OTHER TITLES IN THE SERIES IN
ELECTROMAGNETIC WAVES

Vol. 1 FOCK – Electromagnetic Diffraction and Propagation Problems
Vol. 2 SMITH and MATSUSHITA – Ionospheric Sporadic-*E*
Vol. 3 WAIT – Electromagnetic Waves in Stratified Media
Vol. 4 BECKMANN and SPIZZICHINO – The Scattering of Electromagnetic Waves from Rough Surfaces
Vol. 5 KERKER – Electromagnetic Scattering
Vol. 6 JORDAN – Electromagnetic Theory and Antennas
Vol. 7 GINZBURG – The Propagation of Electromagnetic Waves in Plasmas
Vol. 8 DU CASTEL – Tropospheric Radiowave Propagation beyond the Horizon
Vol. 9 BANOS – Dipole Radiation in the Presence of a Conducting Half-space
Vol. 10 KELLER and FRISCHKNECHT – Electrical Methods in Geophysical Prospecting
Vol. 11 BROWN – Electromagnetic Wave Theory
Vol. 12 CLEMMOW – The Plane Wave Spectrum Representation of Electromagnetic Fields
Vol. 13 KERNS and BEATTY – Basic Theory of Waveguide Junctions and Introductory Microwave Network Analysis
Vol. 14 WATT – VLF Radio Engineering
Vol. 15 GALEJS: Antennas in Inhomogeneous Media

TERRESTRIAL PROPAGATION OF LONG ELECTROMAGNETIC WAVES

BY

JANIS GALEJS
Naval Research Laboratory,
Communication Sciences Division, Washington

PERGAMON PRESS
OXFORD · NEW YORK · TORONTO
SYDNEY · BRAUNSCHWEIG

Umran Inan

Pergamon Press Ltd., Headington Hill Hall, Oxford
Pergamon Press Inc., Maxwell House, Fairview Park, Elmsford, New York 10523
Pergamon of Canada Ltd., 207 Queen's Quay West, Toronto 1
Pergamon Press (Aust.) Pty. Ltd., 19a Boundary Street, Rushcutters Bay, N.S.W. 2011, Australia
Vieweg & Sohn GmbH, Burgplatz 1, Braunschweig

First edition 1972
Library of Congress Catalog Card No. 70–175513

Printed in Hungary
08 016710 1

CONTENTS

ACKNOWLEDGMENTS

THIS monograph reflects to a large extent the author's work at the former Applied Research Laboratory of Sylvania Electronic Systems. The author is particularly indebted to Dr. J. E. Storer, Director of the Laboratory, for his support. This work was also made possible by a long-range interest of the U.S. Navy. Dr. A. Shostak of the Office of Naval Research, Mr. J. Tennyson and Mr. J. Merrill of the Navy Underwater Sound Laboratory, and Mr. J. E. Don Carlos of the Naval Electronics Systems Command have encouraged the investigation of several topics.

Professor K. G. Budden of the University of Cambridge and Dr. J. R. Wait of the Environmental Science Services Administration provided a number of helpful comments. The author did benefit from several discussions with Professor T. R. Madden of Massachusetts Institute of Technology and Dr. E. T. Pierce of Stanford Research Institute. Also acknowledged are comments by Professor K. G. Booker of University of California at San Diego.

ERRATA

Page	*Equation*	*Reads*	*Should Read*
19	(18)	$\pm \frac{k_{zq}}{\omega \epsilon_q}$	$\pm \frac{k_{zq}}{\omega \epsilon_q \epsilon_0}$
19	(19)	$-\frac{k_0 S}{\omega \epsilon_q}$	$-\frac{k_0 S}{\omega \epsilon_q \epsilon_0}$
82	(43)	$\left[\left(\nu + \frac{1}{2}\right)(\pi - \theta) - \frac{4}{\pi}\right]$.	$\left[\left(\nu + \frac{1}{2}\right)(\pi - \theta) - \frac{\pi}{4}\right]$.
106	(164)	$u(t) \pm iv(t) =$ $\sqrt{\pi}\,[Bi(t) \pm iAi(t)]$,	$u(t) \mp iv(t) =$ $\sqrt{\pi}\,[Bi(t) \mp iAi(t)]$,
107	(167)	$[\pm i(x + \pi/4)]$	$\left[\mp i\left(x + \frac{\pi}{4}\right)\right]$

LIST OF PRINCIPAL SYMBOLS

a = radius of the earth = $20000/\pi$ (km)
$[a_n]$ = solution matrix in (92) of Ch. 5
A_e, B_e = amplitudes of T.M. waves
A_h, B_h = amplitudes of T.E. waves
A_{jn} = amplitudes of magneto-ionic modes in (181) to (184) of Ch. 5 or (102) of Ch. 6
$Ai(t)$, $Bi(t)$ = Airy functions in (164) of Ch. 4
B_0 = induction of the geomagnetic field
c = free space velocity of E.M. waves = 3×10^8 m/sec
$[c_n]$ = solution matrix in (102) of Ch. 6
C = received signal due to a median return stroke in Section 3.3.3
$C = \cos\theta = \sqrt{1-S^2}$ = cosine of the wave incidence angle
C_j = normalized radial wave numbers defined by (154) or (179) of Ch. 4
C_k = characteristic function in Section 3.4
$[C_n]$ = column matrix of coefficients defined by (91) or (94) of Ch. 5
$[d_n]$ = matrix product defined by (98) of Ch. 5 or (105) of Ch. 6
$D = a\theta$ = distance along the surface of the earth
$D_a = a(\pi - \theta) = a\delta$ = distance from antipode
D_{ij} = interference distance of modes i and j in (2) of Ch. 8
$\mathcal{D}$ = differential operator defined by (59) of Ch. 4
D_j = down-coming waves in Section 1.5
e_k = charge of a particle
E_j = j-component of electric field
E.W. = east to west
f = frequency in c/s (or Hz)
f_n = resonance frequency
$F(w)$ = attenuation function in (34) of Ch. 9
F_n, F_m = functions defined by (105), (112) of Ch. 4
F_{in}, F_{im} = functions defined by (208), (209), (219) of Ch. 4
$g(i\omega)$, $G(i\omega)$ = power spectrum
$G_q(y)$ or $G_q(z)$ = height-gain function defined in Section 1.5
$G_q^j(y)$ = height-gain function defined by (272) or (275) of Ch. 5
$h(t)$ = impulse response in Section 3.3.3
h = height of the ionospheric boundary
h_u = upper boundary of ionospheric stratifications
he, *hm* (superscripts) = horizontal electric, magnetic

$h_\nu^{(m)}(u)$ = spherical Bessel function defined by (15) of Ch. 4
$h_\nu^e(u)$, $h_\nu^h(u)$ = radial functions of T.M., T.E. modes defined by (31), (40) of Ch. 4
H_j = j-component of the magnetic field
$H_\nu^{(m)}(y)$ or $H_\nu^{(m)}(z)$ = Hankel function of kind m and order ν
i, I = current
I = dip angle in Section 7.3.3
Ids = electric dipole moment (Am)
Im S = imaginary part of S
I_ν^e, I_ν^h = integrals defined by (36) of Ch. 4
i_e = density of electric current (A/m^2)
i_m = density of magnetic current (V/m^2)
$\mathbf{i}_x$ = unit vector in x direction
$J_n(x)$ = Bessel functions of the first kind of order n
J_{se} = electric surface current (A/m)
J_{sm} = magnetic surface current (V/m)
j (superscript or subscript) = e or h
$K_n(z)$ = modified Bessel function of second kind and order n
k = wave number
$k_0 = \omega\sqrt{\mu_0\varepsilon_0}$ = wave number of free space
$k_r = k/k_0$
K = Boltzmann's constant (1.38×10^{-16} erg per °K); radial wave number of the exponential or thin-shell approximations in Sections 4.3 and 5.3; magnetic current (V); a_e/a in Ch. 9
Kds = magnetic dipole moment (V m)
m, M = electron and ion mass
m = index of T.E. modes
M.W. = molecular weight
n = index of T.M. modes
$\mathbf{n}$ = unit vector normal to an interface
$n = \sqrt{\varepsilon}$ = refractive index
N_j = particle density per cm^3
$[p_n]$ = matrix product in (106) of Ch. 6
P = probability
P_j = power flow in the j-direction
$P_n(\cos\theta)$ = Legendre polynomial
$P_\nu^\mu(z)$ = Legendre function of first kind, degree ν, and order μ
q (subscript) = n or m
q_j, q_{sj} = normalized impedance or admittance defined by (176), (188) and (189) of Ch. 4 or following (279) of Ch. 5
q_{ij} = matrix elements in (181) to (184) of Ch. 5 or (109) to (112) of Ch. 6
Q = quality factors defined in Section 7.4.2
r, θ, φ = spherical coordinates
r, φ, z = cylindrical coordinates
$R_e = {}_{\parallel}R_{\parallel}$ = reflection coefficient of T.M. waves
R_g = reflection coefficient of ground surface

$R_h = {}_{\perp}R_{\perp}$ = reflection coefficient of T.E. waves
R_i = reflection coefficient of ionosphere boundary
${}_{\parallel}R_{\perp}$, ${}_{\perp}R_{\parallel}$ = reflection coefficients of Section 6.8.1
Re S = real part of S
$S = \sin\theta = \sqrt{1-C^2}$ = sine of the wave incidence angle
S = propagation parameter; Re $S = c/v_{ph}$, Im $(S) \sim \alpha$
$S' = (a/r)S$
$[S_n(r)]$ = column matrix of tangential field components defined by (90) or (93) of Ch. 5
t = argument of Airy functions defined by (161) of Ch. 4
t_g, t_i = t for $r = a$, $a+h$
T.E. = transverse electric (subscript h)
T.M. = transverse magnetic (subscript e)
T = temperature in degrees (Kelvin)
T = period, time interval or integration time
$u = k_0 r$
$u_g = k_0 a$, $u_i = k_0(a+h)$
$u(t)$, $v(t)$ = Airy functions in (164) of Ch. 4
U_j = upgoing waves in Section 1.5
U_j, V_j = scalar functions in Sections in 7.4.4 and 7.5
$U_n(u)$, $V_n(u)$ = spherical functions defined by (43) of Ch. 7
v = velocity
ve, vm (superscripts) = vertical electric, magnetic
v_{ph} = phase velocity
V = voltage or potential difference
w = Sommerfeld's numerical distance in (37) of Ch. 9
$w(r)$, $W(r)$ = probability densities
$w_{1,2}(t)$ = Airy functions in (162) to (164) of Ch. 4
$W(u, v)$ = Wronskian defined by (151) of Ch. 4
W.E. = west to east
y, y_r = height of the observation point above the ground surface in a cylindrical shell
y_s = height of the source above the ground surface in a cylindrical shell
Y = admittance
z, z_r = height of the observation point above the ground surface in a spherical shell
z_s = height of the source above the ground surface in a spherical shell
Z = pressure in atmospheres in Section 2.2.2
Z_e, Z_h = surface impedance of T.M., T.E. modes at the ionospheric boundary
Z_{eh} = coupling impedance in (284), (217), and (218) of Ch. 5
Z_g = surface impedance of ground
$Z_\nu^e(u)$, $Z_\nu^h(u)$ = cylinder functions defined by (29) and (47) of Ch. 5
α = attenuation rate in db/1000 km
$\Gamma(x)$ = gamma function
Δ_j = normalized impedance $(Z_j/\sqrt{\mu_0/\varepsilon_0})$.
$\Delta_q(y)$ or $\Delta_q(z)$ = normalized height-dependent impedance defined in Section 1.5
$\Delta_q^j(y)$ = normalized height-dependent impedance defined by (273) or (276) of Ch. 5

$\delta = \pi - \theta$
$\delta(x)$ = delta function
ε = complex relative permittivity
ε_i = elements of permittivity tensor in Section 2.2.3
$\varepsilon_0 = (1/36\pi)\times 10^{-9}$ = permittivity of free space
ε_r = real relative permittivity
A_q = excitation factor defined by (91) or (94) of Ch. 4
A_q^I = excitation factor defined by (274) or (277) of Ch. 5
$\lambda = 2\pi/k_0$ = free space wavelength
$\mu_0 = 4\pi\times 10^{-7}$ = permeability of free space
$\nu = k_0 a\, S$ (in cyl. coord.); $k_0 a\, S - 0.5$ (in spher. coord.)
ν_{jk} = collision frequency between particles j and k
σ = conductivity (mho/m)
τ = time constant
φ = phase
ω = angular frequency
ω_c = cyclotron or gyro frequency
ω_p = plasma frequency
ω_i = conductivity parameter in Section 2.2.3
$e^{-i\omega t}$ = implied harmonic time dependence

CHAPTER 1

INTRODUCTION

1.1 Scope and Limitations of the Treatment

The energy of propagating radio waves is confined principally to the shell between the earth and the ionosphere, and this space is frequently denoted as the terrestrial waveguide. For long waves the height of this guide becomes comparable to a wavelength, and characteristics of wave propagation are determined jointly by the properties of the two guide boundaries. There are a number of propagating modes with distinct cutoff frequencies similar to those present in microwave problems. But unlike the highly conducting guides of the microwave range, the upper boundary of the terrestrial guide is diffuse and a poor conductor; the finite conductivity of the ground surface may be also important. The frequency range to be discussed encompasses the extremely-low-frequencies (E.L.F.) from 6 to 3000 c/s, the very-low-frequency (V.L.F.) range from 3 to 30 kc/s, and a brief mention will be made also of low frequencies (L.F.) in the range from 30 to 300 kc/s. The effective waveguide height h is less than the free-space wavelength λ in the E.L.F. range, and only one waveguide mode propagates. For V.L.F. h exceeds λ, and there are several propagating modes. In the L.F. range the number of significant propagating modes may exceed 10.

Wave propagation in this frequency range has been discussed also in several published text and review papers. Sommerfeld [1949] and Bremmer [1949] treat dipole radiation above a plane or curved finitely conducting earth; Bremmer [1949] develops ionospheric reflection characteristics which are used in solutions of geometric optics. Waves in a planar waveguide are treated exhaustively in the monograph by Budden [1961b]. Wait [1962] emphasizes wave propagation in a sharply bounded waveguide; several approximations are developed for curved waveguides in the V.L.F. range; E.L.F. propagation and the earth-to-ionosphere cavity resonances [Schumann, 1952a, b] are also treated. E.L.F. propagation and earth-to-ionosphere cavity resonances are analyzed in more detail by Galejs [1964a] and Madden and Thompson [1965]. In a monograph on long-wave propagation, Volland [1968] develops reflection characteristics and propagation parameters for a flat waveguide, but the curved waveguide is analyzed using ray theory.

The magneto-ionic theory of waves in a generally anisotropic ionosphere and the detailed reflection properties have been discussed by Ratcliffe [1959], Budden [1961a], or Ginzburg [1964]. Watt [1967] and Wait [1968] treat a weakly anisotropic ionosphere. For more general conditions [Baybulatov and Krasnushkin, 1967; Galejs, 1967, 1968, and 1969; Pappert, 1968; Snyder and Pappert, 1969] the effective phase velocity and attenuation rates change for dif-

ferent directions of propagation, and there is a coupling between vertically and horizontally polarized waves.

In this text, wave propagation will be characterized almost exclusively by mode theory. After developing the fundamental concepts of wave propagation in a planar and curved isotropic waveguide, a number of examples will illustrate the effects of an anisotropic ionosphere. The mathematics are developed only for sources at the ground surface or within the waveguide. This includes artificial sources as well as lightning discharges. Emissions generated at ionospheric or higher altitudes by incident extraterrestrial particles and whistlers guided in ionized columns along the geomagnetic field lines [Helliwell, 1965] can be classified as separate topics and will not be treated. The discussion is limited to steady-state solutions in a waveguide that is uniform in the direction of propagation; problems of mode conversion caused by changing boundary properties [Wait, 1968] are not considered.

The remaining part of this chapter summarizes the basic equations and treats plane-wave reflection from a dielectric interface. A planar waveguide is analyzed using a superposition of two obliquely incident plane waves. The properties of waveguide boundaries are implicitly represented by Fresnel reflection coefficients. The propagation parameters of waveguide modes, the field expressions and concepts of height-gain functions and height-dependent impedances are then developed.

Chapter 2 discusses boundaries of the terrestrial guide. The ground surface is frequently approximated as a homogeneous isotropic conductor, but the detailed ground structure is important in studies of horizontal field components. Stratifications cause an effective anisotropy: the conductivity parallel to the interface will differ from the conductivity perpendicular to the interface. The properties of the lower ionosphere are emphasized in the survey of ionosphere characteristics, but some data of the *E*- and *F*-layers are also included. Components of the ionospheric permittivity or conductivity tensor are calculated from the magneto-ionic theory.

Lightning discharges are regarded as a natural source of E.L.F. and V.L.F. radiation in Chapter 3. Apart from return strokes, the more frequent lower amplitude *K*-changes also contribute significantly to the radiated energy. The received noise is the result from integrating several atmospherics during the response time of the receiver. The amplitude distribution of the observed radio noise can be related to the statistics of the lightning discharges by considering return strokes from several thunderstorm centers or by return strokes from a single center in the presence of the more frequent *K*-changes.

The mode theory for waves in an isotropic spherical shell is developed in Chapter 4. The vertically and horizontally polarized modes excited by various dipole sources are characterized by wave numbers, excitation factors, height-gain functions, and height-dependent normalized impedances. An exponential approximation of the radial functions can be interpreted as a modification of the planar solution. These approximations are less accurate than Airy function representations for frequencies in the V.L.F. range. Nonpropagating waveguide modes must be included in the mode summation near the source. Also, antipodal standing wave patterns are illustrated in several examples.

The terrestrial waveguide is closely represented in a spherical geometry, but a cylindrical geometry may be required for the analysis of curved anisotropic waveguide boundaries following Chapter 5. In the Airy function approximation the radial functions are the same in spherical

and cylindrical shells; for a given set of boundary characteristics the parameters of V.L.F. wave propagation are the same in both geometries. The exponential approximation of radial functions is of limited accuracy for waveguide height $h > \lambda$, but it becomes highly accurate in thin shells. A convergent solution of propagation parameters is obtained by subdividing the airspace in a large number of shells; the Airy function solution exhibits an accuracy comparable to an approximately 1 km uncertainty of waveguide height in the V.L.F. range. Equations are developed for determining parameters of transverse electric (T.E.) and magnetic (T.M.) modes, that are coupled by an anisotropic ionosphere.

Waves in stratified and/or anisotropic media can be analyzed by the methods reviewed in Chapter 6. The differential equations for a continuously varying medium can be solved only for several specialized profiles of ionospheric conductivity. In a more general approach the medium is approximated by a series of homogeneous slabs; exponential functions are exact solutions for planar slabs, and modified exponential solutions (or thin-shell approximations) are applicable to curved isotropic or anisotropic shells. The four field components tangential to the shell boundaries are described in a matrix notation. Each field component consists of parts which may exhibit four different radial wave numbers corresponding to the distinct roots of Booker's quartic. This approach requires a multiplication and inversion of a series of 4×4 matrices, and the problem of numerical swamping may arise at higher frequencies if waves are followed deeply in the ionosphere.

Anisotropic ground, which is characterized by different conductivities for different horizontal directions, may be treated by similar methods; such a ground affects the pattern symmetry of horizontally oriented antennas.

E.L.F. propagation parameters are calculated for several ionosphere models in Chapter 7. The simplest sharply bounded homogeneous and isotropic models do not account for the experimentally observed frequency dependence of phase velocity and attenuation rates. Exponential models of daytime electron concentration are more successful, but the corresponding nighttime models exhibit very low attenuation rates. A radial geomagnetic field and the presence of low altitude ions increase the nighttime attenuation rates significantly, but more moderate propagation parameters are obtained by considering *F*-layer reflections and the presence of a residual nighttime *E*-layer.

The Schumann resonances can be adequately treated by assuming a uniform earth-to-ionosphere cavity. Such calculations account for observed resonance frequencies, *Q*-factors, power spectra, diurnal power, and frequency variations. The frequency variations appear to be caused by different amounts of energy spillover from adjacent resonances for various distances between the effective sources and the receiver. The differences between day and night hemispheres cause only a small amount of mode splitting and coupling between T.E. and T.M. modes for realistic ionospheric parameters.

The developments of Chapter 8 emphasize V.L.F. propagation characteristics for anisotropic ionosphere models. Some propagation data can be explained even with the lower accuracy Debye approximations of the radial wave function [Wait, 1957]; more accurate are the Airy function solutions in conjunction with homogeneous [Wait, 1962] or exponentially tapered ionosphere [Galejs, 1964b; Wait and Spies, 1965]; models with a purely horizontal transverse geomagnetic field [Galejs, 1967] do not account for the observed direction dependence of phase velocity [Crombie, 1966]. A finite dip angle of the geomagnetic field is necessary for explaining

such observations. The clear distinction between T.M. and T.E. modes is lost in the presence of anisotropic ionosphere. A vertically polarized source excites also T.M. field components with wave numbers corresponding to T.E. modes, and a horizontally polarized source excites T.E. fields corresponding to T.M. modes, particularly for the higher frequencies at nighttime and for westward propagation. Among the field components tangential to the ground surface T.M. fields tend to dominate, with the exception of T.E. modes at daytime and for lower frequencies at night.

The discussion of E.L.F. and V.L.F. waves was concerned with the composite waveguide fields without including a geometric optics breakdown in ground waves and sky waves that reach the receiver after reflections from the guide boundaries. The period of L.F. waves is less than the time delay between the ground waves and sky waves, and the ground wave represents the initial cycles of the received signal in pulsed transmissions [Johler, 1962]. For a uniform, spherical earth the ground wave is expressed as a residue or mode series in Chapter 9. The individual terms of this series exhibit a phase velocity v_{ph} that is less than the free-space velocity of electromagnetic waves c, and the attenuation rate increases rapidly with an increasing mode number; the mode sum is monotonically decreased with increased distance from the source. The composite L.F. fields observed in the spherical shell between the earth and the ionosphere are also represented by a mode sum. The lower order terms of $v_{ph} < c$ appear earth-detached and are weakly excited, and the higher order terms of $v_{ph} > c$ are attenuated; terms of $v_{ph} \approx c$ dominate in the mode summation, which exhibits irregular distance variations.

1.2 Basic Equations

For harmonically time varying fields with an implied $\exp(-i\omega t)$ time variations, the electric and magnetic fields of a source-free region are related by

$$\nabla\times\mathbf{E} = i\omega\mu_0\mathbf{H}, \tag{1}$$

$$\nabla\times\mathbf{H} = -(i\omega\varepsilon_0\varepsilon_r - \sigma)\,\mathbf{E}. \tag{2}$$

In rationalized M.K.S. units E, H, μ_0, ε_0, and σ are given in volts/meter, amperes/meter, henries/meter (or V s/A m), farads/meter (or A s/V m) and mho/meter (or A/V m) respectively. The relative permittivity ε_r is dimensionless. For free space the permeability is given by $\mu_0 = 4\pi\times10^{-7}$ and the permittivity by $\varepsilon_0 = (1/36\pi)\times10^{-9}$. The real parameters ε_0, ε_r, and σ may be combined in a complex relative permittivity

$$\varepsilon = \varepsilon_r(1 + i\tan\delta), \tag{3}$$

where the loss tangent $\tan\delta = \sigma/(\omega\varepsilon_0\varepsilon_r)$. The permittivity ε is a scalar for isotropic media; for anisotropic media the tensor character of the permittivity is discussed in Chapter 2.

The solutions must satisfy the following boundary conditions in the interface of two source-free regions:

$$\mathbf{n}\times(\mathbf{E}_2 - \mathbf{E}_1) = 0, \tag{4}$$

$$\mathbf{n}\cdot(\varepsilon_2\mathbf{E}_2 - \varepsilon_1\mathbf{E}_1) = 0, \tag{5}$$

$$\mathbf{n}\cdot(\mu_2\mathbf{H}_2 - \mu_1\mathbf{H}_1) = 0, \tag{6}$$

$$\mathbf{n}\times(\mathbf{H}_2 - \mathbf{H}_1) = \mathbf{J}_{se}, \tag{7}$$

where the unit vector $\mathbf{n}$ is normal to the interface and points from region 1 into region 2, and where $\mathbf{J}_{se}$ is the electric surface current in amperes/meter. For a perfectly conducting surface

$$\mathbf{n}\times\mathbf{E}_2 = 0, \tag{8}$$

$$\mathbf{n}\cdot(\mu_2\mathbf{H}_2) = 0, \tag{9}$$

$$\mathbf{n}\times\mathbf{H}_2 = \mathbf{J}_{se}. \tag{10}$$

By analogy with (10), a magnetic surface current $\mathbf{J}_{sm}$ is defined by

$$\mathbf{J}_{sm} = \mathbf{n}\times\mathbf{E}_2, \tag{11}$$

which is assumed to flow on a perfectly conducting surface. The electric fields of an aperture $\mathbf{E}$ are replaced by an equivalent magnetic surface current $\mathbf{J}_{sm}$ that flows on the surface of a conducting plane.

In the formulation of a given boundary value problem it is possible to confine the source currents (7) or (11) to interfaces between two regions. The equivalent dipole moments of sources are defined as **Ids** and **Kds**, where ds designates the length of the current element in meters, I is the electric current in amperes, and K is the magnetic current in volts. The electric and magnetic currents I and K may be computed by integrating the corresponding surface current densities J_{sj} in the direction transverse to the current flow as $\int J_{sj}\,dw$.

The magnetic dipole moment **Kds** of a volume (or surface) distribution of electric current $\mathbf{i}_e$ (or $\mathbf{J}_{se}$) is computed by the integration

$$\mathbf{Kds} = -\frac{i\omega\mu_0}{2}\iiint \mathbf{r}\times\mathbf{i}_e\,dv = -\frac{i\omega\mu_0}{2}\iint \mathbf{r}\times\mathbf{J}_{se}\,da, \tag{12}$$

where $\mathbf{r}$ is the radius vector from a selected point to the current element, dv indicates a volume element, and da indicates an area element. For a small loop of radius r_0 and current I_0,

$$\mathbf{Kds} = -i\omega\mu_0\pi r_0^2 I_0\mathbf{i}_z = -i\omega\mu_0 I_0\mathbf{da}, \tag{13}$$

where $\mathbf{da} = \pi r_0^2\mathbf{i}_z$ is in the direction of loop axis and $\mathbf{i}_z$ is a unit vector in the z-direction.

For a slot in a conducting plane

$$\mathbf{Kds} = \iint \mathbf{J}_{sm}\,da = \iint \mathbf{E}\times\mathbf{da}, \tag{14}$$

where the tangential electric field of the aperture $\mathbf{E}\times\mathbf{n} = \mathbf{J}_{sm}$ is integrated over the area of the slot.

By analogy with (12), the equivalent electric dipole moment **Ids** of a volume (or surface) distribution of magnetic current is determined by

$$\mathbf{Ids} = \frac{i\omega\varepsilon_0}{2}\iiint \mathbf{r}\times\mathbf{i}_m\,dv = \frac{i\omega\varepsilon_0}{2}\iint \mathbf{r}\times\mathbf{J}_{sm}\,da. \tag{15}$$

A small annulus of radius r_0 with a voltage $V = -E_r\,dr$ across it is equivalent to a magnetic current K flowing around a loop of area $da = \pi r_0^2$. Equations (11) and (15) show that

$$\mathbf{Ids} = -\omega\varepsilon_0\pi r_0^2 V\mathbf{i}_z = -i\omega\varepsilon_0 K\mathbf{da}, \tag{16}$$

where **da** and $\mathbf{i}_z$ are in the direction of loop axis.

Loops of electric and magnetic currents are therefore equivalent to magnetic and electric dipoles oriented along the loop axis with dipole moments that increase linearly with frequency in (13) and (16).

The characteristic impedance of free space is denoted as

$$\eta = \sqrt{\mu_0/\varepsilon_0} = 120\pi \text{ (ohms)}. \tag{17}$$

The wave number in free space is

$$k_0 = \omega\sqrt{\mu_0\varepsilon_0} = \omega/c, \tag{18}$$

where $c = 3\times10^8$ m/sec is the free-space velocity of electromagnetic waves. In media characterized by real or complex relative permittivity $\varepsilon \neq 1$ the wave number is

$$k = k_0\sqrt{\varepsilon} = k_0 n, \tag{19}$$

where $n = \sqrt{\varepsilon}$ is the refractive index of the medium.

1.3 Plane Waves

For plane waves the field variations are confined to a single direction without geometric spreading or focusing effects. The basic properties of such waves will be surveyed in this section, but a more detailed discussion can be found in the books of Budden [1961a, b].

A wave is assumed to propagate in a medium of relative permittivity ε at an angle θ with respect to the vertical z direction without any variations along the transverse y direction. The various field components ($j = x, y, z$) will exhibit x and z variations of the form

$$F_j = F_j^0 \exp\left[-i\omega t + ik\,(x\sin\theta + z\cos\theta)\right], \tag{20}$$

where $F_j = E_j$ or H_j. Constant phase surfaces of (20) are characterized by constant values of

$$\varphi = -\omega t + \operatorname{Re} k(x\sin\theta + z\cos\theta) = -\omega t + \operatorname{Re} kr. \tag{21}$$

where $r = (x^2+z^2)^{0.5}$, $x = r\sin\theta$, $z = r\cos\theta$. The phase velocity in the x or θ direction is computed by applying $\partial\varphi/\partial t = 0$. The first part of (21) shows that

$$v_{\text{ph}} = \frac{dx}{dt} = \frac{\omega}{\operatorname{Re} k\sin\theta} = \frac{c}{\operatorname{Re} n\sin\theta} \tag{22}$$

if $dz/dt = 0$. The second part of (21) results in

$$v_{\text{ph}} = \frac{dr}{dt} = \frac{\omega}{\operatorname{Re} k} = \frac{c}{\operatorname{Re} n}, \tag{23}$$

For $\sin\theta \ll 1$, v_{ph} along the x-axis will exceed v_{ph} along the r direction.

In an isotropic medium (1) and (2) are satisfied by two possible sets of F_j. One solution contains the field components E_x, E_z, and H_y; the single component of the magnetic field is transverse to the direction of propagation, and this solution is labeled as a transverse magnetic (T.M.) or E wave. In this wave the amplitudes E_x^0 and E_z^0 are related to H_y^0 by

$$E_x^0 = \eta\cos\theta H_y^0/n; \quad E_z^0 = -\eta\sin\theta H_y^0/n. \tag{24}$$

The other solution contains field components E_y, H_x, and H_z; the single electric field component is transverse to the direction of propagation and this solution is labeled as a transverse electric (T.E.) or H wave. In this wave the amplitudes H_x^0 and H_z^0 are related to E_y^0 by

$$H_x^0 = -n\cos\theta E_y^0/\eta; \quad H_z^0 = n\sin\theta E_y^0/\eta. \tag{25}$$

The ratio between x and z components is computed from (24) and (25) as

$$\frac{E_x^0}{E_z^0} = \frac{H_x^0}{H_z^0} = -\cot\theta. \tag{26}$$

It depends only on the angle θ. The x components vanish for propagation along the x-axis ($\theta = 0$), and the z component is equal to zero for propagation along the z-axis ($\theta = 90°$).

Field components (20) satisfy (1) and (2) also for complex angles θ. Such waves are designated as inhomogeneous plane waves and the field component F_j will change in magnitude during the progression of the wave even for real values k.

1.4 Reflection of Plane Waves

A plane surface is assumed to separate the free space of $z \leqslant h$ from a medium of relative permittivity ε_j for $z \geqslant h$. A plane wave F_i of the form (20) is incident on this boundary at an angle θ measured from the z directed normal to this surface. The reflected wave F_r propagates at the same angle θ away from the interface. After omitting the time factors, these field components are characterized by

$$F_i = F_i^0 \exp\{ik_0(x\sin\theta + z\cos\theta)\}, \tag{27}$$

$$F_r = F_r^0 \exp\{ik_0[x\sin\theta + (2h-z)\cos\theta]\}. \tag{28}$$

After satisfying the boundary conditions (4) to (7) at the interface $z = h$, the ratio of the field components or the reflection coefficient $R = F_r/F_i\Big|_{z=h}$ may be computed following Stratton [1941] as

$$R_e = \frac{n_j^2\cos\theta - \sqrt{n_j^2 - \sin^2\theta}}{n_j^2\cos\theta + \sqrt{n_j^2 - \sin^2\theta}} \tag{29}$$

and

$$R_h = \frac{\cos\theta - \sqrt{n_j^2 - \sin^2\theta}}{\cos\theta + \sqrt{n_j^2 - \sin^2\theta}} \tag{30}$$

for the T.M. and T.E. (or E and H) waves respectively. For T.M. waves the electric vector $\mathbf{E} = \mathbf{i}_x E_x + \mathbf{i}_z E_z$ is parallel to the plane of incidence, which denotes the plane through the direction of the incident wave and the normal to the boundary. The electric field vector remains also parallel to this plane after the reflection, and the reflection coefficient R_e is frequently denoted as ${}_{\|}R_{\|}$. This reflection coefficient applies to waves of essentially vertical polarization. For T.E. waves the electric vector $\mathbf{E} = \mathbf{i}_y E_y$ is normal to the plane of incidence, it remains normal after the reflection, and R_h is denoted also as ${}_{\perp}R_{\perp}$. This reflection coefficient applies to waves of horizontal polarization. After reflection from an anisotropic boundary, the change

of polarization is characterized by further reflection coefficients ${}_{\parallel}R_{\perp}$ and ${}_{\perp}R_{\parallel}$ that are derived in Section 6.8.1.

For a nearly grazing incidence of $\theta \to 90°$, $R_{e,h} \to (-1)$. With a highly conducting medium of $|n_j| \gg 1$, $R_e \to 1$ and $R_h \to (-1)$. These limiting forms suggest a sudden transition of R_e from 1 to (-1) as $\theta \to 90°$ for $|n_j| \gg 1$. An apparent refractive index of $|n_j| \ll 1$ may characterize waves incident on a less dense medium, when $R_e \to -1$ and $R_h \to \exp(-2i\theta)$. In this limit there are no sudden changes of R_e or R_h as $\theta \to 90°$ for near grazing incidence.

The reflection coefficients (29) and (30) can also be expressed by using the normalized surface impedance Δ_j which is related for a homogeneous isotropic medium to the refractive index n_j by

$$n_j = \sqrt{\varepsilon_j} = \frac{\eta}{Z_j} = \frac{1}{\Delta_j}. \tag{31}$$

For an inhomogeneous medium Δ_j is computed from a solution of the appropriate boundary-value problem and it will not be related to the local value of n_j by (31). Letting $C = \cos\theta$ and $S = \sin\theta$, R_e and R_h are approximated for $|n_j^2| \gg 1$ or S^2 by

$$R_e \approx \frac{C - 1/n_j}{C + 1/n_j} = \frac{C - \Delta_{je}}{C + \Delta_{je}} \tag{32}$$

and

$$R_h \approx \frac{C - n_j}{C + n_j} = \frac{C - 1/\Delta_{jh}}{C + 1/\Delta_{jh}}, \tag{33}$$

where the normalized impedances Δ denoted by subscripts e and h may differ for T.M. and T.E. waves.

The magnitude and phase angle of reflection coefficients (29) and (30) are illustrated in Fig. 1.1 for boundary surfaces characterized by constant values of ε_r and σ. A poorly conducting ionospheric boundary of $\varepsilon_r = 1$ and $\sigma = 10^{-6}$ mho/m is represented by the curves A; ground of low conductivity ($\sigma = 10^{-3}$ mho/m), and high conductivity ($\sigma = 1$ mho/m) is represented by the curves B and C respectively. An increasing conductivity σ and/or a decreasing frequency increase the magnitude of reflection coefficients. $|R_h| > |R_e|$ for a given set of boundary parameters. The thin-lined curves indicate a decreasing incidence angle θ; for $\sin\theta = 0.95$, R_e is increased in magnitude, but R_h is decreased relative to the thick-lined curves for $\sin\theta = 0.98$. The phase angle of R_e is near zero for the lower frequencies and for the higher conductivity values. However, for $\sigma = 10^{-6}$ mho/m, R_e is almost real and positive for f near 10 c/s, and real and negative for $f > 10$ kc/s, with a local minimum of the magnitude at frequencies where $\varphi \approx 90°$. The reflection coefficient R_e may be positive or negative for the same boundary at different frequencies. The phase angle of R_h is near $(-180°)$, and R_h may be approximated by a negative real number.

1.5 Planar Waveguide

Aside from texts of low-frequency wave propagation [Budden, 1961b; Wait, 1962; Volland, 1968], parallel plate waveguides have been discussed also in connection with microwave problems [Marcuvitz, 1951]; in distinction from the latter metallic waveguides, the terrestrial guide is characterized by a relatively poor conductivity of its boundaries that may exhibit also

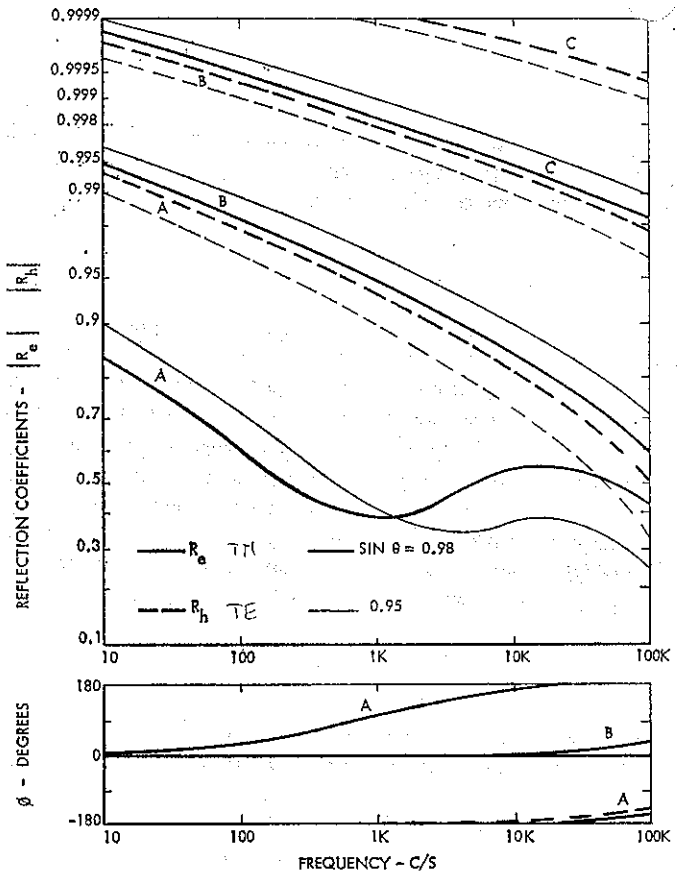

FIG. 1.1 Plane Wave Reflection Coefficients
(A) $\varepsilon_r = 1$, $\sigma = 10^{-6}$; (B) $\varepsilon_r = 10$, $\sigma = 10^{-3}$; (C) $\varepsilon_r = 10$, $\sigma = 1$

some anisotropy. For a given operating frequency the guided waves will exhibit a discrete number of wave numbers k_n (or wavelengths $\lambda_n = 2\pi/\mathrm{Re}\ k_n$). Some of the basic waveguide properties will be illustrated by representing the guided waves as a series of upgoing and downcoming plane waves of the type described by (27) and (28).

1.5.1 *Modal Equation*

In a waveguide of height h shown in Fig. 1.2 the upper boundary is characterized by a reflection coefficient R_t and the lower boundary by R_g, where either (29) or (32) apply for T.M. waves and (30) or (33) apply for T.E. waves. The wave front traverses the height of the guide in a distance $\Delta x = h \tan\theta$. The same plane-wave representation (27) should apply to the

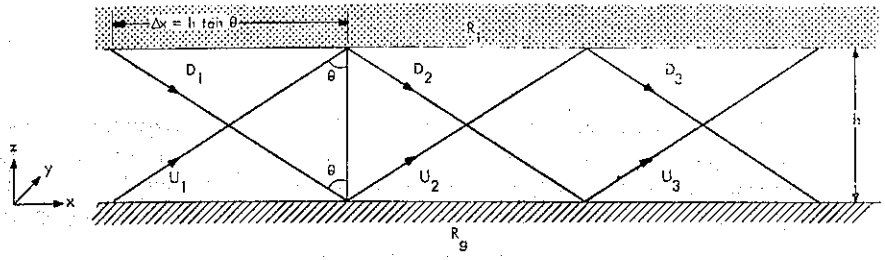

FIG. 1.2 Geometry of the Waveguide

portion of up-going waves U_1, U_2, and U_3; (28) should apply to the down-coming waves D_1, D_2, and D_3, where subscripts 1, 2, and 3 denote the two plane waves at the coordinates x, $x+\Delta x$, and $x+2\,\Delta x$. For z = constant, the waves should satisfy the relation

$$\frac{U_2}{U_1} = \frac{U_3}{U_2} = \frac{D_2}{D_1} = \frac{D_3}{D_2} = \exp(ik_0\,\Delta x \sin\theta). \tag{34}$$

The field components U_1, D_2, and U_3 or D_1, U_2, and U_3 are interrelated by the reflection coefficients R_i and R_g as

$$U_1 = U_1^0 \exp\{ik_0(x_1 \sin\theta + z\cos\theta)\}, \tag{35}$$

$$D_2 = U_1^0 R_i \exp\{ik_0[(x_1+\Delta x)\sin\theta + (h+z')\cos\theta]\}, \tag{36}$$

$$U_3 = U_1^0 R_i R_g \exp\{ik_0[(x_1+2\,\Delta x)\sin\theta + (2h+z)\cos\theta]\}, \tag{37}$$

and

$$D_1 = D_1^0 \exp\{ik_0(x_i \sin\theta + z'\cos\theta)\}, \tag{38}$$

$$U_2 = D_1^0 R_g \exp\{ik_0[(x_1+\Delta x)\sin\theta + (h+z)\cos\theta]\}, \tag{39}$$

$$D_3 = D_1^0 R_i R_g \exp\{ik_0[(x_1+2\,\Delta x)\sin\theta + (2h+z')\cos\theta]\}, \tag{40}$$

where $z' = h - z$. It can be seen that for $\Delta x = 0$, $R_i = D_2/U_1 = D_3/U_2$ at $z = h$, and $R_g = U_3/D_2 = U_2/D$, at $z = 0$, which agrees with the definition of reflection coefficients. The ratios U_3/U_1 and D_3/D_1 computed from (37) and (35) or (40) and (38) are the same as in (34) if

$$R_i R_g \exp(2ik_0\, h\cos\theta) = 1. \tag{41}$$

R_i and R_g are functions of θ, and there will be a discrete set of $\theta = \theta_q$ values that satisfy (41). This equation has been also labeled as the fundamental equation of mode theory [Budden, 1961b].

Applying (32), or (33), (41) is expressed as

$$\frac{C_n - \Delta_e}{C_n + \Delta_e}\,\frac{C_n - \Delta_g}{C_n + \Delta_g} \exp(2ik_0 h C_n) = 1 \tag{42}$$

for T.M. modes and as

$$\frac{C_m \Delta_h - 1}{C_m \Delta_h + 1}\,\frac{C_m \Delta_g - 1}{C_m \Delta_g + 1} \exp(2ik_0 h C_m) = 1 \tag{43}$$

for T.E. modes, where $C_q = \cos\theta_q$, $S_q = \sqrt{1-C_q^2} = \sin\theta_q$. The index $q = n$ (or m) designates

T.M. (or T.E.) modes. The normalized ground impedance Δ_g remains the same for both mode types, and Δ_e and Δ_h denote the normalized ionospheric surface impedance for the T.M. and T.E. modes respectively. In the limit of a flat earth of infinite radius a, (42), and (43) compare with (83) and (89) of Chapter 4 where $K/k_0 \to C$.

Waves of the guide have been represented as a superposition of two obliquely propagating plane waves, both of which are characterized by the same incidence angle θ_q or C_q and S_q values. For such plane waves the phase velocity along the x-axis was given by (22). In free space the refractive index $n = 1$ and

$$S_q = \sin\theta_q = c/v_{\text{ph}}\Big|_q, \tag{44}$$

where S_q is real. For complex angles θ_q, the x variation of the field component (35) to (37) or (38) to (40) is characterized by $\exp(ik_0 x S_q)$; the phase angle is proportional to

$$\text{Re}\, S_q = c/v_{\text{ph}}\Big|_q \tag{45}$$

and the magnitude is decreased as $\exp(-\text{Im}\, S_q k_0 x)$. The attenuation rate in decibels per 1000 km is therefore expressed as

$$\alpha_q = 20(\log_{10} e)\omega\ \text{Im}\, S_q/300$$

$$\approx 0.02895\omega\ \text{Im}\, S_q. \tag{46}$$

For perfectly conducting waveguide walls of refractive index $|n_j| \to \infty$, $R_e \to 1$ for T.M. modes and $R_h \to (-1)$ for T.E. modes. In either case (41) simplifies to

$$C_q = \cos\theta_q = \frac{q\pi}{k_0 h}, \tag{47}$$

where the integer $q \geqslant 0$. The $q = 0$ mode is characterized by $C_q = 0$, $S_q = 1$ and $v_{\text{ph}} = c$. In this mode there are no field variations in the vertical direction [$G_q(z)$ of (55) is equal to unity]; the boundary conditions (8) and (9) can be satisfied with nonvanishing field components only in the T.M. $n = 0$ mode, that may be also designated as the T.E.M. mode. There are no T.E. $m = 0$ modes, which is pointed out also by Budden [1961b] and in Section 4.3.1. The modes of $q \neq 0$ will have cutoff frequencies $f = f_{cq}$, where $C_q = 1$, $S_q = 0$ and $v_{\text{ph}} = \infty$ following (44). For lower frequencies $f < f_{cq}$, k_0 becomes smaller in magnitude, $C_q > 1$ and $S_q = \sqrt{1-C_q^2}$ is purely imaginary. This wave is severely attenuated and exhibits $v_{\text{ph}} = \infty$ following (45).

For a perfectly conducting lower boundary ($|n_g| \gg 1$) and reflecting upper boundary ($|n_i| \ll 1$), $R_i \to (-1)$ and $R_g \to 1$ for T.M. waves. Equation (41) is reduced to

$$C_n = \cos\theta_n = \frac{(2n-1)\pi}{2k_0 h}, \tag{48}$$

where n is restricted to positive integers. This latter approximation may be used to idealize the propagation of lower order T.M. V.L.F. modes following Section 4.3.1, but the approximation (47) remains applicable to T.E. and higher order T.M. modes.

For real values of θ_q, $C_q < 1$, $S_q = \sqrt{1-C_q^2} < 1$ and $v_{ph} > c$ following (44). For V.L.F. modes of $q > 0$, $S_q > 1$ or $v_{ph} < c$ is possible only in curved geometries, which are discussed in Chapters 4 and 5.

For finite complex values of the refractive index n_g the solutions of (41) will be illustrated only for the T.M. $n = 0$ mode in the E.L.F. range, when $k_0 h < 1$, $|n_g| \to \infty$ and $|n_i| \gg 1$. This implies that $R_g \to 1$ and $R_i \approx 1$. For modes of $|k_0 h C_0| \ll 1$, (41) is approximated as

$$R_i(1+2ik_0hC_0) = 1 \tag{49}$$

which can be reduced applying (32) to

$$C_0 = \frac{1-R_i}{2ik_0h} \approx \frac{1-R_i}{1+R_i}\,\frac{1}{ik_0h} = \frac{\Delta_e}{C_0 ik_0h}. \tag{50}$$

Hence

$$S_0 = \sqrt{1-C_0^2} = \sqrt{1-\frac{\Delta_e}{ik_0h}}, \tag{51}$$

which compares in the limit of a flat earth of infinite radius a with (87) of Chapter 4. Although $R_i \to 1$ for frequencies in the E.L.F. range, the complex cosine C_0 is proportional to $(1-R_i)$ and inversely proportional to $k_0h \ll 1$; C_0 is not necessarily small in magnitude. It is seen that $\operatorname{Im} C_0 < 0$, $\operatorname{Re} S_0 > 1$ and $v_{ph} < c$.

1.5.2 *Field Components*

It follows from (34) that $U_2/U_1 = D_2/D_1$. Substituting (35), (36), (38), and (39) and applying (41), one obtains $D_1^0/U_1^0 = 1/[R_g \exp(ikhC)]$. For a given mode of index q the net fields in the guide can be computed from (35) and (38) as

$$F = U_1 + D_1 = U_1^0 \exp(ik_0xS_q)\left[\exp(ik_0zC_q) + \frac{1}{R_g}\exp(-k_0zC_q)\right]. \tag{52}$$

The fields (52) are expressed alternately as

$$F = F_0 G_q(z) \exp(ik_0xS_q), \tag{53}$$

where

$$F_0 = U_1^0(1+1/R_g) \tag{54}$$

and

$$G_q(z) = \frac{R_g \exp(ik_0zC_q) + \exp(-ik_0zC_q)}{R_g+1} = \cos k_0zC_q - i\sin k_0zC_q\,\frac{1-R_g}{1+R_g}. \tag{55}$$

The function $G_q(z)$ characterizes altitude variations of the fields starting with $G_q(0) = 1$. It is denoted as a height-gain function.

It follows from (32) that $(1-R_g)/(1+R_g) = \Delta_g/C_n$ for the T.M. (or n) modes, and (55) becomes identical to (93) of Chapter 4 in the limit of a flat earth. For highly conducting ground surface of $\Delta_g \to 0$, $R_g \to 1$ and (55) is reduced to

$$G_n(z) = \cos k_0zC_n. \tag{56}$$

For nonabsorbing boundaries either (47) or (48) may be substituted for C_n and the argument (k_0zC_n) of (56) is real.

For the T.E. (or m) modes, (33) shows that $(1-R_g)/(1+R_g) = 1/(C_m\Delta_g)$ and (55) is the same as (99) of Chapter 4 for a flat earth of infinite radius a. For T.E. modes $\Delta_g \to 0$ is associated with $R_g \to (-1)$, and $G_m(z)$ may be large in magnitude at altitudes where the sine term of (55) dominates.

F of (52) or (53) is assumed to represent the field component H_y of T.M. modes. The other field components are computed applying (2) as

$$E_x = \frac{1}{i\omega\varepsilon_0\varepsilon}\frac{\partial}{\partial z}H_y; \qquad E_z = -\frac{1}{i\omega\varepsilon_0\varepsilon}\frac{\partial}{\partial x}H_y. \tag{57}$$

Using the notation of (53), these T.M. field components are represented as

$$H_y = \sum_n F_n G_n(z) \exp(ik_0xS_n), \tag{58}$$

$$E_z = -\eta \sum_n S_n F_n G_n(z) \exp(ik_0xS_n), \tag{59}$$

$$E_x = \eta \sum_n F_n \Delta_n(z) G_n(z) \exp(ik_0xS_n), \tag{60}$$

where

$$\left.\begin{aligned}\Delta_n(z) &= \frac{\partial G_n(z)/\partial z}{ik_0G_n(z)} = \frac{i\sin k_0zC_n - \cos k_0zC_n(1-R_g)/(1+R_g)}{\cos k_0zC_n - i\sin k_0zC_n(1-R_g)/(1+R_g)}\\ &= C_n\frac{iC_n\sin k_0zC_n - \Delta_g\cos k_0zC_n}{C_n\cos k_0zC_n - i\Delta_g\sin k_0zC_n}\end{aligned}\right\} \tag{61}$$

denotes a z-dependent normalized impedance of the T.M. modes. Equation (61) is the same as (96) of Chapter 4 in the limit of a flat earth. For $z = 0$, $\Delta_n(0) = -\Delta_g$. For $z = h$ application of (42) shows that $\Delta_n(h) = \Delta_e$. For a highly conducting ground of $R_g \to 1$ or $|\Delta_g| \to 0$, $\Delta_n(z)$ is proportional to $\tan k_0zC_n$, which becomes real for nondissipative boundaries when C_n is given by (47) or (48).

Equations (58) to (60) are of the same form as the field expressions H_φ, E_r and E_θ for a vertical electric dipole in (104) to (107) of Chapter 4 in the limit of a flat earth. However, in the present formulation the source of waveguide excitation has not been specified and the relative mode amplitudes F_n remain undetermined.

For T.E. modes F of (52) or (53) is assumed to represent the E_y field component which can be written as

$$E_y = \sum_m F_m G_m(z) \exp(ik_0xS_m), \tag{62}$$

where the different T.E. modes are distinguished by the subscript m. The other field components are computed applying (1) as

$$H_x = -\frac{1}{i\omega\mu_0}\frac{\partial}{\partial z}E_y = -\frac{1}{\eta}\sum_m \frac{F_m G_m(z)}{\Delta_m(z)} \exp(ik_0xS_m), \tag{63}$$

$$H_z = \frac{1}{i\omega\mu_0}\frac{\partial}{\partial x}E_y = \frac{1}{\eta}\sum_m S_m F_m G_m(z) \exp(ik_0xS_m), \tag{64}$$

where

$$\left.\begin{aligned}\Delta_m(z) &= \frac{ik_0G_m(z)}{\partial G_m(z)/\partial z} = \frac{\cos k_0zC_m - \sin k_0zC_m(1-R_g)/(1+R_g)}{C_m i \sin k_0zC_m - \cos k_0zC_m(1-R_g)/(1+R_g)} \\ &= \frac{C_m\Delta_g \cos k_0zC_m - i \sin k_0zC_m}{C_m[iC_m\Delta_g \sin k_0zC_m - \cos k_0zC_m]}\end{aligned}\right\} \quad (65)$$

denotes a z-dependent normalized impedance of the T.E. mode.

Equation (65) is the same as (100) of Chapter 4 in the limit of a flat earth. For $z = 0$, $\Delta_m(0) = -\Delta_g$; applying (43) for $z = h$, $\Delta_m(h) = \Delta_h$. For a highly conducting ground $R_g \to (-1)$ and $\Delta_g \to 0$. Impedances of T.E. modes $\Delta_m(z)$ become proportional to tan k_0zC_m where the argument (k_0zC_m) is real for nondissipative boundaries when C_m is given by (47).

Equations (62) to (64) are of the same form as the field components of a vertical magnetic dipole E_φ, H_θ and H_r in (111) to (114) of Chapter 4 in the limit of a flat earth of infinite radius a. However, the relative mode amplitudes F_m remain undetermined in the present formulation.

Further examples of height-gain functions $G_q(z)$ and normalized impedances are presented in Chapter 4 for a spherical geometry. The exponential approximation of spherical wave functions appears as a modification of flat-earth formulas, and in the limit of a flat earth they are reduced to the formulas developed in this section. For lossy boundaries the height variations of $G_q(z)$ and $\Delta_q(z)$ differ from the simple cosinusoidal, sinusoidal and tangential variations that are obtained in absence of losses.

1.6 References

Baybulatov, R. B., and P. E. Krasnushkin (1967) Influence of the earth's magnetic field on the propagation of ultra long waves around the earth, *Doklady Akad. Nauk SSSR, Geofiz.* **174** (1), 84–87.

Bremmer, H. (1949) *Terrestrial Radio Waves*, Elsevier Publishing Co., Inc., New York.

Budden, K. G. (1961a) *Radio Waves in the Ionosphere*, Cambridge University Press, Cambridge.

Budden, K. G. (1961b) *The Wave Guide Mode Theory of Wave Propagation*, Logos Press, London.

Crombie, D. D. (1966) Further observations of sunrise and sunset fading of very-low-frequency signals, *Radio Sci.* **1** (1), 47–51.

Galejs, J. (1964a) Terrestrial extremely-low-frequency propagation, in *Natural Electromagnetic Phenomena Below 30 kc/s*, Proc. NATO Advanced Study Institute, Bad Homburg, Germany, 1963 (edited by D. F. Bleil), pp. 205–258, Plenum Press, New York.

Galejs, J. (1964b) Propagation of V.L.F. waves below a curved and stratified anisotropic ionosphere, *J. Geophys. Res.* **69** (17), 3639–3650.

Galejs, J. (1967) Propagation of V.L.F. waves below an anisotropic stratified ionosphere with a transverse static magnetic field, *Radio Sci.* **2** (6), 557–574.

Galejs, J. (1968) Propagation of E.L.F. and V.L.F. waves below an anisotropic ionosphere with a dipping static magnetic field, *J. Geophys. Res.* **73** (1), 339–352.

Galejs, J. (1969) V.L.F. modes below an idealized anisotropic ionosphere, *Radio Sci.* **4** (6), 491–516.

Ginzburg, V. L. (1964) *The Propagation of Electromagnetic Waves in Plasmas*, Pergamon Press, Oxford.

Helliwell, R. A. (1965) *Whistlers and Related Ionosphere Phenomena*, Stanford University Press, Stanford.

Johler, J. R. (1962), Propagation of the low-frequency radio signal, *Proc. IRE* **50** (4), 404–427.

Madden, T., and W. Thompson (1965), Low-frequency electromagnetic oscillations of the earth-ionosphere cavity, *Rev. Geophys.* **3** (2), 211–254.

Marcuvitz, N. (1951) *Waveguide Handbook*, McGraw-Hill, New York, NY.

Pappert, R. A. (1968) A numerical study of V.L.F. mode structure and polarization below an anisotropic ionosphere, *Radio Sci.* **3** (3), 219–233.

Ratcliffe, J. R. (1959) *The Magneto-ionic Theory*, University Press, Cambridge.

Schumann, W. O. (1952a) On the radiation free selfoscillations of a conducting sphere, which is surrounded by an air layer and an ionospheric shell (in German), *Z. Naturforsch.* **72**, 149–154.

Schumann, W. O. (1952b) On the damping of electromagnetic selfoscillations of the system earth-air-ionosphere (in German), *Z. Naturforsch.* **72**, 250–252.

Snyder, F. P., and R. A. Pappert (1969) A parametric study of V.L.F. modes below anisotropic ionospheres, *Radio Sci.* **4** (3), 213–226.

Sommerfeld, A. (1949) *Partial Differential Equations in Physics*, Academic Press, New York, NY.

Stratton, J. A. (1941) *Electromagnetic Theory*, McGraw-Hill, New York, NY.

Volland, H. (1968) *Propagation of Long Waves* (in German), F. Vieweg & Sohn, Braunschweig.

Wait, J. R. (1957) The mode theory of V.L.F. ionosphere propagation for finite ground conductivity, *Proc. IRE* **45** (6), 762–767.

Wait, J. R. (1962) *Electromagnetic Waves in Stratified Media*, Macmillan, New York.

Wait, J. R. (1968) Recent theoretical advances in the terrestrial propagation of V.L.F. electromagnetic waves, in *Advances in Electronics and Electron Physics*, **25**, 145–209, Academic Press, NY.

Wait, J. R., and K. P. Spies (1965) Influence of finite ground conductivity on the propagation of V.L.F. radio waves, *Radio Sci. J. Res. NBS*, **69D** (10), 1359–1373.

Watt, A. D. (1967) *V.L.F. Radio Engineering*, Pergamon Press, Oxford.

CHAPTER 2

BOUNDARIES OF THE TERRESTRIAL WAVEGUIDE

Abstract. The ground surface at the lower waveguide boundary is frequently treated as a homogeneous isotropic medium, but stratifications in either the horizontal or vertical directions may give rise to an effective anisotropy.

The ionospheric upper boundary is characterized by gradually changing electrical properties. Data available on ionospheric composition are reviewed for altitudes below the *F*-layer. Components of the tensor permittivity or conductivity are determined using the conventional magneto-ionic theory for several models of electron and ion densities, collision frequencies, and molecular weights.

2.1 Ground Surface

The ground is usually considered to be a homogeneous isotropic conductor of a given conductivity σ_g, and the displacement currents are negligible for frequencies in the L.F. range and lower. The effective ground conductivity σ_g of 10^{-3} to 5 mho/m is much higher than the effective ionospheric conductivity σ_i, which is estimated to be of the order of 10^{-5} to 10^{-7} mho/m.

The detailed ground characteristics are relatively unimportant for estimating propagation parameters of vertically polarized waves in the air-to-ionosphere wave guide, but more detailed considerations are necessary when considering the excitation of electric field components tangential to the earth's surface or when analyzing the performance of horizontally oriented antennas. The wave penetration in the ground or the skin depth $\delta = \sqrt{2/(\omega\mu_0\sigma_g)}$ are increased with a lowering of the operating frequency, and the lower substrata become more effective. Measurements of the horizontal electric and magnetic field components on the surface of the earth can be interpreted using models of underground stratifications [Cagniard, 1953; Wait, 1962b], and such measurements indicate also significant amounts of anisotropy in the frequency range of Schumann resonances and micro-pulsations [Bostick and Smith, 1962; Dowling, 1968].

The surface impedance of a two-layer ground model will be briefly discussed in this section. It will be shown that a stratified medium can be considered to be anisotropic in the sense that the effective conductivity in the direction perpendicular to the stratifications differs from the conductivity parallel to the stratifications. This anisotropy will be illustrated first in the D.C. limit, and subsequently also for waves propagating above the two-layer model of horizontally stratified ground.

2.1.1 *Stratified Ground*

In a model of a two-layer ground, the top layer is assumed of thickness h and of conductivity σ_1; the lower semi-infinite layer exhibits a conductivity σ_2. The vertically polarized fields are assumed to propagate above the earth's surface in the x direction with no field variations in the y direction. The effective surface impedance is computed in Section 2.1.3 as

$$Z_g = -\frac{E_x}{H_y} = \sqrt{\frac{\omega\mu_0}{i\sigma_1}}\,\frac{1+R}{1-R}, \tag{1}$$

where

$$R = \frac{\sqrt{\sigma_1}-\sqrt{\sigma_2}}{\sqrt{\sigma_1}+\sqrt{\sigma_2}}\exp(i2k_1h), \tag{2}$$

$$k_1 = \sqrt{i\omega\mu_0\sigma_1}. \tag{3}$$

For $\sigma_1 \to \sigma_2$ or $|\mathrm{Im}\, 2k_1h| \gg 1$, $R \to 0$ and Z_g is the same as for a homogeneous medium of conductivity σ_1. Also, the ground impedance is independent of the wave-propagation parameters (or of the sine of the complex angle of wave incidence S) in the airspace. An extension to multilayer ground models is straightforward, and such calculations are similar to the ones reported for isotropic ionosphere models [Galejs, 1964c].

2.1.2 *Equivalent Anisotropy of a Stratified Medium*

A multilayer ground model will exhibit an effective conductivity in the vertical direction (or perpendicular to the stratifications) which will differ from the effective conductivity in the horizontal direction (or parallel to the stratifications).

This can be illustrated most simply by examining a finite sample of the medium with a 1 m^2 cross section in the horizontal xy plane and of layer thicknesses d_1 and d_2 respectively in the z direction. The two layers are characterized by conductivities σ_1 and σ_2.

A potential difference V_z is maintained in the vertical direction, which is perpendicular to the interface between the two media, as shown in Fig. 2.1a. The electric fields of the media E_{zj} are proportional to σ_j^{-1}, and the power dissipated by the current flow in the z direction is simply

$$P_z = I(V_1+V_2) = I^2\left(\frac{d_1}{\sigma_1}+\frac{d_2}{\sigma_2}\right). \tag{4}$$

Alternately, (4) can be expressed as

$$P_z = I^2\,\frac{d_1+d_2}{\sigma_z}, \tag{5}$$

where the effective conductivity σ_z is computed from (4) and (5) as

$$\sigma_z = \frac{d_1+d_2}{(d_1/\sigma_1)+(d_2/\sigma_2)}. \tag{6}$$

Noting that $I = V_1\sigma_1/d_1 = |E_z\sigma_1|$, (4) can be also rearranged as

$$P_z = |E_z|^2(\sigma_1d_1+\sigma_1^2d_2/\sigma_2). \tag{7}$$

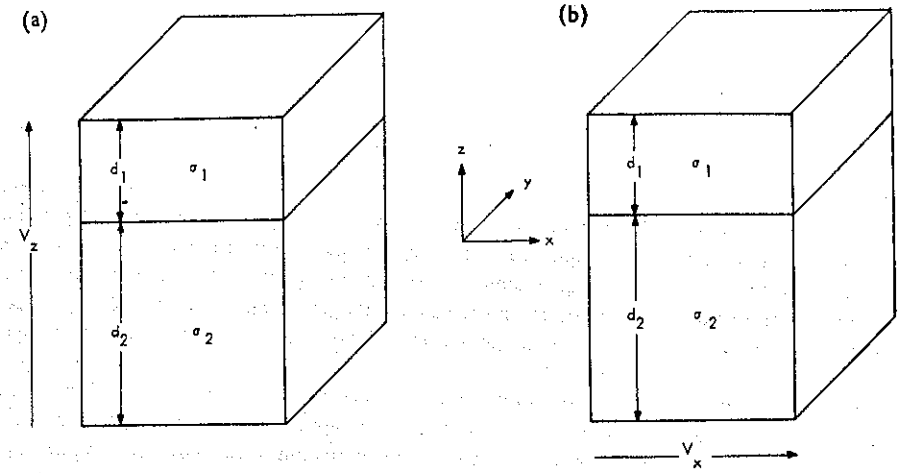

FIG. 2.1 Example of a Two-layer Medium

In Fig. 2.1b, the potential difference V_x is maintained in the x direction. It is seen that

$$P_x = (I_1+I_2)V_x = (\sigma_1 d_1+\sigma_2 d_2)V_x^2 = (\sigma_1 d_1+\sigma_2 d_2)\,|E_x|^2 \tag{8}$$

or

$$P_x = \sigma_x(d_1+d_2)V_x^2, \tag{9}$$

where V_x measured over the length of 1 m is numerically equal to the electric field E_x. The equivalent conductivity of the x direction is computed from (8) and (9) as

$$\sigma_x = \frac{\sigma_1 d_1+\sigma_2 d_2}{d_1+d_2}, \tag{10}$$

which differs from the equivalent conductivity σ_z of the z direction.

The above relations have been derived by assuming that a D.C. field is applied to a medium of finite size. However, similar relations can be also derived when the fields are excited by a wave propagating in the x direction above a two-layer ground, where the upper layer has a thickness h, which is much less than the skin depth δ_1; and the lower medium is semi-infinite. The calculations of Section 2.1.3 show that

$$P_x = |E_x(0)|^2(\sigma_1 h+0.5\sigma_2\delta_2), \tag{11}$$

$$P_z = |E_z(0^-)|^2(\sigma_1 h+0.5\sigma_1^2\delta_2/\sigma_2), \tag{12}$$

which are similar to (8) and (7) except that half of the skin depth δ_2 replaces the thickness d_2 of the finite sample. The analogy with (6) and (10) indicates that a horizontally stratified medium exhibits different conductivities in directions perpendicular (σ_z) and parallel (σ_x) to the interface. The effect of the stratification can be described by an equivalent anisotropy ($\sigma_z \neq \sigma_x$).

It is apparent that a medium with vertically oriented interfaces between parts of different bulk conductivities σ_j will also exhibit different conductivities in directions perpendicular and parallel to these interfaces. Solutions for such a medium can be expressed in terms of integrals

that have been evaluated numerically [d'Erceville and Kunetz, 1962; Weaver, 1963]. This medium will appear anisotropic at distances from the interface that are comparable to a skin depth in the conducting medium, and different conductivity components will be effective for various directions in the horizontal plane. A similar anisotropy can be also expected for tilted substrata of the earth. Such an anisotropy will affect the directional characteristics of horizontally oriented antennas [Galejs, 1969], which are discussed also in Sections 6.7 and 6.8.4.

2.1.3 *Two-layer Ground*

In a medium of relative dielectric constant ε_{rq} and conductivity σ_q, the electric and magnetic fields satisfy the Maxwell's equations

$$\nabla\times\mathbf{E} = i\omega\mu_0\mathbf{H}, \tag{13}$$

$$\nabla\times\mathbf{H} = (-i\omega\varepsilon_0\varepsilon_{rq}+\sigma_q)\,\mathbf{E} = -i\omega\varepsilon_0\varepsilon_q\mathbf{E}, \tag{14}$$

for an implied $\exp(-i\omega t)$ time variation. The fields do not vary in the y direction and exhibit the x and z dependence of

$$F_{jq} = F_{jq}^0 \exp(ik_0 Sx - ik_{zq}z), \tag{15}$$

where $F = E$ or H; $j = x$, y, or z; $q = 1$ or 2. S is the sine of the complex incidence angle (Re $S \sim 1/v_{ph}$, Im $S \sim \alpha$, where v_{ph} = phase velocity, α = attenuation rate), Im $k_{zq} > 0$, and the z-axis is in the direction from the lossy medium into the airspace. The T.M. (E_x, E_z, H_y) and T.E. (E_y, H_x, H_z) fields are not coupled in (13) and (14). The x and z components of (14) are substituted in the y component of (13) to yield

$$k_0^2S^2+k_{zq}^2 = k_0^2\varepsilon_q = k_q^2, \tag{16}$$

or

$$\frac{k_{zq}}{k_0} = \sqrt{\varepsilon_q - S^2} \approx \sqrt{\varepsilon_q}, \tag{17}$$

where for negligible displacement currents of the medium $|\varepsilon_q| \gg 1$. This gives

$$\frac{E_{xq}^0}{H_{yq}^0} = \pm\frac{k_{zq}}{\omega\varepsilon_q\varepsilon_0} = \pm\frac{\eta}{\sqrt{\varepsilon_q}}, \tag{18}$$

$$\frac{E_{zq}^0}{H_{yq}^0} = -\frac{k_0 S}{\omega\varepsilon_q\varepsilon_0} = -\frac{\eta S}{\varepsilon_q}, \tag{19}$$

where $\eta = \sqrt{\mu_0/\varepsilon_0} = 120\pi$ ohms is the characteristic impedance of free space, and the sign of (18) corresponds to the sign of (15). The horizontal field components of the two media will be of the form

$$\left.\begin{aligned} E_{x1}(z) &= [E_{x1-}^0\exp(-ik_{z1}z)+E_{x1+}^0\exp(ik_{z1}z)]\exp(ik_0Sx)\\ H_{y1}(z) &= [H_{y1-}^0\exp(-ik_{z1}z)+H_{y1+}^0\exp(ik_{z1}z)]\exp(ik_0Sx)\end{aligned}\right\}\quad \text{for}\quad (0 \geqslant z \geqslant -h),$$

$$\left.\begin{aligned} E_{x2}(z) &= E_{x2-}^0\exp[-ik_{z2}(z+h)+ik_0Sx]\\ H_{y2}(z) &= H_{y2-}^0\exp[-ik_{z2}(z+h)+ik_0S_x]\end{aligned}\right\}\quad \text{for}\quad (-h \geqslant z). \tag{20}$$

It follows from (18) that

$$\frac{E^0_{x1+}}{H^0_{y1+}} = -\frac{E^0_{x1-}}{H^0_{y1-}} \quad \text{or} \quad \frac{E^0_{x1+}}{E^0_{x1-}} = -\frac{H^0_{y1+}}{H^0_{y1-}} = R. \tag{21}$$

The surface impedance of the ground is computed using (18), (20), and (21) as

$$Z_g = -\frac{E_{x1}(0)}{H_{y1}(0)} = \frac{\eta}{\sqrt{\varepsilon_1}} \frac{1+R}{1-R}. \tag{22}$$

From the continuity of E_x and H_y at $z = -h$, it can be shown that

$$R = \frac{\sqrt{\varepsilon_1/\varepsilon_2}-1}{\sqrt{\varepsilon_1/\varepsilon_2}+1} \exp(i2k_1h). \tag{23}$$

In the limit of $\sigma_q \gg \omega\varepsilon_0\varepsilon_q$, (22) and (23) are reduced to (1) and (2).

The above relations can be also used to compute the power dissipated below the ground surface in terms of the electric fields $E_{x1}(0)$ and $E_{z1}(0^-)$. The power dissipated by E_{jq} in a column of 1 m² cross section in the xy plane is computed as

$$P_j = \sigma_2 \int_{-\infty}^{-h} |E_{j2}(z)|^2\, dz + \sigma_1 \int_{-h}^{0} |E_{j1}(z)|^2\, dz. \tag{24}$$

Letting $\sigma_q \gg \omega\varepsilon_0\varepsilon_q$ and substituting (20), (21), and (23), a calculation shows that

$$P_x = |E_{x1}(0)|^2 \frac{\sigma_1\delta_1}{2(1+r^2e^{-2v}+2re^{-v}\cos v)} \left[(1+r^2e^{-v})(1-e^{-v})+2re^{-v}\sin v + \sqrt{\frac{\sigma_2}{\sigma_1}}(1+r)^2e^{-v}\right] \tag{25}$$

$$P_z = |E_{z1}(0^-)|^2 \frac{\sigma_1\delta_1}{2(1+r^2e^{-2v}-2re^{-v}\cos v)} \left[(1+r^2e^{-v})(1-e^{-v})-2re^{-v}\sin v + \left(\frac{\sigma_1}{\sigma_2}\right)^{1.5}(1-r)^2e^{-v}\right] \tag{26}$$

where $r = (\sqrt{\sigma_1/\sigma_2}-1)/(\sqrt{\sigma_1/\sigma_2}+1)$, $v = 2h/\delta_1$, and $\delta_q = \sqrt{2/(\omega\mu_0\sigma_q)}$. In the limit of $v \ll 1$, (25) and (26) simplify to

$$P_x = |E_{x1}(0)|^2 \sigma_1\delta_1 \left[\frac{h}{\delta_1}+\frac{1}{2}\sqrt{\frac{\sigma_2}{\sigma_1}}\right], \tag{27}$$

$$P_z = |E_{z1}(0^-)|^2 \sigma_1\delta_1 \left[\frac{h}{\delta_1}+\frac{1}{2}\left(\frac{\sigma_1}{\sigma_2}\right)^{1.5}\right]. \tag{28}$$

Noting that $\sqrt{\sigma_1\sigma_2}\,\delta_1 = \sigma_2\delta_2$, (27) and (28) can be rearranged in the form (11) and (12).

2.2 The Ionospheric Boundary

Wave propagation in the terrestrial waveguide is affected principally by the lower ionosphere regions for frequencies in the V.L.F. and E.L.F. ranges with a possible exception of E.L.F. at nighttime when reflections from the F-region affect the wave fields below the ionosphere.

Available data on ionosphere composition will be reviewed with a particular emphasis on the height range below 100 km, and this information will be applied to determine the tensor permittivity (or conductivity) using the conventional magneto-ionic theory and by allowing for the presence of ions. Several ionospheric models will be examined for the height range between 100–300 km, and representative collision frequencies and conductivity components will be calculated.

2.2.1 *Electron and Ion Densities*

Considerable amounts of data have been collected on ionospheric electron densities under a variety of conditions [Belrose, 1964; Frihagen, 1966; Valley, 1965].

Electron-density profiles of the lower ionosphere have been deduced from partial reflection measurements by Deeks [1966a] and by Bain and May [1967]. Such electron-density distributions of the D-region are not unique, and different electron-density distributions may produce nearly identical ground interference patterns [Bain, 1969]. Comparable D-region electron densities can be derived from partial reflection and high-power wave interaction (or pulsed cross modulation) experiments [Thrane *et al.*, 1968]. The wave interaction measurements of Lee and Ferraro [1969] yield midday electron density profiles similar to the ones deduced by Deeks [1966a], and they are also comparable to some of the profiles derived by Belrose *et al.* [1968]. Seasonal variations of the lower ionosphere have been determined using rocket-borne electronic current probes by Mechtly and Smith [1968]; their electron-density profiles are compared with partial reflection results of Deeks [1966a] and Belrose *et al.* [1966]. Several D-region electron density profiles are also quoted in the review of Mittra [1968].

In the measurements of Deeks [1966a], reflection coefficients are calculated by full wave analysis for a postulated electron-density distribution. This electron distribution is then progressively changed until the computed values of reflection parameters agree with experimental data over the frequency range from 16 to 100 kc/s at both steep and oblique incidences for middle latitudes. The sunspot minimum data of Deeks [1966a] of winter nighttime and summer daytime are represented as solid curves in Fig. 2.2. The summer nighttime profile of Deeks, not shown in Fig. 2.2, is characterized by a nearly abrupt change of electron density at a height of 89 km. In the theoretical work of Radicella [1968], abrupt changes of electron density occur at intermediate heights; and only Deeks' winter nighttime electron density profile will be used in the subsequent numerical examples for the V.L.F. range. The above profiles can be also approximated by a sharply bounded ionosphere model and an exponential model, which are also shown in Fig. 2.2. The summer daytime profile has been also modified to show the effects of increased electron concentration in the lower parts of the D-region. This modification is indicated by the dotted line in Fig. 2.2. Deeks' [1966a] midday ionospheric profiles differ by approximately 5 km between winter and summer conditions. The summer daytime profile, which is the lower one, is approximately 5 km higher than the profile by Bain and May [1967], which has been derived using more accurate measurement techniques. Only Deeks' summer daytime profile, shown in Fig. 2.2, will be used in the subsequent computations for the V.L.F. range. The exponential profile, indicated by thin dotted dashed lines in Fig. 2.2, can be considered as the smoothed average of Deeks' and Bain's and May's daytime profiles.

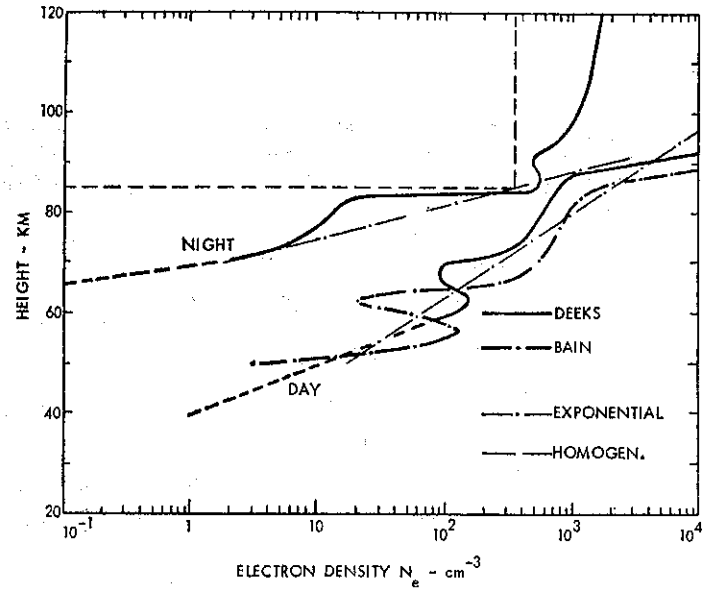

FIG. 2.2 Models of Electron Concentration

A number of ionospheric electron-concentration profiles have also been deduced from measurements made during various geophysical events. Deeks [1966a] and May [1966] have estimated electron concentration profiles during solar-flare induced sudden ionospheric disturbances (S.I.D.) by L.F. and V.L.F. partial reflection experiments. The profile of Deeks is quoted by May [1966] to represent an "average" S.I.D., while the data of May [1966] pertain to observations of October 7, 1948. Jayaram and Chin [1967] have analytically determined the *D*-region response to solar-flare *X*-rays during the April 27, 1962, event. Jespersen *et al.* [1966] report Faraday rotation measurements on a rocket-borne receiver during an auroral absorption event on March 12, 1964. Reid [1966] has calculated electron concentration profiles during polar cap absorption events (P.C.A.). These ionosphere density models are indicated in Fig. 2.3, together with the unperturbed ionosphere model by Piggott and Thrane [1966]. Solar flares tend to increase *D*-region ionization, but there may be altitude ranges where the perturbed electron concentration of one author is less than the unperturbed electron concentration of a different investigation that pertains to a different locality and is based on different measurement techniques. With the exception of P.C.A. events, the electron concentration profiles of the perturbed ionosphere models are comparable in magnitude with those observed under quiet daytime conditions.

The above electron density profiles refer to the *D*-region, which covers the altitude range from approximately 60 to 85 km and the lower part of the *E*-region, which is extended over the altitude range of 85–140 km. At daytime electron densities reach the value of $N_e = 10^5$ cm^{-3} near the altitude of 100 km; N_e is further increased in the F_1-region (140–200 km) and reaches its maximum value in the F_2-region at a height near 300 km. This maximum value may exceed

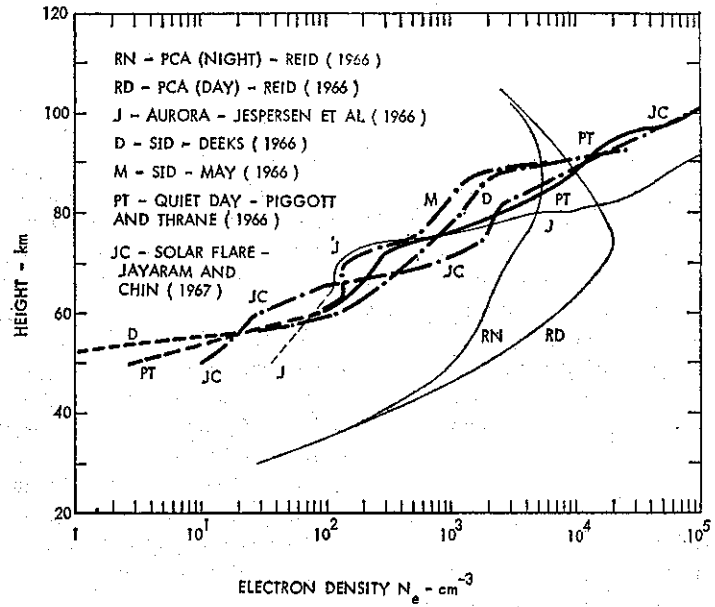

FIG. 2.3 Electron Density in a Perturbed Ionosphere

10^6 cm^{-3}. Above the maximum electron concentration in the F_2-region, the density is decreased to approximately 10^4 cm^{-3} near an altitude of 1000 km [Chan and Colin, 1969]. At nighttime F_1-region merges in the F_2-region; and the maximum electron density exceeds 10^5 cm^{-3}, which is less than at daytime.

The nighttime *F*-region is highly variable, and hourly changes of its altitude levels have been observed [Thomas, 1959; Davies, 1965]. The latitude changes of the electron density profile are also of a comparable magnitude [Chan and Colin, 1969]. Backscatter measurements made in Peru [Farley, 1966] and in Puerto Rico [LaLonde, 1966] indicate that the lower boundary of the *F*-layer tends to change from a level of 250–300 km to a level in the range from 150 to 200 km in the three to four hours following midnight. Midlatitude measurements of Evans [1967b] show a decrease of the *F*-layer maximum density from a height near 300 km around midnight to a height approaching 200 km in the early morning hours. It will not be possible to advance a single model representation of the lower part of the *F*-region at night, but the variability of the *F*-region may be illustrated using several ionosphere models.

There are also uncertainties in the nighttime electron densities in the interval between the *D*- and *F*-layers. It is frequently assumed that the electron density, which is of the order of 10^3 cm^{-3} at an altitude near 100 km, is monotonically increased in the height range between 100 and 200 km; a more rapid increase is observed near the bottom side of the *F*-layer, where N_e exceeds 10^4 [Hanson, 1961; Maeda and Matsumoto, 1962; Prince and Bostick, 1964]. For altitudes between 100 and 200 km, the electron density varies from experiment to experiment; and it is in the range from 300 to 5000 cm^{-3} [Wakai, 1967; Maeda, 1969]. Maeda [1969]

reports also a residual E-layer peak with densities of 3000 to 10^4 cm^{-3} near the altitude of 100 km. The above electron density data will be approximated by the idealized profiles of Fig. 7.8(p. 254), which will be used in subsequent calculations of E.L.F. propagation parameters.

Direct ion-density measurements have been made by rocket-borne instruments mostly for the upper ionosphere, but there are also data available for ions in the upper atmosphere at heights below 30 km [Valley, 1965]. Ion- and electron-density profiles for the height range between 0 and 100 km have been deduced by Cole and Pierce [1965] based on available estimates on production rates, attachment, recombination, and detachment coefficients of the various ionospheric constituents. The resulting profiles of electron and ion densities are shown

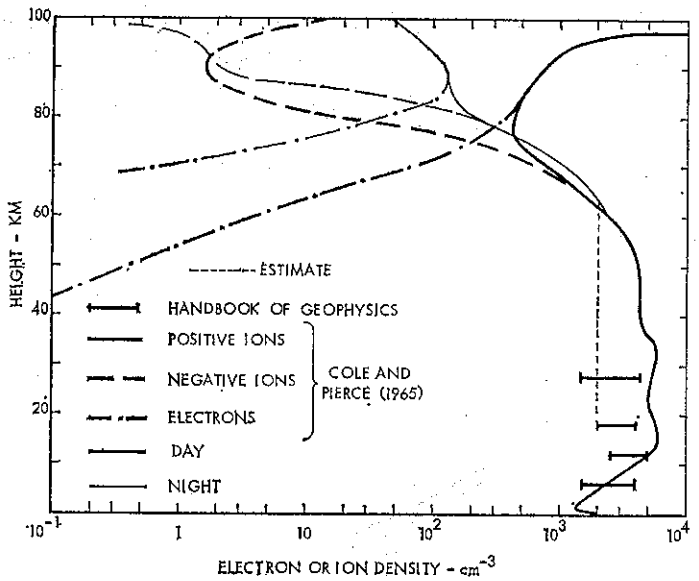

FIG. 2.4 Profiles of Electron and Ion Density

in Fig. 2.4. In this study, the mean ionic mass is assumed to be 29, which is representative for an average of NO^+, O_2^+, N_2^+, O_2^-, and O^- ions. Cole and Pierce [1965] point out that ions of greater mass can be produced by clustering and aerosols or attachment to dust and nuclei. Ions of larger effective mass have been established by mass spectrometric measurements [Narcisi and Bailey, 1965]. The limits of small ion concentration observed in the geomagnetic latitude range of 33°–65° N are indicated by horizontal bars following fig. 8.20 of Valley [1965]. Paltridge [1965] has deduced comparable ion densities of approximately 3000 cm^{-3} in the altitude range of 8–22 km, but he found a density of only 1000 cm^{-3} near 30 km altitude. The ion concentration of Cole and Pierce [1965] appears to be above the upper limit of the horizontal bars in the height range between 20 and 30 km, and calculations will be also made using the estimated dotted profile in the height range between 20 and 60 km.

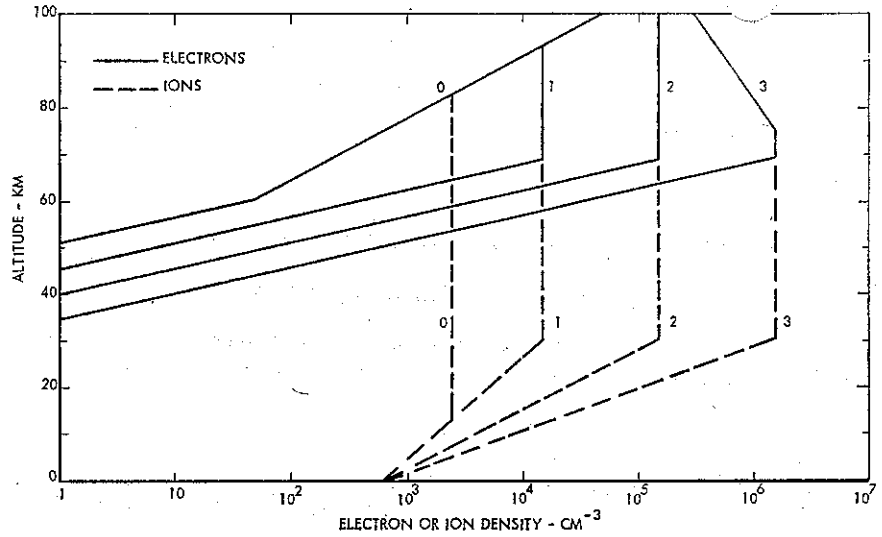

FIG. 2.5 Models of Perturbed Electron and Ion Density

At altitudes above 100 km, the densities of the negative ions become small; and it may be assumed that density of positive ions $N_i = N_+$ are the same as the electron density N_e.

The ion density data of Fig. 2.4 pertain to unperturbed daytime and nighttime conditions. The largest perturbations of daytime profiles may be expected in a nuclear environment; for high ionization production rates, radio-wave absorption is caused principally by ions following Crain and Booker [1964] or Johler and Berry [1966]. Ion and electron-density profiles of P.C.A. events have been investigated by Field [1969]. The ion densities of P.C.A. events are increased by a factor of 10–100 relative to ambient daytime conditions in the height range relative to unperturbed daytime conditions. Such perturbed electron and ion density profiles are idealized in the models of Fig. 2.5. The model 0 refers to unperturbed daytime conditions; models 1 and 2 could approximate P.C.A. events, but model 3 is more typical of nuclear perturbations.

2.2.2 *Collision Frequencies*

In the framework of standard magneto-ionic theory [Ratcliffe, 1959], the collisions between particles i and j exert a retarding force on particles i which is proportional to the mass i, the velocity difference $(\mathbf{v}_j - \mathbf{v}_i)$, and the collision frequency ν_{ij}, as is shown in more detail in Section 2.4. Such a definition of the retarding force ignores the energy distribution of electrons and the energy dependence of collision frequencies. Experiments of Phelps and Pack [1959] have shown that collision frequencies of mono-energetic electrons with nitrogen (and also oxygen) gas are proportional to electron energy or to the square of electron velocity v, which should be considered in the study of radio-wave propagation in the lower ionosphere. Sen and Wyller [1960] have developed a more complete theory using a Maxwellian distribution of electron

velocity v, collision frequencies $\nu \sim v^2$, and by denoting ν_M as the collision frequency of mono-energetic electrons of energy KT, where K is the Boltzmann's constant. However, the original formulas of the magneto-ionic theory can still be used if the collision frequency ν is replaced by ν_{eff}; $\nu_{eff} = 1.5\nu_M$ if $\nu \gg (\omega \pm \omega_{ce})$ and $\nu_{eff} = 2.5\nu_M$ if $\nu \ll (\omega \pm \omega_{ce})$, where ω_{ce} is the gyrofrequency of electrons defined by (44). Based on calculations for $f \approx 600$ kc/s, they caution against the use of Appleton–Hartree equations for intermediate values of ν. Budden [1965] has presented a number of computations which further justify the use of ν_{eff} in formulas of the conventional magneto-ionic theory; and for $f < 100$ kc/s, Deeks [1966b] has indicated that the two asymptotic values of ν_{eff} can be joined by a smooth curve.

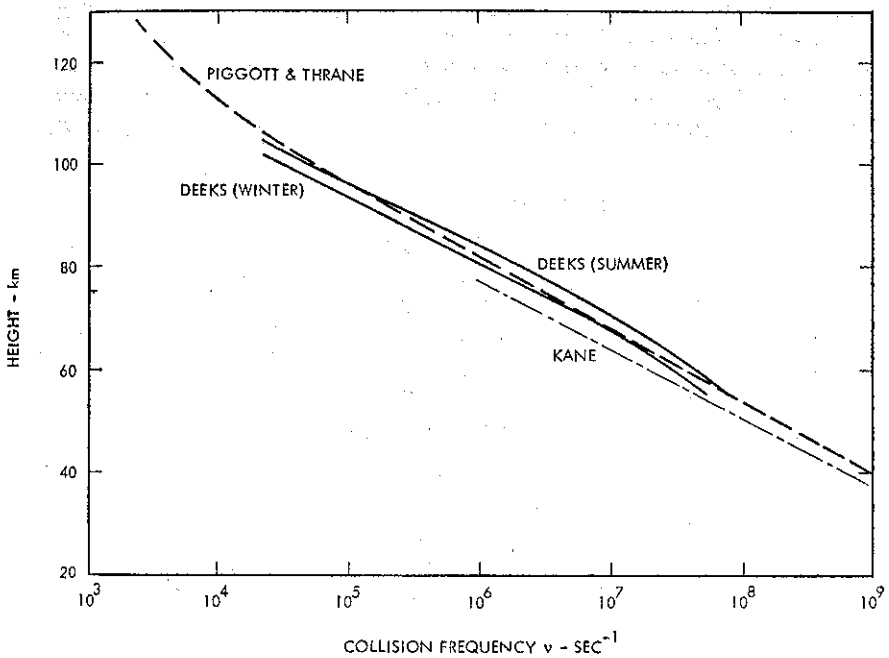

FIG. 2.6 Collision Frequencies ν_{en} at Middle Latitudes

For altitudes below 120 km, the collision frequency between electrons and neutral particles $\nu_{en} = \nu$ can be seen from the measurement data collected in Fig. 2.6, where $\nu = \nu_{eff}$ is obtained by suitably correcting ν_M data. The measurements of Piggott and Thrane [1966] lie halfway between the summer and winter collision-frequency data of Deeks [1966a]. The data of Piggott and Thrane are extrapolated to lower altitudes with the same slope as in the measurements by Kane [1961]. Thrane and Piggott [1966] present a detailed comparison of measured and computed collision-frequency profiles. The recent high-power wave interaction measurements of Lee and Ferraro [1969] compare closely with the collision-frequency data of Thrane and Piggott [1966].

At greater altitudes, the collision frequency ν_{en} is estimated as

$$\nu_{en} = CN_n\sqrt{T}, \tag{29}$$

where the constant C is 5.4×10^{-10} following Chapman [1956] and 3.7×10^{-10} following (6.11) of Ginzburg [1964]. Shkarofsky [1961] differentiates between electron collisions with nitrogen molecules N_2 and atomic oxygen O, where the relative abundance N_{N2}/N_n and N_O/N_n are determined from the molecular weight of the neutral atmosphere. In this formulation

$$\nu_{en} = \nu_{N2}+\nu_O = 2.493\times10^{-11}N_{N2}T+8.282\times10^{-10}N_O\sqrt{T} \tag{30}$$

where $N_n = N_{N2}+N_O$.

Following Chapman [1956], the collision frequency between electrons and ions may be computed from

$$\nu_{ei} = N_eT_e^{-1.5}[33.9+5.44\ln(T_e/N_e^{1/3})], \tag{31}$$

where the number of electrons N_e is defined per cm^3. The collision frequency ν_{ei} in (6.14) of Ginzburg [1964] can be expressed as

$$\nu_{ei} = N_eT_e^{-1.5}[29.7+5.5\ln(T_e/N_e^{1/3})]. \tag{32}$$

The first constant in the square brackets of (32) is 12 percent less than in (31). Under conditions of $T_e \gg T_i$ eqn. (6.15) of Ginzburg [1964] shows that

$$\nu_{ei} = N_eT_e^{-1.5}[a+b\ln(T_e/N_e^{1/3})+c\ln(T_i/T_e)] \tag{33}$$

with $a = 31$, $b = 5.5$, and $c = 1.83$. After replacing N_e with N_i, (33) corresponds to eqn. (A1) of Thrane and Piggott [1966] if $a = 30$, $b = 5.4$, and $c = 1.8$. There is only a minor difference between the constants deduced by Ginzburg [1964] and Thrane and Piggott [1966]. Equation (33) becomes numerically the same as (32) for $T_e/T_i \approx 2$, and the presence of low-temperature ions will tend to reduce ν_{ei} relative to thermal equilibrium conditions only for larger values of T_e/T_i. Equations (31) or (32) may serve as an upper bound of ν_{ei} under conditions where $T_e > T_i$.

Assuming that the molecular weights M.W. of ions and neutral particles are the same, the collision frequency between ions and neutral particles is computed following Chapman [1956] as

$$\nu_{in} = 2.6\times10^{-9}(N_i+N_n)/\sqrt{\text{M.W.}} \tag{34}$$

Valley [1965] indicates that collision frequencies between ions and neutral particles ν_{in} is approximated by the collision frequency of neutral particles ν_{nn} as

$$\nu_{in} \approx \nu_{nn} = 2.775\times10^{-10}N_n\sqrt{T/300}. \tag{35}$$

Following Dalgarno [1961], Banks [1966], or Stubbe [1968], collision frequencies for ions in neutral gases are of the form

$$\nu_{in} = CN_n, \tag{36}$$

where for NO^+ in O_2 and N_2, for O_2^+ in N_2, for O_2^+ and O_2^-, $C = (4.15 \text{ to } 4.35)\times10^{-10}$;

for N_2^+ in N_2, $C = 7.5\times10^{-10}$. Equation (36) applies also to negative ions moving in unlike gases [Dalgarno, 1961]. Crain and Booker [1964] and Field [1969] define

$$\nu_{in} = 4\times10^{9}Z \approx 5.46\times10^{-13}N_nT, \tag{37}$$

where Z, the pressure in atmospheres, is related to N_n by $1.01325\times10^6\ Z = KN_nT$. For $T \approx \approx 250°$ K, (36) gives 65 percent higher values of ν_{in} than (35), and (37) is lower by 44 percent. For M.W. = 29, (34) gives 90 percent higher values of ν_{in} than (35).

The various collision frequencies (29) to (35) can be calculated after establishing a model of atmospheric density N_n, molecular weights M.W., and temperatures T. The parameters of the US Standard Atmosphere 1962 [Valley, 1965] are shown as solid curves in Figs. 2.7 and 2.8.

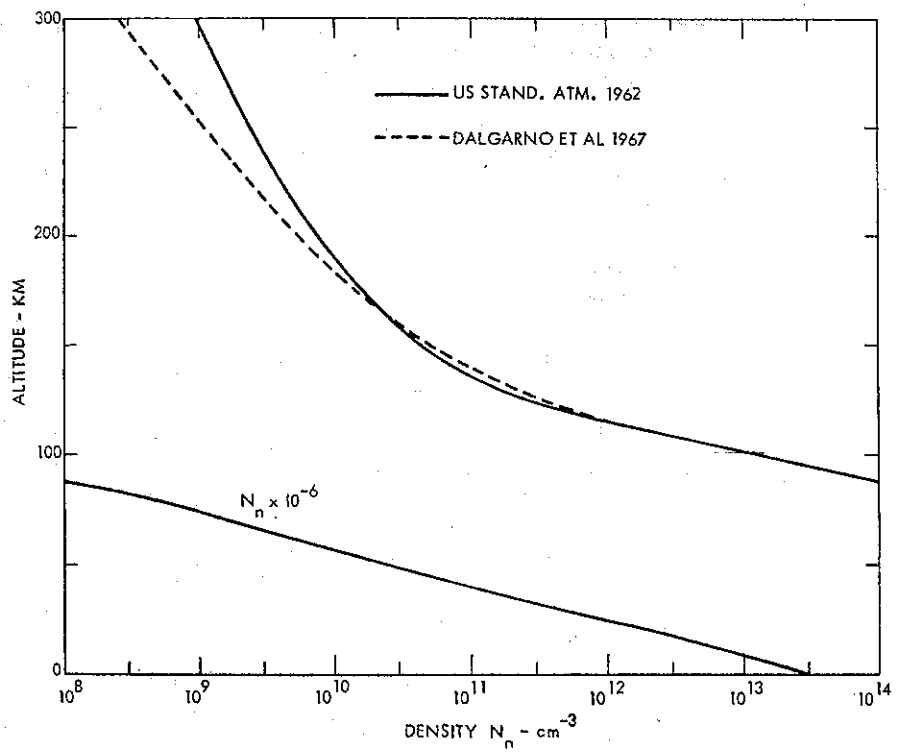

FIG. 2.7 Atmospheric Density

The height variation of the atmospheric density N_n is shown in Fig. 2.7. The early morning model of Dalgarno *et al.* [1967] shows a somewhat lower density for heights above 200 km.

The molecular weight of the neutral particles is M.W. $\approx$ 29 in Fig. 2.8 for altitudes less than 100 km, where the air consists of a mixture of O_2 and N_2 molecules. The molecular weight is decreased at larger heights, where atomic oxygen O becomes the dominant neutral particle. Different models of the neutral atmosphere have been advanced by Johnson [1961], Norton *et al.*

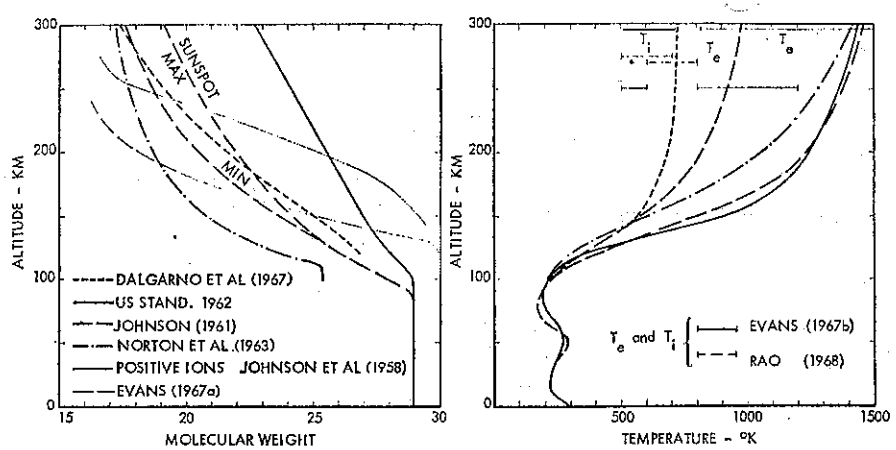

FIG. 2.8 Atmospheric Molecular Weight and Temperature

[1963], and Dalgarno *et al.* [1967] that are also indicated in Fig. 2.8. The molecular weights of the positive ions (O_2^+, NO^+, and O^+) exhibit a different altitude variation following the data of Johnson *et al.* [1958] and of Evans [1967a] that are indicated by thin lines in Fig. 2.8. The positive ions approach the M.W. = 16 of O^+ at a lower altitude than the neutral particles. NO^+ of M.W. = 30 dominates near 100 km. For altitudes below 100 km, the effective M.W. may be beyond the scale of Fig. 2.8. Mass spectrometric measurements of positive ions [Narcisi and Bailey, 1965] show that only 25 percent of ions detected in the altitude range between 64 and 76 km have masses less than 37 and that 50 percent have masses exceeding 45.

The temperature of the neutral particles is in the range between 180° and 300°K for altitudes less than 100 km. It is increased for larger altitudes and is in the range of 700–1500°K at 300 km. The temperature of the neutral particles, electrons, and ions are equal ($T = T_i = T_e$) for heights less than 120 km; but $T \approx T_i < T_e$ for altitudes between 120 and 300 km, as is pointed out by Dalgarno *et al.* [1967]. Evans [1967a] shows that $T_e = T_i$ at an altitude of 130 km, and that T_e is increased significantly for larger altitudes. The nighttime ion and electron temperatures determined by Evans [1967b] at midlatitudes and by Rao [1968] in Puerto Rico are shown by horizontal bars. These measurements suggest that the model of the US Standard Atmosphere [Valley, 1965] may give a realistic electron temperature T_e but that $T = T_i$ may be too high for the altitudes of 250–300 km. The model of Dalgarno *et al.* [1967] represents the measurements of $T = T_i$ more closely.

The collision frequency ν_{nn} of the US Standard Atmosphere has been determined by (35), which is also used for computing ν_{nn} for the ionosphere model of Dalgarno *et al.* [1967] in Fig. 2.9. The ion-neutral collision frequencies ν_{in} of Hanson [1961] based on (34), N_n of the US Standard Atmosphere, and the M.W. data of Johnson [1961], are indicated by horizontal bars, where the lower values are representative of sunspot minimum conditions. The molecular weights of positive ions of Fig. 2.8 indicate that atomic oxygen predominates in the ion mixture at altitudes above 200 km. Indicated by thin lines in Fig. 2.9 are collision frequencies by O^+ ions in O following Dalgarno [1964] and Stubbe [1968], where Stubbe's original values of the

collision frequencies are divided by 2 to correspond to the frictional force term in (49), which is also used in the theory of Dalgarno. The two curves labeled *SA* are computed using T and N_n data of US Standard Atmosphere; the curves labeled *D* are based on T and N_n data of Dalgarno *et al.* [1967]. It is seen that the ν_{in} data do not deviate by more than ± 50 per cent from the corresponding ν_{in} curves. The effects of ion-neutral collisions can be therefore estimated using ν_{nn} data.

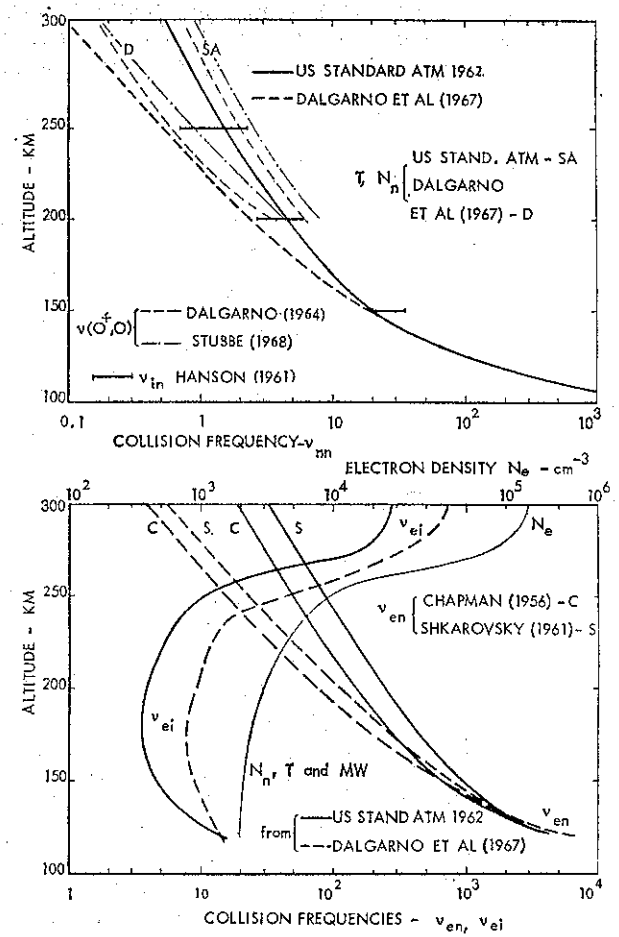

FIG. 2.9 Collision Frequencies in the Altitude Range from 100 to 300 km

The electron-neutral collision frequencies ν_{en} of Fig. 2.9 computed from (29) and (30) are labeled with *C* and *S* respectively. The solid lines indicate that N_n, T, and M.W. are taken from the US Standard Atmosphere, and the dashed curves are based on the atmospheric model of Dalgarno *et al.* [1967]. The electron-ion collision frequencies ν_{ei} are computed from (31) using

the assumed electron-density (N_e) profile of Fig. 2.9 although it should be noted that the temperatures T of Dalgarno's model are not representative of electron temperatures at higher altitudes. The atmospheric model with the higher temperature produces higher values of ν_{ei} and lower values of ν_{en} near an altitude of 300 km, which is an obvious consequence from the T-dependence of equations (29) to (31).

The subsequent calculations will be based on N_n, M.W., and T data of the US Standard Atmosphere 1962; ν_{in} is approximated by ν_{nn}, and the collision frequencies ν_{en} and ν_{ei} are calculated following Chapman [1956] for altitudes above 100 km; ν_{en} of Piggott and Thrane [1966] is used for altitudes below 100 km. Also, the effects of larger values of M.W. and ν_{in} will be considered for altitudes below 100 km.

2.2.3 *Conductivity Tensor*

The electrical properties of the ionosphere will be characterized using Appleton–Hartree formulas for a lightly ionized gas of different ionized species. The electric flux density **D** is related to the electric field **E** by the dielectric permittivity tensor $[\varepsilon]$ as

$$\mathbf{D} = [\varepsilon]\cdot\mathbf{E}. \tag{38}$$

In the case where the static magnetic field is directed along the z-axis of Cartesian x, y, z coordinates, the permittivity tensor $[\varepsilon]$ is of the form

$$[\varepsilon] = \begin{bmatrix} \varepsilon_1 & -\varepsilon_2 & 0 \\ \varepsilon_2 & \varepsilon_1 & 0 \\ 0 & 0 & \varepsilon_3 \end{bmatrix} = \begin{bmatrix} 1+\dfrac{i\sigma_1}{\omega\varepsilon_0} & -\dfrac{i\sigma_2}{\omega\varepsilon_0} & 0 \\ \dfrac{i\sigma_2}{\omega\varepsilon_0} & 1+\dfrac{i\sigma_1}{\omega\varepsilon_0} & 0 \\ 0 & 0 & 1+\dfrac{i\sigma_0}{\omega\varepsilon_0} \end{bmatrix} \tag{39}$$

where ε_j and σ_j may be denoted as permittivity and conductivity components respectively. Neglecting the collisions between different kinds of charged particles and assuming a weakly ionized medium, the components σ_j are computed from the equations

$$\sigma_0 = \varepsilon_0 \sum_k \frac{\omega_{pk}^2}{\nu_k - i\omega}, \tag{40}$$

$$\sigma_1 = \varepsilon_0 \sum_k \frac{\omega_{pk}^2(\nu_k - i\omega)}{(\nu_k - i\omega)^2 + \omega_{ck}^2}, \tag{41}$$

$$\sigma_2 = -\varepsilon_0 \sum_k \frac{\omega_{pk}^2 \omega_{ck}}{(\nu_k - i\omega)^2 + \omega_{ck}^2}, \tag{42}$$

$$\omega_{pk} = \left(\frac{N_k e_k^2}{\varepsilon_0 m_k}\right)^{1/2} \tag{43}$$

is the plasma frequency of the kth charged species and N_k, e_k, m_k are the number density, charge, and mass of the kth species particle.

$$\omega_{ck} = \frac{e_k B_0}{m_k} \tag{44}$$

is the kth species cyclotron or gyrofrequency and ν_k is the effective collision frequency between kth species particle and all other constituents of the plasma. In this notation, ω_{ck} is negative for particles of negative charge e_k.

The conductivity component σ_0 is effective for the direction parallel to the geomagnetic field, and it is the same as the conductivity computed in the absence of this field. The component σ_1 applies to the direction perpendicular to the geomagnetic field, and it is frequently labeled as Pederson conductivity. The component σ_2 is designated as the Hall conductivity. The so-called Cowling conductivity $\sigma_3 = \sigma_1 + \sigma_2^2/\sigma_1$ characterizes energy dissipation per unit volume for a current density $\mathbf{i}_t$ flowing in a plane that is perpendicular to the geomagnetic field [$\mathbf{i}_t \cdot \mathbf{E}_t = i_x E_x + i_y E_y = \sigma_1(E_x^2 + E_y^2) = (i_x^2 + i_y^2)/\sigma_3$]. It can be seen from (40) to (42) that for a single-charged species, $\sigma_3 = \sigma_0$.

It is also possible to allow for electron-to-ion collisions and for an arbitrary degree of ionization. Such a development is shown in Section 2.4 for a neutral gas consisting of electrons (N_e), positive ions ($N_i = N_+$), and neutral particles (N_n), where $N_e = N_+ = N$. The resulting expressions of the tensor conductivity components (55) and (56) differ from (40) to (42) by terms proportional to N/N_n and ν_{ei}. For a weakly ionized gas ($N/N_n \ll 1$), these two sets of equations lead to (61) and (62); the difference between the two latter equations becomes significant in the F-layer where $\nu_{ei} \gg \nu_{en}$. A generalization which allows for electron-to-electron and velocity dependent collisions [Dubs *et al.*, 1969] will not be considered at the present time.

The subsequent examples of the lower ionosphere will be restricted to a plasma of three components: electrons ($k = e$), positively charged ($k = +$), and negatively charged ions ($k = -$) of molecular weight M.W.$_k$.

For electrons, $\omega_{pe}^2 = 3.185 \times 10^9 N_e$, $\omega_{ce} = -0.88 \times 10^7$ for $B_0 = 0.5 \times 10^{-4}$ M.K.S. units (or 0.5 gauss) and $\nu_e = \nu_{en} + \nu_{ei}$. For the ions, $\omega_{pk}^2 = 1.73 \times 10^6 N_k/\text{M.W.}_k$, $|\omega_{ck}| = 4800/\text{M.W.}_k$ for $B_0 = 0.5 \times 10^{-4}$ M.K.S. units, and $\nu_k = \nu_+ = \nu_- = \nu_{in}$. In the above expressions for plasma frequencies ω_{pk}^2, the particle density N_k is defined per cm^3. A quasi-equilibrium implies that $N_+ = N_- + N_e$, and it is necessary to specify N_e and the profiles of either N_+ or N for computing σ_j.

The presence of a static magnetic field alters the conductivity components σ_1 and σ_2, but σ_0 is independent of the gyrofrequencies ω_{ck} (or of the static magnetic field B_0). The conductivity components σ_1 are generally complex, but the imaginary parts approach zero in the limit of low frequencies ω or high collision frequencies $\nu_k (\nu_k \gg \omega)$. The conductivity component σ_0 is illustrated in this limit in Fig. 2.10 for particle-density profiles of Fig. 2.4. Also shown are calculations based on electron-density profiles by Deeks (winter nighttime and summer daytime data) and by Bain and May that are used in conjunction with the estimated negative ion profile of Fig. 2.4. As a consequence of the assumed quasi-equilibrium $N_+ = N_-$ at low altitudes, but N_+ approaches N_e at heights where $N_- \ll N_e$. The two nighttime conductivity profiles indicated by thin lines are in relatively close agreement in Fig. 2.10. The daytime profiles of Deeks or Bain and May are lower by 5–10 km than the profiles of Cole and Pierce. The Deeks' summer daytime profile has been modified in Fig. 2.2 to increase the electron density at lower altitudes [Galejs, 1968]. This empirical modification provides conductivity σ_0 that is of comparable magnitude for heights above 45 km to the data of Bain and May which include also the ion effects. The conductivity below the D-region is lower in the present calculations than in the model of Cole and Pierce [1965]. Even three times lower values are reported in Fig. 8.18 of

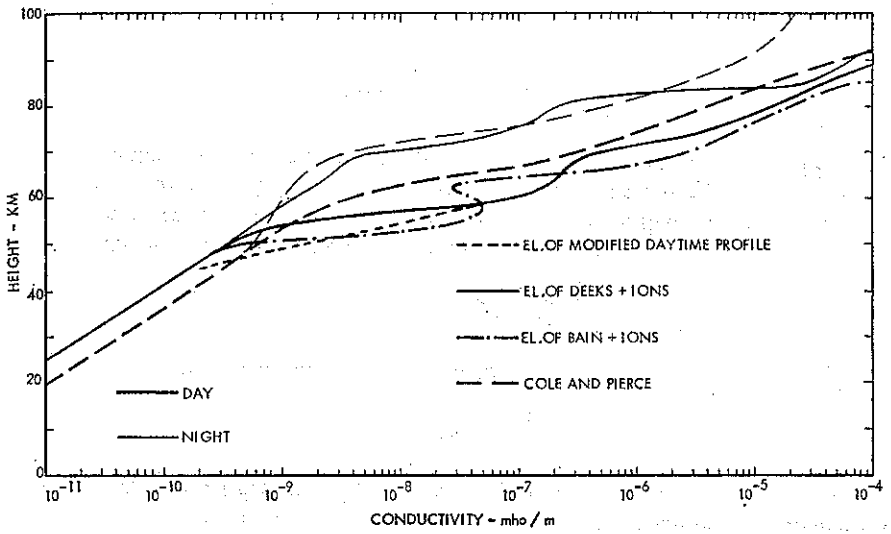

FIG. 2.10 Profiles of the Conductivity σ_0

Valley [1965] for the altitude range between 20 and 30 km; the latter conductivity figures are consistent with the ion conductivity data used in the E.L.F. calculations of Galejs [1961]. These conductivity data of Valley [1965] suggest the use of larger values of M.W. and ν_{in} in the calculation of ion conductivity.

The permittivity elements ε_1 and ε_3 of (39) approach unity if the conductivity components $\sigma_j \ll \omega\varepsilon_0$. The permittivity ε_j will differ by less than 1 percent in magnitude from its free space value of unity when $\sigma_j < (\omega\varepsilon_0/7)$. In the V.L.F. range ($f = 20$ kc/s), parts of the conductivity profile where $\sigma_j < 1.6 \times 10^{-7}$ mho/m will be relatively insignificant; however, near the fundamental Schumann resonance ($f = 8$ c/s), the corresponding value of conductivity is 6.4×10^{-11}. The lower parts of the ionospheric conductivity profile with its smaller conductivity values are therefore more significant at the lower frequencies.

It is also possible to express the permittivity elements ε_j ($j = 1$ or 3) or the corresponding refractive index $n_j = \sqrt{\varepsilon_j}$ as [Wait, 1962a]

$$\varepsilon_j = n_j^2 = 1 + i\omega_{rj}/\omega, \tag{45}$$

where the conductivity parameter ω_{rj} is defined by

$$\omega_{rj} = \sigma_j/\varepsilon_0. \tag{46}$$

The parameter ω_r of (45) eliminates the constant ε_0 from the computation of permittivity elements (39); $\omega \gg \omega_{rj}$ implies that $|\varepsilon_j| \to 1$ while $\omega \ll \omega_{rj}$ is characterized by $|\varepsilon_j| \gg 1$.

The height variations of the other tensor conductivity components are illustrated in Fig. 2.11 for Deeks' winter nighttime and the modified daytime electron density profiles of Fig. 2.2 which are used in conjunction with the collision-frequency data of Piggott and Thrane [1966]

that are shown in Fig. 2.6. The static magnetic field is assumed to be $B_0 = 0.5$ gauss. In the lower ionosphere where the collision frequencies ν are larger than the frequencies ω, Im $\sigma_j <$ $< \mathrm{Re}\,\sigma_j$, and only the real parts of the conductivities are illustrated in Fig. 2.11. The conductivity component σ_0 is the larger one, and σ_1 tends to decrease after reaching a maximum value in the height range between 75 and 85 km. For conductivity components calculated for a single species of charged particles examination of (40) to (42) shows that

$$\sigma_0 = \sigma_1 + \sigma_2^2/\sigma_1 . \tag{47}$$

It is apparent that for small values of σ_2 in Fig. 2.11b, $\sigma_0 \approx \sigma_1$; however, for $\sigma_1 < \sigma_2$ in Fig. 2.11a, $\sigma_0 > \sigma_2$.

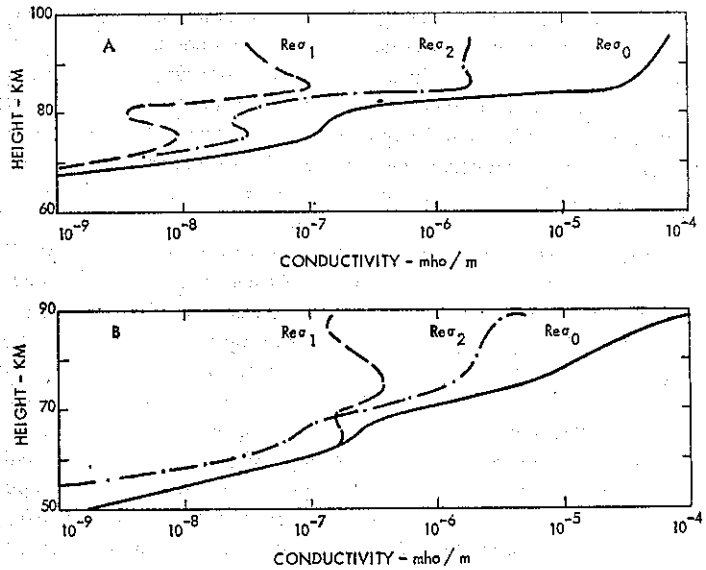

FIG. 2.11 Tensor Conductivity. Deeks' Winter Nighttime Profile (A) and Modified Daytime Profile (B) of Electrons. $f = 20$ kc/s

Further plots of σ_j [Galejs, 1964a, b] show that the real and imaginary parts of σ_j are frequency dependent. It is not convenient to deal with frequency-dependent profiles of complex conductivity component σ_j as an input to numerical calculations. It is more appropriate to establish analytical approximations for N_e, N_i, and ν profiles that can be used for numerically calculating the required components of σ_j or ε_j at the required frequencies.

2.2.4 *The Conductivity of a Partly Ionized Gas*

The conductivity tensor, which relates the current to the components of the applied electric field in a weakly ionized neutral mixture of ions and electrons, is frequently described as a sum of terms, each of which characterizes the contributions of the individual plasma components

[Chapman, 1956; Wait, 1962a]. Such equations can be derived from the mean-free-path theory by neglecting the collisions between different kinds of charged particles. It is also possible to set up the equations for electrons, ions, and neutral gas particles by considering collisions between the various charged particles and by accounting for the presence of the finite number of neutral molecules. In a development which follows Ginzburg [1964], the equations of motion for electrons, ions, and neutral gas particles (subscripts e, i, and n respectively) are expressed as

$$m\dot{\mathbf{v}}_e = e\mathbf{E} + e\mathbf{v}_e \times \mathbf{B} + m\nu_{ei}(\mathbf{v}_i - \mathbf{v}_e) + m\nu_{en}(\mathbf{v}_n - \mathbf{v}_e), \tag{48}$$

$$M\dot{\mathbf{v}}_i = -e\mathbf{E} - e\mathbf{v}_i \times \mathbf{B} + m\nu_{ei}(\mathbf{v}_e - \mathbf{v}_i) + M\nu_{in}(\mathbf{v}_n - \mathbf{v}_i), \tag{49}$$

$$M\dot{\mathbf{v}}_n = -m\nu_{en}\frac{N}{N_n}(\mathbf{v}_n - \mathbf{v}_e) - M\nu_{in}\frac{N}{N_n}(\mathbf{v}_n - \mathbf{v}_i). \tag{50}$$

Ions are assumed to be positive and singly charged of particle density $N_i = N_+ = N_e = N$ and of mass $M_i = M_n = M$. The mass and the charge of the electron are denoted by m and e respectively. The velocities $\mathbf{v}_j$ are averaged over a large number of particles and the collision terms are proportional to ν_{jk} and to the relative mean velocities of the colliding particles j and k. The frequency of collisions of particle j with n is proportional to the density N_j and of particle n with j to N_n; hence, $\nu_{nj} = (N/N_n)\nu_{jn}$. In the subsequent development, it is assumed that $\sqrt{m/M} \ll 1$, $\nu_{en} > \nu_{in}$, and $(m\nu_{en}/M) \ll \nu_{in}$. For an exp $(-i\omega t)$ time variation of the various quantities (48) to (50) can be rearranged into

$$(-i\omega + \nu_{ei} + \nu_{en})\mathbf{w} = \frac{e}{m}\mathbf{E} + \frac{e}{m}\mathbf{w} \times \mathbf{B} + \frac{e}{m}\mathbf{v}_i \times \mathbf{B} + \nu_{en}(\mathbf{v}_n - \mathbf{v}_i), \tag{51}$$

$$-i\omega\mathbf{v}_i = -\frac{e}{M}\mathbf{E} - \frac{e}{M}\mathbf{v}_i \times \mathbf{B} + \frac{m}{M}\nu_{ei}\mathbf{w} + \nu_{in}(\mathbf{v}_n - \mathbf{v}_i), \tag{52}$$

$$(-i\omega + \nu_{in}N/N_n)\mathbf{v}_n = \nu_{in}\frac{N}{N_n}\mathbf{v}_i + \frac{m}{M}\frac{N}{N_n}\nu_{en}\mathbf{w}, \tag{53}$$

where $\mathbf{w} = \mathbf{v}_e - \mathbf{v}_i$. The three vector equations (51) to (53) are written out in their scalar components for a magnetic field $\mathbf{B} = \mathbf{i}_z B_0$ that is applied along the z-axis of a Cartesian coordinate system. The current density along the j-axis can be expressed as

$$i_j = eNw_j = \sum_{k=1}^{3} \sigma_{jk} E_k . \tag{54}$$

The conductivity component $\sigma_{zz} = \sigma_0$ is computed as

$$\sigma_0 \approx \frac{\varepsilon_0 \omega_{pe}^2}{-i\omega + \nu_{ei} + \nu_{en}}, \tag{55}$$

where the plasma frequency of the electrons $\omega_{pe}^2 = Ne^2/(\varepsilon_0 m)$.

It can be readily shown that $\sigma_{xz} = \sigma_{yz} = \sigma_{zx} = \sigma_{zy} = 0$ and that the current density $(i_x \pm i i_y)$ is proportional to $(E_x \pm iE_y)$. Applying (54), this implies that $\sigma_{xx} = \sigma_{yy} = \sigma_1$ and $\sigma_{yx} = -\sigma_{xy} = \sigma_2$. In this notation, the proportionality constant becomes $(\sigma_1 \pm i\sigma_2)$, which is computed as

$$\sigma_1 \pm i\sigma_2 = \frac{-i\omega(1 + \nu_{in}/P)\varepsilon_0 \omega_{pe}^2}{A + B}, \tag{56}$$

where

$$A = (-i\omega \pm i\omega_{ce} + \nu_{ei} + \nu_{en})(-i\omega \pm i\omega_{ci} - i\omega\nu_{in}/P), \tag{57}$$

$$B = [\nu_{ei} + \nu_{en}\nu_{in}N/(PN_n)](\mp i\omega_{ci} + \nu_{en}m/M) + \nu_{en}^2 i\omega Nm/(N_n M), \tag{58}$$

$$P = -i\omega + \nu_{in}N/N_n. \tag{59}$$

The cyclotron or gyrofrequency $\omega_{ij} = e_j B_0/m_j$ is negative for particles of negative charge e_j.

For a fully ionized gas, $N_n \to 0$ and $\nu_{in} = \nu_{en} = 0$. In this limit, (56) simplifies to

$$\sigma_1 \pm i\sigma_2 = \frac{-i\omega\varepsilon_0\omega_{pe}^2}{(-i\omega \pm i\omega_{ce})(-i\omega \pm i\omega_{ci}) - i\omega\nu_{ei}}. \tag{60}$$

For a weakly ionized gas of $N \ll N_n$, (56) is changed to

$$\sigma_1 \pm i\sigma_2 = \frac{(-i\omega + \nu_{in})\varepsilon_0\omega_{pe}^2}{(-i\omega \pm i\omega_{ce} + \nu_{ei} + \nu_{en})(-i\omega \pm i\omega_{ci} + \nu_{in}) + \nu_{ei}(\mp i\omega_{ci} + \nu_{en}m/M)}. \tag{61}$$

In the limit of $\omega \to 0$ and $(m\nu_{en}/M) \ll \nu_{in}$, (61) can be reduced to (57) of Chapman (1956).

The conductivity $\sigma_1 \pm i\sigma_2$ can be also computed from (41) and (42) as

$$\sigma_1 \pm i\sigma_2 = \frac{(-i\omega + \nu_i + \nu_e m/M)\varepsilon_0\omega_{pe}^2}{(-i\omega \pm i\omega_{ce} + \nu_e)(-i\omega \pm i\omega_{ci} + \nu_i)} \tag{62}$$

which can be reduced to (46) of Chapman [1946] in the limit of $\omega \to 0$. Using $\nu_e = \nu_{ei} + \nu_{en}$ and $\nu_i = \nu_{in}$ for the effective collision frequencies of electrons and ions in (62), (62) is seen to differ from (61) by the absence of the second term in the denominator.

2.3 References

Bain, W. C. (1969) Comparison of Russian and British electron density distributions derived from the same v.l.f. and l.f. propagation data, *J. Atmos. Terr. Physics* **31**, 755–758.

Bain, W. C., and B. R. May (1967) *D*-region electron density distributions from propagation data, *Proc. IEE (London)* **114** (11), 1593–1597.

Banks, P. (1966) Collision frequencies and energy transfer ions, *Planet. Space Sci.* **14**, 1105–1122.

Belrose, J. S. (1964) Present knowledge of the lowest ionosphere, *Propagation of Radio Waves at Frequencies Below 300 kc/s* (ed. W. T. Blackband), Pergamon Press, Oxford, pp. 3–24.

Belrose, J. S., I. A. Bourne, and L. W. Hewitt (1966) The winter variability of electron number density in the lower ionosphere over Ottawa, in *Electron Density Profiles in Ionosphere and Exosphere* (ed. J. Frihagen), pp. 48–60.

Belrose, J. S., L. W. Hewitt, and R. Bunker (1968) The partial reflection experiment as a tool for synoptic *D*-region research; and results of recent studies related to winter variability, in *Conference Digest*, Third Conference on Meteorological and Chemical Factors in *D*-Region Aeronomy, University of Illinois, September 23–26, 1968.

Bostick, F. X., and H. W. Smith (1962), Investigation of large-scale inhomogeneities in the earth by the magneto-telluric method, *Proc. IRE* **50** (11), 2339–2346.

Budden, K. G. (1965) Effect of electron collisions on the formulas of magnetoionic theory, *Radio Sci.* **69D** (2), 191–211.

Cagniard, L. (1953), Basic theory of the magneto-telluric method of geophysical prospecting, *Geophysics* **18** (3), 605–635.

Chan, K. L., and L. Colin (1969), Global electron density distributions from topside soundings, *Proc. IEEE* **57** (6), 990–1004.

Chapman, S. (1956), The electrical conductivity of the ionosphere: a review, *Suppl. Nuovo Cimento* **4** (4), 1385–1412.

Cole, R. K., and E. T. Pierce (1965), Electrification in the earth's atmosphere for alti... between 0 and 100 kilometers, *J. Geophys. Res.* **70** (12), 2735–2749.

Crain, C. M., and H. G. Booker (1964), The effects of ions on low frequency and very low frequency propagation in an abnormally ionized atmosphere, *J. Geophys. Res.* **69** (21), 4713–4716.

Dalgarno, A. (1961), Charged particles in the upper atmosphere, *Ann. Geophys.* **17** (1), 16–49.

Dalgarno, A. (1964) Ambipolar diffusion in the *F*-region, *J. Atmos. Terr. Physics* **26**, 939.

Dalgarno, A., M. B. McElroy, and J. C. G. Walker (1967) The diurnal variation of ionospheric temperatures, *Planet. Space Sci.* **15**, 331–345.

Davies, K. (1965) *Ionospheric Radio Propagation*, N.B.S. Monograph 80, US Department of Commerce.

Deeks, D. G. (1966a) *D*-region electron distributions in middle latitudes deduced from the reflection of long radio waves, *Proc. Roy. Soc.* **291** (1426), 413–427.

Deeks, D. G. (1966b) Generalized full wave theory for energy-dependent collision frequencies, *J. Atmos. Terr. Physics* **28**, 839–846.

Dowling, F. L. (1968) A magnetotelluric investigation of the crust and upper mantle across the Wisconsin Arch, Thesis, University of Wisconsin, Madison, Wisconsin.

Dubs, C. W., B. Prasad, and H. K. Sen (1969) Heating of the ionosphere and attenuation of the equatorial hydromagnetic waves, *Radio Sci.* **4** (9), 843–848.

d'Erceville, I., and G. Kunetz (1962) The effect of a fault on the earth's natural electromagnetic field, *Geophysics* **27** (5), 651–665.

Evans, J. V. (1967a) Electron temperature and ion composition in the F_1 region, *J. Geophys. Res.* **72** (13), 3343–3355.

Evans, J. V. (1967b) Midlatitude *F*-region densities and temperatures at sunspot minimum, *Planet. Space Sci.* **15**, 1387–1405.

Farley, D. T. (1966) Observations of the equatorial ionosphere using incoherent backscatter, in *Electron Density Profiles in Ionosphere and Exosphere* (ed. J. Frihagen), North-Holland, Amsterdam, 446–469.

Field, E. C. (1969) The propagation of E.L.F. waves under normally and naturally disturbed conditions, *J. Geophys. Res.* **74** (14), 3639–3650.

Frihagen, J. (ed.) (1966) *Electron Density Profiles in Ionosphere and Exosphere*, North-Holland, Amsterdam.

Galejs, J. (1961) E.L.F. waves in the presence of exponential ionospheric conductivity profiles, *IRE Trans. Antennas Prop. QA-9* (6), 554–562.

Galejs, J. (1964a) Terrestrial extremely-low-frequency propagation, *Natural Electromagnetic Phenomena Below 30 kc/s* (ed. D. F. Bleil), Proc. NATO Advanced Study Institute, Bad Homburg, Germany, 1963, Plenum Press, New York, New York, pp. 205–258.

Galejs, J. (1964b) E.L.F. and V.L.F. waves below an inhomogeneous anisotropic ionosphere, *Radio Sci. J. Res. NBS* **68D** (6), 693–707.

Galejs, J. (1964c) Propagation of V.L.F. waves below a curved and stratified anisotropic ionosphere, *J. Geophys. Res.* **69** (17), 3639–3650.

Galejs, J. (1968) Propagation of E.L.F. and V.L.F. waves below anisotropic ionosphere with a dipping static magnetic field, *J. Geophys. Res.* **73** (1), 339–352.

Galejs, J. (1969) Horizontally oriented antennas in the presence of an anisotropic ground, *Radio Sci.* **4** (11), 1047–1059.

Ginzburg, V. L. (1964) *The Propagation of Electromagnetic Waves in Plasmas*, Pergamon Press, Oxford.

Hanson, W. B. (1961) Structure of the ionosphere, in *Satellite Environment Handbook* (ed. F. S. Johnson), Stanford University Press, Stanford, California, pp. 27–46.

Jayaram, R., and G. Y Chin (1967) Analytical study of the *D*-region response to solar flares monitored by Ariel satellite (UK-1), *J. Geophys. Res.* **72**, 1889.

Jespersen, M., A. Haug, and B. Landmark (1966) Electron density and collision frequency observations in the arctic *D*-region, *Electron Density Profiles in Ionosphere and Exosphere* (ed. J. Frihagen), North-Holland, Amsterdam, p. 29.

Johler, J. R., and L. A. Berry (1966) On the effect of heavy ions on L.F. propagation, with special reference to the nuclear environment, *Radio Sci.* **1** (3), 303–307.

Johnson, C. Y., E. B. Meadows, and J. C. Holmes (1958) Ion composition of the Arctic ionosphere, *J. Geophys. Res.* **63**, 443–444.

Johnson, F. S. (1961) Structure of the upper atmosphere, in *Satellite Environment Handbook*, Stanford University Press, Stanford, California, pp. 9–24.

Kane, J. A. (1961) Reevaluation of ionospheric electron densities and collision frequencies derived from rocket measurements of refractive index and attenuation, *J. Atmos. Terr. Physics* **23**, 92–100.

LALONDE, L. M. (1966) A short-pulse backscatter study of the lower ionosphere, in *Electron Density Profiles in Ionosphere and Exosphere* (ed. J. Frihagen), North-Holland, Amsterdam, 515–522.
LEE, H. S., and A. J. FERRARO (1969) Winter *D*-region electron concentration and collision frequency features obtained with high-power interaction measurements, *J. Geophys. Res.* **74** (5), 1184–1194.
MAEDA, K. (1969) Mid-latitude electron density profile as revealed by rocket experiments, *J. Geomagnet. Geoelectr.* **21** (2), 557–567.
MAEDA, K., and H. MATSUMOTO (1962) Conductivity of the ionosphere and current system, *Rep. Ionosphere Space Res. Japan* **16** (1), 1–26.
MAY, B. R. (1966) The behaviour of the *D*-region at midlatitudes during a sudden ionospheric disturbance, *J. Atmos. Terr. Physics* **28**, 553–564.
MECHTLY, E. A., and L. G. SMITH (1968) Seasonal variation of the lower ionosphere at Wallops Island during the I.Q.S.Y., *J. Atmos. Terr. Physics* **30**, 1555–1561.
MITRA, A. P. (1968) A review of *D*-region processes in non-polar latitudes, *J. Atmos. Terr. Physics* **30**, 1065–1114.
NARCISI, R. S., and A. D. BAILEY (1965) Mass spectrometric measurements of positive ions at altitudes from 64 to 112 kilometres, *J. Geophys. Res.* **70** (15), 3687–3700.
NORTON, R. B., T. E. ZANDT, and J. S. DENISON (1963) A model of the atmosphere and ionosphere in the *E* and F_1 regions, *Procedure of the International Conference on the Ionosphere*, Institute of Physics and the Physical Society, London, pp. 26–34.
PALTRIDGE, G. W. (1965) Experimental measurements of the small-ion density and electrical conductivity of the stratosphere, *J. Geophys. Res.* **70** (12), 2751–2761.
PHELPS, A. V., and J. L. PACK (1959) Electron collision frequencies in nitrogen and in the lower ionosphere, *Phys. Rev. Letters* **3**, 340.
PIGGOTT, W. R., and E. V. THRANE (1966) The electron densities in the *E* and *D* regions above Kjeller, *J. Atmos. Terr. Physics* **28**, 467–479.
PRINCE, C. E., and F. X. BOSTICK (1964) Ionospheric transmission of transversely propagated plane waves at micropulsation frequencies and theoretical power spectrums, *J. Geophys. Res.* **69** (15), 3213–3234.
RADICELLA, S. M. (1968) Theoretical models of electron and ion density in the night-time D-region, *J. Atmos. Terr. Physics* **30** (10), 1745–1760.
RAO, P. B. (1968) Electron concentrations and electron and ion temperatures in the F region for magnetically quiet and disturbed conditions, *J. Geophys. Res.* **73** (5), 1661–1678.
RATCLIFFE, J. A. (1959) *Magnetoionic Theory*, Cambridge University Press.
REID, G. C. (1966) Physics of the D-region at high latitudes, *Electron Density Profiles in Ionosphere and Exosphere*, (ed. J. Frihagen), North-Holland, Amsterdam, p. 18.
SEN, H. K., and A. A. WYLLER (1960) On the generalization of the Appleton–Hartree magnetoionic formulas *J. Geophys. Res.* **65** (12), 3931–3950.
SHKAROFSKY, I. P. (1961) Generalized Appleton–Hartree equation for any degree of ionization and application to the ionosphere, *Proc. IRE* **49** (12), 1857–1871.
STUBBE, P. (1968) Frictional forces and collision frequencies between moving ion and neutral gases, *J. Atmos. Terr. Physics* **30**, 1965–1985.
THOMAS, J. O. (1959) The distribution of electrons in the ionosphere, *Proc. IRE* **47** (2), 162–175.
THRANE, E. V., and W. R. PIGGOTT (1966) The collision frequency in the *E*- and *D*-regions of the ionosphere, *J. Atmos. Terr. Physics* **28** (8), 721–737.
THRANE, E. V., A. HAUG, B. BJELLAND, M. ANASTASSIADES, and E. TSAGAKIS (1968) Measurements of *D*-region electron densities during the International Quiet Sun Years, *J. Atmos. Terr. Physics* **30**, 135–150.
VALLEY, S. L. (ed.) (1965) *Handbook of Geophysics and Space Environments*, Air Force Cambridge Research Laboratories, McGraw-Hill, New York, NY.
WAIT, J. R. (1962a) *Electromagnetic Waves in Stratified Media*, Pergamon Press, Oxford.
WAIT, J. R. (1962b) Theory of magneto-telluric fields, *J. Res. NBS-D Rad. Prop.* **66D** (5), 509–542.
WAKAI, N. (1967) Quiet and disturbed structure and variations of the nighttime E region, *J. Geophys. Res.* **72** (17), 4507–4517.
WEAVER, J. T. (1963) The electromagnetic field within a discontinuous conductor with reference to geomagnetic micropulsations near a coastline, *Canadian J. Phys.* **41**, 484–495.

CHAPTER 3

NATURAL SOURCES OF RADIATION

Abstract. The detailed structure of lightning discharges and the probability distributions of return-stroke currents are reviewed. The time variations of typical currents are used to calculate the frequency spectra of individual atmospherics. The received noise is considered as the result of integrating several atmospherics during the response time of the receiver. The probability distributions of this noise and of current in lightning flashes are formally related by a twofold Hankel transform. Measured amplitude distributions are satisfactorily related by the theoretical model if sources are considered at various distances from the receiver or if noise from low amplitude sources is added to the noise from return strokes.

3.1 Introduction and Summary

Lightning discharges appear as effective sources of radiation in the V.L.F. and E.L.F. ranges of frequency. In the lower E.L.F. range, the Schumann resonances of the earth-to-ionosphere cavity are excited almost exclusively by lightning discharges. In the E.L.F. and V.L.F. range, atmospherics associated with individual lightning discharges are found to propagate to large distances, and they provide convenient means for estimating the effective parameters of wave propagation. In communication systems, the radio signal must exceed the background noise provided by atmospherics; the noise statistics are also significant for determining the error rates of various communication channels.

The detailed structure of individual lightning discharges has been described in a number of survey papers [Schonland, 1956; Horner, 1964; Jones, 1967], and electric near-field measurements of Kitagawa and Brook [1960] are used to illustrate various processes of a typical lightning discharge in Section 3.2.

Based on a number of measurements, probabilities of stroke current distributions have been estimated by McCann [1944], Malan [1962], Wagner [1963], and Muller-Hillebrand [1965]. These results are summarized in Section 3.3.1. The median current of the first return stroke is shown to be in the range of 15–25 kA with no measurement data available for currents exceeding 200 kA. The time variations of typical current waveforms have been investigated by Bruce and Golde [1941], Hepburn [1957], Williams [1959], Berger [1962], and Dennis and Pierce [1964]. Together with estimated velocity variations of the return stroke, this gives means for calculating the effective dipole moments of lightning discharges. The return stroke model of Bruce and Golde [1941], which provides significant radiation only for frequencies in the V.L.F. range, can be supplemented by a model for corona currents between the leader sheath and the return channel in the first stroke [Rao, 1967]. The combination of the return stroke and of the corona current models gives dipole moments comparable to those of Hepburn [1957] over the

frequencies of the E.L.F. and V.L.F. range. However, these estimates of E.L.F. radiation are lower than in the work of Pierce [1963] that are based on estimated gross time variations of the moments in a lightning discharge. The so-called *K*-changes are observed as small rapid field fluctuations, and they are caused by the inhomogeneous charge distribution in the clouds. A model of *K*-changes is described by Arnold and Pierce [1964]; and because of their high frequency, these *K*-changes are shown to radiate also sizable amounts of V.L.F. energy. This work is summarized in Sections 3.3.2.

The spectra of individual atmospherics are calculated in Section 3.3.3 using mode theory of wave propagation in the terrestrial waveguide between the earth and the ionosphere. It is indicated that the frequently used formulas for free-space radiation fields may be misleading, particularly in the E.L.F. range where at distances comparable to the ionospheric heights, the electrostatic and induction fields dominate, while at larger distances the effects of the ionospheric boundary cannot be ignored.

A superposition of atmospherics caused by individual lightning waveforms gives rise to noise in the output of a receiver. The receiver noise is frequently measured and analyzed without specific references to sources or individual source waveforms [Watt and Maxwell, 1957a; Crichlow *et al.*, 1960]. In the theoretical model of Galejs [1966, 1967], the receiver noise is considered as a result of integrating several atmospherics during the response time of the receiver. The amplitude distribution (A.D.) of the received noise and the current in lightning strokes are related by twofold Hankel transforms. This model should consider sources at various distances from the receiver or noise from low-amplitude sources in addition to the noise from return strokes. The A.D. of the received signal is derived in Section 3.4.1 starting out with available estimates on the A.D. of return strokes. However, the return strokes from a single thunderstorm center provide noise of a rather limited dynamic range in Section 3.4.1.2. Better agreement with measured A.D. is obtained in Section 3.4.1.3 if the receiver noise arises from atmospherics arriving less frequently from nearby lightning strokes and more frequently from distant strokes. Section 3.4.2 treats the reciprocal problem of determining the A.D. of lightning currents from measured A.D. of the receiver noise. The derived return stroke current distributions for a single thunderstorm center are inversely proportional to the squared current for large amplitudes, but there is no justification for such a large amplitude extrapolation of available measurements in Section 3.4.2.2. However, the presence of frequent low-amplitude *K*-pulses of clouds-to-ground or intracloud discharges tends to decrease the probability of large amplitude return strokes; and the resulting effective source currents exhibit the theoretically postulated large amplitude behavior in Section 3.4.2.3.

3.2 Description of a Lightning Discharge

The processes of a lightning discharge will be illustrated using the field changes of Fig. 3.1 which have been recorded by Kitagawa and Brook [1960]. The upper and lower traces of the figure represent field variations recorded with short (20 μsec) and long (4 sec) time constants of the input circuit.

Gravitational separation between the lighter positively charged ice splinters and heavier negatively charged pellets of soft hail lead to negative charges near the base of the thundercloud and to positive charges at higher altitudes [Workman, 1967]. The buildup of charges produces

an increase of fields outside the thundercloud. A corona breakdown of water drops initiates a negatively charged pilot streamer or stepped leader, the fields of which are indicated as the part *L* of Fig. 3.1a. The leader requires about 50 msec to reach the ground. This path contains a number of low-intensity luminous steps, each of which corresponds to a single leader pulse lasting for a few microseconds. The return stroke *R* follows from the ground surface upwards along the ionized channel; the ionization density of this channel has diminished at its upper part, and the instantaneous velocity of the return stroke is decreased as it travels upwards. The duration of the return stroke is near 1 msec, and its peak current is of the order of 20 kA.

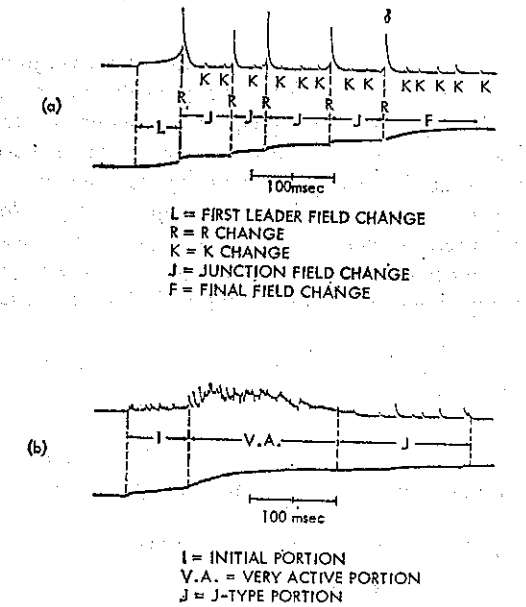

FIG. 3.1 Field Changes of Ground (a) and Cloud (b) Discharges (Adapted from Kitagawa and Brook, 1960)

During the gradual junction field change *J*, one may observe several rapid field changes *K*, which are correlated with the inhomogeneous charge distribution (or junction streamers) in the cloud. Later return strokes are preceded by a dart leader, and ionization is formed in about 1 msec. The return stroke is established in a more uniformly ionized channel, and the speed of growth is nearly constant. There may be several return strokes, and *K*-changes are observed during all of the intermediate intervals *J* and also during the final field change *F*.

The cloud discharge is illustrated in Fig. 3.1b. It is subdivided in an initial portion *I*, a very active portion *VA*, and a junction-type portion *J*. A number of small-amplitude pulses occur during the initial portion, the pulse amplitudes are larger, and pulse shapes or intervals become irregular during the very active portion. Subsequently, the field changes become similar to the

fields of a J-portion of a ground discharge; and one may observe a number of small rapid field changes K.

Kitagawa *et al.* [1962] have also recorded continuous currents (C-changes), where luminosity lasts for 40–500 msec. The luminosity is increased during small surges of current which are designated as M-changes. The M-components of a C-change correspond to K-changes observed during interstroke J and final F portions of a cloud-to-ground flash.

The return strokes R exhibit the largest current moments. The small-energy K-changes occur more frequently, and they are also present in intercloud discharges. The return strokes and K-changes appear to be the main sources of electromagnetic energy, and they will be investigated in more detail in Section 3 of this report.

Detailed descriptions of a lightning discharge and further references on the subject can be found in the papers by Horner [1964], Arnold and Pierce [1964], Jones [1967], or Pierce [1969].

3.3 Mathematical Models of Lightning Discharges

Lightning waveforms exhibit widely varying parameters; and some characteristics like amplitudes, interstroke intervals, or number of return strokes per flash, are described by statistical distributions. Still, a number of authors have defined models of median or average returns strokes, which are based on different measurements and therefore do not agree in all details. Some models are valid only for the V.L.F. range of frequencies; there are also models that consider current components of longer durations, which may produce significant E.L.F. radiation. The amplitude distributions of return strokes and also several models of lightning waveforms are reviewed in this section. The dipole moment of a given lightning waveform will characterize its effect in exciting long-distance radial fields that are observed in the form of individual atmospherics. Discussed also are the distance variations of the frequency spectra of individual atmospherics. It is also possible to compute the radiated fields by assuming the lightning discharge to occur in a semi-infinite free-space region above a perfectly conducting flat ground plane. Such calculations may be difficult to interpret physically, particularly in the E.L.F. range. It may be also misleading to use similar free-space formulas to compute the equivalent dipole moment of experimentally observed waveforms. In the near-field range, this will neglect the sizable electrostatic and induction fields that are extended for E.L.F. sources to distances exceeding the ionospheric height. At larger distances, it may be more appropriate to use the waveguide mode theory to establish a relation between an equivalent dipole moment of a source and the observed field strength. The free-space formulas are still used by several authors, and such field-strength data will be quoted only for purposes of a comparison.

3.3.1 *Amplitude Distribution of Return Strokes*

The amplitude distribution of peak currents is illustrated in Fig. 3.2, where source current estimates of various authors are plotted on a log–log versus log–scale. The uncertainties in the peak-current distributions of the return strokes are illustrated by the spread between the curves reported by McCann [1944], Wagner [1963], Muller-Hillebrand [1965], and Malan [1962]. The largest current reported by McCann [1944] is 160 kA, which compares with 180 kA observed by Berger [1962]. The source current amplitudes are frequently represented by log–

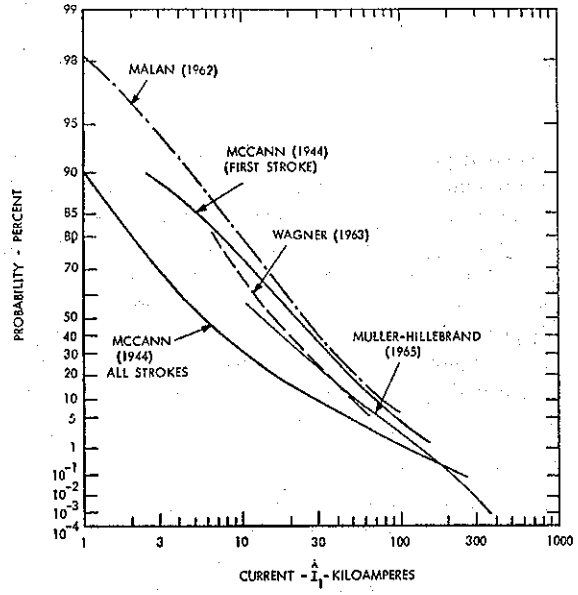

FIG. 3.2 Probability Distribution of Current Peaks in a Lightning Flash $P(\hat{I}_k \geq \hat{I}_1)$

normal distributions. The probability that the peak current of a return stroke $\hat{I}_k$ exceeds the current $\hat{I}_1$ is then given by

$$P(\hat{I}_k \geq \hat{I}_1) = \frac{1}{\sigma\sqrt{2\pi}} \int_{\hat{I}_1}^{\infty} \frac{d\hat{I}_k}{\hat{I}_k} \exp\left[-\frac{(\log \hat{I}_k - m)^2}{2\sigma^2}\right] = \frac{1}{2}\left[1 - \operatorname{erf}\left(\frac{\log \hat{I}_1 - m}{\sigma\sqrt{2}}\right)\right], \quad (1)$$

where m is the median value of $\log \hat{I}_k$, the logarithms are computed with the base e, and σ is the standard deviation. The average value of $\log \hat{I}_k$ is $m \exp(\sigma^2/2)$ and the R.M.S. value is $m \exp(\sigma^2)$. On a probability versus log–scale, a log–normal distribution is characterized by a straight line of a slope inversely proportional to the standard deviation σ. The curves of McCann [1944] measurements are replotted in Fig. 3.3. The all-stroke data appear linear over the whole range of probabilities with $\sigma = 11.2$ db. The first-stroke data exhibit a four times higher median value and appear linear for $P < 50$ percent. In the linear portion, the curve exhibits $\sigma = 7.9$ db. For large amplitudes, the probability for a given current is approximately four times lower when considering all of the return strokes.

3.3.2 *Current Waveforms and Dipole Moments*

The waveforms of lightning discharges are approximated by exponential functions of the form

$$i(t) = \sum_j I_j \exp(-t/\tau_j) \quad (2)$$

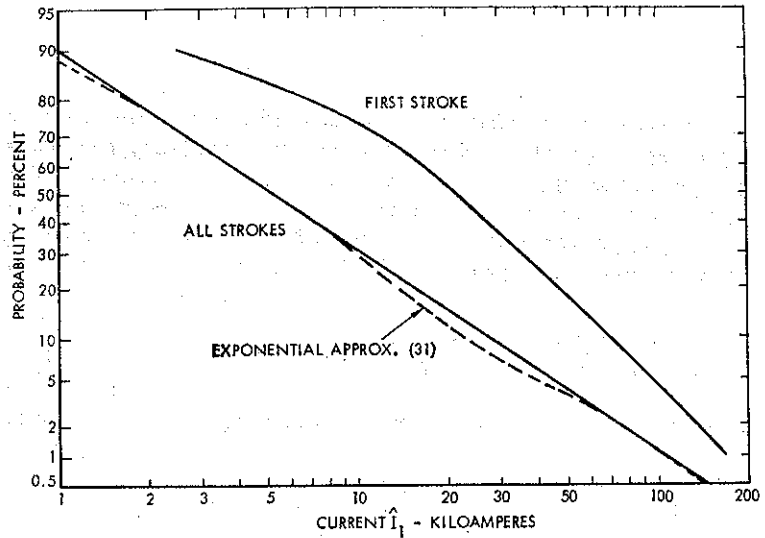

FIG. 3.3 Probability Distribution of Current Peaks in the Lightning Flash $P(\hat{I}_k \geq \hat{I}_1)$. Measurements of McCann (1944)

The waveform parameters suggested by Bruce and Golde [1941], Williams [1959], and Hepburn [1957] are listed in Table 3.1. The paper of Dennis and Pierce [1964] discusses also current waveforms that are representative of Berger's measurements [1961] of first and subsequent strokes, the parameters of which are listed in Table 3.1.

TABLE 3.1. PARAMETERS OF WAVEFORM APPROXIMATIONS
(I_j in kA, τ_j in μsec)

	j	1	2	3	4
Return strokes by: Bruce and Golde	I_j	28.4	−28.4		
	τ_j	22.8	2.18		
Williams	I_j	−16,8	15.35	1	0.45
	τ_j	1.7	33	500	6800
Hepburn	I_j	20	−25	5	
	τ_j	20	2	1430	
Berger (first)	I_j	30	−30		
	τ_j	50	5		
Berger (subsequent)	I_j	10	−10		
	τ_j	71.5	0.166		
Corona by Rao	I_j	3.3	−3.3		
	τ_j	2900	337		
K-Pulse by Arnold and Pierce	I_j	16	−16	(5.3)	(−5.3)
	τ_j	20	5	(200)	(50)

There are also lateral corona currents which are caused by the high potential differences between the leader sheath and the return channel in the first stroke of a lightning flash. Based on the return stroke model of Bruce and Golde [1941], Rao [1967] has reported detailed calculations of the corona currents, which are shown to radiate significant amounts of E.L.F. energy. These corona currents have been represented as a sum of two exponential terms of the form shown in Table 3.1.

Several K-changes occur per each return stroke in a ground discharge, and K changes are considered to be the main source of radiation in intracloud discharges. In tropics, intracloud discharges are believed to be predominant: ground flashes, on a seasonal average, constitute about 10 per cent of all flashes in India [Aiya, 1968], which is in contrast to the 40 per cent figure applicable to moderate latitudes; hence, K-changes may be even more important than the return strokes for fields in the V.L.F. range [Jones, 1967]. The K-pulse waveforms have been represented as a sum of two exponentials by Arnold and Pierce [1964] with parameters that are indicated in Table 3.1. For this representation of K-pulses, the total charge $\int_0^\infty i(t)\,dt = 0.24$ C. Estimates based on the electrostatic component of the field change indicate a charge of about 1 C and a current in excess of 1 kA for durations of several hundred microseconds. Pierce [1969] suggests a modification of the K-pulse waveform by the addition of two more terms, which are indicated in parentheses in Table 3.1. The total charge of the modified K-pulse is 1.04 C, and the spectral dipole moment would be increased sixfold for E.L.F. in Fig. 3.5. However, this modification is not included in the subsequent calculations.

The resulting current waveforms are computed from (2) and are shown in Fig. 3.4. Most of the waveforms exhibit comparable rise times, and the waveforms reach a peak in about

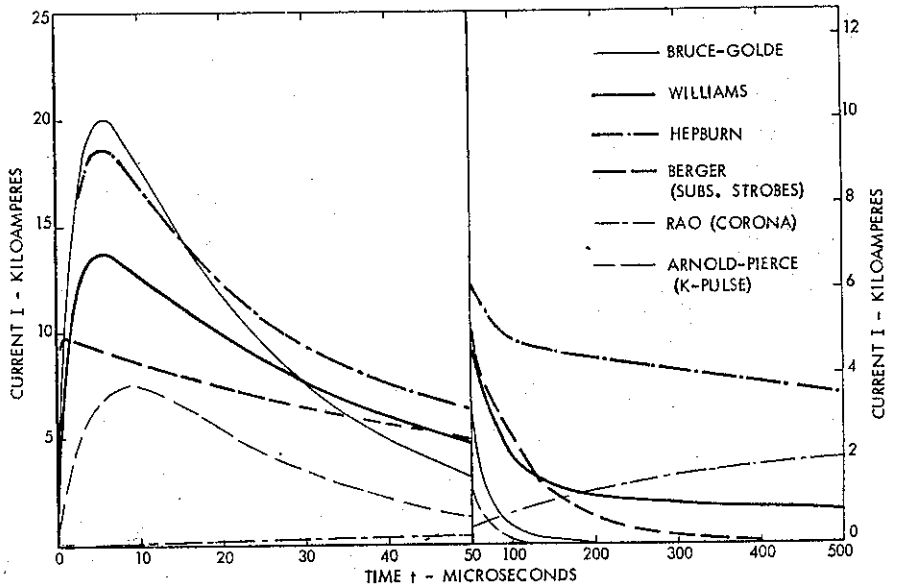

FIG. 3.4 Current Waveforms of Lightning Discharges

5–8 μsec. The subsequent strokes of Berger [1961] peak in 1 μsec; the corona current of Rao [1967] exhibits a very slow rise time, and it reaches its maximum value at 900 μsec, which is beyond the scale limit of Fig. 3.4. The amplitudes of the return strokes in the Bruce and Golde [1941] model and also the *K*-change waveforms, decay to negligible values in about 100 μsec. The subsequent strokes of Berger [1961] reach small amplitudes in about 300 μsec. The first-stroke waveforms of Berger [1961], not shown in Fig. 3.4, exhibit a decay that is intermediate between the subsequent-stroke waveforms and the waveforms of Bruce and Golde [1941]. The waveforms of Williams [1959] and Hepburn [1957] exhibit a gradual decay. The time constant τ_n of the last term of Williams [1959] approximation is even larger than in the corona representation by Rao [1967].

The first stroke follows the leader stroke which lasts for about 50 msec. During this time, the ionization density of the channel has diminished at its upper part; and the rate $v(t)$ at which the return stroke extends upwards in the preionized channel between the ground surface and the thundercloud is decreased with time. The subsequent return strokes are preceded by a dart leader, and ionization is formed in approximately 1 msec. The return stroke penetrates upward along a better ionized channel, and its velocity is assumed to be nearly constant. The velocity of return strokes may be represented as

$$v(t) = \begin{cases} v_0 & \text{for} \quad 0 \leq t \leq t_p, \\ v_0 \exp\left[-(t-t_p)/\tau_v\right] & \text{for} \quad t_p \leq t. \end{cases} \tag{3}$$

Most authors use $t_p = 0$, $v_0 = 8\times10^7$ m/sec, $\tau_v = 33.3$ μsec for the first stroke, and $\tau_v = \infty$ for the subsequent strokes following Bruce and Golde [1941] and Schonland [1956]. In the work of Williams [1959], $t_p = 43$ μsec, $v_0 = 3.5\times10^7$, and $\tau_v = 180$ μsec for a median stroke of a multistroke flash, which is intermediate between the earlier values of τ_v for first and following strokes. For *K*-pulses $v_0 = 2\times10^7$ m/sec and $\tau_v = 25$ μsec.

The dipole moment of the waveform (2) is computed as

$$\begin{aligned} ids(t) = i(t)\int_0^t v(t')\,dt' &= v_0\sum_j I_j \exp\left(-\frac{t}{\tau_j}\right) t[u(t)-u(t-t)] \\ &+ v_0\sum_j I_j \exp\left(-\frac{t}{\tau_j}\right)\left[t_p+\tau_v-\tau_v\exp\left(-\frac{t-t_p}{\tau_v}\right)\right]u(t-t_p) \end{aligned} \tag{4}$$

where $u(x)$ is a unit step function. The frequency spectrum of the dipole moment is defined as

$$Ids(\omega) = \int_{-\infty}^{\infty} i\,ds(t)\exp(-i\omega t)\,dt = v_0\sum_j \frac{I_j\tau_j^2}{(1+i\omega\tau_j)^2}\left[1-\frac{\tau_j\exp\left[-i\omega t_p - t_p/\tau_j\right]}{\tau_j+\tau_v+i\omega\tau_v\tau_j}\right]. \tag{5}$$

The frequency spectra of the dipole moments are calculated for the current waveforms of Fig. 3.4 and are shown in Fig. 3.5. The parameters of $v(t)$ by Bruce and Golde [1941] and Schonland [1956] are used for all the calculations except for the return stroke models of Williams [1959]. The rapidly decaying current wave forms (return strokes of Bruce and Golde, Berger, *K*-pulses of Arnold and Pierce) exhibit nearly constant spectral amplitudes in the E.L.F. range. The slowly decaying current waveforms (return strokes of Hepburn and Williams, corona by

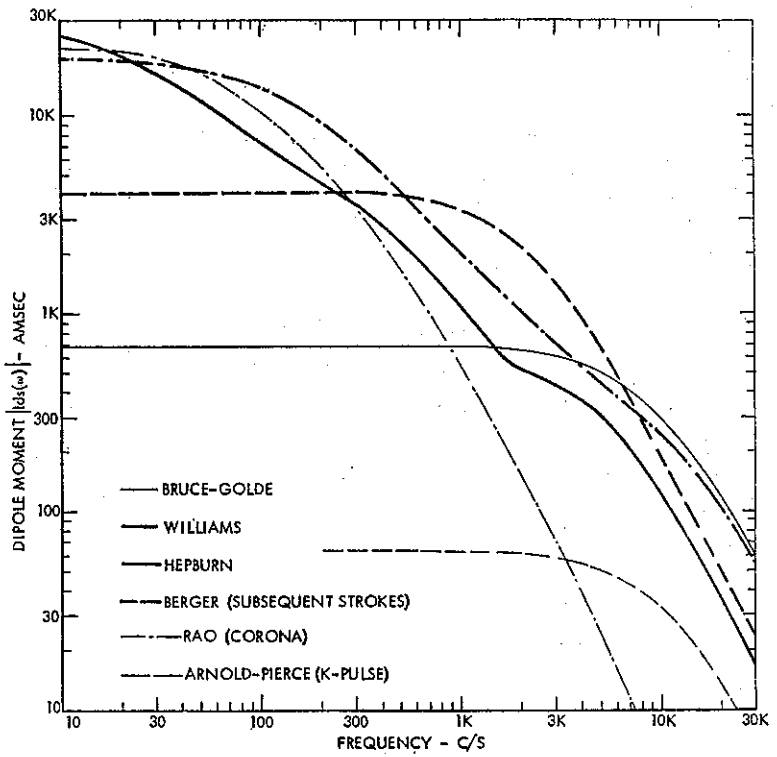

FIG. 3.5 Spectrum of the Dipole Moment for a Median Lightning Flash

Rao) exhibit comparable spectral components in the lower E.L.F. range. The waveform estimate of Williams [1959] contains terms with the longest time constants ($\tau_4 = 6.8$ msec in Table 1), and it is the only one which shows a nonzero slope near the lower Schumann resonances ($f \approx 10$ c/s). For higher frequencies, the current model of Hepburn [1957] approximates the spectra of Bruce and Golde [1941] while the Williams [1959] multiple return-stroke model exhibits spectra that are comparable to Berger's [1961] model of following strokes. The corona spectra of Rao [1967] decay rapidly at higher frequencies. However, the sum of the corona spectrum and the return-stroke spectrum by Bruce and Golde [1941] is comparable to the spectrum of Hepburn [1967] for most of the frequency range shown in Fig. 3.5. The corona spectrum of Rao [1967] was based on the return-stroke model of Bruce and Golde [1941], and it appears to provide a satisfactory extension of the Bruce and Golde lightning model to lower frequencies.

Dennis and Pierce [1964] use the Bruce and Golde [1941] current model of two exponentials and an exponentially decaying return-stroke velocity. They have investigated the effects of a lightning charge which moves in the channel at a finite velocity u, where $c \geq u \geq v_0$, c is the free-space velocity of electromagnetic waves, and v_0 is the maximum rate at which the return

stroke grows upward. The upper bound $u = c$ gives a 5 percent increase in the radiated fields at 25 kc/s, but a 20 percent increase at 1 kc/s. At the lower bound $u = v_0$, the radiated fields are increased by 20 percent at 25 kc/s and by 60 percent at 1 kc/s.

In the previous discussion, the waveform of the first-return stroke was considered to differ from the waveforms observed for subsequent strokes. However, Bradley [1965] has examined the spectra of first and subsequent strokes at the frequencies of 6 and 10 kc/s and has not been able to observe any systematic differences.

An alternate estimate of the effective dipole moment for the E.L.F. range has been provided by Pierce [1963]. The gross time variation of the vertical electric moment of a cloud-to-ground discharge is approximated as

$$ids(t) = \frac{1}{\sqrt{\pi}} \sum_j A_j h_j \exp(-h_j t^2), \tag{6}$$

where $h_1 = 40$, $h_2 = 1000\ h_1$, $h_3 = 25\ h_1$, $A_1 = 80\times10^3$, $A_2 = 5\times10^3$, and $A_3 = 35\times10^3$. The first term represents the contributions from the leader and the final stage of a lightning flash, the second is due to the return strokes, and the third accounts for any continuous currents following the return stroke and also for the increased rate of change of the moment just before the leader reaches the ground surface. Intracloud discharges are modeled similarly, but with only one term of amplitude $A_1 = -120\times10^3$ and with the same value for h_1. The spectrum of the discharge (6) is computed as

$$Ids(\omega) = \sum_j A_j \exp[-(\omega/2h_j)^2]. \tag{7}$$

For a cloud-to-ground discharge and frequencies $f = 10$, 100, and 1000 c/s, equation (7) gives $Ids(\omega) = 8.4\times10^4$, 4×10^4, and 5×10^3 Amsec, which are larger than the spectral dipole moments of Fig. 3.5. The spectra of (7) will exhibit rapid amplitude changes near the frequencies $\omega = 2h_j$, which correspond to $f = 13$, 320, and 13000 c/s.

The power spectrum of the dipole moment for a single lightning stroke will be proportional to the square magnitude of the frequency spectrum of the dipole moment. Based on Williams' [1959] model of multiple strokes, Raemer [1961] has computed the power spectrum by assuming that the interstroke interval T is normally distributed about a median value $T_0 = 33$ msec with a standard deviation $\sigma_T = 7$ msec and by considering the finite probabilities of multiple strokes. The probabilities P_n of n return strokes per flash are approximated by 0.15, 0.22, 0.23, 0.15, 0.09, 0.06, 0.04, 0.03, and 0.01 for n from 1 to 10, with a median value of $n = 2.5$. The calculations of Raemer [1961] have led to the power spectrum estimates shown in Fig. 3.6 for frequencies in the range of Schumann resonances. Rycroft [1963] has calculated the frequency spectrum of the source dipole moment using a representation similar to the one shown in (6). The squared magnitude of this frequency spectrum is also indicated in Fig. 3.6, where the rapid decay in the frequency range between 10 and 20 c/s is caused by the $j = 1$ term of (7). Shown by thin lines is the squared magnitude of the dipole moment of Williams' [1959] average return stroke from Fig. 3.5 that is normalized to unity at $f = 10$ c/s. The decay of this latter curve is more gradual than for the other curves shown in Fig. 3.6.

The median interstroke interval T_0, used in calculating the spectrum of a single lightning flash, will differ from times T_n between pulses in an atmospheric noise envelope, where the

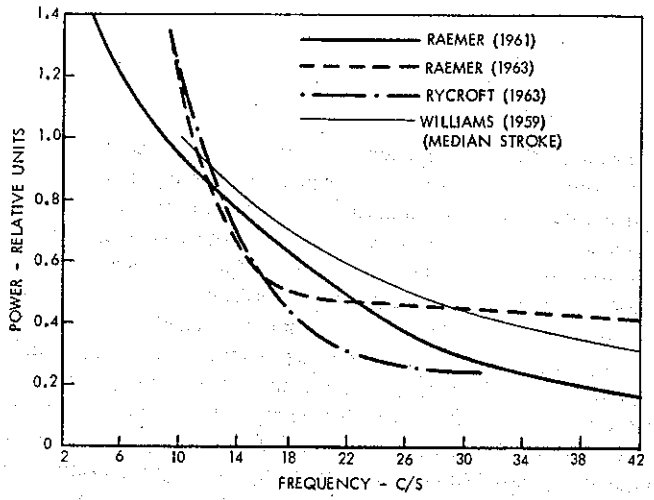

FIG. 3.6 Estimated Lightning Flash Spectrum

successive pulses may be caused by different lightning flashes. For low thresholds, the median interpulse interval is less than 1 msec in V.L.F. measurements; for high thresholds, it can exceed 100 msec. For threshold fields near 1 mV/m, the median value of $T_n \approx 100$ msec; but the probability density $\Delta P/\Delta T_n$ exhibits its maximum value at $T_n \approx 15$ msec [Watt and Maxwell, 1957a; Nakai, 1968].

3.3.3 *Spectra of Individual Atmospherics*

The spectrum of individual atmospherics can be calculated from the dipole moment of a lightning waveform in a fixed source and receiver geometry. It is also possible to compute the radiated fields by assuming the lightning discharge to occur above an infinite conducting ground plane. However, in the interpretation of such calculations, it must be remembered that the actual radiation occurs in the earth-to-ionosphere waveguide. In the near-field measurements, the effects of the upper guide boundary may be neglected; but one may not neglect the sizable electrostatic or induction fields that are extended to distances exceeding the waveguide height for frequencies in the E.L.F. range. At larger distances, the field variations can be conveniently described using mode theory. The resulting field variations will be functionally different from the free-space fields. Although the free-space radiation fields are often quoted in the literature even for the E.L.F. range, such calculations appear to be a carryover from the work at higher frequencies, where the power radiated by the antenna may be legitimately estimated from the simple free-space formulas. The field strength estimates of this section will be based on mode theory; but a few examples will also consider the free-space radiation fields, where such data will be quoted in the literature. The concept of free-space radiation fields is used only in comparisons, and it is not implied that these are the actual fields observed at the quoted reference distances.

The frequency spectrum of the received signal can be computed from standard expressions of mode theory. The vertically polarized source and the receiver are both at the ground level, and (104) of Chapter 4 simplifies to

$$\left|\frac{E_r(\omega)}{Ids(\omega)}\right| \approx \frac{\omega\mu_0}{h} \frac{|A_n S_n^{1.5}|}{\sqrt{2\pi a k_0 \sin\theta}} \exp\left[-ak_0\,\theta\,\mathrm{Im}\,(S_n)\right]. \tag{8}$$

In the above expression, a is the radius of the earth, h is the height of the lower ionosphere edge, θ is the polar angle between the source and receiver, and n designates the modes. For E.L.F., $n = 0$ and the excitation factor $A_0 = 0.5$; for V.L.F., $n = 1$ and $A_1 \approx 1$ for purposes of a crude estimate. More accurate values of A_n are seen in Figs. 4.6 and 4.9 (pp. 96 and 115). S_n can be interpreted as the ratio between the complex phase constant for propagation along the surface of the earth in mode n and the phase constant of free space k_0. Hence, Re S is inversely proportional to the phase velocity and Im S is proportional to the attenuation rate. Equation (8) is not valid in the immediate vicinity of the source or of its antipode when the inequalities $|\nu\theta| \gg 1$ and $|\nu(\pi-\theta)| \gg 1$, (where $\nu = k_0 aS - 0.5$) are not satisfied.

The signal spectrum $S(\omega)$ at the output of the I.F. amplifier or at the input of the linear detector is related to the input spectrum $E_r(\omega)$ by the effective transfer function of the R.F. and I.F. amplifiers $H(\omega)$ as

$$S(\omega) = H(\omega)\, E_r(\omega). \tag{9}$$

The filter impulse response $h(t)$ is related to $H(\omega)$ by

$$h(t) = \frac{1}{2\pi} \int_{-\infty}^{\infty} H(\omega) \exp(i\omega t)\, d\omega. \tag{10}$$

The filter is assumed to be an ideal integrator at the frequency ω_0 with

$$h(t) = \frac{A}{T} \exp(i\omega_0 t) \quad \text{for} \quad 0 \leqslant t \leqslant T \tag{11}$$

and with $h(t) = 0$ for other values of t. The corresponding transfer function $H(\omega)$ is

$$|H(\omega)| = A\left|\frac{\sin x}{x}\right|, \tag{12}$$

where $x = (\omega - \omega_0)\, T/2$. This $\sin x/x$ shaped band-pass filter has a 3 db bandwidth of $\Omega = 2\pi\, 0.89/T$. The spectrum of the wide-band signal $E_r(\omega)$ will be relatively constant over the narrow pass-band of the filter and

$$S(\omega) \approx H(\omega)\, E_r(\omega_0). \tag{13}$$

Hence

$$S(t) = \frac{1}{2\pi} E_r(\omega_0) \int_{-\infty}^{\infty} H(\omega) \exp(i\omega t)\, d\omega = E(\omega_0)\, h(t). \tag{14}$$

The observed signal $S(t)$ is therefore proportional to the impulse response $h(t)$ and to the input spectrum $E_r(\omega_0)$. The received signal which is due to the median return stroke of current moment $ids(t)$ is observed in a narrow frequency band around the frequency ω, and its spectrum is

$$C = Ids(\omega)\, F(\omega), \tag{15}$$

where $F(\omega)$ is given by

$$|F(\omega)| = \frac{E_r(\omega_0)}{Ids(\omega_0)} \frac{A}{T}. \tag{16}$$

In (16), T is the integration time of the filter and A is the receiver gain at the center of the pass-band. The parameter C relates the signal $S(t)$ to the median current of the lightning waveform I_{med}, where C depends on the frequency spectrum $Ids(\omega)$, the excitation efficiency of the waveguide modes in the earth-ionosphere waveguide, the distance between the source and the receiver, and on the receiver bandwidth.

The transfer function of the earth-to-ionosphere waveguide in (8) is computed using the parameters of an exponential isotropic daytime ionosphere [Galejs, 1962, 1964b]. After considering the effects of the finite receiver bandwidth as shown in (16), it is possible to compute the field strength at a distance d from the source which is due to the median lightning flash with a dipole moment of Fig. 3.5. The parameter $C = |Ids(\omega)\, F(\omega)|$ designates the fields observed in the receiver of integration time T (the 3 db bandwidth is $0.89/T$ c/s) at a distance d from the medium lightning stroke, and it is shown in Fig. 3.7 and 3.8 for fields in the E.L.F. and V.L.F. ranges respectively.

In the E.L.F. range, the fields exhibit a maximum for frequencies from 15 to 30 c/s; and they exhibit a rapid decay for frequencies exceeding a few hundred cycles per second. Fischer [1965] has reported spectrum measurements from 50 to 20 μV/m in 1 c/s bandwidths in the frequency range from 10 to 100 c/s, and similar field intensities for frequencies near 100 c/s have been obtained from frequency spectra of atmospheric waveforms [Mikhaylova, 1967]. This compares with 100 to 50 μV/m field strength in a 6 c/s bandwidth for a distance of 3000 km from the source for a single atmospheric as shown in Fig. 3.7. Both sets of numbers are of comparable order of magnitude but are difficult to compare directly because measurements refer to the integrated effect of numerous lightning discharges over a wide range of distances, and the computations are made for a single atmospheric. The measurements by Balser and Wagner [1960] made in the frequency range from 60 to 100 c/s indicate also a gradual decay of the frequency spectrum. Barr [1968] has recorded the E.L.F. amplitude spectra of a number of atmospherics propagated over a distance of 1050 km. The arithmetic mean of the spectral amplitudes is equal to 80, 80, 45, and 12 μV sec/m at frequencies $f = 35$, 100, 300, and 1000 c/s respectively. This compares with C of 175, 135, 93, and 24 μV/m in Fig. 7 for fields of the median lightning stroke of Williams [1959] that are observed at a distance of 1000 km with 0.166 sec integration time. After converting C to spectral amplitudes, the median fields are approximately three times lower than the average fields of Barr [1968]. This can be attributed in part to differences between averages and median values of the recorded waveforms, which are also discussed in connection with V.L.F. observations.

In the V.L.F. range, the present calculations of 0.2 mV/m at 10 kc/s over a 50 c/s bandwidth at a distance of 1000 km from a source compare with the computations of Watt and Maxwell

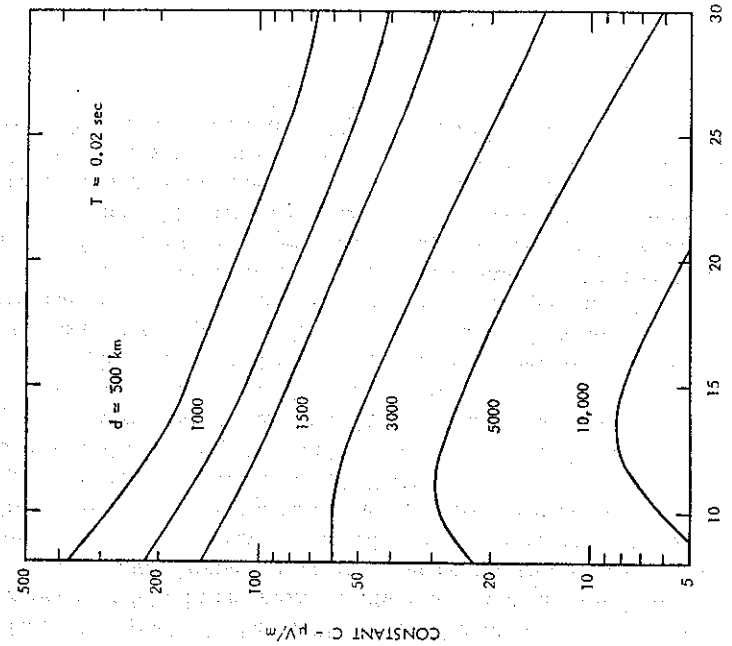

FIG. 3.8 Fields of the Median Lightning Flash in the V.L.F. Range

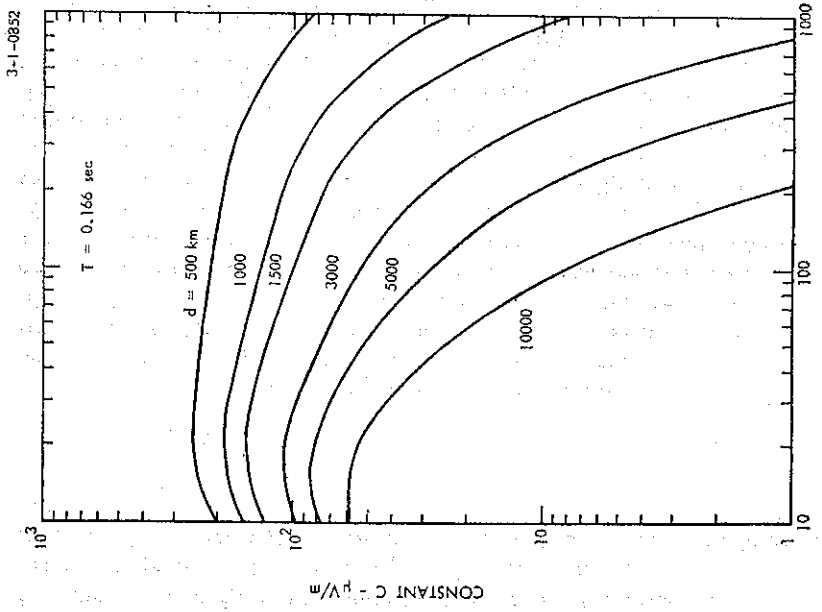

FIG. 3.7 Fields of the Median Lightning Flash in the E.L.F. Range

[fig. 8, 1957b], who report 18 mV/m in a 1 kc/s bandwidth. The filter output will be proportional to the bandwidth for a single lightning waveform, and the field strength computed in Fig. 3.8 is about four times lower than in the computations by Watt and Maxwell [1957b], who used a different model of the average lightning discharge. Taylor [1960] has measured V.L.F. frequency spectra of single atmospherics at various distances d. At $f = 10$ kc/s and $d = 1600$ km, the measured spectral amplitude is 60 μV sec/m; at $d = 4500$ km, it is 16 μV sec/m. After converting the constants C to the bandwidth of 1 c/s, Fig. 3.8 gives the spectral amplitudes 2.74 and 0.62 μV sec/m for distances $d = 1500$ and 5000 km respectively. The relative distance variation is approximately the same in measurements and calculations, but the measured magnitudes are much larger, which indicates that the waveforms of Taylor have amplitudes that exceed the median amplitudes of the theoretical model by more than 26 db.

A quantitative justification of the present lightning model [Williams, 1959] can be obtained by computing the hypothetical free-space fields radiated by the current moment of Fig. 3.5 and by comparing the resulting field strength with similarly reduced near field measurements. The radiated fields can be computed from the usual free-space formula ($E = 120\pi\, Ids/\lambda d$, where the distance d and the wavelength λ are in meters). When normalizing to $d = 1$ km, the median spectral component at $f = 10$ kc/s is 1.53 mV sec/m. Dennis and Pierce [1964] report an average measured value of 2.6 mV sec/m, and the theoretical model of Hill [1966] gives also a comparable field strength figure. For the statistics under consideration, the average of an amplitude distribution is higher than its median value [Watt and Maxwell, 1957a], and also the average of spectral components is nearly two times its median value [table 2, Horner, 1961]. This can be also seen from the relations listed following (1).

The radiation fields of the present lightning model are therefore consistent with the measurements reported by Dennis and Pierce [1964]. Volland [1964, 1966] uses an average figure of 1.65–1.7 mV sec/m for 10 kc/s, and the strong indidual atmospherics observed by Taylor and Jean [1959] at a distance of 150–600 km exhibit a spectrum of 6.6 mV sec/m when referred to $d = 1$ km. Also, the transient waveform of the radiation fields in the present model of the median, return stroke [fig. 7.1 of Williams, 1959] compares closely with waveform observations reported by the University of Florida [Sullivan *et al.*, 1955, 1956].

The preceding discussion of atmospheric spectra has been restricted to vertically oriented source currents, and it neglected the effects of finite source heights. Horizontal current components are present also in cloud-to-ground lightning discharges [Hill, 1969]. In E.L.F. measurements, waveforms with an initial positive polarity are usually associated with cloud-to-ground discharges; but the more frequent small amplitude slow-tail waveforms of negative polarity are generated principally by intracloud strokes following Tepley [1961]. The presence of clouds prevents a detailed optical examination of intracloud discharges. However, such discharges may be uniquely identified by measuring the difference in arrival times between signals reflected from the ionosphere and signals reflected from ground surface and ionosphere, which leads in the work of Taylor [1969] to source elevations of 5–11 km.

The fields at the ground surface of an elevated source of altitude z_s are related to the fields of a ground-based source ($z_s = 0$) by the height-gain function $G_n(z_s)$, which is essentially unity for frequencies in the E.L.F. range. In the V.L.F. range $|G_n(z_s)|$ deviates by less than 20 percent from unity for the two lowest T.M. modes for frequencies between 10 and 30 kc/s following Fig. 4.10 (p. 116).

There is a problem of determining the effective horizontal and vertical dipole moments of a given lightning discharge. For equal dipole moments and source altitudes, the ratio of the vertical electric fields on the ground surface excited by horizontal and vertical currents may be computed from (131) of Chapter 4. Along the axis of the horizontal dipole, this ratio is in the first approximation equal to the normalized impedance $\Delta_n(z_s)$, where z_s is the altitude of the source. The plots of $\Delta_n(z_s)$ are shown for the E.L.F. and V.L.F. range in Fig. 4.5 and 4.11 (p. 95 and 117) respectively. The magnitude of $\Delta_n(z_s)$ is less than unity, and the horizontal dipole will excite the weaker fields.

3.4 Statistical Models for Relating Source and Receiver Waveforms

A superposition of atmospherics caused by individual lightning waveforms gives rise to noise in a receiver output. This noise is generally measured and analyzed without specific references to sources or individual atmospherics. Measured amplitude distributions of terrestrial V.L.F. noise have been reported in the literature, and the measured envelope of the received noise exhibits for high signal levels significant deviations from a Rayleigh distribution which characterizes the envelope of a narrow-band Gaussian noise [Watt and Maxwell, 1957a; Crichlow *et al.*, 1960]. Fulton [1961] has considered the effects of the receiver bandwidth on the amplitude distribution of the low-probability nonoverlapping high-intensity noise bursts, and a more general method for converting amplitude distributions from one bandwidth to another has been developed by Spaulding *et al.* [1962]. Impulsive random noise that may be representative of atmospheric waveforms has been discussed by Middleton [1960], and amplitude distributions of Poisson noise have been compared with a number of measurements by Furutsu and Ishida [1961]. Beckmann [1964] assumes that an individual atmospheric exhibits an exponential rise and decay and shows that the computed amplitude distribution for a superposition of such individual atmospherics is in a good agreement with measurements by Crichlow *et al.* [1960]. Volland [1963] shows that the measured amplitude distribution of V.L.F. noise is related by an integral equation to the geographical distribution of lightning sources, to the transfer function of the earth-to-ionosphere waveguide, and to the lightning waveforms. Measuring the amplitude distribution of V.L.F. noise at a single station and using the transfer function of the waveguide, he obtains estimates of the distance from the lightning sources to the receiver [Volland, 1964].

The amplitude distributions (A.D.) of E.L.F. and V.L.F. noise can be related to the A.D. of the source dipole moments or to the A.D. of lightning waveforms. In the mathematical model, all the lightning strokes are assumed to have the shape of the median return stroke, but varying amplitudes. The probability distribution of waveform amplitudes is assumed to be the same as for current peaks in cloud-to-ground flashes. This latter amplitude distribution is approximated in a numerical example as a sum of two exponentials. Frequency spectra of received atmospherics that correspond to a median return stroke have been discussed in Section 3.3.3. These spectra will present a scale factor C between the probability densities of source currents and of the received noise waveforms, as will be shown in Section 3.4.1.1. The observed signal is due to a number of lightning discharges. This number n is proportional to the thunderstorm activity (flashes per unit time) and also to the effective integration time T of the receiver. The computations will show the probability P that the amplitude of the signal exceeds the value r if n atmospheric waveforms arrive at the narrow-band receiver tuned to frequency ω during its integration time T from a thunderstorm center over a distance d. For a large number of lightning waveforms (small bandwidths or frequent lightning discharges), the probability distribution of the received signal approaches that of a Rayleigh distribution for small signal amplitudes. However, large signal amplitudes are more probable than in an envelope of Gaussian noise which is characterized by a Rayleigh distribution, as will be shown in Section 3.4.1.2.

Available measurements of lightning currents or of the near-field radiation are carried out over a dynamic range of approximately 30 db [McCann, 1944; Dennis and Pierce, 1964] while A.D. of receiver noise is frequently reported over a range exceeding 80 db [Watt and Maxwell, 1957a; Crichlow *et al.*, 1960]. Receiver noise with a dynamic range of 60–70 db has been observed for sources from a distance range of 2000–4000 km [Watt and Maxwell, 1957b]. Assuming identical source characteristics, the above distance variation accounts only for approximately 6 db in the amplitude range of the received noise. The scale factor C between the probability densities of the source current and the received noise depends on the median value of source current and on the distance between the source and receiver. A constant scale factor would produce amplitude distributions of the received noise and source currents of comparable dynamic range. The dynamic range of the received noise can be increased considering the contributions of atmospheric noise originating at various distances or by examining sources other than return strokes of lightning flashes. An example of Section 3.4.1.2 will consider atmospherics arriving from different distances; and the effects of lower amplitude K-changes will be examined in Section 3.4.2.3, where the A.D. of lightning waveforms are computed by starting out with the A.D. of the received noise. The effects of bandwidth transformation are discussed in Section 3.4.1.4; and it is shown that the bandwidth transformation of Fulton [1961] is justified for large amplitudes, when nonoverlapping pulses may be assumed within the memory time of the filters.

3.4.1 Probability Distribution of the Received Signal

3.4.1.1 Formal Solution

Probability distributions of current peaks in cloud-to-ground lighting flashes have been listed in Fig. 3.2 and 3.3. A random variable

$$z_k = I_k / I_{\text{med}} \tag{17}$$

is defined as the ratio between the peak current I_k of a particular stroke k and the median value I_{med} of the peak current for a number of strokes. The measurement data can be represented by the cumulative probability

$$P(z_k \geq z_0) = \int_{z_0}^{\infty} w(z_k)\, dz_k. \tag{18}$$

The amplitude of the received signal, which is due to a lightning stroke of peak current amplitude I_k, is defined as $r_k = Cz_k$, and its probability density is

$$w_1(r_k) = (1/C)\, w(r_k/C). \tag{19}$$

The scale factor C is given in (15) as

$$C = \left| Ids(\omega) \frac{E_r(\omega)}{Ids(\omega)} \frac{A}{T} \right|. \tag{20}$$

This scale factor is proportional to the frequency spectrum of the current moment in a median lightning waveform $Ids(\omega)$ and to the receiver's gain A and inversely proportional to the integration time T. The scale factor C is also proportional to the transfer function between the received signals $E_r(\omega)$ and the spectrum $Ids(\omega)$, which depends on the excitation efficiency of the waveguide mode in the earth-to-ionosphere guide, on the propagation characteristics, and on the distance d between the source and the receiver. The received signal $r \exp(i\varphi)$, which is due to n lightning strokes is obtained by summing n values of r_k with an assumed random phase angle φ_k of the individual terms. Thus

$$re^{i\varphi} = \sum_{k=1}^{n} r_k \exp(i\varphi_k) \quad \text{or} \quad x+iy = \sum_{k=1}^{n} (x_k+iy_k). \tag{21}$$

The random phase angle φ_k does not affect the probability distribution of the signal amplitude r_k, and the two-dimensional probability density of random phase can be expressed as

$$w(r_k, \varphi_k) = w_1(r_k)\, w_2(\varphi_k) = \frac{1}{2\pi} w_1(r_k). \tag{22}$$

The density $w(r_k, \varphi_k)$ of (22) represents the amplitude and phase distributions of a received signal due to a single lightning waveform. The probability density of the signal r of (21) will be determined after first computing the characteristic function of the variables x_k and y_k as

$$C_k(u, v) = \int_{-\infty}^{\infty} \int_{-\infty}^{\infty} dx_k\, dy_k \exp(iux_k) \exp(ivy_k)\, w(x_k, y_k). \tag{23}$$

Changing to polar coordinates and evaluating the φ integral for a φ-independent density $w(r_k, \varphi_k)$, (23) can be also expressed as

$$C_k(\varrho) = 2\pi \int_0^{\infty} dr_k\, J_0(\varrho r_k)\, w(r_k, \varphi_k), \tag{24}$$

where $\varrho = \sqrt{u^2+v^2}$ and $J_m(x)$ is the Bessel function of first kind of order m. The characteristic function of a sum of uncorrelated variables (21) is the product of their characteristic functions. If all the probability densities $w(x_k, y_k)$ are the same, the probability density of x and y of (21) is computed as the integral

$$W(x, y) = \frac{1}{4\pi^2} \int_{-\infty}^{\infty} \int_{-\infty}^{\infty} du\, dv \exp(-iux) \exp(-ivy)\, [C_k(u, v)]^n. \tag{25}$$

Changing to polar coordinates $\varrho = \sqrt{u^2+v^2}$, $\psi = \tan^{-1}(v/u)$, evaluating the ψ integral for a ψ-independent characteristic function $C_k(\varrho)$, changing from x, y to polar coordinates r, φ; and integrating over φ, it follows that

$$W(r) = r \int_0^{\infty} d\varrho \varrho J_0(\varrho r)\, [C_k(\varrho)]^n. \tag{26}$$

The cumulative probability $P(r \geqslant r_0)$ is computed as

$$P(r \geqslant r_0) = \int_{r_0}^{\infty} W(r)\, dr. \tag{27}$$

Substituting (26) in (27), evaluation of the r integral results in

$$P(r \geqslant r_0) = \int_0^{\infty} d\varrho [C_k(\varrho)]^n \left[\lim_{r \to \infty} rJ_1(\varrho r) - r_0 J_1(\varrho r_0) \right]. \tag{28}$$

Noting that

$$\lim_{r \to \infty} \left\{ r \int_0^{\infty} d\varrho [C_k(\varrho)]^n J_1(\varrho r) \right\} = \lim_{r \to \infty} \int_0^{\infty} dx \left[C_k\left(\frac{x}{r}\right) \right]^n J_1(r) = [C_k(0)]^n, \tag{29}$$

and substituting the $\varrho = 0$ value of (24), it follows that

$$P(r \geqslant r_0) = 1 - r_0 \int_0^{\infty} d\varrho\, J_1(\varrho r_0)\, [C_k(\varrho)]^n. \tag{30}$$

The second term of (30) is zero for $r_0 \to 0$ and $P(r \geqslant 0) = 1$. For $r_0 \to \infty$, a substitution of (29) in (30) shows $P(r \geqslant \infty) = 0$.

3.4.1.2 *Signals Received from a Single Thunderstorm Center*

The probability distribution of return stroke current peaks was nearly log-normal over the limited range of measurements shown in Fig. 3.3, and it can be approximated as a sum of two exponentials. An exponential large amplitude decay of the A.D. has been reported also by Muller-Hillebrand [1965]. In this approximation, $P(z_k \geqslant z_0)$ of (18) is represented by

$$P(z_k \geqslant z_0) = \int_{z_0}^{\infty} w(z)\, dz = (1-\delta) \exp(-\alpha_1 z_0) + \delta \exp(-\alpha_2 z_0), \tag{31}$$

where $\delta = 0.1$, $\alpha_1 = 0.81$, and $\alpha_1/\alpha_2 = 6.66$. The corresponding probability density is computed as

$$w(z) = \frac{\partial P}{\partial z} = (1-\delta)\alpha_1 \exp(-\alpha_1 z) + \delta\alpha_2 \exp(-\alpha_2 z) \tag{32}$$

and the characteristic function $C_k(\varrho)$ follows from (22) and (24) as

$$C_k(\varrho) = (1-\delta) \frac{\beta_1}{(\beta_1^2+\varrho^2)^{0.5}} + \delta \frac{\beta_2}{(\beta_2^2+\varrho^2)^{0.5}}, \tag{33}$$

where $\beta_j = \alpha_j/C$.

In the limiting case of $\delta = 0$, the cumulative probability is computed for a superposition of n-signals as

$$P(r \geqslant r_0) = 1 - r_0 \int_0^{\infty} \frac{d\varrho\, J_1(\varrho r_0)}{[1+(\varrho/\beta)^2]^{0.5}} = \frac{(\beta r_0)^{0.5n} K_{0.5n}(\beta r_0)}{2^{0.5n-1}\Gamma(0.5n)} = Q_{0.5n}(\beta r_0), \tag{34}$$

where $\beta = \beta_1$. Using the small argument approximations of the modified Bessel function $K_m(z)$, it can be seen that $P(r \geq 0) = 1$. Simplified forms of (34) can be obtained in the special case of $p = 0.5n \gg 1$ using the asymptotic expansion [eqn. 7.13. 2–10 of Erdélyi, 1953]

$$K_p(z) \approx \frac{\sqrt{\pi/2}}{(p^2+z^2)^{1/4}} \exp\left[-\sqrt{p^2+z^2}+p \sinh^{-1}(p/z)\right]. \tag{35}$$

For $0.5n \gg \beta r_0$, substitution of (35) in (34) and an approximation of the gamma function by the Stirling's formula gives

$$P(r \geq r_0) = \exp\left(-\frac{\beta^2 r_0^2}{2n}\right), \tag{36}$$

which is recognized as a Rayleigh distribution. It represents the envelope of narrow-band Gaussian noise of zero mean and variance $\sigma^2 = n/\beta^2$. For $0.5n \ll \beta r_0$, a substitution of (35) in (34) gives

$$P(r \geq r_0) = \frac{\sqrt{\pi}}{\Gamma(p)}\left(\frac{z}{2}\right)^{p-0.5} \frac{\exp\left[-z+p^2/(2z)\right]}{1+[p/(2z)]^2}, \tag{37}$$

where $p = 0.5n$ and $z = \beta r_0$. For large values of z, (37) is proportional to $z^{0.5n-0.5} \exp(-z)$; and large values of r are more probable for atmospheric noise than for the envelope of a Gaussian noise (36).

For $\delta \neq 0$ and $n > 1$, the integral (30) is evaluated numerically over the range of ϱ from 0 to ϱ_1; and the remainder term is computed analytically using the asymptotic expansion of the Bessel function and by simplifying $C_k(\varrho)$ for $\varrho \gg \beta_1, \beta_2$. For large values of r_0, the probability distribution (30) will be determined primarily by the more slowly decaying second term of (32) or by the small ϱ behavior of $C_k(\varrho)$. After letting ϱ equal to zero in the first term of (33) and expanding $[C_k(\varrho)]^n$ in powers of δ, the resulting integrals are evaluated in closed form to give

$$\left.\begin{aligned} P(r \geq r_0) \approx\ & n\,\delta Q_{0.5}(\beta_2 r_0) - \frac{n(n-1)}{2!}\,\delta^2[2Q_{0.5}(\beta_2 r_0) - Q_1(\beta_2 r_0)] \\ & + \frac{n(n-1)(n-2)}{3!}\,\delta^3[3Q_{0.5}(\beta_2 r_0) - 3Q_1(\beta_2 r_0) + Q_{1.5}(\beta_2 r_0)] - \ldots, \end{aligned}\right\} \tag{38}$$

where $Q_v(z)$ is defined as in (34). This approximation is useful for large values of r_0, where the numerical integration becomes inaccurate due to the highly oscillatory behavior of the integrand in (30). When observing a single signal at a time ($n = 1$), the integral (30) can be evaluated in closed form to give $P(r \geq r_0)$ in the form of (31), where α_j is replaced by $\beta_j = \alpha_j/C$, and C is defined by (20).

The cumulative probability distribution of amplitudes of the received waveforms is shown in Fig. 3.9 as a function of the normalized signal amplitude $\beta_1 r$ for several values of the number n of the lightning waveforms which have occurred during the integration time of the filter. The parameter β_1 is defined as α_1/C, where $\alpha_1 = 0.81$ in (31) and where $C = |Ids(\omega)\,F(\omega)|$ gives the received field strength due to a single median lightning stroke in a receiver with an integration time T, as was shown in Fig. 3.7 and 3.8. The parameter β_1 will be constant for a given receiver at a fixed distance from the source, and the cumulative probability computed

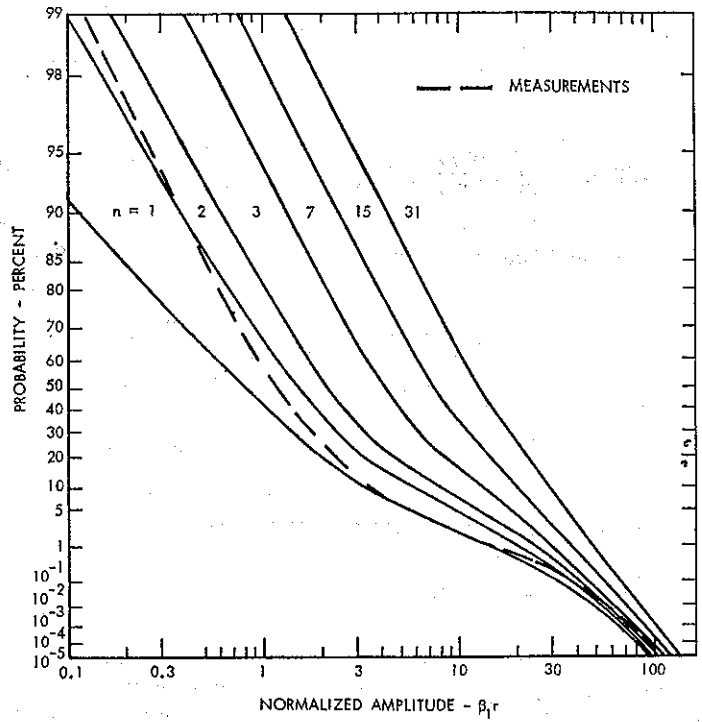

FIG. 3.9 Probability Distribution of the Received Noise. Source Current Distribution Represented by Two Exponentials

for normalized signal amplitudes $\beta_1 r$ is representative of the observed relative signal amplitudes, as long as $\beta_1 \simeq$ constant for the various signals. In the log–log versus log–scale used for graphing the results, the exponential distribution of $n = 1$ has a slope of (-1) for r small, the Rayleigh distribution of n large and r small has a slope of (-2). The decay of the curves becomes more gradual for r large. Although curves similar to the one indicated by dashed lines have been reported in some E.L.F. measurements [Farstadt, 1969], most measurements show A.D. which are inversely proportional to the squared amplitudes for larger signals [Watt and Maxwell, 1957a; Crichlow *et al.*, 1960]. In the above computations, the probability of the received signal is defined by assuming that n atmospherics caused by return strokes arrive during time T over a distance d from a single thunderstorm center. However, the measurements refer to the probability that the received signal exceeds a certain amplitude in a given noise environment, where atmospherics may arrive from a large number of different sources located at various distances from the receiver.

3.4.1.3 Signals Received from Two Thunderstorm Centers

The previous development will be generalized to allow atmospherics to arrive from two different thunderstorm centers of distances d_k and d_j. The corresponding scale factors computed from (20) are denoted as C_k and C_j, and the characteristic functions of (24) are denoted as $C_k(\varrho)$ and $C_j(\varrho)$ respectively. It is further assumed that only one atmospheric contributes from the distance d_k and that $(n-1)$ atmospherics from distance $d_j \gg d_k$ (scale factor $C_k = uC_j$ with $u \gg 1$) contribute to the receiver output. The mathematics of the development remain similar to the one shown in Section 3.4.1.1 except that $[C_k(\varrho)]^n$ of (26) is replaced by a product $C_k(\varrho)\,[C_j(\varrho)]^{n-1}$. The modified equation (30) is evaluated numerically; but for r large, an approximation corresponding to (38) is obtained as

$$\left.\begin{aligned} P(r \geqslant r_0) = {} & Q_{0.5}(\beta_{2k} r_0)\,\delta\left(1-\frac{m\delta}{u^2}\right) + Q_1(\beta_{2k} r_0)\,\frac{m\delta^2}{u^2} \\ & + Q_{0.5}(\beta_{1k} r_0)\,(1-\delta)\left[1-\frac{mq^2\delta}{u^2}+\frac{m(m-1)}{2}\left(\frac{\delta q^2}{u^2}\right)^2\right] \\ & + Q_1(\beta_{1k} r_0)\,\delta(1-\delta)\,\frac{mq^2}{u^2}\left[1-\frac{(m-1)\,\delta q^2}{u^2}\right] \\ & + Q_{1.5}(\beta_{1k} r_0)\,\delta^2(1-\delta)\,\frac{m(m-1)}{2u^4}\,q^4, \end{aligned}\right\} \tag{39}$$

where $\beta_{jk} = \alpha_j/C_k$, $q = \beta_{1k}/\beta_{2k}$, $m = n-1$, and $u = C_k/C_j$.

In the numerical calculations, it is assumed that atmospherics from the larger distance d_j are more frequent than from the smaller distance d_k. Atmospherics from d_k contribute only 10 percent of the time to the filter output and the only one at a time. If a total of n atmospherics contribute to the receiver output, then 90 percent of the time these outputs are caused by n atmospherics from d_j, and 10 percent of the time by $(n-1)$ atmospherics from d_j and one atmospheric from d_k. Thus

$$P(r \geqslant r_0) = 0.9P(n, d_j) + 0.1\,P(1, d_k;\, n-1, d_j). \tag{40}$$

$P(n, d_j)$ is taken from the curves of Fig. 3.9, but by noting that $\beta_{1j} = u\beta_{1k}$; $P(1, d_k;\, n-1, d_j)$ is computed numerically using $C_k(\varrho)\,[C_j(\varrho)]^{n-1}$ in (30) or from (39) for large values of r. The curves of Fig. 3.10 and 3.11 are calculated for $C_k/C_j = 10$ and 30 respectively. These probability curves are normalized using $\beta_{1k} = \alpha_1/C_k$. For $n = 1$, the calculated curves exhibit a (-1) slope for r small; the other curves exhibit (-2) slope of a Rayleigh distribution, which corresponds to the envelope of a narrow-band Gaussian noise. For r large, the probability distribution is determined by the second term of (40), which can be approximated from (39) as

$$P(r \geqslant r_0) \to 0.1\delta \exp(-\beta_{2k} r_0). \tag{41}$$

Increasing the value of $u = C_k/C_j$ (u is increased with increasing distance ratio d_j/d_k) extends the relatively flat center portion of the A.D. curves and increases the dynamic range of the distribution. The calculated curves of Fig. 3.10 and 3.11 are compared with the measured probability distributions from fig. 6 and 9a of Watt and Maxwell [1957a]. The two experimental curves approximate the calculations made for $n \approx 7$.

For atmospherics generated by return strokes at a fixed distance, the probability distributions of Fig. 3.9 exhibit slopes similar to those shown in Figs. 3.10 and 3.11 for r small. The addition of frequent waveforms from distant sources to the less frequent waveforms received from nearby sources appears to introduce the relatively flat center portions of the probability curves in Figs. 3.10 and 3.11, and it decreases also the slope of the decay for very large values of r. The parameters of the numerical examples of Figs. 3.10 and 3.11 have been quite arbitrary defined

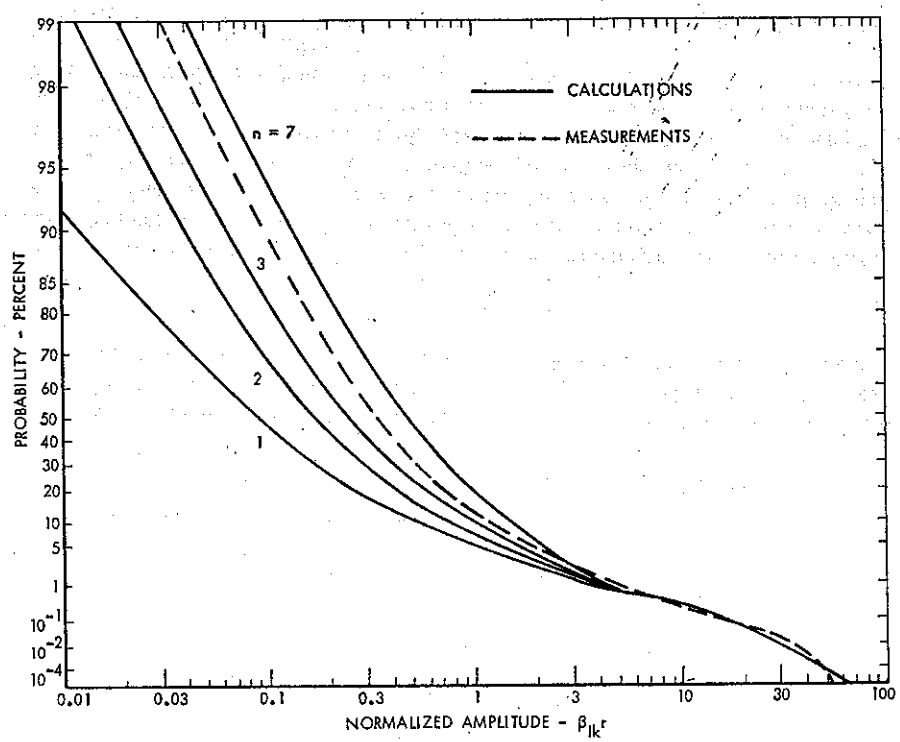

FIG. 3.10 Probability Distribution of the Noise Received from Distances d_1 and $d_2 > d_1$. 90% of Time n Waveforms Received from d_2, 10% of Time 1 Waveform from d_1 Is Added to $(n-1)$ Waveform from d_2; $u = 10$

in (41), and one may choose also different parameters. However, it is shown that atmospherics caused by return strokes and arriving from a single thunderstorm center are not sufficient for explaining the statistics of the received noise. The computational model should consider contributions from more frequent, low-amplitude sources, which in the example of (40) or Figs. 3.10 and 3.11 have been provided by more frequent atmospherics of same statistics arriving from larger distances. Alternately, one may also consider lower amplitude radiation processes of the lightning discharge of a single thunderstorm center. An example of such calculations is shown in Section 3.4.2.3.

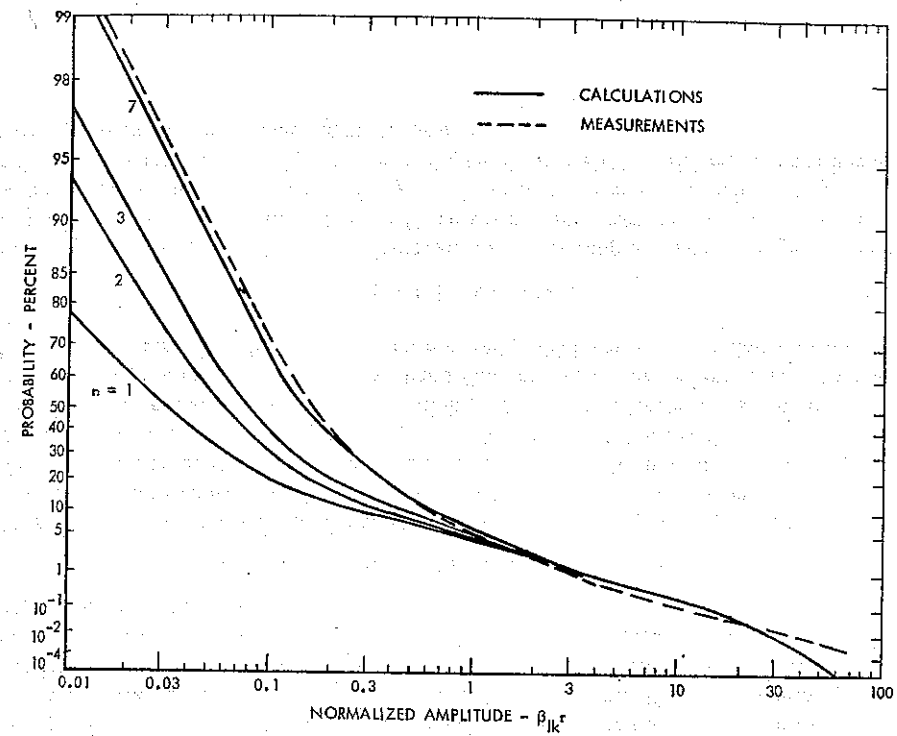

FIG. 3.11 Probability Distribution of the Noise Received from Distances d_1 and $d_2 > d_1$. 90% of Time n Waveforms Received from d_2; 10% of Time 1 Waveform from d_1 Is Added to $(n-1)$ Waveforms from d_2; $u = 30$

3.4.1.4 *Bandwidth Transformations*

For a given lightning environment or a constant number of lightning flashes per unit time, a change of receiver bandwidth or of the integration time T will change the number of lightning discharges which occur during T and will also change the value of the normalization parameter β_1 while leaving the ratio α_1/α_2 constant. The mathematical model of Section 3.4.1.2 serves to illustrate a change of bandwidth from Ω_1 (or $n_1 = 31$) to a bandwidth $\Omega_2 = 10.3\Omega_1$ (or $n_2 = 3$) in Fig. 3.12. The bandwidth transformation from one solid curve to the other is made assuming that the receiver output is proportional to the filter bandwidth and that the number of the atmospheric waveforms to be summed in the filter is inversely proportional to the bandwidth. The curves for $n_1 = 31$ and $n_2 = 3$ are taken from Fig. 3.9. The curve $P(r_1, n_1)$ for Ω_1 is reproduced in Fig. 3.12, and it is compared with a shifted version of the curve $P(r_2, n_2)$ for Ω_2. The transformation between the two solid curves of Fig. 3.12 is given as

$$P(r_1, n_1) = P(mr_2, n_1/m) \tag{42}$$

if $\Omega_2 = m\Omega_1$. (The shifting of the second curve is not necessary if the two curves are plotted

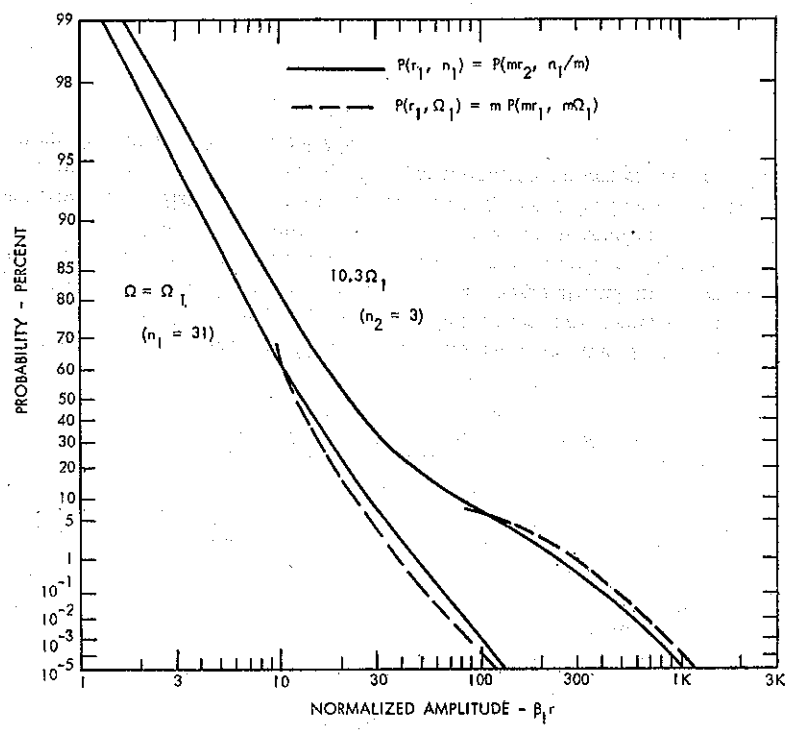

FIG. 3.12 Probability Distribution of the Received Noise for Two Bandwidths of the Receiver

using normalizing parameters β_1 which are appropriate to the respective bandwidths; in the present plot, the normalizing parameter refers to the bandwidth Ω_1.) The solid curves of Fig. 3.12 can be transformed into the dashed curves of the other bandwidths using the transformation

$$P(r_1, \Omega_1) = mP(mr_1, m\Omega_1), \tag{43}$$

which was derived by Fulton [1961] by assuming nonoverlapping pulses within the memory time of the filter. This criterion does not consider the change in the number of atmospherics n which the filter is integrating for different bandwidths. Some of the high-amplitude bursts are due to the addition of several lower amplitude signals during the integration time of the filters. When increasing the bandwidth, (43) gives a higher probability of the high-amplitude signals than (42), which considers the decrease of n. When decreasing the bandwidth, (43) gives lower probability of the high-amplitude signals than (42), which considers the increase of n during the change of the bandwidth.

The lower amplitude portion of the curve for $\Omega_2 = 10.3\Omega_1$ is obtained by shifting the lower bandwidth curve to the right by a factor of 1.3 to 1.6. This factor is increased for decreasing values of the parameter α_1/α_2 and is 2–2.4 for the same frequency change width $\alpha_1/\alpha_2 = 1$. This compares with a factor 1.9 measured with $\Omega_2 = 9.4\Omega_1$ [Watt and Maxwell, fig. 6, 1957a].

V.L.F. atmospherics have durations of less than 0.5 msec at distances of less than 500 km from source [Taylor and Jean, 1959] and durations of approximately 1 msec at larger distances [Obayashi, 1960; Taylor and Jean, 1959]. It is estimated that about 100 lightning flashes per second occur on an average over the surface of the earth with about 90 percent of this number occurring on the sunlit hemisphere [Volland, 1963]. The average separation between two atmospherics should therefore be of the order of 10 msec, and nonoverlapping atmospherics can be expected frequently in receivers where the bandwidth is of the order of 1000 c/s. It is therefore of interest to examine the amplitude probability of the received noise for $n = 1$ when only a single atmospheric contributes to the filter output. With a further increased bandwidth, there should be times of zero output even for low thresholds.

The computed curves for $n = 1$ are characterized by a (-1) slope for small signal amplitudes in Figs. 3.9–3.11, and there are several experimental curves which exhibit a slope of nearly (-1) for small signal amplitudes. The quiet-day curve in Fig. 3.3, the wide-band curve in Fig. 3.6, and also the curves in figs. 9a, 11a, and 15 of Watt and Maxwell [1957a] exhibit this behavior. Recent measurements by Maxwell (private communication, 1965) show a (-1) slope for small signals in the presence of strong nearby thunderstorms. In this example, secondary processes of nearby thunderstorms appear to generate signals of larger amplitudes than the

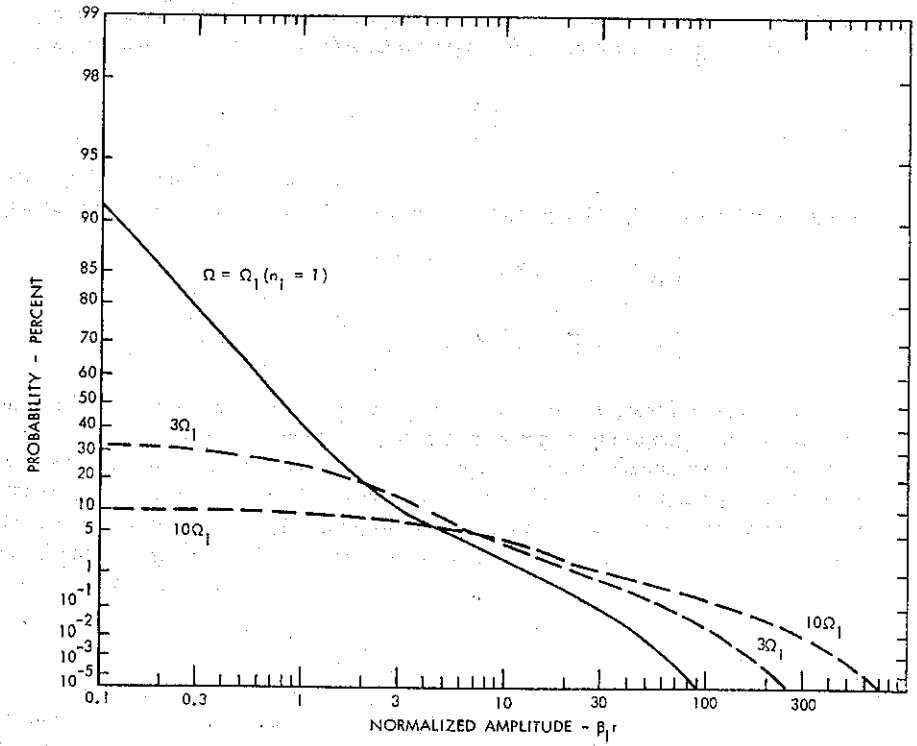

FIG. 3.13 Probability Distribution of the Received Noise for Several Bandwidths with Nonoverlapping Noise Waveforms

superposition of more frequent ($n > 1$) long-distance atmospherics. For even wider bandwidths, there should be times of zero filter output; and in this case, the bandwidth transformation of Fulton [1961] should apply for all signal amplitudes. Such a bandwidth transformation is shown in Fig. 3.13. However, experimental observations show that an increased bandwidth is always associated with an increased signal level; and curves similar to those shown in Fig. 3.13 have not been observed for small signal levels. At sufficiently low signal levels, the noise is apparently due to several atmospherics. The previous estimate of 1 msec waveforms occurring at a rate of less than 100 per second may be inaccurate. There may be lower amplitude long tails of the atmospherics which do not appear on the linear scale atmospheric records, or there may be also other local noise sources. In the E.L.F. range, atmospherics are of a longer duration. Daytime waveforms of 5 msec and nighttime waveforms of 100 msec durations have been reported by Liebermann [1956]. The observation bandwidths are smaller in this frequency range, and the possibility of nonoverlapping atmospheric waveforms is remote.

3.4.2 *Amplitude Distributions of Lightning Waveforms*

In Section 3.4.1, the received noise was considered as a result of integrating several atmospherics during the response time of the receiver. The probability distributions of this noise and of current in the lightning flashes were related by a twofold Hankel transform. In Section 3.4.2.1, this method is inverted to derive lightning statistics from measured A.D.s of received noise. Assuming that the received noise is caused by return strokes from a single thunderstorm center, the computed A.D. of the source currents becomes inversely proportional to the squared amplitudes for very large signals in Sections 3.4.2.2. At present, there is no justification for extrapolating measured return-stroke currents to larger amplitudes using this inverse-square dependence.

However, there is evidence that the so-called *K*-pulses are more frequent than the return strokes and that they contribute to the lower amplitudes of V.L.F. noise [Arnold and Pierce, 1964]. These *K*-pulses will predominate at lower amplitudes of the source-current distribution, and they will tend to decrease the probability of large-amplitude return strokes. The shape of the resulting large amplitude distribution of the effective source current is approximately proportional to the inverse square of the amplitudes when considering the increased velocity of the higher amplitude return strokes in Section 3.4.2.3.

3.4.2.1 *Formal Solution*

The probability $P(z_k \geqslant z_0)$ of $z_k = I_k/I_{\text{med}}$ will be derived starting out with a given cumulative probability $P(r \geqslant r_0)$ of the received noise. Equation (30) can be inverted using the fundamental pair of Hankel transforms (eqn. 8.1.1 of Erdélyi, 1953). It follows that

$$[C_k(\varrho)]^n = \varrho \int_0^\infty dr_0\, J_1(\varrho r_0)\,[1 - P(r \geqslant r_0)]. \tag{44}$$

Equations (22) and (24) are inverted as

$$w_1(r_k) = r_k \int_0^\infty d\varrho\; \varrho J_0(r_k \varrho)\, C_k(\varrho) \tag{45}$$

and the cumulative probability $P(r_k \geq r_1)$ is computed by integrating (45) as

$$P(r_k \geq r_1) = \int_{r_0}^{\infty} w_1(r_k)\, dr_k = 1 - r_1 \int_0^{\infty} d\varrho\, J_1(\varrho r_1)\, C_k(\varrho). \tag{46}$$

A substitution of (44) into (46) gives for $n = 1$ a trivial identity. Substitution of (19) into (46) shows that

$$P(r_k \geq r_1) = \frac{1}{C} \int_{r_1}^{\infty} w(r_k/C)\, dr_k = P(z_k \geq z_1) \tag{47}$$

if r_k and z_k are related as indicated before.

Starting out with $P(r \geq r_0)$ of the received noise and evaluating the two integrals of (44) and (46) permits a determination of $P(z_k \geq z_1)$ of the random variable z_k, which characterizes the A.D. of the current in a lightning flash. These integrations require an analytical representation of $P(r \geq r_0)$. The representation of $P(r \geq r_0)$ is selected to be such that it approximates measured A.D.s of the received noise and that it also permits a closed-form evaluation of the integrals amplitude for large signal levels. The cumulative probability $P(r \geq r_0)$ is approximated by

$$\left.\begin{aligned} P(r \geq r_0) = {} & \left[1 - \left(\frac{b}{a}\right)^2 - \left(\frac{d}{a}\right)^2\right] \exp\left[-\left(\frac{r_0}{\sigma}\right)^2\right] \\ & + \frac{b^2}{r_0^2 + a^2 + r_0(r_0^2 + a^2)^{1/2}} + \left(\frac{d}{a}\right)^2 \exp(-s r_0) \end{aligned}\right\} \tag{48}$$

which is equal to unity for $r_0 = 0$ and decays monotonically with increasing values of r_0. For r_0 sufficiently large, (48) is approximated by

$$P(r \geq r_0) = \frac{1}{2}\left(\frac{b}{r_0}\right)^2. \tag{49}$$

For very large values of r_0, $P(r \geq r_0)$ is characterized by the parameter b. The other parameters a, d, s, and σ can be selected by matching (48) to an experimental curve at four different values of r.

Substituting (48) in (44), the integrals can be evaluated using the relations (8.6.8), (8.5.38), and (8.4.6) of Erdélyi [1953], which give

$$\left.\begin{aligned} [C_k(\varrho)]^n = {} & \left[1 - \left(\frac{b}{a}\right)^2 - \left(\frac{d}{a}\right)^2\right] \cdot \exp\left[-\left(\frac{\varrho\sigma}{2}\right)^2\right] + \left(\frac{b}{a}\right)^2 \\ & \times \left[1 - a\varrho I_1\left(\frac{a\varrho}{2}\right) K_0\left(\frac{a\varrho}{2}\right)\right] + \left(\frac{d}{a}\right)^2 \frac{s}{(s^2 + \varrho^2)^{1/2}} \end{aligned}\right\} \tag{50}$$

where $I_m(x)$ and $K_m(x)$ are the modified Bessel functions of order m and of the first and second kind respectively. For large values of ϱ, $C_k(\varrho)$ is approximated by

$$C_k(\varrho) = \left\{\left[\frac{b^2}{a^3} + \frac{d^2 s}{a^2}\right]\frac{1}{\varrho} + \left[\frac{b^2}{a^2} 3\left(\frac{3}{4a}\right)^3 - \left(\frac{d}{a}\right)^2 \frac{s^3}{2}\right]\frac{1}{\varrho^3}\right\}^{1/n} \approx \left\{\left[\frac{b^2}{a^3} + \frac{d^2 s}{a^2}\right]\frac{1}{\varrho}\right\}^{1/n}. \tag{51}$$

The approximation (51) is valid if the exponential term of (50) is negligible, $\varrho \gg s$ and $a\varrho \gg 1$. It will be used for $\varrho > \varrho_0$, where ϱ_0 is determined as

$$\varrho_0 = \max(\varrho_1, \varrho_2, \varrho_3)$$

with $\varrho_1 = 50/a$, $\varrho_2 = 50s$, and with ϱ_3 determined from the solution of

$$0.001\left(\frac{\sigma}{2a}\right)\frac{b^2 + d^2 sa}{a^2 - b^2 - d^2} = \frac{\varrho_3 \sigma}{2} \exp\left[-\left(\frac{\varrho_3 \sigma}{2}\right)^2\right]. \tag{52}$$

Substituting (51) in (46), $P(r_k \geq r_1)$ is rewritten as

$$\left.\begin{aligned} P(r_k \geq r_1) = {} & 1 - r_1 \int_0^{\varrho_0} d\varrho\, J_1(r_1\varrho)\, C_k(\varrho) \\ & - r_1 \int_{\varrho_0}^{\infty} d\varrho\, J_1(r_1 p)\left[\left(\frac{b^2}{a^3} + \frac{d^2 s}{a^2}\right)\frac{1}{\varrho}\right]^{1/n}. \end{aligned}\right\} \tag{53}$$

$C_k(\varrho)$ of (50) is used in the first integral. The last integral is evaluated between the limits of 0 and ∞, and (53) is rewritten as

$$\left.\begin{aligned} P(r_k \geq r_1) = {} & 1 - \left[\left(\frac{b^2}{a^3} + \frac{d^2}{a^2} s\right)\frac{r_1}{2}\right]^{1/n} \cdot \frac{\Gamma(1 - \frac{1}{2}n)}{\Gamma(1 + \frac{1}{2}n)} - r_1 \int_0^{\varrho_0} d\varrho\, J_1(r_1\varrho) \\ & \times \left\{C_k(\varrho) - \left[\left(\frac{b^2}{a^3} + \frac{d^2}{a^2} s\right)\frac{1}{\varrho}\right]^{1/n}\right\}, \end{aligned}\right\} \tag{54}$$

where $\Gamma(x)$ is the gamma function. There may still be difficulties in the numerical evaluation of the integral for large values of r_1 when $r_1\varrho_0$ may exceed 10^3 or 10^4 in magnitude and when the integral is carried out over a large number of cycles of the Bessel function. For $r_1 \gg 1$, $J_1(\varrho r_1)$ is small in magnitude except when ϱ is near 0 and when the behavior of $P(r_k \geq r_1)$ is determined primarily from the behavior of $C_k(\varrho)$ near zero. $C_k(\varrho)$ of (50) is rewritten as

$$\left.\begin{aligned} C_k(\varrho) = {} & \left\{1 - \left(\frac{b}{a}\right)^2 a\varrho I_1\left(\frac{a\varrho}{2}\right) K_0\left(\frac{a\varrho}{2}\right) - \left(\frac{d}{a}\right)^2 \left[1 - \frac{s}{(s^2 + \varrho^2)^{1/2}}\right] \right. \\ & \left. - \left[1 - \left(\frac{b}{a}\right)^2 - \left(\frac{d}{a}\right)^2\right] \cdot \left[1 - \exp\left[-\left(\frac{\varrho\sigma}{2}\right)^2\right]\right]\right\}^{1/n}. \end{aligned}\right\} \tag{55}$$

For ϱ small, $C_k(\varrho)$ is nearly unity, and (55) is approximated as

$$\left.\begin{aligned} C_k(\varrho) \approx {} & 1 - \left(\frac{b}{a}\right)^2 \frac{a\varrho}{n} I_1\left(\frac{a\varrho}{2}\right) K_0\left(\frac{a\varrho}{2}\right) - \left(\frac{d}{a}\right)^2 \frac{1}{n}\left[1 - \frac{s}{(s^2 + \varrho^2)^{1/2}}\right] \\ & - \left[1 - \left(\frac{b}{a}\right)^2 - \left(\frac{d}{a}\right)^2\right]\frac{1}{n} \cdot \left\{1 - \exp\left[-\left(\frac{\varrho\sigma}{2}\right)^2\right]\right\}. \end{aligned}\right\} \tag{56}$$

Substituting (5[illegible] (46),

$$P(r_k \geqslant r_1) \approx \frac{1}{n}\left\{\left[1-\left(\frac{b}{a}\right)^2-\left(\frac{d}{a}\right)^2\right]\cdot\exp\left[-\left(\frac{r_1}{\sigma}\right)^2\right] + \frac{b^2}{r_1^2+a^2+r_1(r_1^2+a^2)^{1/2}}+\left(\frac{d}{a}\right)^2\exp\left(-sr_1\right)\right\} = \frac{1}{n}P(r \geqslant r_1). \tag{57}$$

The representation in (57) is based on the approximation of (55) by (56), which is inaccurate for ϱ large when $J_1(\varrho r_1)$ is also very small for r_1 large. The adequacy of the approximation (56) can be seen from numerical calculations. $P(r_k \geqslant r_1)$ is computed by (54) and (57). For sufficiently large values of r_1, both computations give nearly the same numerical results; and there is no need to carry out time-consuming numerical integrations of (54) for even larger values of r_1.

3.4.2.2 *Return-stroke Currents for a Single Thunderstorm Center*

According to (47), the probability $P(z_k \geqslant z_1)$ of the current in a lightning discharge is numerically the same as the probability $P(r_k \geqslant r_1)$ of hypothetical receiver noise, which is due to a single lightning waveform. This latter probability will be calculated from (54) and (57). The receiver noise distribution shown in fig. 9a of Watt and Maxwell [1957a] is considered as an example, and it is indicated as the measured $P(r \geqslant r_0)$ curve in Fig. 3.14. This probability distribution is approximated by (48), which is shown as the dashed curve. The current distribution of lightning discharges would have an identical shape if the received noise would be due to the arrival of a single atmospheric waveform during the integration time of the receiver. Generally, the number of atmospheric waveforms n occurring during the integration time of the receiver exceeds 1, and the resulting shapes of the probability distributions of the current in the lightning discharges are as indicated in Fig. 3.14. The $P(z_k \geqslant z_1)$ curves exhibit various slopes for small values of z_1; but they exhibit a z_1^{-2} dependency for larger values of z_1, which is a consequence of the approximation (57). Equation (57) applies for $r_1 > 20$, and the z_1^{-2} dependency is observed for $r_1 > 200$.

The approximation of the measured distribution of the received noise is quite accurate for large-signal amplitudes, but the slope of the curve (48) is less than (-2) in magnitude for smaller amplitudes in the log–log versus log–scale used in the graph. As a consequence, the computed probability distribution $P(z_k \geqslant z_1)$ is relatively flat for the larger values of n and smaller values of z_1. This may be avoided possibly by using an improved form for approximating the measured probability distribution. The modification of (48) in such a way that the second and third term of the expression approach zero for r_0 approaching zero may be desirable. In this case, the derivatives of the two terms will be negative for r small, but the coefficients of the individual terms might be selected such that $P(r \geqslant r_0)$ is still monotonically decreasing with increasing values of r_0. Such calculations will not be reported in this section.

The theoretical source current distributions can be compared with available statistics of return strokes. The curves of Fig. 3.14 have been replotted using the probability versus log–scale where a log–normal distribution is characterized by a straight line of a slope inversely proportional to the standard deviation σ. The maximum slope of the $n = 1$–5 curves corresponds to a log–normal distribution of $\sigma = 7.6$–9.8 db. For larger values of n, $\sigma \approx 12$ db.

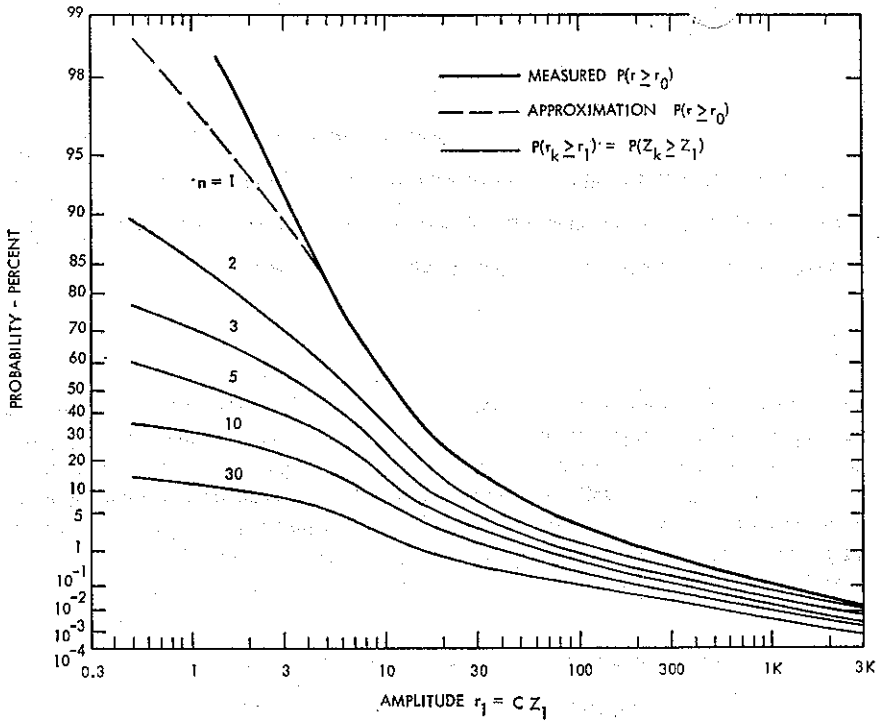

FIG. 3.14 Probability Distributions of Received Noise $P(r \geqslant r_0)$ and of Current in a Lightning Flash $P(z_k \geqslant z_1)$

This is not out of line with a range of $\sigma = 6.5$–9.5 db reported by Dennis and Pierce [1964] or $\sigma = 6$–12 db quoted by Horner [1960].

However, none of the experimental return-stroke distributions of Fig. 3.2 or 3.3 exhibit the theoretically postulated inverse-square dependence for large amplitudes. It is possible to extrapolate the measured amplitude distributions to larger amplitudes using the theoretically postulated inverse-square dependency. However, this will give finite probabilities for current exceeding 1000 kA, but only currents of approximately 200 kA have been reported in experimental observations [McCann, 1944; Berger, 1962].

3.4.2.3 *Effects of Low-amplitude Sources*

Only the return stroke was considered as a signal source in the above discussion, and it may be appropriate to examine also other processes as sources of atmospherics. Small, rapid, field changes—the so-called *K*-changes—are generated as a result of inhomogeneous charge distributions in the clouds. Their V.L.F. spectrum is nearly of the same shape as for return strokes, but a single *K*-pulse excites field components of approximately 5–10 times smaller amplitude

than the first return stroke following Fig. 3.5. Figure 3.1 shows approximately three *K*-changes for one return stroke. The *K*-changes are present also in intercloud discharges, and the intercloud discharges have been estimated to be 4–10 times more frequent than flashes to earth [Horner, 1964; Arnold and Pierce, 1964]. The *K*-changes are therefore more frequent than return strokes, and they should be considered in estimating statistics of effective source distributions.

The presence of frequent low-amplitude *K*-changes will decrease the probability that a particular large-amplitude return stroke contributes to the receiver noise. The probability of the return stroke is simply decreased by a factor of $(n+1)$ if n *K*-changes occur for every return stroke. [For every return stroke there are n *K*-changes; and the probability of a return stroke is $1/(1+n)$.]

Assuming $n = 9$ (three *K*-changes per return stroke plus six intercloud *K*-changes per return stroke), the all-stroke probability data of McCann [1944] should be decreased by a factor of 10 for the larger amplitudes. Similarly, the Muller-Hillebrand [1965] probabilities, which consider only the current of the first stroke can be divided by 30 (nine *K*-changes per ground flash and twenty intercloud *K*-changes per ground flash) or 100 (nine *K*-changes per ground flash and ninety intercloud *K*-changes per ground flash). The large amplitude part of the resulting probability curves are shown in Fig. 3.15.

The calculations of the scale factor C of (15) and of the median dipole moment $Ids(\omega)$ of (5) were made using the return-stroke velocity $v_0 \approx 0.12c_0$ (c_0 = free-space velocity of electromagnetic waves) following Williams [1959]. Similar velocity figures are used by Muller-Hillebrand [page 104, 1962] for low current return strokes, but Wagner [1963] points out how the velocity is increased with increasing current of the return stroke. An increasing velocity v_0 increases the dipole moment (5) and the scale factor of (15). Alternately, the increase of the velocity can be considered by defining an effective source current $I_{\text{eff}} = Iv/v_0$. This increase of the return-stroke velocity v tends to increase the dynamic range of the effective current as is shown in Fig. 3.15. The effective current is defined using the v/v_0 expressions of Lundholm-Rusck and Wagner [Wagner, 1962]. These expressions are of the form

$$\frac{v}{c} = \sqrt{\frac{I}{\alpha_1 I + \alpha_2}}, \tag{58}$$

where c is the free-space velocity of electromagnetic waves. Following Lundholm-Rusck, $\alpha_1 = 1$, $\alpha_2 = 500$, and I is given in kiloamperes. In the formula of Wagner, the parameters α_1 and α_2 depend on I, and α_1 is larger in magnitude. As a consequence, v/c is smaller for large values of I in the formula of Wagner [1962]. The effective-current distributions are approximately proportional to the inverse square of the amplitude as was required from theoretical considerations.

A number of *K*-pulses per return stroke determines the scale factor of the probability transformation between Figs. 3.2 and 3.15. The result is not very sensitive to this number as shown for the Muller-Hillebrand data. The exponential decay of the Muller-Hillebrand [1965] data eventually takes over for very large amplitudes. There is also a large amplitude cutoff in the measured statistics of radio noise [Watt and Maxwell, 1957a], although this is not considered in the theoretical model of Section 3.4.2.1. Only the *K*-pulses have been considered in the transformation of the return stroke probabilities. The leader pulses are of smaller

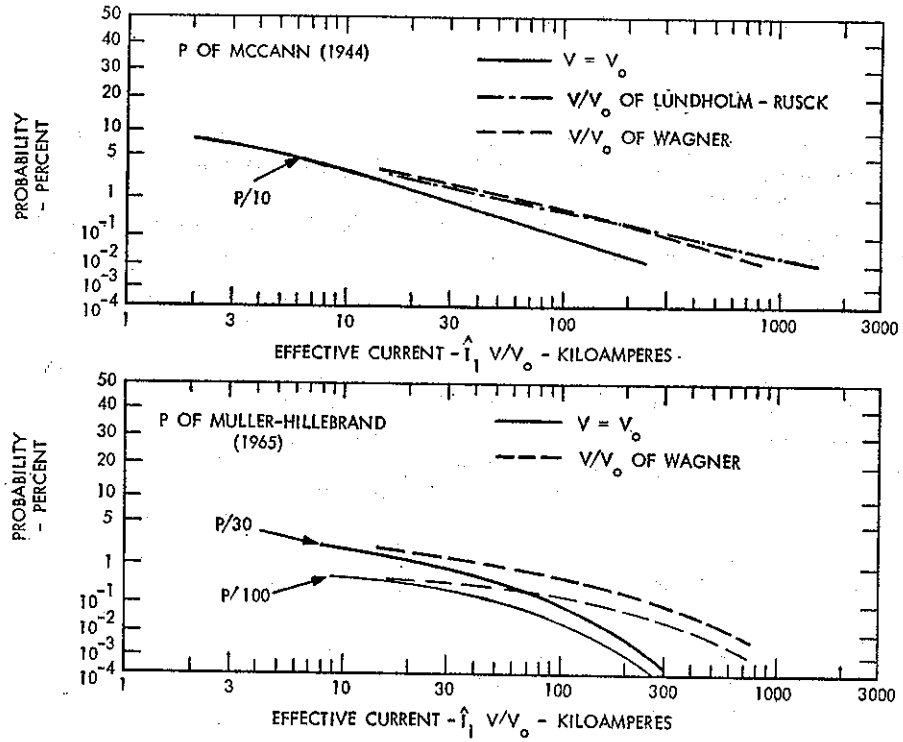

FIG. 3.15 Probability Distribution of the Effective Large Amplitude Current

amplitudes than *K*-pulses, and there is only one group of leader pulses for a lightning flash. The presence of leader pulses can be considered in the definition of the scale factor of the probability transformation. Their effect can be expected to be small in view of the uncertainties regarding the relative frequencies of the more significant *K*-changes.

A theoretical estimate of the effective source-current distribution is derived starting out from measured distribution of the received noise. The presence of frequent lower amplitude discharge processes alters the large amplitude statistics of the return strokes in a way that is consistent with these theoretical estimates.

3.5 References

AIYA, S. V. C. (1968) Lightning and power systems, *Electro Technology, J. Soc. of Electronic Engineers, Bangalore* **12** (1), 1–12.

ARNOLD, H. R., and E. T. PIERCE (1964) Leader and junction processes in the lightning discharge as a source of V.L.F. atmospherics, *Radio Sci.* **68D** (7), 771–776.

BALSER, M., and C. A. WAGNER (1960) Measurements of the spectrum of radio noise from 50 to 100 c/s, *J. Res. NBS (Radio Propagation)* **64D** (4), 415–418.

BARR, R. (1968) Ph.D. thesis, University of London, King's College.

BECKMANN, P. (1964) Amplitude probability distribution in atmospheric radio noise, *Radio Sci. J. Res. NBS*, **68D** (6), 723–736.

BERGER, K. (1962) Front duration and current steepness of lightning strokes to the earth, in *Gas Discharges and Electricity in Supply Industry*, Proc. Intern. Conf., Central Electricity Res. Lab., Leatherhead, Surrey, England, May 1962 (edited by J. S. Forrest), Butterworths, London, pp. 63–73.

BRADLEY, P. A. (1965) The V.L.F. energy spectra of first and subsequent return strokes of multiple lightning discharges to ground, *J. Atmosph. Terr. Phys.* **27**, 1045–1053.

BRUCE, C. E. R., and R. H. GOLDE (1941) The lightning discharge, *Inst. of Elect. Eng. J.* **88**, Part II, 487–505.

CRICHLOW, W. Q., C. J. ROUBIQUE, A. D. SPAULDING, and W. M. BERRY (1960) Determination of the amplitude probability distribution of atmospheric radio noise from statistical moments, *J. Res. NBS Radio Propagation*, **64D** (1), 49–56.

DENNIS, A. S., and E. T. PIERCE (1964) The return stroke of the lightning flash to earth as a source of V.L.F. atmospherics, *Radio Sci.* **68D**, 772–794.

ERDÉLYI, A. (1953) *Higher Transcendental Functions*, Vol. 2, McGraw-Hill, New York, NY.

FARSTADT, A. J. (1969) *Atmospheric Noise*, Final Report, Contract No. N00039-69-C-1541, Westinghouse Electric Corporation, Georesearch Laboratory, Boulder, Colorado.

FISCHER, W. H. (1965) The radio noise spectrum from E.L.F. to E.H.F., *J. Atmosph. Terr. Phys.* **27**, 475–480.

FULTON, S. F. (1961) Effects of the receiver bandwidths on the amplitude distributions of V.L.F. atmospheric noise, *J. Res. NBS Radio Propagation* **65D** (3), 299–304.

FURUTSU, K., and T. ISHIDA (1961) On the theory of amplitude distribution of impulse noise, *J. Appl. Phys.* **32** (7), 1206–1221.

GALEJS, J. (1962) A further note on terrestrial extremely low-frequency propagation in the presence of an isotropic ionosphere with an exponential conductivity-height profile, *J. Geophys. Res.* **67** (7), 2715–2728.

GALEJS, J. (1964) E.L.F. and V.L.F. waves below an inhomogeneous anisotropic ionosphere, *Radio Science J. Res. NBS* **68D** (6), 693–707.

GALEJS, J. (1966) Amplitude distributions of radio noise at E.L.F. and V.L.F., *J. Geophys. Res.* **71**, 201–216.

GALEJS, J. (1967) Amplitude statistics of lightning discharge currents and E.L.F. and V.L.F. radio noise, *J. Geophys. Res.* **72** (11), 2943–2953.

HEPBURN, F. (1957) Atmospheric waveforms with very-low-frequency components below 1 kc/s known as slow tails, *J. Atmosph. Terr. Phys.* **10**, 266–287.

HILL, R. D. (1966) Electromagnetic radiation from the return stroke of a lightning discharge, *J. Geophys. Res.* **71**, 1963–1967.

HILL, R. D. (1969) Electromagnetic radiation from erratic paths of lightning strokes, *J. Geophys. Res.* **74** (8), 1922–1929.

HORNER, F. (1960) The design and use of instruments for counting local lightning flashes, *Proc. IEE (London)* **107B**, 321–330.

HORNER, F. (1961) Narrow band atmospherics from two local thunderstorms, *J. Atmosph. Terr. Phys.* **21**, 13–25.

HORNER, F. (1964) Radio noise from thunderstorms, in *Advances in Radio Research* (edited by J. A. Saxton), Vol. 2, Academic Press, New York, p. 146.

JONES, D. L. (1967) Atmospherics, *M.F., L.F., and V.L.F. Radio Propagation*, IEE Conference Publication, 36.

KITAGAWA, N., and M. BROOK (1960) A comparison of intercloud and cloud-to-ground lightning discharges, *J. Geophys. Res.* **65**, 1189–1201.

KITAGAWA, N., M. BROOK, and E. J. WORKMAN (1962) Continuing currents in cloud-to-ground lightning discharges, *J. Geophys. Res.* **67** (2), 637–647.

LIEBERMANN, L. (1956) Extremely-low-frequency electromagnetic waves: 1, Reception from lightning, *J. Appl. Phys.* **27** (12), 1473–1476.

MCCANN, G. D. (1944) The measurement of lightning currents in direct strokes, *Trans. IEE* **63**, 1157–1164, see fig. 13.

MALAN, D. J. (1962) Lightning counter for flashes to ground, in *Gas Discharges and the Electricity Supply Industry*, Proc. Intern. Conf., Central Electricity Res. Lab., Leatherhead, Surrey, England, May 1962 (edited by J. S. Forrest), Butterworths, London, p. 121.

MIDDLETON, D. (1960) *Introduction to Statistical Communication Theory*, McGraw-Hill, New York, pp. 490–497.

MIKHAYLOVA, G. A. (1967) Spectra of atmospherics at ultra low frequencies during nighttime, *Geomag. Aeron.* **7** (2), 285–287.

MULLER-HILLEBRAND, D. (1962) The magnetic field of the lightning discharge, in *Gas Discharges and Electricity Supply Industry*, Proc. Intern. Conf., Central Electricity Res. Lab., Leatherhead, Surrey, England, May 1962 (edited by J. S. Forrest), Butterworths, London, pp. 89–111.

MULLER-HILLEBRAND, D. (1965) Lightning protection, in *Problems of Atmospheric and Space Electricity*, Proc. 3rd Intern. Conf. Atmospheric and Space Electricity, Montreaux, Switzerland, 1963 (edited by S. C. Coroniti), Elsevier, New York, pp. 408–429.

NAKAI, T. (1968) On the time functions of atmospheric noise, *Proc. Res. Inst. Atmospherics, Nagoya University* **15**, 17–28.

OBAYASHI, T. (1960) Measured frequency spectra of V.L.F. atmospherics, *J. Res. NBS Radio Propagation* **64D** (2), 41–48.

PIERCE, E. T. (1963) Excitation of earth-ionosphere cavity resonances by lightning flashes, *J. Geophys. Res.* **68** (13), 4125–4127.

PIERCE, E. T. (1969) *The Thunderstorm as a Source of Atmospheric Noise at Frequencies Between 1 and 100 kHz*, Report DASA 2299, Stanford Research Institute, Menlo Park, California.

RAEMER, H. R. (1961) On the spectrum of terrestrial radio noise at E.L.F., *J. Res. NBS Radio Propagation* **65D** (6), 581–594.

RAO, M. (1967) Corona currents after the return stroke and the emission of E.L.F. waves in a lightning flash to earth, *Radio Sci.* **2** (2), 241–244.

RYCROFT, M. J. (1963) Low frequency disturbances of natural origin of the electric and magnetic fields of the earth, Ph.D. thesis, University of Cambridge.

SCHONLAND, B. F. J. (1956) The lightning discharge, *Handbuch der Physik* **22**, 576–628.

SPAULDING, A. D., C. J. ROUBIQUE, and W. Q. CRICHLOW (1962) Conversion of the amplitude probability distribution function for atmospheric radio noise from one bandwidth to another, *J. Res. NBS Radio Propagation* **66D** (6), 713–720.

SULLIVAN, A. W., S. P. HERSPERGER, R. F. BROWN, and E. L. AITON, (1955) *Investigation of Atmospheric Radio Noise*, Progr. Rept. No. 7, Contract No. A.F. 19(604)-876, Dept. Elec. Engr., University of Florida, Gainesville, Florida.

SULLIVAN, A. W., S. P. HERSPERGER, and R. F. BROWN (1956) *Investigation of Atmospheric Radio Noise*, Sci. Rept. No. 10, Dept. Elec. Engr., University of Florida, Gainesville, Florida.

TAYLOR, W. L. (1960) Daytime attenuation rates in the V.L.F. band using atmospherics, *J. Res. NBS Radio Propagation* **64D**, 349–355.

TAYLOR, W. L. (1969) Determining lightning stroke height from ionospheric components of atmospheric waveform, *J. Atmosph. Terr. Phys.* **31** (7), 983–990.

TAYLOR, W. L., and A. G. JEAN (1959) V.L.F. radiation spectra of lightning discharges, *J. Res. NBS Radio Propagation* **63D**, 199–204.

TEPLEY, L. R. (1961) Sferics from intracloud lightning strokes, *J. Geophys. Res.* **66** (1), 111–123.

VOLLAND, H. (1963) The statistical amplitude spectrum of atmospherics, *Z. Angew. Phys.* **15**, 541–547.

VOLLAND, H. (1964) Investigation of the statistical amplitude spectrum of atmospheric disturbances from individual storm centers, *Nachr. Tech. Z.* **17**, 407–412.

VOLLAND, H. (1966) On the theory of the sudden enhancement of atmospherics, *J. Atmosph. Terr. Phys.* **28**, 409–423.

WAGNER, C. F. (1962) The lightning stroke in relation to overhead transmission lines, in *Gas Discharges and the Electrical Supply Industry*, Proc. Intern. Conf., Central Electricity Res. Lab., Leatherhead, Surrey, England, May 1962 (edited by J. S. Forrest), Butterworths, London, pp. 54–62.

WAGNER, C. F. (1963) The lightning stroke as related to transmission line performance, *Elec. Engr.* **82**, 339–347.

WATT, A. D., and E. L. MAXWELL (1957a) Measured statistical characteristics of V.L.F. atmospheric noise, *Proc. IRE* **45**, 55–62.

WATT, A. D., and E. L. MAXWELL (1957b) Characteristics of atmospheric noise from 1 to 100 kc, *Proc. IRE* **45**, 787–794.

WILLIAMS, J. C. (1959) Thunderstorms and V.L.F. radio noise, Ph.D. thesis, Harvard University, Div. Engr. and Applied Phys.

WORKMANN, E. J. (1967) The production of thunderstorm electricity, *J. Frank. Inst.* **283** (6), 540–557.

CHAPTER 4

WAVES IN A SPHERICAL GUIDE

Abstract. The waveguide is excited by vertical or horizontal electric or magnetic dipole sources, and its boundaries are characterized by surface impedances. The resulting waves are expressed as a superposition of T.M. and T.E. modes. The wave numbers, excitation factors, height-gain functions, and height-dependent impedances are examined for both types of modes. A thin-shell approximation of the radial wave functions is shown to be adequate for phase-velocity estimates, but other propagation parameters are of restricted validity in the V.L.F. range, where Airy integral approximations provide more reliable data. A horizontal electric dipole is shown to provide a nearly omnidirectional coverage of horizontal field components in the frequency range of the lower Schumann resonances; and for an elevated source, the horizontal fields are essentially omnidirectional also in the V.L.F. range. Near fields of vertical and horizontal electric dipoles are expressed as a summation of waveguide modes. At the antipode the horizontal field components vanish for a vertical electric dipole, and the vertical electric field vanishes for a horizontal electric dipole.

4.1 Introduction and Summary

Wave propagation in the spherical waveguide between the earth and the ionosphere has been treated in a number of monographs and review papers [Budden, 1961; Wait, 1962; Krasnushkin, 1962; Galejs, 1964; Madden and Thompson, 1965]. The waveguide solutions are discussed in great detail for excitation by vertical electric dipoles. There are also formulations for other types of excitation, but these solutions are not developed to a comparable degree; there is only very scanty information on T.E. modes that are significant in the analysis of radiation from horizontal current elements or from loop antennas.

This chapter discusses the problem of wave propagation in a spherical shell between the earth and the ionosphere in the geometry shown in Fig. 4.1. The source is located at $\theta = 0$ and $z = z_s$, and the fields are observed at z and θ in a spherical coordinate system. Field expressions are derived for excitation by vertical electric dipoles and by vertical magnetic dipoles or horizontal loops in Section 4.2.3; the reciprocity theorem is used to obtain the field expressions for horizontal electric and magnetic dipoles in Sections 4.2.4 and 4.2.5. In the formal solution of the problem, the azimuthal field variations are expressed in terms of Legendre functions; and there are simple approximations valid near the source, the antipode, and for intermediate distances. The radial field variations are represented by spherical Bessel functions or Hankel functions of complex arguments ν. For spherical shells thin relative to the wavelength (e.g. E.L.F.), it is permissible to approximate the radial functions by exponentials and to refer the propagation parameter from the center of the shell to its lower boundary as indicated in Section 4.3. Such an approximation procedure has been proposed for the V.L.F. range by Volland [1964a, b], but its accuracy and limitations have not been established in detail.

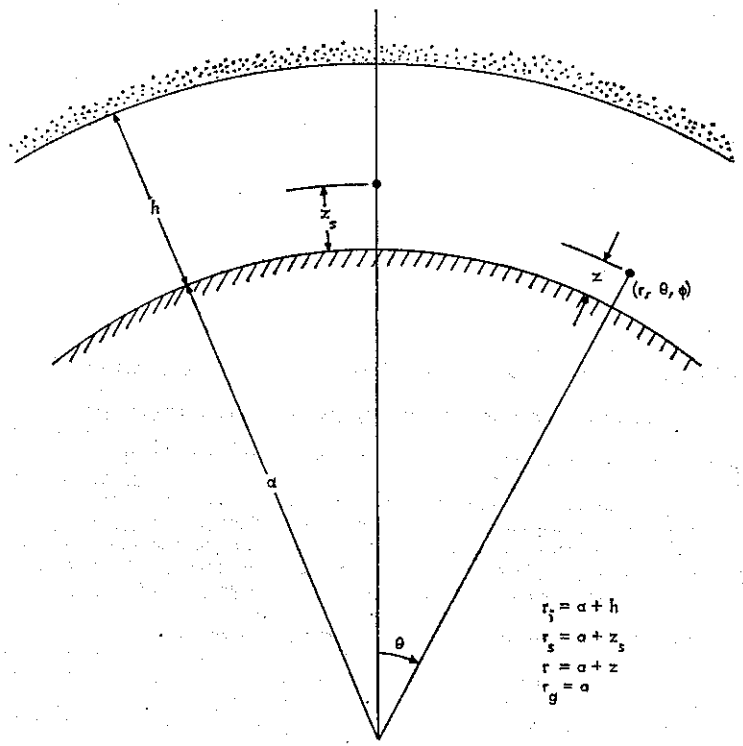

FIG. 4.1 Geometry of the Spherical Shell

It will be shown that this approximation gives a reasonable accuracy to phase-velocity data, but the other propagation parameters are of a more restricted validity. Another thin-shell approximation is developed in Section 4.4 by a Taylor series expansion of the spherical wave functions, which may be used for calculations in the E.L.F. range. For the V.L.F. range, a more accurate representation of the radial functions is derived in Section 4.5 using the so-called third order or Watson approximation, which replaces spherical Bessel functions by Hankel functions of order 1/3 or Airy functions. The accuracy of these approximations are adequate for most purposes, but a more exact reference solution can be derived using the thin-shell approximations in a multilayer representation of the airspace between the earth and the ionosphere [Galejs, 1967], which are also discussed in Section 5.5.

The waveguide boundaries are characterized by surface impedances, and waves excited by the various elementary sources can be expressed as a superposition of T.M. and T.E. modes. These waves may be coupled at the source and at the ionospheric boundary if the wave coupling in the anisotropic ionosphere makes the surface impedance of the T.E. modes Z_h and amplitudes of the T.E. waves dependent on the surface impedance of the T.M. modes Z_e and their amplitudes. The mechanism of this latter coupling will not be treated in this chapter, but the analysis allows for values of Z_e and Z_h that differ and may subsequently account

for such wave coupling beyond the ionospheric boundaries. The surface impedance boundary conditions at $z = 0$ and h lead to a transcendental conditional or modal equation involving the radial wave functions. The solution of this equation determines the permissible wave numbers for propagation in the azimuthal θ direction, or the propagation parameter S, where Re S is inversely proportional to the phase velocity v_{ph} and Im S is proportional to the attenuation rate α. The effective refractive index of the ionospheric boundary n_i is not necessarily large compared to unity, and the surface impedance Z_i (where $i = e$ or h) may depend on S. The initial estimate of Z_i may be inaccurate, and the calculations must be iterated until the Z_i and S sequences converge. The final propagation parameter S is the same as the propagation parameter S used in the Z_i computations. This final solution provides the same wave number for propagation in the θ direction for the waves inside and below the ionospheric boundary, and it assures the continuity of the tangential electric and magnetic fields across the boundary.

The various field expressions contain a number of common combinations of radial functions that can be interpreted as excitation factors; height-gain functions, and height-dependent normalized impedances. These functions are defined in Section 4.3.2, and the excitation factor characterizes the effectiveness of a ground-based source; the height-gain function denotes the altitude variations of the principal field components. The excitation efficiency of an elevated source may be determined from a combination of the excitation factor with a height-gain function for the appropriate transmitter altitude. The normalized impedance or refractive index denotes the height variations of the wave tilt.

There are significant differences between the characteristics of T.M. and T.E. modes, as is pointed out in Sections 4.5.1 and 4.5.2. For T.M. waves, the ionosphere appears in the V.L.F. range as a nearly perfect reflector of $\sigma_i \to 0$; but for T.E. waves the same ionospheric model acts as a nearly perfect conductor of $\sigma_i \to \infty$. A decrease of the ionospheric conductivity σ decreases the attenuation rate α of T.M. waves but increases the attenuation of T.E. waves. For T.M. modes, the excitation factor A_n is of the order of 0.1 to 1, the height-gain function $G_n(z)$ is of the order of 1, while the normalized impedance $\Delta_n(z)$ is of the same order of magnitude as the normalized impedances of the two boundary surfaces. For T.E. modes, the excitation factor A_m is inversely proportional to the ground conductivity σ_g and is several orders of magnitude less than the excitation factor A_n of the T.M. modes. The height-gain function $G_m(z)$ is proportional to $\sigma_g^{0.5}$ and is large in magnitude except at the ground surface where it is equal to 1 by definition. The T.E. modes are excited more efficiently by an elevated source. The normalized impedance of the T.E. modes $\Delta_m(z)$ is much larger in magnitude than the normalized impedances of the boundary surfaces over most of the height range z.

The fields of the horizontal current element have been examined in Section 4.3.2.3. Although the vertical electric field component E_r exhibits the familiar cos φ angular variation, it is not generally recognized that the horizontal field components of the same dipole exhibit different angular characteristics in several limiting geometries. In the E.L.F. range at 7.5 c/s, which is near the fundamental Schumann resonance, the horizontal electric and magnetic field components are of comparable magnitudes in the directions parallel and perpendicular to the dipole axis; however, the field components of the perpendicular direction are decreased in magnitude at higher frequencies. For an elevated source in the V.L.F. range, the horizontal electric and magnetic field components are also of comparable magnitude in directions perpendicular and

parallel to the dipole axis: quasi-T.M. fields predominate in the direction parallel to the dipole axis; quasi-T.E. fields predominate in the perpendicular direction.

Near fields of a vertical electric dipole are expressed as a series of zonal harmonics in Section 4.9 or as a summation of waveguide modes in Section 4.6. These representations are compared with dipole fields on a conducting ground plane and with field calculations using the method of images or ray theory. The series of zonal harmonics and the mode sum provide identical near fields; their difference characterizes the contribution of so-called branch-cut waves and is negligible in the present computational model. Approximately 100 T.M. modes are necessary for representing the fields of a vertical electric dipole at a distance of 5 km from the source, but a smaller number of modes is sufficient at larger distances. In the near-field range, the method of images gives the simplest field representation for E.L.F.; for V.L.F, a useful approximation is provided by combining the ground wave and a single sky wave. For horizontal electric dipoles, T.E. as well as T.M. modes are required in the near-field representations; these near-field expressions apply to any of the field components at arbitrary heights within the waveguide, and they consider also the finite conductivity of the boundary surface. In the vicinity of the source, the mode summations for the horizontal electric dipole compare with the relatively simple expressions for dipole fields on a flat finitely conducting ground plane. Section 4.7 discusses the antipodal fields of vertical electric and horizontal electric dipoles. For vertical electric dipoles, the field components E_θ and H_φ are shown to vanish at the antipode. For horizontal electric dipoles, the field component E_r vanishes, but the other field components remain finite in the vicinity of the antipode. The field variations over the complete distance range which starts near the source and ends at the antipode are briefly illustrated in Section 4.8.

4.2 Formal Solution

4.2.1 *Field Components*

For an assumed exp $(-i\omega t)$ time dependence, the fields in the spherical shell satisfy the equations

$$\nabla \times \mathbf{H} = -i\omega\varepsilon_0 \mathbf{E}, \tag{1}$$

$$\nabla \times \mathbf{E} = i\omega\mu_0 \mathbf{H}. \tag{2}$$

For no φ variations of the fields, the components of (1) and (2) may be written out as

$$\frac{1}{r^2 \sin\theta} \frac{\partial}{\partial\theta}(r \sin\theta H_\varphi) = -i\omega\varepsilon_0 E_r, \tag{3}$$

$$-\frac{1}{r \sin\theta} \frac{\partial}{\partial r}(r \sin\theta H_\varphi) = -i\omega\varepsilon_0 E_\theta, \tag{4}$$

$$\frac{1}{r}\left[\frac{\partial}{\partial r}(rH_\theta) - \frac{\partial}{\partial\theta} H_r\right] = -i\omega\varepsilon_0 E_\varphi, \tag{5}$$

$$\frac{1}{r^2 \sin\theta} \frac{\partial}{\partial\theta}(r \sin\theta E_\varphi) = i\omega\mu_0 H_r, \tag{6}$$

$$-\frac{1}{r \sin\theta} \frac{\partial}{\partial r}(r \sin\theta E_\varphi) = i\omega\mu_0 H_\theta, \tag{7}$$

$$\frac{1}{r}\left[\frac{\partial}{\partial r}(rE_\theta) - \frac{\partial}{\partial\theta} E_r\right] = i\omega\mu_0 H_\varphi. \tag{8}$$

There is no coupling between the T.M. (E_r, E_θ, and H_φ) and the T.E. (E_φ, H_r, and H_θ) fields. The T.M. and T.E. field components can be treated separately in the spherical shell between the earth and the ionosphere, and the T.M. fields will be considered first.

Equations (3), (4), and (8) can be combined to give the differential equation

$$\frac{\partial^2}{\partial r^2} G + \frac{1}{r^2}\left(-\cot\theta \frac{\partial}{\partial \theta} G + \frac{\partial^2}{\partial \theta^2} G\right) + k_0^2 G = 0, \tag{9}$$

where $G = r \sin\theta H_\varphi$ and $k_0 = \omega\sqrt{\mu_0 \varepsilon_0}$ is the wave number of free space. Substituting $G = R(r)T(\theta)$, (9) can be separated into an r-dependent and a θ-dependent part, each of which is set to be equal to a constant $\nu(\nu+1)$. The resulting differential equation in $T(\theta)$

$$T'' - \cot\theta T' + \nu(\nu+1) T = 0 \tag{10}$$

can be rearranged using the substitution $T(\theta) = \sin\theta W(-\cos\theta)$ into

$$\sin^2\theta W'' + 2\cos\theta W' + [\nu(\nu+1) - \mu(\sin\theta)^{-2}] W = 0$$

or

$$\frac{1}{\sin\theta}\frac{\partial}{\partial\theta}\left[\sin\theta \frac{\partial}{\partial\theta} W(-\cos\theta)\right] + [\nu(\nu+1) - \mu(\sin\theta)^{-2}] W(-\cos\theta) = 0, \tag{11}$$

where $\mu = 1$. Equation (11) is recognized as Legendre's equation of degree ν and order $\mu = 1$. Its solution can be written in terms of Legendre functions as

$$W(-\cos\theta) = P_\nu^1(-\cos\theta) = \frac{d}{d\theta} P_\nu(-\cos\theta), \tag{12}$$

where $P_\nu^\mu(z)$ is a Legendre function of first kind, degree ν, and order μ. This function is singular only for $\theta \to 0$. The Legendre functions of the second kind $Q_\nu(-\cos\theta)$ are singular for $\theta \to 0$ and π and are not included in the solution.

The r-dependent part of (9) becomes

$$r^2 R'' + [(k_0 r)^2 - \nu(\nu+1)] R = 0$$

or

$$r^2(R/r)'' + 2r(R/r)' + [(k_0 r)^2 - \nu(\nu+1)](R/r) = 0. \tag{13}$$

The solution of (13) can be expressed in terms of spherical Bessel functions as

$$R(r) = r[A h_\nu^{(1)}(u) + B h_\nu^{(2)}(u)], \tag{14}$$

where

$$h_\nu^{(m)}(u) = \left(\frac{\pi}{2u}\right)^{0.5} H_{\nu+0.5}^{(m)}(u). \tag{15}$$

$H_{\nu+0.5}^{(m)}(u)$ is the Hankel function of kind m and order $(\nu+0.5)$, and $u = k_0 r$. The magnetic field component $H_\varphi(r, \theta)$ is computed as

$$H_\varphi(r, \theta) = \frac{R(r)\,T(\theta)}{r\sin\theta} = C_e[A_e h_\nu^{(1)}(u) + B_e h_\nu^{(2)}(u)] \frac{\partial}{\partial\theta} P_\nu(-\cos\theta). \tag{16}$$

The electric field component $E_r(r, \theta)$ is computed substituting (16) in (3) and by applying (11) with the parameter μ set equal to zero. It follows that

$$E_r(r, \theta) = C_e \frac{\sqrt{\mu_0/\varepsilon_0}\,\nu(\nu+1)}{iu} [A_e h_\nu^{(1)}(u) + B_e h_\nu^{(2)}(u)] P_\nu(-\cos\theta). \tag{17}$$

$E_\theta(r, \theta)$ is computed from (4) and (16) as

$$E_\theta(r, \theta) = C_e \frac{\sqrt{\mu_0/\varepsilon_0}}{iu}\left\{A_e \frac{\partial}{\partial u}[u h_\nu^{(1)}(u)] + B_e \frac{\partial}{\partial u}[u h_\nu^{(2)}(u)]\right\} \frac{\partial}{\partial\theta} P_\nu(-\cos\theta). \tag{18}$$

The T.E. field components E_φ, H_r, and H_θ satisfy equations (5), (6), and (7) which are similar to the equations (8), (3), and (4) satisfied by H_φ, E_r, and E_θ respectively, except that E and H, μ_0 and ε_0, and i and $(-i)$ are mutually interchanged. Applying a similar modification to (16), (17), and (18), it follows that

$$E_\varphi(r, \theta) = C_h[A_h h_\nu^{(1)}(u) + B_h h_\nu^{(2)}(u)] \frac{\partial}{\partial\theta} P_\nu(-\cos\theta) \tag{19}$$

$$H_r(r, \theta) = C_h \frac{i\sqrt{\varepsilon_0/\mu_0}\,\nu(\nu+1)}{u} [A_h h_\nu^{(1)}(u) + B_h h_\nu^{(2)}(u)] P_\nu(-\cos\theta) \tag{20}$$

$$H_\theta(r, \theta) = C_h \frac{i\sqrt{\varepsilon_0/\mu_0}}{u}\left\{A_h \frac{\partial}{\partial u}[u h_\nu^{(1)}(u)] + B_h \frac{\partial}{\partial u}[u h_\nu^{(2)}(u)]\right\} \frac{\partial}{\partial\theta} P_\nu(-\cos\theta), \tag{21}$$

where $u = k_0 r$.

Expressions (16) to (21) represent a formal solution of the field problem. The fields must satisfy boundary conditions at the cavity walls, which determine the amplitudes A_e, B_e, A_h, and B_h and the values ν as will be shown in Section 4.2.2. The remaining constants C_e and C_h, discussed in Section 4.2.3, are proportional to the dipole moments of the sources.

4.2.2 *Modal Equation*

The field components (16) to (21) should satisfy the boundary conditions

$$Z_g = -\frac{E_\theta(a)}{H_\varphi(a)} = \frac{E_\varphi(a)}{H_\theta(a)} \tag{22}$$

and

$$Z_e = \frac{E_\theta(a+h)}{H_\varphi(a+h)} \qquad Z_h = -\frac{E_\varphi(a+h)}{H_\theta(a+h)} \tag{23}$$

at the ground surface and the ionospheric boundary respectively. Substituting (16) and (18) in (22), the resulting equation can be solved for the amplitude ratio B_e/A_e, which gives

$$\frac{B_e}{A_e} = -\frac{h_1'(u_g) + i\Delta_g h_1(u_g)}{h_2'(u_g) + i\Delta_g h_2(u_g)}, \tag{24}$$

where $h_m(u) = h_\nu^{(m)}(u)$, $h_m'(u) = (1/u)\,\partial[u h_\nu^{(m)}(u)]/\partial u$, $u_g = k_0 a$, $\Delta_g = Z_g/\sqrt{\mu_0/\varepsilon_0}$. Field components (16) to (18) will satisfy the boundary condition (22) at $r = a$ for any value of ν if

B_e/A_e ratio is computed from (24). Substituting (16) and (18) in (23), the resulting equation is solved for B_e/A_e, which gives

$$\frac{B_e}{A_e} = -\frac{h_1'(u_i) - i\,\Delta_e h_1(u_i)}{h_2'(u_i) - i\,\Delta_e h_2(u_i)}, \tag{25}$$

where $u_i = k_0(a+h)$, $\Delta_e = Z_e/\sqrt{\mu_0/\varepsilon_0}$, and the other symbols are defined as in (24). Using this B_e/A_e ratio, field components (16) to (18) will satisfy the boundary condition (23) at $r = a+h$ for any value of ν. However, the field components (16) to (18) must satisfy the boundary conditions (22) and (23) simultaneously. There will be only a discrete set of ν values which make B_e/A_e of (24) equal to B_e/A_e of (25).

Eliminating B_e/A_e from (24) and (25), it follows that the permissible eigenvalues ν are determined from the solution of

$$\frac{h_2'(u_g) + i\,\Delta_g h_2(u_g)}{h_1'(u_g) + i\,\Delta_g h_1(u_g)} \cdot \frac{h_1'(u_i) - i\,\Delta_e h_1(u_i)}{h_2'(u_i) - i\,\Delta_e h_2(u_i)} = 1, \tag{26}$$

which represents the conditional or modal equation for the T.M. modes. The subsequent equations (45) to (48) show that $(\nu+0.5)$ is proportional to the wave number in the θ-direction.

For T.E. modes, (iE_θ/H_φ) of the above development should be replaced by $(-iH_\theta/E_\varphi)$ and $\sqrt{\mu_0/\varepsilon_0}$ should be replaced by $\sqrt{\varepsilon_0/\mu_0}$. After defining $\Delta_h = Z_h/\sqrt{\mu_0/\varepsilon_0}$, the modal equation (26) can be used for determining the eigenvalues ν of T.E. modes if Δ_g is replaced by $(1/\Delta_g)$ and Δ_e is replaced by $(1/\Delta_h)$. The amplitude ratio B_h/A_h of the T.E. field components (19) to (21) is given by (24) if Δ_g is replaced by $(1/\Delta_g)$, or by (25) if Δ_e is replaced by $(1/\Delta_h)$.

The modal equation for the T.M. modes (26) or its modification for the T.E. modes contains spherical Bessel functions of complex order ν and large arguments u. There are no simple analytical representations for such functions, and further approximations are necessary to make the solution of these equations practicable. A relatively simple earth-flattening or thin-shell approximation is developed in Section 4.3.1, which is strictly valid only in spherical shells thin relative to wavelength. Another thin-shell approximation is developed in Section 4.4 using a Taylor series expansion of the spherical wave functions. Approximations suitable in the V.L.F. range involve Hankel functions of order $\frac{1}{3}$ or Airy functions. These approximations are discussed in Section 4.5.1.

4.2.3 *Vertical Electric or Magnetic Dipoles*

A radial electric dipole or an electric current element of moment $I\,ds$ is located at $r_s = a+z_s$ on the $\theta = 0$ axis of the spherical shell. The magnetic field component H_φ can be readily calculated in the vicinity of this current element. Thus

$$\lim_{\theta \to 0} 2\pi r\theta H_\varphi(r, \theta) = \begin{cases} I & \text{if} \quad (r_s - ds/2) < r < (r_s + ds/2) \\ 0 & \text{elsewhere} \end{cases} \tag{27}$$

or

$$\lim_{\theta \to 0} \int_{r_g}^{r_i} H_\varphi(r, \theta)\, dr \approx \lim_{\theta \to 0} \frac{I\,ds}{2\pi r_s \theta}. \tag{28}$$

The value of the integral (28) remains unchanged if H_φ is assumed of the form

$$\lim_{\theta \to 0} H_\varphi(r, \theta) = \lim_{\theta \to 0} \frac{I\,ds}{2\pi r_s \theta}\, \delta(r - r_s), \tag{29}$$

where $\delta(x)$ is a delta function. In the limit of $\theta \to 0$, the Legendre function $P_\nu(-\cos\theta)$ is approximated by

$$P_\nu(-\cos\theta) \approx \frac{2\sin\nu\pi}{\pi}\,[\log\theta + f(\nu)]. \tag{30}$$

Introducing a simplified notation,

$$h_\nu^e(u) = A_e h_\nu^{(1)}(u) + B_e h_\nu^{(2)}(u), \tag{31}$$

substituting (16) in (29), applying (30), it follows that

$$\frac{I\,ds}{2\pi r_s}\,\delta(r - r_s) = \sum_\nu C_e h_\nu^e(u)\,\frac{2\sin\nu\pi}{\pi}, \tag{32}$$

where the summation is extended over those discrete values of $\nu = \nu_n$ which satisfy the modal equation (26). Multiplying both sides of (32) with a function $h_\mu^e(u)$, an integration results in

$$\frac{I\,dsk_0}{4r_s}\,h_\mu^e(u_s) = \sum_\nu C_e \sin\nu\pi \int_{u_g}^{u_i} h_\nu^e(u)\, h_\mu^e(u)\, du. \tag{33}$$

The function $h_\nu^e(u)$ of (31) is the same as $R(r)/r$ of (14). The differential equation (13) is therefore satisfied by $h_\nu^e(u)$ and $h_\mu^e(u)$ functions. The differential equation for $h_\nu^e(u)$ is multiplied with $h_\mu^e(u)$ and integrated between u_g and u_i. The differential equation for $h_\mu^e(u)$ is multiplied with $h_\nu^e(u)$ and is also integrated. The difference of these two sets of integrals is integrated by parts to give [Sommerfeld, 1949]

$$\int_{u_g}^{u_i} h_\nu^e(u)\, h_\mu^e(u)\, du = \frac{u\left\{h_\mu^e(u)\,\dfrac{\partial}{\partial u}\,[uh_\nu^e(u)] - h_\nu^e(u)\,\dfrac{\partial}{\partial u}\,[uh_\mu^e(u)]\right\}}{\nu(\nu+1) - \mu(\mu+1)}\Bigg|_{u=u_g}^{u_i}. \tag{34}$$

For $\nu \neq \mu$, the numerator of the right-hand side of (34) vanishes if modes μ and ν satisfy identical impedance boundary conditions

$$\Delta_b = Z_b/\sqrt{\mu_0/\varepsilon_0} = \pm\frac{\partial}{\partial u}\,[uh_\nu^e(u)]/[iuh_\nu^e(u)]\Big|_{u=u_b}, \tag{35}$$

where the plus sign refers to Z_e with $u = u_i$ and the minus sign to Z_g with $u = u_g$. The modes μ and ν will not be strictly orthogonal if the impedance Z_e of mode μ will differ from the impedance Z_e of mode ν. This possibility is ignored for the present, and the right-hand side of (34) is assumed to become zero if $\mu \neq \nu$. The only nonzero term with $\mu = \nu$ on the right-hand side of (33) is computed after differentiating the numerator and denominator of (34) with respect to μ as

$$I_\nu^e = \int_{u_g}^{u_i} [h_\nu^e(u)]^2\, du = \lim_{\mu \to \nu} \frac{-u^2}{2\mu+1}\left[\frac{\partial}{\partial\mu}\,h_\mu^e(u)\,\frac{\partial}{\partial u}\,h_\nu^e(u) - h_\nu^e(u)\,\frac{\partial^2}{\partial\mu\,\partial u}\,h_\mu^e(u)\right]_{u=u_g}^{u_i}. \tag{36}$$

The validity of this relation can be established also by substituting (31) and (15) and by comparing the resulting expression with the integral (7.14.1.11) of Erdélyi [1953]. After evaluating I_ν^e of (36), C_e of (33) is computed as

$$C_e = \frac{I\, dsk_0}{4r_s \sin \nu\pi} \frac{h_\nu^e(u_s)}{I_\nu^e}, \tag{37}$$

which completes the specification of the T.M. field components (16) to (18).

Integration of (2) shows that

$$\lim_{\theta \to 0} 2\pi r_s \theta E_\varphi(r, \theta) = i\omega\mu_0 \iint H_z(r, \theta)\, da = i\omega\mu_0 H_z(r, 0)\, da$$

or

$$\lim_{\theta \to 0} \int_{r_g}^{r_t} E_\varphi(r, \theta)\, dr = \lim_{\theta \to 0} \frac{i\omega\mu_0 I\, da}{2\pi r_s \theta}, \tag{38}$$

where the integral $\int H_z(r, 0)\, dr = I$ can be verified for the fields of a small loop from Section 7.10 of Smythe [1950]. Equation (38) replaces (28) for fields excited by a small loop or by a magnetic dipole of moment $K\, ds = -i\omega\mu_0 I\, da$. A similar development shows that the amplitude C_h of the T.E. field components (19) to (21) is given by

$$C_h = \frac{i\omega\mu_0 I\, dak_0}{4r_s \sin \nu\pi} \frac{h_\nu^h(u_s)}{I_\nu^h}, \tag{39}$$

where

$$h_\nu^h(u) = A_h h_\nu^{(1)}(u) + B_h h_\nu^{(2)}(u) \tag{40}$$

and I_ν^h is obtained by replacing $h_\nu^e(u)$ with $h_\nu^h(u)$ in (36). The amplitudes A_h and B_h are computed from the B_e/A_e expression (24) or (25) following the procedure summarized in Section 4.2.2. For T.E. modes, the right-hand side of (35) represents $1/\Delta_h = \sqrt{\mu_0/\varepsilon_0}/Z_c$, where the plus sign refers to Z_h with $u = u_i$ and the minus sign to Z_g with $u = u_g$.

Substituting (37) in (17) and applying (31),

$$E_r(r, \theta) = \frac{I\, dsk_0 \sqrt{\mu_0/\varepsilon_0}\, \nu(\nu+1)}{4 \sin \nu\pi\, r_s I_\nu^e iu} h_\nu^e(u_s)\, h_\nu^e(u)\, P_\nu(-\cos\theta). \tag{41}$$

The other T.M. field components are similarly obtained from (16) and (18). Substituting (3) in (20) and applying (40)

$$H_r(r, \theta) = \frac{-I\, dak_0^2 \nu(\nu+1)}{4 \sin \nu\pi\, r_s I_\nu^h u} h_\nu^h(u_s)\, h_\nu^h(u)\, P_\nu(-\cos\theta). \tag{42}$$

The other T.E. field components are similarly obtained from (19) and (21).

The azimuthal field variations are characterized by the Legendre function $P_\nu(-\cos\theta)$. The asymptotic form of the functions is valid for $\nu\theta \gg 1$, and it provides a convenient traveling-wave representation of the field variations in (41) and (42). It follows from (3.9.1.2) of Erdélyi [1953] that

$$P_\nu(-\cos\theta) \approx \sqrt{\frac{2}{\pi(\nu+0.5)\sin\theta}} \cos\left[\left(\nu+\frac{1}{2}\right)(\pi-\theta) - \frac{\pi}{4}\right]. \tag{43}$$

For $\nu \gg 1$ with $\operatorname{Im} \nu > 0$, $\operatorname{Im}\left[\left(\nu+\frac{1}{2}\right)(\pi-\theta)\right] \gg 0$. A further simplification gives

$$\frac{P_\nu(-\cos\theta)}{\sin \nu\pi} \approx -\sqrt{\frac{2}{\pi(\nu+0.5)\sin\theta}} \exp\left[i(\nu+0.5)\theta + i\pi/4\right]. \tag{44}$$

The distance along the surface of the earth between the source at $\theta = 0$ and the receiver at θ is designated as $D = a\theta$. Hence

$$i(\nu+0.5)\theta = \frac{\nu+0.5}{k_0 a} ik_0 D. \tag{45}$$

The factor

$$\frac{\nu+0.5}{k_0 a} = \frac{\nu+0.5}{u_g} = S \tag{46}$$

of (45) can be interpreted as the ratio between the wave number along the surface of the earth k_θ and the wave number of the free space k_0. The real part of S is inversely proportional to the phase velocity v_{ph} of the waves, and the imaginary part of S is proportional to the attenuation rate α. It is seen that

$$c/v_{ph} = \operatorname{Re} S, \tag{47}$$

$$\alpha = 20(\log_{10} e)\omega \operatorname{Im} S/300 \approx 0.02895\omega \operatorname{Im} S, \quad \text{in db/1000 km}, \tag{48}$$

where $c = 1/\sqrt{\mu_0/\varepsilon_0}$ is the free-space velocity of electromagnetic waves.

The radial functions of the various field expressions can be related to excitation factors, height-gain functions, or normalized height-dependent impedances that are defined in Section 4.3.2. Such representations of the radial functions are used in conjuction with the asymptotic form (44) to obtain the fields of vertical electric and magnetic dipoles in Sections 4.3.2.1 and 4.3.2.2.

The asymptotic form (44) is not valid in the vicinity of sources ($\nu\theta \ll 1$) or in the vicinity of the antipode ($\theta \to \pi$). Approximations suitable for this range of θ are developed in Sections 4.6 and 4.7.

4.2.4 *Horizontal Electric Dipole*

The fields of a horizontal electric dipole can be related to the fields of vertical electric and vertical magnetic dipoles by the reciprocity theorem [Wait, 1962]. This theorem states that the voltage V_2 induced in antenna 2 by current I_1 of antenna 1 is the same as the voltage V_1 induced in antenna 1 by an indentical current I_2 flowing in antenna 2.

A vertical electric (V.E.) dipole of length ds at $z_0' = z_s$ and a horizontal electric (H.E.) dipole parallel to the x-axis at $z_0 = z_r$ are shown in Fig. 4.2, where subscripts r and s refer to receiver and source coordinates respectively. $E_{\varphi'}$ is the only electric field component generated by the V.E. dipole which lies in the plane of the H.E. dipole. The magnitude of the voltage induced in the H.E. dipole V^{he} is maximum if $E_{\varphi'}$ is parallel to the x-axis, which occurs for $\varphi = 0$ and π. It follows that

$$V^{he} = -E_{\varphi'}^{ve}(z_0' = z_s, z_0 = z_r) \cos\varphi\, ds^{he}, \tag{49}$$

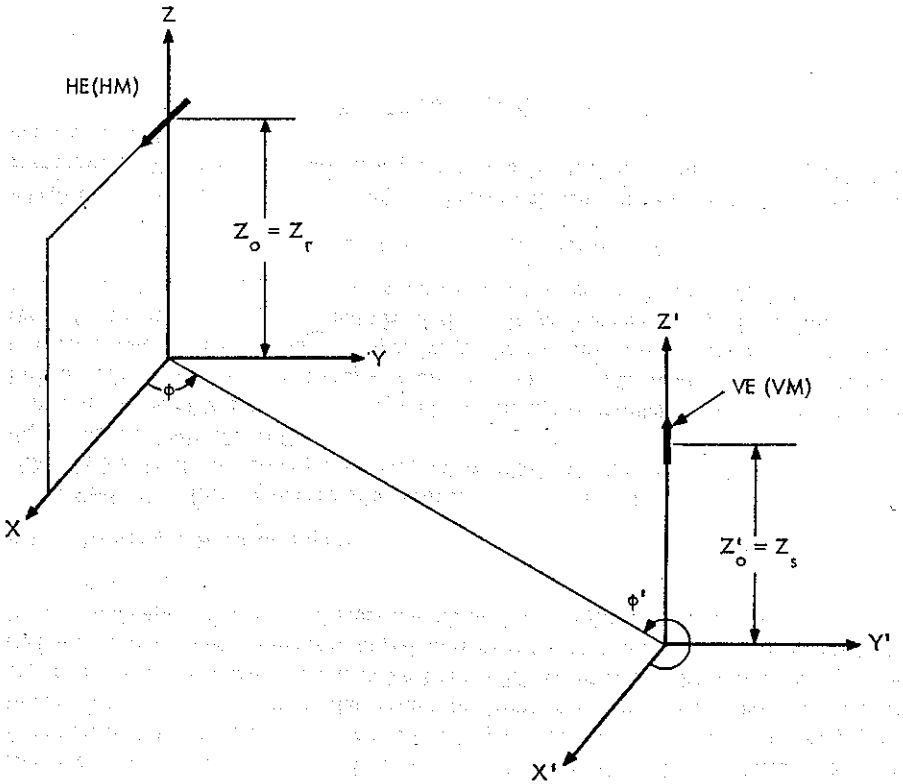

FIG. 4.2 Coordinate Systems for Defining Reciprocity Relations

where the superscripts *he* and *ve* refer to horizontal and vertical electric dipoles respectively. With the same current applied to the H.E. dipole, only the V.E. field E_z will contribute to V^{ve} and

$$V^{ve} = E_z^{he}(z_0 = z_s,\ z_0' = z_r)\, ds^{ve}. \tag{50}$$

Equating (49) and (50) and letting $ds^{he} = ds^{ve}$ results in

$$E_z^{he}(z_0 = z_s, z_0' = z_r) = -E_{\varphi'}^{ve}(z_0' = z_s, z_0 = z_r)\cos\varphi. \tag{51}$$

A vertical magnetic (V.M.) dipole (or a horizontal loop of area da^{vm} parallel to the x', y' plane) at $z_0' = z_s$ and a (H.E.) dipole parallel to the x-axis at $z_0 = z_r$ may be considered in the geometry shown in Fig. 4.2. The only nonzero electric component generated by the V.M. dipole is $E_{\varphi'}$. The magnitude of the voltage induced in the H.E. dipole V^{he} is maximum if $E_{\varphi'}$ is parallel to the x-axis, which occurs for $\varphi = \pi/2$ or $3\pi/2$. Hence

$$V^{he} = E_{\varphi'}^{vm}(z_0' = z_s, z_0 = z_r)\sin\varphi\, ds^{he}, \tag{52}$$

where the superscript *vm* refers to the V.M. dipole. With the same current applied to the H.E. dipole only the V.M. field H_z will contribute to V^{vm} and

$$V^{vm} = i\omega\mu_0 H_z^{he}(z_0 = z_s,\ z_0' = z_r)\, da^{vm}. \tag{53}$$

Equating (52) and (53) gives

$$H_z^{he}(z_0 = z_s, z_0' = z_r) = \frac{1}{i\omega\mu_0} E_{\varphi'}^{vm}(z_0' = z_s, z_0 = z_r)\sin\varphi\, ds^{he}/da^{vm}. \tag{54}$$

For spherical coordinates the z component of (51) or (54) is replaced by r component and the ϱ component of (51) by the θ component of the fields. Substituting (18) in (51) and applying (31) and (37), it follows that

$$E_r^{he}(r, \theta, \varphi) = \frac{I\, dsk_0\sqrt{\mu_0/\varepsilon_0}}{4\sin\nu\pi\, I_\nu^e iu_s r}\frac{\partial}{\partial u}[uh_\nu^e(u)]\Big|_{u=u_s} h_\nu^e(u)\frac{\partial}{\partial\theta}P_\nu(-\cos\theta)\cos\varphi, \tag{55}$$

where θ derivatives change sign when interchanging the coordinates of source and receiver. Substituting (19) in (54) and applying (39) and (40), it follows that

$$H_r^{he}(r, \theta, \varphi) = \frac{-I\, dsk_0}{4\sin\nu\pi\, I_\nu^h r} h_\nu^h(u_s)\, h_\nu^h(u)\frac{\partial}{\partial\theta}P_\nu(-\cos\theta)\sin\varphi \tag{56}$$

where $h_\nu^q(u)$ is defined by (31) and (40) and where the eigenvalues ν are determined from solutions of modal equations as discussed in Section 4.2.2. The other field components are related to E_r and H_r by (1) and (2). The φ component of (1) and the θ component of (2) can be manipulated to yield

$$\mathcal{D}(r\sin\theta H_\theta) = -i\omega\varepsilon\frac{\partial}{\partial\varphi}E_r + \sin\theta\frac{\partial^2}{\partial r\,\partial\theta}H_r, \tag{57}$$

$$\mathcal{D}(r\sin\theta E_\varphi) = \frac{\partial^2}{\partial\varphi\,\partial r}E_r - i\omega\mu_0\sin\theta\frac{\partial}{\partial\theta}H_r, \tag{58}$$

where the differential operator $\mathcal{D}$ is defined as

$$\mathcal{D} = \left(k_0^2 + \frac{\partial^2}{\partial r^2}\right). \tag{59}$$

A similar manipulation of the θ component of (1) and of the φ component of (2) gives

$$\mathcal{D}(r\sin\theta H_\varphi) = i\omega\varepsilon\sin\theta\frac{\partial}{\partial\theta}E_r + \frac{\partial^2}{\partial\varphi\,\partial r}H_r, \tag{60}$$

$$\mathcal{D}(r\sin\theta E_\theta) = \sin\theta\frac{\partial^2}{\partial\theta\,\partial r}E_r + i\omega\mu_0\frac{\partial}{\partial\varphi}H_r. \tag{61}$$

A similar differential operator can be introduced in the right-hand sides of (57), (58), (60), and (61) by noting that $rh_\nu^q(u)$ computed from (31) or (40) satisfies the differential equation (13). This results in

$$\frac{h_\nu^q(u)}{r} = \frac{1}{\nu(\nu+1)}\mathcal{D}[rh_\nu^q(u)]. \tag{62}$$

After substituting (62) in (55) and (56), the differential operators are cancelled on both sides of (57), (58), (60), and (61). This gives

$$E_\theta = (r \sin\theta)^{-1}\left[\sin\theta \frac{\partial^2}{\partial\theta\,\partial r}(rU) + i\omega\mu_0 \frac{\partial}{\partial\varphi}(rV)\right], \tag{63}$$

$$E_\varphi = (r \sin\theta)^{-1}\left[\frac{\partial^2}{\partial\varphi\,\partial r}(rU) - i\omega\mu_0 \sin\theta \frac{\partial}{\partial\theta}(rV)\right], \tag{64}$$

$$H_\theta = (r \sin\theta)^{-1}\left[-i\omega\varepsilon_0 \frac{\partial}{\partial\varphi}(rU) + \sin\theta \frac{\partial^2}{\partial r\,\partial\theta}(rV)\right], \tag{65}$$

$$H_\varphi = (r \sin\theta)^{-1}\left[i\omega\varepsilon_0 \sin\theta \frac{\partial}{\partial\theta}(rU) + \frac{\partial^2}{\partial\varphi\,\partial r}(rV)\right], \tag{66}$$

where

$$U = \frac{I\,dsk_0\sqrt{\mu_0/\varepsilon_0}}{4\sin\nu\pi\, I_\nu^e i u_s \nu(\nu+1)} \frac{\partial}{\partial u}[uh_\nu^e(u)]\Big|_{u=u_s} h_\nu^e(u) \frac{\partial}{\partial\theta} P_\nu(-\cos\theta)\cos\varphi, \tag{67}$$

$$V = \frac{-I\,dsk_0}{4\sin\nu\pi\, I_\nu^h \nu(\nu+1)} h_\nu^h(u_s)\, h_\nu^h(u) \frac{\partial}{\partial\theta} P_\nu(-\cos\theta)\sin\varphi. \tag{68}$$

Noting that $E_r = \mathcal{D}(rU)$ and $H_r = \mathcal{D}(rV)$, equations (63) to (66) can be seen to be consistent with (57), (58), (60), and (61).

The above field expressions are reduced in Section 4.3.2.3 to a form that is suitable for numerical calculations. The radial functions of (55), (56), (67), and (68) are related to excitation factors, height-gain functions, and normalized height-dependent impedances; and the Legendre functions have been replaced by the asymptotic forms. Approximations valid near the source or the antipode are found in Sections 4.6.2 and 4.7.2 respectively. The height-gain functions, excitation factors, and normalized impedances of the field expressions can be defined using the thin-shell approximations of Section 4.3.2 or the Airy functions of Section 4.5.2.

4.2.5 *Horizontal Magnetic Dipole*

The fields of a H.M. dipole (or of a vertical loop) are also related to the fields of V.E. and V.M. dipoles by the reciprocity theorem [Galejs, 1961], which was applied in Section 4.2.4 to determine the fields of a H.E. dipole.

A V.E. dipole of length ds at $z_0' = z_s$ and a H.M. dipole parallel to the x-axis (or a vertical loop of area da in the yz plane) at $z_0 = z_r$ are shown in Fig. 4.2, where subscripts r and s refer to receiver and source coordinates respectively. The only nonzero H component generated by the V.E. dipole is $H_{\varphi'}$. The magnitude of the voltage induced in the H.M. dipole V^{hm} is maximum if $H_{\varphi'}$ is parallel to the x-axis, which occurs for $\varphi = \pi/2$ and $3\pi/2$. Thus

$$V^{hm} = i\omega\mu_0 H_{\varphi'}^{ve}(z_0' = z_s,\, z_0 = z_r)\sin\varphi\, da, \tag{69}$$

where the superscripts *hm* and *ve* refer to horizontal magnetic and vertical electric dipoles respectively. With the same current applied to the H.M. dipole, only the V.E. field E_z will contribute to V^{ve} and

$$V^{ve} = E_z^{hm}(z_0 = z_s,\, z_0' = z_r)\, ds. \tag{70}$$

Equating (69) and (70) results in

$$E_z^{hm}(z_0 = z_s,\, z_0' = z_r) = i\omega\mu_0 \sin\varphi H_{\varphi'}^{ve}(z_0' = z_s,\, z_0 = z_r)\, da/ds. \tag{71}$$

A V.M. dipole (or a horizontal loop of area da^{vm} parallel to the $x'y'$ plane) at $z_0' = z_s$ and a H.M. dipole parallel to the x-axis (or a vertical loops of area da^{hm} in the yz plane) at $z_0 = z_r$ may be considered in the geometry shown in Fig. 4.2. $H_{\varrho'}$ is the only nonzero H component generated by the V.M. dipole which lies in the plane of the H.M. dipole. The magnitude of the voltage induced in the H.M. dipole V^{hm} is maximum, if $H_{\varrho'}$ is parallel to the x-axis, which occurs for $\varphi = 0$ or π. Hence

$$V^{hm} = -i\omega\mu_0 H_{\varrho'}^{vm}(z_0' = z_s,\, z_0 = z_r)\cos\varphi\, da^{hm}, \tag{72}$$

where the superscript *vm* refers to the vertical magnetic dipole. With the same current applied to the H.M. dipole, only the V.M. field H_z will contribute to V^{vm} and

$$V^{vm} = i\omega\mu_0 H_z^{hm}(z_0 = z_s,\, z_0' = z_r)\, da^{vm}. \tag{73}$$

Equating (64) and (65) gives for $da^{vm} = da^{hm}$

$$H_z^{hm}(z_0 = z_s,\, z_0' = z_r) = -\cos\varphi H_{\varrho'}^{vm}(z_0' = z_s,\, z_0 = z_r). \tag{74}$$

For spherical coordinates, the z component of (71) or (74) is replaced by r component and the ϱ component of (74) by the θ component of the fields. Substituting (16) in (71) and applying (31) and (37), it follows that

$$E_r^{hm}(r,\theta,\varphi) = -\frac{i\omega\mu_0 I\, dak_0}{4\sin\nu\pi\, I_\nu^e} h_\nu^e(u_s) \frac{h_\nu^e(u)}{r} \frac{\partial}{\partial\theta} P_\nu(-\cos\theta)\sin\varphi, \tag{75}$$

where θ derivates change sign when interchanging the coordinates of source and receiver. Substituting (21) in (74) and applying (39) and (40), H_r^{hm} becomes

$$H_r^{hm}(r,\theta,\varphi) = -\frac{I\,dak_0^2}{4\sin\nu\pi\, I_\nu^h u_s} \frac{\partial}{\partial u}[uh_\nu^h(u)]\Big|_{u=u_s} \frac{h_\nu^h(u)}{r} \frac{\partial}{\partial\theta} P_\nu(-\cos\theta)\cos\varphi. \tag{76}$$

E_r^{hm} and H_r^{hm} of (75) and (76) exhibit the same r and θ dependence as E_r^{he} and H_r^{he} in (55) and (56). Equations (57) to (66) apply also to the other field components excited by a horizontal magnetic dipole, but the functions U and V of (63) to (66) are now defined by

$$U = -\frac{i\omega\mu_0 I\, dak_0}{4\sin\nu\pi\, I_\nu^e \nu(\nu+1)} h_\nu^e(u_s)\, h_\nu^e(u) \frac{\partial}{\partial\theta} P_\nu(-\cos\theta)\sin\varphi, \tag{77}$$

$$V = -\frac{I\,dak_0^2}{4\sin\nu\pi\, I_\nu^h u_s \nu(\nu+1)} \frac{\partial}{\partial u}[uh_\nu^h(u)]\Big|_{u=u_s} h_\nu^h(u) \frac{\partial}{\partial\theta} P_\nu(-\cos\theta)\cos\varphi. \tag{78}$$

The field expressions listed in the subsequent Section 4.3.2.4 are developed starting out with (75) to (78) and making use of the asymptotic form (44) of the Legendre function. The excitation factors, height-gain functions, and normalized impedances of these field expressions can be defined using the thin-shell approximation of Section 4.3.2 or the Airy functions of Section 4.5.2.

4.3 Exponential or Thin-shell Approximations

The solutions of the preceding sections have been carried out using Legendre functions for the θ variations and spherical Bessel functions for the r variations of the fields. The approximation (43) or (44) is adequate for the θ dependence in a number of applications, but there appears to be no simple representations for the spherical Bessel functions of large complex order ν and large arguments $u = k_0 r$ that are equally applicable to E.L.F. and V.L.F. ranges. Approximations which neglect the earth's curvature can be used in the E.L.F. range but give inaccurate results in most of the V.L.F. range. A simple approximation which becomes accurate in the limit of zero earth curvature ($r \to \infty$) or for thin shells ($h/r \to 0$) will be developed in this section.

The radial field variation was computed from the differential equation (13). For $r \to \infty$ or for fields in a thin shell of $h/r \to 0$, the factors r are approximated by their average value in the shell $r_m = a + 0.5h$ and (13) becomes

$$R'' + \left[k_0^2 - \frac{\nu(\nu+1)}{r_m^2}\right] R = 0, \tag{79}$$

solutions of which are of the form

$$R = Ae^{iKr} + Be^{-iKr} \tag{80}$$

with

$$K^2 = k_0^2 - [\nu(\nu+1)/r_m^2] = k_0^2[1 - (aS/r_m^2)]. \tag{81}$$

A comparison of (80) and (14) indicates that

$$h_\nu^{(1,2)}(u) \sim \exp(\pm iKr)/r_m. \tag{82}$$

The approximation (82) will be substituted in the modal equation and will be also used for field computations.

Other work will show that the representation (82) is adequate for frequencies in the E.L.F. range. In the V.L.F. range, this radial function gives results of qualitative accuracy although it illustrates some of the basic mode characteristics. For detailed numerical work, (82) can be used in a multishell approximation of the airspace between the ground and the ionosphere, where the height of the individual shells h is small compared to the free-space wavelengths [Galejs, 1968].

A similar approximation has been proposed by Volland [1964a, b]. He considers the first-order curvature effects of earth-to-ionosphere wave guide by analyzing it in a planar geometry, and by transforming the resultant propagation parameter S' from a radius $(a+h/2)$ to the earth's surface at a as $S = S'[1+h/(2a)]$.

4.3.1 Modal Equation

Using the approximate functions (81) and (82) and noting that $h'_{1,2}(u) \approx \pm(iK/k_0) \cdot h_{1,2}(u)$, the modal equation (26) of the T.M. modes is changed into

$$\frac{K - \Delta_e k_0}{K + \Delta_e k_0} \cdot \frac{K - \Delta_g k_0}{K + \Delta_g k_0} \exp(2iKh) = \exp(2in\pi). \tag{83}$$

where n is zero or an arbitrary integer.

This modal equation of T.M. modes can be simplified under the restriction $(\Delta_g k_0/K) \ll 1$ and $(\Delta_e k_0/K) \gg 1$. It follows that

$$\frac{K}{k_0} \approx \frac{i(n-0.5)\pi + \sqrt{-(n-0.5)^2\pi^2 - 4\,\Delta_g/\Delta_e + 4ihk_0\,\Delta_g}}{2(ik_0h - 1/\Delta_e)}. \tag{84}$$

For $\Delta_g \to 0$ and $|\Delta_e k_0 h| \gg 1$, (84) simplifies further to $2Kh = (2n-1)\pi$, where $n \gg 1$. Applying (81), this yields

$$S = \frac{r_m}{a}\sqrt{1 - \left[\frac{(n-0.5)\pi}{k_0 h}\right]^2}. \tag{85}$$

Equation (85) is strictly valid for a perfectly conducting ground surface ($\Delta_g = 0$) and a perfectly reflecting ionosphere ($\Delta_e = \infty$) which may idealize the boundaries for the lower order propagating T.M. waves in the V.L.F. range. At a mode cutoff $k_0 = k_c = (n-0.5)\pi/h$, $S = 0$; and the phase velocity is infinite following (47). S is imaginary for lower frequencies and the waves are severely attenuated. In the high-frequency limit, $S > 1$ and the phase velocity v_{ph} becomes less than the free-space velocity of electromagnetic waves c. However, the high-frequency limit of the propagation parameter S depends on the choice of the value r_m. For $r_m = a$, S will remain less than unity and the phase velocity v_{ph} exceeds c, which is also observed when using the second-order or Debye approximation of the spherical wave functions [Schumann, 1954; Wait, 1957].

An approximation that is valid for the $n = 0$ mode in the limit of $|\Delta_e k_0 h| \gg 1$ will be derived after examining the modal equation (83) for a purely reactive surface impedance of the ionosphere (Re $\Delta_e = 0$). It can be shown that in this limit $K \to k_0$ Im Δ_e. For a lossy ionosphere (Re $\Delta_e > 0$), it is therefore appropriate to examine the limit of $K \to \Delta_e k_0$. Substituting $\Delta_g = 0$ and $K = \Delta_e k_0 + \delta$ in (83), it follows that

$$\left.\begin{aligned} \delta &\approx \frac{1}{4ih}\left[1 - \exp(-2i\,\Delta_e k_0 h) - \sqrt{1 + 2(8i\,\Delta_e k_0 h - 1)\exp(-2i\,\Delta_e k_0 h) + \ldots}\right] \\ &\approx 2\,\Delta_e k_0 \exp(-2i\,\Delta_e k_0 h). \end{aligned}\right\} \tag{86}$$

It is seen that $\delta \to 0$ and $K \to \Delta_e k_0$ in the V.L.F. range, where $|\Delta_e k_0 h| \gg 1$.

In the E.L.F. range where only the $n = 0$ mode propagates, the waveguide boundaries appear as nearly perfect conductors. Substituting $(\Delta_e k_0/K_0)$, $(\Delta_g k_0/K_0) \ll 1$, and $n = 0$ in (83), it is seen that

$$\left.\begin{aligned} K^2 &\approx \frac{(\Delta_e + \Delta_g)k_0}{2ih}\left[1 + \sqrt{1 + \tfrac{4}{3}(\Delta_e - 2\Delta_g)ik_0 h}\right] \\ &\approx \frac{(\Delta_e + \Delta_g)k_0}{ih} \quad \text{for} \quad |\Delta_e k_0 h| \ll 1 \end{aligned}\right\} \tag{87}$$

or

$$S \approx \frac{r_m}{a}\sqrt{1 + \frac{i(\Delta_e + \Delta_g)}{k_0 h}}.$$

It is seen that $K \to 0$ and $S \to (r_m/a)$ as Δ_e and $\Delta_g \to 0$. The phase velocity of E.L.F. waves in a lossless waveguide is nearly equal to the free-space velocity of electromagnetic waves. For the

higher order cutoff modes ($n \neq 0$), K_n is almost real and is approximated by

$$K_n \approx \frac{n\pi}{h} + \frac{(\Delta_e + \Delta_g)k_0}{in\pi}. \tag{88}$$

The modal equation of T.E. modes is obtained by replacing Δ_g with $(1/\Delta_g)$ and Δ_e with $(1/\Delta_h)$ in (83), which results in

$$\frac{K\Delta_h - k_0}{K\Delta_h + k_0} \cdot \frac{K\Delta_g - k_0}{K\Delta_g + k_0} \exp(2iKh) = \exp(2im\pi), \tag{89}$$

where m is an integer. In the limit of $(K\Delta_h/k_0)$ and $(K\Delta_g/k_0) \ll 1$, (89) simplifies to

$$K \approx \frac{m\pi}{h}\left[1 - \frac{\Delta_h + \Delta_g}{ik_0 h}\right]^{-1}. \tag{90}$$

In the $m = 0$ mode, $K = 0$ even if Δ_h and $\Delta_g \neq 0$. For $K = 0$, the amplitude ratio B_h/A_h, defined in Section 4.2.2, becomes (-1). Substituting (82) and $K = 0$ in the field expressions (19) to (21), it is seen that the T.E. fields are not excited in the $m = 0$ mode. A similar observation is made when synthesizing the T.E. modes of a parallel plate waveguide by two crossing plane waves [Budden, 1961].

In the examples of Fig. 4.3, the phase velocities and attenuation rates of E.L.F. waves are calculated using (87), (47), and (48). The normalized impedances Δ_e and Δ_g are computed following (97). It is evident from (87) that σ_g is of no consequence for calculating the propagation parameters as long as $\sigma_g \gg \sigma_i$. The attenuation rate α and the reciprocal normalized phase velocity Re S are lower for the ionosphere models of higher h and σ_i values. The ionosphere model of $\sigma_i = 10^{-5}$ mho/m and $h = 85$ km gives an attenuation rate α that compares with the Schumann resonance measurements near 30 c/s by Balser and Wagner [1960] or with the measurements of Jean *et al.* [1961] above 100 c/s. However, the attenuation rate α of this model is much too low for frequencies near 1000 c/s where the ionosphere model of $h = 70$ km provides more realistic α figures. A particular sharply bounded homogeneous ionosphere model can be used only over a limited frequency range, which has prompted introduction of models where the height h is frequency dependent [Pierce, 1960]. However, such an ionosphere model does not account simultaneously for the phase-velocity and attenuation-rate measurements. The Schumann resonance data by Balser and Wagner [1960] imply that Re $S \approx 1.25$ near $f = 30$ c/s, which is more in line with the phase velocity data of the lower ionosphere model that gives excessive attenuation rates. These apparent difficulties have led to the use of tapered ionosphere models in this frequency range [Galejs, 1965].

The phase velocities and attenuation rates are shown in Fig. 4.4 for a more extended range of frequencies using a ground conductivity $\sigma_g = 10^{-3}$ mho/m. In the $n = 0$ mode, the attenuation becomes very high for frequencies exceeding 3–5 kc/s; for $f = 20$ kc/s, the attenuation rate α of the $n = 0$ mode exceeds 200 db/1000 km for the ionosphere models used in Fig. 4.4. In the V.L.F. range, the exponential approximations of the $n \neq 0$ modes are compared with the more accurate solutions based on Airy function approximation of the radial functions that are developed in Section 4.5.1. The exponential approximation of the radial functions appears to be satisfactory for the $n = 1$ and 2 modes only for frequencies below 10 kc/s, but the approximate solution of the $n = 3$ mode can be used for frequencies $f \leq 20$ kc/s respectively.

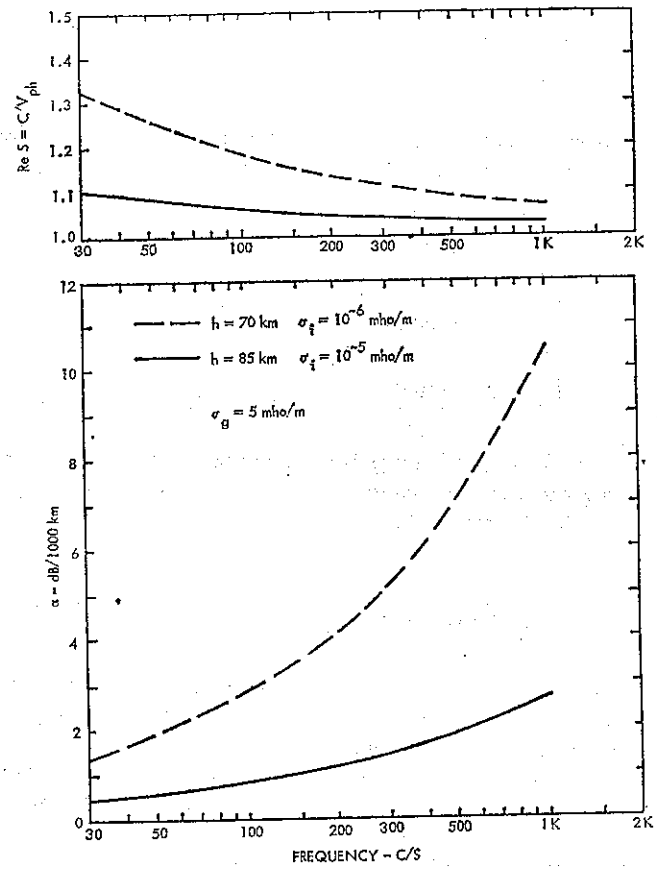

FIG. 4.3 Phase Velocity and Attenuation Rates of E.L.F. Waves. Sharply Bounded Homogeneous and Isotropic Ionosphere Models

Further comparisons between the exponential (or thin-shell) and Airy function approximations are shown in Figs. 4.7 and 4.8 (p. 111) for frequencies in the V.L.F. range. The thin-shell approximations (83) or (89) produce a reasonable approximation to the phase-velocity data, but the attenuation rates of the thin-shell approximations are consistently too low. The exponential or thin-shell approximations appear to be most accurate at the lower frequencies when the height of the waveguide is smaller relative to the wavelength.

Using the thin-shell field representations, the approximations (84) or (90) produce nearly the same data as the numerical solution of equations (83) or (89) respectively. For $f = 20$ kc/s, $h = 85$ km and $\sigma_i = 10^{-5}$ mho/m, and the $n = 1$ mode, the approximation (84) gives $S = 1.0056 + i\,0.0001519$, while the numerical solution of (83) results in $S = 1.005599 + i\,0.0001515$. For the $m = 1$ mode, the approximation (90) gives $S = 1.00280 + i\,0.0000481$,

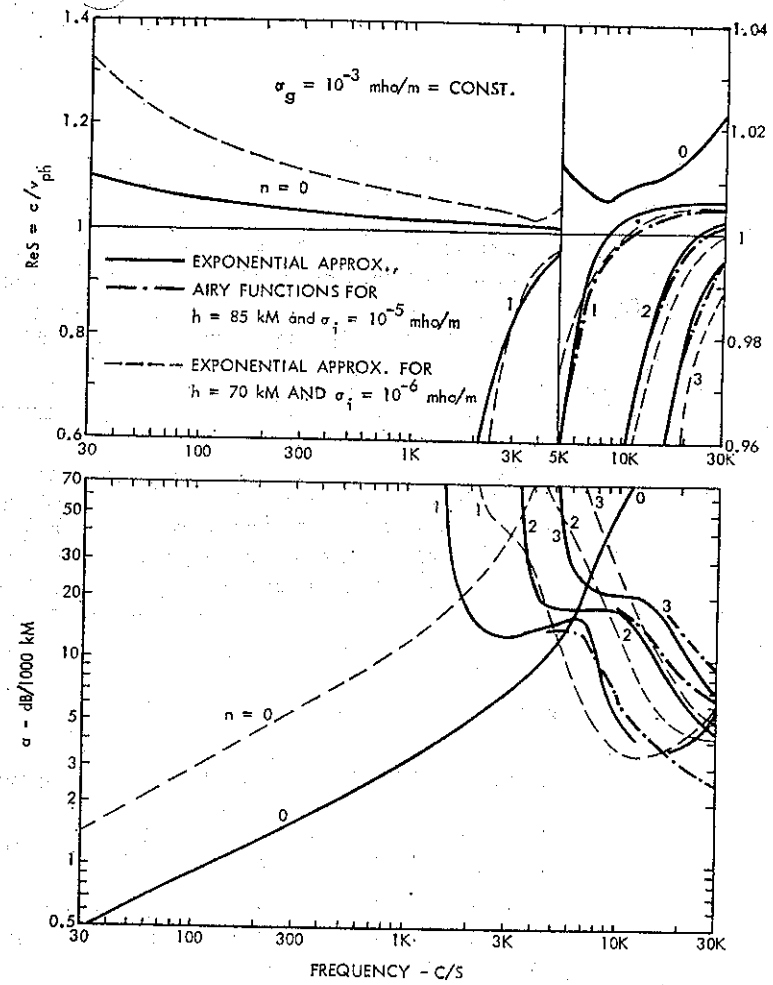

FIG. 4.4 Phase Velocity and Attenuation Rates of T.M. Modes for Sharply Bounded Homogeneous and Isotropic Ionosphere

while the numerical solution of (89) gives $S = 1.002805 + i\,0.0000479$. The approximation (84) of the T.M. modes is based on the assumption that the ground surface approximates a perfect conductor of $\Delta_g \to 0$ and that the ionospheric boundary acts as a nearly perfect reflector of $\Delta_e \to \infty$. However, the approximation (90) of the T.E. modes implies that both the ground surface and the ionosphere appear as nearly perfect conductors of Δ_g, $\Delta_h \to 0$. A given ionosphere model may therefore act essentially as a reflector ($\Delta_e k_0/K \gg 1$) for the T.M. modes and as a conductor ($\Delta_h K/k_0 \ll 1$) for the T.E. modes, even though $\Delta_e \approx \Delta_h$.

4.3.2 Field Expressions

The field expressions (41), (42), (55), (56), (75), and (76) of the various elementary dipoles contain a number of common combinations of spherical Bessel functions which have simple physical interpretations. The effectiveness of a source can be characterized by an excitation factor A, and the height variation of the fields by height-gain functions $G(z)$ that are defined following Wait [1962]. The fields depend also on a height-dependent normalized impedance $\Delta(z)$.

For T.M. modes, the excitation factor A_n will be defined as

$$A_n = \frac{k_0 h}{2} \cdot \frac{[h_\nu^e(u_g)]^2}{I_\nu^e}. \tag{91}$$

Substituting (82) in (36), the integral can be readily evaluated to give

$$A_n = \left[1 + \frac{\sin 2Kh}{2Kh} + \left(\frac{\Delta_g k_0}{K}\right)^2 \left(\frac{\sin 2Kh}{2Kh} - 1\right) - \frac{i\Delta_g k_0}{hK^2}(1 - \cos 2Kh)\right]^{-1}. \tag{92}$$

In the E.L.F. range, $Kh \to 0$ according to (87), and it follows that $A_0 \approx 0.5$. In the V.L.F. range for a perfectly conducting ground ($\Delta_g = 0$) and a perfectly reflecting ionosphere ($\Delta_e = \infty$) K of (84) results in $A_n = 1$. The same result is obtained for a perfectly conducting ionosphere ($\Delta_e = 0$) and $h \neq 0$.

A height-gain function is defined as

$$G_n(z) = \frac{h_\nu^e(u)}{h_\nu^e(u_g)} = \cos Kz - \frac{i\Delta_g k_0}{K} \sin Kz \tag{93}$$

and $G_n(0) = 1$ for points on the surface of the spherical earth. Recalling the definition of I_ν^e in (36), the excitation factor A_n of (91) can be expressed alternately as

$$A_n = \frac{h}{2}\left\{\int_0^h [G_n(z)]^2\, dz\right\}^{-1}. \tag{94}$$

In the E.L.F. range, $G_0(z) \approx 1$ and $A_0 \approx 0.5$. A_n is increased in magnitude if $|G_n(z)| < 1$, but A_n is decreased and modes of $|G_n(z)| \gg 1$ are weakly excited from a ground-based source.

A z-dependent normalized impedance is defined following (35) as

$$\Delta_n(z) = \frac{Z_e(z)}{\sqrt{\mu_0/\varepsilon_0}} = \frac{\partial}{\partial u}[uh_\nu^e(u)]/[iuh_\nu^e(u)], \tag{95}$$

which gives

$$\Delta_n(z) = \left(\frac{K}{k_0}\right)\frac{iK \sin Kz - \Delta_g k_0 \cos Kz}{K \cos Kz - \Delta_g k_0 i \sin Kz}. \tag{96}$$

For $z = 0$, $\Delta_n(0) = -\Delta_g$; and for $z = h$, $\Delta_n(h) = \Delta_e$ following (83).

The impedance of the ground surface $Z_g = \sqrt{\mu_0/\varepsilon_0}\,\Delta_g$ and of the ionosphere $Z_e = \sqrt{\mu_0/\varepsilon_0}\,\Delta_e$ have been treated as known quantities in the preceding derivations. For a homogeneous and

isotropic medium beyond the boundaries ($z < 0, z > h$), it is possible to compute the impedance of the medium similarly as in (96). Only waves receding away from the boundary will exist in a homogeneous medium. For $z < 0$ $A = 0$, for $z > h$ $B = 0$ in (31); also k_0 is replaced by $k_j = \sqrt{\varepsilon_j + i\sigma_j/(\omega\varepsilon_0)}\, k_0$ in (79), where ε_j is the relative dielectric constant, σ_j is the conductivity of the medium, the subscript $j = g$ designates ground and $j = i$ designates the ionosphere. Also u is now defined as $u = k_j r$. It follows that

$$\frac{Z_q}{\sqrt{\omega\mu_0/(\omega\varepsilon_0\varepsilon_j + i\sigma_j)}} = \pm\frac{\dfrac{\partial}{\partial u}[uh_\nu^e(u)]}{iuh_\nu^e(u)} = \sqrt{1 - \frac{\nu(\nu+1)}{k_j^2 r_m^2}} = \sqrt{1 - \left(\frac{k_0 aS}{k_j r_m}\right)^2}, \tag{97}$$

where the plus and minus signs refer to $j = i$ and g or $q = e$ and g respectively. The impedance Z_q is generally dependent on S, or on the wave number of the fields in the spherical shell that is determined from a solution of the modal equation. The magnitude of the square-root expression of (97) is near one in the limit of $|k_j| \gg k_0$ and the impedance Z_g or Z_e becomes independent of S. Only in this limit can $\Delta_q \approx \sqrt{\omega\varepsilon_0/(\omega\varepsilon_0\varepsilon_j + i\sigma_j)}$ of (35) be treated as constant in the modal equation (26) or (83). These simplified forms of the normalized impedance Δ_q are equal to the reciprocal of the refractive index n_j of the medium j.

For T.E. modes, a similarly defined excitation factor is computed as

$$A_m = -\left(\frac{\Delta_g K}{k_0}\right)^2 \left[1 - \frac{\sin 2Kh}{2Kh} - \left(\frac{\Delta_g K}{k_0}\right)^2 \left(1 + \frac{\sin 2Kh}{2Kh}\right) - \frac{i\Delta_g}{k_0 h}(\cos 2Kh - 1)\right]^{-1}. \tag{98}$$

A_m approaches zero as Δ_g and/or $K \to 0$. The height-gain function

$$G_m(z) = \frac{h_\nu^h(u)}{h_\nu^h(u_g)} = \cos Kz - \frac{ik_0}{\Delta_g K}\sin Kz. \tag{99}$$

is unity for points on the ground surface ($z = 0$), but it increases rapidly with increasing altitude z, particularly for highly conducting ground of $\Delta_g \to 0$. Equation (94) applies also to T.E. modes, and modes of $|G_m(z)| \gg 1$ are weakly excited from a ground-based source. For source and receiver above the highly conducting ground surface ($z, z_s \neq 0$) and $K \neq 0$, the product $A_m G_m(z)\, G_m(z_s)$ remains finite, although Δ_g may approach zero. However, the same product approaches zero for any value of z if $K \to 0$. A z-dependent normalized impedance may be computed using the definitions of Section 4.2.3. It follows that

$$\Delta_m(z) = \frac{Z^h(z)}{\sqrt{\mu_0/\varepsilon_0}} = [iuh_\nu^h(u)]\Big/\frac{\partial}{\partial u}[uh_\nu^h(u)] = \frac{k_0}{K}\,\frac{\Delta_g K\cos Kz - ik_0 \sin Kz}{i\Delta_g K \sin Kz - k_0\cos Kz} \approx -\Delta_g + ik_0 z \tag{100}$$

The last approximation, valid for $Kz \ll 1$, applies in the E.L.F. range to z in the range of $0 \ll z \ll h$. For $z = 0$, $\Delta_m(0) = -\Delta_g$, and for $z = h$, $\Delta_m(h) = \Delta_h$ following (89).

For a homogeneous and isotropic medium beyond the boundaries ($z < 0, z > h$), the impedances $Z_g = \sqrt{\mu_0/\varepsilon_0}\,\Delta_g$ and $Z_h = \sqrt{\mu_0/\varepsilon_0}\,\Delta_h$ are computed as

$$\frac{Z_q}{\sqrt{\omega\mu_0/(\omega\varepsilon_0\varepsilon_j + i\sigma_j)}} = \pm\frac{iuh_\nu^h(u)}{\dfrac{\partial}{\partial u}[uh_\nu^h(u)]} = \left[1 - \left(\frac{k_0 aS}{k_j r_m}\right)^2\right]^{-0.5}, \tag{101}$$

where $j = i$ or g, $u = k_j r$, $k_j = \sqrt{\varepsilon_j + i\sigma_j/(\omega\varepsilon_0)}\, k_0$ and where the plus and minus signs refer to $q = h$ and g respectively. Similarly, as in (97), Z_q becomes independent of S only in the limit of $|k_j| \gg k_0$, when $\Delta_q = \sqrt{\omega\varepsilon_0/(\omega\varepsilon_0\varepsilon_j + i\sigma_j)} = 1/n_j$, and n_j is the refractive index of the medium $j = i$ or g.

The excitation factor A_0, the height-gain function $G_0(z)$, and the normalized impedances $\Delta_0(z)$ have been computed in the E.L.F. range from the ionosphere parameters indicated in Fig. 4.3. The height-gain function is near 1 [$1 \ll G_0(z) \ll G_0(85) \approx 1.008$ at $f = 300$ c/s], and it follows from (94) that A_0 differs only negligibly from 0.5. The normalized impedance $\Delta_0(z)$, which characterizes the wave tilt following (108), is shown in Fig 4.5. It starts with

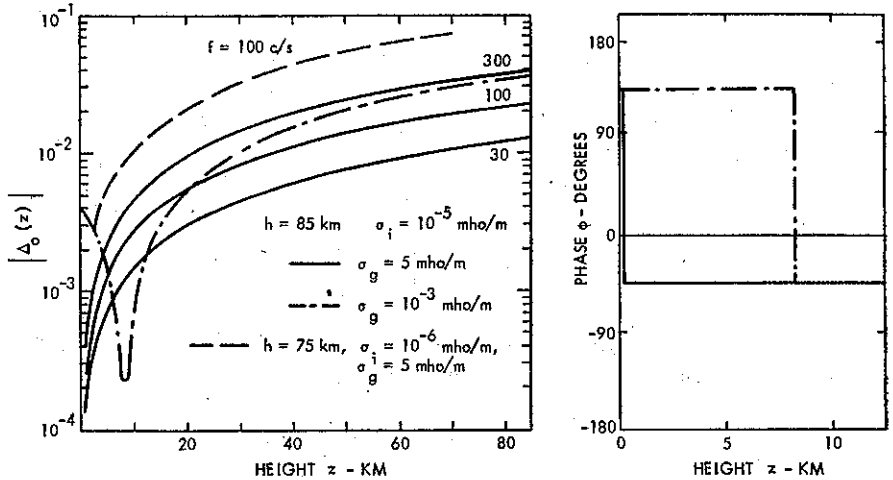

FIG. 4.5 Normalized Impedance $\Delta_0(z) = |\Delta_0(z)| \exp(i\varphi)$ of E.L.F. Waves. Sharply Bounded Homogeneous and Isotropic Ionosphere Models

$\Delta_0(0) = -\Delta_g$ at $z = 0$, reverses its phase near the ground surface, and with increasing values of z approaches gradually $\Delta_0(h) = \Delta_e$, which is proportional to $\sigma_i^{-0.5}$. The heights of this phase reversal and of an associated amplitude minimum are increased with decreasing ground conductivity. In the vicinity of the ionospheric boundary, $\Delta_0(z)$ is proportional to z [$\Delta_0(z)/z \approx \approx$ const]; but the decrease of $\Delta_0(z)$ becomes more rapid when approaching the height of phase reversal.

The excitation factors A_n are further illustrated in Fig. 4.6. The excitation factor A_0, which is approximately equal to 0.5 in the E.L.F. range, becomes negligible for V.L.F.; thus, $A_0 < < 10^{-6}$ for $f = 20$ kc/s. Because of the small values of A_0, the presence of the $n = 0$ mode can be neglected even in the near-field range for V.L.F. In the E.L.F. range, K_n is almost real for the higher order cutoff modes ($n = 0$) following (88), and the excitation factors $A_n \approx 1$. It is therefore not permissible to neglect the nonpropagating ($n \neq 0$) modes in the near-field range for E.L.F. In the V.L.F range, the exponential approximations of the $n \neq 0$ modes are compared with the more accurate solutions based on Airy function approximation of the radial functions that are developed in Section 4.5.1. The exponential approximation of the radial functions appears to be satisfactory for the $n = 1$ mode only for frequencies below 7 kc/s,

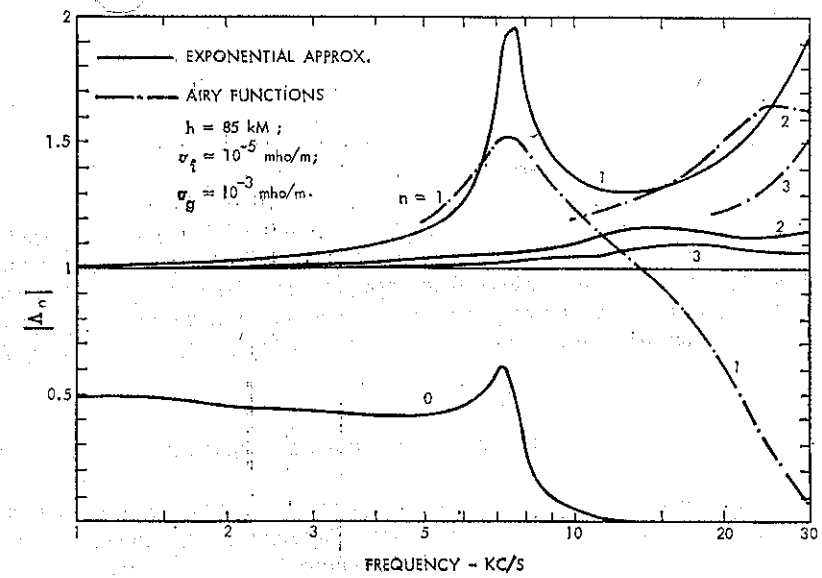

FIG. 4.6 Excitation Factor $|A_n|$ of T.M. Modes for a Sharply Bounded Homogeneous and Isotropic Ionosphere Model

but the approximate solutions of the $n = 2$ and 3 modes can be used for frequencies $f \leqslant 10$ kc/s and 20 kc/s respectively.

For the V.L.F. range, the excitation factors, height-gain functions, and normalized impedances of the T.M. and T.E. modes are shown in Figs. 4.9–4.14 together with the more accurate results of Section 4.5.2 that are based on Airy function representations of the radial field variations. A_1 of the thin-shell approximations decreases very gradually with increasing frequency. This can be related by (94) to the height-gain functions $G_1(z)$ which do not exhibit the required increase in amplitude with increasing frequency. Still $G_n(z)$ and $G_m(z)$ are qualitatively correct for $z < 10$ and 20 km respectively. The normalized impedances of the thin-shell approximations appear to be qualitatively correct within 10 km from the waveguide boundaries except for the T.M. modes in Fig. 4.11, when differences of the order of 2 are noted for $f = 20$ kc/s and $z = 5$ km. These limitations are described in more detail in the discussion of Section 4.5.2.

The best accuracy of the thin-shell approximations is noted for frequencies near 10 kc/s; at higher frequencies the computed attenuation rates are too low, excitation factors may be high, height-gain functions are too low, and the normalized impedances are reliable only in the direct vicinity of the ionospheric boundary. The analytical simplicity of the thin-shell approximations may suggest their use for qualitatively estimating propagation parameters, but the above limitations should be noted when interpreting any such results.

It will be shown in the following sections that the field components of the various dipole sources can be written in a compact form by using the definitions of the excitation factors, height-gain functions, or normalized impedances, and by substituting either the thin-shell approximations of this section or the Airy function representations of Section 4.5.2.

The Legendre functions of the field expressions can be approximated by their asymptotic expansions as indicated in (43) and (44). The derivatives of $P_\nu(-\cos\theta)$ are computed using the relation

$$\frac{d}{d\theta}P_\nu(-\cos\theta) = \nu[\cos\theta P_\nu(-\cos\theta)+P_{\nu-1}(-\cos\theta)]/\sin\theta. \tag{102}$$

Substituting the approximation (44), it follows that

$$\frac{d}{d\theta}P_\nu(-\cos\theta) \approx i\nu P_\nu(-\cos\theta). \tag{103}$$

4.3.2.1 *Vertical Electric Dipole*

Applying the approximation (44), equation (41) may be written as

$$E_r^{ve}(r,\theta) = i\sqrt{\mu_0/\varepsilon_0}\, I\, ds \sum_n S_n^{1.5} F_n, \tag{104}$$

where

$$F_n = \frac{1}{\sqrt{D\lambda h}}\sqrt{\frac{D/a}{\sin(D/a)}}\, G_n(z)\, G_n(z_s)\, A_n \exp(i\pi/4 + ik_0 DS_n), \tag{105}$$

$D = a\theta$, $\lambda = (2\pi/k_0)$ is the free-space wavelength, and the excitation factor A_n and the height-gain functions $G_n(z)$ are given by (94) and (95). The subscript n designates modes with eigenvalues S_n of (46) determined from a solution of (83) or from the more approximate expressions (88) to (90). Equations (18) and (16) can be similarly rearranged into

$$E_\theta^{ve}(r,\theta) = -i\sqrt{\mu_0/\varepsilon_0}\, I\, ds \sum_n S_n^{0.5}\, A_n(z)\, F_n, \tag{106}$$

$$H_\varphi^{ve}(r,\theta) = -iI\, ds \sum_n S_n^{0.5} F_n, \tag{107}$$

where $A_n(z)$ is defined by (96) and where use has been made of the approximation (103).

The field components (104), (106), and (107) are proportional to $F_n \sim G_n(z)\, G_n(z_s) A_n$. For the source and receiver located near ground level ($z = z_s \approx 0$), $G_n(0) = 1$. The excitation factor A_n was shown to be approximately 0.5 in the E.L.F. range, but $A_n = 1$ in the V.L.F. range if the boundaries are either perfectly conducting or reflecting ($\Delta_g = 0, \Delta_e = 0$ or ∞).

The tilt of the electric vector is computed as

$$E_\theta^{ve}/E_r^{ve}\Big|_n = -A_n(z)/S_n. \tag{108}$$

Noting that $A_n(0) = -\Delta_g$ and $A_n(h) = \Delta_e$ from (96), the wave tilt at the boundary surfaces is numerically equal to the normalized surface impedances of the ground and the ionospheric boundary divided by the propagation parameter S_n. For $S_n \approx 1$, the wave tilt (108) becomes the same as in the far fields of a V.E. dipole above a finitely conducting ground plane [equations (57) and (70) of Norton, 1937]. The ratio

$$E_\theta^{ve}/H_\varphi^{ve}\Big|_n = \sqrt{\mu_0/\varepsilon_0}\, A_n(z) \tag{109}$$

becomes equal to the surface impedances $(-Z_g)$ and Z_e for $z = 0$ and h, which is in agreement with the boundary conditions (22) and (23). The ratio

$$E_r^{ve}/H_\varphi^{ve}\Big|_n = -\sqrt{\mu_0/\varepsilon_0}\, S_n \tag{110}$$

approximates the characteristic impedance of free space for $S_n \approx 1$.

4.3.2.2 Vertical Magnetic Dipole

Applying the approximation (44), equation (42) may be written as

$$H_r^{vm}(r, \theta) = I\, dak_0 \sum_m S_m^{1.5} F_m, \tag{111}$$

where

$$F_m = \frac{1}{\sqrt{D\lambda h}} \sqrt{\frac{D/a}{\sin (D/a)}}\, G_m(z)\, G_m(z_s) \Lambda_m e^{i\pi/4 + ik_0 D S_m} \tag{112}$$

and the excitation factor Λ_m and the height-gain functions $G_m(z)$ are given by (98) and (99). The subscript m designates modes with eigenvalues S_m of (46) determined from a solution of (89) or from the more approximate expression (90). Equations (21) and (19) can be similarly rearranged into

$$H_\theta^{vm} = -I\, dak_0 \sum_m S_m^{0.5} F_m/\Delta_m(z), \tag{113}$$

$$E_\varphi^{vm} = I\, dak_0 \sqrt{\mu_0/\varepsilon_0} \sum_m S_m^{0.5} F_m, \tag{114}$$

where $\Delta_m(z)$ is defined by (100) and where use has been made of the approximation (103).

The field components (111), (113), and (114) are proportional to a factor $F_m \sim G_m(z)\, G_m(z_s) \Lambda_m$ which was briefly discussed following equation (99). For a source on a perfectly conducting ground ($\Delta_g = 0$, $z_s = 0$), $F_m = 0$ and no fields are excited because $\Lambda_m \sim \Delta_g^2$. For the source above the perfectly conducting ground ($z_s \neq 0$) and the receiver on the ground surface ($z = 0$), $F_m = 0$, but $F_m/\Delta_m(0)$ remains finite. Hence, H_r, $E_\varphi = 0$, but H_θ is finite corresponding to boundary conditions on a perfectly conducting ground of $\Delta_g \to 0$.

In the $m = 0$ mode, $K = 0$ following Section 4.3.1. It can be seen that F_m and $F_m/\Delta_m = 0$ and that no field components are excited in the $m = 0$ mode even for arbitrary values of z and z_s.

The ratio of the magnetic field components is computed as

$$H_r^{vm}/H_\theta^{vm}\Big|_m = -S_m\, \Delta_m(z). \tag{115}$$

Noting that $\Delta_m(0) = -\Delta_g$ and $\Delta_m(h) = \Delta_h$, the ratio of the two magnetic field components at the boundary surfaces is numerically equal to the normalized surface impedance of the ground or of the ionospheric boundary multiplied with the propagation parameter S_m. The magnetic fields are nearly tangential to highly conducting boundary ($\Delta_g, \Delta_h \to 0$), but nearly normal to a highly reflecting boundary ($\Delta_h \to \infty$). The ratio

$$E_\varphi^{vm}/H_\theta^{vm}\Big|_m = -\sqrt{\mu_0/\varepsilon_0}\, \Delta_m(z) \tag{116}$$

becomes equal to surface impedances Z_g and $(-Z_h)$ for $z = 0$ and h, which is in agreement with the boundary conditions (22) and (23). The ratio

$$E_\varphi^{vm}/H_r^{vm}\Big|_m = \sqrt{\mu_0/\varepsilon_0}/S_m \tag{117}$$

approximates the characteristic impedance of free space for $|S_m| \approx 1$.

4.3.2.3 Horizontal Electric Dipole

Applying the approximations (44) and (103) and using the notation of equations (93) to (95), (98), and (99), equation (55) and (56) may be written as

$$E_r^{he}(r, \theta, \varphi) = i\sqrt{\mu_0/\varepsilon_0} I\, ds \cos\varphi \sum_n \Lambda_n(z_s) S_n^{0.5} F_n. \tag{118}$$

$$H_r^{he}(r, \theta, \varphi) = -i\, I\, ds \sin\varphi \sum_m S_m^{0.5} F_m, \tag{119}$$

where

$$F_q = \frac{1}{\sqrt{D\lambda h}} \sqrt{\frac{D/a}{\sin (D/a)}}\, G_q(z)\, G_q(z_s) \Lambda_q \exp\left(i\pi/4 + ik_0 D S_q\right) \tag{120}$$

and $q = n$ or m. The other field components are computed from (63) to (68) as

$$E_\theta^{he}(r, \theta, \varphi) = -\sqrt{\mu_0/\varepsilon_0} I\, ds \cos\varphi \left[i \sum_n \Lambda_n(z)\, \Lambda_n(z_s) S_n^{-0.5} F_n - \frac{1}{k_0 a \sin\theta} \sum_m S_m^{-1.5} F_m \right], \tag{121}$$

$$E_\varphi^{he}(r, \theta, \varphi) = -\sqrt{\mu_0/\varepsilon_0} I\, ds \sin\varphi \left[-\frac{1}{k_0 a \sin\theta} \sum_n \Lambda_n(z)\, \Lambda_n(z_s) S_n^{-1.5} F_n + i \sum_m S_m^{-0.5} F_m \right], \tag{122}$$

$$H_\theta^{he}(r, \theta, \varphi) = -I\, ds \sin\varphi \left[\frac{1}{k_0 a \sin\theta} \sum_n \Lambda_n(z_s) S_n^{-1.5} F_n - i \sum_m S_m^{-0.5} F_m/\Delta_m(z) \right], \tag{123}$$

$$H_\varphi^{he}(r, \theta, \varphi) = -I\, ds \cos\varphi \left[i \sum_n \Lambda_n(z_s) S_n^{-0.5} F_n - \frac{1}{k_0 a \sin\theta} \sum_m S_m^{-1.5} F_m/\Delta_m(z) \right], \tag{124}$$

where $\Delta_q(z)$ is defined by (95) and (100). The above summations do not include the $m = 0$ term which is not excited according to the discussion of Section 4.3.2.2.

The definition of T.M. modes n implies that the longitudinal magnetic field component H_θ be zero. Similarly, T.E. modes m imply that the longitudinal electric field component E_θ is zero. However, the above field expressions contain a summation over n in the H_θ and a summation over m in the E_θ expression. The fields excited by a H.E. dipole cannot be separated into strictly T.E. and T.M. modes. It is more appropriate to relabel the n terms of the summations as quasi-T.M. modes and the m terms of the summations as quasi-T.E. modes. Only the E_r and H_r components are expressed as a single summation of quasi-T.M. modes n and quasi-T.E. modes m respectively. The other field components contain both summations and are expressed as a super-position of quasi-T.M. or quasi-T.E. modes. Only for φ-symmetrical excitation, the field components become strictly T.M. and T.E. in character; thus the fields of a vertical electric dipole contain only E_r, E_θ, and H_φ components [equations (104), (106), and (107)], while the fields of a vertical magnetic dipole contain H_r, H_θ, and E_φ compo-

nents [equations (112), (113), and (114)]. However, for φ-dependent E_r and H_r fields, the quasi-T.M. fields contain also the E_φ and H_θ components, and the quasi-T.E. fields contain also E_θ and H_φ components, which is a consequence of equations (57) to (61) or (63) to (68).

The ratios of the quasi-T.M. field components $E_\theta^{he}/E_r^{he}\big|_n$, $E_\theta^{he}/H_\varphi^{he}\big|_n$, $E_r^{he}/H_\varphi^{he}\big|_n$ remain the same as for the V.E. dipole in (108) to (110). The T.M. mode contributions to E_φ^{he} and H_θ^{he} are characterized by the ratios

$$\frac{E_\theta^{he}}{E_\varphi^{he}}\bigg|_n = -\frac{H_\varphi^{he}}{H_\theta^{he}}\bigg|_n = -\frac{ik_0aS_n \sin\theta\cos\varphi}{\sin\varphi}. \tag{125}$$

The $E_\theta^{he}\big|_n$ and $H_\varphi^{he}\big|_n$ field components exhibit their maximum values in the axial or endfire directions ($|\cos\varphi| = 1$), and they are generally larger in magnitude than the $E_\varphi^{he}\big|_n$ and $H_\theta^{he}\big|_n$ components, that have their maximum values in the broadside direction ($|\sin\varphi| = 1$). The ratio (125) reaches its maximum value for $\sin\theta = 1$ or $D \approx 10{,}000$ km. This ratio has a magnitude of unity for $k_0a = 1$ or $f = 7.5$ Hz. For frequencies in the vicinity of the fundamental Schumann resonance, a horizontally directed current excites distant fields tangential to the ground surface that are of comparable magnitudes in the $\varphi = 0$ and $\pi/2$ directions. The relative magnitudes of E_φ^{he} and H_θ^{he} components are decreased at higher frequencies when they tend to fill in the nulls of the principal E_θ^{he} and H_φ^{he} components that are observed in the $\varphi = \pi/2$ and $3\pi/2$ directions. The E_φ^{he} and H_θ^{he} components become negligible in the V.L.F. range when $k_0a \gg 1$.

The ratios of the quasi-T.E. field components $H_r^{he}/H_\theta^{he}\big|_m$, $E_\varphi^{he}/H_\theta^{he}\big|_m$, $E_\varphi^{he}/H_r^{he}\big|_m$ remain the same as for the V.M. dipole in (115) to (117). The T.E. mode contributions to E_θ^{he} and H_φ^{he} are characterized by the ratios

$$\frac{E_\varphi^{he}}{E_\theta^{he}}\bigg|_m = -\frac{H_\theta^{he}}{H_\varphi^{he}}\bigg|_m = -\frac{ik_0aS_m \sin\theta\sin\varphi}{\cos\varphi}. \tag{126}$$

The $E_\varphi^{he}\big|_m$ and $H_\theta^{he}\big|_m$ field components are generally larger in magnitude than the $E_\theta^{he}\big|_m$ and $H_\varphi^{he}\big|_m$ components, that become negligible if $k_0a \gg 1$ with increasing frequency.

At higher frequencies $E_\theta^{he}\big|_n$, $E_\varphi^{he}\big|_m$, $H_\theta^{he}\big|_m$, $H_\varphi^{he}\big|_n$ are the principal field components tangential to the boundary surface. It follows that

$$\frac{E_\theta^{he}}{E_\varphi^{he}}\bigg|_m = \frac{\cos\varphi}{\sin\varphi}\frac{\sqrt{S_m}}{\sqrt{S_n}}\frac{\Delta_n(z_s)\,\Delta_n(z)F_n}{F_m}, \tag{127}$$

$$\frac{H_\varphi^{he}}{H_\theta^{he}}\bigg|_m = -\frac{\cos\varphi}{\sin\varphi}\frac{\sqrt{S_m}}{\sqrt{S_n}}\frac{\Delta_n(z_s)\,\Delta_m(z)F_n}{F_m}, \tag{128}$$

where $F_q \approx \Delta_q G_q(z_s)\,G_q(z)$. For a source and receiver on the ground surface, $z_s = z = 0$, $\Delta_n(0) = \Delta_m(0) = -\Delta_g$, and $G_q(0) = 1$. Noting that the excitation factors $\Delta_n \approx 1$ and

$\Delta_m \approx -(\Delta_g K_m/k_0)^2$, it is seen that

$$\frac{E_\theta^{he}}{E_\varphi^{he}}\bigg|_n = -\frac{H_\varphi^{he}}{H_\theta^{he}}\bigg|_m = -\frac{\cos\varphi\sqrt{S_m}k_0^2}{\sin\varphi\sqrt{S_n}K_m^2}. \tag{129}$$

Equation (81) shows that $K_m^2/k_0^2 = 1-(aS_m/r_m)^2 \ll 1$ for $|S_m| \approx 1$. $E_\theta^{he}\big|_n$ and $H_\varphi^{he}\big|_n$ will be the predominant field component for $z_s = z = 0$. For an elevated source ($z_s \neq 0$), the ratio (127) or (128) will be computed for a ground-based observer ($z = 0$) under the restriction of $|\Delta_g k_0/K| \ll 1$. It follows that $\Delta_n(z_s) \approx (iK_n/k_0)\tan K_n z_s$, $G_n(z_s) \approx \cos K_n z_s$, and $G_m(z_s) \approx -(ik_0/\Delta_g K_m)\sin K_m z_s$ and the ratio becomes

$$\frac{E_\theta^{he}}{E_\varphi^{he}}\bigg|_n = -\frac{H_\varphi^{he}}{H_\theta^{he}}\bigg|_m \approx -\frac{\cos\varphi\sqrt{S_m}K_n \sin K_n z_s}{\sin\varphi\sqrt{S_n}K_m \sin K_m z_s}, \tag{130}$$

which is valid for source heights z_s, satisfying the inequality $k_0 z_s[1-(aS/r_m)^2] \gg \Delta_g$. The net electric field tangential to the boundary surface $\mathbf{E}_t = \mathbf{i}_\theta E_\theta + \mathbf{i}_\varphi E_\varphi$ will remain constant in magnitude and parallel to the direction of the elevated electric dipole for any value of φ to the extent that $S_n = S_m$ (or $K_n = K_m$). Similarly, the net magnetic field remains constant and perpendicular to the direction of the dipole. It is implied that the exponential factors of (120) in the two modes are the same, which requires identical attenuation rates of the modes n and m in (129) and (130). Although the radial or V.E. field component radiated from an elevated horizontal dipole exhibits a $\cos\varphi$ angular dependence following (118), the horizontal field components remain essentially independent of φ. The different excitation efficiencies of quasi-T.M. and quasi-T.E. modes have been considered within the accuracy of the thin-shell approximation, the limitations of which have been discussed in Section 4.3.2. The excitation factors of the thin-shell approximations are larger in magnitude than the excitation factors based on Airy functions of Section 4.5.2. However, a comparison of Figs. 4.9 and 4.12 shows that for $f = 20$ kc/s, Δ_n of the thin-shell approximations is high by a factor of 2.5 in the $n = 1$ mode, which compares with an error in Δ_m by a factor of 2.8 in the $m = 1$ mode. Hence, the ratio of Δ_n/Δ_m remains qualitatively correct at this frequency. The height-gain functions can be used for $z_s \ll 10$ km, but some inaccuracies can be anticipated from the $\Delta_n(z)$ expressions. The above uncertainties imply that the actually observed radiation pattern of an elevated horizontal dipole will exhibit some angular variations, but a pronounced null of the horizontal field components cannot be anticipated in the $\varphi = \pi/2$ or $3\pi/2$ directions. Equations (126) to (130) do not apply to the E.L.F. range because the $m = 0$ mode is not excited.

The comparisons of equations (125) to (130) have been restricted to the various field components excited by a H.E. dipole. The radial electric field component of a H.E. dipole (118) may be compared also with the fields of V.E. dipole (104). It is seen that

$$\frac{E_r^{he}}{E_r^{ve}}\bigg|_n = \frac{\cos\varphi\,\Delta_n(z_s)}{S_n}. \tag{131}$$

The fields of a H.E. dipole located at the surface of the ground ($z_s = 0$) are decreased with increasing conductivity of the ground or decreasing values of the normalized impedance

$\Delta_n(0) = -\Delta_g$. With $S \approx 1$, the ratio (131) becomes the same as in the far fields of dipoles above a flat ground plane [equations (212) with $q = 0$ and (223) for $k_0 D \gg 1$]. A substitution of (96) shows that an increased elevation of the horizontal dipole ($z_s > 0$) will tend to increase the ratio (131). The radial magnetic field component of a H.E. dipole is related to the corresponding component of a V.M. dipole from (111) and (119) as

$$\left.\frac{H_r^{he}}{H_r^{vm}}\right|_m = -\frac{iI\,ds^{he}\sin\varphi}{I\,da^{vm}k_0 S_m} = -\frac{\sqrt{\mu_0/\varepsilon_0}\,I\,ds^{he}\sin\varphi}{K\,ds^{vm}S_m}, \tag{132}$$

where the magnetic dipole moment $K\,ds = -i\omega\mu_0 I\,da$. The two field components of (132) are comparable in magnitude for comparable dipole moments $I\,ds^{he}$ and $(K\,ds^{vm}/\sqrt{\mu_0/\varepsilon_0})$ of the two sources.

4.3.2.4 *Horizontal Magnetic Dipole*

Applying the approximations (44) and (103) and using the notation of equations (93), (94), and (98) to (100), equations (75) and (76) may be rewritten as

$$E_r^{hm}(r, \theta, \varphi) = \omega\mu_0 I\,da \sin\varphi \sum_n S_n^{0.5} F_n, \tag{133}$$

$$H_r^{hm}(r, \theta, \varphi) = I\,dak_0 \cos\varphi \sum_m S_m^{0.5} F_m/\Delta_m(z_s), \tag{134}$$

where

$$F_q = \frac{1}{\sqrt{D\lambda}\,h}\sqrt{\frac{D/a}{\sin(D/a)}}\,G_q(z)\,G_q(z_s)\Delta_q \exp(i\pi/4 + ik_0 D S_q) \tag{135}$$

and $q = n$ or m. The other field components are computed from (63) to (66) and (77) and (78) as

$$E_\theta^{hm}(r, \theta, \varphi) = \omega\mu_0 I\,da \sin\varphi\left[-\sum_n \Delta_n(z) S_n^{-0.5} F_n - \frac{i}{k_0 a \sin\theta}\sum_m S_m^{-1.5} F_m/\Delta_m(z_s)\right], \tag{136}$$

$$E_\varphi^{hm}(r, \theta, \varphi) = \omega\mu_0 I\,da \cos\varphi\left[-\frac{i}{k_0 a \sin\theta}\sum_n \Delta_n(z) S_n^{-1.5} F_n + \sum_m S_m^{-0.5} F_m/\Delta_m(z_s)\right], \tag{137}$$

$$H_\theta^{hm}(r, \theta, \varphi) = k_0 I\,da \cos\varphi\left[\frac{i}{k_0 a \sin\theta}\sum_n S_n^{-1.5} F_n - \sum_m S_m^{-0.5} F_m/[\Delta_m(z)\,\Delta_m(z_s)]\right], \tag{138}$$

$$H_\varphi^{hm}(r, \theta, \varphi) = k_0 I\,da \sin\varphi\left[-\sum_n S_n^{-0.5} F_n - \frac{i}{k_0 a \sin\theta}\sum_m S_m^{-1.5} F_m/[\Delta_m(z)\,\Delta_m(z_s)]\right], \tag{139}$$

where $\Delta_q(z)$ is defined by (96) and (100).

The field components $E_\theta^{hm}/E_r^{hm}\big|_n$, $E_\theta^{hm}/H_\varphi^{hm}\big|_n$, and $E_r^{hm}/H_\varphi^{hm}\big|_n$ of mode n are seen to be related similarly as for a V.E. dipole in (108) to (110). The field components $H_r^{hm}/H_\theta^{hm}\big|_m$, $E_\varphi^{hm}/H_\theta^{hm}\big|_m$, and $E_\varphi^{hm}/H_r^{hm}\big|_m$ of mode m are related similarly as for a V.M. dipole in (115) to (117). The ratios of the horizontal field components

$$\left.\frac{E_\theta^{hm}}{E_\varphi^{hm}}\right|_n = -\left.\frac{H_\varphi^{hm}}{H_\theta^{hm}}\right|_n = -\frac{ik_0 a S_n \sin\theta\sin\varphi}{\cos\varphi} \tag{140}$$

and

$$\left.\frac{E_\varphi^{hm}}{E_\theta^{hm}}\right|_m = -\left.\frac{H_\theta^{hm}}{H_\varphi^{hm}}\right|_m = \frac{ik_0 a S_m \sin\theta\cos\varphi}{\sin\varphi} \tag{141}$$

are similar to the corresponding expressions for a H.E. dipole in (125) and (126) except for a change of sign and an interchange of sin φ and cos φ functions. The $E_\theta^{hm}\big|_n$ and $H_\varphi^{hm}\big|_n$ components of mode n are the dominant ones, and they exhibit maximum values in a direction perpendicular to the dipole (loop) axis ($|\sin\varphi| = 1$). For the mode m, the horizontal field components, $E_\varphi^{hm}\big|_m$ and $H_\theta^{hm}\big|_m$ are generally of a larger magnitude than the components $E_\theta^{hm}\big|_m$ and $H_\varphi^{hm}\big|_m$ respectively; maximum values of the dominant field components occur in the axial direction ($|\cos\varphi| = 1$).

The ratios $E_\theta^{hm}\big|_n/E_\varphi^{hm}\big|_n$ and $H_\varphi^{hm}\big|_n/H_\theta^{hm}\big|_n$ are similar to the ratios shown in (127) and (128) except for a sign change, an interchange of sin φ and cos φ functions and the replacement of $\Delta_n(z_s)$ by $\Delta_m(z_s)$. For a source and receiver at the ground level ($z = z_s = 0$)

$$\frac{E_\theta^{hm}\big|_n}{E_\varphi^{hm}\big|_m} = -\frac{H_\varphi^{hm}\big|_n}{H_\theta^{hm}\big|_m} = \frac{\sin\varphi\sqrt{S_m}k_0^2}{\cos\varphi\sqrt{S_n}K_m^2}, \tag{142}$$

$K_m^2/k_0^2 \ll 1$ and the $E_\theta^{hm}\big|_n$ and $H_\varphi^{hm}\big|_n$ components are dominant in the tangential fields. For an elevated source ($z_s > 0$), it is seen that

$$\frac{E_\theta^{hm}\big|_n}{E_\varphi^{hm}\big|_m} = -\frac{H_\varphi^{hm}\big|_n}{H_\theta^{hm}\big|_m} = \frac{\sin\varphi\sqrt{S_m}\sin K_n z_s k_0^2}{\cos\varphi\sqrt{S_n}\sin K_m z_s K_n K_m}, \tag{143}$$

which is essentially the same as (142) if $K_n \approx K_m$. $E_\theta^{hm}\big|_n$ and $H_\varphi^{hm}\big|_n$ field components are the dominant ones also for elevated sources.

The radial electric field component of a H.M. dipole (133) will be compared with the corresponding field component of a V.E. dipole (104). It is seen that

$$\left.\frac{E_r^{hm}}{E_r^{ve}}\right|_n = \frac{k_0 I\,da^{hm}\sin\varphi}{iI\,ds^{ve}S_n} = \frac{K\,ds^{hm}\sin\varphi}{I\,ds^{ve}S_n\sqrt{\mu_0/\varepsilon_0}}, \tag{144}$$

where the magnetic dipole moment $K\,ds = -i\omega\mu_0\,I\,da$. The two field components of (144) are comparable in magnitude for comparable dipole moments Ids^{ve} and $(Kds^{hm}/\sqrt{\mu_0/\varepsilon_0})$ of the two sources. The radial magnetic field component of a H.M. dipole is related to the corresponding component of a V.M. dipole from (111) and (134) as

$$\left.\frac{H_r^{hm}}{H_r^{vm}}\right|_m = \frac{\cos\varphi}{\Delta_m(z_s)\,S_m}. \tag{145}$$

$|H_r^{hm}| \gg |H_r^{vm}|$ if the normalized impedance $\Delta_m(z_s)$ of (100) is much less than unity. For $z_s = 0$, $H_r^{vm} \sim \Delta_g^2$ and $H_r^{hm} \sim \Delta_g$; both radial field components tend to zero as the conductivity of the ground surface is increased or as $\Delta_g \to 0$.

4.4 Taylor Series Expansion of the Radial Functions

The radial functions of the field representation in the earth-to-ionosphere waveguide can be expressed in terms of functions and their derivatives evaluated at one of the waveguide boundaries [Schumann, 1952; Galejs, 1964]. This Taylor series expansion of the spherical Bessel functions will be rapidly convergent in the E.L.F. range, where the height of the earth-to-ionosphere waveguide is small relative to the guide wavelength. Explicit representations of the radial functions are not required for evaluating quantities which involve their products, but use can be made of simple Wronskian expressions. The wave functions (31) with the amplitudes A_e and B_e determined from (24) or (25), the modal equation (26), the excitation factor Λ_n, the height-gain function $G_u(z)$, and the height-dependent impedance $\Delta_n(z)$ can be readily evaluated in this approach; and the results will be shown to be consistent with the planar approximations of Sections 4.3.1 and 4.3.2.

The spherical Bessel functions (15) will be denoted as

$$U(u) = uh_\nu^{(1)}(u), \tag{146}$$

$$V(u) = uh_\nu^{(2)}(u), \tag{147}$$

where special values of the variable $u = k_0 r$ are designated by $u_g = k_0 a$, $u_i = k_0(a+h)$, $\delta = k_0 h$. The function $U(u_i)$ can be represented by the series

$$U(u_i) = U(u_g+\delta) = U(u_g)+\delta U'(u_g)+(\delta^2/2)\,U''(u_g)+(\delta^3/6)\,U'''(u_g)+\ \ldots, \tag{148}$$

where primes denote derivatives with respect to the argument of the function. The function $U(u)$ satisfies the differential equation (13), and $U''(u)$ is related to $U(u)$ by

$$U''(u) = -\left[1-\frac{\nu(\nu+1)}{u^2}\right]U(u). \tag{149}$$

Differentiation of (149) shows that

$$U'''(u) = -\frac{2\nu(\nu+1)}{u^3}\,U(u)-\left[1-\frac{\nu(\nu+1)}{u^2}\right]U'(u). \tag{150}$$

The relations (148), (149), and (150) apply also to the functions $V(u_g)$ and $V(u_i)$. The Wronskian of the two functions is computed as

$$W[V(u),\,U(u)] = V(u)\,U'(u)-U(u)\,V'(u) = 2i. \tag{151}$$

Using the above notation, the modal equation (26) is rewritten as

$$[U'(u_g)+i\Delta_g U(u_g)]\,[V'(u_i)-i\Delta_e V(u_i)] = [U'(u_i)-i\Delta_e U(u_i)]\,[V'(u_g)+i\Delta_g V(u_g)]. \tag{152}$$

Expanding $U(u_i)$ and $V(u_i)$ in the series (148) and applying (151), it follows that

$$\frac{\nu(\nu+1)}{u_g^2}\left(1-\frac{\delta}{u_g}\right) \approx 1+i\frac{\Delta_g+\Delta_e}{\delta}, \tag{153}$$

where terms involving products and higher powers of Δ_g and Δ_e have been neglected. Noting

that $\nu(\nu+1) = (k_0 aS)^2$ and that $u_g^2/(1-\delta/u_g) \approx (k_0 r_m)^2$, where $r_m = a+h/2$, (153) is seen to agree with (87).

Introducing the notation

$$C_g^2 = \left(\frac{K_g}{k_0}\right)^2 = 1-\frac{\nu(\nu+1)}{u_g^2}, \tag{154}$$

the excitation factor Λ_n of (92) is computed as

$$\Lambda_n = 0.5\left(1-\frac{h}{a}\right)^{-1}\left\{1-i\Delta_g k_0 h\left(1-\frac{h}{3a}\right)+\frac{(k_0 h)^2}{3}\,[\Delta_g^2+C_g^2]\right\}^{-1}. \tag{155}$$

A series expansion of the sine and cosine functions of (93) shows that (155) and (93) agree in the limit of $(h/a) \ll 1$.

The height-gain function is computed as

$$G_n(z) = \frac{h_\nu^e(u)}{h_\nu^e(u_g)} = \left(1-\frac{z}{a}\right)\left(1-i\Delta_g k_0 z-\frac{1}{2}K_g^2 z^2\right), \tag{156}$$

which agrees with (94) in the limit of $K_g z \ll 1$ and $(z/a) \ll 1$.

The z-dependent normalized impedance is defined following (95). It follows that

$$\Delta_n(z) = \frac{Z_e(z)}{\sqrt{\mu_0/\varepsilon_0}} = \frac{ik_0 zC_g^2+ik_0 z\left(\frac{z}{a}\right)[1-C_g^2]-\Delta_g\left[1-\frac{1}{2}(K_g z)^2\right]}{1-\frac{1}{2}(K_g z)^2-i\Delta_g k_0 z}. \tag{157}$$

Also, (157) agrees with (96) in the limit of $K_g z \ll 1$ and $(z/a) \ll 1$.

In the E.L.F. range, the Taylor series expansion of the radial wave functions gives a modal equation identical to the one obtained in Section 4.3.1 using a planar approximation. The two methods give excitation factors Λ_n, height-gain functions $G_n(z)$, and impedances $\Delta_n(z)$ that exhibit differences of the order (h/a). The expressions for Λ_n, $G_n(z)$, and $\Delta_n(z)$ derived in this section can be substituted in the field expressions for the various dipole sources derived in Sections 4.3.2.1 to 4.3.2.4. The resulting fields will differ negligibly from the planar approximation of Section 4.3.2.

The method of Taylor series expansions is restricted to shells thin relative to the wavelength [$\delta = k_0 h < 1$ and $|K_g h| < 1$]. These conditions are satisfied for the $n = 0$ mode, but not for the cutoff ($n = 0$) modes in the E.L.F. range. In the V.L.F. range, Taylor series expansions can be used in a multilayer representation of the space between the earth and the ionosphere, where each layer is thin relative to the wavelength [Galejs, 1967].

4.5 Airy Function Approximation of the Radial Functions

In the formal solution of the earth-ionosphere waveguide spherical Bessel functions,

$$h_\nu^{(1,2)}(u) = \left(\frac{\pi}{2u}\right)^{0.5} H_{\nu+0.5}^{(1,2)}(u) \tag{158}$$

represent the radial field variations in (14). In Section 4.3, these radial functions were approx-

imated by simple exponentials that may be of limited accuracy in the V.L.F. range. In this section, the same radial functions will be represented by the so-called third-order or Watson approximation, which replaces spherical Bessel functions of large arguments and large complex order by Hankel functions of order (1/3) or by Airy functions. These approximations have been extensively studied by Wait [1962], and a similar notation will be used for some of the functions.

Following Sommerfeld [section 21, 1949], the Hankel function of order ν is expressed in terms of Hankel functions of order (1/3) which are replaced by Airy functions [Miller, 1946; Abramowitz and Stegun, 1964]. It can be shown that

$$\left.\begin{aligned} H_\nu^{(1,2)}(u) &= \frac{1}{\sqrt{3}}\sqrt{(u/\nu)^2-1}\,\exp\left[\pm if(\nu)\pm i\pi/6\right] H_{1/3}^{(1,2)}\left[(\nu/3)\left(\frac{u^2}{\nu^2}-1\right)^{1.5}\right] \\ &\approx \mp\frac{i}{\sqrt{\pi}}\left(\frac{2}{k_0a}\right)^{1/3}\exp\left[\pm if(\nu)\right] w_{2,1}(t), \end{aligned}\right\} \tag{159}$$

where

$$\left.\begin{aligned} f(\nu) &= \nu\left\{\sqrt{(u/\nu)^2-1}-(1/3)\left[(u/\nu)^2-1\right]^{1.5}-\sin^{-1}\sqrt{1-(\nu/u)^2}\right\} \\ &\approx (2/5)(-t)^{2.5}(k_0a/2)^{-2/3}+\ \ldots, \end{aligned}\right\} \tag{160}$$

$$-t = (\nu/2)^{2/3}\left[(u/\nu)^2-1\right] \approx \left(\frac{k_0a}{2}\right)^{2/3}\left[1-S^2+2(r-a)/a\right], \tag{161}$$

and where $w_j(t)$ represents Airy functions [Wait, 1962]. Re $S \approx 1$ and Im $S \ll 1$ for V.L.F. modes of low attenuation. In products S may be approximated by 1, but not in difference terms $(1-S)$. This approximation has been used in deriving the simplified forms of (160) or (161), and it will be also used throughout this section. The function $f(\nu)$ is small in magnitude for the lower modes, and the exponent of $f(\nu)$ is approximated by 1.

The Airy functions $w_{1,2}(t)$ satisfy the differential equation

$$w''(t)-tw(t) = 0 \tag{162}$$

and the Wronskian is given by

$$W[w_1(t),\ w_2(t)] = w_1(t)\,w_2'(t)-w_1'(t)\,w_2(t) = -2i. \tag{163}$$

The functions $w_{1,2}(t)$ can be expressed alternately as

$$w_{1,2}(t) = u(t) \mp iv(t) = \sqrt{\pi}\left[Bi(t) \mp iAi(t)\right], \tag{164}$$

where $Ai(t)$ and $Bi(t)$ are defined by Miller [1946] or Abramowitz and Stegun [1964]. The functions $u(t)$ and $v(t)$ are represented by the series

$$\left.\begin{aligned} u(t) &= \sqrt{3\pi}\left[c_1f(t)+c_2g(t)\right], \\ v(t) &= \sqrt{\pi}\left[c_1f(t)-c_2g(t)\right], \end{aligned}\right\} \tag{165}$$

where

$$\left.\begin{aligned} f(t) &= 1+\frac{1}{3!}t^3+\frac{1.4}{6!}t^6+\frac{1.4.7}{9!}t^9+\ \ldots, \\ g(t) &= t+\frac{2}{4!}t^4+\frac{2.5}{7!}t^7+\frac{2.5.8}{10!}t^{10}+\ \ldots, \end{aligned}\right\} \tag{166}$$

and where $c_1 = [3^{3/2}\Gamma(2/3)]^{-1}$, $c_2 = [3^{1/3}\Gamma(1/3)]^{-1}$, and $\Gamma(x)$ is the gamma function. These series representations are valid also for complex arguments t and are convenient for numerical calculations.

For arguments with large negative real parts,

$$\left.\begin{aligned} w_{1,2}(t) &= (-t)^{-0.25}\exp\left[\mp i(x+\pi/4)\right]\sum_{n=0}^{N}(\pm i)^n c_n x^{-n}, \\ w_{1,2}'(t) &= (-t)^{0.25}\exp\left[\mp i(x+\pi/4)\right]\sum_{n=0}^{N}(\pm i)^{n+1} d_n x^{-n}, \end{aligned}\right\} \tag{167}$$

where $x = (2/3)(-t)^{3/2}$, and where a prime denotes a derivative with respect to t. The coefficients c_n and d_n are computed from the relations

$$\left.\begin{aligned} c_0 &= d_0 = 1, \\ c_n &= c_{n-1}(6n-5)(6n-3)(6n-1)/[216n(2n-1)], \\ d_n &= -c_n(6n+1)/(6n-1). \end{aligned}\right\} \tag{168}$$

$N = 11$ gives an approximate 10-digit accuracy of the functions (167) for $\mathrm{Re}(t) < (-8)$.

The differential equation (162) can be also derived directly from the differential equation of the spherical Bessel functions. Changing the variable of the differential equation (13) from r to t and replacing $\nu(\nu+1)$ by ν^2, it can be shown that

$$(k_0r/\nu)^4 R''(t)-(k_0r/\nu)^2(2\nu^2)^{-1/3}R'(t)-tR(t) = 0. \tag{169}$$

This simplifies to (162) if $k_0r \approx \nu = k_0aS-0.5$ and if the term proportional to $R'(t)$ is negligible. The r-dependence of the coefficient of the $R(r)$ term of (13) has not been compromised in this derivation. The approximation (162) should be, therefore, more accurate than the thin-shell approximation (79), which was derived by replacing all the r factors of the differential equation (13) by their average values r_m.

Budden [section 15.5, 1961] shows that (162) can be obtained by introducing the approximation

$$\frac{1}{r^2} \approx \frac{1}{(a+h)^2}\left[1-2(z-h)/(a+h)\right] \tag{170}$$

in the differential equation (13). The solution of (162) differs from the solution of (13) by a term of the order $\nu(\nu+1)\left[(z-h)/(a+h)\right]^4/4$. Approximating ν by k_0a, this indicates an approximately 5 percent error for $f = 20$ kc/s and $h = 85$ km. This error is larger than in (159) which represents the complete third-order approximation of the Hankel functions. The error of (159) is estimated to be less than $\left|24\sqrt{2}/\nu\right|$ [Magnus and Oberhettinger, 1949], which is less than 1 percent for $f > 25$ kc/s.

More accurate solutions can be obtained by subdividing the airspace between the two waveguide boundaries in a large number of concentric thin shells. The fields in each of the shells can be adequately represented by functions of either Section 4.3 or Section 4.4 [Galejs 1967].

4.5.1 Modal Equation

Substituting (158) and (159), the wave functions (31) or (40) are approximated by

$$h_v^q(u) \approx \frac{i}{\sqrt{2u}} \left(\frac{2}{k_0 a}\right)^{1/3} [-A_q w_2(t) + B_q w_1(t)], \tag{171}$$

where $q = e$ or h and

$$-t = \left(\frac{v+0.5}{2}\right)^{2/3} \left[\left(\frac{u}{v+0.5}\right)^2 - 1\right] \approx \left(\frac{k_0 a}{2}\right)^{2/3} [1 - S^2 + 2(r-a)/a]. \tag{172}$$

The amplitude ratio B_e/A_e of the T.M. modes in (24) can be expressed as

$$\frac{B_e}{A_e} = \frac{w_2(t_g)\,[i\,\Delta_g + 1/(2u_g)] + w_2'(t_g)\,\partial t_g/\partial u}{w_1(t_g)\,[i\,\Delta_g + 1/(2u_g)] + w_1'(t_g)\,\partial t_g/\partial u} \tag{173}$$

or

$$\frac{B_e}{A_e} \approx \frac{w_2'(t_g) - q_g w_2(t_g)}{w_1'(t_g) - q_g w_1(t_g)}, \tag{174}$$

where t_g is computed by substituting $u = u_g = k_0 a$ or $r = a$ in (172),

$$\frac{\partial t}{\partial u} = -\frac{2^{1/3}}{(v+0.5)^{4/3}} \approx -\left(\frac{2}{k_0 a}\right)^{1/3}, \tag{175}$$

and where

$$q_j = i(k_0 a/2)^{1/3}\,\Delta_j \tag{176}$$

with $j = g$ or e. The simplified form (174) will be accurate if $|2u_g\,\Delta_g| \gg 1$. For $f = 20$ kHz and sea water of $\sigma_g = 5$ mho/m $|2u_g\,\Delta_g| \approx 2.5$, and it will become much larger for lower conductivities σ_g. The amplitude ratio B_e/A_e of (25) is obtained similarly as

$$\frac{B_e}{A_e} \approx \frac{w_2'(t_i) + q_e w_2(t_i)}{w_1'(t_i) + q_e w_1(t_i)}, \tag{177}$$

where t_i is computed by substituting $u = u_i = k_0(a+h)$ or $r = a+h$ in (172), and q_e is defined by (176). The modal equation (26) may be rewritten as

$$\left[\frac{w_1'(t_g) - q_g w_1(t_g)}{w_2'(t_g) - q_g w_2(t_g)}\right] \left[\frac{w_2'(t_i) + q_e w_2(t_i)}{w_1'(t_i) + q_e w_1(t_i)}\right] - \exp(i2\pi n) = 0 \tag{178}$$

which can be also obtained by equating the B_e/A_e ratios of (174) and (177).

The transcendental equation (178) simplifies in several limiting cases which will be examined first. For a perfectly conducting ground $q_g = 0$, substitution of the approximations for large negative arguments (167) and (168) in (178) shows that

$$\frac{C_i - \Delta_e}{C_i + \Delta_e} \exp\left\{\frac{2i}{3} k_0 a[(C_i)^3 - C_g^3]\right\} = \exp(i2\pi n), \tag{179}$$

where $C_g^2 = 1 - S^2$, $C_i^2 = 1 - S^2 + 2h/a = C_g^2 + 2h/a$, and where C_g and C_i may be complex.

For $(2h/a) \ll C_g^2$ and $|\Delta_e| = \infty$ or 0, (179) simplifies to

$$2k_0 h C_g[1 + h/(2aC_g^2)] = \begin{cases} (2n-1)\pi & \text{if } |\Delta_e| = \infty \\ 2n\pi & \text{if } |\Delta_e| = 0 \end{cases} \tag{180}$$

which can be seen to agree with (83) or (85), including the first-order terms in (h/a); both methods give comparable corrections for the earth curvature. Although t_i has a negative real part and generally is larger than unity in magnitude, t_g will have a positive real part and may be less than unity in the $n = 1$ mode for most of the frequencies in the V.L.F. range. However, (179) can be used for estimating the roots C_g of higher order modes ($n > 1$).

A more general solution of (178) should consider arbitrary numerical values of t, and it will be assumed that the roots t_i and t_g are real. For a perfectly conducting ground ($q_g = 0$) and real values of t, the first factor of (178) will be of unity magnitude. Substituting the large argument approximations in the second factor, the logarithm of (178) may be written as

$$\frac{2k_0 a}{3}(C_i)^3 - \frac{\pi}{2}(4n-1) - 2\tan^{-1}\left[\frac{v'(t_g)}{u'(t_g)}\right] - 2\tan^{-1}\left[\frac{C_i}{i\Delta_e}\right] = 0. \tag{181}$$

For a purely reactive surface impedance Δ_e is imaginary, all the terms of (181) are real, and the equation has real solutions, which justifies its derivation from (178). For Δ_e imaginary, q_e is real; and for t_i and t_g real, (178) can be written alternately as

$$\tan^{-1}\frac{v'(t_i) + q_e v(t_i)}{u'(t_i) + q_e u(t_i)} - \tan^{-1}\frac{v'(t_g)}{u'(t_g)} = \pi n, \tag{182}$$

which can be solved for real roots C_g by substituting the power series representations (165) and (166) of u and v functions. The surface impedance Δ_e is complex for realistic ionosphere models, but the imaginary part of this surface impedance is used in (181) or (182) to obtain a first estimate of C_g. However, in cases where Δ_e has a real part which is larger than $C_g \approx \sqrt{2h/a}$, $|\Delta_e| = \infty$ may be used in (181).

The effects of a reactive surface impedance can be examined also using a further simplified form of (181). For small arguments t, it can be shown that

$$\tan^{-1}\left[\frac{v'(t)}{u'(t)}\right] \approx -\frac{\pi}{6} + 0.4t^2 + \dots . \tag{183}$$

Substituting (183) in (181) and approximating C_i as

$$(C_i)^m = \left(\frac{2h}{a}\right)^{m/2} + \frac{m}{2}\left(\frac{2h}{a}\right)^{-1+m/2}, \tag{184}$$

it follows that

$$C_g^2 \approx \frac{(12n-5)(\pi/6) - \dfrac{2k_0 a}{3}\left(\dfrac{2h}{a}\right)^{1.5} + 2\dfrac{\sqrt{2h/a}}{i\Delta_e} - \dfrac{2}{3}\left[\dfrac{\sqrt{2h/a}}{i\Delta_e}\right]^3}{k_0 a\sqrt{\dfrac{2h}{a}} - 0.8\left(\dfrac{k_0 a}{2}\right)^{4/3} C_g^2 - \dfrac{1}{i\Delta_e\sqrt{2h/a}} + \dfrac{\sqrt{2h/a}}{(i\Delta_e)^3}}, \tag{185}$$

which is valid only if $|C_i/(i\Delta_e)| \ll 1$. The term proportional to C_g^2 in the denominator can be

neglected, which is equivalent to approximating (183) by its $t = 0$ value. It can be shown that an inductive (capacitive) surface impedance with Im $\Delta_e < 0$ (> 0) increases (decreases) C_g^2 and decreases (increases) $S = \sqrt{1-C_g^2}$, relative to their values for $|\Delta_e| = \infty$.

After computing approximate real values of C_g^2 for a finite reactive or infinite surface impedance from (181) or (182), more accurate complex values of t_g or C_g^2 are computed by applying Newton's iteration method to (178). Noting that

$$-t_i = -t_g + \left(\frac{k_0 a}{2}\right)^{2/3} \frac{2h}{a}, \tag{186}$$

the left-hand side of (178) can be designated as $f(t_g)$. A Taylor series expansion of the function $f(t_g)$ about its approximate zero $f(t_0)$ gives a corrected t_g estimate for its zero as

$$t_g = t_0 - \frac{f(t_0)}{df/dt_q\big|_{t_q \simeq t_0}}, \tag{187}$$

where use can be made of (162) and (163) in the evaluation of the derivative. Iterations may be used to improve the accuracy of the roots provided that this process is convergent.

Equations (173) to (185) apply to T.M. or n-modes only. A similar development shows that the amplitude ratios B_h/A_h of (171) can be calculated from (174) and (177) and that the modal equation (178) applies to T.E. or m-modes if n, Δ_g, and Δ_e are replaced by m, $1/\Delta_g$, and $1/\Delta_h$ respectively. Therefore q_g is defined as

$$q_g = i(k_0 a/2)^{1/3}/\Delta_g \tag{188}$$

and q_e is replaced by

$$q_h = i(k_0 a/2)^{1/3}/\Delta_h \tag{189}$$

for calculation of T.E. modes. An approximate real value of C_g^2 is computed for $\Delta_g = \Delta_h = 0$ or $q_g = q_h = \infty$; more accurate complex values of t_g or C_g^2 are obtained using (187).

The phase velocities and attenuation rates of V.L.F. waves have been calculated for the two lower T.M. and T.E. modes and are shown in Fig. 4.7 and 4.8 respectively. The ionospheric boundary heights $h = 70$ or 85 km, the ionospheric conductivity $\sigma_i = 10^{-6}$ or 10^{-5}, and the ground conductivity $\sigma_g = 10^{-3}$ or 5 mho/m. The parameter Re $S = c/v_{ph}$ is decreased, and the attenuation rate α is increased with a decreasing frequency; these changes are more pronounced for the n or $m = 2$ modes. It was indicated in Section 4.3.1 that for the T.M. modes the ionosphere approximates a perfect reflector ($\sigma_i \approx 0$) and for the T.E. modes the same ionosphere approximates the characteristics of a perfect conductor of $\sigma_i = \infty$. As a consequence, a decreasing conductivity (σ_i is changed from 10^{-5} to 10^{-6} mho/m) makes the T.M. modes to approach the low loss conditions and the attenuation rate is *decreased*, particularly in the $n = 1$ mode. A similar decrease of the ionospheric conductivity causes the ionosphere to deviate more from the low loss condition of high conductivity for the T.E. modes, and the attenuation rates are *increased*. A decreasing ground conductivity increases the attenuation rates of both T.E. and T.M. modes. For $h = 85$ km, $\sigma_i = 10^{-5}$, and for the $n = 1$ mode at $f = 20$ kc/s, the attenuation rate $\alpha = 2.2$ and 3.3 db/1000 km for $\sigma_g = 5$ and 10^{-3} respectively; for the $m = 1$ mode, the corresponding α figures are 0.365 and 0.372 db/1000 km respectively. Such a decrease of the ground conductivity causes a small increase of Re S which can be seen for the

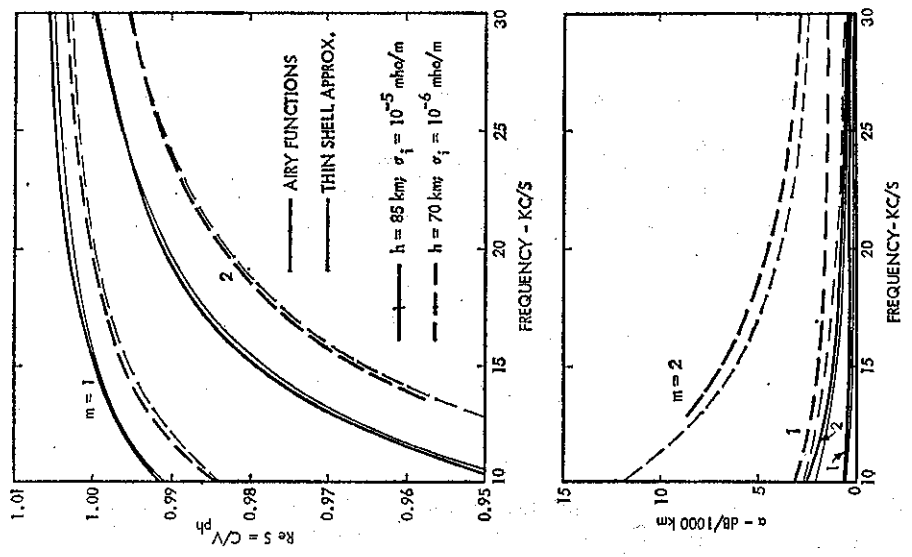

FIG. 4.8 Phase Velocity and Attenuation Rates of V.L.F. Waves. T.E. Modes for Sharply Bounded Homogeneous and Isotropic Ionosphere Models

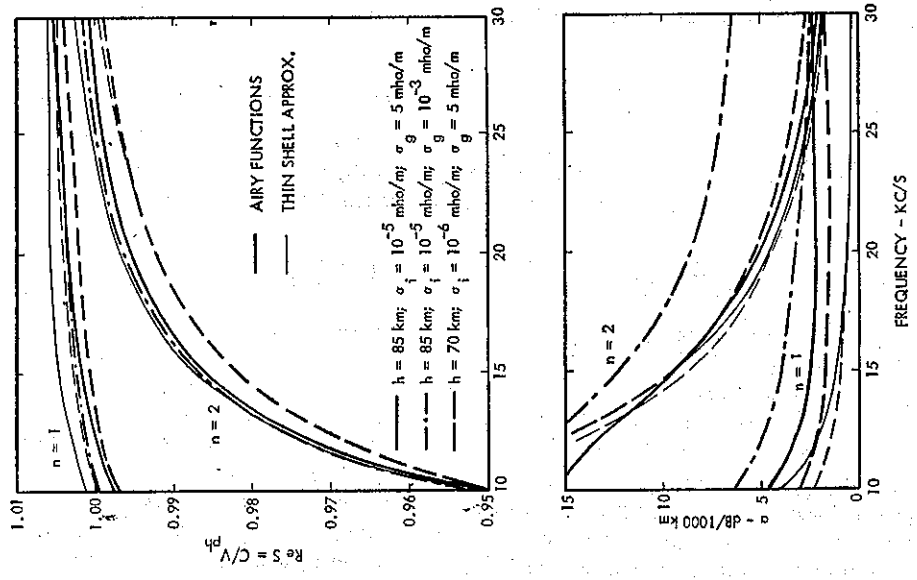

FIG. 4.7 Phase Velocity and Attenuation Rates of V.L.F. Waves. T.M. Modes for Sharply Bounded Homogeneous and Isotropic Ionosphere Models

T.M. modes in Fig. 4.7, but this increase is only 2 parts in 10^6 for the T.E. modes, and appears negligible within the accuracy of the plotted curves.

The thin-shell field representations of Section 4.3.1 provide the propagation parameters indicated by thin lines in Fig. 4.7 and 4.8. The Re S curves (or the phase velocity data) are approximated with a reasonable accuracy; but the attenuation rates are too low, particularly in the $n = 1$ and $m = 1$ modes at the higher frequencies. The thin-shell approximations are most inaccurate for the $n = 1$ mode.

4.5.2 *Field Components*

Expressions for field components of the various dipole sources have been listed in Sections 4.3.2.1 to 4.3.2.4 in terms of excitation factors A_q, height-gain function $G_q(z)$, and height-dependent normalized impedances $\Delta_q(z)$ (where $q = n$ or m) that have been defined in Section 4.3.2 in terms of spherical Bessel functions. Also, the Airy function approximations of Section 4.5 can be substituted in these expressions to obtain a better accuracy of A_q, $G_q(z)$, and $\Delta_q(f)$ for frequencies in the V.L.F. range.

The excitation factor A_n is defined by (91) and (36) as

$$A_n = 0.5k_0h[h_\nu^e(u_g)]^2 \left\{ \lim_{\mu\to\nu} \frac{-u^2}{2\mu+1} \left[\frac{\partial}{\partial\mu} h_\mu^e(u) \frac{\partial}{\partial u} h_\nu^e(u) - h_\nu^e(u) \frac{\partial^2}{\partial\mu\,\partial u} h_\mu^e(u) \right]_{u=u_g}^{u_t} \right\}^{-1}. \tag{190}$$

In this expression, $h_\nu^e(u)$ of (31) or (171) has eigenvalues $\nu = \nu_n$ (or $S = S_n$) which satisfy the boundary conditions at the surfaces $u = u_g$ and u_t or which makes B_e/A_e of (174) equal to B_e/A_e of (177). A modified value $\mu \neq \nu_n$ should not satisfy the boundary conditions, which can be achieved by defining $h_\mu^e(u)$ from (171), but with B_e/A_e determined for $\nu = \nu_n$. As a consequence, A_e and B_e of the function $h_\mu^e(u)$ do not depend on μ and $\partial A_e/\partial\mu = \partial B_e/\partial\mu = 0$. The coefficients A_e and B_e are computed for constant values $t = t_g$ or t_i from (174) or (177), and also $\partial A_e/\partial t = \partial B_e/\partial t = 0$. The function (171) can be expressed as

$$\left.\begin{aligned} h_\nu^e(u) &= \frac{i}{\sqrt{2u}} \left(\frac{2}{k_0a}\right)^{1/3} [-A_e(t_g)\, w_2(t) + B_e(t_g)\, w_1(t)] \\ &= \frac{i}{\sqrt{2u}} \left(\frac{2}{k_0a}\right)^{1/3} \frac{A_e(t_g)}{A_e(t_i)} [-A_e(t_i)\, w_2(t) + B_e(t_i)\, w_1(t)], \end{aligned}\right\} \tag{191}$$

where $A_e(t_g)$ and $B_e(t_g)$ refer to (B_e/A_e) computed from (174), and $A_e(t_i)$ and $B_e(t_i)$ refer to (B_e/A_e) computed from (177). Both expressions are identical if t_i and t_g satisfy the modal equation (178). The first expression of (191) is more convenient to use for evaluating terms of (190) involving $u = u_g$, while the second expression of (191) is used for $u = u_t$. Noting that

$$\frac{\partial t}{\partial \nu} = \frac{1}{3} \left(\frac{2}{\nu+0.5}\right)^{1/3} \left[2\left(\frac{u}{\nu+0.5}\right)^2 + 1\right] \approx \left(\frac{2}{k_0a}\right)^{1/3}, \tag{192}$$

$$\frac{\partial^2 t}{\partial \nu\, \partial u} = \frac{u}{3} \left(\frac{2}{\nu+0.5}\right)^{7/3} \approx \frac{2}{3} \left(\frac{2}{k_0a}\right)^{4/3}, \tag{193}$$

and applying (162), (163), and (175), it follows that

$$\left.\begin{aligned} A_n = 0.5k_0h\left(\frac{2}{k_0a}\right)^{1/3} \Bigg\{ & t_g - q_g^2 - \frac{2}{3} q_g \left(\frac{2}{k_0a}\right)^{2/3} \\ & - \left[\frac{w_1'(t_g) - q_g w_1(t_g)}{w_1'(t_i) + q_e w_1(t_i)}\right]^2 \left[t_i - q_e^2 + \frac{2}{3} q_e \left(\frac{2}{k_0a}\right)^{2/3}\right] \Bigg\}^{-1}. \end{aligned}\right\} \tag{194}$$

For $|q_j| \gg \left(\frac{2}{3}\right)[2/(k_0a)]^{2/3}$ or $|\Delta_j| \gg 4/(3k_0a)$, (194) simplifies to the A_n expression (VII-68) of Wait [1962]. In the V.L.F. range, this inequality is satisfied for $\sigma_j \prec 0.1$ mho/m. [For $f = 20$ kHz and $\sigma_j = 0.1$ mho/m, $|\Delta_j| = \left|Z_j/\sqrt{\mu_0/\varepsilon_0}\right| \approx 3.3\times10^{-3} \succ 4/(3k_0a) = 5\times10^{-4}$, where Z_j is computed for a homogeneous medium from (97).] For larger conductivities, the terms proportional to q_j become negligible $\left(\left|\left(\frac{2}{3}\right) q_g(2/k_0a)^{2/3}/t_g\right| = |4\Delta_g/[3k_0a(1-S^2)]|\right.$ $\left.\prec |4\Delta_g/(6k_0a\ \mathrm{Im}\ S)| \approx 3\times10^{-3}\right.$ for $f = 20$ kHz, $\sigma_g = 0.1$ mho/m and $\alpha = 1$ db/1000 km), and the boundary medium will appear similar to a perfect conductor of $q_j = 0$.

In the limit of $q_g = 0$, $|q_e| = \infty$, $(2h/a) \ll C_g^2$, and large negative values of t, A_n simplifies to

$$\left.\begin{aligned} A_n &= 0.5k_0h\left(\frac{2}{k_0a}\right)^{1/3} \{t_g + [w_1'(t_g)/w_1(t_i)]^2\}^{-1} \\ &= -\frac{h}{aC_g^2} \left\{1 + \left(1 + \frac{h}{aC_g^2}\right) \exp\left[2ik_0hC_g\left(1 + \frac{h}{2aC_g^2}\right)\right]\right\}^{-1}. \end{aligned}\right\} \tag{195}$$

Application of (180) shows that $A_n = 1$. The same value of A_n is obtained in a similar development also for $q_g = q_e = 0$.

The height-gain function $G_n(z)$ is defined by (94), and it is computed using (163), (171), and (174) as

$$\left.\begin{aligned} G_n(z) = \frac{h_\nu^e(u)}{h_\nu^e(u_g)} &= 0.5i[-A_e w_2(t) + B_e w_1(t)] \\ &= -0.5i\{[w_1'(t_g) - q_g w_1(t_g)]\, w_2(t) - [w_2'(t_g) - q_g w_2(t_g)]\, w_1(t)\}. \end{aligned}\right\} \tag{196}$$

For small values of $z = r - a$, the functions $w_j(t)$ are approximated as $w_j(t_g) + (t - t_g)\, w_j'(t_g)$, and $G_n(z) \approx 1 - i\Delta_g k_0 z$, which is in agreement with a small Kz approximation of (93).

Following (95), the z-dependent normalized impedance is obtained as

$$\Delta_n(z) = \frac{Z_e(z)}{\sqrt{\mu_0/\varepsilon_0}} = \frac{\partial}{\partial u}[uh_\nu^e(u)]/[iuh_\nu^e(u)] \approx i\left(\frac{2}{k_0a}\right)^{1/3} \frac{-A_e w_2'(t) + B_e w_1'(t)}{-A_e w_2(t) + B_e w_1(t)}, \tag{197}$$

where either (174) or (177) can be used for A_e and B_e. In the limit of $z = 0$, $\Delta_n(0) = -\Delta_g$ and for $z = h$, $\Delta_n(h) = \Delta_e$, which agrees with (96).

For T.E. modes, the amplitude ratios B_h/A_h of (171) are computed from (173) or (177), the excitation factor A_m from (194), and the height-gain function $G_m(z)$ from (196) by replacing subscripts n by m, subscripts or superscripts e by h, and with q_g and q_h defined by (188) and (189).

In the limit of a highly conducting ionosphere and conducting ground (Δ_h, $\Delta_g \to 0$), $|q_h|$ and $|q_g| \to \infty$, and the excitation factor A_m becomes

$$A_m = (h/a)\, \Delta_g^2 \{1 + [w_1(t_g)/w_1(t_i)]^2\}^{-1}. \tag{198}$$

Substituting the large negative argument approximations (167) and (168), assuming $(2h/a) \ll C_g^2$, and applying the modal equation (178), it is seen that $A_m \approx -A_g^2 C_g^2[1+h/(2aC_g^2)]$, the leading term of which agrees with (98). A_m remains proportional to A_g^2 as $A_g \to 0$.

For small values of $z = r-a$, the height-gain function is approximated as $G_m(z) \approx 1 - ik_0 z/A_g$. $G_m(0) = 1$, but $G_m(z)$ increases rapidly with increasing values of z if $A_g \to 0$. Although $A_m \to 0$ if $A_g \to 0$, the field components proportional to $A_m G_m(z_s) G_m(z)$ will remain finite for elevated sources and observation points (z_s, $z \neq 0$).

The z-dependent normalized impedance defined by (100) is computed as

$$A_m(z) = \frac{Z^h(z)}{\sqrt{\mu_0/\varepsilon_0}} = [iuh_1^h(u)]\Big/\frac{\partial}{\partial u}[uh_2^h(u)] = -i\left(\frac{k_0 a}{2}\right)^{1/3} \frac{-A_h w_2(t) + B_h w_1(t)}{-A_h w_2'(t) + B_h w_1'(t)}, \qquad (199)$$

where A_h and B_h are computed as indicated earlier. For $z = 0$, $A_m(0) = -A_g$, and for $z = h$, $A_m(h) = A_h$.

The excitation factors A_n, the height-gain functions $G_n(z)$, and the normalized impedances $A_n(z)$ of the T.M. modes are shown in Figs. 4.9–4.11 for the same ionosphere and ground conductivity models considered in Fig. 4.7.

The excitation factors $A_n \approx 1$ near $f = 10$ kc/s; but the magnitude of A_1 is decreased with increasing frequency, particularly for the larger ionospheric boundary heights h. However, for the thin-shell approximations of Section 4.3.2, which are indicated by thin lines in Fig. 4.9, the magnitude of A_1 remains nearly constant with frequency. A_n is essentially real and the phase angle is less than 20° in magnitude.

The height-gain function $G_n(z)$, shown in Figs. 4.10A and 4.10B characterizes the height variations of the E_r^{vn} or H_φ^{ve} field components following (104), (105), and (107). It is seen that the magnitude of $G_1(z) < 1$ for $f = 10$ kc/s; it exhibits portions larger in magnitude than 1 at $f = 20$ kc/s, but it is larger than 1 at nearly all heights for $f = 30$ kc/s. It follows from (94) that modes with height-gain functions of large magnitude are poorly excited, which can be also seen from a direct comparison of Figs. 4.9, 4.10A, and 4.10B. $G_1(z)$ is not significantly affected by changes in the ground conductivity σ_g. The thin-shell approximation of Section 4.3.2, indicated by thin lines in Figs. 4.10A and 4.10B, does not produce the increase of $G_1(z)$ that is observed in the Airy function representations at larger heights and higher frequencies. The excitation factor A_1 of the thin-shell approximation is therefore too large in magnitude at the higher frequencies. In the $n = 2$ mode, the magnitude of $G_2(z) < 1$; and there are two minima, the heights of which are increased with increasing frequency. The phase of $G_2(z)$ changes rapidly near the minima, and $G_2(z)$ is nearly imaginary at the minima. The thin-shell approximations do not reproduce the frequency dependence of these minima, but the magnitude of $G_2(z)$ is adequately represented at height intervals within 10 km from the waveguide boundaries.

In modes characterized by small excitation factors, energy is concentrated below the base of the ionosphere; and the field strength near the ground is small. Such earth-detached modes appear to be repeatedly reflected at the inside spherical surface of the ionosphere. A similar process is observed for sound waves inside a whispering gallery [Rayleigh, 1910], and these modes are described as "whispering gallery modes" [Budden and Martin, 1962; Wait, 1962]. The lower order T.M. modes are also earth detached in the L.F. range following Section 9.3; all T.E. modes exhibit height-gain functions $|G_m(z)| \gg 1$ for $z > 0$, as seen from Fig. 4.13 (p. 119).

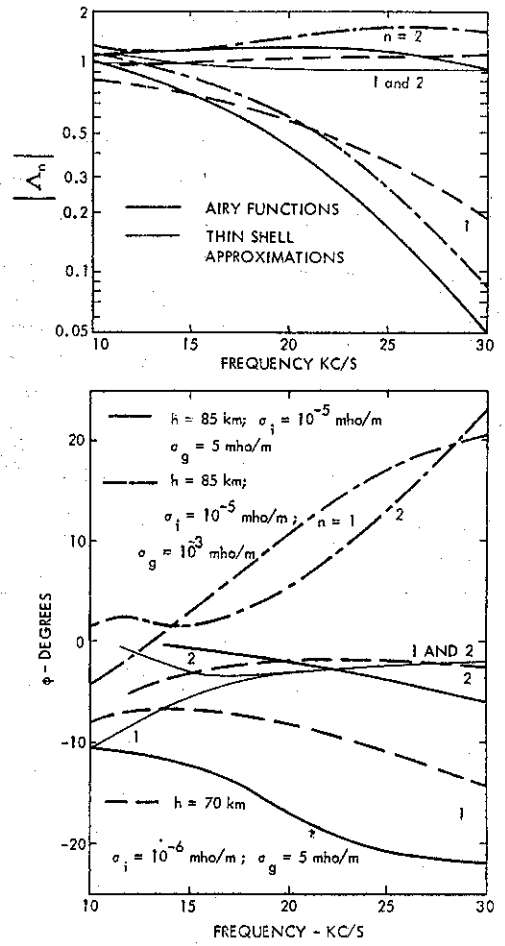

FIG. 4.9 Excitation Factors $A_n = |A_n| \exp(i\varphi_n)$ of V.L.F. Waves. T.M. Modes for Sharply Bounded Homogeneous and Isotropic Ionosphere Models

The normalized impedance $A_n(z)$, shown in Fig. 4.11, characterizes the wave tilt E_θ^{ve}/E_r^{ve} according to (109). It was pointed out, following (197), that $A_n(0) = -A_g$. As a consequence, the phase angle of $A_n(z)$ is 135° at $z = 0$; but there is a rapid change of the phase angle near $z = 0$ for a highly conducting ground surface. The phase angle $\varphi = 0$ and $A_n(z)$ is real at the maxima and minima of the magnitude curves. The magnitude of $A_1(z)$ is maximum near the ionospheric boundary at $z = h$; but there are several maxima of the $A_2(z)$ curves, which significantly exceed the normalized ionospheric surface impedance A_e in magnitude. The maxima of $A_2(z)$ exceed 1 in magnitude for $f = 10$ and 20 kc/s; at these heights, which correspond to the heights z of the lower minima of $G_2(z)$ in Figs. 4.10A and 4.10B, the horizontal component of the E vector is

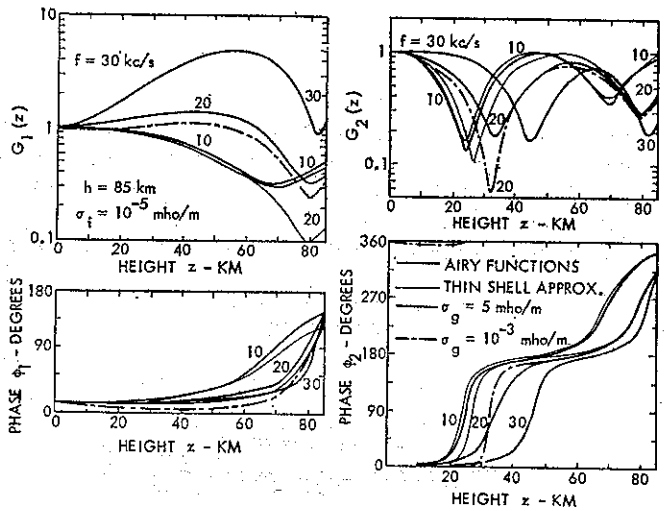

FIG. 4.10A Height-gain Functions $G_n(z) = |G_n(z)| \exp(i\varphi_n)$ of V.L.F. Waves. T.M. Modes for Sharply Bounded Homogeneous and Isotropic Ionosphere Models

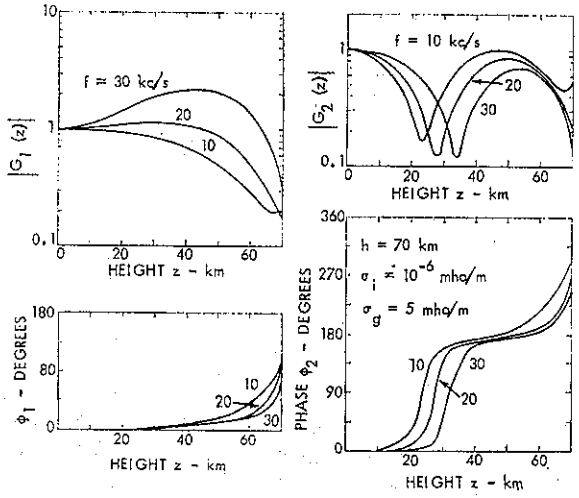

FIG. 4.10B Height-gain Functions $G_n(z) = |G_n(z)| \exp(i\varphi_n)$ of V.L.F. Waves. T.M. Modes for Sharply Bounded Homogeneous and Isotropic Ionosphere Models

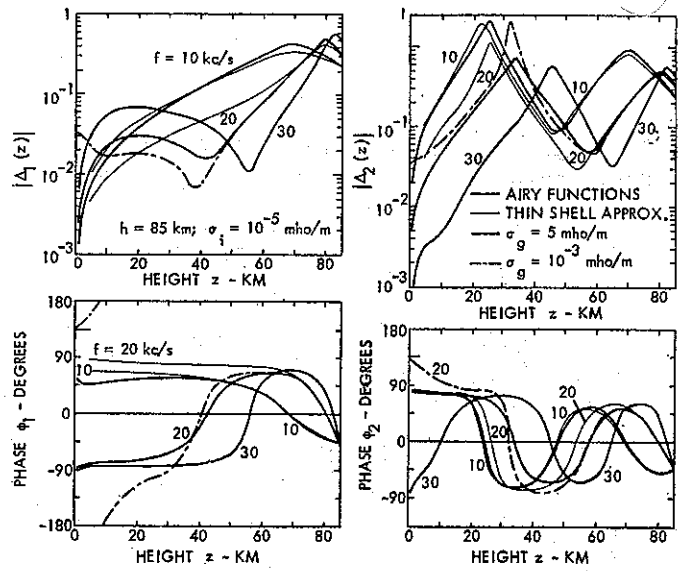

FIG. 4.11A Normalized Impedance $\Delta_n(z) = |\Delta_n(z)| \exp(i\varphi_n)$ of V.L.F. Waves. T.M. Modes for Sharply Bounded Homogeneous and Isotropic Ionosphere Models

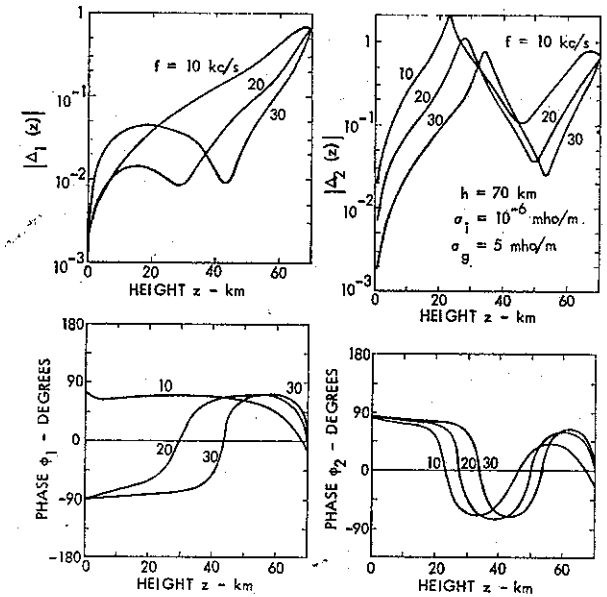

FIG. 4.11B Normalized Impedance $\Delta_n(z) = |\Delta_n(z)| \exp(i\varphi_n)$ of V.L.F. Waves. T.M. Modes for Sharply Bounded Homogeneous and Isotropic Ionosphere Models

larger than its vertical component. The thin-shell approximations appear to be adequate for $f = 10$ kc/s, but at higher frequencies these approximations can be used only in the vicinity of the ionospheric boundary.

The excitation factors Λ_m, the height-gain functions $G_m(z)$, or the normalized impedances $\Delta_m(z)$ of the T.E. modes, shown in Figs. 4.12–4.14, are quite different from the corresponding parameters of the T.M. modes shown in Figs. 4.9–4.11.

The excitation factor Λ_m, shown in Fig. 4.12, is inversely proportional to the ground conductivity σ_g. It is nearly imaginary and is of a small magnitude. The magnitude of Λ_m is decreased with increasing frequency, but the thin-shell approximations of Section 3.2 produce a similar frequency dependence only to a lesser degree.

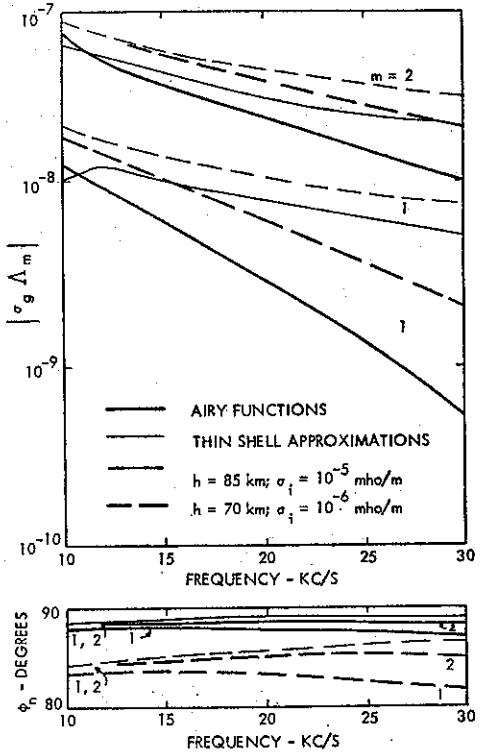

FIG. 4.12 Excitation Factors $\Lambda_m = |\Lambda_m| \exp(i\varphi_m)$ of V.L.F. Waves. T.E. Modes for Sharply Bounded Homogeneous and Isotropic Ionosphere Models

The height-gain functions $G_m(z)$, shown in Figs. 4.13A and 4.13B, characterize the height variations of the H_r^{vm} or E_φ^{vm} field components following (111), (112), and (114). The function $G_m(0) = 1$ by definition, but it exhibits a rapid increase with increasing heights z. The height-gain function $|G_m(z)| \gg 1$ corresponds to an excitation factor $|\Lambda_m| \ll 1$ following (94). As a consequence, $G_m(z)$ is proportional to the square root of the ground conductivity σ_g, which

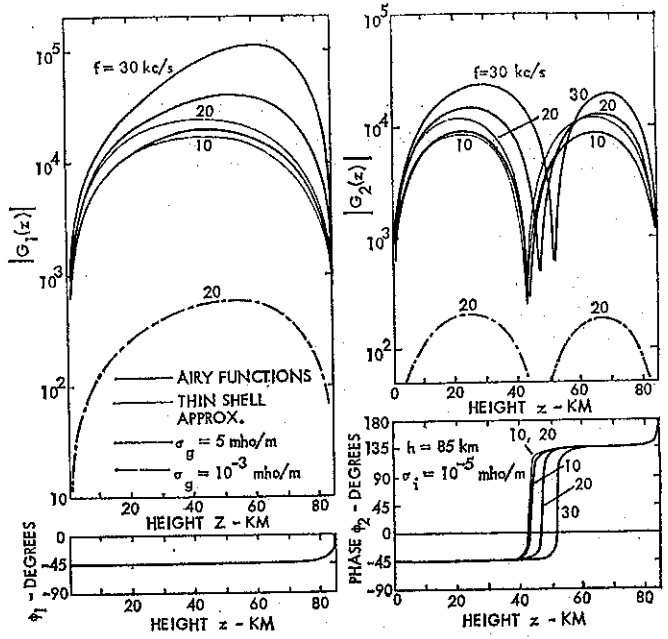

FIG. 4.13A Height-gain Functions $G_m(z) = |G_m(z)| \exp(i\varphi_m)$ of V.L.F. Waves. T.E. Modes for Sharply Bounded Homogeneous and Isotropic Ionosphere Models

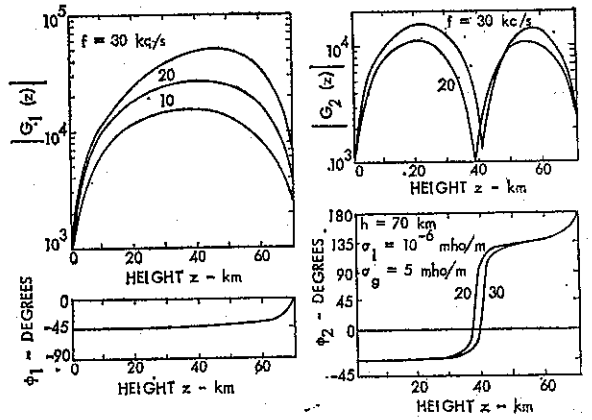

FIG. 4.13B Height-gain Functions $G_m(z) = |G_m(z)| \exp(i\varphi_m)$ of V.L.F. Waves. T.E. Modes for Sharply Bounded Homogeneous and Isotropic Ionosphere Models

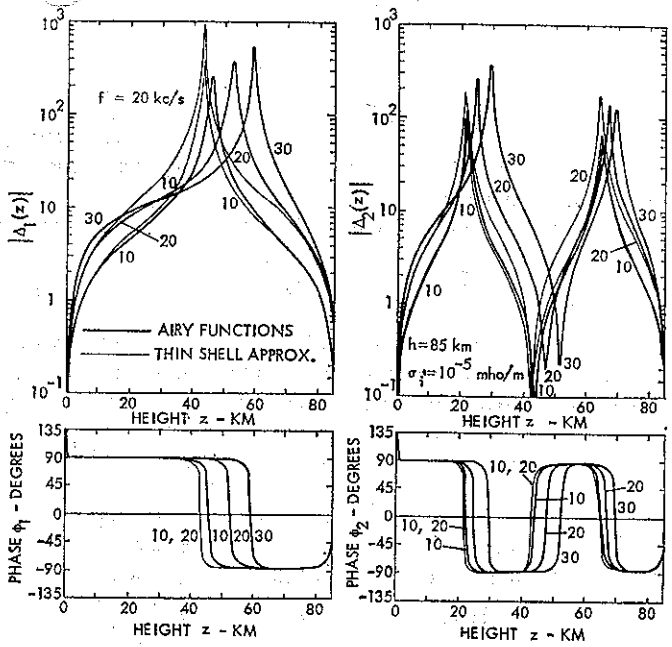

FIG. 4.14A Normalized Impedance $\Delta_m(z) = |\Delta_m(z)| \exp(i\varphi_m)$ of V.L.F. Waves. T.E. Modes for Sharply Bounded Homogeneous and Isotropic Ionosphere Models

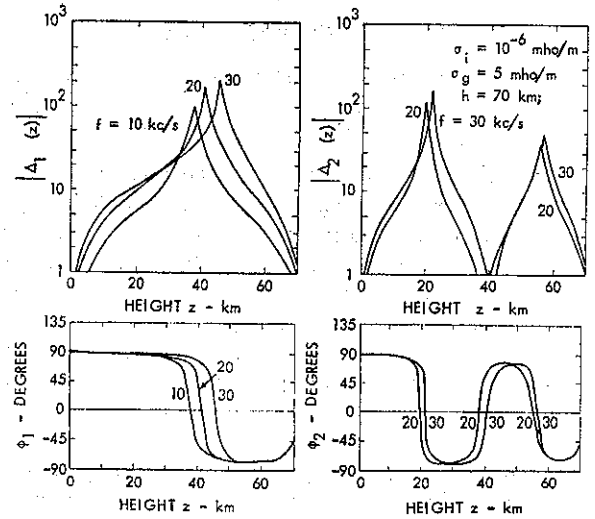

FIG. 4.14B Normalized Impedance $\Delta_m(z) = |\Delta_m(z)| \exp(i\varphi_m)$ of V.L.F. Waves. T.E. Modes for Sharply Bounded Homogeneous and Isotropic Ionosphere Models

can be also seen by a comparison of the curves shown in Figs. 4.13A and 4.13B. The phase angle of $G_1(z) \approx 45°$ for most values of z; the phase angle of $G_2(z)$ changes from $-45°$ to $135°$ with $\varphi \approx 45°$ at the minima of $G_2(z)$ curves. The minimum magnitudes of $G_2(z)$ occur at heights which increase with increasing frequency f. The thin-shell approximations appear adequate for $f \approx 10$ kc/s; at higher frequencies, these approximations can be used only for $z < 20$ km.

The normalized impedance $\Delta_m(z)$, shown in Figs. 4.14A and 4.14B, characterizes the wave tilt H_r^{vm}/H_θ^{vm} following (115). Except for the immediate vicinity of the waveguide boundaries and the minima of the $\Delta_2(z)$ curves, the magnitude of $\Delta_m(z) \ll 1$ and H_r^{vm} is the principal magnetic field component of the T.E. modes. The minima and maxima of the plotted curves correspond to a zero phase angle $\varphi_m(z)$ or to real values of $\Delta_m(z)$, but $\Delta_m(z)$ is nearly imaginary at other heights z. The thin-shell approximations appear to be adequate within 10 km from the waveguide boundaries, but they become less accurate near the minima and maxima of the $\Delta_m(z)$ curves.

The thin-shell approximations of Section 4.3.2 have been compared with solutions based on Airy function representations in Figs. 4.9–4.14. The thin-shell approximations can be used for qualitatively estimating the excitation factors, height-gain functions, and normalized height-dependent impedances of T.M. and T.E. modes without a detailed examination of their validity only for frequencies near 10 kc/s. For T.M. modes, the thin-shell approximations do not produce the required higher frequency decrease of Λ_1 or the increase of $G_1(z)$. $G_2(z)$ is reasonably accurate within approximately 10 km from the waveguide boundaries, but $\Delta_n(z)$ appears to be adequate within approximately 10 km from the ionospheric boundary. For T.E. modes at higher frequencies, the thin-shell approximations do not provide an adequate decrease of Λ_m; and, as a consequence, $G_m(z)$ tends to be too small in magnitude. $\Delta_m(z)$ is adequate only within approximately 10 km from the waveguide boundaries.

4.6 Fields in the Vicinity of Sources

There are several possible representations for the E.L.F. or V.L.F. near fields in the space between the spherical boundaries of earth and the ionosphere. For distances in excess of several waveguide heights from the source, the fields are adequately represented as a sum of a few propagating modes. In the immediate vicinity of a ground-based or low-altitude source, the fields can be computed by neglecting the presence of the upper waveguide boundary. Another useful approximation is provided by the method of images that is strictly valid for perfectly conducting flat ground surface and ionosphere. The near fields can be alternately represented by the series of zonal harmonics or as a summation of a large number of waveguide modes.

The series of zonal harmonics appears to be the more fundamental of the above-field representations. The Watson transformation [Bremmer, 1949; Sommerfeld, 1949] changes this series into a complex integral, the residues of which can be identified as contributions of individual modes. In addition to the waves of the residue type, there will also be a continuous wave spectrum or lateral waves, which propagate in the earth or the ionosphere. In the limit of a planar waveguide, these so-called branch-cut waves have been studied by Budden [1961] or Anderson [1962]; but their relative contributions have not been investigated in the near-field range of the earth-to-ionosphere waveguide. It will be shown that both the series of zonal harmonics and the mode sum produce numerically identical near fields. The difference of the two representations,

which should characterize the contributions of branch-cut waves, is negligible in the present computational model.

The series of zonal harmonics and the Watson transformation are discussed in Section 4.9. The field expressions of Section 4.2 can be applied to the near-field range after developing a suitable approximation for the Legendre function $P_\nu(-\cos\theta)$ that characterizes the distance or θ-dependence of the various field components.

The near-field approximation (30) of Legendre functions satisfies equations (11) and (12) in the limit of $\nu(\nu+1) \ll 1/(\sin\theta)^2$ or $(\nu+0.5)\,\theta \ll 1$, but the asymptotic form (44) satisfies (11) and (12) even for $\theta \ll 1$ if $(\nu+0.5)\,\theta \gg 1$. Propagating modes as well as modes below cutoff must be considered for representing the fields in the vicinity of sources. For propagating modes, $\nu+0.5 = k_0 aS$ is nearly real and is less in magnitude than for the cutoff modes, where $K \approx n\pi/h$ and $\nu+0.5 \approx in\pi(r_m/h)$ following (81) and (83). For the cutoff modes, the representation (30) may be changed over into (44) in a relatively small distance, and it is desirable to have a θ representation which varies continuously from the form (30) to the form (44). Such an approximation can be derived most readily by examining the differential equation (10) in the limit of $\theta \ll 1$. This limit may be interpreted as the flat earth approximation for distant fields ($\theta = D/a$, with $a \to \infty$), or the short-range approximation for curved earth ($D \ll a$).

Using the small θ approximation of the cot θ function, the differential equation (10) becomes

$$\theta^2 T'' - (\theta - \theta^3/3)\,T' + \nu(\nu+1)\,\theta^2 T = 0. \tag{200}$$

Neglecting the θ^3 term, the solution of (200) can be expressed as

$$T(\theta) = C_1 \theta H_1^{(1)}\left(\sqrt{\nu(\nu+1)}\,\theta\right), \tag{201}$$

where $H_1^{(1)}(x)$ is the Hankel function of the first kind of order one. For $\theta \ll 1$, the neglected θ^3 term can be expected to produce a minor perturbation, and approximate solutions of (201) may be expected to have the form

$$T(\theta) = C_1(\theta + b\theta^n)\,H_1^{(1)}\left(\sqrt{\nu(\nu+1)}\,\theta\right). \tag{202}$$

Substitution of (202) shows that the differential equation (200) is satisfied including terms proportional to θ^4 if $n = 3$ and $b = -1/12$. Other choices of n can be shown to produce larger residual errors. Applying (12), it follows that

$$\frac{\partial}{\partial\theta} P_\nu(-\cos\theta) \approx \frac{T(\theta)}{\sin\theta} = C_1(1+\theta^2/12)\,H_1^{(1)}[(\nu+0.5)\theta], \tag{203}$$

where $\sin\theta$ has been replaced by a two-term expansion. It may be seen that $C_1 = i(\nu+0.5)$ $\sin\nu\pi$ makes the approximation (203) consistent with (30) and also with (44) if it is noted that $(\theta/\sin\theta)^{0.5} \approx 1+\theta^2/12$. Integration of (203) leads to

$$P_\nu(-\cos\theta) \approx -i\sin\nu\pi\left\{H_0^{(1)}[(\nu+0.5)\,\theta] - \frac{\theta^2}{12}\,H_2^{(1)}[(\nu+0.5)\,\theta]\right\}. \tag{204}$$

A similar equation has been listed also by Wait [1962], but in a misprinted form.

The approximations (203) and (204) can be substituted in the field expressions of the various dipole sources. Subsequent examples will consider the fields excited by vertical electric and horizontal electric dipoles.

4.6.1 Vertical Electric Dipole

The field expressions (41), (18), and (16) can be rewritten as

$$E_r^{ve} = \frac{\sqrt{\mu_0/\varepsilon_0}\,I\,ds}{hD}\,\frac{k_0 a}{2i}\sum_n S_n^2 \Lambda_n G_n(z)\,G_n(z_s)\,F_{0n}, \tag{205}$$

$$E_\theta^{ve} = \frac{\sqrt{\mu_0/\varepsilon_0}\,I\,ds}{hD}\,\frac{1}{\pi}\sum_n \Lambda_n(z)\,\Lambda_n G_n(z)\,G_n(z_s)\,F_{1n}, \tag{206}$$

$$H_\varphi^{ve} = \frac{I\,ds}{hD}\,\frac{1}{\pi}\sum_n \Lambda_n G_n(z)\,G_n(z_s)\,F_{1n}, \tag{207}$$

where the excitation factor Λ_n, height-gain functions $G_n(z)$, and the impedances $\Delta_n(z)$ are defined by (92) to (96). The functions

$$F_{0n} = \frac{\theta}{\sin\nu\pi} P_\nu(-\cos\theta) \tag{208}$$

and

$$F_{1n} = \frac{\theta\pi}{2\sin\nu\pi}\,\frac{\partial}{\partial\theta} P_\nu(-\cos\theta) \tag{209}$$

are computed from (204) and (203). It is seen from (30) that $F_{0n} \to 0$ and $F_{1n} \to 1$ in the limit of $\theta \to 0$. Using the earth-flattening or thin-shell approximations of Section 3, the propagation parameter

$$S_n = \frac{r_m}{a}\sqrt{1-(K_n/k_0)^2}$$

is computed from (83). For $n = 0$, S is given by (87). In the E.L.F. range, S_n of the higher-order cutoff modes ($n \neq 0$) is computed using (88).

A large number of terms are required in the summations (205) to (207) in order to reproduce the field singularity that is observed near the source. An alternate field representation can be derived using the method of images for a waveguide of perfectly conducting walls and of zero curvature ($a \to \infty$). For a vertical electric dipole on a perfectly conducting ground plane, the fields are twice the free-space fields. The presence of a second conducting plane at a height h above the ground plane is accounted for by a series of in-phase images at heights $\pm 2qh$, where $q = 1, 2, \ldots$, and where each image has twice the dipole moment of the original source. The total field in the space between the two conducting planes is simply the sum of the free-space source and image fields. Starting out with the free-space fields of a single electric dipole (Stratton, 1941, section 8.5), the field components E_r^{ve} and H_φ^{ve} are computed as

$$\left.\begin{aligned} E_r^{ve} = \frac{\sqrt{\mu_0/\varepsilon_0}I\,ds}{hD}\,\frac{ik_0 h}{2\pi}\sum_{q=-\infty}^{\infty}\Bigg\{&\left[1+\frac{i}{k_0 r_q}-\frac{1}{(k_0 r_q)^2}\right] \\ &-\left(\frac{z+2qh}{r_q}\right)^2\left[1+\frac{3i}{k_0 r_q}-\frac{3}{(k_0 r_q)^2}\right]\Bigg\}\frac{D}{r_q}\exp(ik_0 r_q), \end{aligned}\right\} \tag{210}$$

$$H_\varphi^{ve} = -\frac{I\,ds}{hD}\,\frac{ik_0 h}{2\pi}\sum_{q=-\infty}^{\infty}\left[1+\frac{i}{k_0 r_q}\right]\left(\frac{D}{r_q}\right)^2\exp(ik_0 r_q), \tag{211}$$

where $r_q = \sqrt{D^2+(z+2qh)^2}$ and where z is the height of the observation point above the ground

plane ($0 \ll z \ll h$). Similar equations are also listed in section 10.6 of Wait [1962]. In the immediate vicinity of the dipole (D, $z \ll h$), the $q = 0$ terms of the summations will predominate; the fields are nearly the same as for a dipole on a conducting plane, and the upper conducting boundary has small effects in this distance range.

The method of images can be also applied to a planar waveguide with a perfectly conducting lower boundary but with a perfectly reflecting (or magnetically conducting) upper boundary. In this geometry, each term of q summations of (210) and (211) should be multiplied by $(-1)^q$.

For a sharply bounded homogeneous and isotropic ionosphere and a perfectly conducting flat ground plane, the vertical electric fields of a ground-based ($z_s = 0$) dipole observed at a distance D and $z = 0$ are given by the ray theory or the geometric optic series [Bremmer, 1949; Wait and Murphy, 1957; Volland, 1961] as

$$E_r = \frac{\sqrt{\mu_0/\varepsilon_0}I\,ds}{hD}\,\frac{ik_0h}{2\pi}\left\{\exp(ik_0D)+2\sum_{q=1}^{\infty}\sin^3\theta_q\,[R_i(\theta_q)]^q\exp(ik_0r_q)\right\}, \tag{212}$$

where

$$R_i(\theta_q) = \frac{n^2\cos\theta_q-\sqrt{n^2-\sin^2\theta_q}}{n^2\cos\theta_q+\sqrt{n^2-\sin^2\theta_q}}, \tag{213}$$

$\sin\theta_q = D/r_q$, $r_q = \sqrt{D^2+(2qh)^2}$, $n = \sqrt{\mu_0/\varepsilon_0}/Z_e$, and Z_e is the surface impedance of the ionosphere for T.M. fields. The individual terms of (212) can be interpreted as a ground wave and sky waves that have been reflected q times from the ionospheric boundary. The field expression (212) becomes identical to (210) in the limit of $z = 0$, $k_0r_q \gg 1$, and $Z_e = 0$ or $R_i = 1$.

The method of images [equations (210) and (211)] and the series of zonal harmonics [equations (261), (275), and (283)] are used for the field calculations shown in Fig. 4.15 for various distances $D = a\theta$. The ionosphere model is sharply bounded of conductivity $\sigma_i = 10^{-5}$ mho/m, height $h = 85$ km, and the frequency $f = 100$ c/s. The amplitude plots are dimensionless and proportional to (DE_r). The ($1/D$) distance variation of the free-space far fields is divided out from the amplitude plot, and this normalization helps also to compress the vertical scale of the plot. The representation (283) of the series of zonal harmonics can be used for any of the distances shown if $z = 0$. However, the integral approximation (277) of the summation (275) is satisfactory for $z = 0$ only if $N_s\theta > 15$–20. Most of the curves are plotted using $N_s = 500 = 37.5k_0a$ terms in the summations; for a smaller number of terms ($N_s = 200 = 15k_0a$), the dotted curves differ from the more accurate calculations near the amplitude minimum at $D \approx 150$ km, and a further decrease of N_s to $100 = 7.5k_0a$ (not shown in Fig. 4.15) introduces a 30–40° phase error in the distance range from $D = 100$–600 km. The series of zonal harmonics agrees very closely in the near-field range with the series of images except for a small amplitude difference near the amplitude minimum. For fields at the ionospheric boundary ($z = h$), the terms of the summation (261) become negligible in magnitude for $nh \gg a$; and the integral approximation of the summation (275) provides a close agreement with the method of images, particularly for the smaller values of the distance D.

Figure 4.16 illustrates the near fields in the mode series representation (205) to (207). The ionosphere and the earth are assumed to be isotropic and homogeneous with conductivities

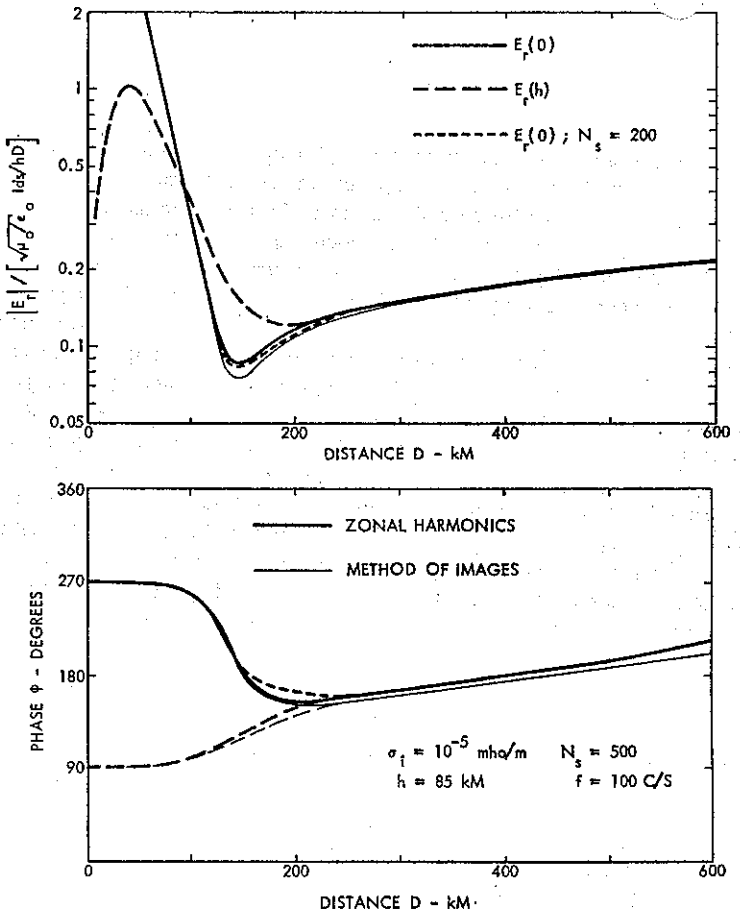

FIG. 4.15 E.L.F. Near Fields of a Vertical Electric Dipole. Series of Zonal Harmonics

$\sigma_i = 10^{-5}$ mho/m and $\sigma_g = 10^{-3}$ mho/m respectively. For small values of the distance $D = a\theta$, the plots indicate that $DE_r(0) \sim D^{-2}$, $DE_\theta(0) \sim D^{-1}$, $DH_\varphi(0) \sim D^{-1}$, which correspond to the field variations of a vertical electric dipole on a finitely conducting ground plane [equations (57), (70), and (117) of Norton, 1937]. $DE_r(0)$ exhibits a minimum between $D = 100$–200 km, and it increases gradually for larger distances. For $D = 1000$ km, the method of images for a flat perfectly conducting waveguide gives higher field intensities at the higher frequencies, where attenuation of the waveguide modes becomes noticeable in the imperfectly conducting spherical shell. At the ionospheric boundary $z = h$, $DE_r(h) \sim D$, $DE_\theta(h) \sim D^2$, and $DH_\varphi(h) \sim D^2$; it is apparent that $E_\theta(h)$ and $H_\varphi(h) \to 0$ as $D \to 0$. The E_r and H_φ field components exhibit the same values at the two boundaries for distances $D > 200$–300 km, but the E_θ components are proportional to $\sigma_j^{-0.5}$ at the boundaries $j = g$ or i

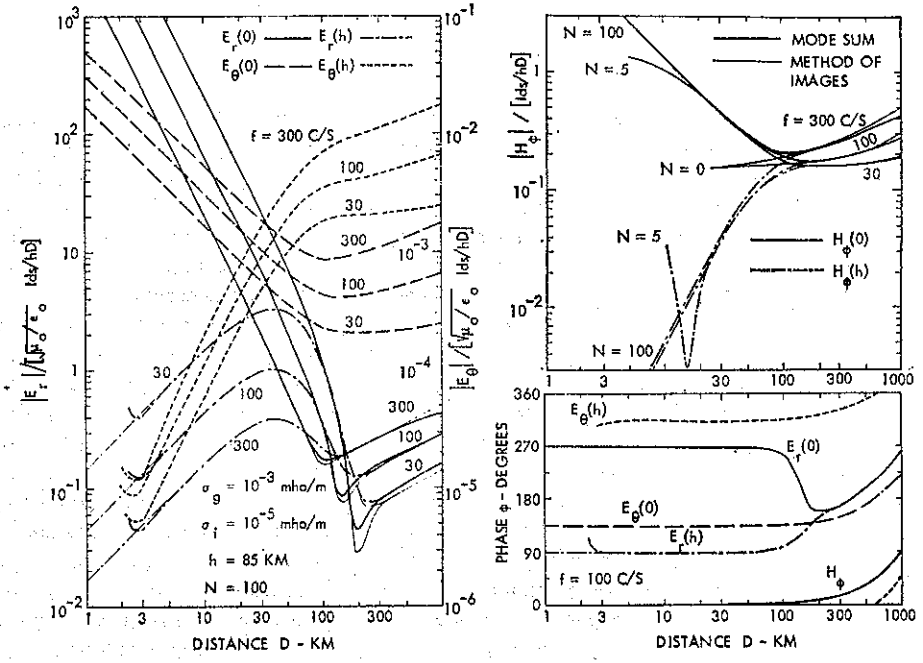

FIG. 4.16 Near Fields of a Vertical Electric Dipole

and are out of phase at these two boundaries for larger distances. A change of σ_i will modify E_θ components, but E_r and H_φ will remain in the near-field range essentially the same as for perfectly conducting boundaries.

The field components are calculated using a maximum number of $N = 100$ terms in the summations of (205) to (207). For fields at the ionospheric boundary ($z = h$), this number of terms is adequate for $D > 5$ km; the mode summation differs from the results obtained using the method of images for $D < 4$ km, which can be seen by examining the $E_r(h)$ curves of Fig. 4.16. Only a smaller number of terms N is necessary for larger distances D. The calculations of the H_φ components show that $N = 5$ is adequate for distances $D > 30$ km, and only the leading term of the mode sum ($N = n = 0$) is required for distances larger than 200 km.

The V.L.F. near fields are illustrated in Fig. 4.17 for the same ionosphere model that is used in the E.L.F. calculations of Fig. 4.16. The exponential approximation of the radial functions is indicated by dashed lines. The exponential approximation is inaccurate for the $n = 1$ and 2 modes at $f = 20$ kc/s following Figs. 4.4 and 4.6. The solid curves represent the fields of a curved waveguide and are obtained by substituting the Airy function approximation for the parameters of $n = 1$ and 2 modes. For fields at the ground surface ($z = 0$), the exponential approximation appears satisfactory for $D < 200$ km; but significant differences between the exponential approximation and the curved waveguide solutions are observed for $D > 350$ km. However, for fields at the ionospheric boundary ($z = h$), the difference between these two mode summations is less significant.

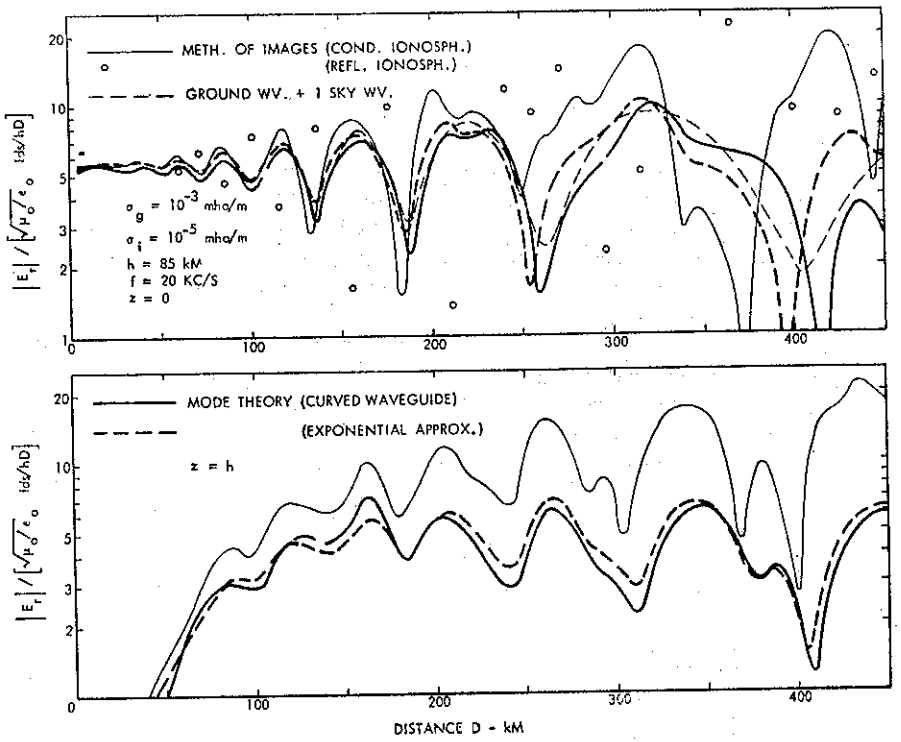

FIG. 4.17 V.L.F. Near-field Comparisons

The method of images for a perfectly conducting ground and ionospheric surface, indicate by thin solid lines in Fig. 4.17 is adequate for representing the field variations only for $D < 10$ km. For $z = h$, the agreement between mode theory and the method of images is less satis factory. For a perfectly reflecting ionosphere, the method of images results in the field-strengt values shown by circles in Fig. 4.17 for $z = 0$. The circles indicate minima and maxima tha occur near the maxima and minima of the other calculations. For a perfectly reflecting ionc sphere, the method of images results in $E_r(h) = 0$, which is obviously incorrect. Although i long distance V.L.F. propagation, the dominant modes are similar as in computations for perfectly reflecting ionosphere, such an approximation is not suited for near-field calculatior when the method of images gives more satisfactory results by assuming perfectly conductir boundaries.

Analytically simplest is the ray theory for a perfectly conducting flat ground and a finite conducting ionosphere when the ground wave and a single sky wave [$q = 1$ term of (212 approximate quite closely the mode representations of the near fields in Fig. 4.17. The simplified equations of the ray theory do not reproduce the deep minima that are observed i mode calculations. However, the ray theory can be readily extended to consider the fini ground conductivity, the ionospheric stratifications and anisotropy, and earth-curvatu

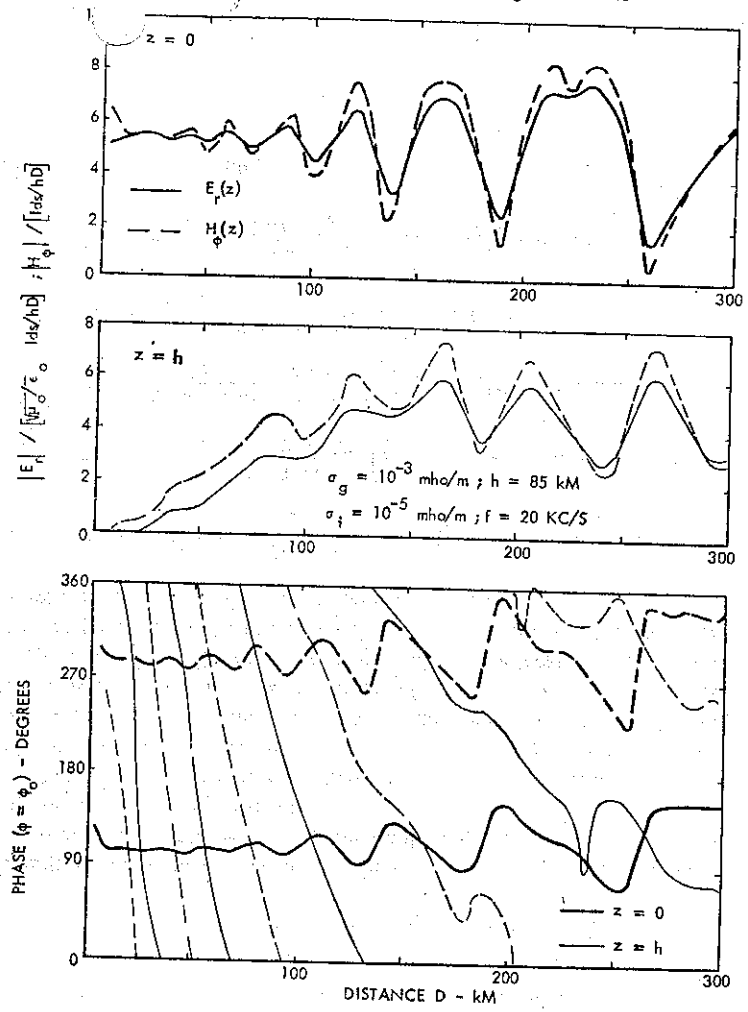

FIG. 4.18 V.L.F. Near Fields of a Vertical Electric Dipole. Mode Theory for a Curved Waveguide. $\varphi_0 = \arg [\exp (ik_0 D)]$

effects. The addition of a ground wave and single sky wave is quite satisfactory for explaining a number of near-field measurements [Weekes, 1950; Bain and May, 1967].

The distance dependence of E_r and H_φ field components is illustrated in Fig. 4.18 using the mode theory of curved waveguides, where Airy function solutions are used for the $n = 1$ and 2 terms of the summations (205) and (207). In the normalization used in Fig. 4.18, the $|E_r|$ and $|H_\varphi|$ curves should coincide if the ratio $|E_r/H_\varphi|$ is equal to the free-space impedance of $\sqrt{\mu_0/\varepsilon_0} = 120\pi$ ohms. The plots indicate that this ratio differs from the free-space impedance near

the minima and maxima of the E_r curves. The difference between the normalized E_r and H_φ curves is larger for $z = h$ and $D < 100$ km. The phase variations of the free-space wave $\varphi_0 = \exp(ik_0 D)$ have been subtracted from the phase plots of Fig. 4.18. The phase velocity of free-space electromagnetic waves would appear as a horizontal line in the phase plots. The phase velocity of the waves is nearly equal to that of free-space waves for distances $D = 100$ km and less if $z = 0$. At larger distances, the phase changes become rapid near the minima of amplitude plots. For $z = h$, the slope of the $(\varphi - \varphi_0)$ curves becomes increasingly negative for decreasing distances D. For D small, most of the indicated phase change arises from φ_0 and φ is nearly constant because the ionospheric boundary is tangential to the equiphase surface at $\theta = 0$. The propagating waveguide modes with $v_{ph} \approx c$ could possibly account for the average of the phase curves indicated at $z = 0$, but not for the slanted phase curves for $z = h$, which can be explained only by invoking higher order modes. At a distance where only a few of the waveguide modes propagate, the average of the $(\varphi - \varphi_0)$ curves should be essentially horizontal for $z = 0$ and h. Higher-order modes are obviously present over the whole distance range shown in Fig. 4.18.

In the E.L.F. range, the series of zonal harmonics provides nearly the same near fields as the method of images in Fig. 4.15, and the method of images compares closely with the mode summations in Fig. 4.16. The difference between the mode summation and the series of zonal harmonics is small, and the contribution of branchcut or lateral waves may be neglected following the argument that has been summarized in the introductory part of Section 4.6. In the V.L.F. range, the number of terms N_s in the series of zonal harmonics is further increased, and $N_s > 3000 = 2.25k_0 a$ terms are necessary for obtaining an agreement between the mode summation and the series of zonal harmonics for $f = 10$ kc/s. The exponential functions used in the mode summation have a restricted validity in the curved waveguide for V.L.F.; and the series of zonal harmonics, which also uses exponential functions for the radial field variations, may become similarly inaccurate at these frequencies. The number of terms N_s required for obtaining a convergence of the series becomes very large, and its has not been attempted to develop expressions for the coefficients a_n and b_n of (261) that would be of better accuracy in the V.L.F. range.

4.6.2 *Horizontal Electric Dipole*

The field expressions (55) and (63) to (66) are rewritten as

$$E_r^{he} = -\frac{\sqrt{\mu_0/\varepsilon_0}\, I\, ds}{hD} \frac{\cos\varphi}{\pi} \sum_n H_n S_n^2 F_{1n}, \tag{214}$$

$$E_\theta^{he} = \frac{\sqrt{\mu_0/\varepsilon_0}\, I\, ds}{hD} \frac{i\cos\varphi}{\pi k_0 D} \left[\sum_n H_n \Delta_n(z) F_{2n} + \frac{\theta}{\sin\theta} \sum_m H_m F_{1m} \right], \tag{215}$$

$$E_\varphi^{he} = \frac{\sqrt{\mu_0/\varepsilon_0}\, I\, ds}{hD} \frac{i\sin\varphi}{\pi k_0 D} \left[\frac{\theta}{\sin\theta} \sum_n H_n \Delta_n(z) F_{1n} + \sum_m H_m F_{2m} \right], \tag{216}$$

$$H_\theta^{he} = -\frac{I\, ds}{hD} \frac{i\sin\varphi}{\pi k_0 D} \left[\frac{\theta}{\sin\theta} \sum_n H_n F_{1n} + \sum_m H_m F_{2m}/\Delta_m(z) \right], \tag{217}$$

$$H_\varphi^{he} = \frac{I\, ds}{hD} \frac{i\cos\varphi}{\pi k_0 D} \left[\sum_n H_n F_{2n} + \frac{\theta}{\sin\theta} \sum_m H_m F_{1m}/\Delta_m(z) \right], \tag{218}$$

where F_{0n} and F_{2n} are defined by (208) and (209),

$$F_{2n} = -\frac{\theta^2\pi}{2\sin\nu\pi}\frac{\partial^2}{\partial\theta^2}P_\nu(-\cos\theta), \tag{219}$$

$$H_n = \Delta_n(z_s)\,S_n^{-2}\Delta_n G_n(z_s)\,G_n(z), \tag{220}$$

$$H_m = S_m^{-2}\Delta_m G_m(z_s)\,G_m(z). \tag{221}$$

F_{jm} is computed from the F_{jn} expressions (208), (209), or (219) by using the ν or S values appropriate to the quasi-T.E. (m) modes. The excitation factors Δ_q, height-gain functions $G_q(z)$, and the impedances $\Delta_q(z)$ (where $q = n$ or m) are defined by (92) to (96) and (98) to (100). For the quasi-T.M. modes, the propagation parameter S_n of (210) is computed from (87) or (88). For the quasi-T.E. modes, the m summation does not include the $m = 0$ mode which is not excited. For the lower-order cutoff modes ($m \neq 0$), K_m is of the same order of magnitude or less than $|k_0/\Delta_q|$ (with $q = g$ or h); K_m is determined from a numerical solution of (89), where the initial estimates of K_m are based on (90) with small values of Δ_h and Δ_g. For larger values of m, where $K_m \approx (m\pi/h) \gg |k_0/\Delta_q|$, this numerical solution is approximated by

$$K_m \approx (m-1)\frac{\pi}{h} - \frac{ik_0}{(m-1)\pi}\left(\frac{1}{\Delta_g}+\frac{1}{\Delta_h}\right). \tag{222}$$

Substituting the above inequality in (89), the right-hand side of (222) characterizes the mode K_{m-1}. This apparent discrepancy in mode numbering is caused by the presence of modes not satisfying the inequality for m small.

The method of images provided an alternate near-field representation for a vertical electric dipole in Section 4.6.1. It was shown that in the immediate vicinity of the source, the fields are not affected by the presence of the reflecting upper boundary of the waveguide. Also, the near fields of a horizontal electric dipole (D, $z \ll h$) located in the waveguide at $z_s = 0$ can be expected to be similar to the near fields of a dipole located on a flat finitely conducting ground plane [Wait, 1961; Baños, 1966]. For $z = z_s = 0$ and $D \ll h$, the expressions (214) to (218) should exhibit the simple distance dependence of the equations

$$E_r^{he} \approx \frac{\sqrt{\mu_0/\epsilon_0}I\,ds}{hD}\,\frac{h\cos\varphi}{2\pi D}\,\frac{k_0}{k_g}\,[1-ik_0D]\exp(ik_0D), \tag{223}$$

$$E_\theta^{he} \approx \frac{\sqrt{\mu_0/\epsilon_0}I\,ds}{hD}\,\frac{hi\cos\varphi}{2\pi k_0D^2}\left(\frac{k_0}{k_g}\right)^2[1-ik_0D-(k_0D)^2]\exp(ik_0D), \tag{224}$$

$$E_\varphi^{he} \approx \frac{\sqrt{\mu_0/\epsilon_0}I\,ds}{hD}\,\frac{hi\sin\varphi}{\pi k_0D^2}\left(\frac{k_0}{k_g}\right)^2[1-ik_0D]\exp(ik_0D), \tag{225}$$

$$H_\theta^{he} \approx \frac{I\,ds}{hD}\,\frac{hi\sin\varphi}{\pi k_0D^2}\,\frac{k_0}{k_g}\,[1-ik_0D]\exp(ik_0D), \tag{226}$$

$$H_\varphi^{he} \approx -\frac{I\,ds}{hD}\,\frac{hi\cos\varphi}{2\pi k_0D^2}\,\frac{k_0}{k_g}\,[1-ik_0D-(k_0D)^2]\exp(ik_0D), \tag{227}$$

where $k_0/k_g = \Delta_g \approx \sqrt{\omega\epsilon_0/(i\sigma_g)}$.

These field expressions may be compared with the fields of a dipole in a homogeneous lossy medium. The axial electric field E_r^{ve} of a dipole is obtained by replacing $\sqrt{\mu_0/\epsilon_0}$ with $\sqrt{\omega\mu_0/i\sigma_g}$, k_0 with $\sqrt{i\omega\mu_0\sigma_g}$ in the $q = 0$ term of (210), and by letting $D = 0$. For a homogeneous space, the factor $\left(\frac{1}{2}\right)$ of (210) is replaced by $\left(\frac{1}{4}\right)$; it follows that $E_r^{ve} \approx I\,ds/(2\pi\sigma_g z^3)$, where z is the axial distance from the dipole. In the $\varphi = 0$ plane, the axial electric field of the horizontal electric dipole is computed from (224) as $E_\theta^{he} \approx I\,ds/(2\pi\sigma_g D^3)$, which is identical to the axial near fields of a dipole in a homogeneous lossy medium. Similarly, computed parallel electric field components $E_r^{ve}(z = 0)$ and $-E_\varphi^{he}(\varphi = 90°)$ differ by a factor of 4. The above near-field components of a dipole in a homogeneous medium exhibit distance variations that are functionally similar to the near-field variations of a dipole on a conducting plane. The derivation of (210) and (211) is straightforward, but the derivations of (223) to (227) are analytically rather involved. However, the above comparison indicates that there are no apparent phase or sign inconsistencies between these two sets of equations.

Figure 4.19 illustrates the waveguide fields of a horizontal electric dipole, and it provides a further comparison with the fields of a dipole on a flat finitely conducting ground plane. The plots refer to the directions φ where the field components exhibit maximum amplitudes ($\cos\varphi = 1$ in the plots of E_r^{he}, E_θ^{he}, H_φ^{he}; $\sin\varphi = 1$ in the plots of E_φ^{he}, H_θ^{he}). For small values of $D = a\theta$, $DE_r^{he}(0) \sim D^{-1}$, while the plots of all the other field components are proportional to D^{-2}. The summations over $N = 100$ T.M. modes and $M = 100$ T.E. modes appear to be

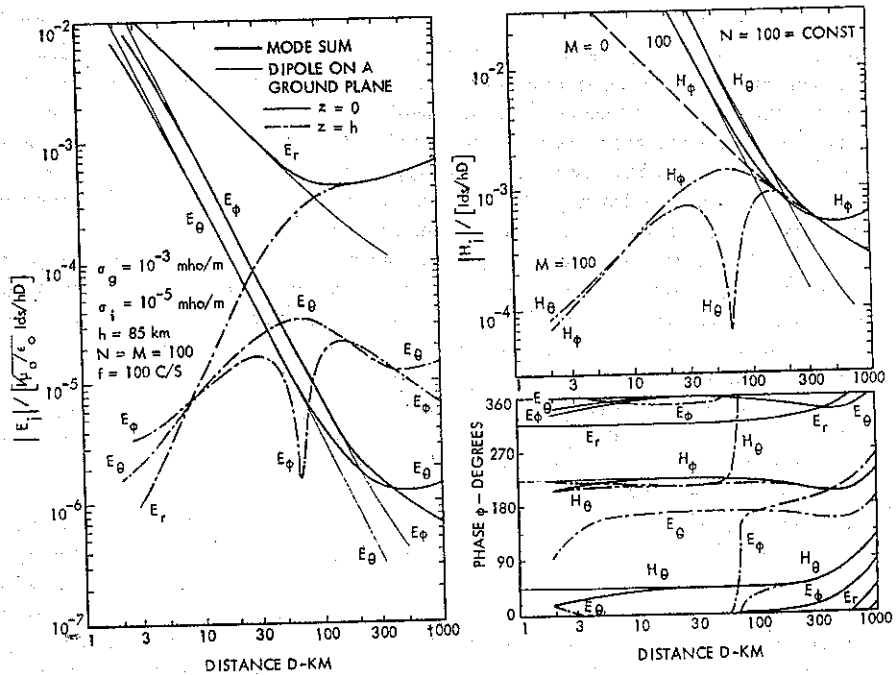

FIG. 4.19 Near Fields of a Horizontal Electric Dipole

adequate for distances $D > 5$ km; the mode sum representation of $E_\theta^{he}(0)$ and $E_\varphi^{he}(0)$ field components deviates from the field representations (224) to (225) for smaller values of D, which can be noted in both the magnitude and phase plots of the field components. At larger distances, the dipole fields on a conducting ground plane are much weaker than the waveguide fields, which have an approximately $D^{-0.5}$ distance dependence. At the ionospheric boundary, $DE_r^{he}(h) \sim D^2$ for small distances $D = a\theta$, while the plots of the other field components are approximately proportional to D. For distances D exceeding 200–300 km, the field components E_r^{he}, H_θ^{he}, H_φ^{he} have the same values at both waveguides boundaries; but the E_θ^{he} and E_φ^{he} components are proportional to $\sigma_j^{-0.5}$ for the boundaries $j = g$ or i and are out of phase at these two boundaries for large distances.

The significance of T.E. modes is illustrated by the dashed curve for the H_φ^{he} component which is computed for $z = 0$ and h using $N = 100$ T.M. modes, but $M = 0$ T.E. modes. For small values of D, this curve differs from the computations which consider $M = 100$ T.E. modes, and it differs also from the dipole fields on flat ground plane. The nonpropagating T.E. modes appear to be as significant as the nonpropagating T.M. modes for establishing the near-field characteristics of a horizontal dipole.

4.7 Fields Near the Antipode

The wave front which emanates from the source is divergent in the spherical shell for $\theta < \pi/2$, but it starts to converge (or focus) for $\theta > \pi/2$. The contraction of the circular wave front tends to increase the density of the power flow, and there may be a range of angles $\theta \to \pi$ where the amplitude of the field is increasing with increasing distance from the source.

The earlier approximations of the Legendre functions (30), (44), or (204) are not valid in this distance range. However, near the antipode [$\delta = (\pi - \theta) \to 0$], the Legendre functions can be expressed using Bessel functions and ascending powers of sin ($\delta/2$). Equation (3.5.10) of Erdélyi [1953] shows that

$$P_\nu(-\cos\theta) = J_0(y) + \sin^2(\delta/2)\left[\frac{J_1(y)}{2y} - J_2(y) + \frac{y}{6}J_3(y)\right] + \ldots, \tag{228}$$

where $\delta = \pi - \theta$, $y = 2(\nu+0.5)\sin(\delta/2)$, and $J_n(y)$ is the Bessel function of the first kind of order n. Expanding $J_0(y)$ in a Taylor series and applying the recurrence relation

$$J_{n+1}(y) = \frac{2n}{y}J_n(y) - J_{n-1}(y), \tag{229}$$

equation (228) can be rearranged into

$$P_\nu(-\cos\theta) \approx \left(1 + \frac{\delta^2}{12}\right)J_0(x) - \frac{\delta}{24(\nu+0.5)}J_1(x), \tag{230}$$

where $x = (\nu+0.5)\delta$. The leading term of the $P_\nu(-\cos\theta)$ expression is proportional to $J_0(x)$; the asymptotic expansion (43) can be verified by substituting the asymptotic form of the Bessel function $J_0(x)$ in (230). For $x \ll 1$, (230) becomes

$$P_\nu(-\cos\theta) \approx 1 - \frac{\delta^2}{4}\left[\left(\nu+\frac{1}{2}\right)^2 - \frac{1}{4}\right] + \frac{\delta^4}{64}\left(\nu+\frac{1}{2}\right)^2\left[\left(\nu+\frac{1}{2}\right)^2 - \frac{7}{6}\right] + \ldots. \tag{231}$$

The derivatives of the Legendre functions are computed as

$$\left.\begin{aligned}\frac{\partial}{\partial\theta}P_\nu(-\cos\theta) &= -\frac{\delta}{8}J_0(x) + (\nu+0.5)(1+\delta^2/12)J_1(x)\\ &\approx \frac{\delta}{2}\left[(\nu+0.5)^2 - \frac{1}{4}\right] - \frac{\delta^3}{16}(\nu+0.5)^2\left[(\nu+0.5)^2 - \frac{7}{6}\right] + \ldots\end{aligned}\right\} \tag{232}$$

and

$$\left.\begin{aligned}\frac{\partial^2}{\partial\theta^2}P_\nu(-\cos\theta) &= -\left[(\nu+0.5)^2(1+\delta^2/12) - \frac{1}{8}\right]J_0(x) + \frac{\nu+0.5}{\delta}J_1(x)(1-\delta^2/24) + \ldots\\ &\approx -\frac{1}{2}\left[(\nu+0.5)^2 - \frac{1}{4}\right] + \frac{3\delta^2}{16}(\nu+0.5)^2\left[(\nu+0.5)^2 - \frac{7}{6}\right] + \ldots.\end{aligned}\right\} \tag{233}$$

It is seen that $P_\nu(-\cos\theta)$ of (231) and the second derivative (233) remain finite as $\delta \to 0$, but the first derivative (232) vanishes proportionally to δ.

The fields near the antipode of the source can be computed from (205) to (207) or (214) to (218) after substituting (230) to (233) in the F_{jn} expressions of (208), (209), and (219). The factors sin $\nu\pi$ become large in magnitude in the denominators of F_{jn} for the attenuated modes, and only propagating modes of low attenuation contribute to the antipodal fields.

4.7.1 *Vertical Electric Dipole*

For a vertical electric dipole, the radial electric field component E_r^{ve} of (205) is proportional to $F_{0n} \sim P_\nu(-\cos\theta)$, which remains finite near antipode following (231). The field components E_θ^{ve} and H_φ^{ve} of (206) and (207) are proportional to $F_{1n} \sim \partial P_\nu(-\cos\theta)/\partial\theta$, which vanishes proportionally to $\delta = \pi - \theta$ at the antipode. A similar distance dependence was observed also for the near fields at the ionospheric boundary in Fig. 4.16.

This behavior of the field components can be shown to be consistent with the field equations (3) and (4). The radial electric field can be represented as $E_r^{ve} = E_0 + \delta^2 E_2$ near $\delta = 0$. Equation (3) shows that $\partial(\sin\theta H_\varphi^{ve})/\partial\theta = 0$, which implies that $H_\varphi^{ve} \sim \delta^n$ where $n \geq 1$. Also, E_θ^{ve} must be proportional to δ^n following (4). Finite values of E_r^{ve} at the antipode are therefore associated with vanishing E_θ^{ve} and H_φ^{ve} components.

Figures 4.20 and 4.21 illustrate the antipodal fields of a vertical electric dipole. The sharply bounded homogeneous ionosphere model has the same parameters as in the near-field studies of Figs. 4.16–4.18. In Figs. 4.20 and 4.21 the distance from the antipode $D_a = a(\pi - \theta) = 20{,}000 - D$ (km) is used in the abscissa; but the field components are normalized in the ordinate of the curves with respect to the distance from the source D. The radial electric field component E_r^{ve} is approximately constant in the vicinity of the antipode, while the E_θ^{ve} and H_φ^{ve} components are proportional to the distance from the antipode $D_a = a(\pi - \theta)$. The minima of the E_r^{ve} field components occur at the nulls of the $J_0(x)$ function; the minima of E_θ^{ve} and H_φ^{ve} field components occur at the nulls of the $J_1(x)$ function, where $x = (\nu+0.5)\delta = k_0 S D_a$. The distances between successive minima of the field components are therefore inversely proportional to the free-space wave number k_0 or inversely proportional to the frequency f. The near field plots of Fig. 4.16 indicate that E_r and H_φ field components have the same values at both

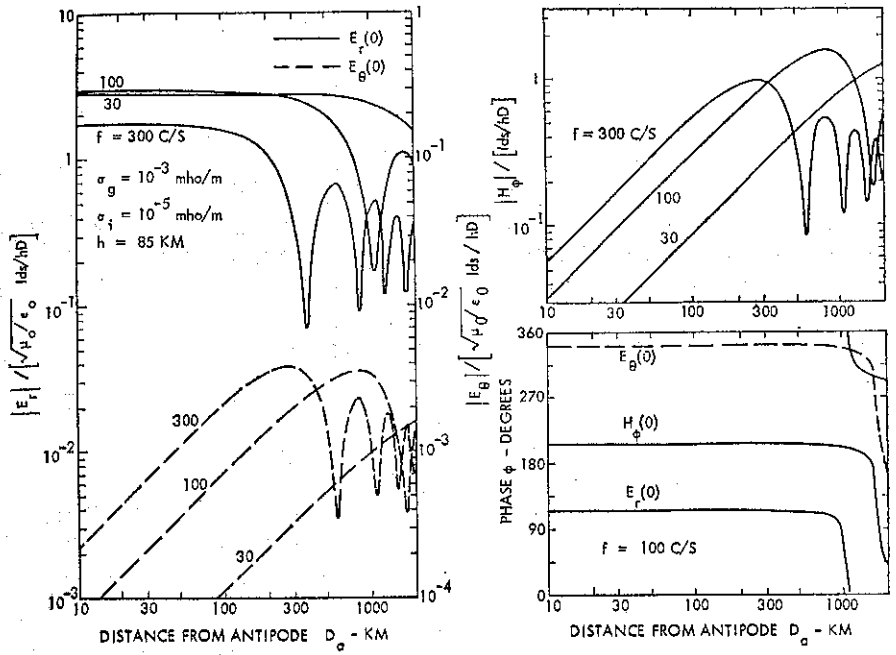

FIG. 4.20 Antipodal E.L.F. Fields of a Vertical Electric Dipole

boundaries for $D > 300$ km; the field component E_θ is proportional to $\sigma_j^{-0.5}$ at the boundaries, where σ_j is the conductivity of the boundary surface and E_θ is out of phase at the two boundaries for $D > 300$ km. The field variations at the ionospheric boundary can be readily extrapolated from the E.L.F. fields indicated for $z = 0$ in Fig. 4.20. A phase change of 180° is observed at the minima of the amplitude plots. The phase-angle variations of the various field components near the antipode are related to the phase angles of the near-field components by the argument of the $\sin \nu\pi$ function. For Re $(S) = 1.06$ and $f = 100$ c/s, this gives a phase shift of approximately 200°. A similar phase shift is obtained by comparing the phase curves of Figs. 4.16 and 4.20.

For the V.L.F. range, the antipodal fields are computed using Airy function approximations for the parameters of the $n = 1$ mode in (205) to (207). Figure 4.21 shows that in the V.L.F. range, the antipodal field variation is similar; but the distance between minima of the amplitude curves is much smaller. The fields at the ionospheric boundary can be computed similarly as for E.L.F., except that all the field components should be multiplied with the height-gain function $G_1(h)$, which can be seen from Fig. 4.10.

The previous calculations have been restricted to an idealized perfectly symmetrical earth-to-ionosphere cavity. The asymmetries of the actual geometry will tend to obscure the deep nulls indicated in Figs. 4.20 and 4.21 although 10–12 db amplitude differences (or scatter) have been reported in some antipodal measurements [Rogerson, 1967].

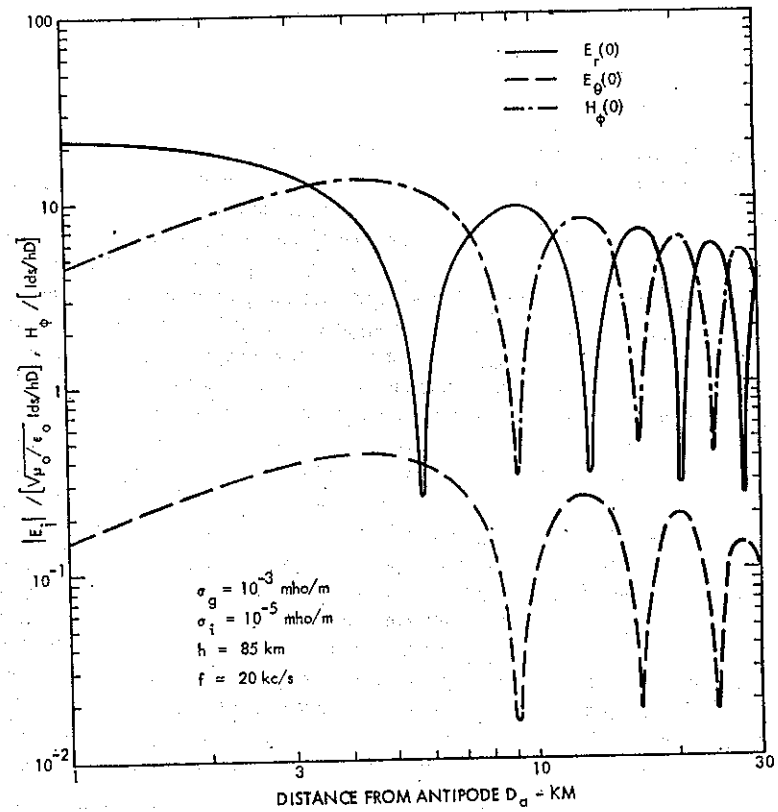

FIG. 4.21 Antipodal V.L.F. Fields of a Vertical Electric Dipole

4.7.2 *Horizontal Electric Dipole*

For a horizontal electric dipole, the radial electric field component E_r^{he} of (214) is proportional to $F_{1n} \sim \partial P_\nu(-\cos\theta)/\partial\theta$, which vanishes proportionally to δ at the antipode. However, the other field components are proportional to $F_{1n}/\sin\theta$ and to $F_{2n} \sim \partial^2 P_\nu(-\cos\theta)/\partial\theta^2$, which remain finite at $\delta = 0$.

This θ-dependence of the field components can be also established from (63) to (68). For the horizontal electric dipole, $E_r^{he} \sim \delta E_1$ and the U and V functions of (67) and (68) exhibit a similar θ-dependence. The field components given by (63) to (66) are proportional to $\partial U/\partial\theta$, $\partial V/\partial\theta$, $U/\sin\theta$ and $V/\sin\theta$, which remain finite for $\delta = \pi - \theta \to 0$.

Substituting the leading terms of the power series approximations (232) and (233) into F_{1n} and F_{2n} of (209), it is seen that $\theta F_{1n}/(\sin\theta F_{2n}) = 1$; the field components computed from (215) to (218) satisfy the relation

$$\frac{E_\theta^{he}}{E_\varphi^{he}} = -\frac{H_\varphi^{he}}{H_\theta^{he}} = \frac{\cos\varphi}{\sin\varphi}. \tag{234}$$

As a consequence, the electric field vector is parallel to the $\varphi = 0$ plane, which intersects the dipole axis in the source centered spherical coordinates; and the magnetic field vector is perpendicular to this plane near the antipode.

The antipodal fields of a horizontal electric dipole are illustrated in Fig. 4.22 for directions of φ, where the field components exhibit maximum magnitude ($\cos\varphi = 1$ in the plots of E_r^{he}, E_z^{he}, H_φ^{he}; $\sin\varphi = 1$ in the plots of E_φ^{he} and H_θ^{he} field components). The horizontal field components (E_θ, E_φ, H_θ, H_φ) are of constant magnitude near the antipode, while the radial electric field component E_r^{he} increases linearly with the distance from the antipode $D_a = a(\pi-\theta)$. The minima of the E_r^{he}, E_φ^{he}, and H_θ^{he} field components occur at the nulls of the $J_0(x)$ function while the minima of the E_θ^{he}, H_φ^{he} occur at the nulls of the function $J_1(x)-xJ_0(x)$, where $x = (\nu+0.5)\delta = k_0 S D_a$. The phase angle of the various field components at the antipode is related to the phase angle of the near-field components by the argument of the sin $\nu\pi$ function, which gives an approximately 200° phase shift between the phase plots of Figs. 4.19 and 4.22.

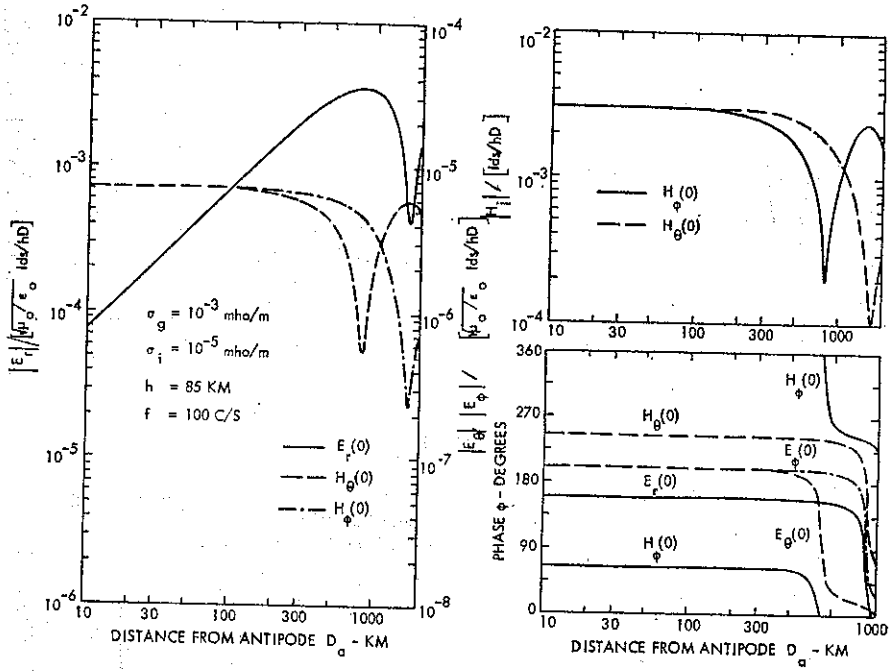

FIG. 4.22 Antipodal E.L.F. Fields of a Horizontal Electric Dipole

4.8 Overall Field Variations

The fields in the vicinity of the source and near its antipode have been discussed in Sections 4.6 and 4.7 respectively. It was shown that the near-field representation of the Legendre functions (204) is changed to the asymptotic form (44) for larger values of θ. Similarly, the

Legendre function representation (228) valid near the antipode where $\delta = (\pi-\theta)$ approaches zero is changed to the asymptotic form (43) as δ is increased. There should be a smooth transition from the near-field form to the asymptotic and antipodal forms provided that θ values exist where (43) is closely approximated by (44). However, discrepancies may arise under conditions when attenuation rates of the fields are so low that the standing-wave pattern observed near the antipode in Figs. 4.20-4.22 is still noticeable in the vicinity of the source.

This overall field variation will be illustrated for frequencies in the E.L.F. range, where for the ionospheric model of $h = 85$ km and $\sigma_i = 10^{-5}$ mho/m used in the calculations of Figs. 4.15-4.22, the attenuation rate $\alpha = 0.8$ db per 1000 km following Fig. 4.3. The ground conductivity is assumed to be $\sigma_g = 10^{-3}$ mho/m in the vicinity of the source. Such a ground conductivity is obviously too low for the intermediate distance range, where the propagating wave must by necessity cross ground surface of higher conductivity and also sea water of conductivity $\sigma_g = 5$ mho/m. However, the attenuation rate α is not affected in the E.L.F. range by ground conductivity to the extent that $\sigma_g \gg \sigma_i$; and only the vertical electric fields and the horizontal magnetic field components will be indicated in the subsequent graphs. The horizontal electric field components are related to the horizontal magnetic field components following (206), (207), and (215) to (218) as

$$\frac{E_\theta^{ve}}{H_\varphi^{ve}} = \frac{E_\theta^{he}}{H_\varphi^{he}} = -\frac{E_\varphi^{he}}{H_\theta^{he}} = \Delta_0(z)\sqrt{\mu_0/\varepsilon_0}, \tag{235}$$

where for $z = 0$, $\Delta_0(0) = -\Delta_g$. The horizontal electric field components tangential to the earth's surface are therefore related to the corresponding magnetic field components by the ground impedance at the particular point of observation.

The field components of a vertical electric and horizontal electric dipole sources are plotted in Figs. 4.23 and 4.24 in the same normalization as in the earlier figures of Sections 4.6 and 4.7. The field components E_r^{ve} and H_φ^{ve} of the vertical electric dipole are rotationally symmetrical; the plots of E_r^{he} and H_φ^{he} refer to the axial $\varphi = 0$ direction, and H_θ^{he} refer to the broadside $\varphi = \pi/2$ direction where the field components of the horizontal electric dipole exhibit their maximum values following (214) to (218). In the vicinity of the source (small values of D) or near the antipode (D approaches 20 Mm), the plotted curves are numerically the same as in Figs. 4.16, 4.19, 4.20, and 4.22. The fields appear to change between adjacent minima and maxima by approximately 10, 6, 2, and 1 db at distances $D = 18$, 15, 10, and 5 Mm; and there are noticeable fluctuations even at smaller distances. The decay rate of the standing waves depends on the attenuation rate α, while the locations of the minima or maxima of the standing-wave pattern depend on the free-space wavelengths λ_0 and on the phase velocity v_{ph} or $\mathrm{Re}\, S = c/v_{ph}$.

In the numerical calculations, $\partial P_\nu/\partial\theta$ of (209) was computed from (102) and $\partial^2 P_\nu/\partial\theta^2$ of (219) from (11) and (102) over the validity range of (43). However, the θ-dependence of the various field components may be estimated by noting that $P_\nu(-\cos\theta)$ and $\partial^2 P_\nu(-\cos\theta)/\partial\theta^2$ are in the first approximation proportional to $\cos\psi$ and that $\partial P_\nu(-\cos\theta)/\partial\theta \sim \sin\psi$, where $\psi = (\nu+0.5)(\pi-\theta) - 0.25\pi$. In this approximation, E_r^{ve} and H_φ^{he} will exhibit local maxima if the distance from the antipode $D_a = a(\pi-\theta) = 0.5\lambda_0(m+0.25)/\mathrm{Re}\, S$ and minima if $D_a = 0.5\lambda_0(m+0.75)/\mathrm{Re}\, S$, where m is an integer and $\lambda_0 = 2\pi/k_0$ is the free-space wavelength. For field components H_φ^{ve}, E_r^{he}, and H_θ^{he}, the conditions for maxima and minima are inter-

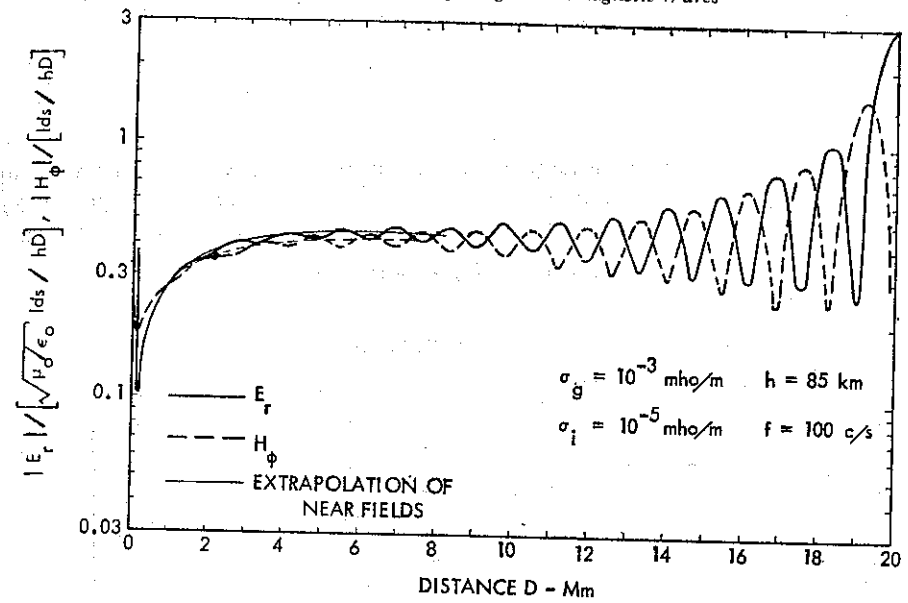

FIG. 4.23 E.L.F. Fields of a Vertical Electric Dipole

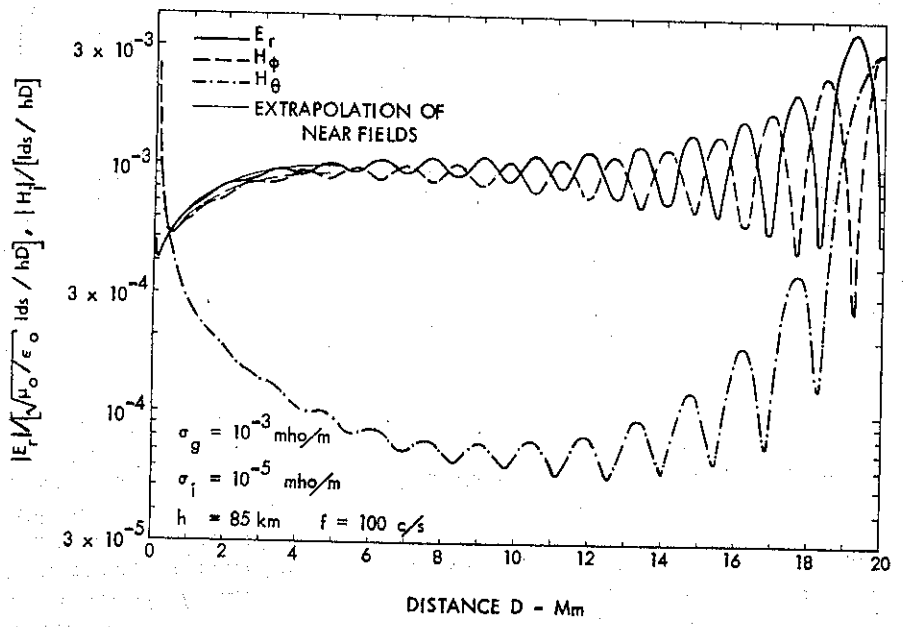

FIG. 4.24 E.L.F. Fields of a Horizontal Electric Dipole

changed. In either case, the distance between two adjacent minima or maxima is $D_m = 0.5\lambda_0/\mathrm{Re}\ S$.

The extrapolated near fields shown by thin lines in Figs. 4.23 and 24 are representative of the asymptotic form (44) of the Legendre function, which can be interpreted as a single wave receding from the source in the θ direction. It cannot account for the standing waves of the asymptotic form (43), which can be decomposed in two waves—one of which recedes from the source and the second of which recedes from the antipode. In the above examples, the asymptotic form (44) provided a smooth transition into the near-field representation (204) at the distance of approximately 1000 km. However, larger differences may be anticipated for frequencies in the Schumann resonance range when the standing waves will decrease at an even slower rate. The attenuation rates, and hence the amplitudes of the standing-wave pattern, are believed to be realistic in Figs. 4.23 and 24. Because of the limitations of the sharply bounded ionosphere model outlined in the discussion of Fig. 4.3, Re S is too low; and the locations of the minima and maxima will be shifted when using more realistic ionosphere models.

4.9 Appendix. Series of Zonal Harmonics and the Watson Transformation

The modal expansions for the various dipoles have been derived in Sections 4.2 to 4.6 by examining the field expressions in the space between the earth and the ionosphere and by determining a discrete set of eigenvalues ν (or wave numbers in the θ direction) which satisfy impedance-type boundary conditions at the ground surface and at the ionosphere. These field expressions involve spherical Bessel functions and Legendre functions of complex orders ν.

Alternately, it is possible to expand the fields in a series of zonal harmonics, which involves spherical Bessel functions of integral orders n and Legendre polynomials. Such field expressions can be readily used for frequencies in the Schumann resonance range, where the circumference of the earth is comparable to a free-space wavelength. These series representations are slowly convergent at higher frequencies, where it is convenient to transform the series of zonal harmonics into a mode sum using the so-called Watson transformation. These series representations and the Watson transformation will be illustrated only for an excitation by a vertical electric dipole. This vertical electric dipole excites transverse magnetic (T.M.) field components which are not coupled to the transverse electric (T.E.) components following Sections 4.2.1 and 4.2.3. Schumann [1952] or Wait [1962] has shown that these T.M. field components can be derived from a Hertz potential which has only a single radial component Π.

4.9.1 *Series of Zonal Harmonics*

Within a spherical shell shown in Fig. 4.1, the field components are given by

$$E_r = -\frac{1}{rr_s}\frac{1}{\sin\theta}\frac{1}{\partial\theta}\left(\sin\theta\frac{\partial\Pi}{\partial\theta}\right) = \left(k_0^2+\frac{\partial^2}{\partial r^2}\right)(r\Pi), \tag{236}$$

$$E_\theta = \frac{1}{rr_s}\frac{\partial^2}{\partial r\,\partial\theta}(r\Pi), \tag{237}$$

$$H_\varphi = -\frac{k_0^2}{i\omega\mu r_s}\frac{\partial\Pi}{\partial\theta}, \tag{238}$$

where the inner radius is $r_g = a$; the outer radius is $r_i = a+h$; $r_s = a+z_s$ is the radius of the source ($r_g \ll r_s \ll r_i$); and where $k_0 = \omega\sqrt{\mu_0\varepsilon_0}$. The primary excitation is given by

$$\Pi_0 = -\frac{I\,ds}{4\pi i\omega_0\varepsilon R}\exp(ik_0R), \tag{239}$$

where R is the distance from the source. This primary excitation can be expressed in terms of spherical wave functions following Bremmer [1949] as

$$\Pi_0 = -\frac{k_0 I\,ds}{\omega\varepsilon\,4\pi}\sum_{n=0}^{\infty}(2n+1)\,P_n(\cos\theta)\quad\begin{cases} j_n(k_0r)\,h_n^{(1)}(k_0r_s) & \text{for}\quad r \ll r_s,\\ h_n^{(1)}(k_0r)\,j_n(k_0r_s) & \text{for}\quad r \gg r_s.\end{cases} \tag{240}$$

The secondary Hertz vector components satisfy the homogeneous wave equation, and they can be expressed as

$$\Pi_s = \sum_{n=0}^{\infty}[A_n h_n^{(1)}(k_0r) + B_n j_n(k_0r)]\,P_n(\cos\theta), \tag{241}$$

where $P_n(\cos\theta)$ is the Legendre polynomial of order n. The spherical Bessel functions are defined as

$$\left.\begin{aligned} j_n(u) &= \sqrt{\frac{\pi}{2u}}\,J_{n+(1/2)}(u),\\ h_n^{(1)}(u) &= \sqrt{\frac{\pi}{2u}}\,H_{n+(1/2)}^{(1)}(u),\end{aligned}\right\} \tag{242}$$

where $J_n(u)$ is the Bessel function and $H_n^{(1)}(u)$ is the Hankel function of the first kind. The net potential

$$\Pi = \Pi_0 + \Pi_s \tag{243}$$

must satisfy the impedance boundary conditions at the earth ($r = a$) and at the lower edge of the ionosphere ($r = r_i$). For $r \ll r_s$, the potential is expressed as

$$\Pi = \sum_n (2n+1)\frac{G_n}{D_n}[j_n(k_0r) + R_{gn}h_n^{(1)}(k_0r)]\,P_n(\cos\theta). \tag{244}$$

For a perfectly conducting ground $E_\theta\big|_{r=a} = 0$ leads to

$$\frac{\partial}{\partial u}(u\Pi) = 0\Big|_{u=k_0a} \tag{245}$$

or to

$$R_{gn} = -\left.\frac{\left[\dfrac{\partial}{\partial u}uj_n(u)\right]}{\dfrac{\partial}{\partial u}[uh_n^{(1)}(u)]}\right|_{u=k_0a}. \tag{246}$$

For $r \gg r_s$, the potential is expressed as

$$\Pi = \sum_n (2n+1)\frac{F_n}{D_n}[h_n^{(1)}(k_0r) + R_{in}j_n(k_0r)]\,P_n(\cos\theta). \tag{247}$$

The impedance boundary condition $E_\theta = Z_e H_\varphi\big|_{r=r_i}$ leads from (237) and [illegible] to

$$\frac{\partial}{\partial u}(u\Pi) = i\,\Delta_e u\Pi\Big|_{u=k_0r_i}, \tag{248}$$

where $\Delta_e = \sqrt{\varepsilon_0/\mu_0}\,Z_e$. For an homogeneous sharply bounded ionosphere

$$\Delta_e = \sqrt{\frac{\varepsilon_0}{\mu_0}}\,Z_e \approx (n_i)^{-1} = \left[1 + \frac{i\sigma_i}{\omega\varepsilon_0}\right]^{-1/2}, \tag{249}$$

where n_i is the refractive index of the ionosphere. Substituting (247) in (248) results in

$$R_{in} = -\left.\frac{\dfrac{\partial}{\partial u}[uh_n^{(1)}(u)] - i\Delta_e uh_n^{(1)}(u)}{\dfrac{\partial}{\partial u}[uj_n(u)] - i\,\Delta_e uj_n(u)}\right|_{u=k_0r_i}. \tag{250}$$

The five equations (240), (241), (243), (244), and (247) contain the unknowns A_n, B_n, G_n/D_n, and F_n/D_n. It follows that

$$F_n = -\frac{k_0 I\,ds}{4\pi\omega\varepsilon_0}[j_n(k_0r_s) + R_{gn}h_n^{(1)}(kr_s)] \tag{251}$$

$$G_n = -\frac{k_0 I\,ds}{4\pi\omega\varepsilon_0}[h_n^{(1)}(k_0r_s) + R_{in}j_n(k_0r_s)], \tag{252}$$

and

$$D_n = 1 - R_{gn}R_{in}, \tag{253}$$

which completes the determination of Π in (244) and (247).

The further considerations are restricted to geometries where the source is located on the ground surface ($r_s = a$ or $z_s = 0$), but the height of the observation point is arbitrary ($r_g \ll r \ll r_i$ or $0 \ll z \ll h$).

Letting

$$U_n(u) = uh_n^{(1)}(u) \tag{254}$$

and

$$V_n(u) = uj_n(u) \tag{255}$$

the Wronskian of the two functions is computed as

$$W[V_n(u), U_n(u)] = V_n(u)\,U_n'(u) - U_n(u)\,V_n'(u) = i. \tag{256}$$

Applying (256), Π of (247) is rewritten as

$$\Pi = -\frac{iI\,ds}{4\pi\omega\varepsilon_0 k_0 ar}\sum_n (2n+1)\frac{a_n}{b_n}P_n(\cos\theta) \tag{257}$$

with

$$a_n = V_n(u)\,U_n'(u_i) - U_n(u)\,V_n'(u_i) + i\,\Delta_e[U_n(u)\,V_n(u_i) - V_n(u)\,U_n(u_i)], \tag{258}$$

$$b_n = V_n'(u_g)\,U_n'(u_i) - U_n'(u_g)\,V_n'(u_i) - i\,\Delta_e[U_n(u_i)\,V_n'(u_g) - V_n(u_i)\,U_n'(u_g)], \tag{259}$$

and $u = k_0r$, $u_g = k_0r_g = k_0a$, and $u_i = k_0r_i = k_0(a+h)$. The radial electric field is computed

from (236) by applying the differential equation of Legendre polynomials

$$\frac{1}{\sin\theta}\frac{\partial}{\partial\theta}\left[\sin\theta\frac{\partial}{\partial\theta}P_n(\cos\theta)\right]+n(n+1)P_n(\cos\theta)=0. \tag{260}$$

It follows that

$$E_r=-\frac{iI\,ds}{4\pi\omega\varepsilon_0 k_0(ar)^2}\sum_n n(n+1)(2n+1)\frac{a_n}{b_n}P_n(\cos\theta). \tag{261}$$

The Legendre polynomials $P_n(x)$ of (257) or (261) can be evaluated using the recurrence relation

$$P_{n+1}(x)=\frac{1}{n+1}[(2n+1)xP_n(x)-nP_{n-1}(x)] \tag{262}$$

for $n \geqslant 1$ and starting with $P_0(x)=1$ and $P_1(x)=x$. The radial functions $U_n(u)$ or $V_n(u)$ are expressed as a sum of terms that involve powers of u and exponential or trigonometric functions [Abramowitz and Stegun, 1964]. After writing down explicit expressions for $U_0(u)$ and $U_1(u)$, the higher-order functions may be computed from the recurrence relations

$$U_{n+1}(u)=\frac{2n+1}{u}U_n(u)-U_{n-1}(u), \tag{263}$$

$$U_n'(u)=U_{n-1}(u)-\frac{n}{u}U_n(u). \tag{264}$$

Equations (263) and (264) apply also to $V_n(u)$ functions.

The formal solution of the problem is given by equations (257) to (261) with the various functions defined by (262) to (264). However, the convergence of the series is very slow, and the series must be rearranged for numerical calculations. These numerical problems can be illustrated using simplified representations of the radial functions $U_n(u)$ and $V_n(u)$. The Taylor series expansions of Section 4.4 are not valid for large values of n, as is pointed out in Section 4.9.1.1; but the convergence problems can be discussed using the exponential approximations of Section 4.3. It is shown in Section 4.9.1.2 that the tail end of the summation can be approximated by an integral. Alternatively, the convergence rate of the series is made more rapid by subtracting from each term of the series an asymptotic value, which the term would approach for n large. The sum of the asymptotic terms is evaluated in closed form and is added to the modified series. This latter approach, which is also discussed in Section 4.9.1.2, has been commonly used in past formulations of this problem [Johler and Berry, 1962].

4.9.1.1 Taylor Series Expansion

The functions $U_n(u)$ and $V_n(u)$ can be expanded in the Taylor series (148). A series representation of the derivatives $U_n'(u)$ and $V_n'(u)$ is obtained by differentiation of (148). The derivatives U_n'' and U_n''' are related to U_n and U_n' by (149) and (150). A corresponding expression for U_n^{IV} is derived by differentiating (150) and by applying (149). The parameters a_n and b_n of (258) and (259) are evaluated as

$$\left.\begin{aligned} a_n &= i[1+0.5\,k_0^2(h-z)^2(N-1)-Nk_0^2(h-z)^3/(6a+3h)] \\ &\quad +\Delta_e k_0(h-z)\,[1+(N-1)\,k_0^2(h-z)^2/6]\approx i, \end{aligned}\right\} \tag{265}$$

$$\left.\begin{aligned} b_n &= -ik_0h\left[(N-1)+N\left(\frac{h}{2a+h}\right)^2+(N-1)^2k_0^2h^2/6\right] \\ &\quad -\Delta_e[1+0.5(N-1)k_0^2h^2+Nk_0^2h^3/(6a+3h)]\approx ik_0h(1-N)-\Delta_e \end{aligned}\right\} \tag{266}$$

with

$$N=\frac{n(n+1)}{k_0^2(a+h/2)^2}. \tag{267}$$

Using only the leading terms of a_n and b_n, E_r of (261) simplifies to

$$E_r=\frac{iI\,ds}{4\pi\omega\varepsilon_0(k_0ar)^2h}\sum_n\frac{n(n+1)(2n+1)P_n(\cos\theta)}{\dfrac{n(n+1)}{k_0^2(a+h/2)^2}-\left(1+\dfrac{i\Delta_e}{k_0h}\right)}. \tag{268}$$

In this approximation, the z variations of E_r are neglected.

A Taylor series expansion will be accurate only if its higher-order terms are smaller in magnitude than its lower-order terms. The expansions (265) and (266) will be valid for $nh \ll a$, and they will become inaccurate for larger values of n. The accuracy of (268) is similarly limited.

4.9.1.2 Exponential Approximation

The functions a_n of (258) and b_n of (259) may be also expressed using the exponential approximation (82). The functions $U_n(u)$ and $V_n(u)$ of (254) and (255) are approximated by

$$U_n(u)\sim\exp(iKr), \tag{269}$$

$$V_n(u)\sim\cos(Kr), \tag{270}$$

with

$$K^2=k_0^2-[n(n+1)/(a+h/2)^2]. \tag{271}$$

Substituting (269) and (270) in (258) and (259),

$$\frac{a_n}{b_n}=\frac{i\cos K(h-z)+(\Delta_e k_0/K)\sin K(h-z)}{(iK/k_0)\sin Kh-\Delta_e\cos Kh}. \tag{272}$$

Using small argument approximations of the trigonometric functions, the leading terms of (272) are seen to agree with (265) and (266) that were obtained from a Taylor series expansion of the radial functions.

For $n \gg k_0a$, the arguments of the sine and cosine functions of (272) become imaginary; and a_n/b_n may be approximated as

$$\frac{a_n}{b_n}\approx-\frac{k_0(a+h/2)}{n+\frac{1}{2}}\exp\left[-\frac{(n+\frac{1}{2})z}{a+h/2}\right]. \tag{273}$$

For $n\theta \gg 1$, the Legendre polynomial is replaced by the asymptotic expansion

$$P_n(\cos\theta)\approx\sqrt{\frac{2}{\pi(n+\frac{1}{2})\sin\theta}}\cos\left[\left(n+\frac{1}{2}\right)\theta-\frac{\pi}{4}\right]. \tag{274}$$

Substituting (273) and (274) in (272), the tail end ($n \gg k_0 a$, $n\theta \gg 1$) of the summation (261) is given by

$$\left.\begin{aligned}\Sigma(N_s) &= \sum_{n=N_s}^{\infty} n(n+1)\,(2n+1)\,\frac{a_n}{b_n} P_n(\cos\theta) \\ &\approx -2k_0\left(a+\frac{h}{2}\right)\sqrt{\frac{2}{\pi \sin\theta}} \sum_{n=N_s}^{\infty}\left(n+\frac{1}{2}\right)^{1.5} \\ &\quad \times \cos\left[\left(n+\frac{1}{2}\right)\theta - \frac{\pi}{4}\right] \exp\left[-\frac{(n+\frac{1}{2})z}{a+h/2}\right].\end{aligned}\right\} \tag{275}$$

The exponential decay of the terms becomes significant only for $n > (a/z)$, and the summation will converge very slowly for small values of z. An estimate of $\Sigma(N)$ can be obtained after approximating the summation over n as an integral of a continuous variable x. A Taylor series expansion of $f(x)$ about $x = n$ shows that

$$f(n) \approx \int_{n-\frac{1}{2}}^{n+\frac{1}{2}} [f(x) - \tfrac{1}{24} f''(x) + \ldots]\, dx = \int_{n-\frac{1}{2}}^{n+\frac{1}{2}} f(x)\, dx - \tfrac{1}{24} f'(x)\Big|_{x=n-\frac{1}{2}}^{n+\frac{1}{2}}. \tag{276}$$

A sum of $f(n)$ is therefore approximated by the integral of the function $f(x)$ and the first derivative $f'(x)$ that is evaluated at the limits of integration. Such an integration gives terms with exponential functions and Fresnel integrals of large arguments. Using the asymptotic forms of Fresnel integrals, (275) becomes

$$\Sigma(N_s) = -2k_0\left(a+\frac{h}{2}\right)\sqrt{\frac{2}{\pi \sin\theta}}\ \mathrm{Re}\,[I(x_1) + D(x_1)], \tag{277}$$

where

$$\left.\begin{aligned}I(x_1) &= \int_{x_1}^{\infty} x^{1.5} \exp(ax)\, dx = \frac{x_1^{1.5}}{\alpha}\left[-1 + \frac{3}{2}(\alpha x_1)^{-1} - \frac{3}{4}(\alpha x_1)^{-2}\right. \\ &\quad \left. - \frac{3}{8}(\alpha x_1)^{-3} - \frac{9}{16}(\alpha x_1)^{-4} - \frac{45}{32}(\alpha x_1)^{-5} + \ldots\right] \exp(\alpha x_1 - i\pi/4)\end{aligned}\right\} \tag{278}$$

and

$$D(x_1) = \frac{\alpha x_1^{1.5}}{24}\left[1 + \frac{3}{2}(\alpha x_1)^{-1}\right] \exp(\alpha x_1 - i\pi/4) \tag{279}$$

with $x_1 = N_s$ and

$$\alpha = i\theta - \frac{z}{(a+h/2)}. \tag{280}$$

The ratio D/I is of the order of $\alpha^2/24$. The derivative term $D(x_1)$ will not make a noticeable contribution for near fields of $\theta \ll 1$.

The n summation of (275) converges very slowly for small values of z, but a different method of evaluating the summation may be used in the limit of $z \to 0$. The n summation can be transformed into a more rapidly converging series by subtracting from each of its terms their asymptotic (large n) value and by subsequently adding the sum of the subtracted parts that

can be expressed in a simple closed form. It follows from p. 53 of Magnus and Oberhettinger [1949] that

$$\sum_{n=0}^{\infty} P_n(\cos\theta) = \frac{1}{\sqrt{2}\sqrt{1-\cos\theta}} = \frac{\frac{1}{2}}{\sin\theta/2}. \tag{281}$$

Applying the differential equation (260), it can be shown that

$$\sum_{n=0}^{\infty} n(n+1)\, P_n(\cos\theta) = -\frac{1 + (\frac{1}{2})\,(\cot\theta/2)^2}{4 \sin\theta/2}. \tag{282}$$

Applying (282), the summation of (261) is rearranged as

$$\left.\begin{aligned}\Sigma(0) &= \sum_{n=0}^{\infty} n(n+1)\,(2n+1)\,\frac{a_n}{b_n} P_n(\cos\theta) \\ &\approx \sum_{n=0}^{N_s} n(n+1)\left[\frac{(2n+1)a_n}{b_n} + 2k_0\left(a+\frac{h}{2}\right)\right] P_n(\cos\theta) \\ &\quad + 2k_0\left(a+\frac{h}{2}\right)\frac{1 + (\frac{1}{2})\,(\cot\theta/2)^2}{4 \sin\theta/2},\end{aligned}\right\} \tag{283}$$

where in the upper limit of the summation ∞ has been replaced by N_s. Substitution of (273) indicates that the expression in the square brackets of (283) approaches zero for $z = 0$ and $n \gg k_0 a$, which justifies the finite limit $N_s \gg k_0 a$ of the summation.

Equations (261), (275), and (283) have been used in the numerical example shown in Fig. 4.15. The discussion of Section 4.6.1 indicates that for $z = 0$, the integral approximation (277) of the summation (275) is satisfactory only if $N_s\theta > 15$–20. There are no θ limitations for the representation (283); $N_s = 200$–500 terms are required for $f = 100$ c/s. For fields at the ionospheric boundary ($z = h$), the terms of the summation (261) become negligible in magnitude for $nh \gg a$; and the integral approximation of the summation (275) can be used also for smaller values of the distance D. In the V.L.F. range, the number of terms N_s in the series of zonal harmonics is further increased, and $N_s > 3000 = 2.25\ k_0 a$ terms are necessary for obtaining an agreement between the mode summation and the series of zonal harmonics for $f = 10$ kc/s. The exponential functions used in the mode summation have a restricted validity in the curved wave guide for V.L.F; and the series of zonal harmonics, which also uses exponential functions for the radial field variations, may become similarly inaccurate at these frequencies. The number of terms N_s required for obtaining a convergence of the series becomes very large, and it has not been attempted to develop expressions for the coefficients a_n and b_n of (261) that would be of better accuracy in the V.L.F. range.

Series of zonal harmonics have been also used for field calculations by Johler and Berry [1962]. They compute the radial and azimuthal functions from recurrence relations (262) to (264), and the convergence rate of the series is improved similarly as in (283). However, the approximations leading to (275) of the present calculations illustrate more clearly the convergence problems of this approach.

4.9.2 Watson Transformation

The series representations (247), (257), (261), or (268) are very slowly converging; and, even in the modified summations (275) or (283), the number of modes N_s required for an accurate field representation is estimated as 2 to 20 k_0a. Although the series can be used in the frequency range of earth-to-ionosphere cavity resonances [Madden and Thompson, 1965; Row, 1962], computations at higher frequencies are feasible only with the aid of high-speed computers [Johler and Berry, 1962]. It is generally advantageous to use the Watson transform to change the series (247) into a more rapidly converging representation. The Watson transformation has been discussed in detail by Sommerfeld [1949], Bremmer [1949], or Wait [1962]. It changes the summation over n into a complex integral, the residues of which are evaluated at the poles of the integrand ν which are the zeros of the denominator

$$D_n = [1 - R_{gn}R_{in}].$$

The series (247) can be written in an abbreviated form as

$$\Pi = \sum_{n=0}^{\infty} (2n+1)\, f(n)\, (-1)^n P_n(-\cos\theta). \tag{284}$$

The summation is transformed into the contour integral

$$\Pi = \frac{1}{i} \int_{C_1} \frac{m\, dm}{\cos m\pi} f\left(m-\frac{1}{2}\right) P_{m-\frac{1}{2}}(-\cos\theta), \tag{285}$$

where the contour C_1 encloses the positive part of the real axis in a clockwise direction. The integrand has poles at $m = 1/2, 3/2, 5/2, \ldots$, which correspond to zeros of the cos $m\pi$ function. The residue theorem shows that the integral (285) is equivalent to the summation (284). The Legendre function $P_{m-\frac{1}{2}}(x)$ and the cosine function cos $m\pi$ are even with respect to m. The function $f(n)$ of (284) is proportional to (a_n/b_n) of (257). The series expansions of a_n and b_n in (265) and (266) contain factors $n(n+1) = (m-\frac{1}{2})(m+\frac{1}{2})$ which are also even with respect to m. The function $f(m-\frac{1}{2})$ of (284) will be even with respect to m to the extent that the possible n (or m) dependence of the surface impedance Δ_e is negligible. The integrand of (285) is odd, and the part of the contour C_1 which lies below the real axis may be replaced by a part of C_2 which lies entirely above the real axis in the negative half plane. Replacing $(m-\frac{1}{2})$ by ν, (285) becomes

$$\Pi = i \int_{C_2} \frac{\nu+\frac{1}{2}}{\sin \nu\pi} f(\nu)\, P_\nu(-\cos\theta)\, d\nu, \tag{286}$$

where C_2 is a straight line above the real axis extending from $\nu = -\infty + i\delta$ to $\nu = +\infty + i\delta$. The path of integration C_2 is closed by an infinite semicircle in the upper half-plane, which does not contribute to the numerical value of the integral. The integral is now computed as $2\pi i$ times the sum of residues of the integrand which are evaluated at the poles of $f(\nu)$ located in the upper half-plane. This results in

$$\Pi = -\pi \sum_{\nu} \frac{2\nu+1}{\sin \nu\pi} \frac{F_\nu[h_\nu^{(1)}(k_0r) + R_{i\nu} j_\nu(k_0r)]}{\partial D_n/\partial n\big|_{n=\nu}} P_\nu(-\cos\theta). \tag{287}$$

In addition to the waves of the residue type (287), there will be a continuous wave spectrum or lateral waves which propagate within the earth and ionosphere. The lateral waves will be negligible if the second order or Debye approximations of the spherical functions can be used for representing the fields beyond the boundaries [Wait, 1962]. In the limit of a planar waveguide, these so-called branch-cut waves have been studied by Budden [1961] and Anderson [1962]. The propagation constant of these waves is determined by the properties of the ionosphere; these waves are rapidly attenuated and do not contribute significantly to the net field. This is also borne out in the numerical examples of Section 4.6.1, where field representations based on (284) are shown to agree with the residue series or mode sum (287).

For the lowest-order (propagating) E.L.F. mode, the spherical Bessel functions can be expanded in a Taylor series. Omitting the summation sign and applying (236) and the differential equation of Legendre functions [equation (11) with $\mu = 0$], it follows that

$$E_r = \frac{iI\, ds}{4} \sqrt{\frac{\mu_0}{\varepsilon_0}} \frac{\nu(\nu+1)(2\nu+1)}{(k_0ar)^2 \sin \nu\pi} \frac{a_\nu}{b'_\nu} P_\nu(-\cos\theta), \tag{288}$$

where a_ν and b_ν are defined by (265) and (266) and where $b'_\nu = \partial b_n/\partial n\big|_{n=\nu}$. The eigenvalues ν are determined from the solution $b_\nu = 0$. The function b_ν of (266) is quadratic with respect to $N = 4\nu(\nu+1)/(u_g+u_i)^2$, and it can be shown that

$$\frac{\nu(\nu+1)}{(k_0a)^2}\left(1-\frac{h}{a}\right) = 1 + \frac{i\Delta_e}{k_0h}\left(1+\frac{h}{a}\right) - \frac{1}{3}\Delta_e^2 \approx 1 + \frac{i\Delta_e}{k_0h}, \tag{289}$$

which agrees with (153) in the limit of a perfectly conducting ground ($\Delta_g = 0$). The derivative b'_ν is computed from (266) as

$$b'_\nu = -\frac{ih(2\nu+1)}{k_0(a+h/2)^2}\left\{1 + \left(\frac{h}{2a+h}\right)^2 + \frac{1}{3}(N-1)(k_0h)^2 - \frac{i\Delta_e k_0 h}{2}\left[1 + \frac{h}{3(a+h/2)}\right]\right\} \approx -\frac{ih(2\nu+1)}{k_0(a+h/2)^2} \tag{290}$$

Substituting the approximate values of a_ν and b'_ν in (288) gives

$$E_r \approx -\frac{iI\, ds}{4\omega\varepsilon_0 ha^2} \frac{\nu(\nu+1)}{\sin \nu\pi} P_\nu(-\cos\theta), \tag{291}$$

which is a commonly used expression. However, its validity depends on the approximations (265) and (290). The electric field (291) is the same as in (41) if the excitation factor A_n of (91) is equal to 0.5 and the height-gain function $G_n(z)$ of (93) is equal to 1. It can be used to calculate the E.L.F. fields of the propagating ($n = 0$) mode. It does not apply to the nonpropagating modes where $A_n \approx 1$ following (92) and (88).

The Legendre function $P_\nu(-\cos\theta)$ of (291) may be also expanded in a series of Legendre polynomials $P_n(\cos\theta)$ following Magnus and Oberhettinger [1949] as

$$P_\nu(-x) = -\frac{\sin \nu\pi}{\pi} \sum_{n=0}^{\infty} P_n(x) \frac{2n+1}{n(n+1)-\nu(\nu+1)}. \tag{292}$$

Substituting (292) in (291) gives

$$E_r = \frac{iI\, ds\nu(\nu+1)}{4\pi\omega\varepsilon_0 ha^2} \sum_{n=0}^{\infty} P_n(\cos\theta) \frac{2n+1}{n(n+1)-\nu(\nu+1)}. \tag{293}$$

After substituting the approximate form of (289) for the $\nu(\nu+1)$ term of the denominator, (293) becomes

$$E_r = \frac{iI\,ds\nu(\nu+1)}{4\pi\omega\varepsilon_0 ha^2} \sum_{n=0}^{\infty} P_n(\cos\theta)\,\frac{2n+1}{n(n+1)-\left(1+\frac{i\,\Delta_e}{k_0 h}\right)\left(1+\frac{h}{a}\right)(k_0 a)^2} \tag{294}$$

which is similar to (268) except that a factor $\nu(\nu+1)$ of (294) corresponds to a factor $n(n+1)$ in (268). The resonant terms of E_r where $|\nu(\nu+1)| \approx n(n+1)$ will be approximately the same in (268) and (294), but differences between corresponding terms will occur as n deviates from this resonance condition. It should be recalled that (268) is an expansion of the total field while (294) represents only the propagating fundamental mode. In the near-field range, (268) should, therefore, provide larger fields than (294), all terms of which add only to a single waveguide mode.

4.10 References

Abramowitz, M., and I. A. Stegun (1964) *Handbook of Mathematical Functions*, National Bureau of Standards, A.M.S. 55.

Anderson, W. L. (1962) Fields of electric dipoles in sea water—the earth-air-ionosphere problem, *J. Res. NBS* **66D** (1), 63–72.

Bain, W. C., and B. R. May (1967) D-region electron density distributions from propagation data, *Proc. IEE* **114** (11), 1593–1597.

Balser, M., and C. A. Wagner (1960) Observations of earth-ionosphere cavity resonances, *Nature* **188**, 638–641.

Baños, A. (1966) *Dipole Radiation in the Presence of a Conducting Half-Space*, Pergamon Press, New York.

Bremmer, H. (1949) *Terrestrial Radio Waves*, Elsevier, New York and Amsterdam.

Budden, K. G. (1961) *The Wave Guide Mode Theory of Wave Propagation*, Logos Press, London.

Budden, K. G., and H. G. Martin (1962) The ionosphere as a whispering gallery, *Proc. Royal Society* **A265**, 554–569.

Erdélyi, A. (1953) *Higher Transcendental Functions*, McGraw-Hill, New York.

Galejs, J. (1961) Excitation of V.L.F. and E.L.F. radio waves by a horizontal magnetic dipole, *NBS J. Res.* **65D**, 305–311.

Galejs, J. (1964) Terrestrial extremely low frequency propagation, *Natural Electromagnetic Phenomena below 30 kc/s* (ed. by D. F. Bleil), Plenum Press, New York, pp. 205–258. (The right-hand sides of (23), (63), and (145) should be multiplied with -1.)

Galejs, J. (1965) Schumann resonances, *Radio Sci.* **69D**, 1043–1055.

Galejs, J. (1967) Propagation of V.L.F. waves below an anisotropic stratified ionosphere with a transverse static magnetic field, *Radio Sci.* **2**, 557–574.

Galejs, J. (1968) Propagation of E.L.F. and V.L.F. waves below an anisotropic ionosphere with a dipping static magnetic field, *J. Geophys. Res.* **73**, 339–352.

Jean, A. G., Jr., A. C. Murphy, J. R. Wait, and D. F. Wasmundt (1961) Propagation attenuation rates at E.L.F., *J. Res. NBS* **65D** *Radio Propagation*, No. 5, 475–479.

Johler, J. R., and L. A. Berry (1962) Propagation of terrestrial radio waves of long wavelength—theory of zonal harmonics with improved summation techniques, *J. Res. NBS* **66D** (6), 737–772.

Krasushkin, P. E. (1962) On the propagation of long and very long radio waves around the earth, *Nuovo Cimento*, Suppl. **26**, 50–112.

Madden, T. R., and W. Thompson (1965) Low-frequency electromagnetic oscillations of the earth-ionosphere cavity, *Rev. Geophys.* **3**, 211–254.

Magnus, F., and F. Oberhettinger (1949) *Special Functions of Mathematical Physics*, Chelsea Publishing Co., New York.

Miller, J. C. P. (1946) *The Airy Integral*, British Association Mathematical Tables, Part-Volume B, University Press, Cambridge.

Norton, K. A. (1937) The propagation of radio waves over the surface of the earth and in the upper atmosphere, Pt. II, *Proc. IRE* **25**, (9), 1203–1236.

Pierce, E. T. (1960) The propagation of radio waves of frequency less than 1 kc, *Proc. IRE* **48**, 329–331.

Rayleigh, Lord (1910) The problem of whispering gallery, *Phil. Mag.* **20**, 1001–1004.

Rogerson, J. E. (1967) Airborne field strength measurements in the region of the N.P.M. antipode, *Radio Sci.* **2** (6), 581–587.

Row, R. V. (1962) On the electromagnetic resonant frequencies of the earth ionosphere cavity, *Trans. IRE PGAP* **AP-10** (6), 766–769.

Schumann, W. O. (1952) On the propagation of very long electrical waves and of the lightning discharge around the earth (in German), *Z. Angew. Phys.* **4**, 474–480.

Schumann, W. O. (1954) On the modal fields in the propagation of long electrical waves in the system earth-air-ionosphere and two applications (horizontal and vertical dipole) (in German), *Z. Angew. Phys.* **6** (1), 35–43.

Smythe, W. R. (1950) *Static and Dynamic Electricity*, second edition, McGraw-Hill, New York, NY.

Sommerfeld, A. (1949), *Partial Differential Equations in Physics*, Academic Press, New York, NY.

Stratton, J. A. (1941) *Electromagnetic Theory*, McGraw-Hill, New York, NY.

Volland, H. (1961) Comparison between mode theory and ray theory of V.L.F. propagation, *J. Res. NBS* **65D** (4), 357–361.

Volland, H. (1964a) On the theory of the propagation of long electromagnetic waves, Part II, Curved anisotropic waveguide (in German), *Arch. El. Uebertr.* **18** (3), 181–188.

Volland, H. (1964b) Remarks on Austin's formula (in German), *NTZ* **17** (12), 641–652.

Wait, J. R. (1957) The mode theory of V.L.F. ionosphere propagation for finite ground conductivity, *Proc. IRE* **45** (6), 762–767.

Wait, J. R. (1961) The electromagnetic fields of a horizontal dipole in the presence of a conducting half-space, *Canadian J. Phys.* **39**, 1017–1028.

Wait, J. R. (1962) *Electromagnetic Waves in Stratified Media*, Macmillan, New York.

Wait, J. R., and A. Murphy (1957) The geometrical optics of V.L.F. sky wave propagation, *Proc. IRE* **45** (6), 754–760.

Weekes, K. (1950) The ground interference pattern of very-low-frequency radio waves, *Proc. IEE* **97**, 100–107.

CHAPTER 5

WAVES IN A CYLINDRICAL GUIDE

Abstract. In the cylindrical shell between a homogeneous ground surface and an isotropic ionosphere, the T.M. and T.E. fields are excited by vertically and horizontally polarized line sources. The azimuthal field variations are characterized by exponentials and the radial variations by cylindrical functions that are approximated by exponentials or Airy functions. In the Airy function approximation, the radial field variations are the same as in a spherical geometry.

The airspace between the earth and the ionosphere is subdivided into a number of thin, concentric layers, where fields of each layer are represented using Debye approximations, Taylor series expansion of radial functions, or exponential approximations. The multilayer field representations allow arbitrarily accurate solutions, while Airy function solutions of wave-propagation parameters exhibit an accuracy comparable to a 1 km uncertainty in the height of the lower ionospheric boundary.

The T.M. and T.E. field components are coupled in the presence of ionospheric anisotropy, and the derivation of excitation factors, height-gain functions, and normalized impedances considers also the presence of T.M. (or T.E.) field components with wave numbers corresponding to T.E. (or T.M.) modes.

5.1 Introduction

The boundaries of the terrestrial waveguide between the earth and the ionosphere are nearly spherical. Waves in such a spherical waveguide have been investigated in Chapter 4.

A cylindrical geometry represents the terrestrial waveguide with lesser accuracy, but it offers several analytical advantages. In long-distance propagation, a cylindrical waveguide provides a two-dimensional model; but the principal advantages of the cylindrical geometry are in the treatment of anisotropy effects. The differential equations of the fields in the ionosphere are separable for arbitrary directions of the static magnetic field only for cylindrical stratifications. Although it is possible to assume a cylindrical ionosphere on the top of a spherical air shell and a spherical earth [Madden and Thompson, 1965], the mathematical formalism appears to be more consistent by assuming a cylindrical geometry for the ionosphere, the airspace, and also for the ground surface. This geometry can be readily treated for excitation by vertically and horizontally polarized line sources. However, in this approach it will be necessary to relate the line source excited fields in a cylindrical shell to the more realistic dipole excited fields of a spherical shell.

This chapter treats in Section 5.2 a line source excited cylindrical shell between a homogeneous ground surface of radius $r_g = a$ and an isotropic ionosphere of radius $r_i = a+h$. The source is located at $r_s = a+y_s$ and $\varphi = 0$, and the fields are observed at $r = a+y$ and at the azimuthal angle φ, as is shown in Fig. 5.1. A vertically polarized line source, or a continuous line of radial electric dipoles, excites T.M. waves; a horizontally polarized source excites T.E. waves. The azimuthal field variations are characterized by simple exponentials,

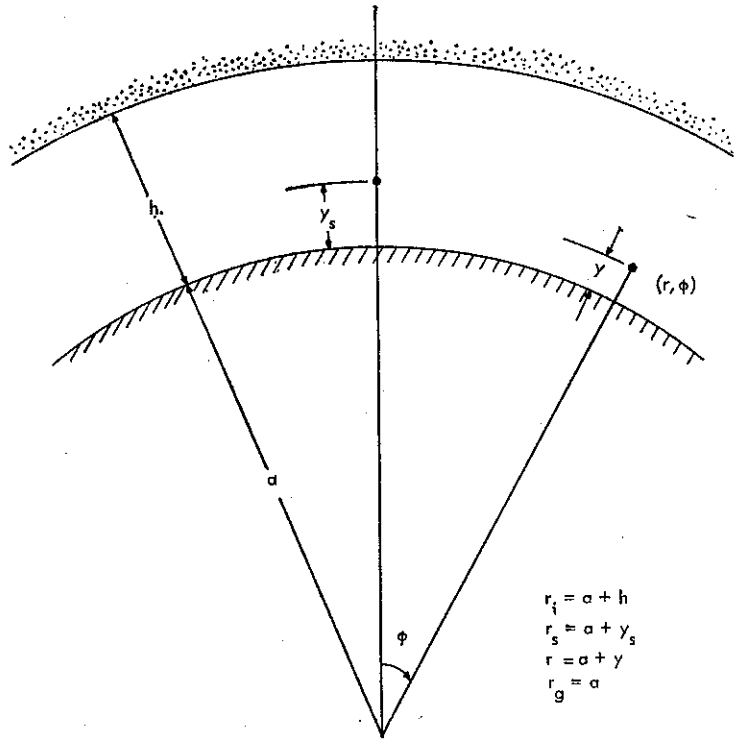

FIG. 5.1 Geometry of the Cylindrical Shell

and the radial field variations are denoted by Hankel functions of large complex order and arguments. These radial functions are approximated by simple exponentials in Section 5.3. The analogy with a spherical shell of Chapter 4 suggests that these exponential representations are valid for the airspace between the ground and the ionosphere only for frequencies near 10 kc/s and lower. The so-called third order or Airy function approximation of the radial cylinder functions of Section 5.4 is more accurate. In this approximation, the radial functions of the cylindrical shell are identical to those of a spherical shell in Chapter 4, and there is no difference between the radial field variations in cylindrical and spherical geometries. The excitation factors, the height-gain functions, and the impedance calculations can be done interchangeably in cylindrical and spherical geometries.

The airspace between the ground surface and the ionosphere has been subdivided into a number of thin shells in Section 5.5. Such multilayer representations are commonly used for approximating a medium of continuously varying properties as a series of homogeneous layers. A subdivision of a homogeneous space in a number of thin shells will have advantages if the radial functions are of limited accuracy, which is improved by decreasing the thickness of a layer. This approach requires a large number of repetitive mathematical operations than can be conveniently described in a matrix notation. These representations are based on second-

order or Debye approximations of Hankel functions, Taylor series approximations, and on thin-shell (or exponential) approximations. It is also possible to determine propagation parameters (or permissible azimuthal wave numbers) from a sequence of multilayer field representations. A comparison between multilayer and Airy function solutions shows that the Airy functions exhibit a solution accuracy that is comparable to an approximate 1 km uncertainty of the waveguide height between the earth and the ionosphere; the propagation parameters can be determined with arbitrary accuracy when using multilayer field representations.

The fields below an anisotropic ionosphere are considered in Section 5.6. The ionospheric fields have been discussed in detail by Galejs [1967b, 1968a], and these results are applied to the derivation of field expressions in the space between the earth and the ionosphere. The line source excited fields are expressed in a harmonic series, which is transformed into a residue series in Section 5.7. The final expressions of these residue series (or mode summations) involve height-gain functions and normalized impedances that are identical to those computed under isotropic conditions although the functions of T.M. (or T.E.) field components must be also computed with wave numbers corresponding to T.E. (or T.M.) modes. However, the rather lengthy derivations are necessary for deriving the excitation factors, which can be reduced to, but cannot be deduced from, the excitation factors of the isotropic shell. There appear no simple methods for deducing the amplitudes of T.M. field components excited by vertically polarized sources with wave numbers corresponding to T.E. modes (or T.E. field components excited by horizontally polarized sources with wave numbers corresponding to T.M. modes). The T.E. field components excited by a vertically polarized source and the T.M. field components excited by a horizontally polarized source will also depend on a coupline impedance Z_{eh} that is defined as the ratio between the transverse horizontal electric and magnetic fields at the ground surface. The field expressions are listed in Section 5.6.2 for line source excitation, and dipole fields are discussed in Section 5.6.3. The azimuthal wave numbers of the coupled T.M. and T.E. modes are determined from modal equations that are summarized in Section 5.6.1.

5.2 Formal Solution

5.2.1 *Field Components*

For an assumed $\exp(-i\omega t)$ time dependence, the fields in the spherical shell satisfy the equations

$$\nabla\times\mathbf{H} = -i\omega\varepsilon_0\mathbf{E}, \tag{1}$$

$$\nabla\times\mathbf{E} = i\omega\mu_0\mathbf{H}, \tag{2}$$

For no z variations of the fields, the components of (1) and (2) may be written out as

$$E_r = \frac{i}{\omega\varepsilon_0 r}\frac{\partial}{\partial\varphi}H_z, \tag{3}$$

$$E_\varphi = -\frac{i}{\omega\varepsilon_0}\frac{\partial}{\partial r}H_z, \tag{4}$$

$$E_z = \frac{i}{\omega\varepsilon_0 r}\left[\frac{\partial}{\partial r}(rH_\varphi) - \frac{\partial}{\partial\varphi}H_r\right], \tag{5}$$

$$H_r = -\frac{i}{\omega\mu_0 r}\frac{\partial}{\partial\varphi}E_z, \tag{6}$$

$$H_\varphi = \frac{i}{\omega\mu_0}\frac{\partial}{\partial r}E_z, \tag{7}$$

$$H_z = -\frac{i}{\omega\mu_0 r}\left[\frac{\partial}{\partial r}(rE_\varphi) - \frac{\partial}{\partial\varphi}E_r\right]. \tag{8}$$

There is no coupling between the T.M. (E_r, E_φ, and H_z) and the T.E. (E_z, H_r, and H_φ) fields. The T.M. and T.E. field components can be treated separately in the cylindrical shell between the earth and the ionosphere, and the T.M. fields will be considered first.

Equations (3), (4), and (8) can be combined to give the differential equation

$$\frac{\partial^2}{\partial r^2}H_z + \frac{1}{r}\frac{\partial}{\partial r}H_z + \frac{1}{r^2}\frac{\partial^2}{\partial\varphi^2}H_z + k^2H_z = 0, \tag{9}$$

where $k = k_0 = \omega\sqrt{\mu_0\varepsilon_0}$ in the shell between the earth and the ionosphere. Substituting $H_z = R(r)F(\varphi)$, (9) can be separated into an r-dependent and a φ-dependent part, each of which is set to be equal to a constant ν^2. The resulting differential equation in $R(r)$

$$r^2R'' + rR' + (k^2r^2 - \nu^2)R = 0 \tag{10}$$

is recognized as Bessel's differential equation. The differential equation in $F(\varphi)$ becomes

$$F'' + \nu^2F = 0, \tag{11}$$

which has simple exponentials for solutions. H_z is therefore of the form

$$H_z(r, \varphi) = [A_eH_\nu^{(1)}(u) + B_eH_\nu^{(2)}(u)][C_e\exp(i\nu\varphi) + D_e\exp(-i\nu\varphi)], \tag{12}$$

where $u = kr$ and $H_\nu^{(m)}(u)$ is the Hankel function of order ν and kind m. E_r and E_φ are computed from (3) and (4) as

$$E_r(r, \varphi) = -\frac{\nu}{\omega\varepsilon_0 r}[A_eH_\nu^{(1)}(u) + B_eH_\nu^{(2)}(u)][C_e\exp(i\nu\varphi) - D_e\exp(-i\nu\varphi)], \tag{13}$$

$$E_\varphi(r, \varphi) = -\frac{ik}{\omega\varepsilon_0}[A_eH_\nu^{(1)}(u)' + B_eH_\nu^{(2)}(u)'][C_e\exp(i\nu\varphi) + D_e\exp(-i\nu\varphi)], \tag{14}$$

where the prime denotes a derivative with respect to the argument.

The T.E. field components E_z, H_r, and H_φ satisfy equations (5), (6), and (7) which are similar to the equations (8), (3), and (4) satisfied by H_z, E_r and E_φ respectively, except that E and H, μ_0 and ε_0, and i and $(-i)$ are mutually interchanged. Applying a similar modification to (12), (13), and (14), it follows that

$$E_z(r, \varphi) = [A_hH_\nu^{(1)}(u) + B_hH_\nu^{(2)}(u)][C_h\exp(i\nu\varphi) + D_h\exp(-i\nu\varphi)], \tag{15}$$

$$H_r(r, \varphi) = -\frac{\nu}{\omega\mu_0 r}[A_hH_\nu^{(1)}(u) + B_hH_\nu^{(2)}(u)][C_h\exp(i\nu\varphi) - D\exp(-i\nu\varphi)], \tag{16}$$

$$H_\varphi(r, \varphi) = \frac{ik}{\omega\mu_0}[A_hH_\nu^{(1)}(u)' + B_hH_\nu^{(2)}(u)'][C_h\exp(i\nu\varphi) + D_h\exp(-i\nu\varphi)], \tag{17}$$

Expressions (12) to (17) represent a formal solution of the field problem. The fields must satisfy boundary conditions at the cavity walls, which determine the amplitudes A_e, B_e, A_h, and B_h and the values ν as will be shown in Section 5.2.2. The remaining constants C_e, D_e and C_h, D_h, discussed in Section 5.2.3, are proportional to the dipole moments of the sources.

5.2.2 *Modal Equation*

The field components (12) to (17) should satisfy the boundary conditions

$$Z_g = -\frac{E_\varphi(a)}{H_z(a)} = \frac{E_z(a)}{H_\varphi(a)} \tag{18}$$

and

$$Z_e = \frac{E_\varphi(a+h)}{H_z(a+h)}, \quad Z_h = -\frac{E_z(a+h)}{H_\varphi(a+h)}, \tag{19}$$

at the ground surface and the ionospheric boundary respectively. Substituting (12) and (14) in (18), the resulting equation can be solved for the amplitude ratio B_e/A_e, which gives

$$\frac{B_e}{A_e} = -\frac{H_\nu^{(1)}(u_g)' + i\,\Delta_g H_\nu^{(1)}(u_g)}{H_\nu^{(2)}(u_g)' + i\,\Delta_g H_\nu^{(2)}(u_g)}, \tag{20}$$

where $u_g = k_0 a$, $\Delta_g = Z_g/\sqrt{\mu_0/\varepsilon_0}$. Field components (12) to (14) will satisfy the boundary condition (18) at $r = a$ for any value of ν, if B_e/A_e ratio is computed from (20). Substituting (12) and (14) in (19), the resulting equation is solved for B_e/A_e, which gives

$$\frac{B_e}{A_e} = -\frac{H_\nu^{(1)}(u_i)' - i\,\Delta_e H_\nu^{(1)}(u_i)}{H_\nu^{(2)}(u_i)' - i\,\Delta_e H_\nu^{(2)}(u_i)}, \tag{21}$$

where $u_i = k_0(a+h)$, $\Delta_e = Z_e/\sqrt{\mu_0/\varepsilon_0}$. Using this B_e/A_e ratio, field components (12) to (14) will satisfy the boundary condition (19) at $r = a+h$ for any value of ν. However, the field components (12) to (14) must satisfy the boundary conditions (18) and (19) simultaneously. There will be only a discrete set of ν values which make B_e/A_e of (20) equal to B_e/A_e of (21). Eliminating B_e/A_e from (20) and (21), it follows that the permissible eigenvalues ν are determined from the solution of

$$\frac{H_\nu^{(2)}(u_g)' + i\,\Delta_g H_\nu^{(2)}(u_g)}{H_\nu^{(1)}(u_g)' + i\,\Delta_g H_\nu^{(1)}(u_g)} \cdot \frac{H_\nu^{(1)}(u_i)' - i\,\Delta_e H_\nu^{(1)}(u_i)}{H_\nu^{(2)}(u_i)' - i\,\Delta_e H_\nu^{(2)}(u_i)} = 1, \tag{22}$$

which represents the conditional or modal equation for the T.M. modes.

For T.E. modes (iE_φ/H_z) of the above development should be replaced by ($-iH_\varphi/E_z$) and $\sqrt{\mu_0/\varepsilon_0}$ should be replaced by $\sqrt{\varepsilon_0/\mu_0}$. After defining $\Delta_h = Z_h/\sqrt{\mu_0/\varepsilon_0}$, the modal equation (22) can be used for determining the eigenvalues ν of T.E. modes, if Δ_g is replaced by $(1/\Delta_g)$ and Δ_e is replaced by $(1/\Delta_h)$. The amplitude ratio B_h/A_h of the T.E. field components (15) to (17) is given by (20), if Δ_g is replaced by $(1/\Delta_g)$, or by (21), if Δ_e is replaced by $(1/\Delta_h)$.

The distance along the surface of the earth between the source at $\varphi = 0$ and the receiver at φ is designated as $D = a\varphi$. The exponents in the field expressions (12) to (17) may be rearranged as

$$i\nu\varphi = \frac{\nu}{k_0 a}\, ik_0 D. \tag{23}$$

The factor

$$\frac{\nu}{k_0 a} = \frac{\nu}{u_g} = S \tag{24}$$

of (23) can be interpreted as the ratio between the wave number along the surface of the earth k_φ and the wave number of the free space k_0. The real part of S is inversely proportional to the phase velocity v_{ph} of the waves, and the imaginary part of S is proportional to the attenuation rate α.

The modal equation for the T.M. modes (22) or its modification for the T.E. modes contains Hankel functions of complex order ν and large arguments u. There are no simple analytical representations for such functions, and further approximations are necessary to make the solution of these equations practicable. A relatively simple earth-flattening or thin-shell approximation is developed in Section 5.3, which is strictly valid only in cylindrical shells thin relative to wavelength. Approximations suitable for the V.L.F. range involve Airy functions or multilayer representations. These approximations are discussed in Sections 5.4 and 5.5 respectively.

5.2.3 *Excitation by Line Source*

5.2.3.1 *T.M. Fields*

The T.M. fields are excited by a radially directed line current of density J_{ser} per unit length in the z-direction which is located at $r_s = a+y_s$ in the $\varphi = 0$ plane of the cylindrical shell. This line current can be also visualized as a continuous line of radial electric dipoles of current J_{ser} per each meter in the z-direction. The magnetic field in the direct vicinity of the $\varphi = 0$ plane is determined from the boundary condition

$$\mathbf{i}_\varphi \times [\mathbf{H}(\varphi = 0^+) - \mathbf{H}(\varphi = 0^-)] = \mathbf{J}_{se} \tag{25}$$

or

$$H_z(r, 0^+) - H_z(r, 0^-) = \begin{cases} J_{ser} & \text{if } (r_s - ds/2) < r < (r_s + ds/2), \\ 0 & \text{elsewhere.} \end{cases} \tag{26}$$

Integrating (26) from $r_g = a$ to $r_i = a+h$ gives

$$\int_{r_g}^{r_i} [H_z(r, 0^+) - H_z(r, 0^-)]\, dr = J_{ser}\, ds. \tag{27}$$

The integral (27) remains unchanged if (26) is replaced by

$$H_z(r, 0^+) - H_z(r, 0^-) = J_{ser}\, ds\, \delta(r - r_s), \tag{28}$$

where $\delta(x)$ is a delta function. In the field representations (12) to (14), C_e and D_e characterize

wave amplitudes propagating in the positive and negative φ-directions respectively. For a source located at $\varphi = 0$, $C_e = 0$ at $\varphi = 0^-$ and $D_e = 0$ at $\varphi = 0^+$. Introducing a simplified notation

$$Z_\nu^e(u) = A_e H_\nu^{(1)}(u) + B_e H_\nu^{(2)}(u), \tag{29}$$

a substitution of (12) into (28) shows that

$$J_{ser}\, ds\, \delta(r - r_s) = \sum_\nu (C_e - D_e)\, Z_\nu^e(u). \tag{30}$$

$E_r(r, \varphi)$ is continuous across the $\varphi = 0$ plane if $C_e = -D_e$. Multiplying both sides of (30) with a function $Z_\mu^e(u)/u$, an integration results in

$$\frac{1}{r_s} J_{ser}\, ds\, Z_\mu^e(u_s) = 2 \sum_\nu C_e \int_{u_g}^{u_t} Z_\nu^e(u)\, Z_\mu^e(u) \frac{du}{u}, \tag{31}$$

where $u_s = k_0 r_s$, $u_g = k_0 a$, and $u_t = k_0(a+h)$. The differential equation (10) is satisfied by $Z_\nu^e(u)$ and $Z_\mu^e(u)$ functions. The differential equation for $Z_\nu^e(u)$ is multiplied with $Z_\mu^e(u)$ and integrated between u_g and u_t. The differential equation for $Z_\mu^e(u)$ is multiplied with $Z_\nu^e(u)$ and is also integrated. The difference of these two sets of integrals is integrated by parts to give

$$\int_{u_g}^{u_t} Z_\nu^e(u)\, Z_\mu^e(u) \frac{du}{u} = \frac{u\left\{Z_\mu^e(u) \frac{\partial}{\partial u}[Z_\nu^e(u)] - Z_\nu^e(u) \frac{\partial}{\partial u}[Z_\mu^e(u)]\right\}}{\nu^2 - \mu^2}\Bigg|_{u=u_g}^{u_t}. \tag{32}$$

For $\nu \neq \mu$, the numerator of the right-hand side of (32) vanishes, if modes μ and ν satisfy identical impedance boundary conditions

$$\Delta_b = Z_b/\sqrt{\mu_0/\varepsilon_0} = \pm \frac{\partial}{\partial u}[Z_\nu^e(u)]/[iZ_\nu^e(u)]\Big|_{u=u_b}, \tag{33}$$

where the plus sign refers to Z_e with $u = u_t$ and the minus sign to Z_g with $u = u_g$. The modes μ and ν will not be strictly orthogonal if the impedance Z_e of mode μ will differ from the impedance Z_e of mode ν. This possibility is ignored for the present, and the right-hand side of (32) is assumed to become zero, if $\mu \neq \nu$. The only nonzero term with $\mu = \nu$ on the right-hand side of (31) is computed after differentiating the numerator and denominator of (32) with respect to μ as

$$I_\nu^e = \int_{u_g}^{u_t} [Z_\nu^e(u)]^2 \frac{du}{u} = \lim_{\mu \to \nu} \frac{-u}{2\mu}\left[\frac{\partial}{\partial \mu} Z_\mu^e(u) \frac{\partial}{\partial u} Z_\nu^e(u) - Z_\nu^e(u) \frac{\partial^2}{\partial \mu\, \partial u} Z_\mu^e(u)\right]\Bigg|_{u=u_g}^{u_t}. \tag{34}$$

After evaluating I_ν^e of (34), C_e of (31) is computed as

$$C_e = \frac{J_{ser}\, ds\, Z_\nu^e(u_s)}{2 r_s I_\nu^e}, \tag{35}$$

which completes the specification of the T.M. field components.

Substituting (35) in (12) to (14) and applying (23) and (24), it follows that

$$E_r(r, \varphi) = -\sqrt{\mu_0/\varepsilon_0} \frac{J_{ser}\, ds}{h} \sum_n S_n G_n(y)\, G_n(y_s) \Lambda_n \exp(ik_0 D S_n), \tag{36}$$

$$E_\varphi(r, \varphi) = \sqrt{\mu_0/\varepsilon_0} \frac{J_{ser}\, ds}{h} \sum_n \Lambda_n(y)\, G_n(y)\, G_n(y_s) \Lambda_n \exp(ik_0 D S_n), \tag{37}$$

$$H_z(r, \varphi) = \frac{J_{ser}\, ds}{h} \sum_n G_n(y)\, G_n(y_s) \Lambda_n \exp(ik_0 D S_n), \tag{38}$$

where the subscript n designates T.M. modes with eigenvalues S_n of (24) determined from the solution of (22). The excitation factors Λ_n, height-gain functions $G_n(y)$, and y-dependent normalized impedances $\Delta_n(y)$ are defined as

$$\Lambda_n = \frac{h[Z_\nu^e(u_g)]^2}{2 r_s I_\nu^e} = \frac{h}{2 r_s}\left\{\int_0^h [G_n(y)]^2 \frac{dy}{r}\right\}^{-1}, \tag{39}$$

$$G_n(y) = Z_\nu^e(u)/Z_\nu^e(u_g), \tag{40}$$

$$\Delta_n(y) = \frac{Z^e(y)}{\sqrt{\mu_0/\varepsilon_0}} = \frac{\partial}{\partial u}[Z_\nu^e(u)]/[iZ_\nu^e(u)], \tag{41}$$

where $Z_\nu^e(u)$ is given by (29). The functions (39) to (41) will be further discussed in Sections 5.3.2 and 5.4.2 for several approximate representations of the cylinder functions $Z_\nu^e(u)$. The field components (36) to (38) are functionally similar to the field components of a vertical electric dipole in a spherical waveguide [equations (104) to (107) of Chapter 4]. The tilt of the electric vector is computed as

$$E_\varphi/E_r\Big|_n = -\Delta_n(y)/S_n, \tag{42}$$

which is the same as the wave tilt $E_\theta^{ve}/E_r^{ve}\Big|_n$ of a vertical electric dipole in (108) of Chapter 4. The ratios

$$E_\varphi/H_z\Big|_n = \sqrt{\mu_0/\varepsilon_0}\, \Delta_n(y) \tag{43}$$

and

$$E_r/H_\varphi\Big|_n = -\sqrt{\mu_0/\varepsilon_0} S_n \tag{44}$$

are the same as the ratios $E_\theta^{ve}/H_\varphi^{ve}\Big|_n$ and $E_r^{ve}/H_\varphi^{ve}\Big|_n$ in (109) and (110) of Chapter 4. It will be shown in Sections 5.3.2 and 5.4.2 that the functions Λ_n, $G_n(y)$, and $\Delta_n(y)$ are comparable in spherical and cylindrical geometries. A vertical electric dipole of moment $I\, ds$ will excite at the distance D fields comparable to those of a line source of moment $J_{ser}\, ds$ (per unit length in z-direction) if

$$J_{ser}\, ds = \frac{I\, ds \sqrt{S_n}}{\sqrt{a\lambda \sin(D/a)}} \exp(-i\pi/4). \tag{45}$$

The dipole moment of this equivalent line source will be increased with decreasing wavelength λ and decreasing distance D.

5.2.3.2 T.E. Fields

The T.E. fields are excited by a z-directed line current of linear density J_{sez} located at $r_s = a+y_s$ in the $\varphi = 0$ plane of the cylindrical shell. The magnetic field satisfies the boundary condition (25) in the direct vicinity of the $\varphi = 0$ plane, which leads to

$$H_r(r, 0^-) - H_r(r, 0^+) = J_{sez}\, ds\, \delta(r - r_s), \tag{46}$$

where the line element ds is taken in the r direction. Noting that $C_h = 0$ at $\varphi = 0^-$ and $D_h = 0$ at $\varphi = 0^+$, the continuity of E_z across the $\varphi = 0$ plane leads to $D_h = C_h$ in the field expressions for $\varphi = 0^-$ and 0^+ respectively. Letting

$$Z_\nu^h(u) = A_h H_\nu^{(1)}(u) + B_h H_\nu^{(2)}(u) \tag{47}$$

and substituting (16) in (46), it can be shown that

$$J_{sez}\, ds\, Z_\mu^h(u_s) = \frac{2}{\omega\mu_0} \sum_\nu \nu C_h \int_{u_g}^{u_t} Z_\nu^h Z_\mu^h \frac{du}{u}. \tag{48}$$

Equation (48) is similar in form to (31), that was derived for T.M. modes. A similar development shows that the amplitude C_h of the T.E. field components (15) to (17) is given by

$$C_h = \frac{\omega\mu_0 J_{sez}\, ds\, Z_\nu^h(u_s)}{|2\nu I_\nu^h}, \tag{49}$$

where I_ν^h is obtained by replacing $Z_\nu^e(u)$ with $Z_\nu^h(u)$ in (34). The amplitudes A_h and B_h are computed from the B_e/A_e expression (20) or (21) following the procedure summarized in Section 5.2.2. For T.E. modes, the right-hand side of (33) represents $1/\Delta_b = \sqrt{\mu_0/\varepsilon_0}/Z_b$, where the plus sign refers to Z_h with $u = u_t$ and the minus sign to Z_g with $u = u_g$.

Substituting (49) in (15) to (17) and applying (23) and (24), it follows that

$$E_z(r, \varphi) = \sqrt{\mu_0/\varepsilon_0}\, \frac{J_{sez}\, ds}{h} \sum_m S_m^{-1} G_m(y)\, G_m(y_s) \Lambda_m \exp(ik_0 D S_m), \tag{50}$$

$$H_r(r, \varphi) = \frac{J_{sez}\, ds}{h} \sum_m G_m(y)\, G_m(y_s) \Lambda_m \exp(ik_0 D S_m), \tag{51}$$

$$H_\varphi(r, \varphi) = -\frac{J_{sez}\, ds}{h} \sum_m \frac{G_m(y)\, G_m(y_s) \Lambda_m}{S_m\, \Delta_m(y)} \exp(ik_0 D S_m), \tag{52}$$

where the subscript m designates T.E. modes with eigenvalues S_m of (24) determined from the solution of a modal equation, which is discussed following (22). The excitation factor Λ_m and the height-gain function $G_m(y)$ are defined similarly as for T.M. modes in (39) and (40). A y-dependent normalized impedance $\Delta_m(y)$ may be computed from

$$\Delta_m(y) = \frac{Z^h(u)}{\sqrt{\mu_0/\varepsilon_0}} = iZ_\nu^h(u) \Big/ \frac{\partial}{\partial u}[Z_\nu^h(u)], \tag{53}$$

where $Z_\nu^h(u)$ is given by (47). The field components (50) to (52) are functionally similar to the

T.E. field components of a horizontal electric dipole in a spherical waveguide [equations (119), (122), and (123) of Chapter 4]. The field component ratios

$$H_r/H_\varphi\Big|_m = -S_m\, \Delta_m(y), \tag{54}$$

$$E_z/H_\varphi\Big|_m = -\sqrt{\mu_0/\varepsilon_0}\, \Delta_m(y), \tag{55}$$

$$E_z/H_r\Big|_m = \sqrt{\mu_0/\varepsilon_0}/S_m, \tag{56}$$

are the same as the ratios $H_r^{he}/H_\theta^{he}\Big|_m$, $E_\varphi^{he}/H_\theta^{he}\Big|_m$, and $E_\varphi^{he}/H_r^{he}\Big|_m$ of horizontal electric or vertical magnetic dipoles in (115) to (117) of Ch. 4. It will be shown in Sections 5.3.2 and 5.4.2 that the functions Λ_m, $G_m(y)$, and $\Delta_m(y)$ are comparable in spherical and cylindrical geometries. A horizontal electric dipole of moment Ids will excite at the distance D in the direction of its maximum radiation ($|\sin\varphi| = 1$) T.E. fields comparable to those of a line current of moment $J_{sez}\, ds$ (per unit length in the z direction) if

$$J_{sez}\, ds = \frac{I\, ds \sqrt{S_m}}{\sqrt{a\lambda}\, \sin(D/a)} \exp(-i\pi/4). \tag{57}$$

A comparison of (45) and (57) shows that for comparable T.M. fields, the moments of a line of radial electric dipoles and of a single vertical electric dipole are related similarly as the moments of a line current and of a single horizontal electric dipole for comparable T.E. fields.

5.3 Exponential or Thin-shell Approximations

The solutions of the preceding section have been carried out using cylindrical functions for the r variations of the fields, but there appears to be no simple representations for the Hankel functions of large complex order ν and large arguments $u = k_0 r$ that are equally applicable to E.L.F. and V.L.F. ranges. An approximation which becomes accurate in the limit of zero earth curvature ($r \to \infty$) or for thin shells ($h/r \to 0$) will be described in this section.

The radial field variation was computed from the differential equation (10). For $r \to \infty$ or for fields in a thin shell of $h/r \to 0$, the factors r are approximated by their average value in the shell $r_m = a + 0.5h$ and (10) becomes

$$R'' + \frac{1}{r_m} R' + [k^2 - (\nu/r_m)^2] R = 0 \tag{58}$$

the solutions of which are of the form

$$R = A \exp(iK_1 r) + B \exp(iK_2 r) \tag{59}$$

with

$$K_{1,2} = \frac{i}{2r_m} \pm K \tag{60}$$

and

$$K = \sqrt{k^2 - \frac{\nu^2 + 0.25}{r_m^2}} = k\sqrt{1 - \left(\frac{k_0 aS}{kr_m}\right)^2 - \frac{0.25}{(kr_m)^2}}. \tag{61}$$

In this approximation

$$H_\nu^{(m)}(kr) \sim \exp(iK_m r). \tag{62}$$

The approximation (62) will be substituted in the modal equation and will be also used for field computations.

It will be shown that the representation (62) is adequate for frequencies in the E.L.F. range. In the V.L.F. range, this radial function gives results of qualitative accuracy, although it illustrates some of the basic mode characteristics. For detailed numerical work, (62) can be used in a multishell approximation of the airspace between the ground and the ionosphere, where the height of the individual shells h is small compared to the free-space wavelengths. These multishell approximations will be discussed in Section 5.5.

5.3.1 Modal Equation

Using the approximate functions (60) and (62) and noting that $H_\nu^{(m)}(u)' \approx (iK_m/k) H_\nu^{(m)}(u)$, the modal equation (26) of the T.M. modes is changed into

$$\frac{K-\Delta_e' k_0}{K+\Delta_e' k_0} \cdot \frac{K-\Delta_g' k_0}{K+\Delta_g' k_0} \exp(2iKh) = \exp(2in\pi), \tag{63}$$

where $\Delta_g' = \Delta_g + i/(2r_m k_0)$, $\Delta_e' = \Delta_e - i/(2r_m k_0)$ and where n is zero or an arbitrary integer.

In the V.L.F. range, $k_0 r_m \gg 1$ and (63) with K defined by (61) differs negligibly from the corresponding approximations for a spherical shell (81) and (83) of Chapter 4.

In the E.L.F. range, only the $n = 0$ mode propagates. Substituting $(\Delta_e' k_0/K)$, $(\Delta_g' k_0/K) \ll 1$, and $n = 0$ in (63), it is seen that

$$iKh - \frac{k_0}{K}(\Delta_e + \Delta_g) = 0 \tag{64}$$

or

$$S \approx \frac{r_m}{a}\sqrt{1 + \frac{i(\Delta_e+\Delta_g)}{k_0 h} - \frac{1}{(2k_0 r_m)^2}}. \tag{65}$$

The last term under the square-root expression contributes less than one part in 10^3 for $f > 85$ c/s, and (65) will differ negligibly from the modal equation for a spherical shell [equation (87) of Chapter 4].

The modal equation of T.E. modes is obtained by replacing Δ_g with $(1/\Delta_g)$, Δ_e with $(1/\Delta_h)$, and n with m in (63). The resulting equation will be quite similar to (89) of Chapter 4, which is the T.E. modal equation for a spherical shell. The T.E. modal equation for the cylindrical shell will not be examined in more detail.

The accuracy of the thin-shell approximations has been investigated for a spherical geometry in Chapter 4. The phase-velocity data are approximated with a reasonable accuracy; but the attenuation rates are too low, particularly in the $n = 1$ and $m = 1$ modes at the higher frequencies.

5.3.2 Field Expressions

The field expressions (36) to (38) and (50) to (52) can be evaluated after obtaining suitable representations for the excitation factors A_q, height-gain functions $G_q(y)$, and the height-dependent normalized impedances $\Lambda_q(y)$, where $q = n$ or m.

Noting the approximation (62), a substitution of (20), (29), and (34) in (39) leads for T.M. modes (n) to

$$\left.\begin{aligned} A_n \approx \Bigg\{ & 1 + \frac{\sin 2Kh}{2Kh}\exp(-h/r_m) + \left(\frac{\Delta_g' k_0}{K}\right)^2 \left[\frac{\sin 2Kh}{2Kh}\exp(-h/r_m) - 1\right] \\ & - \frac{i\Delta_g' k_0}{hK^2}[1 - \cos 2Kh \exp(-h/r_m)] + \frac{1}{4K^2 r_m h}\left[\left[1 + \left(\frac{\Delta_g' k_0}{K}\right)^2\right]\right. \\ & \left. \times [1 - \cos 2Kh \exp(-h/r_m)] + \sin 2Kh \exp(-h/r_m)(4i\Delta_g' k_0/K)\right]^{-1}\Bigg\}, \end{aligned}\right\} \tag{66}$$

where $\Delta_g' = \Delta_g + i/(2r_m k_0)$. For $\Delta_g' \approx \Delta_g$, $(h/r_m) \ll 1$, and $Kr_m \gg 1$, (66) simplifies to the A_n field expression (92) of Chapter 4 for a spherical shell. In the E.L.F. range, $Kh \to 0$ according to (64), and it follows that $A_0 \approx 0.5$. In the V.L.F. range, it can be shown that $A_n \approx 1$.

Using similar approximations, the height-gain function $G_n(y)$ of (40) is expressed as

$$G_n(y) = \left[\cos Ky - \frac{i\Delta_g' k_0}{K}\sin Ky\right]\exp(-y/r_m), \tag{67}$$

which compares with (93) of Chapter 4 for a spherical shell. It is seen that $G_n(0) = 1$ for points on the surface of the cylindrical earth.

The y-dependent normalized impedance is computed from (41) as

$$\Lambda_n(y) = \frac{K}{k_0}\,\frac{[iK + \Delta_g' k_0/(2r_m K)]\sin Ky - \Delta_g k_0 \cos Ky}{K\cos Ky - \Delta_g' k_0 i \sin Ky}, \tag{68}$$

which also compares closely with with the corresponding expression for a spherical shell [equation (96) of Chapter 4].

The corresponding expressions for the T.E. modes A_m, $G_m(y)$, and $1/\Lambda_m(y)$ are obtained by substituting $(1/\Delta_g)$ for Δ_g in (66) to (68).

The previous examples demonstrate the close similarity between the A_q, $G_q(y)$, and $\Lambda_q(y)$ expressions in cylindrical and spherical geometries. For a spherical geometry, it has been shown in Chapter 4 that the thin-shell approximations can be used for qualitatively estimating the excitation factors, height-gain functions, and normalized height-dependent impedances of T.M. and T.E. modes without a detailed examination of their validity only for frequencies near 10 kc/s and lower. For T.M. modes, the thin-shell approximations do not produce the required higher frequency decrease of A_1 or the increase of $G_1(y)$. $G_2(y)$ is reasonably accurate within approximately 10 km from the waveguide boundaries, but $\Lambda_n(y)$ appears to be adequate within approximately 10 km from the ionospheric boundary. For T.E. modes at higher frequencies, the thin-shell approximations do not provide an adequate decrease of A_m; and, as a consequence, $G_m(y)$ tends to be too small in magnitude. $\Lambda_m(y)$ is adequate only within approximately 10 km from the waveguide boundaries.

5.4 Airy Function Approximation of the Cylindrical Functions

In the formal solution of the earth-to-ionosphere wave guide, Hankel functions of large complex order ν represent the radial field variations in (12) to (17). In Section 5.3 these cylindrical functions were approximated by simple exponentials that are of limited accuracy in the V.L.F. range. In this section, the same cylindrical functions will be represented by the so-called third-order or Watson approximation, which replaces spherical Bessel functions of large arguments and large complex order by Hankel functions of order (1/3) or by Airy functions. It follows from (159) to (163) of Chapter 4 that

$$H_\nu^{(1,2)}(u) \approx \mp \frac{i}{\sqrt{\pi}} \left(\frac{2}{k_0 a}\right)^{1/3} w_{2,1}(t), \tag{69}$$

$$-t = (\nu/2)^{2/3}\,[(u/\nu)^2 - 1] \approx \left(\frac{k_0 a}{2}\right)^{2/3} [1 - S^2 + 2(r-a)/a]. \tag{70}$$

The Airy functions $w_{1,2}(t)$ satisfy the differential equation

$$w''(t) - tw(t) = 0 \tag{71}$$

and the Wronskian is given by

$$W[w_1(t),\, w_2(t)] = w_1(t)\, w_2'(t) - w_1'(t)\, w_2(t) = -2i. \tag{72}$$

5.4.1 *Modal Equation*

Noting that

$$\frac{\partial t}{\partial u} = -(2/\nu)^{1/3}\,(u/\nu) \approx -(2/k_0 a)^{1/3} \tag{73}$$

a substitution of (69) in (22) shows that the T.M. modal equation is given by

$$\left[\frac{w_1'(t_g) - q_g w_1(t_g)}{w_2'(t_g) - q_g w_2(t_g)}\right]\left[\frac{w_2'(t_i) + q_e w_2(t_i)}{w_1'(t_i) + q_e w_1(t_i)}\right] - e^{i2\pi n} = 0, \tag{74}$$

where t_g and t_i are computed substituting $u_g = k_0 a$ and $u_i = k_0(a+h)$ in (70) and where

$$q_j = i(k_0 a/2)^{1/3}\, \Delta_j. \tag{75}$$

with $j = g$ or e. Equation (74) is identical to the corresponding modal equation of the spherical geometry [equation (178) of Chapter 4].

The modal equation (74) applies to T.E. or m modes if n, Δ_g, and Δ_e are replaced by m, $1/\Delta_g$, and $1/\Delta_h$ respectively. Therefore, q_g is defined as

$$q_g = i(k_0 a/2)^{1/3}/\Delta_g \tag{76}$$

and q_e is replaced by

$$q_h = i(k_0 a/2)^{1/3}/\Delta_h \tag{77}$$

for calculation of T.E. modes.

The modal equation (74), that was based on (22), was derived by computing the amplitude ratio B_e/A_e of the Hankel functions in (29) which satisfies the boundary conditions at the earth (20) or at the ionosphere (21) and by finally determining a sequence of eigenvalues $\nu = k_0 a S$, which satisfy these boundary conditions simultaneously. This transcendental equation can be solved directly only for nondissipative boundaries when the roots ν are real. For dissipative boundaries and complex values of ν, an iterative procedure outlined in Chapter 4 can be used for successively improving the accuracy of an initial ν estimate.

The modal equation (74) can be solved alternately by examining the impedance reflected at the ground surface $\Delta_n(0)$ using inaccurate eigenvalues ν. Then it is possible to compute a corrected value $\nu + \delta\nu$ such that $\Delta_n(0)$ tends to the normalized ground impedance $(-\Delta_g)$. Such a formulation is particularly useful in a multilayer approximation of the space between the earth and the ionosphere, when $\Delta_n(0)$ is computed after multiplying out a sequence of matrices. In the Airy function approximation of the cylinder functions, that represent the fields in the space between the earth and the ionosphere, this alternate method does not provide any clear-cut advantages relative to the method of solution described in Chapter 4. Still, this alternate method will be described to illustrate the procedure to be used in the subsequent multilayer calculations of Section 5.5.5.

The normalized impedance of the T.M. modes reflected by the ionosphere at the ground surface $\Delta_n(0)$ is computed substituting (29) with B_e/A_e ratio of (21) in (41) and by using the Airy function approximation (69) for the Hankel functions. Thus,

$$\Delta_n(0) = i\left(\frac{2}{k_0 a}\right)^{1/3} \frac{A_e w_2'(t_g) - B_e w_1'(t_g)}{A_e w_2(t_g) - B_e w_1(t_g)} \tag{78}$$

with

$$A_e = w_1'(t_i) + q_e w_1(t_i), \tag{79}$$

$$B_e = w_2'(t_i) + q_e w_2(t_i). \tag{80}$$

It can be seen that $\Delta_n(0)$ is equal to the negative of the normalized ground impedance Δ_g, if t_i and t_g satisfy the modal equation (74). However, for inaccurate values of t or S, $\Delta_n(0) \neq -\Delta_g$, and it is possible to compute a correction δS, which will make

$$\Delta_n(0) + \delta S[\partial \Delta_n(0)/\partial S] \to -\Delta_g. \tag{81}$$

The derivative $\partial\Delta_n(0)/\partial S$ is computed by differentiating $\Delta_n(0) = \sqrt{\varepsilon_0/\mu_0}\, E_\varphi(0)/H_z(0)$ as

$$\frac{\partial \Delta_n(0)}{\partial S} = \frac{1}{H_z(0)}\left[\sqrt{\frac{\varepsilon_0}{\mu_0}}\,\frac{\partial E_\varphi(0)}{\partial S} + \Delta_g \frac{\partial H_z(0)}{\partial S}\right], \tag{82}$$

where

$$\frac{\partial E_\varphi(0)}{\partial S} = \sqrt{\frac{\mu_0}{\varepsilon_0}}\, 2S\left(\frac{2}{k_0 a}\right)^{2/3} \{A_e' w_2'(t_g) - B_e' w_1'(t_g) + [A_e w_2(t_g) - B_e w_1(t_g)]t_g\}, \tag{83}$$

$$\frac{\partial H_z(0)}{\partial S} = 2iS\left(\frac{2}{k_0 a}\right)^{1/3} \{-A_e' w_2(t_g) + B_e' w_1(t_g) - A_e w_2'(t_g) + B_e w_1'(t_g)\}, \tag{84}$$

$$H(0) = \frac{2i}{k_0 a}\,[-A_e w_2(t_g) + B_e w_1(t_g)], \tag{85}$$

and where the primes of the coefficients A_e and B_e denote derivatives with respect to the argument t_i. After evaluating (78) and (82) to (85) for an approximate value of S_0, an improved

propagation parameter $S_1 = S_0 + \delta S$ is obtained using

$$\delta S = -[\Delta_n(0) + \Delta_g] \Big/ \left[\frac{\partial \Delta_n(0)}{\partial S}\right]. \tag{86}$$

For T.E. modes, the normalized impedance is defined as $\Delta_m(0) = -\sqrt{\varepsilon_0/\mu_0}\, E_z(0)/H_\varphi(0)$. The correction to S is computed as

$$\delta S = -\left[\frac{1}{\Delta_m(0)} + \frac{1}{\Delta_g}\right] \Big/ \left\{\frac{\partial}{\partial S}\left[\frac{1}{\Delta_m(0)}\right]\right\}, \tag{87}$$

where

$$\frac{\partial}{\partial S}\left[\frac{1}{\Delta_m(0)}\right] = -\frac{1}{E_z(0)}\left[\sqrt{\frac{\mu_0}{\varepsilon_0}}\,\frac{\partial H_\varphi(0)}{\partial S} - \frac{1}{\Delta_g}\,\frac{\partial E_z(0)}{\partial S}\right]. \tag{88}$$

The right-hand sides of (78) and (83) to (85) represent $1/\Delta_m(0)$, $\partial H_\varphi(0)/\partial S$, $\partial E_z(0)/\partial S$, and $E_z(0)$ respectively, if A_e and B_e are replaced by A_h and B_h that are obtained from (79) and (80) by replacing q_e with q_h of (77). Furthermore, $\sqrt{\mu_0/\varepsilon_0}$ of (83) should be replaced by its reciprocal.

5.4.2 *Field Expressions*

The Airy functions can be also used for representing the radial functions in the field expressions (36) to (38) or (50) to (52), where r or y functions enter in the definitions of Δ_q, $G_q(y)$, and $\Delta_q(y)$. The excitation factor Δ_n of (39), the height-gain functions $G_n(y)$ of (40), and the normalized impedances $\Delta_q(y)$ of (41) or (53) can be evaluated by substituting the approximations (69) and (70) and by applying (71) to (73). The results are identical to equations (194), (196), (197), and (199) of Chapter 4 for a spherical geometry; and these equations will not be reproduced in this section.

It is apparent that in the Airy function approximation, there is no difference between the wave numbers or the radial field variations in spherical and cylindrical geometries. The results of the numerical calculations shown in Section 4.5 apply also to cylindrical geometries. The accuracy of Airy function approximations are adequate for most purposes, but more exact reference solutions can be derived using the thin-shell approximations in a multilayer representation of the airspace between the earth and the ionosphere, as will be shown in Section 5.5.

5.5 Multilayer Representations

Multilayer representations are commonly used for approximating a medium of continuously varying properties as a series of homogeneous layers. It is also possible to subdivide a homogeneous medium (like the space between the earth and the ionosphere) into a series of thin shells. This method will have definite advantages if the functions representing the field variations are of limited accuracy, which is improved with a decreasing thickness of the layers. Although the cumulative error due to a multiplication of the field representations of individual layers is increased with an increasing number of layers, the accuracy of the functions in each of the

layers is improved sufficiently to provide a net improvement of the solution accuracy [Galejs, 1967a].

This approach requires a large number of repetitive mathematical operations that can be conveniently described in a matrix notation. After developing the basic matrix formalism, further examples will consider representations based on second-order or Debye approximations of Hankel functions, Taylor series approximations, and the thin-shell approximation of Section 5.3. The latter functions are of the simplest form, and these functions will be used for determining the propagation parameters in a formulation similar to the one described in Section 5.4.1. The developments of this section are limited to field representations in the shell of free space between the earth and the ionosphere. Still, the formulations and the derivations are sufficiently general, and they can be readily adapted for representing the fields within the ionosphere.

5.5.1 *Formulation*

The space above the cylindrical earth of radius a is subdivided in a number of concentric cylindrical shells as is indicated in Fig. 5.2. For purposes of the present discussion, the upper medium represents a homogeneous and sharply bounded model ionosphere. However, this representation can be generalized to include parts of the ionosphere in the stratified regions.

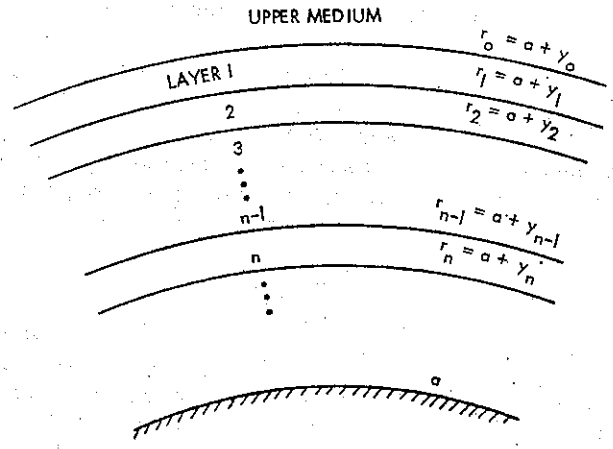

FIG. 5.2 A Cylindrically Stratified Medium

The fields within the nth layer and on its boundaries can be represented in matrix form as

$$[S_n(r)] = [a_n(r)] \cdot [C_n], \tag{89}$$

where $[S_n(r)]$ is a column matrix of the tangential field components, $[C_n]$ is a column matrix of coefficients or wave amplitudes, and $[a_n(r)]$ is a matrix of the functions or the solution matrix.

For T.M. field components (12) to (14), the column matrix of the tangential field components is

$$[S_n(r)] = \begin{bmatrix} E_\varphi(r) \\ H_z(r) \end{bmatrix}; \tag{90}$$

the column matrix of coefficients is

$$[C_n] = \begin{bmatrix} A_e \\ B_e \end{bmatrix}; \tag{91}$$

and the solution matrix has the form

$$[a_n(r)] = \begin{bmatrix} \alpha_1 H_\nu^{(1)}(kr) + \beta [H_\nu^{(1)}(kr)]' & \alpha_1 H_\nu^{(2)}(kr) + \beta [H_\nu^{(2)}(kr)]' \\ H_\nu^{(1)}(kr) & H_\nu^{(2)}(kr) \end{bmatrix}, \tag{92}$$

where the prime denotes a derivative with respect to the argument. For T.M. fields in layers of free space $\alpha_1 = 0$ and $\beta = -i\sqrt{\mu_0/\varepsilon_0}$. For T.E. field components (15) to (17), the column matrix of the tangential field components is

$$[S_n(r)] = \begin{bmatrix} H_\varphi(r) \\ E_z(r) \end{bmatrix} \tag{93}$$

and the column matrix of coefficients is

$$[C_n] = \begin{bmatrix} A_h \\ B_h \end{bmatrix}. \tag{94}$$

For T.E. fields, the solution matrix has also the form (92), where for layers of free space $\alpha_1 = 0$ and $\beta = i\sqrt{\varepsilon_0/\mu_0}$. By noting the differences in the definitions of the various matrices, the subsequent development applies to T.M. as well as T.E. field components.

At the two boundaries, r_{n-1} and r_n of the nth layer, (89) may be written as

$$[S_n(r_{n-1})] = [a_n(r_{n-1})] \cdot [C_n], \tag{95}$$

$$[S_n(r_n)] = [a_n(r_n)] \cdot [C_n]. \tag{96}$$

$[S_n(r_{n-1})]$ is related to $[S_n(r_n)]$ by eliminating $[C_n]$ from (95) and (96) as

$$[S_n(r_n)] = [d_n] \cdot [S_n(r_{n-1})], \tag{97}$$

where

$$[d_n] = [a_n(r_n)] \cdot [a_n^{-1}(r_{n-1})]. \tag{98}$$

The boundary condition at r_{n-1} between the layers (n) and $(n-1)$ is given as

$$[S_n(r_{n-1})] = [S_{n-1}(r_{n-1})] \tag{99}$$

if there are no sources on the boundary. When combining (97) and (99), the fields at the boundary r_n are related to the fields at the boundary r_0 as

$$[S_n(r_n)] = [d_n] \cdot [d_{n-1}] \dots [d_2] \cdot [d_1] \cdot [S_1(r_0)], \tag{100}$$

where the fields at the upper boundary of layer 1

$$[S_1(r_0)] = [a_1(r_0)] \cdot [C_1] \tag{101}$$

can be replaced by fields at the lower boundary of the upper medium

$$[S_u(r_0)] = [a_u(r_0)] \cdot [C_u] \tag{102}$$

following (99). Substituting (101) or (102) in (100), the fields at the boundary r_n are expressed as

$$[S_n(r_n)] = [b_n] \cdot [C_j], \tag{103}$$

where the 2×2 matrix $[b_n]$ is given by

$$[b_n] = [d_n] \cdot [d_{n-1}] \dots [d_2] \cdot [d_1] \cdot [a_j(r_0)] \tag{104}$$

and where the subscript $j = 1$ or u.

An impedance-type boundary condition at the bottom of the ionosphere (19) determines the amplitude B_e/A_e of the waves in the cylindrical shell between the earth and the ionosphere. Similarly, an impedance-type boundary condition at r_0 will determine the ratio between the elements of $[S_1(r_0)]$ of (100) or the ratio of the two amplitudes in the column matrix $[C_1]$ in (101). The fields $[S_n(r_n)]$ at $y = y_n$ are then determined except for one multiplicative constant.

In (102) the matrix $[a_u(r_0)]$ considers the properties of the upper medium, that differs from the free space below $r = r_0$. For a homogeneous upper medium (a homogeneous sharply bounded ionosphere), there will be only up-going waves in the upper medium; and the coefficient matrix becomes

$$[C_u] = \begin{bmatrix} A_q^u \\ 0 \end{bmatrix} \tag{105}$$

where the subscript $q = e$ or h. Substituting (105) in (103) determines the fields at r_n or y_n except for the numerical value of the amplitude A_q^u. The elements of the matrix in $[a_u(r_0)]$ of (102) determine uniquely the ratio of the field components in $[S_u(r_0)]$. This ratio was interpreted as an impedance boundary condition in the earlier approach.

For 2×2 matrices, the matrix $[d_n]$ of (98) can be readily evaluated. After computing the inverse matrix, the matrix elements d_{11} and d_{12} of $[d_n]$ are obtained as

$$d_{11} = \frac{1}{q}[a_{11}(r_n)\, a_{22}(r_{n-1}) - a_{12}(r_n)\, a_{21}(r_{n-1})], \tag{106}$$

$$d_{12} = \frac{1}{q}[a_{12}(r_n)\, a_{11}(r_{n-1}) - a_{11}(r_n)\, a_{12}(r_{n-1})], \tag{107}$$

with

$$q = a_{11}(r_{n-1})\, a_{22}(r_{n-1}) - a_{12}(r_{n-1})\, a_{21}(r_{n-1}). \tag{108}$$

The elements d_{21} and d_{22} are obtained from the expressions for d_{12} and d_{11} by interchanging the indices 1 and 2. The matrices $[d_n]$ will be computed in the following sections for several approximations to the Hankel functions of (92).

5.5.2 *Second-order or Debye Approximation*

For large arguments and $(kr - \nu) \gg (kr)^{1/3}$, the Hankel functions can be approximated by the Debye expansion

$$H_\nu^{(1,2)}(kr) = \sqrt{\frac{2/\pi}{\sqrt{(kr)^2 - \nu^2}}} \exp\{\pm i[g_\nu(kr) - \pi/4]\}, \tag{109}$$

where

$$g_\nu(z) = \sqrt{z^2-\nu^2} - \nu \cos^{-1}(\nu/z) \approx z\left[1 - \frac{\pi}{2}\left(\frac{\nu}{z}\right) + \frac{1}{2}\left(\frac{\nu}{z}\right)^2 + \frac{1}{24}\left(\frac{\nu}{z}\right)^4 + \dots\right] \quad (110)$$

or

$$\left.\begin{aligned} g_\nu(z) &= \sqrt{z^2-\nu^2} - \nu \sin^{-1}\sqrt{1-(\nu/z)^2} = iz\{\sqrt{(\nu/z)^2-1} \\ &\quad -(\nu/z)\log[(\nu/z)+\sqrt{(\nu/z)^2-1}]\}, \end{aligned}\right\} \quad (111)$$

where the square roots are defined with positive real parts. Equation (110) is used for $|\nu/z| \ll 1$ and (111) is used for larger values of $|\nu/z|$. The validity of (109) is further discussed by Watson [1958] for arbitrary complex values of the ratio ν/kr. For typical ionosphere parameters, the right-hand side of (109) may also represent $H_\nu^{(1)}(kr)$ and $2J_\nu(kr)$, where $J_\nu(x)$ is the Bessel function of the first kind, which are also two distinct solutions of the Bessel's differential equations. The function changes are determined primarily by the altitude changes of k and only to a very small degree by changes of r or by ν in the various forms of $g_\nu(kr)$ which enter into the subsequent calculation of the d matrix. The functions remain the same in a given homogeneous layer, and the accuracy of the matrix product $[b_n]$ is not affected by a possible change of functions in two adjacent layers.

Substituting (109) in (92), the elements d_{ij} can be expressed as

$$d_{11} = \frac{1}{P}\left\{\sin[g_{\nu-1}(kr_n) - g_\nu(kr_{n-1})] + \frac{\alpha}{\beta} Q \sin[g_\nu(kr_n) - g_\nu(kr_{n-1})]\right\}, \quad (112)$$

$$\left.\begin{aligned} d_{12} = \frac{1}{P}\Big\{&\alpha \sin[g_{\nu-1}(kr_{n-1}) - g_\nu(kr_n)] - \alpha \sin[g_{\nu-1}(kr_n) - g_\nu(kr_{n-1})] \\ &+ \frac{\alpha^2}{\beta} Q \sin[g_\nu(kr_{n-1}) - g_\nu(kr_n)] + \frac{\beta}{Q}\sin[g_{\nu-1}(kr_{n-1}) - g_{\nu-1}(kr_n)]\Big\}, \end{aligned}\right\} \quad (113)$$

$$d_{21} = \frac{1}{P}\frac{Q}{\beta}\{\sin[g_\nu(kr_n) - g_\nu(kr_{n-1})]\}, \quad (114)$$

$$d_{22} = \frac{1}{P}\left\{\sin[g_{\nu-1}(kr_{n-1}) - g_\nu(kr_n)] + \frac{\alpha Q}{\beta}\sin[g_\nu(kr_{n-1}) - g_\nu(kr_n)]\right\}, \quad (115)$$

where

$$P = \sin[g_{\nu-1}(kr_{n-1}) - g_\nu(kr_{n-1})], \quad (116)$$

$$Q = \left[\frac{(kr_m)^2-(\nu-1)^2}{(kr_m)^2-\nu^2}\right]^{0.25}, \quad (117)$$

and $r_m = (r_n + r_{n-1})/2$. For T.M. fields in free space, $\alpha = -\nu/(i\omega\varepsilon_0 r)$; for T.E. fields $\alpha = \nu/(i\omega\mu_0 r)$. For $\nu \ll kr$, $g_\nu(kr)$ of (110) can be approximated by its three first terms and the elements d_{ij} simplify to

$$d_{11} = \cos(2k\Delta) - \frac{\alpha_1}{\beta} Q \sin(2k\Delta), \quad (118)$$

$$d_{12} = \left[\frac{\beta}{Q} + \frac{\alpha_1^2}{\beta} Q\right]\sin(2k\Delta), \quad (119)$$

$$d_{21} = -\frac{Q}{\beta}\sin(2k\Delta), \quad (120)$$

$$d_{22} = \cos(2k\Delta) + Q\frac{\alpha_1}{\beta}\sin(2k\Delta). \quad (121)$$

where $2\Delta = r_{n-1} - r_n$ and $Q \approx 1$. The matrix elements (118) to (121) are the same as for a planar ionosphere, where the field components exhibit an $\exp(\pm ikr)\, r$ variation.

The Debye approximation (109) is valid for $(kr-\nu) = (kr - k_0 aS) \gg (kr)^{1/3}$. For $S \approx 1$ in free space of $k = k_0$ at $r = a+h$, the inequality can be rearranged into $k_0 h \gg (k_0 r)^{1/3}$. For $h = 80$ km and $f = 15$ kc/s, $k_0 h/(k_0 r)^{1/3} \approx 2$, which satisfies the above inequality only marginally. The Debye approximation appears to be marginally valid for the V.L.F. range in the airspace near the ionospheric boundary, although it may be used for representing the fields within the ionosphere, where $k > k_0$.

5.5.3 *Taylor Series Expansion*

The radial functions of the spherical shell have been expanded in a Taylor series in Section 4.4. A similar expansion can be also used for the Hankel functions of (92).

In the numerators of the matrix elements d_{ij}, the Hankel functions are evaluated at two different values of r, and they can be expanded in a Taylor series about $r_m = r_{n-1} - \Delta = r_n + \Delta$. It follows that

$$\left.\begin{aligned} H_\nu^{(m)}(kr) = H_\nu^{(m)}[k(r_m+\Delta)] = H(w+\delta) &= H(w) + \delta H'(w) + \frac{\delta^2}{2}H''(w) \\ &+ \frac{\delta^3}{6}H'''(w) + \frac{\delta^4}{24}H^{iv}(w). \end{aligned}\right\} \quad (122)$$

The derivative of $H_\nu^{(m)}(kr)$ is computed by differentiating the Taylor series (122) with respect to δ. The higher derivatives of (122) are related to $H(w)$ and $H'(w)$ by Bessel's differential equation and its derivatives. It follows that

$$H'' = -\left[1 - \left(\frac{\nu}{w}\right)^2\right]H - \frac{1}{w}H', \quad (123)$$

$$H''' = \frac{H}{w}\left[1 - 3\left(\frac{\nu}{w}\right)^2\right] + H'\left[-1 + \left(\frac{\nu}{w}\right)^2 + \frac{2}{w^2}\right], \quad (124)$$

$$H^{iv} = H\left\{\left[1 - \left(\frac{\nu}{w}\right)^2\right]^2 - \frac{3}{w^2} + \frac{11}{w^2}\left(\frac{\nu}{w}\right)^2\right\} + \frac{2H'}{w}\left[1 - \frac{3}{w^2} - 3\left(\frac{\nu}{w}\right)^2\right]. \quad (125)$$

After substituting the matrix elements (92), the denominator (108) of d_{ij} becomes

$$q = -\beta W[H_\nu^{(1)}(kr_{n-1}),\, H_\nu^{(2)}(kr_{n-1})] = -\frac{4i\beta}{\pi k r_{n-1}}, \quad (126)$$

$$W[u(x),\, v(x)] = u(x)\,v'(x) - u'(x)\,v(x), \quad (127)$$

denotes the Wronskian. Substitution of (122) in (106) and (107) shows that the following combinations of Hankel functions and their derivatives are required for the evaluation of d_{ij}:

$$P_1 = \{H_\nu^{(1)}(w-\delta)\,H_\nu^{(2)}(w+\delta) - H_\nu^{(1)}(w+\delta)\,H_\nu^{(2)}(w-\delta)\}/W, \quad (128)$$

$$P_2 = \{H_\nu^{(1)}(w+\delta)\,[H_\nu^{(2)}(w-\delta)]' - H_\nu^{(2)}(w+\delta)\,[H_\nu^{(1)}(w-\delta)]'\}/W, \quad (129)$$

$$P_3 = \{H_\nu^{(1)}(w-\delta)\,[H_\nu^{(2)}(w+\delta)]' - H_\nu^{(2)}(w-\delta)\,[H_\nu^{(1)}(w+\delta)]'\}/W, \quad (130)$$

$$P_4 = \{[H_\nu^{(1)}(w-\delta)]'\,[H_\nu^{(2)}(w+\delta)]' - [H_\nu^{(1)}(w+\delta)]'\,[H_\nu^{(2)}(w-\delta)]'\}/W, \quad (131)$$

where $w = kr_m$, $\delta = k\Delta$ and

$$W = W[H_\nu^{(1)}(w),\ H_\nu^{(2)}(w)]. \tag{132}$$

Substitution of (122) to (125) results in

$$P_1 = 2\delta\left\{1-\frac{2}{3}\delta^2\left[1-\left(\frac{\nu}{w}\right)^2\right]+\frac{1}{3}\left(\frac{\delta}{w}\right)^2+\ldots\right\}, \tag{133}$$

$$P_2 = 1+\frac{\delta}{w}-2\delta^2\left[1+\frac{1}{3}\,\frac{\delta}{w}-\left(\frac{\nu}{w}\right)^2\left(1+\frac{\delta}{w}\right)\right]+\left(\frac{\delta}{w}\right)^2\left(1+\frac{\delta}{w}\right)+\ldots, \tag{134}$$

$$P_3 = 1-\frac{\delta}{w}+2\delta^2\left[-1+\frac{1}{3}\,\frac{\delta}{w}+\left(\frac{\nu}{w}\right)^2\left(1-\frac{\delta}{w}\right)\right]+\left(\frac{\delta}{w}\right)^2\left(1-\frac{\delta}{w}\right)+\ldots, \tag{135}$$

$$P_4 = 2\delta\left\{1-\left(\frac{\nu}{w}\right)^2-\frac{2}{3}\delta^2\left[1-\left(\frac{\nu}{w}\right)^2\right]^2+\left(\frac{\delta}{w}\right)^2\left[1-\frac{4}{3}\left(\frac{\nu}{w}\right)^2\right]+\ldots\right\}. \tag{136}$$

Using (133) to (136), the elements d_{ij} are expressed as

$$d_{11} = \left[P_2-\frac{\alpha_1}{\beta}P_1\right]\left(1+\frac{\delta}{w}\right), \tag{137}$$

$$d_{12} = \left[\frac{\alpha_1^2}{\beta}P_1+\alpha_1(P_3-P_2)+\beta P_4\right]\left(1+\frac{\delta}{w}\right), \tag{138}$$

$$d_{21} = -\frac{P_1}{\beta}\left(1+\frac{\delta}{w}\right), \tag{139}$$

$$d_{22} = \left[P_3+\frac{\alpha_1}{\beta}P_1\right]\left(1+\frac{\delta}{w}\right). \tag{140}$$

The above matrix elements can be simplified in the limit of $\nu \ll w$ and $\delta \ll w$ to

$$d_{11} = (1-2\delta^2)-\frac{\alpha_1}{\beta}2\delta\left(1-\frac{2}{3}\delta^2\right), \tag{141}$$

$$d_{12} = \left(\frac{\alpha_1^2}{\beta}+\beta\right)2\delta\left(1-\frac{2}{3}\delta^2\right), \tag{142}$$

$$d_{21} = -\frac{1}{\beta}2\delta\left(1-\frac{2}{3}\delta^2\right), \tag{143}$$

$$d_{22} = (1-2\delta^2)+\frac{\alpha_1}{\beta}2\delta\left(1-\frac{2}{3}\delta^2\right). \tag{144}$$

The expressions $(1-2\delta^2)$ and $2\delta\left(1-\frac{2}{3}\delta^2\right)$ can be recognized as the leading terms in the expansion of $\cos 2k\Delta$ and $\sin 2k\Delta$. The simplified expressions (141) to (144) are therefore in agreement with the corresponding approximations (118) to (121).

The above expressions of the matrix elements include terms proportional to Δ^3, and the error of the expressions can be anticipated to be of the order of Δ^4. After multiplying a number of matrices, the error will be increased proportionally to the number of terms used. When subdividing the height integral (Δy) into m parts, the number of layers $m = (\Delta y)/\Delta$ is inversely proportional to $\Delta = \delta/k$. The total error is also of the order of δ^3, and it is decreased by decreasing the thickness of the layer Δ or by increasing the number of layers n, provided that $\delta < 1$.

5.5.4 *Thin-shell Approximations*

The thin-shell approximations of Section 5.3 can be also used in the multilayer matrix representations. Substitution of (60) and (62) in (92) shows that

$$[a_n(r)] = \begin{bmatrix}(\alpha_1+\alpha_2+\alpha_3)\exp(iK_1r) & (\alpha_1-\alpha_2+\alpha_3)\exp(iK_2r)\\ \exp(iK_1r) & \exp(iK_2r)\end{bmatrix}, \tag{145}$$

where $\alpha_2 = i\beta K/k$, $\alpha_3 = \beta/(2kr_m)$, α_1 and β remain as defined in (92), and K is given by (61). The elements d_{ij} of (106) to (108) are expressed as

$$d_{11} = \frac{1}{q}\left[-i(\alpha_1+\alpha_3)\sin(2K\Delta)+\alpha_2\cos(2K\Delta)\right], \tag{146}$$

$$d_{12} = \frac{i}{q}\left[(\alpha_1+\alpha_3)^2-\alpha_2^2\right]\sin(2K\Delta), \tag{147}$$

$$d_{21} = -\frac{i}{q}\sin(2K\Delta), \tag{148}$$

$$d_{22} = \frac{1}{q}\left[i(\alpha_1+\alpha_3)\sin(2K\Delta)+\alpha_2\cos(2K\Delta)\right], \tag{149}$$

with $q = \alpha_2\exp(-\Delta/r_m)$ and $2\Delta = r_{n-1}-r_n$. In the limit of $|\nu| \ll |k_j r_m|$, the expressions (146) to (149) become identical to the planar approximations (118) to (121). The expressions (146) to (149) are valid for arbitrary values of ν, and they are simpler than the representations (112) to (117) or (133) to (140) which are based on the Debye approximation or the Taylor series expansion of the cylindrical wave functions.

The matrix elements of (145) contain factors $(\nu/r_m) = (k_0 aS/r_m)$ in the parameter K of (61). The root of the modal equation S which was defined at the surface of the earth at $r = a$ is therefore replaced by an effective propagation parameter $S' = Sa/r_m$ of decreased magnitude in a layer with $r = r_m$. This implies an increased phase velocity $v_{ph} \sim 1/\mathrm{Re}\,S'$ and decreased attenuation rate $\alpha \sim \mathrm{Im}\,S'$ with an increasing radius r_m. The radial wave fronts of the cylindrical geometry shown in Fig. 5.3a are characterized by φ = constant. They would exhibit a continuously changing propagation parameter per unit distance in the φ direction with a changing radius r. The radial field variations are exponential in the thin-shell approximation (145), which denotes planar layers. The concentric cylindrical shells shown in Fig. 5.3a are approximated by a number of planar layers of Fig. 5.3b, where the cylindrical wave front is replaced by a stepped wave front in the approximate representation. It may be noted that the wave has travelled a larger physical distance in the upper layer and that this corresponds to an increased phase velocity in these layers.

These stepped wave fronts of Fig. 5.3b can be also replaced by vertical wave fronts. The larger physical distance of the upper layers of Fig. 5.3b has been replaced by a larger electrical distance in Fig 5.3c by defining a height dependent modified permeability or permittivity by

$$[\varepsilon\mu]_{r_m} = (r_m/a)^2\,[\varepsilon\mu]_a \approx \left(1+2\,\frac{r_m-a}{a}\right)[\varepsilon\mu]_a. \tag{150}$$

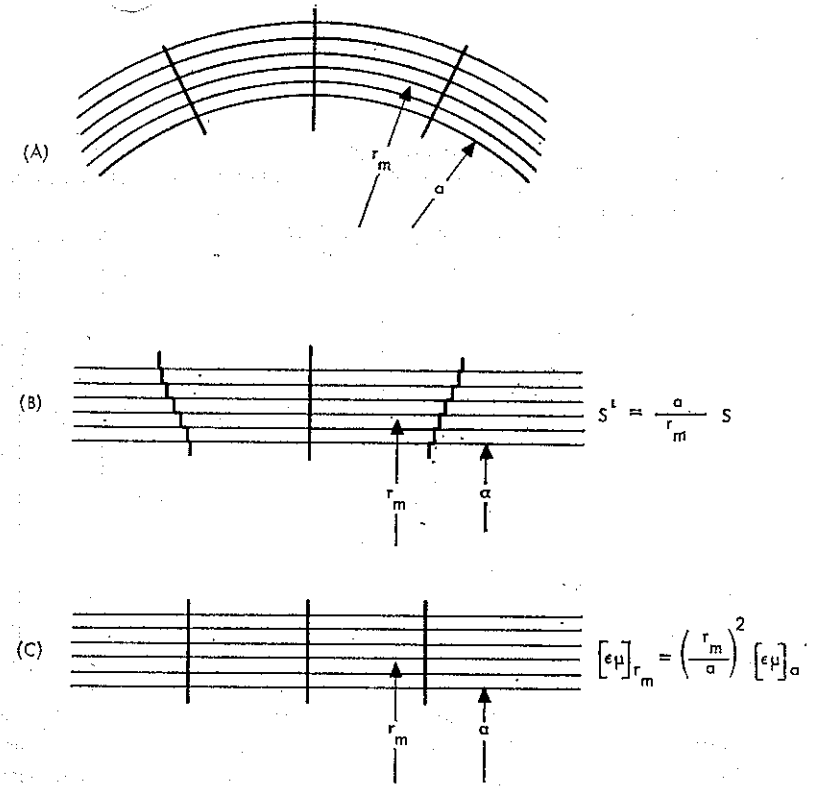

FIG. 5.3 A Cylindrically Stratified Geometry and Its Planar Approximation

The mathematical background for this curved-earth approximation has been developed by Bremmer [1949] and Budden [1961]. In this approach, permeability should be scaled for the T.M. modes and the permittivity for T.E. modes following Richter [1966], and it is also possible to treat anisotropy effects [Pappert *et al*, 1967]. The thin-shell approximations of (145) appear to be closely analogous to the method of modified refractive index in (150).

5.5.5 *Impedance Calculations*

A numerical example will illustrate the use of multilayer field representations in the calculation of the ionospheric surface impedance $Z_b = \sqrt{\mu_0/\varepsilon_0}\,\Delta_b$ ($b = e$ or h) or of the impedance $Z_q(0) = \sqrt{\mu_0/\varepsilon_0}\,\Delta_q(0)$, which is reflected to the ground surface ($y = 0$) in the modes $q = n$ or m by the ionospheric boundary.

For a homogeneous ionosphere model, $Z_e = E_\varphi(a+h)/H_z(a+h) = a_{11}/a_{21}$ and $Z_h = -E_z(a+h)/H_\varphi(a+h) = -a_{21}/a_{11}$ are defined using the elements a_{ij} of the matrix $[a_u(r_0)]$ following (92) and (102). In an isotropic medium, the parameter $\alpha_1 = 0$, but ε_0 should be

replaced by $\varepsilon\varepsilon_0$ in the definitions of β. The wave number k is now defined as $k = \sqrt{\varepsilon}k_0$ with $\varepsilon = 1 + i\sigma_i/(\omega\varepsilon_0)$. After computing the normalized impedances Δ_e or Δ_h using either the Debye approximation of Section 5.5.2 or the thin-shell approximations of Section 5.5.4, the propagation parameter S is determined by solving the modal equation of Section 5.4.1. This value of S (or the corresponding values of $\nu = k_0 aS$) is substituted in the matrix elements (137) to (140) of the Taylor series representation or (146) to (149) of the thin-shell approximations, which relate the tangential electric fields in the successive cylindrical shells. After multiplying out a sequence of $[d_n]$ matrices over the height range from $r_i = a+h$ to $r_g = a$, the fields at the ground surface are determined as shown in (103) and (104). The impedance reflected to the ground surface $Z(0)$ of the T.M. or T.E. modes is determined as $E_\varphi(a)/H_z(a) = b_{11}/b_{21}$ or $-E_z(a)/H_\varphi(a) = -b_{21}/b_{11}$, where b_{ij} are elements of the matrix $[b_n]$ that is defined by (104) with $j = u$.

A homogeneous sharply bounded ionosphere model of $\sigma_i = 10^{-5}$ mho/m and $h = 85$ km has been considered in the examples of Chapter 4, and the same model will be used also in the present calculations. For $f = 20$ kc/s, the normalized ionospheric surface impedances are obtained as $\Delta_e = Z_e/\sqrt{\mu_0/\varepsilon_0} \approx 0.250 - i0.227$ and $\Delta_h = Z_h/\sqrt{\mu_0/\varepsilon_0} \approx 0.222 - i0.251$, where impedances based on the Debye approximation differ from thin-shell approximations by less than 10^{-5}. These numerical impedances are substituted together with the normalized ground impedances Δ_g in the modal equation of Section 5.4.1 to determine the propagation parameters Re $S = c/v$ and α, that are shown in Table 5.1. The various approximations give nearly identical propagation parameters for a given mode and a given ground conductivity σ_g.

TABLE 5.1 IMPEDANCE COMPUTATIONS USING MULTILAYER FIELD REPRESENTATIONS
Airy functions in the modal equation. Sharply bounded isotropic ionosphere of $h = 85$ km and $\sigma_i = 10^{-5}$ mho/m, $f = 20$ kc/s, $C = 0.5$

σ_g (mho/m)		5			0.001		
Fields in	ionosphere / air	Debye approx. Taylor series		Thin-shell approx.	Debye approx. Taylor series		Thin-shell approx.
$n = 1$	Re $(S) = c/v$	1.00351	1.00351	1.00351	1.00386	1.00386	1.00386
	α(db/1000 km)	2.2104	2.2105	2.2139	3.3802	3.3802	3.3826
	$-Z(0)/Z_g$	4.1742	4.1742	4.1672	1.0084	1.0084	1.0083
		$-i1.6284$	$-i1.6283$	$-i1.6206$	$-i0.0276$	$-i0.0276$	$-i0.0275$
$n = 2$	Re $(S) = c/v$	0.99564	0.99564	0.99565	0.99653	0.99653	0.99653
	α(db/1000 km)	5.1482	5.1483	5.1561	8.6817	8.6817	8.6893
	$-Z(0)/Z_g$	4.8788	4.8788	4.8707	1.0373	1.0373	1.0373
		$-i4.5000$	$-i4.5000$	$-i4.4934$	$-i0.0619$	$-i0.0619$	$-i0.0618$
$m = 1$	Re $(S) = c/v$	1.00338	1.00338	1.00338	1.00338	1.00338	1.00338
	α(db/1000 km)	0.3657	0.3657	0.3650	0.3722	0.3722	0.3715
	$-Z(0)/Z_g$	885.44	885.44	885.10	13.514	13.514	13.509
		$-i832.86$	$-i832.86$	$-i832.64$	$-i11.845$	$-i11.845$	$-i11.842$
$m = 2$	Re $(S) = c/v$	0.99119	0.99119	0.99119	0.99121	0.99121	0.99121
	α(db/1000 km)	0.8384	0.8384	0.8369	0.8930	0.8930	0.8915
	$-Z(0)/Z_g$	451.08	451.08	451.05	7.3421	7.3421	7.3418
		$-i434.70$	$-i434.70$	$-i434.69$	$-i6.1826$	$-i6.1826$	$-i6.1825$

A decrease of the ground conductivity from $\sigma_g = 5$ to 0.001 mho/m increases Re S and α for T.M. (n) modes, but the resulting changes are almost negligible for T.E. (m) modes. The impedance reflected to the ground surface $Z(0)$ differs from the negative of the ground impedance $(-Z_g)$ in the examples of Table 5.1. The ratio $-Z(0)/Z_g$ differs from unity only slightly in the T.M. modes for a poorly conducting ground. This ratio is higher for a highly conducting ground surface, and it is particularly high for the T.E. modes. The deviations of the ratio $-Z(0)/Z_g$ are increased in the $n = 2$ relative to the $n = 1$ mode and in the $m = 1$ relative to the $m = 2$ modes.

The impedance boundary conditions at the ground surface and the ionospheric boundary should be satisfied for accurately determined propagation parameters. However, the modal equation of Section 5.4.1 involves Airy functions, and its solution will satisfy the boundary conditions only in the Airy function approximation of the cylindrical wave functions. The accuracy of the multilayer field representations is increased by subdividing the airspace between the ionospheric boundary and the ground surface in an increasing number of layers following the discussion of Section 5.5.3. The impedance $Z(0)$ is not changed by decreasing the layer thickness from $r_{n-1} - r_n = 0.6$ km to 0.2 or 0.1 km, and is believed to be accurate for any of these layer thicknesses. The ratio $-Z(0)/Z_g$ is nearly the same for the Taylor series and thin-shell approximations in Table 5.1, which implies comparable accuracies of these two field representations. The magnitude of the ratio $-Z(0)/Z_g$ differs significantly for various ground conductivities and mode types. The propagation parameters are quite insensitive to changes of σ_g when σ_g is large, and the relatively large deviations of $-Z(0)$ from Z_g for σ_g large may affect the accuracy of the computed propagation parameters in about the same way as the relatively small deviations of $-Z(0)$ from Z_g for the smaller values of σ_g. The large differences between the $-Z(0)/Z_g$ figures for the T.E. and T.M. modes will be further clarified by examining the height variations of the normalized impedance $\Delta_q(y)$.

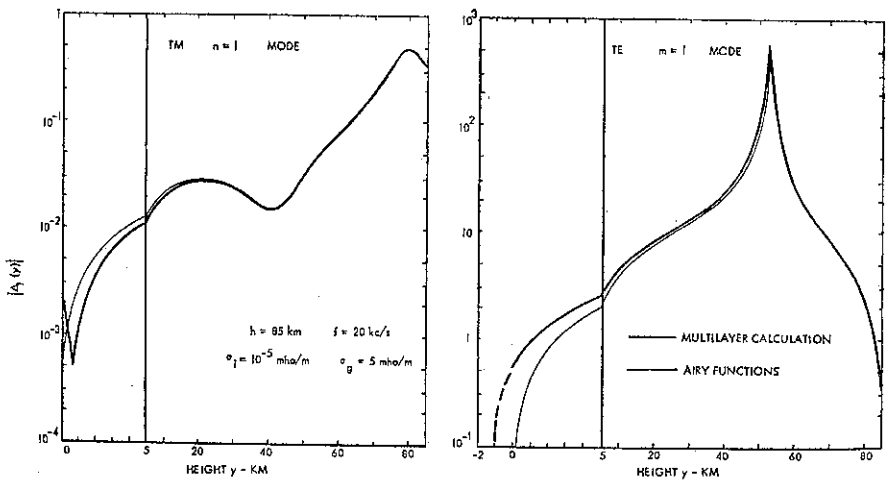

FIG. 5.4 Normalized Impedance $|\Delta_1(y)|$ for a Sharply Bounded Homogeneous and Isotropic Ionosphere Model

The height variations of the impedance $\Delta_q(y)$ are examined in Fig. 5.4 in the Airy function and multilayer approximation of the cylindrical functions. The normalized impedance $\Delta_q(y)$ satisfies the boundary conditions at the earth $[\Delta_q(0) = -\Delta_g]$ and at the ionosphere $[\Delta_n(h) = \Delta_e, \Delta_m(h) = \Delta_h]$ in the Airy function approximation of the cylindrical functions as is seen from the thin line curves of Fig. 5.4. The normalized impedance of the multilayer representations start with the ionospheric surface impedance near the ionospheric boundary, but it differs from the Airy function approximation of the impedance $\Delta_q(y)$ near the ground surface. For the T.M. mode, the impedance reaches a minimum at a height of approximately 1 km above the ground, for the T.E. mode at the height of approximately 1 km below the ground surface. A solution that is based on the Airy function approximation of the cylindrical wave functions is characterized by an approximately 1 km uncertainty in the waveguide height in both the T.E. and T.M. modes. The large values of the ratio $-Z_g/Z(0)$ of the T.E. modes shown in Table 5.1 are caused by the rapid variations of $\Delta_m(y)$ near the ground surface, which is further illustrated by the curve shown in Fig. 4.14 (p. 120). However, the large $-Z_g/Z(0)$ ratios of the T.E. modes correspond to approximately the same uncertainty in the waveguide height as for the T.M. modes.

The height variations of $\Delta_q(y)$ are more cumbersome to calculate, and the impedance ratio $-Z(0)/Z_g$ will be listed in the further examples to illustrate the accuracy of a given approximate solution. However, these ratios should be interpreted in the light of the data shown in Table 5.1 and Fig. 5.4.

5.5.6 *The Modal Condition*

A sequence of thin-layer representations provides accurate fields in the space between the earth and the ionosphere, and an accurate impedance $Z(0)$, which is reflected at the ground level by the ionosphere. Using a propagation parameter S_0 determined in the Airy function approximation from the modal equations of Section 5.4.1, this impedance $Z(0)$ differs from the impedance $(-Z_g)$, which has been attributed to inaccuracies of the Airy functions. It should be possible to compute a corrected propagation parameter $S_1 = S_0 + \delta S$ that would make $Z(0)$ approach $(-Z_g)$. Such calculations have been carried out in Airy function approximation of the cylindrical wave functions in Section 5.4.1, and a similar procedure can be also used with the multilayer field representations. In this approach, it is necessary to determine the variations of the normalized impedances $\Delta_n(0)$ or $\Delta_m(0)$ with the propagation parameter S in (86) or (87), which have been related to the derivatives of the tangential field components (82) or (88). In the multilayer representations, it will be also necessary to compute the derivatives of the tangential field components $\partial E_\varphi(0)/\partial S$ and $\partial H_z(0)/\partial S$ for T.M. modes or $\partial_\varphi H(0)/\partial S$ and $\partial E_z(0)/\partial S$ for the T.E. modes. A given field representation is valid only in one of the layers, and the derivatives must be also computed for each of the many layers. The thin-shell approximations of Section 5.5.4 have provided the simplest expressions for the $[d_n]$ matrix that characterizes the field changes in the successive layers. The above derivatives will be also computed using this same field representation.

For T.M. modes in free space, (89) to (91) and (145) can be rewritten as

$$E_\varphi(r) = a_{11}(r)A_e + a_{12}(r)B_e, \tag{151}$$

$$H_z(r) = a_{21}(r)A_e + a_{22}(r)B_e, \tag{152}$$

with

$$\left.\begin{aligned} a_{11} &= (K_1/\omega\varepsilon_0)\exp(iK_1 r), \quad & a_{12} &= (K_2/\omega\varepsilon_0)\exp(iK_2 r) \\ a_{21} &= \exp(iK_1 r), & a_{22} &= \exp(iK_2 r), \end{aligned}\right\} \tag{153}$$

where for the shell n, $r_{n-1} \geqslant r \geqslant r_n$ and where

$$K_{1,2} = \frac{i}{2r_m} \pm K \tag{154}$$

with

$$K = \sqrt{k_0^2 - \frac{\nu^2+0.25}{r_m^2}}\,. \tag{155}$$

The derivatives of the field components are formally computed as

$$\frac{\partial}{\partial S}E_\varphi(r) = a_{11}\frac{\partial}{\partial S}A_e + A_e\frac{\partial}{\partial S}a_{11} + a_{12}\frac{\partial}{\partial S}B_e + B_e\frac{\partial}{\partial S}a_{12}, \tag{156}$$

$$\frac{\partial}{\partial S}H_z(r) = a_{21}\frac{\partial}{\partial S}A_e + A_e\frac{\partial}{\partial S}a_{21} + a_{22}\frac{\partial}{\partial S}B_e + B_e\frac{\partial}{\partial S}a_{22}. \tag{157}$$

The S-dependence of the matrix elements a_{ij} can be seen from the definitions in (153), but the S-dependence of the amplitudes A_e and B_e will become more apparent after relating them to E_φ and H_z at the upper boundary $r = r_{n-1}$ of the shell n, which will be denoted as r_u in the subsequent development. The elements of the matrix $[a_n(r_{n-1})]$ are denoted similarly as a_{ij}^u. Substituting $r = r_u$ in (151) and (152) and solving for A_e and B_e gives

$$A_e = [a_{12}^u H_z(r_u) - a_{22}^u E_\varphi(r_u)]/f, \tag{158}$$

$$B_e = [a_{21}^u E_\varphi(r_u) - a_{11}^u H_z(r_u)]/f, \tag{159}$$

where

$$f = a_{12}^u a_{21}^u - a_{11}^u a_{22}^u. \tag{160}$$

The S-dependence of A_e and B_e is therefore related to the S-dependence of the field components and of the matrix elements a_{ij} that are all evaluated at the upper boundary $r_{n-1} = r_u$ of the shell n. Substituting (158) to (160) in (156) and (157) and carrying out the differentiations leads to

$$\left.\begin{aligned} \frac{\partial}{\partial S}E_\varphi(r) = \frac{\exp\left(\frac{r_u-r}{2r_m}\right)}{K}\Bigg\{ & E_\varphi(r_u)\frac{\partial K}{\partial S}\left[\left(1+\frac{r_u-r}{2r_m}\right)\cos K(r_u-r) - K(r_u-r)\sin K(r_u-r)\right] - \frac{iH_z(r_u)}{\omega\varepsilon_0}\frac{\partial K}{\partial S}\left[(r_u-r)\times\left(K^2+\frac{1}{4r_m^2}\right)\cos K(r_u-r) + 2K\sin K(r_u-r)\right] - \frac{i}{\omega\varepsilon_0}\left[\frac{\partial H_z(r_u)}{\partial S} - \frac{H_z(r_u)}{K}\frac{\partial K}{\partial S}\right]\left[K^2+\frac{1}{4r_m^2}\right]\sin K(r_u-r) + \left[\frac{\partial E_\varphi(r_u)}{\partial S} - \frac{E_\varphi(r_u)}{K}\frac{\partial K}{\partial S}\right]\left[K\cos K(r_u-r) + \frac{1}{2r_m}\sin K(r_u-r)\right]\Bigg\} \end{aligned}\right. \tag{161}$$

and

$$\left.\begin{aligned} \frac{\partial}{\partial S}H_z(r) = \frac{\exp\left(\frac{r_u-r}{2r_m}\right)}{K}\Bigg\{ & -i\omega\varepsilon_0 E_\varphi(r_u)\frac{\partial K}{\partial S}(r_u-r)\cos K(r_u-r) + H_z(r_u)\frac{\partial K}{\partial S}\left[\left(1-\frac{r_u-r}{2r_m}\right)\cos K(r_u-r) - K(r_u-r)\sin K(r_u-r)\right] + \left[\frac{\partial H_z(r_u)}{\partial S} - \frac{H_z(r_u)}{K}\frac{\partial K}{\partial S}\right]\left[K\cos K(r_u-r) - \frac{1}{2r_m}\sin K(r_u-r)\right] - i\omega\varepsilon_0\left[\frac{\partial E_\varphi(r_u)}{\partial S} - \frac{E_\varphi(r_u)}{K}\frac{\partial K}{\partial S}\right]\sin K(r_u-r)\Bigg\}. \end{aligned}\right. \tag{162}$$

The limit $r \to r_u$ of (161) and (162) shows that the derivatives are continuous across the boundary $r = r_u$ of the layer. After computing the surface impedance Z_e at the ionospheric boundary $r = r_0$, the propagation parameter S has been formerly calculated by assuming Z_e to remain constant during the initial solution of the modal equation [(74), see Section 5.4.1]. A similar assumption is also made in the present development, which implies that $\partial E_\varphi(r_0)/\partial S$ and $\partial H_z(r_0)/\partial S = 0$. It can be seen that $\partial E_\varphi(r)/\partial S$ will increase linearly and $\partial H_\varphi(r)/\partial S$ quadratically with the distance $(r_0 - r)$ from the ionospheric boundary. The derivatives $\partial E_\varphi(r)/\partial S$ and $\partial H_z(r)/\partial S$ of a given layer n depend on the derivatives $\partial E_\varphi(r_u)/\partial S$, $\partial H_z(r_u)/\partial S$, and on the field components $E_\varphi(r_u)$ and $H_z(r_u)$ evaluated at the upper boundary $r_{n-1} = r_u$ of this layer. A successive application of (161) and (162) requires also a knowledge of $E_\varphi(r)$ and $H_z(r)$ at every boundary of the shells.

The field components $E_\varphi(r)$ and $H_z(r)$ of layer n will depend on the fields $E_\varphi(r_u)$ and $H_z(r_u)$ at the upper boundary $r_{n-1} = r_u$ of the layer. Substituting (158) to (160) in (151) and (152), it follows that

$$\left.\begin{aligned} E_\varphi(r) = \frac{\exp\left(\frac{r_u-r}{2r_m}\right)}{K}\Bigg\{ & E_\varphi(r_u)\left[K\cos K(r_u-r) + \frac{1}{2r_m}\sin K(r_u-r)\right] - \frac{iH_z(r_u)}{\omega\varepsilon_0}\left[K^2+\frac{1}{4r_m^2}\right]\sin K(r_u-r)\Bigg\}, \end{aligned}\right. \tag{163}$$

$$\left.\begin{aligned} H_z(r) = \frac{\exp\left(\frac{r_u-r}{2r_m}\right)}{K}\Bigg\{ & -i\omega\varepsilon_0 E_\varphi(r_u)\sin K(r_u-r) + H_z(r_u)\left[K\cos K(r_u-r) - \frac{1}{2r_m}\sin K(r_u-r)\right]\Bigg\}. \end{aligned}\right. \tag{164}$$

These equations are reduced to trivial identities in the limit of $r \to r_u$.

Alternately, $E_\varphi(r_u)$ and $H_z(r_u)$ at the upper boundary $r_{n-1} = r_u$ of shell n are obtained using elements b_{ij} of the matrix $[b_{n-1}]$ of (103) and (104) with $j = 1$. It is seen that

$$E_\varphi(r_u)\big|_n = b_{11} + b_{12}(B_e/A_e)_{n=1}, \tag{165}$$

$$H_z(r_u)\big|_n = b_{21} + b_{22}(B_e/A_e)_{n=1}, \tag{166}$$

where the field components of shell n are defined using the matrix $[b_{n-1}]$ and the amplitudes A_e and B_e of the coefficient matrix $[C_1]$ of the shell just below the ionospheric boundary ($n = 1$). The amplitude ratio B_e/A_e is determined from the impedance boundary condition (19) at $r = r_0$, which gives

$$\left.\frac{B_e}{A_e}\right|_{n=1} = \frac{a_{11}(r_0) - Z_e a_{21}(r_0)}{Z_e a_{22}(r_0) - a_{12}(r_0)}, \tag{167}$$

where $a_{ij}(r_0)$ are elements of the matrix $[a_1(r_0)]$.

For T.E. modes, E_φ of the previous development can be replaced by H_φ and H_z by E_z, if ε_0 is replaced by $(-\mu_0)$ in (153) and (161) to (164) and if the subscripts e are changed to h. The ratio $\left.B_h/A_h\right|_{n=1}$ is determined from the impedance boundary condition (19) at $r = r_0$ as

$$\left.\frac{B_h}{A_h}\right|_{n=1} = -\frac{a_{21}(r_0) + Z_h a_{11}(r_0)}{a_{22}(r_0) + Z_h a_{12}(r_0)}. \tag{168}$$

The initial value $S = S_0$ of the calculations is obtained from a modal equation that involves Airy functions. Using this value of S_0, the S-derivatives of the field components and also the field components are evaluated in the successive layers from $r_i = a + h$ down to $r_g = a$. A corrected value $S_1 = S_0 + C\,\delta S$ is then computed using (82) and (86) for T.M. modes or (87) and (88) for T.E. modes, where the constant C is less than one. These calculations are iterated and S_n is computed using S_{n-1} in the calculation of the field components and their S-derivatives.

The numerical calculations are made for a sharply bounded homogeneous model ionosphere, that was considered in the examples shown in Table 5.1. The effects of various choices of the convergence constant C are illustrated in Table 5.2 for a fixed number of four iterations in the

TABLE 5.2 THE S VALUES AND IMPEDANCE RATIO $-Z(0)/Z_e$ FOR THE MODAL EQUATION BASED ON MULTILAYER FIELD REPRESENTATIONS

$h = 85$ km, $\sigma_i = 10^{-5}$ mho/m, $\sigma_g = 5$ mho/m, $f = 20$ kc/s

	C	S	$-Z(0)/Z_e$
$n = 1$	0.5	1.0034885 + i0.00060719	1.011 − i0.0018
	0.65	1.0034885 + i0.00060721	0.9991 − i0.0058
	0.8	1.0034885 + i0.00060722	0.9989 − i0.0014
	0.9	1.0034885 + i0.00060772	0.9995 − i0.0002
$m = 1$	0.5	1.0033327 + i0.00010211	4.28 − i2.10
	0.65	1.0033327 + i0.00010101	1.57 − i0.054
	0.8	1.0033327 + i0.00010101	1.07 − i0.088
	0.9	1.0033327 + i0.00010101	1.01 − i0.025

S computations. The ratio $-Z(0)/Z_g$ deviates more from unity for the smaller values of C, although the corresponding S changes are negligible. For larger values of C, the sequence of $-Z(0)/Z_g$ is not changing monotonically between successive iterations, and there is a possibility of divergence. The calculations shown in Table 5.3 are made for $C = 0.5$ and illustrate the effects of higher modes ($n, m = 2$) and changes in the ground conductivity σ_g. The multilayer

TABLE 5.3 MODAL EQUATIONS USING AIRY FUNCTIONS AND MULTILAYER FIELD REPRESENTATIONS

Thin-shell approximations in impedance calculation. Sharply bounded isotropic ionosphere of $h = 85$ km and $\sigma_i = 10^{-5}$ mho/m, $f = 20$ kc/s. $C = 0.5$

σ_g(mho/m)		5		0.001	
Modal equations		Airy function	Multilayer	Airy function	Multilayer
$n = 1$	Re $(S) = c/v$	1.00351	1.00349	1.00386	1.00384
	α(db/1000 km)	2.2139	2.2077	3.3826	3.3984
		4.1672	1.0107	1.0083	0.9999
	$-Z(0)/Z_e$	$-i$1.6206	$-i$0.0184	$-i$0.0275	$-i$0.0002
$n = 2$	Re $(S) = c/v$	0.99565	0.99554	0.99653	0.99643
	α(db/1000 km)	5.1561	5.1885	8.6893	8.7363
		4.8707	1.0055	1.0372	0.999999
	$-Z(0)/Z_e$	$-i$4.4934	$-i$0.0125	$-i$0.0618	$-i$0.0002
$m = 1$	Re $(S) = c/v$	1.00338	1.00333	1.00338	1.00333
	α(db/1000 km)	0.3650	0.3673	0.3715	0.3740
		885.10	4.2776	13.509	1.0464
	$-Z(0)/Z_e$	$-i$832.64	$-i$2.1004	$-i$11.842	$-i$0.0299
$m = 2$	Re $(S) = c/v$	0.99119	0.99100	0.99121	0.99101
	α(db/1000 km)	0.8369	0.84362	0.8915	0.899653
		451.05	1.3900	7.3418	1.0055
	$-Z(0)/Z_e$	$-i$434.69	$-i$0.5146	$-i$6.1825	$-i$0.0073

solution of the modal equation provides ratios of $-Z(0)/Z_g$ that differ much less from unity than in the Airy function solution, although the difference between the corresponding Re $S = c/v$ figures is less than 10^{-4} and between attenuation rates α is less than 10^{-2}. It is possible to reduce the deviations of $-Z(0)/Z_g$ even further by increasing the number of iterations of the S computations or by increasing the value of the convergence constant C, as has been illustrated in Table 5.2. However, such calculations cannot be expected to yield a noticeable change of the propagation parameters Re S or α.

It has been shown that the boundary conditions at the earth and the ionosphere can be satisfied with arbitrary accuracy in the multilayer solution of the modal equation. Although accuracies of the type shown in Table 5.2 can be achieved, there are no obvious merits for developing solutions with accuracies beyond those indicated in Table 5.3.

5.6 Fields Below an Anisotropic Ionosphere

5.6.1 *Modal Equation*

In developments of the preceding sections, the ground surface was characterized by an impedance Z_g and the ionospheric boundary by surface impedances Z_e and Z_h for the T.M. and T.E. modes respectively. It was also observed that T.E. and T.M. waves are not coupled within the cylindrical waveguide between the earth and the ionosphere. In a generally anisotropic

ionosphere, the T.E. and T.M. wave components are coupled; and the resulting surface impedance Z_e will depend on Z_h or vice versa. This leads to coupling between the T.E. and T.M. wave components in the earth-to-ionosphere waveguide and to more complicated conditions for determining the permissible propagation parameters $\nu = k_0 aS$.

In the cylindrical coordinate system of Fig. 5.1, the fields are assumed to exhibit no variations in the z direction. The wave propagation is in the φ direction, and all the field components exhibit a φ variation of the form $\exp(i\nu\varphi)$. Equations (12) to (17) show that in the airspace of $a \ll r \ll (a+h)$, the φ and z components of the fields are of the form

$$E_\varphi(r) = i-\eta[A_e H_\nu^{(1)}(k_0 r)' + B_e H_\nu^{(2)}(k_0 r)'], \tag{169}$$

$$H_z(r) = A_e H_\nu^{(1)}(k_0 r) + B_e H_\nu^{(2)}(k_0 r), \tag{170}$$

$$H_\varphi(r) = (i/\eta)\,[A_h H_\nu^{(1)}(k_0 r)' + B_h H_\nu^{(2)}(k_0 r)'], \tag{171}$$

$$E_z(r) = A_h H_\nu^{(1)}(k_0 r) + B_h H_\nu^{(2)}(k_0 r), \tag{172}$$

where $H_\nu^{(m)}(x)$ denotes a Hankel function of complex order ν and kind m, the primes denote derivatives with respect to the argument, and $\eta = \sqrt{\mu_0/\varepsilon_0} = 120\pi$ ohms.

The T.M. (E_φ, H_z) and the T.E. (H_φ, E_z) field components are coupled only in the anisotropic medium, and the boundary conditions at h will determine a relation between A_e, B_e and A_h, B_h. After imposing boundary conditions at the ground surface $r = a$ and the ionospheric boundary $r = a+h$, equations (169) to (172) will be combined into a modal equation, the solutions of which determine permissible eigenvalues $\nu = k_0 aS$.

At the ground surface

$$Z_g = -\frac{E_\varphi(a)}{H_z(a)} = \frac{E_z(a)}{H_\varphi(a)}. \tag{173}$$

Substituting (169) to (172) in (173), it follows that

$$\frac{B_e}{A_e} = -\frac{H_\nu^{(1)\prime}(u_g) + i\Delta_g H_\nu^{(1)}(u_g)}{H_\nu^{(2)\prime}(u_g) + i\Delta_g H_\nu^{(2)}(u_g)}, \tag{174}$$

$$\frac{B_h}{A_h} = -\frac{H_\nu^{(1)}(u_g) - i\Delta_g H_\nu^{(1)\prime}(u_g)}{H_\nu^{(2)}(u_g) - i\Delta_g H_\nu^{(2)\prime}(u_g)}, \tag{175}$$

where $\Delta_g = Z_g/\eta$ and $u_g = k_0 a$. At the ionospheric boundary $r = a+h$, the surface impedance of the T.M. and T.E. field components is computed from (169) to (172) as

$$Z_e = \frac{E_\varphi(a+h)}{H_z(a+h)} = -i\eta\,\frac{H_\nu^{(1)\prime}(u_l) + H_\nu^{(2)\prime}(u_l)\,(B_e/A_e)}{H_\nu^{(1)}(u_l) + H_\nu^{(2)}(u_l)\,(B_e/A_e)}, \tag{176}$$

$$Z_h = -\frac{E_z(a+h)}{H_\varphi(a+h)} = i\eta\,\frac{H_\nu^{(1)}(u_l) + H_\nu^{(2)}(u_l)\,(B_h/A_h)}{H_\nu^{(1)\prime}(u_l) + H_\nu^{(2)\prime}(u_l)\,(B_h/A_h)}, \tag{177}$$

where $u_l = k_0(a+h)$. The electric field components E_φ and E_z can be related at $r = a+h$ by an impedance matrix to the magnetic field components H_φ and H_z. Thus

$$E_\varphi = Z_{11} H_\varphi + Z_{12} H_z, \tag{178}$$

$$E_z = -Z_{21} H_\varphi - Z_{22} H_z. \tag{179}$$

After computing $Z_e = E_\varphi/H_z$ and $Z_h = -E_z/H_\varphi$, the unknown ratio H_φ/H_z can be eliminated from the two equations which gives

$$(Z_e - Z_{12})\,(Z_h Z_{21}) = Z_{11} Z_{22}, \tag{180}$$

where Z_e and Z_h are defined in terms of fields below the ionosphere by (176) and (177). The impedances Z_{ij} are related to the ionospheric reflection coefficients [Wait, 1963]. The impedances Z_{ij} can be also computed from the solution of the fields within the ionosphere, as will be commented on below. Equation (180) can be solved for the eigenvalues ν. For uncoupled T.E. and T.M. modes, the right-hand side of (180) is equal to zero; and two factors on the left-hand side represent modal equations of T.M. and T.E. modes respectively, which have been discussed in Section 5.2.2. A modal condition, expressed in terms of reflection coefficients [Budden, 1962], has been used by Pappert *et al.* [1967] in a similar problem.

In the ionosphere model of Fig. 5.1, the upper region is unbounded; and it can support waves in two outgoing magneto-ionic modes, the amplitudes of which are designated as A_{1u} and A_{3u}. The fields at $r = a+h$ are formally expressed in terms of these wave amplitudes as

$$E_\varphi(a+h) = q_{11}\,A_{1u} + q_{13}\,A_{3u}, \tag{181}$$

$$H_z(a+h) = q_{21}\,A_{1u} + q_{23}\,A_{3u}, \tag{182}$$

$$H_\varphi(a+h) = q_{31}\,A_{1u} + q_{33}\,A_{3u}, \tag{183}$$

$$E_z(a+h) = q_{41}\,A_{1u} + q_{43}\,A_{3u}, \tag{184}$$

where q_{ij} are determined from field solutions in the anisotropic medium. A substitution of (181) to (184) in (178) and (179) shows that

$$Z_{11} = (q_{11}\,q_{23} - q_{13}\,q_{21})/D_1, \tag{185}$$

$$Z_{21} = (q_{43}\,q_{21} - q_{41}\,q_{23})/D_1, \tag{186}$$

$$Z_{12} = (q_{11}\,q_{33} - q_{13}\,q_{31})/D_2, \tag{187}$$

$$Z_{22} = (q_{43}\,q_{31} - q_{41}\,q_{33})/D_2, \tag{188}$$

with

$$D_1 = q_{31}\,q_{23} - q_{33}\,q_{21}, \tag{189}$$

$$D_2 = q_{21}\,q_{33} - q_{23}\,q_{31}. \tag{190}$$

Substituting (185) to (190) in (180), a lengthy algebraic manipulation leads to

$$(Z_e\,q_{23} - q_{13})\,(Z_h\,q_{31} + q_{41}) = (Z_e\,q_{21} - q_{11})\,(Z_h q_{33} + q_{43}), \tag{191}$$

where Z_e and Z_h are defined in terms of fields below the ionosphere by (176) and (177). Equation (191) can be derived with less analytical effort by computing Z_e and Z_h from (181) to (184) in terms of the ionosphere fields as

$$Z_e = \frac{E_\varphi(a+h)}{H_z(a+h)} = \frac{q_{11} + q_{13}(A_{3u}/A_{1u})}{q_{21} + q_{23}(A_{3u}/A_{1u})}, \tag{192}$$

$$Z_h = -\frac{E_z(a+h)}{H_\varphi(a+h)} = -\frac{q_{41} + q_{43}(A_{3u}/A_{1u})}{q_{31} + q_{33}(A_{3u}/A_{1u})}, \tag{193}$$

and by eliminating the unknown amplitude ratio from (192) and (193). Equation (191) or the

two coupled equations (192) and (193) are equivalent to the modal equation (180), and any of these equations can be used for determining the eigenvalue $\nu = k_0 aS$ of the waves. In this chapter, the parameter ν is determined from an iterative solution of (192) and (193) and also from a direct solution of (191).

5.6.1.1 *Iterative Solution of Coupled Equations*

At first, the surface impedance of T.E. modes Z_h is computed from (175) and (177) for an assumed value $\nu = \nu_0$. Using this value of Z_h, (193) can be solved for the amplitude ratio (A_{3u}/A_{1u}) as

$$\frac{A_{3u}}{A_{1u}} = -\frac{q_{41}+q_{31}Z_h}{q_{43}+q_{33}Z_h}, \tag{194}$$

which determines uniquely the relative amplitudes of the two upgoing waves of the upper half-space. The surface impedance Z_e, which is seen by the T.M. fields at the bottom of the ionosphere ($r = a+h$), is computed substituting (A_{3u}/A_{1u}) of (194) into (192). This value of Z_e is substituted in the left-hand side of (176). Using the (B_e/A_e) ratio of (174), (176) can be rearranged into

$$\frac{H_\nu^{(2)}(u_g)' + i\Delta_g H_\nu^{(2)}(u_g)}{H_\nu^{(1)}(u_g)' + i\Delta_g H_\nu^{(1)}(u_g)} \cdot \frac{H_\nu^{(1)}(u_i)' - i\Delta_e H_\nu^{(1)}(u_i)}{H_\nu^{(2)}(u_i)' - i\Delta_e H_\nu^{(2)}(u_i)} = 1, \tag{195}$$

where $u_g = k_0 a$, $u_i = k_0(a+h)$, where $\Delta_g = Z_g/\eta$, $\Delta_e = Z_e/\eta$, and where Z_e is given by (192). Equation (195) may be recognized as the modal equation of T.M. modes (22), but Δ_e (or Z_e) of this equation reflects the presence of the T.E. modes in the space between the earth and the ionosphere. The solution of (195) will give an improved estimate of $\nu = \nu_1$, which should be used in a repeated calculation of Z_h, (A_{3u}/A_{1u}), Z_e, and ν_2. This calculation is iterated until the resulting ν or S sequence converges, and usually three or four iterations are sufficient.

Alternately, the surface impedance of T.M. modes Z_e may be computed from (174) and (176) for an assumed value $\nu = \nu_0$. Using this value of Z_e, (192) can be solved for the amplitude ratio (A_{3u}/A_{1u}) as

$$\frac{A_{3u}}{A_{1u}} = \frac{q_{11}-q_{21}Z_e}{q_{23}Z_e-q_{13}}. \tag{196}$$

The surface impedance Z_h, which is seen by the T.E. fields at the bottom of the ionosphere $(r = a+h)$, is computed substituting (A_{3u}/A_{1u}) of (196) in (193). This value of Z_h is substituted in the left-hand side of (177). Using the (B_h/A_h) ratio of (175), (177) can be rearranged into the modal equation for T.E. modes, where Z_h reflects the presence of T.M. modes in the space between the earth and the ionosphere. The solution of this modal equation gives an improved estimate $\nu = \nu_1$, and the calculations may be iterated until the ν sequence converges.

The impedances Z_h of (177) or (194) and Z_e of (176) or (196) can be also computed using the multilayer representations of Section 5.5. The T.E. fields at the upper boundary of the cylindrically stratified medium are given by (93), (94), and (101) as

$$\begin{bmatrix} H_\varphi(r_0) \\ E_z(r_0) \end{bmatrix} = [a_1^h(r_0)] \cdot \begin{bmatrix} A_h \\ B_h \end{bmatrix}. \tag{197}$$

The fields at the ground surface are obtained from (103) with $j = 1$ as

$$\begin{bmatrix} H_\varphi(a) \\ E_z(a) \end{bmatrix} = [b_n^h] \cdot \begin{bmatrix} A_h \\ B_h \end{bmatrix}, \tag{198}$$

where the matrix $[b_n^h]$ is defined by (104). It is obtained by continuing the matrix multiplication from the upper boundary of the cylindrically stratified medium $r = r_0$ to the ground surface $r = a$. Then, A_h and B_h refer to the wave amplitudes in the upper shell ($n = 1$). The ground impedance can be expressed in terms of the T.E. field components as

$$Z_g = \sqrt{\frac{\omega\mu_0}{\omega\varepsilon_g + i\sigma_g}} = \frac{E_z(a)}{H_\varphi(a)}. \tag{199}$$

Substituting this in the left-hand side of (198), the amplitudes A_h and B_h of the up-going and down-coming waves of the upper shell ($n = 1$) are computed as

$$\frac{B_h}{A_h} = -\frac{b_{21}^h - Z_g b_{11}^h}{b_{22}^h - Z_g b_{12}^h}. \tag{200}$$

Z_h of (177) is now expressed as

$$Z_h' = -\frac{E_z(r_0)}{H_\varphi(r_0)} = -\frac{a_{21}^h + a_{22}^h(B_h/A_h)}{a_{11}^h + a_{12}^h(B_h/A_h)}. \tag{201}$$

Using this value of Z_h in (194), Z_e is computed from (192), and the propagation parameter ν can be determined using the method of Section 5.5.6.

In an analogous development, Z_e of (176) is expressed as

$$Z_e = \frac{E_\varphi(r_0)}{H_z(r_0)} = \frac{a_{11}^e + a_{12}^e(B_e/A_e)}{a_{21}^e + a_{22}^e(B_e/A_e)} \tag{202}$$

with

$$\frac{B_e}{A_e} = -\frac{b_{11}^e + Z_g b_{21}^e}{b_{12}^e + Z_g b_{22}^e}. \tag{203}$$

Using this value of Z_e in (196), Z_h is computed from (193); and the propagation parameter ν can be determined as shown in Section 5.5.6.

5.6.1.2 *Direct Solution*

The modal equation for the coupled T.M. and T.E. waves can be also solved directly. The elements of the q_{ij} matrix in (191) are computed for an assumed propagation parameter S_0 of the waves below the ionosphere. The impedances $Z_e = \eta\Delta_n(h)$ and $Z_h = \eta\Delta_m(h)$ are computed from (174) to (177) or from (197) and (199) of Chapter 4 for an approximate representation of the radial functions. The impedances $\Delta_n(h)$ and $\Delta_m(h)$ depend on ν (or S), and it is possible to find a corrected value $S_1 = S_0 + \delta S$ which satisfies (191). The corrected value S_1 is used to recompute the elements q_{ij}, and a further improved estimate $S = S_2$ is computed from (191).

This procedure will be illustrated using the Airy function approximation of the radial functions. It follows from (197) and (199) of Chapter 4 that

$$\frac{Z_e}{\eta} = i\left(\frac{2}{k_0 a}\right)^{1/3} \frac{-A_e w_2'(t_i) + B_e w_1'(t_i)}{-A_e w_2(t_i) + B_e w_1(t_i)}, \tag{204}$$

$$\frac{Z_h}{\eta} = -i\left(\frac{k_0 a}{2}\right)^{1/3} \frac{-A_h w_2(t_i) + B_h w_1(t_i)}{-A_h w_2'(t_i) + B_h w_1'(t_i)}, \tag{205}$$

where

$$A_j = w_1'(t_g) - q_g^j w_1(t_g), \tag{206}$$

$$B_j = w_2'(t_g) - q_g^j w_2(t_g), \tag{207}$$

and where

$$j = e \quad \text{or} \quad h,$$

$$q_g^e = i\left(\frac{k_0 a}{2}\right)^{1/3} \Delta_g,$$

$$q_g^h = i\left(\frac{k_0 a}{2}\right)^{1/3} \Big/ \Delta_g,$$

$$-t_g = (k_0 a/2)^{2/3}(1 - S^2),$$

$$t_i = t_g - (k_0 a/2)^{2/3}(2h/a).$$

Equation (191) can be regarded as a function of t_g. Thus

$$f(t_g) = (Z_e\ q_{23} - q_{13})(Z_h\ q_{31} + q_{41}) - (Z_e\ q_{21} - q_{11})(Z_h\ q_{33} + q_{43}). \tag{208}$$

A Taylor series expansion of the function $f(t_g)$ about its approximate zero $f(t_0)$ gives a corrected t_g estimate for its zero as

$$t_g = t_0 - \frac{f(t_0)}{df/dt_g\big|_{t_g = t_0}}. \tag{209}$$

The derivative of (209) can be computed from

$$\left.\begin{aligned} \frac{df}{dt_g} = {} & \frac{dZ_e}{dt_g}[q_{23}(Z_h\ q_{31} + q_{41}) - q_{21}(Z_h\ q_{33} + q_{43})] \\ & + \frac{dZ_h}{dt_g}[q_{31}(Z_e\ q_{23} - q_{13}) - q_{33}(Z_e\ q_{21} - q_{11})]. \end{aligned}\right\} \tag{210}$$

The differentiation of Z_e and Z_h involves the derivatives of A_j and B_j, which are readily computed from (206) and (207) making use of (71).

The solution of (191) can be shown to converge more rapidly than the iterative solution of (192) and (193) examined in Section 5.6.1.1. The parameters q_{ij} characterize the ionosphere and are less dependent on S than the impedances Z_e and Z_h, which are reflected to the ionospheric boundary by T.M. and T.E. waves of the cylindrical shell. In the present solution, one iteration is characterized by a set of q_{ij} values which are computed for an estimated value of $S = S_0$; subsequently, both Z_e and Z_h are recomputed for corrected values of S. In the iterative solution of Section 5.6.1.1, q_{ij} and Z_h (or Z_e) are computed for an estimated value of $S = S_0$, and subsequent computations of the first iteration tend to optimize S by recomputing only Z_e (or Z_h), even though Z_h (or Z_e) of this iteration may be also inaccurate.

5.6.2 Field Components

The T.M. field components E_r, E_φ, and H_z of (36) to (38) are excited by a continuous line of radial dipoles of heights ds and of current J_{ser} per each meter in z direction. Under isotropic conditions, these T.M. field components are not coupled to the T.E. field components E_z, H_r, and H_φ of (50) to (52) that are excited by a z-directed line current of linear density J_{sez} and of a vertical dimension ds. For an anisotropic ionosphere, the field components become coupled; and all of the field components may be excited by either one of the two different line sources. In Sections 5.2.3.1 and 5.2.3.2, the various field components have been expressed using excitation factors Λ_q, height-gain functions $G_q(y)$, and normalized impedances $\Delta_q(y)$ of T.M. modes ($q = n$) or T.E. modes ($q = m$). This notation must be generalized for anisotropic conditions when either one of the two sources may excite field components with wave numbers corresponding to n or m modes.

In the definition of the excitation factor, a superscript e (or h) will be introduced to denote vertically (or horizontally) polarized sources. A subscript $q = n$ or m will denote wave numbers corresponding to T.M. or T.E. modes. In this notation, Λ_m^e denotes the excitation factor of T.E.(m) modes by a vertically polarized source; and Λ_n^h denotes the excitation of T.M.(n) modes by a horizontally polarized source. The excitation factors Λ_n^e and Λ_m^h can be designated as Λ_n and Λ_m following the notation of Section 5.2.3.

For the height-gain functions and normalized impedances, the superscripts e or h denote T.M. or T.E. components; and the subscripts $q = n$ or m denote wave numbers corresponding to T.M. or T.E. modes. In this notation, $G_m^e(y)$ or $G_n^h(y)$ denote height-gain functions of T.M. or T.E. field components with wave numbers corresponding to T.E. or T.M. modes; the height-gain function $G_n^e(y)$ and $G_m^h(y)$ can be designated as G_n and G_m following the notation of Section 5.2.3. The normalized impedances $\Delta_q^j(y)$ are interpreted similarly for superscripts $j = e$ or h and subscripts $q = n$ or m.

The development of the Appendix shows that for a given wave number $q = n$ or m, the function $G_q^e(y)$ of (272) and Δ_q^e of (273) are computed similarly as $G_n(y)$ and $\Delta_n(y)$ of Sections 5.2.3.1 or 5.4.2 for same wave numbers ν; also $G_q^h(y)$ of (275) and $\Delta_q^h(y)$ of (276) are computed similarly as $G_m(y)$ and $\Delta_m(y)$ of Sections 5.2.3.2 or 5.4.2. In the Airy function approximation of the radial functions, these expressions are the same as (196), (197), or (199) of Chapter 4 that have been derived for fields in an isotropic spherical shell. However, the excitation factors Λ_q^j of (274) and (277) contain explicitly parameters of both T.E. and T.M. field components, and they cannot be derived from the simpler relations that are valid under isotropic conditions.

For a vertically polarized line source, the various field components are expressed as

$$E_r(y) = -\frac{\eta J_{ser}\, ds}{h} \sum_q \Lambda_q^e G_q^e(y_s)\, G_q^e(y)\, S_q \exp(ik_0 D S_q), \tag{211}$$

$$E_\varphi(y) = \frac{\eta J_{ser}\, ds}{h} \sum_q \Lambda_q^e G_q^e(y_s)\, G_q^e(y)\, \Delta_q^e(y) \exp(ik_0 D S_q), \tag{212}$$

$$E_z(y) = \frac{J_{ser}\,ds}{h} \sum_q A_q^e G_q^e(y_s)\, Z_{eh} G_q^h(y) \exp(ik_0 D S_q), \tag{213}$$

$$H_r(y) = \frac{J_{ser}\,ds}{\eta h} \sum_q A_q^e G_q^e(y_s)\, Z_{eh} G_q^h(y)\, S_q \exp(ik_0 D S_q), \tag{214}$$

$$H_\varphi(y) = -\frac{J_{ser}\,ds}{\eta h} \sum_q A_q^e G_q^e(y_s)\, Z_{eh} G_q^h(y) \exp(ik_0 D S_q)/\Delta_q^h(y), \tag{215}$$

$$H_z(y) = \frac{J_{ser}\,ds}{h} \sum_q A_q^e G_q^e(y_s)\, G_q^e(y) \exp(ik_0 D S_q), \tag{216}$$

where $J_{ser}\,ds$ is the dipole moment per unit length in z-direction and $D = a\varphi$. All of the field components are proportional to the excitation factor A_q^e and the height-gain function $G_q^e(y_s)$ The T.M. components E_r, E_φ, and H_z are proportional to the height-gain function $G_q^e(y)$ and remain of same form as in (36) to (38). The T.E. components E_z, H_r, and H_φ are proportional to the height-gain function $G_q^h(y)$ and to the coupling impedance Z_{eh} of (284). Equations (211) to (216) show that

$$\left.\frac{H_\varphi(0)}{H_z(0)}\right|_q = -\left.\frac{E_z(0)}{E_\varphi(0)}\right|_q = \frac{Z_{eh}}{Z_g} \tag{217}$$

or

$$\left.\frac{E_z(0)}{E_r(0)}\right|_q = -\frac{Z_{eh}}{\eta S_q}; \quad \left.\frac{H_r(0)}{H_z(0)}\right|_q = \frac{Z_{eh} S_q}{\eta}. \tag{218}$$

The coupling impedance Z_{eh} denotes the ratio of the horizontal field components perpendicular to direction of propagation in (284), the ratio of horizontal field components in (217), or the wave tilt in plane perpendicular to direction of propagation in (218).

For a horizontally polarized line source of dipole moment $J_{sez}\,ds$ per unit length in z-direction the field components are expressed as

$$E_r(y) = -\eta^2 \frac{J_{sez}\,ds}{h} \sum_q \frac{A_q^h G_q^h(y_s)}{Z_{eh} S_q} S_q G_q^e(y) \exp(ik_0 D S_q), \tag{219}$$

$$E_\varphi(y) = \eta^2 \frac{J_{sez}\,ds}{h} \sum_q \frac{A_q^h G_q^h(y_s)}{Z_{eh} S_q} G_q^e(y)\, A_q^e(y) \exp(ik_0 D S_q), \tag{220}$$

$$E_z(y) = \frac{\eta J_{sez}\,ds}{h} \sum_q A_q^h G_q^h(y_s)\, S_q^{-1} G_q^h(y) \exp(ik_0 D S_q), \tag{221}$$

$$H_r(y) = \frac{J_{sez}\,ds}{h} \sum_q A_q^h G_q^h(y_s)\, G_q^h(y) \exp(ik_0 D S_q), \tag{222}$$

$$H_\varphi(y) = -\frac{J_{sez}\,ds}{h} \sum_q \frac{A_q^h G_q^h(y_s)\, G_q^h(y)}{S_q\, A_q^h(y)} \exp(ik_0 D S_q), \tag{223}$$

$$H_z(y) = \frac{\eta J_{sez}\,ds}{h} \sum_q \frac{A_q^h G_q^h(y_s)}{Z_{eh} S_q} G_q^e(y) \exp(ik_0 D S_q). \tag{224}$$

The field components (219) to (226) are proportional to the excitation factor A_q^h and to the height-gain function $G_q^h(y_s)$. The T.M. components E_r, E_φ, and H_z are proportional to the height-gain function $G_q^e(y_s)$ and are inversely proportional to the coupling impedance Z_{eh} of (284). The T.E. components are proportional to the height-gain function $G_q^h(y)$ and remain of same form as in (50) to (52).

5.6.3 *Application to Dipole Sources*

The line source excitation has been selected for mathematical convenience in the treatment of cylindrical geometries, and it is desirable to relate the field components of Section 5.6.2 to those excited by more realistic dipole-type sources in a spherical geometry.

5.6.3.1 *Vertical Electric Dipole*

The excitation factor A_n, the height-gain function $G_n(z)$, and the normalized impedance $\Delta_n(z)$ of a spherical geometry [Galejs, 1968c] are identical to A_n^e, $G_n^e(y)$, and $\Delta_n^e(y)$ of a cylindrical geometry under isotropic conditions in the Airy function approximation of the radial wave functions. The field components E_r, E_θ, and H_φ excited by a vertical electric dipole in a spherical geometry correspond to E_r, E_φ, and H_z of (211), (212), and (216) respectively. A vertical electric dipole of moment Ids will excite at the distance D fields comparable to those of a line source of moment $J_{ser}\,ds$ (per unit length in z-direction) if

$$J_{ser}\,ds = \frac{I\,ds\sqrt{S_q}}{\sqrt{a\lambda}\sin(D/a)} \exp(-i\pi/4). \tag{225}$$

The dipole moment of this equivalent line source will be increased with decreasing wavelength λ and decreasing distance D. It is assumed that (225) applies also in the presence of an anisotropic ionosphere; then the field components E_φ, H_r, and H_θ of a spherical geometry are estimated by applying (225) to (213), (214), and (215) respectively.

5.6.3.2 *Horizontal Electric Dipole*

The horizontal electric dipole excites T.M. field components that are coupled to T.E. field components even under isotropic conditions. However, in the V.L.F. range, the field components proportional to cos φ (the angle φ is measured from the dipole axis) are caused principally by n modes, and components proportional to sin φ are excited by m modes. The field components E_r, E_φ, and H_z of (211), (212), and (216) of a vertically polarized line source will be comparable to the T.M. field components of a horizontal electric dipole E_r, E_θ, and H_φ of (28), (29), and (33) of Galejs [1968c] if

$$J_{ser}\,ds = \frac{I\,ds\cos\varphi\,\Delta_q(z_s)}{\sqrt{a\lambda}\sin D/a\sqrt{S_q}} \exp(-i\pi/4). \tag{226}$$

The T.E. field components E_z, H_r, and H_φ of (221) to (223) excited by a horizontally polarized line source of moment $J_{sez}\,ds$ (per unit length in z direction) in a cylindrical geometry will be

comparable to the field components of a horizontal electric dipole E_φ, H_r, and H_θ of (30) to (32) of Galejs [1968c] if

$$J_{sez}\,ds = \frac{\sin\varphi I\,ds\sqrt{S_q}}{\sqrt{a\lambda}\sin(D/a)}\exp(-i\pi/4). \tag{227}$$

Ionospheric coupling will give rise to T.E. field components of the horizontal electric dipole E_φ, H_r, and H_θ with a cos φ angular dependence. These components can be estimated by applying (226) to the line source excited field components (213) to (215). Similarly, the T.M. field components E_r, E_θ, and H_φ with a sin φ angular dependence can be estimated by applying (227) to (219), (220), and (224). However, the equivalence expressions between the moments of line sources and the dipole (226) and (227) have been derived by neglecting the small amount of coupling between T.E. and T.M. components observed in the dipole fields under isotropic conditions. As a consequence, the dipole field components deduced applying (226) to (211) to (216) and (227) to (219) to (224) will exhibit n and m mode components with a strict cos φ and sin φ angular dependence in the limit of an isotropic ionosphere.

5.7 Appendix. Excitation of the Air Space Below an Anisotropic Ionosphere

The cylindrical air space is bounded by a homogeneous isotropic ground and by an anisotropic ionosphere. The ionospheric fields have been discussed in detail by Galejs [1967b, 1968a]; and the results, summarized in Section 5.7.2, will be applied to the derivation of field expressions in the space between the earth and the ionosphere. The line source excited fields will be expressed in a harmonic series in Sections 5.7.1 and 5.7.3, which are transformed in a residue series in Section 5.7.4. The final expressions of these residue series (or mode summations) involve height-gain functions and normalized impedances that are identical to those computed under isotropic conditions. However, the rather lengthy derivations are necessary for deriving the excitation factors, which can be reduced to, but cannot be deduced from, the excitation factors of the isotropic shell. There appear no simple methods for deducing the amplitudes of T.M. field components excited by vertically polarized sources with wave numbers corresponding to T.E. modes (or T.E. field components excited by horizontally polarized sources with wave numbers corresponding to T.M. modes). The T.E. field components excited by a vertically polarized source and the T.M. field components excited by a horizontally polarized source will also depend on a coupling impedance Z_{eh} that is defined as the ratio between the transverse horizontal electric and magnetic fields at the ground surface.

5.7.1 *The Primary Fields*

The propagation in the cylindrical shell between the earth and the ionosphere in Fig. 5.1 can be treated in two dimensions if the fields are excited by line sources. A vertically polarized source can be visualized as a continuous line of radially oriented electric dipoles of current J_{ser} per unit length in the z direction. A horizontally polarized source is represented by a z-directed line current of linear density J_{sez}. The primary fields excited by these line currents can be readily deduced from the more familiar primary fields of elementary dipoles.

In a source-centered cylindrical coordinate system (ϱ', φ', z'), the φ' component of the magnetic field of an elementary dipole is given by

$$H_{\varphi'} = -\frac{I\,ds}{4\pi}\frac{d}{d\varrho'}\left(\frac{e^{ik_0r'}}{r'}\right), \tag{228}$$

where k_0 is the wave number of free space, the current element ds is oriented in the z' direction, and $r' = \sqrt{\varrho'^2+z'^2}$ is the distance from the elementary source to the observation point. In the cylindrical coordinates of Fig. 5.1, the z component of the magnetic field of a single radial electric dipole is computed as $H_z = (r_s\varphi/\varrho')H_{\varphi'}$ or as

$$H_z = -\frac{I\,ds}{4\pi r_s}\frac{d}{d\varphi}\left(\frac{e^{ik_0r'}}{r'}\right), \tag{229}$$

where $r' = \sqrt{\varrho'^2+(r-r_s)^2}$ and $\varrho' = \sqrt{z^2+(r_s\varphi)^2}$. For a continuous line of radial electric dipoles of moment $J_{ser}\,ds$ per unit length in z direction, the field component H_z is computed as

$$H_z = -\frac{J_{ser}\,ds}{4\pi r_s}\frac{d}{d\varphi}\int_{-\infty}^{\infty} dz(e^{ik_0r'}/r') = -\frac{i}{4r_s}J_{ser}\,ds\frac{d}{d\varphi}H_0^{(1)}(k_0\varrho), \tag{230}$$

where $\varrho^2 = r_s^2+r^2-2rr_s\cos\varphi$ and $H_n^{(m)}(x)$ is the Hankel function of kind m and order n. The addition theorem of Bessel functions shows that

$$H_0^{(1)}(k_0\varrho) = \sum_{n=0}^{\infty}\varepsilon_n\cos n\varphi\begin{cases} J_n(k_0r)\,H_n^{(1)}(k_0r_s) & \text{if} \quad r \ll r_s, \\ J_n(k_0r_s)\,H_n^{(1)}(k_0r) & \text{if} \quad r \gg r_s, \end{cases} \tag{231}$$

where $J_n(x)$ is the Bessel function of the first kind of order n, $\varepsilon_n = 1$ for $n = 0$, and $\varepsilon_n = 2$ for $n \neq 0$. Noting that $E_\varphi = -(i/\omega\varepsilon_0)\,\partial H_z/\partial r$ and applying the Wronskian

$$J_n(x)\,H_n^{(1)}(x)' - J_n(x)'\,H_n^{(1)}(x) = 2i/(\pi x) \tag{232}$$

it can be shown that

$$\lim_{\Delta\to 0}[E_\varphi(r_s+\Delta)-E_\varphi(r_s-\Delta)] = \frac{iJ_{ser}\,ds}{\omega\varepsilon_0\pi r_s^2}\sum_{n=1}^{\infty} n\sin n\varphi. \tag{233}$$

$H_{\varphi'}$ of (228) applies also to the fields excited by a horizontally oriented elementary dipole if the z'-axis coincides with the z-axis of Fig. 5.1 and if $\varrho' = \varrho = \sqrt{r_s^2+r^2-2rr_s\cos\varphi} \approx$ $\approx \sqrt{(r-r_s)^2+(r_s\varphi)^2}$. It can be shown that

$$H_\varphi = -\frac{r-r_s}{\varrho}H_{\varphi'} = -\frac{d\varrho}{dr}H_{\varphi'}, \tag{234}$$

The fields of a z-directed line source of moment $J_{sez}\,ds$ per unit length are computed by integrating (234), which gives

$$H_\varphi = \frac{J_{sez}\,ds}{4\pi}\frac{d}{dr}\int_{-\infty}^{\infty} dz(e^{ik_0r'}/r') = \frac{iJ_{sez}\,ds}{4}\frac{d}{dr}H_0^{(1)}(k_0\varrho). \tag{235}$$

Applying (231) and (232), it is seen that

$$\lim_{\Delta \to 0} [H_\varphi(r_s+\Delta)-H_\varphi(r_s-\Delta)] = -\frac{J_{sez}\, ds}{2\pi r_s} \sum_{n=0}^{\infty} \varepsilon_n \cos n\varphi. \tag{236}$$

Vertically and horizontally polarized line sources are characterized by (233) and (236) respectively. These equations will be used as boundary conditions in the field formulation of Section 5.7.3.

5.7.2 *Fields at the Anisotropic Ionosphere*

A vertically polarized line source excites T.M. field components E_r, E_φ, and H_z that are not coupled to the T.E. field components H_r, H_φ, and E_z excited by a horizontally polarized line source in the space between the earth and the ionosphere. However, the field components are coupled at the boundary of the anisotropic ionosphere. The ionospheric model is assumed to be stratified for values of r in the range $r_l = a+h \ll r \ll r_u = a+h_u$, and the space of $r > r_u$ is considered to be homogeneous. Then it is possible to relate the field components tangential to the lower ionospheric boundary to outgoing wave amplitudes A_{1u} and A_{3u} of the two magneto-ionic modes in the upper region following Galejs [1968a] as

$$\left.\begin{aligned} E_\varphi(h) &= q_{11}A_{1u}+q_{13}A_{3u},\\ H_z(h) &= q_{21}A_{1u}+q_{23}A_{3u},\\ H_\varphi(h) &= q_{31}A_{1u}+q_{33}A_{3u},\\ E_z(h) &= q_{41}A_{1u}+q_{43}A_{3u}. \end{aligned}\right\} \tag{237}$$

The ionospheric surface impedances of the T.E. and T.M. field components are defined as

$$Z_e = \frac{E_\varphi(h)}{H_z(h)}; \qquad Z_h = -\frac{E_z(h)}{H_\varphi(h)}. \tag{238}$$

After substituting (237) in (238) and eliminating the amplitude A_{3u}/A_{1u}, Z_e and Z_h are related by

$$Z_e = \frac{a_{11}+a_{12}\,Z_h}{a_{21}+a_{22}\,Z_h} \quad \text{or} \quad Z_h = -\frac{a_{11}-a_{21}\,Z_e}{a_{12}-a_{22}\,Z_e}, \tag{239}$$

where

$$\left.\begin{aligned} a_{11} &= q_{11}\,q_{43}-q_{13}\,q_{41}; \qquad a_{12} = q_{11}\,q_{33}-q_{13}\,q_{31};\\ a_{21} &= q_{21}\,q_{43}-q_{23}\,q_{41}; \qquad a_{22} = q_{21}\,q_{33}-q_{23}\,q_{31}. \end{aligned}\right\} \tag{240}$$

The surface impedance Z_e is related to the surface impedance Z_h by matrix elements q_{ij}, the calculation of which has been described in detail in earlier work [Galejs, 1968a, b].

5.7.3 *The Harmonic Series*

For vertically polarized sources, the E_φ field component will be discontinuous across the source at $r = r_s$ following (233); and different definitions of the T.M. field components will apply to region 1 of $a \ll r \ll r_s$ and region 2 of $r_s \ll r \ll r_l$. The tangential field components

will exhibit the φ-dependence of the excitation in (233), and H_{zj} of region j can be written in the form

$$H_{zj} = \sum_{n=1}^{\infty} [A_{enj}H_n^{(1)}(u)+B_{enj}H_n^{(2)}(u)] \sin n\varphi, \tag{241}$$

where $u = k_0 r$ and $j = 1$ or 2. The other T.M. field components are related to H_z as

$$E_\varphi = -\frac{i}{\omega\varepsilon_0}\frac{\partial}{\partial r}H_z; \qquad E_r = \frac{i}{\omega\varepsilon_0 r}\frac{\partial}{\partial \varphi}H_z. \tag{242}$$

Applying (242), $E_{\varphi j}$ is expressed as

$$E_{\varphi j} = -i\eta \sum_{n=1}^{\infty} [A_{enj}H_n^{(1)}(u)'+B_{enj}H_n^{(2)}(u)'] \sin n\varphi, \tag{243}$$

where $\eta = \sqrt{\mu_0/\varepsilon_0} = 120\pi$ ohms is the characteristic impedance of free space, and the prime denotes differentiation with respect to the argument. Because of wave coupling in the ionosphere, there will be also T.E. wave components in the airspace between the ionosphere and the ground surface. The E_z component will be of the form

$$E_z = \sum_{n=1}^{\infty} [A_{hn}H_n^{(1)}(u)+B_{hn}H_n^{(2)}(u)] \sin n\varphi, \tag{244}$$

where $u = k_0 r$ and $a \ll r \ll r_l$.

The other T.E. field components are related to E_z as

$$H_\varphi = \frac{i}{\omega\mu_0}\frac{\partial}{\partial r}E_z; \qquad H_r = -\frac{i}{\omega\mu_0 r}\frac{\partial}{\partial \varphi}E_z. \tag{245}$$

Applying (245), H_φ is expressed as

$$H_\varphi = \frac{i}{\eta} \sum_{n=1}^{\infty} [A_{hn}H_n^{(1)}(u)'+B_{hn}H_n^{(1)}(u)'] \sin n\varphi. \tag{246}$$

The boundary condition of the ground surface $Z_g = E_z(0)/H_\varphi(0)$ determines the amplitude ratio B_{hn}/A_{hn}, and the surface impedance $Z_h = -E_z(h)/H_\varphi(h)$ is uniquely determined for each of the harmonics n. Z_h is related to Z_e by (239). The remaining four amplitude coefficients A_{enj} and B_{enj} ($j = 1$ and 2) are determined from the boundary conditions $Z_g = -E_{\varphi 1}(0)/H_{z1}(0)$, $Z_e = E_{\varphi 2}(h)/H_{z2}(h)$, $H_{z1}(y_s) = H_{z2}(y_s)$ and the condition (233). A lengthy calculation shows that

$$H_{z2}(r) = \frac{J_{ser}\, ds\, \eta}{4ir_s} \sum_{n=1}^{\infty} \frac{n \sin n\varphi}{D_n} Z_{n1}^e(u_s)\, Z_{n2}^e(u) \cdot [a_{21}Z_n^h(u_l)'+a_{22}i\eta Z_n^h(u_l)], \tag{247}$$

$$E_z(r) = \frac{J_{ser}\, ds\, \eta^2}{i\pi k_0 r_s r_l}(q_{41}\,q_{33}-q_{43}\,q_{31}) \sum_{n=1}^{\infty} \frac{n \sin n\varphi}{D_n} Z_{n1}^e(u_s)\, Z_n^h(u), \tag{248}$$

where

$$D_n = -\eta\, Z^e_{n1}(u_i)'\,[a_{21}Z^h_n(u_i)' + ia_{22}\eta Z^h_n(u_i)] + iZ^e_{n1}(u_i)\,[a_{11}Z^h_n(u_i)' + ia_{12}\eta Z^h_n(u_i)], \quad (249)$$

$$Z^e_{nj}(u) = A_{enj}H^{(1)}_n(u) + B_{enj}H^{(2)}_n(u), \quad (250)$$

$$Z^h_n(u) = A_{hn}H^{(1)}_n(u) + B_{hn}H^{(2)}_n(u), \quad (251)$$

$$A_{en1} = H^{(2)}_n(u_g)' + i\Delta_g H^{(2)}_n(u_g), \quad (252)$$

$$B_{en1} = -H^{(1)}_n(u_g)' - i\Delta_g H^{(1)}_n(u_g), \quad (253)$$

$$A_{en2} = H^{(2)}_n(u_i)' - i\Delta_{en}H^{(2)}_n(u_i), \quad (254)$$

$$B_{en2} = -H^{(1)}_n(u_i)' + i\Delta_{en}H^{(2)}_n(u_i), \quad (255)$$

$$A_{hn} = H^{(2)}_n(u_g)' + \frac{i}{\Delta_g}H^{(2)}_n(u_g), \quad (256)$$

$$B_{hn} = -H^{(1)}_n(u_g)' - \frac{i}{\Delta_g}H^{(1)}_n(u_g), \quad (257)$$

and where $u = k_0 r$, $u_g = k_0 a$, $u_s = k_0 r_s$, $u_i = k_0 r_i = k_0(a+h)$, $\Delta_g = Z_g/\eta$, and $\Delta_{en} = Z_e/\eta$. The surface impedance Z_e is computed from (239) with $Z_h = -E_z(h)/H_\varphi(h)$ determined for the harmonic n from (244) and (246). A prime denotes a differentiation with respect to the argument. The parameters q_{ij} and a_{ij} are defined by (237) and (240). $H_{z1}(r)$ is obtained by interchanging u and u_s in (247). The other field components are obtained substituting (247) in (242) and (248) in (245).

For a horizontally polarized source, the T.E. field components E_{zj} and $H_{\varphi j}$ are defined in two regions ($a \ll r \ll r_s$ and $r_s \ll r \ll r_i$), but the T.M. components H_z and E_φ are defined in a single region ($a \ll r \ll r_i$). The individual terms of the harmonic series exhibit cosinusoidal φ variations following (236). A calculation shows that

$$E_{z2}(r) = \frac{-J_{sez}\, ds\eta k_0}{8ir_s}\sum_{n=0}^{\infty}\frac{\varepsilon_n \cos n\varphi}{D_n}\, Z^h_{n1}(u_s)\, Z^h_{n2}(u)\cdot[a_{11}Z^e_n(u_i) + i\eta a_{21}Z^e_n(u_i)'], \quad (258)$$

$$H_z(r) = \frac{J_{sez}\, ds\eta}{2\pi i r_s}(q_{11}\, q_{23} - q_{12}\, q_{21})\sum_{n=0}^{\infty}\frac{\varepsilon_n \cos n\varphi}{D_n}\, Z^h_{n1}(u_s)\, Z^e_n(u). \quad (259)$$

The various symbols are defined similarly as in (247) and (248) except that $Z^h_{n1}(u) = Z^h_n(u)$ of (251) and $Z^e_n(u) = Z^e_{n1}(u)$ of (250). $Z^h_{n2}(u)$ is defined by

$$Z^h_{n2}(u) = A_{hn2}H^{(1)}_n(u) + B_{hn2}H^{(2)}_n(u) \quad (260)$$

with

$$A_{hn2} = H^{(2)}_n(u_i)' - \frac{i}{\Delta_{hn}}H^{(2)}_n(u_i), \quad (261)$$

$$B_{hn2} = -H^{(1)}_n(u_i)' + \frac{i}{\Delta_{hn}}H^{(1)}_n(u_i), \quad (262)$$

where $\Delta_{hn} = Z_h/\eta$ is computed from (239) with $Z_e = E_\varphi(h)/H_z(h)$ determined from the field expressions for the harmonic n. $E_{z1}(r)$ is obtained by interchanging u and u_s in (258). The other field components are obtained substituting (258) in (245) and (259) in (242).

A comparison of (247) and (248) with (258) and (259) shows that the field components excited by vertically and horizontally polarized sources are characterized by different φ variations in their harmonic series representations.

5.7.4 The Residue Series

5.7.4.1 Formal Solution

For frequencies in the V.L.F. range, the harmonic series converge very slowly; and it is advantageous to transform the summations in a complex integral that can be evaluated using residue theory following Sensiper [1957] or Wait [1959].

The field expressions (247), (248), (258), and (259) are of the form

$$F = \sum_{n=1}^{\infty}\frac{f(n)}{D(n)}\, n \sin n\varphi; \qquad G = \sum_{n=0}^{\infty}\frac{g(n)}{D(n)}\,\varepsilon_n \cos n\varphi, \quad (263)$$

where $f(n)$, $g(n)$, and $D(n)$ contain products of an even number of Hankel functions $H^{(1,2)}_n(x)$ and derivatives $H^{(1,2)}_n(x)'$. Noting that $H^{(1,2)}_{-n}(x) = e^{\pm in\pi}H^{(1,2)}_n(x)$, the functions $f(n)$, $g(n)$, and $D(n)$ are seen to be even with respect to n; and the summations (263) are rewritten as

$$F = \frac{1}{2i}\sum_{n=-\infty}^{\infty}\frac{f(n)}{D(n)}\, ne^{in\varphi}; \qquad G = \sum_{n=-\infty}^{\infty}\frac{g(n)}{D(n)}\, e^{in\varphi}. \quad (264)$$

The summations can be represented by the complex integrals

$$F = \frac{1}{4}\int_{C_1}\frac{e^{-i\nu\pi}}{\sin\nu\pi}\frac{f(\nu)}{D(\nu)}\,\nu e^{i\nu\varphi}\,d\nu; \qquad G = -\frac{1}{2i}\int_{C_1}\frac{e^{-i\nu\pi}}{\sin\nu\pi}\frac{g(\nu)}{D(\nu)}\, e^{i\nu\varphi}\,d\nu. \quad (265)$$

The clockwise contour C_1 encloses the poles of the integrand which occur at the zeros of the $\sin\nu\pi$ function or at integer values $\nu = n$ on the real axis. The contributions to the integral from portions of C_1 which cross the real axis at $\pm\infty$ approach zero. Thus, C_1 becomes identical to two line integrals. The two line integrals are joined by large semicircles in counterclockwise direction in the upper and lower half plane respectively. The integrals along these closed contours are evaluated as $2\pi i$ times the sum of residues of the integrands by neglecting the contributions of the continuous wave spectrum or of lateral waves. The poles of the integrands correspond to zeros of $D(\nu)$. Only the poles of the 1. quadrant correspond to attenuated waves propagating in the φ-direction (Re ν, Im $\nu > 0$). (There are also poles in the 3. quadrant which correspond to waves attenuated in the negative φ direction. However, identical wave numbers for propagation in the φ direction are obtained by reversing the direction of the static magnetic field in the calculation of the ionosphere parameters. These 3. quadrant poles will not be considered in more detail.) Noting that $e^{-i\nu\pi}/\sin\nu\pi \approx -2i$, the integrals (265) are changed to

$$F = \pi\sum_{\nu}\frac{\nu f(\nu)}{D'(\nu)}\, e^{i\nu\varphi}, \qquad G = 2\pi i\sum_{\nu}\frac{g(\nu)}{D'(\nu)}\, e^{i\nu\varphi}, \quad (266)$$

where $D'(\nu) = dD(n)/dn\Big|_{n=\nu}$ and the complex eigenvalues ν are determined from the solutions of $D(\nu) = 0$. The eigenvalue ν can be related to a propagation parameter S as $\nu = k_0 a S$, where Re S is inversely proportional to the phase velocity and Im S is proportional to the attenuate rate.

The transformation of (263) into (266) changes also the order of the various Hankel functions and their derivatives from real integer values n to complex values ν. For frequencies in the V.L.F range, these Hankel functions can be approximated by Airy functions as

$$H_\nu^{(1,2)}(u) \approx \mp \frac{i}{\sqrt{\pi}} \left(\frac{2}{k_0 a}\right)^{1/3} w_{2,1}(t), \tag{267}$$

$$-t = (\nu/2)^{2/3}\,[(u/\nu)^2 - 1] \approx \left(\frac{k_0 a}{2}\right)^{2/3} [1 - S^2 + 2(r-a)/a]. \tag{268}$$

The Airy functions $w_{1,2}(t)$ satisfy the differential equation

$$w''(t) - t w(t) = 0 \tag{269}$$

and the Wronskian is given by

$$W[w_1(t), w_2(t)] = w_1(t)\, w_2'(t) - w_1'(t)\, w_2(t) = -2i. \tag{270}$$

In the evaluation of the derivatives, it may be noted that

$$\frac{\partial t}{\partial u} = -(2/\nu)^{1/3}\,(u/\nu) \approx -(2/k_0 a)^{1/3}. \tag{271}$$

5.7.4.2 Field Expressions

The various field expressions can be reduced to a compact form by introducing a simplifying notation for several common combinations of functions. The effectiveness of the source will be characterized by an excitation factor A, the height variations of the fields by height-gain functions $G(y)$; the fields also depend on a height-dependent normalized impedance $\Delta(y)$ These functions will differ for the various modes q (or eigenvalues ν) and for T.M. and T.E field components or sources that will be denoted by superscripts e and h respectively.

For T.M. components or sources, the functions are defined as

$$G_q^e(y) = \frac{Z_\nu^e(u)}{Z_\nu^e(u_g)} = 0.5i[-A_{eg} w_2(t) + B_{eg} w_1(t)], \tag{272}$$

$$\Delta_q^e(y) = \frac{\dfrac{\partial}{\partial u}\,[Z_\nu^e(u)]}{iZ_\nu^e(u)} = i\left(\frac{2}{k_0 a}\right)^{1/3} \frac{-A_{eg} w_2'(t) + B_{eg} w_1'(t)}{-A_{eg} w_2(t) + B_{eg} w_1(t)}, \tag{273}$$

$$A_q^e = -\frac{2h}{r_s}\,\frac{A_{ei}}{A_{eg}}\,\frac{(a_{21} + a_{22} Z_h)\,\eta (k_0 a/2)^{1/3}}{[-A_{eg} w_2(t_i) + B_{eg} w_1(t_i)]\,(\partial D_\nu/\partial t)}. \tag{274}$$

For T.E. components or sources, the functions become

$$G_q^h(y) = \frac{Z_\nu^h(u)}{Z_\nu^h(u_g)} = 0.5i[-A_{hg} w_2(t) + B_{hg} w_1(t)], \tag{275}$$

$$\Delta_q^h(y) = \frac{iZ_\nu^h(u)}{\dfrac{\partial}{\partial u}\,[Z_\nu^h(u)]} = -i\left(\frac{k_0 a}{2}\right)^{1/3} \frac{-A_{hg} w_2(t) + B_{hg} w_1(t)}{-A_{hg} w_2'(t) + B_{hg} w_1'(t)}, \tag{276}$$

$$A_q^h = \frac{2ih}{r_s}\,\frac{A_{hi}}{A_{hg}}\,\frac{Z_h (a_{12} - a_{22} Z_e)\,(k_0 a/2)^{2/3}}{[-A_{hg} w_2'(t_i) + B_{hg} w_1'(t_i)]\,(\partial D_\nu/\partial t)}. \tag{277}$$

The various coefficients are defined as

$$A_{jg} = w_1'(t_g) - q_{gj} w_1(t_g), \quad B_{jg} = w_2'(t_g) - q_{gj} w_2(t_g), \tag{278}$$

$$A_{ji} = w_1'(t_i) + q_j w_1(t_i), \quad B_{ji} = w_2'(t_i) + q_j w_2(t_i), \tag{279}$$

with $j = e$ or h, $q_e = i(k_0 a/2)^{1/3}(Z_e/\eta)$, $q_{ge} = i(k_0 a/2)^{1/3}\,\Delta_g$, $q_h = i(k_0 a/2)^{1/3}\cdot(\eta/Z_h)$, and $q_{gh} = i(k_0 a/2)^{1/3}/\Delta_g$. The parameters t_i and t_g denote values of the variable t that correspond to $r = r_i$ and r_g respectively. Z_e and Z_h of the above expressions are computed as $\eta\Delta_q^e(h)$ and $\eta\Delta_q^h(h)$ respectively. The function D_ν is given by

$$D_\nu = (Z_e q_{21} - q_{11})(Z_h q_{33} + q_{43}) - (Z_e q_{23} - q_{13})(Z_h q_{31} + q_{41}), \tag{280}$$

where eigenvalues $\nu = k_0 a S$ are determined from solution of $D_\nu = 0$. This modal condition has been deduced also as (191) in Section 5.6.1.

Under isotropic conditions, the T.M. modes have been denoted by numbers n and T.E. modes by numbers m [Galejs, 1968c]. In the presence of an anisotropic ionosphere, a vertically polarized source will excite field components with wave numbers corresponding to n or m modes; and also a horizontally polarized source will excite field components with wave numbers corresponding to both n and m modes. The subscript q, which designates the mode number in (272) to (277), can be set equal to n or m.

The height-gain function $G_q^e(y)$ and the normalized impedance $\Delta_q^e(y)$ contain only amplitude coefficients of T.M. field components A_{eg} and B_{eg}; similarly, $G_q^h(y)$ and $\Delta_q^h(y)$ depend only on coefficients A_{hg} and B_{hg}. For a given wave number, $G_q^j(y)$ and $\Delta_q^j(y)$ are computed similarly as under isotropic conditions. However, the excitation factors A_q^j contain explicitly the parameters of both T.E. and T.M. field components.

For T.M. modes, the surface impedance Z_e will not depend on Z_h if in (239) $a_{12} = a_{22} = 0$ or $a_{11} = a_{21} = 0$, which implies that $Z_e = a_{12}/a_{22}$. In either case, $\partial D_\nu/\partial t = (a_{21} + Z_h a_{22})\,\partial Z_e/\partial t$ and (274) will not depend on Z_h or on any other parameters of T.E. field components. Under these conditions, $A_q^e = A_n^e$ can be rearranged into

$$A_n^e = 0.5 k_0 h \left(\frac{2}{k_0 a}\right)^{1/3} \left\{t_g - q_{ge}^2 - \left(\frac{A_{eg}}{A_{ei}}\right)^2 (t_i - q_{ei}^2)\right\}^{-1}, \tag{281}$$

where in the derivation use has been made of (269) and (270) and where A_{eg} and A_{ei} are defined by (278) and (279). Equation (281) is recognized as the excitation factor of T.M. modes A_n

[Wait, 1962], which is related to the height-gain function $G_n^e(y)$ as

$$\Lambda_n^e = \frac{h}{2}\left\{\int_0^h [G_n^e(y)]^2\, dy\right\}^{-1}. \tag{282}$$

For T.E. modes, Z_h will not depend on Z_e in (239) if $a_{21} = a_{22} = 0$ or $a_{11} = a_{12} = 0$, which implies that $Z_h = -a_{21}/a_{22}$. In either case, $\partial D_n/\partial t = (-a_{12}+Z_e a_{22})\ \partial Z_n/\partial t$, and (277) will not depend on Z_e. Subsequently, $\Lambda_q^h = \Lambda_m^h$ assumes the form (281) (where subscripts and superscripts e are replaced by h). This excitation factor $\Lambda_m^h = \Lambda_m$ is related to $G_m^h(y)$ in the same way as Λ_n and $G_n^e(y)$ in (282).

The relations (281) and (282) for Λ_n^e and $G_n^e(y)$ and their modification for Λ_m^h and $G_m^h(y)$ provide a useful approximation even under anisotropic conditions. However, there are *no* simple relations of the form (282) for calculating the excitation of quasi-T.E. modes m by a vertically polarized source Λ_m^e or the excitation of quasi-TM modes n by a horizontally polarized source Λ_n^h.

The coupling between the T.E. and T.M. field components can be characterized by the ratio E_z/H_z. At the ionospheric boundary, $E_z(h)$ and $H_z(h)$ may be computed from (237), where the amplitude ratio A_{3u}/A_{1u} is expressed using either $E_\varphi(h)$ and $H_z(h)$ (or Z_e) or $H_\varphi(h)$ and $E_z(h)$ (or Z_h). This results in

$$\frac{E_z(h)}{H_z(h)} = \frac{a_{11}-a_{21}Z_e}{q_{11}q_{23}-q_{13}q_{21}} = \frac{(q_{41}q_{33}-q_{43}q_{31})\,Z_h}{a_{21}+a_{22}Z_h}, \tag{283}$$

where a_{ij} are defined by (240). This ratio, referred to the ground level $y = 0$, will be denoted as a coupling impedance

$$Z_{eh} = \frac{E_z(0)}{H_z(0)} = \frac{E_z(h)}{H_z(h)} \cdot \frac{G_q^e(h)}{G_q^h(h)}. \tag{284}$$

Noting the difference between (263) and (266) and applying (267) to (284), the fields of a vertically polarized line source of (242), (245), (247), and (248) may be rearranged into (211) to (216) of Section 5.6.2.

It can also be shown [Galejs, 1971] that the coupling impedance Z_{eh} is related to the excitation factors Λ_q^e and Λ_q^h as

$$\frac{\Lambda_q^e}{\Lambda_q^h} = \left(\frac{\eta}{Z_{eh}}\right)^2. \tag{285}$$

For a horizontally polarized line source of dipole moment $J_{sez}\,ds$ per unit length in z direction, the fields of (242), (245), (258), and (259) are rearranged into (219) to (224) of Section 5.6.2.

The excitation factors of waves below an anisotropic ionosphere can be also expressed in terms of reflection coefficients [Budden, 1962; Pappert *et al.*, 1967; Pappert, 1970].

5.8 References

Bremmer, H. (1949) *Terrestrial Radio Waves*, Elsevier, New York, pp. 137 and 214.

Budden, K. G. (1961) *The Wave Guide Mode Theory of Wave Propagation*, Logos Press, London, sections 9.8 and 15.11.

Budden, K. G. (1962) The influence of the earth's magnetic field on radio propagation by waveguide modes, *Proc. Royal Society* **A265**, 538–553.

Galejs, J. (1967a) Propagation of V.L.F. waves below an anisotropic stratified ionosphere with a transverse static magnetic field, *Radio Sci.* **2** (6), 557–574.

Galejs, J. (1967b) Propagation of V.L.F. waves below anisotropic ionosphere models with a dipping static magnetic field, *Radio Sci.* **2** (12), 1497–1512.

Galejs, J. (1968a) Propagation of E.L.F. and V.L.F. waves below an anisotropic ionosphere with a dipping static magnetic field, *J. Geophys. Res.* **73** (1), 339–352.

Galejs, J. (1968b) Propagation of E.L.F. and V.L.F. waves below a generally anisotropic ionosphere, *Radio Sci.* **3** (8), 781–786.

Galejs, J. (1968c) E.L.F. and V.L.F. fields of a horizontal electric dipole, *IEEE Trans. Antennas Propagation*, vol. AP-16, no. 6, 689–700.

Galejs, J. (1971) On the excitation of V.L.F. waves, *IEEE Trans. Antennas Propagation*, vol. AP-19, no. 4.

Madden, T., and W. Thompson (1965) Low frequency electromagnetic oscillations of the earth-ionosphere cavity, *Rev. Geophys.* **3** (2), 211–254.

Pappert, R. A. (1970) The effects of elevation and ground conductivity on horizontal dipole excitation of the earth ionosphere wave guide, *Radio Sci.* **5** (3), 579–590.

Pappert, R. A., E. E. Gossard, and I. J. Rothmuller (1967) A numerical investigation of classical approximations used in V.L.F. propagation, *Radio Sci.* **2** (4), 387–400.

Richter, J. H. (1966) Application of conformal mapping to earth flattening procedures, *Radio Sci.* **1** (2), 1435 1438.

Sensiper, S. (1957) Cylindrical radio waves, *IRE Trans. Antennas Propagation*, vol. AP-5, no. 1, 56–70.

Wait, J. R. (1959) *Electromagnetic Radiation from Cylindrical Structures*, Pergamon Press, London.

Wait, J. R. (1962) *Electromagnetic Waves in Stratified Media*, Pergamon Press, New York, NY.

Wait, J. R. (1963) The mode theory of V.L.F. radio propagation for a spherical earth and a concentric anisotropic ionosphere, *Canadian J. Phys.* **41**, 299–315.

Watson, G. N. (1958) *Treatise on the Theory of Bessel Functions*, University Press, Cambridge, sections 8.6 and 8.61.

CHAPTER 6

FIELDS IN STRATIFIED AND ANISOTROPIC MEDIA

Abstract. Several models of stratified and/or anisotropic ionosphere are introduced in calculations of surface impedances that can be subsequently used for determining propagation parameters of waves in the terrestrial waveguide. The matrix formulations also yield amplitude and phase data for all the field components tangential to the boundaries of the various ionospheric shells which are concentric with the surface of the earth.

Similar methods are applied to the treatment of anisotropic ground which exhibits different conductivities for different horizontal directions.

6.1 Introduction and Summary

Wave propagation under sharply bounded homogeneous and isotropic model ionospheres has been discussed in Chapters 4 and 5 for spherical and cylindrical geometries. For sharply bounded ionosphere models, the refractive index n is changed suddenly from $n = 1$ in the atmosphere to $|n| \gg 1$ at the ionospheric boundary. The lower boundary of realistic ionosphere models is diffuse, and the refractive index n will change gradually as a wave penetrates upwards into the ionosphere. The characteristics of such a diffuse lower ionospheric boundary may be also described by a surface impedance.

The surface impedance is determined from the differential equations of the medium. For a stratified medium, this impedance depends also on the parameters of wave propagation in the airspace between the ground surface and the ionosphere (or on the complex angle of wave incidence at the ionospheric boundary). The initial calculation of the surface impedance is made for an assumed propagation parameter S_0 ($\mathrm{Re}\, S = c/v_{ph}$, $\mathrm{Im}\, S \approx \alpha$, where c is the free-space velocity of electromagnetic waves, v_{ph} is the phase velocity and α is the attenuation rate), and the resulting surface impedance (or impedance components) is used to calculate a corrected propagation parameter S_1 from the modal equations developed in Chapters 4 and 5. For isotropic ionosphere in a spherical geometry, S_1 is determined following Sections 4.3.1 or 4.5.1 or in a cylindrical geometry following Sections 5.3.1, 5.4.1, or 5.5.6 for uncoupled T.E. and T.M. field components. Section 5.6.1 discusses the modal equations under conditions when T.E. and T.M. field components are coupled by an anisotropic ionosphere. After computing S_1, the surface impedance is recomputed, which gives a second estimate S_2. These calculations can be repeated until the S sequence converges. More iterations of the S computations are required when the local refractive index of the ionospheric boundary is low and when the initial estimate S_0 differs significantly from the final value S_n.

Isotropic ionosphere models with exponentially varying refractive index or conductivity

are discussed in Section 6.2. Such models are particularly useful in the lower E.L.F. range, where anisotropy effects due to the earth's static magnetic field are less significant.

A cylindrically stratified ionosphere with a horizontal static magnetic field transverse to the direction of propagation represents a further refinement. Such ionosphere models may be treated by numerically integrating the differential equations of a continuously varying medium or by approximating the medium by a number of concentric homogeneous shells, as is shown in Section 6.3. The multilayer approximations of the fields are expressed using a sequence of 2×2 matrices, and it is permissible to use a larger step size for larger values of the local refractive index (at larger altitudes). The computation time is reduced relative to solutions based on numerical integrations of differential equations. In this geometry, T.E. and T.M. field components are uncoupled by the medium; and the solutions are comparable in complexity to the solutions for an isotropic medium. The field components are shown to be rapidly attenuated at heights where the collision frequency ν is much smaller than the cylotron frequency ω_c.

Section 6.4 shows that a radial static magnetic field facilitates the field penetration in the ionosphere, but the solutions of T.E. and T.M. components are coupled in the ionosphere. The permissible radial wave numbers of the waves are determined from the solution of a quartic equation in a spherical geometry, and the field components tangential to the boundaries of the spherical shells become circularly polarized at altitudes where displacement currents of the medium are negligible. A multilayer representation involves 4×4 matrices, and the impedance components at the lower edge of the ionosphere are determined similarly as in the 2×2 matrix formulation of Section 5.5.

A cylindrically stratified anisotropic medium with a dipping static magnetic field is discussed in Section 6.5, where propagation is restricted along a constant magnetic latitude. The differential equations are separable, but their solutions are obtained only after approximating factors r of the differential equations with their average values r_m of a given cylindrical shell. The cylindrical stratifications are treated in the same accuracy as in the thin-shell approximations of Section 5.5.4, where for a homogeneous medium, a sequence of such thin shells gives more accurate fields than the Airy function approximation of the radial functions following Section 5.5.6. The method used in the field computations is subject to numerical swamping, but this problem is not encountered when avoiding computations at heights that exceed appreciably the effective reflection height of the waves.

Section 6.6 treats the more general problem of an arbitrary dip angle and arbitrary direction of propagation. The fields are considered in planar layers, but with a height-dependent local propagation parameter $S(r)$. In the special case of propagation along a constant magnetic latitude, this planar approximation gives results comparable to those of the cylindrical geometry of Section 6.5. The radial wave numbers are determined from a fourth-order algebraic equation, the solutions of which are derived analytically. The multilayer representations of fields for an arbitrary direction of propagation are deduced from the representations that were discussed in Section 5.5.

This chapter develops the mathematical formalism for the treatment of a number of stratified and anisotropic ionosphere models. The discussion emphasizes the calculation of surface impedances that can be used for determining wave-propagation parameters in conjunction with the formulas given in Chapters 4 and 5. The matrix formulations also yield amplitude and phase data for all the field components tangential to the boundaries of the various ionospheric

shells that are co...itric with the surface of the earth; the height variation of these field components can be readily computed. In an alternate approach, one may determine the reflection coefficients of the ionosphere for complex incidence angles although some work on the interpretation of short-range V.L.F. measurements has been limited to real angles of incidence. A number of methods used in determining ionospheric reflection coefficients have been summarized in the survey of Budden [1969]. The reflection coefficients will yield wave-propagation parameters of the terrestrial waveguide, but they cannot be used for determining height variation of the field components.

Anisotropic ground, which exhibits different conductivities for different horizontal directions, can be treated more simply than an anisotropic ionosphere. It is shown in Section 6.7 that the anisotropic ground produces coupled T.M. and T.E. field components. For an excitation by vertically or horizontally polarized waves, the net horizontal fields are modified by the anisotropy, except for the horizontal magnetic fields of the T.M. modes which remain the same as under isotropic conditions; the horizontal electric fields are decreased near the directions of higher ground conductivity and increased for directions approaching the axis of the lower conductivity. This results in null shifts and nonsymmetrical radiation patterns of horizontal dipole antennas which differ from the angular field variations derived in Chapter 4 for an isotropic ground surface.

6.2 Isotropic Ionosphere Models with a Diffuse Lower Boundary

In this section the surface impedance is determined for a continuously varying isotropic medium. The differential equations for such a medium are solved in the special case of exponentially varying refractive index and with some restrictions also for an exponentially varying conductivity following Galejs [1961], but solutions available for other specialized electron density profiles [chapter 17 of Budden, 1961a; chapter 3 of Wait, 1962] are not treated. For arbitrary variations of the refractive index, the medium may be approximated by a series of homogeneous shells. The multilayer field representations from Section 5.5 apply to the individual shells by noting that the wave number $k = \sqrt{\varepsilon}\, k_0$, where k_0 is the wave number for free space, $\varepsilon = 1 + i\sigma/(\omega\varepsilon_0)$, and σ is the average conductivity within a given shell. This multilayer field representation will not be discussed in more detail in this section.

The ionosphere is described in rectangular coordinates, where z is in the vertical direction. The fields exhibit no variations in the y direction and are assumed to have a wave number $k_x = k_0 S$ for propagation in the x direction, where S is the yet undetermined root of the modal equation. It follows from Maxwell's equations and from the equation of continuity that the vertical electric field component E_z in a vertically stratified lossy medium of complex relative dielectric constant

$$\varepsilon = 1 + \frac{i\sigma}{\omega\varepsilon_0} \tag{1}$$

is of the form

$$E_z = Z(z) \exp(ik_x x - i\omega t). \tag{2}$$

$Z(z)$ satisfies the differential equation

$$Z'' + \frac{\varepsilon'}{\varepsilon} Z' + \left[\varepsilon k_0^2 + \frac{\varepsilon''}{\varepsilon} - \frac{\varepsilon'^2}{\varepsilon} - k_x^2\right] Z = 0, \tag{3}$$

where primes denote derivatives with respect to z. With E_z determined, the field components E_x and H_y follow from Maxwell's equations as

$$E_x = \frac{1}{ik_x\varepsilon} \frac{\partial}{\partial z}(\varepsilon E_z) \tag{4}$$

and

$$H_y = -\frac{\omega\varepsilon}{k_x} E_z. \tag{5}$$

The field components (2), (4), and (5) will be examined first, for an exponentially increasing refractive index $n = \sqrt{\varepsilon/\varepsilon_0}$, and, second for exponentially increasing conductivity σ.

6.2.1 *Exponential Changes of the Refractive Index*

For exponential variation of the refractive index n, the variable in (3) is changed from z to

$$u = n^2 = \frac{\varepsilon}{\varepsilon_0} = iBe^{\beta z}. \tag{6}$$

This results in

$$Z''(u) + \frac{2}{u} Z'(u) + \frac{k_0^2 u - k_x^2}{u^2\beta^2} Z(u) = 0. \tag{7}$$

A solution of (7) is given by Kamke [1948] as

$$Z(u) = An^{-1} K_\nu(-iw), \tag{8}$$

where K_ν is the modified Bessel function of the second kind of order $\nu = (1 + 4k_x^2/\beta^2)^{0.5}$ and where $w = 2k_0 n/\beta$. Substitution of (8) in (2) and in (4) and (5) results in

$$Z_e = \frac{E_x}{H_y} = \sqrt{\frac{\mu_0}{\varepsilon_0}} \frac{1}{n} \frac{K_{\nu-1}(-iw)}{K_\nu(-iw)} + \frac{\beta}{2i\omega\varepsilon_0} \frac{1-\nu}{n^2}. \tag{9}$$

For $|w| \ll 1$, (9) may be approximated by

$$Z_e = \frac{E_x}{H_y} = \sqrt{\frac{\mu_0}{\varepsilon_0}} \frac{k_0}{\beta} \left[-2i\left(0.116 - \log\frac{2k_0|n|}{\beta}\right) + \frac{\pi}{2} + \frac{ik_x^2}{k_0^2 n^2}\right]. \tag{10}$$

The variation of n^2 in (6) applies only to those regions of the ionosphere where $|n| \gg 1$. It cannot be used in ionosphere models where $\sigma \ll \omega\varepsilon_0$.

6.2.2 *Exponential Changes of the Conductivity*

For an exponential variation of the ionospheric conductivity σ, the variable in (3) is changed from z to

$$v = \frac{\sigma}{\omega\varepsilon_0} = Be^{\beta z}. \tag{11}$$

The surface impedance is computed following Galejs [1961] as

$$Z_e = \frac{E_x}{H_y} = \sqrt{\frac{\mu_0}{\varepsilon_0}}\,\frac{k_0}{\beta}\left[-2i\left(0.116-\log\frac{2k_0}{\beta}\right)+\frac{\pi}{2}\,\frac{k_0^2+k_x^2}{k_0^2}\right.$$
$$\left.-i\,\frac{k_x^2-k_0^2}{k_0^2}\log v - i\,\frac{k_x^2}{k_0^2}\sum_{m=1}^{\infty}\frac{(-iv)^m}{m}\right]. \tag{12}$$

The validity of (12) is restricted by the inequality

$$\frac{|k_x^2-k_0^2|}{\beta^2} < \frac{k_0^2}{\beta^2} \ll v \ll \frac{\beta}{k_0}. \tag{13}$$

For $\beta = 1/3.25$ km^{-1} and $f = 1000$ c/s, v should satisfy $0.46\times10^{-2} \ll v \ll 15$. It is readily seen that (12) is valid in E.L.F, but not in the V.L.F. range of frequencies.

The models of exponential refractive index n and conductivity σ do not differ for $|n| \gg 1$, and the surface impedances (9) and (12) agree in this limit.

6.3 Propagation Transverse to a Horizontal Static Magnetic Field in a Cylindrical Geometry

A purely horizontal static magnetic field appears to provide the simplest computational model that may account for differences in propagation characteristics between the general east–west and west–east directions of propagation. Such a model is strictly valid only for propagation along the magnetic equator, but it provides a great analytical simplification of the problem. In the presence of a transverse horizontal static magnetic field, the T.E. and T.M. field components are not coupled in the ionosphere similarly as in an isotropic medium.

Reflections from a sharply bounded planar ionosphere model are discussed by Barber and Crombie [1959] and Wait [1962]. The reflection coefficients for an exponentially varying planar ionosphere model [Wait and Walters, 1964] are used by Wait and Spies [1965] to calculate wave-propagation parameters in the cylindrical space between the earth and the ionosphere; Galejs [1964a, b] discusses planar ionosphere models of arbitrary density variations, and curved ionosphere models have been also treated [Galejs, 1964c, 1967a; Pappert *et al.*, 1967].

In this section, the fields in the ionosphere are determined by numerically integrating the differential equations describing continuously varying ionospheric conductivity components [Galejs, 1964c] and also by approximating the ionosphere by a number of homogeneous thin shells [Galejs, 1967a]. These formulations lead to expressions for surface impedances that are effective for T.M. (or T.E.) field components propagating in the space between the ground surface and the lower ionospheric boundary.

6.3.1 *Differential Equation for a Continuously Varying Medium*

In a magneto-ionic medium, the relative tensor permittivity is for cylindrical coordinates (r, φ, z) of the form

$$[\varepsilon] = \begin{bmatrix} \varepsilon_1 & -\varepsilon_2 & 0 \\ \varepsilon_2 & \varepsilon_1 & 0 \\ 0 & 0 & \varepsilon_3 \end{bmatrix} = \begin{bmatrix} 1+\dfrac{i\sigma_1}{\omega\varepsilon_0} & -\dfrac{i\sigma_2}{\omega\varepsilon_0} & 0 \\ \dfrac{i\sigma_2}{\omega\varepsilon_0} & 1+\dfrac{i\sigma_1}{\omega\varepsilon_0} & 0 \\ 0 & 0 & 1+\dfrac{i\sigma_0}{\omega\varepsilon_0} \end{bmatrix} \tag{14}$$

if the static magnetic field is in the z direction. For a cold electron plasma, the permittivity components are given by

$$\varepsilon_1 = 1+\frac{\omega_p^2(\omega+iv)/\omega}{\omega_c^2-(\omega+iv)^2}, \tag{15}$$

$$\varepsilon_2 = \frac{i\omega_p^2\omega_c/\omega}{\omega_c^2-(\omega+iv)^2}, \tag{16}$$

$$\varepsilon_3 = 1-\frac{\omega_p^2}{\omega(\omega+iv)}, \tag{17}$$

where v is the effective collision frequency and where the plasma frequency ω_p and the cyclotron frequency ω_c of electrons are defined in terms of the electron density N_e, charge e, mass m, and the applied static magnetic induction B_0 as $\omega_p^2 = e^2N_e/(m\varepsilon_0)$ and $\omega_c = |e|\,B_0/m$. Substituting the appropriate parameters, it follows that $\omega_p^2 = 3.185N_e\times10^9$ for N_e in electrons per cm^3 and $\omega_c = 0.88\times10^7$ for $B_0 = 0.5$ gauss (or 0.5×10^{-4} M.K.S. units). In the presence of a multi-component plasma, the conductivity components σ_0, σ_1, and σ_2 can be computed from the formulas listed in Section 2.2.3.

It is assumed that the field components exhibit no variation in the z direction and that $[\varepsilon]$ is changing only in the r direction, which would be the south–north and vertical directions for equatorial propagation. The field equations

$$\nabla\times\mathbf{H} = -i\omega\varepsilon_0[\varepsilon]\cdot\mathbf{E} \tag{18}$$

and

$$\nabla\times\mathbf{E} = i\omega\mu_0\mathbf{H} \tag{19}$$

may be written in cylindrical components. Multiplying the r component of (18) with ε_1 and the φ component of (18) with ε_2, and adding the two equations, gives

$$E_r = [i\omega\varepsilon_0(\varepsilon_1^2+\varepsilon_2^2)]^{-1}\left(-\frac{\varepsilon_1}{r}\,\frac{\partial}{\partial\varphi}H_z+\varepsilon_2\frac{\partial}{\partial r}H_z\right). \tag{20}$$

Multiplying the r component of (18) with ε_2 and the φ component of (18) with ε_1, and sub-

tracting the two equations, gives

$$E_\varphi = [i\omega\varepsilon_0(\varepsilon_1^2+\varepsilon_2^2)]^{-1}\left(\frac{\varepsilon_2}{r}\frac{\partial}{\partial\varphi}H_z+\varepsilon_1\frac{\partial}{\partial r}H_z\right). \tag{21}$$

Substitution of (20) and (21) into the z component of (19) gives for r-dependent ε_1 and ε_2 the differential equation

$$\left.\begin{aligned}\frac{\partial^2}{\partial r^2}H_z+\frac{1}{r^2}\frac{\partial^2}{\partial\varphi^2}H_z+k_0^2\frac{\varepsilon_1^2+\varepsilon_2^2}{\varepsilon_1}H_z+\frac{\varepsilon_1^2+\varepsilon_2^2}{\varepsilon_1}\left[\frac{1}{r}\left(\frac{\partial}{\partial r}\frac{r\varepsilon_1}{\varepsilon_1^2+\varepsilon_2^2}\right)\right.\right.\\ \left.\left.\frac{\partial}{\partial r}H_z+\frac{1}{r}\left(\frac{\partial}{\partial r}\frac{\varepsilon_2}{\varepsilon_1^2+\varepsilon_2^2}\right)\frac{\partial}{\partial\varphi}H_z\right]=0.\end{aligned}\right\} \tag{22}$$

In the limit of $\varepsilon_1 = 1$ and $\varepsilon_2 = 0$, (22) is reduced to the simple wave equation in cylindrical coordinates.

The fields in the ionosphere should exhibit the same φ variation as the fields in the airspace between the ground surface and the ionospheric boundary. It follows from (12) and (24) of Chapter 5 that the solution for the fields in the ionosphere should exhibit the φ dependence of

$$H_z = \exp(i\nu\varphi)\,R(r), \tag{23}$$

where $\nu = k_0 aS$, a is the radius at the surface of the earth, and S is the yet unknown root of the modal equation. Substituting (23) in (22), $R(r)$ is determined from a solution of the differential equation

$$\frac{d^2R}{dr^2}+P(r)\frac{dR}{dr}+QR = 0, \tag{24}$$

where

$$P(r) = \frac{d}{dr}\log\left(\frac{\varepsilon_1}{\varepsilon_1^2+\varepsilon_2^2}\right)+\frac{1}{r} \tag{25}$$

and

$$Q(r) = \frac{\varepsilon_1^2+\varepsilon_2^2}{\varepsilon_1}k_0^2-\left(\frac{\nu}{r}\right)^2+\frac{i\nu}{r}\frac{\varepsilon_2}{\varepsilon_1}\log\left(\frac{\varepsilon_2}{\varepsilon_1^2+\varepsilon_2^2}\right). \tag{26}$$

In the limit of a and $r \to \infty$, equations (24) to (26) correspond to equations (10) to (12) of Galejs [1964b].

There is no coupling by the anisotropic medium between the field components E_r, E_φ, H_z and E_z, H_r, H_φ. If the excitation is such that the latter components are not excited (e.g. far fields of a vertical electric dipole of dipole moment $I\,dr$), the surface impedance in the anisotropic medium is simply

$$Z_e = E_\varphi/H_z. \tag{27}$$

Substituting (21) and (23), Z_e becomes

$$Z_e = \frac{1}{i\omega\varepsilon_0(\varepsilon_1^2+\varepsilon_2^2)}\left[\varepsilon_1\frac{1}{R}\frac{dR}{dr}+\frac{\varepsilon_2 i\nu}{r}\right]. \tag{28}$$

The variable $U = R'/R$ satisfies the differential equation

$$\frac{dU}{dr}+U^2(r)+P(r)\,U(r)+Q(r) = 0, \tag{29}$$

which can be integrated numerically after determining the surface impedance Z_e at the upper edge $y = y_u$ of the ionosphere model. Assuming that ε_1 and ε_2 are constant for $y > y_u$, it can be shown, following Galejs and Row [1964], that

$$U(y_u) = ik_0\sqrt{1+(\varepsilon_2/\varepsilon_1)^2}. \tag{30}$$

The impedance (28) applies for west–east propagation along the magnetic equator. The sign of ε_2 is reversed for east–west propagation, which causes an obvious nonreciprocity. The surface impedance computations start with an assumed value of $S = S_0$. Z_e of (28) is computed at the lower ionospheric boundary $r_l = a+h$. After assuming free space for $y < h$, this value of Z_e is used in the modal equation to obtain the first estimate of S. The Z_e and S computations are repeated until the S sequence converges.

A similar formulation has been also developed for propagation in the south–north direction across the magnetic equator [Galejs and Row, 1964; Galejs 1964b]. The numerical integration of differential equations of the type (29) requires a small step size at larger heights where the refractive index is large even though the fields are of negligible magnitude. The multilayer representations in Section 6.3.2 are less sensitive to the selection of layer thicknesses.

6.3.2 *Multilayer Representations*

A medium of radially varying properties can be approximated by a number of concentric thin shells, where each shell is assumed to be homogeneous. A large number of such shells is readily treated using the matrix notation that has been developed in Section 5.5.1. Field representations suitable for individual shells in an isotropic medium have been listed in Sections 5.5.2 to 5.5.4. It will be shown that these multilayer representations of an isotropic medium can be readily modified to consider the anisotropy caused by the static magnetic field which is horizontal and transverse to the direction of propagation [Galejs, 1967a].

The T.M. field components (E_r, E_φ, H_z) will be considered first. Equations (14) to (21) apply also to a homogeneous medium, and the differential equations (22) simplify for r-independent permittivity elements ε_1 and ε_2 to

$$\frac{\partial^2}{\partial r^2}H_z+\frac{1}{r}\frac{\partial}{\partial r}H_z+\frac{1}{r^2}\frac{\partial^2}{\partial\varphi^2}H_z+k_0^2\frac{\varepsilon_1^2+\varepsilon_2^2}{\varepsilon_1}H_z = 0. \tag{31}$$

For propagation in the φ direction, the magnetic field component H_z will have the φ and r dependence of (23). Substitution of (23) in (31) shows that $R(r)$ is determined from a solution of the Bessel's differential equation. Hence

$$H_z = e^{i\nu\varphi}[A_e H_\nu^{(1)}(k_e r)+B_e H_\nu^{(2)}(k_e r)], \tag{32}$$

where $k_e^2 = k_0^2(\varepsilon_1^2+\varepsilon_2^2)/\varepsilon_1$, $H_\nu^{(m)}(x)$ is the Hankel function of order ν and kind m. It follows from

(21) and (32) that the field representation (89) to (92) of Chapter 5 applies to the present geometry if $k = k_e$, $\alpha_1 = i\varepsilon_2 \nu/D$, $\beta = \varepsilon_1 kr/D$, and $D = i\omega\varepsilon_0(\varepsilon_1^2+\varepsilon_2^2)r$.

The T.E. field components (E_z, H_r, H_φ) can be determined from the remaining components of (18) and (19). The r and φ components of (19) give

$$H_r = \frac{1}{i\omega\mu_0 r}\frac{\partial}{\partial\varphi}E_z, \tag{33}$$

$$H_\varphi = -\frac{1}{i\omega\mu_0}\frac{\partial}{\partial r}E_z. \tag{34}$$

Substitution of (33) and (34) in the z component of (18) gives the differential equation

$$\frac{\partial^2}{\partial r^2}E_z+\frac{1}{r}\frac{\partial}{\partial r}E_z+\frac{1}{r^2}\frac{\partial^2}{\partial\varphi^2}E_z+k_0^2\varepsilon_3 E_z = 0. \tag{35}$$

Equation (35) is similar to (31), and its solution can be written from analogy with (32) as

$$E_z = e^{i\nu\varphi}[A_h H_\nu^{(1)}(k_h r)+B_h H_\nu^{(2)}(k_h r)], \tag{36}$$

where $k_h^2 = k_0^2\varepsilon_3$. It follows from (34) and (36) that the field representation (89) and (92) to (94) of Chapter 5 applies to the present geometry if $k = k_h$, $\alpha_1 = 0$, and $\beta = ik_h/(\omega\mu_0)$.

The Debye approximations of Section 5.5.2 can be used for T.M. fields substituting $k = k_e$, $\alpha = (i\varepsilon_2-\varepsilon_1)\nu/D$, $D = i\omega\varepsilon_0(\varepsilon_1^2+\varepsilon_2^2)r$, and for T.E. fields substituting $k = k_h$, $\alpha = \nu/(i\omega\mu_0 r)$. The appropriate values of k, α_1, and β should be also used in the Taylor series expansion of Section 5.5.3 or in the thin-shell approximations of Section 5.5.4.

The T.M. field components (E_r, E_φ, H_z) are determined from (20), (21), and (32) that are separate from the set of equations (33), (34), and (36), which describe the T.E. field components (E_z, H_r, H_φ). The T.M. and T.E. field components are not coupled by the anisotropic ionosphere if the static magnetic field is horizontal and transverse to the direction of propagation.

For T.M. modes, $k^2 = k_e^2$ is computed substituting (15) and (16) for ε_1 and ε_2 and by assuming $\nu \gg \omega$. For T.E. modes, $k^2 = k_h^2$ is computed substituting (17) for ε_3. It follows that

$$k_e^2 = k_0^2\frac{1+\dfrac{2\omega_p^2 i\nu}{\omega(\omega_c^2+\nu^2)}-\dfrac{\omega_p^4}{\omega^2(\omega_c^2+\nu^2)}}{1+\dfrac{\omega_p^2 i\nu}{\omega(\omega_c^2+\nu^2)}}, \tag{37}$$

$$k_h^2 = k_0^2\left[1-\frac{\omega_p^2}{i\nu\omega}\right]. \tag{38}$$

Assuming $\omega_c \gg \nu$, noting that $\omega_p \gg \omega$ and that ω_p is comparable to ω_c, (37) and (38) simplify to

$$k_e^2, \quad k_h^2 \approx k_0^2\frac{i\omega_p^2}{\omega\nu}. \tag{39}$$

The nearly imaginary solutions of k_e^2 and k_h^2 correspond to rapidly attenuated waves in the ionosphere layers where $\omega_c \gg \nu$.

Using the multilayer formalism of Section 5.5.1, the T.M. field components (E_φ, H_z) or the T.E. field components (H_φ, E_z) tangential to the lower ionosphere boundary $r = a+h$ are determined except for a multiplicative constant that represents the up-going wave amplitude in the upper homogeneous medium of $r > r_u$. The quotient of the tangential field components gives the surface impedances of T.M. or T.E. modes as $Z_e = E_\varphi(a+h)/H_z(a+h)$ or $Z_h = -E_z(a+h)/H_\varphi(a+h)$, which can be used for determining the wave-propagation parameters from the modal equation.

6.4 Spherical Layers with a Radial Static Magnetic Field

The anisotropic ionosphere can be also idealized by assuming a purely radial direction of the static magnetic field. This appears to be the only orientation of the magnetic field which leads to separable differential equations in a spherical geometry. In this model, the propagation parameters will be independent of the direction of propagation of the fields in the airspace between the lower ionospheric boundary and the ground surface. However, the radial magnetic field will introduce a coupling of T.E. and T.M. field components in the ionosphere and will facilitate the penetration of the fields into the ionosphere. This is analogous to the whistler-type of signals that are guided with a relatively small attenuation along the lines of the earth dipole field [Helliwell, 1965].

The effects of the static magnetic field have been estimated by Wait [1962] in the quasi-longitudinal approximation. A radial static magnetic field has been investigated also by Krasnushkin [1962]. Volland [1962, 1964] considers propagation below an inhomogeneous and anisotropic ionosphere using matrices of reflection coefficients. A formalism for treating a multilayer ionosphere has been presented by Wait [1963], and the formal solution for an M layer ionosphere is shown to require the solution of $4M+2$ simultaneous equations in $4M+2$ unknowns. A solution intended for frequencies in the Schumann resonance range (30 c/s and lower) has been derived in the thesis of Thompson [1963] and shown by Galejs [1964a]. This procedure considers each resonant mode (characterized by a Legendre polynomial of order n) separately and requires the multiplication of a sequence of 4×4 matrices. Similar solutions have been further developed by Large and Wait [1968], who consider added refinements such as mode coupling between T.M. and T.E. modes and the effects of a surface impedance discontinuity between the day and night hemispheres.

In this section, the solutions for a radial static magnetic field will be illustrated by expressing the fields in terms of waveguide modes, which involves Legendre functions of complex order ν, similarly as in Chapter 4 for isotropic boundaries of the shell. The solution will be carried out only for a single homogeneous layer; it will be only indicated how a multilayer treatment similar to the one described in Section 5.5 may be used to compute the fields in a sequence of such layers and to obtain impedance elements that characterize the anisotropic ionosphere.

The wave solutions for the fields in the anisotropic ionosphere can be derived from Maxwell's equations (18) and (19). For an assumed $\exp(-i\omega t)$ time dependence of the fields and an r-directed static magnetic field, the permittivity tensor $[\varepsilon]$ is given by the classical magneto-ionic theory as

$$[\varepsilon] = \begin{bmatrix} \varepsilon_3 & 0 & 0 \\ 0 & \varepsilon_1 & \varepsilon_2 \\ 0 & -\varepsilon_2 & \varepsilon_1 \end{bmatrix} = \begin{bmatrix} 1+\frac{i\sigma_0}{\omega\varepsilon_0} & 0 & 0 \\ 0 & 1+\frac{i\sigma_1}{\omega\varepsilon_0} & -\frac{i\sigma_2}{\omega\varepsilon_0} \\ 0 & \frac{i\sigma_2}{\omega\varepsilon_0} & 1+\frac{i\sigma_1}{\omega\varepsilon_0} \end{bmatrix}. \tag{40}$$

For a cold electron plasma, the permittivity components ε_j are computed from (15) to (17). More general formulas which account also for the presence of ions are listed by Galejs [1964a]. Fields in the anisotropic ionosphere should exhibit θ variations identical to the variations of fields below it. Equations (16) to (21) of Chapter 4 show that the field components E_r and H_r are proportional to $f_\nu(\theta) = P_\nu(-\cos\theta)$ while E_θ, H_θ, E_φ, and H_φ are proportional to $f_\theta(0) = f_\varphi(\theta) = dP_\nu(-\cos)/d\theta$. After writing out the two vector equations (18) and (19) in their six scalar components, the θ functions can be canceled leaving six scalar equations in the r-dependent components $E_j^0(r) = E_j/f_j(\theta)$, $H_j^0(r) = H_j/f_j(\theta)$, where $j = r$, θ, or φ. This gives

$$-\nu(\nu+1)\frac{E_\varphi^0}{r} = i\omega\mu_0 H_r^0, \tag{41}$$

$$-\frac{1}{r}\frac{\partial}{\partial r}(rE_\varphi^0) = i\omega\mu_0 H_\theta^0, \tag{42}$$

$$\frac{1}{r}\frac{\partial}{\partial r}(rE_\theta^0) - \frac{E_r^0}{r} = i\omega\mu_0 H_\varphi^0, \tag{43}$$

$$\nu(\nu+1)\frac{H_\varphi^0}{r} = i\omega\varepsilon_0\varepsilon_3 E_r^0, \tag{44}$$

$$\frac{1}{r}\frac{\partial}{\partial r}(rH_\varphi^0) = i\omega\varepsilon_0[\varepsilon_1 E_\theta^0 + \varepsilon_2 E_\varphi^0], \tag{45}$$

$$\frac{1}{r}\frac{\partial}{\partial r}(rH_\theta^0) - \frac{H_r^0}{r} = i\omega\varepsilon_0[\varepsilon_2 E_\theta^0 - \varepsilon_1 E_\varphi^0]. \tag{46}$$

After introducing the notation

$$k_j^2 = \omega^2\mu_0\varepsilon_0\varepsilon_j \tag{47}$$

($j = 1, 2, 3$), a manipulation of (41) to (46) results in

$$\frac{\partial^3}{\partial r^3}(rE_\varphi^0) + k_1^2\frac{\partial}{\partial r}\left\{\left[1-\frac{\nu(\nu+1)}{k_1^2r^2}\right]rE_\varphi^0\right\} + \frac{k_2^2k_3^2}{\nu(\nu+1)}\left[1-\frac{\nu(\nu+1)}{k_3^2r^2}\right]r^2E_r^0 = 0, \tag{48}$$

$$k_2^2\frac{\partial}{\partial r}(rE_\varphi^0) = \frac{k_3^2}{\nu(\nu+1)}\left\{\frac{\partial^2}{\partial r^2}(r^2E_r^0) + k_1^2\left[1-\frac{\nu(\nu+1)}{k_3^2r^2}\right]r^2E_r^0\right\}, \tag{49}$$

and

$$\left\{k_2^4 + k_1^4\left[1-\frac{\nu(\nu+1)}{k_1^2r^2}\right]\right\}rE_\varphi^0 + k_1^2\frac{\partial^2}{\partial r^2}(rE_\varphi^0) = k_2^2\frac{k_3^2}{\nu(\nu+1)}\frac{\partial}{\partial r}(r^2E_r^0), \tag{50}$$

E_φ^0 can be eliminated from (48) to (50), which gives a fourth-order differential equation for computing E_r^0. The parameter ν is defined by $\nu(\nu+1) = (k_0aS)^2$, where $k_0 = \omega\sqrt{\varepsilon_0\mu_0}$, a is the

radius of earth, and S is the yet undetermined root of the modal equation. The factors $\nu(\nu+1)/(k_jr)^2$ change gradually relative to $(r^2E_r^0)$, and only the first-order change is considered. These factors and their first derivatives are replaced by constants

$$q_j = \frac{\nu(\nu+1)}{(k_jr_m)^2}, \tag{51}$$

$$q_j' = \frac{\partial}{\partial r}q_j = -\frac{2}{r_m}q_j, \tag{52}$$

where r_m is the mean radius of an ionospheric layer. This results in

$$\frac{\partial^4}{\partial r^4}(r^2E_r^0) + b_3\frac{\partial^3}{\partial r^3}(r^2E_r^0) + B_2\frac{\partial^2}{\partial r^2}(r^2E_r^0) + b_1\frac{\partial}{\partial r}(r^2E_r^0) + (B_0+b_0)r^2E_r^0 = 0, \tag{53}$$

where

$$b_3 = \frac{q_1'k_1^4}{k_1^4(1-q_1)+k_2^4}, \tag{54}$$

$$B_2 = k_1^2(2-q_1-q_3), \tag{55}$$

$$b_1 = k_1^2\left[2q_3' + q_1'\frac{k_2^4-k_1^4(1-q_3)}{k_2^4+k_1^4(1-q_1)}\right], \tag{56}$$

$$B_0 = k_1^4(1-q_1)(1-q_3) + k_2^4(1-q_3), \tag{57}$$

$$b_0 = -\frac{q_1'q_3'k_1^6}{k_2^4+k_1^4(1-q_1)}. \tag{58}$$

A first-order solution of (53) is obtained by neglecting the small terms proportional to b_n. This solution is of the form

$$r^2E_r^0 = \exp(ikr), \tag{59}$$

where

$$k^2 = k_\pm^2 = k_1^2\left[1-\frac{1}{2}q_1-\frac{1}{2}q_3\right] \pm ik_2^2\sqrt{1-q_3-\frac{1}{4}\left(\frac{k_1}{k_2}\right)^4(q_3-q_1)^2}. \tag{60}$$

Equation (60) is seen to be in agreement with (34) to (36) of Wait [1963]. For negligible displacement currents, $k_j \gg k_0 = \omega\sqrt{\varepsilon_0\mu_0}$. Noting that $\nu(\nu+1) \approx (k_0r)^2$, $q_j \ll 1$ and (60) simplifies further to

$$k^2 = k_1^2 \pm ik_2^2. \tag{61}$$

The second-order solution (designated by primes) is obtained by a single iteration substituting (59) in (53), solving for k^2, and by using (60) for k in the right-hand side of this equation. This procedure gives

$$k_j'^2 = \frac{1}{B_2}(k_j^4 - ib_3k_j^3 + ib_1k_j + B_0 + b_0) = k_j^2 + \frac{ik_j}{B_2}(b_1 - b_3k_j^2) + \frac{b_0}{B_2}, \tag{62}$$

where $j = +$ or $-$. The second solution which corresponds to the negative of k_j is designated as $k_j''^2$. Although there are only minor differences between the solutions (60) and (62), it is

essential to use (62) in the subsequent expression (67) because (60) does not result in decoupled T.E. and T.M. field components as $\varepsilon_2 \to 0$ and $\varepsilon_3 \to 1$ in (40).

The field components will be derived using the planar approximation (51) to (52). The field components will be related to the amplitude of the radial electric field. The component E_r is assumed to be of the form

$$E_r^0 = a_r \nu(\nu+1) \frac{1}{r^2} \exp(ikr), \tag{63}$$

where k has four possible values according to (60) or (62). H_φ^0 follows from (44) as

$$H_\varphi^0 = a_r i\omega\varepsilon_0\varepsilon_3 \frac{1}{r} \exp(ikr). \tag{64}$$

E_θ^0 is obtained from (43)

$$E_\theta^0 = \frac{a_r i(1-q_3)k_3^2}{kr} \exp(ikr). \tag{65}$$

Computing the second derivative of (rH_θ^0) from (46), applying (41) and substituting (42) and (43) for the derivatives of (rE_φ^0) and (rE_θ^0) gives

$$H_\theta^0 = a_r i\omega\varepsilon_0\varepsilon_3 \frac{F}{r} \exp(ikr), \tag{66}$$

with

$$F = \frac{k_2^2(1-q_3)}{[k^2 - k_1^2(1-q_1)]}. \tag{67}$$

E_φ^0 and H_r^0 follow from (42) and (41) respectively as

$$E_\varphi^0 = -\frac{a_r i k_3^2 F}{kr} \exp(ikr), \tag{68}$$

$$H_r^0 = \frac{a_r \nu(\nu+1) k_3^2 F}{\omega\mu_0 k r^2} \exp(ikr). \tag{69}$$

When using (62) for k^2 in (67), there is no coupling between the T.M. components $(E_r^0, E_\theta^0, H_\varphi^0)$ and the T.E. components $(E_\varphi^0, H_r^0, H_\theta^0)$ for ε_2 or $k_2^2 \to 0$ in (41) to (46), and E_φ^0, H_r^0, and H_θ^0 of (68), (69), and (66) approach zero.† For negligible displacement currents, $q_j \ll 1$ and the expressions (63) to (69) are simplified to

$$E_r^0 = a_r \nu(\nu+1) \frac{1}{r^2} \exp(ikr), \tag{70}$$

† For decoupled field components, F of (67) should approach zero. However, the field components are not decoupled when using (60) for k^2 in (67). For $k_3 = k_1$, F is finite and independent of k_2. For $k_3 \neq k_1$ and $k_2 \to 0$, $F \sim k_3^2/(k_3^2 - k_1^2)$. After relating k_j^2 to the tensor permittivity components ε_j by (47), k_j^2 can be expressed in terms of collision frequencies ν, plasma frequencies ω_p, and gyrofrequencies ω_c of the charged particles of the ionosphere, as shown by (15) to (17). The last expression given above for F becomes $F \sim \nu/|\omega_c|$ which is increasing with a decreasing altitude contrary to expectations.

$$E_\theta^0 = a_r \frac{\varepsilon_3}{\varepsilon_1 \pm i\varepsilon_2} \frac{ik}{r} \exp(ikr), \tag{71}$$

$$E_\varphi^0 = a_r \frac{\varepsilon_3}{\varepsilon_2 \pm i\varepsilon_1} \frac{ik}{r} \exp(ikr), \tag{72}$$

$$H_r^0 = -a_r \nu(\nu+1) \frac{\varepsilon_3}{\varepsilon_2 \pm i\varepsilon_1} \frac{k}{\omega\mu_0 r^2} \exp(ikr), \tag{73}$$

$$H_\theta^0 = \pm a_r \omega\varepsilon_0\varepsilon_3 \frac{1}{r} \exp(ikr), \tag{74}$$

$$H_\varphi^0 = +ia_r \omega\varepsilon_0\varepsilon_3 \frac{1}{r} \exp(ikr). \tag{75}$$

The θ and φ components of the above equations are related as $E_\varphi^0/E_\theta^0 = H_\varphi^0/H_\theta^0 = \pm i$ which denotes circular polarization.

For a radial static magnetic field, the approximate wave number (61) may be computed substituting (15) to (17) and (47). For $\nu \gg \omega$, it follows that

$$k^2/k_0^2 = \begin{cases} 1 - \dfrac{\omega_p^2}{\omega(\omega_c + i\nu)}, \\ 1 + \dfrac{\omega_p^2}{\omega(\omega_c - i\nu)}. \end{cases} \tag{76}$$

Assuming $\omega_c \gg \nu$, noting that $\omega_p \gg \omega$ and that ω_p is comparable to ω_c, one of the solutions k^2 is almost real and negative corresponding to a rapidly attenuated wave; the other solution is essentially real and positive and will be attenuated to a lesser degree during its upward penetration of an ionospheric layer. This is contrasted with the solution for a horizontal static magnetic field in Section 6.3.2, where the waves corresponding to either T.E. or T.M. modes were severely attenuated. The radial static magnetic field facilitates, therefore, wave penetration in the ionosphere.

For a given mode characterized by a parameter ν and for a homogeneous layer of a finite thickness, the amplitudes a_r of the field components (64) to (69) or of (70) to (75) can have four different values corresponding to the four different roots k'_+, k'_-, k''_+, and k''_- of (53). These roots denote two up-going and two down-coming waves in each layer. In the notation of Section 5.5, the field components tangential to the boundaries of a spherical layer are characterized by a 4×4 matrix. The column matrix $[S_n]$ denotes the field components $E_\theta^0(r)$, $H_\varphi^0(r)$, $E_\varphi^0(r)$ and $H_\theta^0(r)$; and the coefficient matrix $[C_n]$ has four nonzero coefficients in a finite layer and two coefficients in $[C_u]$ for the upper unbounded space. The fields at the bottom of the ionosphere $[S_n(r_n)]$ are related by a matrix product to the up-going waves of the upper medium $[C_u]$, similarly as in (100) to (104) of Chapter 5; it is possible to compute the impedance reflected by the anisotropic ionosphere to the upper boundary of the airspace at $r = a+h$. Details of this development may be seen from Galejs [1965].

One of the waves characterized by (76) is rapidly attenuated with increasing height, and in a downward matrix multiplication procedure this inhomogeneous solution will rapidly increase in amplitude. Because of numerical inaccuracies in carrying out the matrix multiplications and

inversions, the r terms will tend to corrupt the smaller terms of the other solutions; this loss of linearity between different solutions of the quartic is described as numerical swamping. Swamping is inherent in methods where field components are the dependent variables of integration, and it may be avoided by an orthogonalization process which detects and systematically subtracts the inhomogeneous solution from terms representing the other waves [Pitteway, 1965; Walsh, 1967]. The undesirable wave components have been excluded also in the numerical solution of Inoue and Horowitz [1966]. For a purely radial geomagnetic field, numerical swamping is avoided by Galejs [1965] using a technique which becomes less accurate with increasing electrical contrast between adjacent layers. Methods where reflection coefficients are obtained by numerical integration of nonlinear equations of admittance matrices are free from numerical instabilities [Budden, 1969]. Such procedures have been used by Budden [1955], Pappert *et al.* [1967], and Aksenov and Lishin [1967]. In the thin-film optical method of Altman and Cory [1969], the dependent variables are reflection and transmission coefficient matrices; and the method is free from tendencies to numerical swamping.

6.5 Cylindrical Layers with a Dipping Static Magnetic Field

Ionosphere models with a dipping static magnetic field can be expected to be more representative of average propagation conditions than idealizations with a purely horizontal or radial static magnetic field that have been discussed in Sections 6.3 and 6.4. A purely horizontal transverse static magnetic field produced solutions that exhibited different characteristics for different directions of propagation, while for a radial magnetic field some waves exhibited little attenuation during their upward penetration of the ionosphere. A combination of these effects can be expected for ionosphere models with a dipping static magnetic field.

Formulations for an arbitrary direction of the earth's magnetic field are more involved [Budden, 1961a, b]. Reflection coefficients have been derived by Crombie [1961] and Johler [1961] for a sharply bounded homogeneous ionosphere in a planar geometry; Johler and Harper [1962] and Martin [1965] have considered wave propagation for tapered ionosphere models in a planar geometry, and Pappert [1968] follows Budden [1962] in treatment of a cylindrically curved geometry. Madden and Thompson [1965] use a combination of spherical geometry for the airspace between the earth's surface and the ionosphere and cylindrical stratifications of the ionosphere in their detailed analysis of Schumann resonances.

In this section, wave propagation is investigated for an arbitrary dip angle of the static magnetic field using a cylindrically stratified ionosphere model, but the wave propagation is restricted to west–east and east–west directions along a constant magnetic latitude. In planar layers, the fields can be expressed as a sum of four exponential functions, the wave numbers of which are determined from the solution of Booker's quartic. In a layer with cylindrical boundaries, the differential equations of the various field components are separable, but their solutions cannot be expressed in terms of known functions for arbitrary angles of the static magnetic field. Subsequently, the factors r of the radial variable of the differential equations are approximated by constants r_m, where r_m is the average radius of an ionospheric layer, similarly as for the thin-shell approximations in Section 5.5.4. The resulting field variation in a curved layer is expressed by the same exponential functions as in planar layers, but it considers the increase

of the phase velocity and decrease of the attenuation rate with the altitude of the layer [$S'(r_m) = (a/r_m)\,S(a)$, where Re S is inversely proportional to the phase velocity v_{ph}, Im S is proportional to the attenuation rate α, and a is the radius of the earth]. A homogeneous cylindrical region is assumed as the upper layer of the stratified regions shown in Fig. 6.1. The four tangential field components (E_φ, E_z, H_φ, H_z) computed at the bottom of this stratified region ($r = a+h$) will be related to the two up-going wave amplitudes of the upper half-space ($r > a+h_u$). Such a relation was postulated in Section 5.6 for the computation of phase velocities, attenuation rates, and excitation factors of the various modes that are excited in the airspace below an anisotropic ionosphere.

6.5.1 *Fields of a Homogeneous Layer*

The cylindrically stratified regions are described in the coordinates shown in Fig. 6.1. The coordinate axis r is in the vertical direction and z is in the south–to–north (S.N.) direction. The propagation is in the φ direction, which corresponds to the west–east (W.E.) direction. The static

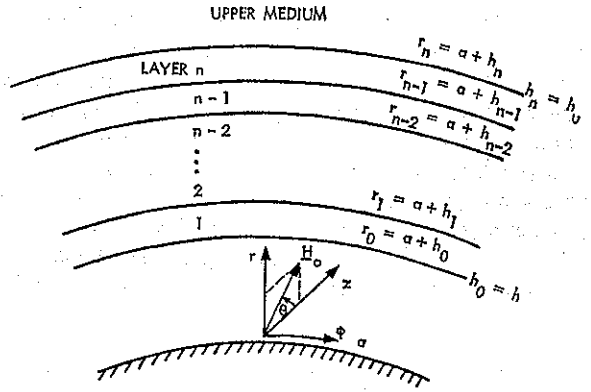

FIG. 6.1 A Cylindrically Stratified Medium

magnetic field is in the rz plane at an angle θ with respect to the z axis: $\theta = \pi/2$, 0, and $-\pi/2$ for the south pole, magnetic equator, and the north pole respectively; the dip angle $I = -\theta$. For propagation in the east–west (E.W.) direction, the z direction is reversed and $\theta = \pi/2, \pi$, and $3\pi/2$ for the south pole, magnetic equator, and the north pole respectively. For a z-directed static magnetic field, the electric flux density $\mathbf{D}$ is related to the electric field $\mathbf{E}$ by the dielectric permittivity tensor (14). For a θ-directed static magnetic field, the permittivity tensor is modified and $\mathbf{D}$ is related to $\mathbf{E}$ by

$$\begin{bmatrix} D_r \\ D_\varphi \\ D_z \end{bmatrix} = \begin{bmatrix} \varepsilon_{11} & \varepsilon_{12} & \varepsilon_{13} \\ -\varepsilon_{12} & \varepsilon_{22} & \varepsilon_{23} \\ \varepsilon_{13} & -\varepsilon_{23} & \varepsilon_{33} \end{bmatrix} \cdot \begin{bmatrix} E_r \\ E_\varphi \\ E_z \end{bmatrix}, \tag{77}$$

where

$$\varepsilon_{11} = \varepsilon_1 \cos^2\theta + \varepsilon_3 \sin^2\theta, \qquad \varepsilon_{22} = \varepsilon_1,$$
$$\varepsilon_{12} = -\varepsilon_2 \cos\theta, \qquad \varepsilon_{23} = -\varepsilon_2 \sin\theta,$$
$$\varepsilon_{13} = (\varepsilon_3 - \varepsilon_1)\sin\theta\cos\theta, \qquad \varepsilon_{33} = \varepsilon_1 \sin^2\theta + \varepsilon_3 \cos^2\theta.$$

For propagation in the φ direction, the fields will not vary with z. Using this restriction, the r and φ components of the field equations

$$\nabla \times \mathbf{H} = -i\omega\varepsilon_0[\varepsilon]\cdot\mathbf{E} \tag{78}$$

and

$$\nabla \times \mathbf{E} = i\omega\mu_0\mathbf{H} \tag{79}$$

can be rearranged into

$$E_r = \frac{1}{f}\left[gE_z - \frac{1}{i\omega\varepsilon_0}\left(\varepsilon_{22}\frac{1}{r}\frac{\partial}{\partial\varphi}H_z + \varepsilon_{12}\frac{\partial}{\partial r}H_z\right)\right], \tag{80}$$

$$E_\varphi = \frac{1}{f}\left[-hE_z + \frac{1}{i\omega\varepsilon_0}\left(\varepsilon_{11}\frac{\partial}{\partial r}H_z - \varepsilon_{12}\frac{1}{r}\frac{\partial}{\partial\varphi}H_z\right)\right], \tag{81}$$

$$H_r = \frac{1}{i\omega\mu_0 r}\frac{\partial}{\partial\varphi}E_z, \tag{82}$$

$$H_\varphi = -\frac{1}{i\omega\mu_0}\frac{\partial}{\partial r}E_z, \tag{83}$$

where

$$f = \varepsilon_{11}\varepsilon_{22} + \varepsilon_{12}^2 = (\varepsilon_1^2 + \varepsilon_2^2)\cos^2\theta + \varepsilon_1\varepsilon_3\sin^2\theta, \tag{84}$$
$$g = \varepsilon_{12}\varepsilon_{23} - \varepsilon_{13}\varepsilon_{22} = (\varepsilon_1^2 - \varepsilon_1\varepsilon_3 + \varepsilon_2^2)\sin\theta\cos\theta, \tag{85}$$
$$h = \varepsilon_{11}\varepsilon_{23} + \varepsilon_{12}\varepsilon_{13} = -\varepsilon_2\varepsilon_3\sin\theta. \tag{86}$$

Substitution of (80) to (83) in the z components of (78) and (79) results in

$$\frac{\partial^2}{\partial r^2}E_z + \frac{1}{r}\frac{\partial}{\partial r}E_z + \frac{1}{r^2}\frac{\partial^2}{\partial\varphi^2}E_z + \frac{k_0^2}{f}(\varepsilon_{13}g + \varepsilon_{23}h + \varepsilon_{33}f)E_z + \frac{i\omega\mu_0}{f}\left[h\frac{\partial}{\partial r}H_z - \frac{g}{r}\frac{\partial}{\partial\varphi}H_z\right] = 0 \tag{87}$$

and

$$\varepsilon_{11}\frac{\partial^2}{\partial r^2}H_z + \frac{\varepsilon_{11}}{r}\frac{\partial}{\partial r}H_z + \frac{\varepsilon_{22}}{r^2}\frac{\partial^2}{\partial\varphi^2}H_z + k_0^2 f H_z - i\omega\varepsilon_0\left[h\frac{\partial}{\partial r}E_z + \frac{h}{r}E_z + \frac{g}{r}\frac{\partial}{\partial\varphi}E_z\right] = 0, \tag{88}$$

where $k_0 = \omega\sqrt{\varepsilon_0\mu_0}$. The ionosphere layers are assumed to have a thickness 2Δ, which is much less than their average radius r_m or the wavelength λ. The factors r of the differential equations are approximated by their average values r_m. This is equivalent to the thin-shell or exponential approximations developed in Section 5.3 for an isotropic medium or in Section 6.3.2 for anisotropic layers with a horizontal static magnetic field. In multilayer representations, these approximations are more accurate than Airy function approximations of the radial functions following Section 5.5.6. These modified differential equations are satisfied by field components

of the form

$$F_j(r, \varphi, z, t) = F_j^0 \exp(-i\omega t + ik_0 S a\varphi + ikr), \tag{89}$$

where $F_j = E_j$ or H_j and where the root S of the modal equation and the wave number k of the r dependence remain to be determined. After substituting (89) in (87) and (88), a rather lengthy algebraic manipulation leads to

$$A_2X^2 + A_1X + A_0 = 0 \tag{90}$$

with

$$X = k_r\left(k_r + \frac{1}{ik_0 r_m}\right), \tag{91}$$

$$A_2 = \varepsilon_1\cos^2\theta + \varepsilon_3\sin^2\theta, \tag{92}$$

$$A_1 = S'^2[\varepsilon_3\sin^2\theta + \varepsilon_1(1+\cos^2\theta)] - \varepsilon_1\varepsilon_3(1+\sin^2\theta) - (\varepsilon_1^2+\varepsilon_2^2)\cos^2\theta, \tag{93}$$

$$\left.\begin{aligned} A_0 = {} & S'^4\varepsilon_1 - S'^2(\varepsilon_1^2 + \varepsilon_1\varepsilon_3 + \varepsilon_2^2) + (\varepsilon_1^2+\varepsilon_2^2)\varepsilon_3 \\ & - \frac{iS'}{k_0 r_m}\varepsilon_2\varepsilon_3\sin^2\theta\cos\theta\frac{\varepsilon_1^2+\varepsilon_2^2-\varepsilon_1\varepsilon_3}{(\varepsilon_1^2+\varepsilon_2^2)\cos^2\theta + \varepsilon_1\varepsilon_3\sin^2\theta}, \end{aligned}\right\} \tag{94}$$

$$k_r = k/k_0, \tag{95}$$

$$S' = aS/r_m. \tag{96}$$

For $|k_r| \gg 1/(k_0 r_m)$, (90) is reduced to a biquadratic equation. The term proportional to $1/(k_0 r_m)$ becomes negligible also for the coefficient A_2, and (90) compares closely with the quartic equation (116) when the parameter $\varphi = 0$ is substituted in the latter. For a given mode characterized by a particular value of k_r, the amplitudes E_z^0 and H_z^0 are determined substituting (89) in (87) or (88); and the other field components follow from (80) to (83).

For a horizontal static magnetic field ($\theta = 0$) $h = g = 0$, E_z^0 and H_z^0 are not coupled by (87) or (88); and the T.E. field components (H_r, H_φ, E_z) can have amplitudes independent of T.M. fields (E_r, E_φ, E_z). For radial static magnetic field ($\theta = \pm\pi/2$) $g = 0$, but $h = 0$ if the off-diagonal terms ε_2 of (14) approach zero. This was also noted in the discussion following (69) of Section 6.4. For intermediate values of θ, the T.E. and T.M. fields are decoupled only if $\varepsilon_1 \to \varepsilon_3$, which implies isotropic propagation.

With the exception of quasi-T.E. modes at daytime, the T.M. field components will predominate in the lower ionosphere regions and in the space between the earth and the ionosphere [Galejs, 1969a]. It is therefore convenient to express the fields in terms of one of the T.M. components (E_r, E_φ, H_z), and the vertical component E_r may be selected. After applying (89), the H_j components of (79) are substituted in the φ and z components of (78). The resulting two equations contain only the electric field components E_r, E_φ, and E_z, which can be combined to give

$$E_\varphi^0 = \frac{1}{D}\left\{(k_r S' - \varepsilon_{12})\left[\varepsilon_{33} - S'^2 - k_r\left(k_r + \frac{1}{ik_0 r}\right)\right] - \varepsilon_{23}\varepsilon_{13}\right\}E_r^0, \tag{97}$$

$$E_z^0 = \frac{1}{D}\left\{\left[\varepsilon_{22} - k_r\left(k_r + \frac{1}{ik_0 r}\right)\right]\varepsilon_{13} + \varepsilon_{23}(k_r S' - \varepsilon_{12})\right\}E_r^0, \tag{98}$$

where

$$D = \left[\varepsilon_{22} - k_r\left(k_r + \frac{1}{ik_0 r}\right)\right]\left[\varepsilon_{33} - S'^2 - k_r\left(k_r + \frac{1}{ik_0 r}\right)\right] + \varepsilon_{23}^2. \tag{99}$$

H_φ of (83) is rewritten as

$$H_\varphi^0 = -\sqrt{\frac{\varepsilon_0}{\mu_0}}\, k_r E_z^0. \tag{100}$$

H_z is computed from the z component of (79) as

$$H_z^0 = \sqrt{\frac{\varepsilon_0}{\mu_0}}\left[\left(k_r + \frac{1}{ik_0 r}\right)E_\varphi^0 - S' E_r^0\right]. \tag{101}$$

6.5.2 *Multilayer Representations*

In each of the ionosphere layers, fields consist of components having four different wave numbers which correspond to the four different roots of the quartic (90). The net fields of a given layer can be written as

$$\begin{bmatrix} E_\varphi(r) \\ H_z(r) \\ H_\varphi(r) \\ E_z(r) \end{bmatrix} = [c_n(r)] \cdot \begin{bmatrix} A_{1n} \\ A_{2n} \\ A_{3n} \\ A_{4n} \end{bmatrix} \tag{102}$$

where the matrix elements c_{1j}, c_{2j}, c_{3j}, and c_{4j} are determined from (97), (101), (100), and (98) respectively and where A_{jn} represents the amplitude E_r^0 of a wave characterized by a root k_j of the quartic (90). Equation (102) can be written more compactly as

$$[S_n(r)] = [c_n(r)] \cdot [A_n]. \tag{103}$$

Fields at the upper boundary $r = r_m + \Delta$ of the layer n are related to the fields at the lower boundary $r = r_m - \Delta$ as

$$[S_n(r_m + \Delta)] = [d_n] \cdot [S_n(r_m - \Delta)] \tag{104}$$

with

$$[d_n] = [c_n(r_m + \Delta)] \cdot [c_n^{-1}(r_m - \Delta)]. \tag{105}$$

Equations (103) to (105) are analogous to the matrix relations (95) to (98) developed for 2×2 matrices in Section 5.5.1.

Similarly, fields at the boundary h_u of the upper medium are related to the fields at lower boundary h of the stratified medium as

$$[S_n(a + h_u)] = [d_n] \cdot [d_{n-1}] \ldots [d_2] \cdot [d_1] \cdot [S_1(a + h)] = [p_n] \cdot [S_1(a + h)]. \tag{106}$$

This relation is inverted as

$$[S_1(a + h)] = [p_n^{-1}] \cdot [S_n(a + h_u)] = [p_n^{-1}] \cdot [S_u(a + h_u)] = [p_n^{-1}] \cdot [c_u(a + h_u)] \cdot [A_u], \tag{107}$$

where the subscript u refers to the upper medium. Only two up-going waves with Im $k_j > 0$ exist in the upper medium. Their amplitudes are designated as A_{1u} and A_{3u}. Introducing the notation

$$[q] = [p_n^{-1}] \cdot [c_u(a + h_u)], \tag{108}$$

(107) is changed to

$$E_\varphi(h) = q_{11} A_{1u} + q_{13} A_{3u}, \tag{109}$$

$$H_z(h) = q_{21} A_{1u} + q_{23} A_{3u}, \tag{110}$$

$$H_\varphi(h) = q_{31} A_{1u} + q_{33} A_{3u}, \tag{111}$$

$$E_z(h) = q_{41} A_{1u} + q_{43} A_{3u}. \tag{112}$$

These equations serve as an input in the computation of propagation parameters for the waves below the anisotropic ionosphere following (181) to (184) of Section 5.6.1 or of Section 5.7.2. The matrix elements q_{ij} are uniquely related to the reflection coefficients ${}_{\|}R_{\|}$, ${}_{\perp}R_{\|}$, ${}_{\|}R_{\perp}$ and ${}_{\perp}R_{\perp}$ of the anisotropic ionosphere [Budden, 1961a] following the development of the Appendix (Section 6.8.1).

The calculation of the fields in the ionosphere starts from the lower boundary at h and proceeds upwards. The numerical evaluation of the matrix products will eventually lead to numerical inaccuracies, loss of linearity between the different solutions of the quartic or to numerical swamping, which has been discussed in the conclusion of Section 6.4. The fields decay during the penetration into the ionosphere, and numerical errors become noticeable only at heights above the effective reflection height. The computations start from h_b, and it is possible to select the height h_u in such a way that the possible numerical errors do not affect the resulting propagation characteristics of the fields below the ionosphere. For E.L.F. waves, the effective reflection height occurs near the boundary h_u of the upper half space of Fig. 6.1, which is in the range from 95 to 120 km for the various ionosphere models. For V.L.F. waves, the effective nighttime reflection height is in the vicinity of 85 km, and the computed propagation characteristics remain constant for $95 < h_u < 115$ km. Numerical errors affect the calculations of surface impedances and propagation data only for $h_u \geq 120$ km when a calculated field strength ratio $H_z(h_u)/H_z(h)$ shows a sudden increase in magnitude [Galejs, 1968a].

6.6 Exponential Approximation for Arbitrary Directions of Propagation Below an Anisotropic Ionosphere

The ionosphere model of Section 6.5 considered a dipping static magnetic field, but the propagation was restricted along a constant magnetic latitude. An exponential height variation of the various field components was obtained by simplifying the differential equations for the cylindrical geometry. In the ionosphere model of this section, the static magnetic field is also dipping; but the direction of propagation is arbitrary [Galejs, 1967b, 1968b]. The fields within the ionospheric layers are described in the rectangular coordinates of Fig. 6.2, but by considering the increase of phase velocity and a decrease of the attenuation rate with the altitude of the layer [$S'(r_m) = (a/r_m)\, S(a)$]. Following Section 5.5.4 and Fig. 5.3 (p. 172), such a multilayer

representation approximates the earth's curvature effects in a cylindrical geometry. This method will be further justified by comparing the results in the special case of E.W. or W.E. propagation with the earlier results of Section 6.5.

6.6.1 *Fields of a Homogeneous Layer*

The ionosphere is assumed to be stratified as indicated in Fig. 6.2. The coordinate axes are chosen so that z is in the vertical direction, y points north, and x points east. The static magnetic field is directed away from the origin in the yz plane at an angle θ with respect to the xy plane. ($\theta = \pi/2$, 0 and $-\pi/2$ for the south magnetic pole, magnetic equator, and north magnetic pole respectively.) The propagation is considered in the φ direction with respect to the x-axis, and the field components are assumed of the form

$$F_j(x, y, z, t) = F_j^0 \exp\left[-i\omega t + ik_0 S'(x\cos\varphi + y\sin\varphi) + ikz\right], \tag{113}$$

where $F_j = D_j, E_j$, or H_j, $k_0 = \omega\sqrt{\mu_0\varepsilon_0}$ and where the root $S = S'r_m/a$ of the modal equation and the wave number k of the z dependence remain to be determined. In the case where the

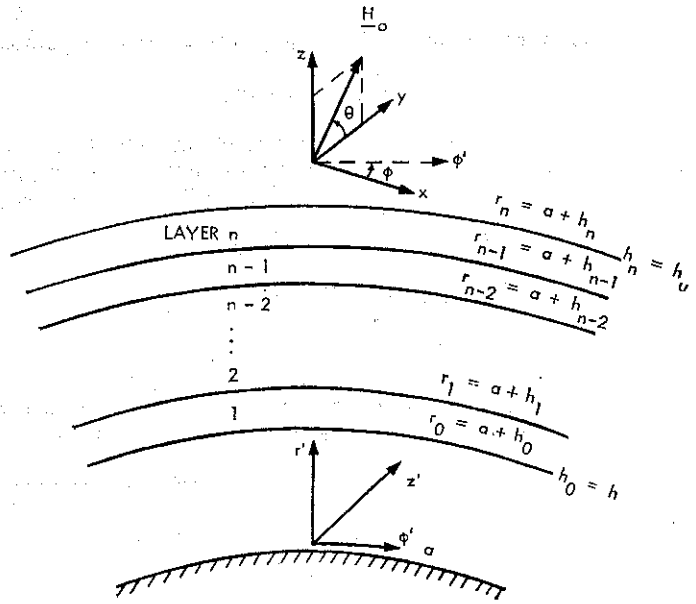

FIG. 6.2 A Cylindrically Stratified Medium

static magnetic field is directed along the z-axis, the electric flux density **D** is related to the electric field **E** by the dielectric permittivity tensor (14). For a θ-directed magnetic field and the x, y, z coordinates of Fig 6.2, **D** is related to **E** by

$$\begin{bmatrix} D_x \\ D_y \\ D_z \end{bmatrix} = \begin{bmatrix} \varepsilon_1 & -\varepsilon_2\sin\theta & \varepsilon_2\cos\theta \\ \varepsilon_2\sin\theta & (\varepsilon_1\sin^2\theta + \varepsilon_3\cos^2\theta) & (\varepsilon_3-\varepsilon_1)\sin\theta\cos\theta \\ -\varepsilon_2\cos\theta & (\varepsilon_3-\varepsilon_1)\sin\theta\cos\theta & (\varepsilon_1\cos^2\theta + \varepsilon_3\sin^2\theta \end{bmatrix} \cdot \begin{bmatrix} E_x \\ E_y \\ E_z \end{bmatrix} \tag{114}$$

The field equations (78) and (79) are written out in rectangular coordinates. Substituting (114) in (78) and (79) and applying (113), it follows that

$$\begin{bmatrix} a_{11}-k_r^2 & a_{12} & a_{13}+k_r\alpha_c \\ a_{21} & a_{22}-k_r^2 & a_{23}+k_r\alpha_s \\ -a_{13}+k_r\alpha_c & a_{23}+k_r\alpha_s & a_{33} \end{bmatrix} \cdot \begin{bmatrix} E_x^0 \\ E_y^0 \\ E_z^0 \end{bmatrix} = 0, \tag{115}$$

where

$$\begin{aligned} a_{11} &= \varepsilon_1 - S'^2\sin^2\varphi, & a_{23} &= (\varepsilon_3-\varepsilon_1)\sin\theta\cos\theta, \\ a_{12} &= -\varepsilon_2\sin\theta + S'^2\sin\varphi\cos\varphi, & a_{33} &= \varepsilon_1\cos^2\theta + \varepsilon_3\sin^2\theta - S'^2 \\ a_{13} &= \varepsilon_2\cos\theta, & \alpha_c &= S'\cos\varphi, \\ a_{21} &= \varepsilon_2\sin\theta + S'^2\sin\varphi\cos\varphi, & \alpha_s &= S'\sin\varphi, \\ a_{22} &= \varepsilon_1\sin^2\theta + \varepsilon_3\cos^2\theta - S'^2\cos^2\varphi, & k_r &= k/k_0. \end{aligned}$$

This system of three linear equations has a solution if its determinant of coefficients vanishes. After some algebra, this gives

$$k_r^4 a_4 + k_r^3 a_3 + k_r^2 a_2 + k_r a_1 + a_0 = 0 \tag{116}$$

with

$$\begin{aligned} a_4 &= \varepsilon_1\cos^2\theta + \varepsilon_3\sin^2\theta, \\ a_3 &= 2S'(\varepsilon_3-\varepsilon_1)\sin\varphi\sin\theta\cos\theta, \\ a_2 &= S'^2[\varepsilon_1+\varepsilon_3^*+\cos^2\theta\cos^2\varphi(\varepsilon_1-\varepsilon_3)] - \varepsilon_1\varepsilon_3(1+\sin^2\theta) - (\varepsilon_1^2+\varepsilon_2^2)\cos^2\theta, \\ a_1 &= 2S'[(\varepsilon_3-\varepsilon_1)(S'^2-\varepsilon_1)+\varepsilon_2^2]\sin\varphi\sin\theta\cos\theta, \\ a_0 &= S'^4[\varepsilon_1\cos^2\varphi + (\varepsilon_1\sin^2\theta + \varepsilon_3\cos^2\theta)\sin^2\varphi] + S'^2[-\varepsilon_1\varepsilon_3(1+\cos^2\theta\sin^2\varphi) \\ &\quad -(\varepsilon_2^2+\varepsilon_1^2)(\cos^2\varphi + \sin^2\varphi\sin^2\theta)] + \varepsilon_3(\varepsilon_1^2+\varepsilon_2^2). \end{aligned}$$

The wave number k_r is determined from the solution of (116) which is equivalent to the familiar Booker quartic [Budden, 1961]. The four complex roots of the quartic represent two up-going and two down-coming waves; for a semi-infinite medium ($r > a+h_u$), only the up-going waves are excited. A method of solving the quartic (116) is outlined in the Appendix (Section 6.8.2). The roots of the quartic are computed from a root of an auxiliary cubic equation and the solutions of three quadratic equations.

For propagation in W.E. ($\varphi = 0$) and E.W. ($\varphi = \pi$ directions, the coefficients a_3 and a_1 of the quartic (116) are zero; and the solutions of this biquadratic equation are the same as for (90) of Section 6.5 in the limit of $k_0 r_m \gg 1$. The two solutions of the biquadratic equation will be designated as $k_+^2 = (k_0 k_{r+})^2$ and $k_-^2 = (k_0 k_{r-})^2$.

The field components E_x and E_y are related to E_z from (115)

$$E_x^0 = \frac{1}{D}\left[(a_{22}-k_r^2)(a_{13}+k_r\alpha_c) - a_{12}(a_{23}+k_r\alpha_s)\right]E_z^0, \tag{117}$$

$$E_y^0 = \frac{1}{D}\left[(a_{11}-k_r^2)(a_{23}+k_r\alpha_s) - a_{21}(a_{13}+k_r\alpha_c)\right]E_z^0, \tag{118}$$

with

$$D = a_{12}a_{21} - (a_{11} - k_r^2)(a_{22} - k_r^2). \tag{119}$$

The magnetic field components are obtained by substituting (113) in (79). It follows that

$$H_x^0 = \sqrt{\frac{\varepsilon_0}{\mu_0}}(S' \sin\varphi E_z^0 - k_r E_y^0), \tag{120}$$

$$H_y^0 = \sqrt{\frac{\varepsilon_0}{\mu_0}}(k_r E_x^0 - S' \cos\varphi E_z^0), \tag{121}$$

$$H_z^0 = \sqrt{\frac{\varepsilon_0}{\mu_0}} S'(E_y^0 \cos\varphi - E_x^0 \sin\varphi). \tag{122}$$

In the special case of transverse propagation and a horizontal magnetic field, $\theta = 0$ and $\varphi = 0$ or π. The coefficients $a_1 = a_3 = 0$; the quartic (116) is reduced to a biquadratic equation and its solutions are

$$k^2 = \left[\frac{\varepsilon_1^2 + \varepsilon_2^2}{\varepsilon_1} - S'^2\right] k_0^2, \tag{123}$$

$$k^2 = [\varepsilon_3 - S'^2] k_0^2. \tag{124}$$

The field components E_x, E_z, and H_y are uncoupled from the field components E_y, H_x, and H_z. These two sets of field components have the wave numbers (123) and (124) respectively. The same result is obtained by examining the differential equations (31) and (35) of Section 6.3.2 at $r' = a + h_u$ in the limit of $(kr) \to \infty$.

For a vertical static magnetic field ($\theta = \pi/2$), the coefficients $a_1 = a_3 = 0$ and the remaining coefficients a_4, a_2, and a_0 are independent of φ. Equation (116) becomes biquadratic and its solutions are

$$k_r^2 = k^2/k_0^2 = \varepsilon_1 - \frac{1}{2} S'^2\left(1 + \frac{\varepsilon_1}{\varepsilon_2}\right) \pm i\varepsilon_2 \sqrt{1 - \frac{S'^2}{\varepsilon_3} - \frac{1}{4}\frac{\varepsilon_1^2}{\varepsilon_2^2} S'^4 \left(\frac{1}{\varepsilon_3} - \frac{1}{\varepsilon_1}\right)^2}. \tag{125}$$

Equation (125) agrees with (60) of Section 6.4. For negligible displacement currents, $|S'^2| \ll |\varepsilon_j|$; and the horizontal field components computed from (117) to (121) are circularly polarized ($E_x^0/E_y^0 = H_x^0/H_y^0 = \pm i$). This is also in agreement with equations (71), (72), (74), and (75) of Section 6.4.

In the limit of decreasing anisotropy ($\varepsilon_2 \to 0$), the T.E. (H_x, E_y, H_z) and the T.M. (E_x, H_y, E_z) field components should become uncoupled. This limit will be examined for small and large values of the ratio $\varepsilon_2/(\varepsilon_3 - \varepsilon_1)$. For an electron plasma, this ratio can be expressed alternately applying (15) to (17) as $(\nu - i\omega)/\omega_c$, where ν is the effective collision frequency and ω_c is the cyclotron frequency.

For $|\varepsilon_2| \ll |\varepsilon_3 - \varepsilon_1|$, the two solutions of (125) become $k_{r+}^2 = \varepsilon_1 - S'^2(\varepsilon_1/\varepsilon_3) - \varepsilon_2^2 Q$ and $k_{r-}^2 = \varepsilon_1 - S'^2 - \varepsilon_2^2 Q$, where $Q = (\varepsilon_3 - S'^2)/[S'^2(\varepsilon_1 - \varepsilon_3)]$. Substituting k_{r+} or k_{r-} in (117) and (118), it follows that $E_x^0/E_y^0 = S'^2(\varepsilon_3 - \varepsilon_1)/(\varepsilon_3\varepsilon_2)$ or $-\varepsilon_2 Q$. The wave numbers k_+ and k_- characterize therefore T.M. and T.E. modes in the limit of $\varepsilon_2 \to 0$.

For $|\varepsilon_2| \gg |\varepsilon_3 - \varepsilon_1|$ (or $|\nu - i\omega| \gg \omega_c$), it can be shown that $\varepsilon_3 \approx \varepsilon_1$; under these conditions, the solutions of (125) simplify to $k_r^2 \approx \varepsilon_1 - S'^2 \pm i\varepsilon_2\sqrt{1 - S'^2/\varepsilon_1}$. Substitution of k_{r+} or k_{r-} for $\theta = \pi/2$ and $\varphi = 0$ in (117) and (118) shows that $E_x^0/E_y^0 = \pm i\sqrt{1 - S'^2/\varepsilon_1}$, which is independent of ε_2 and is of the same magnitude for both wave numbers. The solutions of form (113) with wave numbers $k/k_0 = k_{r+}$ and k_{r-} are not linearly independent in the limit of $\varepsilon_2 \to 0$ and $\varepsilon_3 = \varepsilon_1$ when the four distinct roots of the quartic (116) degenerate into two pairs. However, the solutions corresponding to the four roots of the quartic can be combined in such a way that the T.M. and T.E. field components become uncoupled by the medium as $\varepsilon_2 \to 0$. The development summarized in the Appendix (Section 6.8.3) shows that the surface impedance E_x/H_y (or $-E_y/H_x$) which a given layer presents to the T.M. (or T.E.) field components of the lower regions remains unaltered in the modified solution. A proper solution of the boundary value problem requires a continuity of the tangential field components across the boundary between the lower ionosphere and the airspace or a boundary impedance E_x/H_y that matches the surface impedance Z_e reflected by the T.M. field components and $-E_y/H_x$ that matches the surface impedance Z_h reflected by the T.E. field components of the airspace. The solutions of this section provide the same impedances as the solutions of Section 6.8.3, and there is no need to modify the present field formulations in the limit of $\varepsilon_2 \to 0$ with $|\nu - i\omega| \gg \omega_c$.

6.6.2 *Multilayer Representations*

In the stratified medium, the fields consist of components having four different wave numbers, which correspond to the four different roots k_j of the quartic (116). The net fields of a given layer can be written as

$$\begin{bmatrix} E_x(r) \\ H_y(r) \\ H_x(r) \\ E_y(r) \end{bmatrix} = [c_n(r)] \cdot \begin{bmatrix} A_{1n} \\ A_{2n} \\ A_{3n} \\ A_{4n} \end{bmatrix} \tag{126}$$

where A_{jn} represents the amplitudes E_z^0 of a wave characterized by a root k_j of the quartic and where the matrix elements c_{1j}, c_{2j}, c_{3j}, and c_{4j} are determined from (117), (121), (120), and (118) respectively. This equation is similar to (102), and the matrix manipulation technique described in Section 6.5.2 can be applied to the calculation of fields in the ionosphere. It follows that fields at the bottom of the ionosphere $h = h_b$ are related to the two up-going wave amplitudes of the upper medium as

$$E_x(h) = q_{11}A_{1u} + q_{13}A_{3u}, \tag{127}$$

$$H_y(h) = q_{21}A_{1u} + q_{23}A_{3u}, \tag{128}$$

$$H_x(h) = q_{31}A_{1u} + q_{33}A_{3u}, \tag{129}$$

$$E_y(h) = q_{41}A_{1u} + q_{43}A_{3u}, \tag{130}$$

where the q matrix is defined by (108). In changing to the primed coordinates of Fig. 6.2, it should be noted that

$$F_{\varphi'} = F_x \cos\varphi + F_y \sin\varphi, \tag{131}$$

$$F_{z'} = -F_x \sin\varphi + F_y \cos\varphi, \tag{132}$$

where $F = E$ or H. Substitution of (127) to (130) in (131) and (132) shows that

$$E_{\varphi'}(h) = q'_{11}A_{1u}+q'_{13}A_{3u}, \tag{133}$$
$$H_{x'}(h) = q'_{21}A_{1u}+q'_{23}A_{3u}, \tag{134}$$
$$H_{\varphi'}(h) = q'_{31}A_{1u}+q'_{33}A_{3u}, \tag{135}$$
$$E_{z'}(h) = q'_{41}A_{1u}+q'_{43}A_{3u}, \tag{136}$$

where

$$q'_{1j} = (q_{1j}\cos\varphi+q_{4j}\sin\varphi),$$
$$q'_{2j} = (q_{2j}\cos\varphi-q_{3j}\sin\varphi),$$
$$q'_{3j} = (q_{3j}\cos\varphi+q_{2j}\sin\varphi),$$
$$q'_{4j} = (q_{4j}\cos\varphi-q_{1j}\sin\varphi).$$

$E_{\varphi'}$, $H_{x'}$, $H_{\varphi'}$, and $E_{z'}$ of (133) to (136) can be used for E_φ, H_z, H_φ, and E_z in (181) to (184) or in (237) of Chapter 5 for computing the propagation parameters of waves below the anisotropic ionosphere.

The numerical problems in the computation of the matrix elements q'_{ij} are similar to the ones encountered in computing q_{ij} and are discussed in the last paragraph of Section 6.5.2

6.7 Anisotropy of the Ground

The ground is usually considered as a homogeneous lossy half-space [Baños, 1966]. There are also treatments of the effects of isotropic vertically stratified layers and of the related anisotropy, where the effective conductivity in the vertical direction is different from the conductivity in a horizontal direction [Wait, 1966]. In the magnetotelluric analysis [Cagniard, 1953], measurements of electric and magnetic fields on the earth's surface are interpreted using a mathematical model of a vertically stratified isotropic earth. The magnetotelluric method has been extended to a generally anisotropic earth by Cantwell [1960] and by Bostick and Smith [1962]. Dowling [1968] has used such analysis techniques to interpret a number of measurements, which show that the effective ground conductivity is anisotropic in the horizontal plane. The maximum conductivity is 3 to 10 times higher than the minimum conductivity for frequencies in the range from 30 to 10^{-3} c/s, with the maximum horizontal conductivity component in the range from 1 to 3 mho/m in northern and central Wisconsin. Clark [1966] reports measured coefficients of anisotropy for sedimentary and metamorphic rock from 1.01 for limestone to 2.75 for graphic slate. Also, vertical or tilted interfaces between rocks of different bulk conductivities will contribute to the anisotropy. (In the vicinity of an interface, the effective measured conductivity will differ for directions parallel and perpendicular with the interface over distances comparable to the skin depth following d'Erceville and Kunetz [1962], Weaver [1963], or Swift [1967]]).

The ground surface will present different conductivities to horizontal electric fields impressed in different directions, and this anisotropy will also affect the performance of horizontal wire antennas. The ground surface is considered as the lower boundary of the spherical earth-to-ionosphere waveguide of Fig. 6.3. The fields above the ground surface are described in (r, θ, φ) coordinates, but the fields below the ground surface in x, y, z coordinates, where the

θ-axis is at an angle ψ relative to the x-axis. The ionosphere is approximated by an isotropic conductor of conductivity σ_i, and the waveguide is excited by E.L.F. or V.L.F. waves propagating in the θ direction. The ground is characterized by a conductivity ellipsoid of axes σ_1, σ_2, and σ_3. Ideally, the current flow will be in the direction of the impressed electric field if the

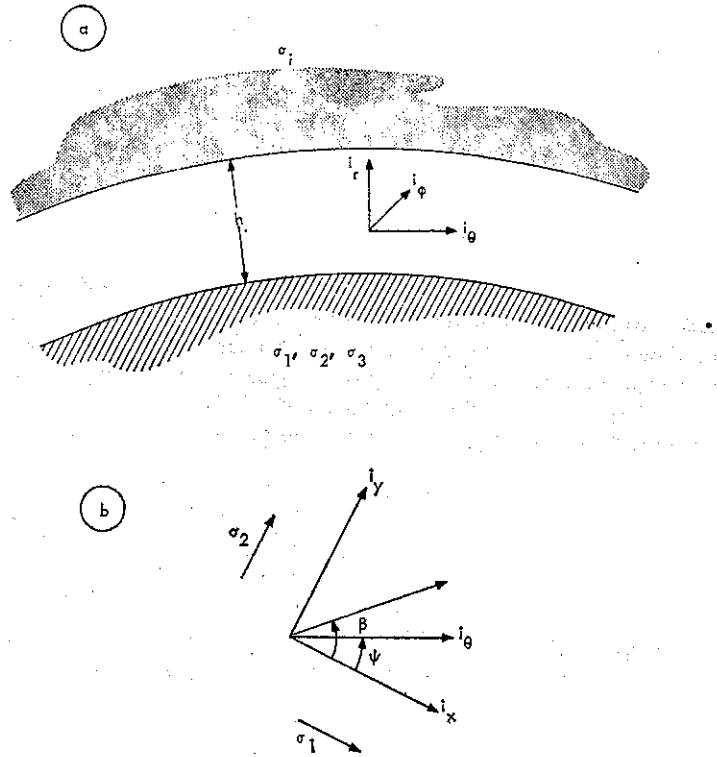

FIG. 6.3 Propagation Geometry

field is oriented along one of the axes of the diagonal conductivity tensor. In practical measurement, noise, near surface inhomogeneities or multi-dimensional subsurface structures will cause small current components in other directions; but the presence of these off-diagonal terms will be ignored in the present study. For a diagonal tensor, the component σ_1 is assumed to exhibit the highest conductivity; its axis is in the x direction, which is at an angle ψ with respect to the θ direction. The component σ_2 denotes the smaller of the two horizontal conductivity components, and it is in the y direction. The conductivity component σ_3 will apply to the vertical (z) direction. The fields excited on the ground surface will be examined at various angles β relative to the x-axis, which will generally differ from the angle of wave incidence ψ. Strictly T.M. (or T.E.) waves can exist below the ground surface only in conjunction with waves of the airspace that propagate along the x and y axes ($\psi = 0$ and $\pi/2$), but the underground

waves will be coupled for other directions of propagation. The analysis of wave propagation in the anisotropic ground is similar to the treatment of wave propagation in an anisotropic ionosphere, and the permissible wave numbers for propagation in the vertical direction are determined from a solution of a quartic equation. The wave number for propagation in the Θ direction (or for propagation at an angle ψ relative to the x-axis) is computed by considering a coupling of T.E. and T.M. modes of the airspace by the anisotropy of ground.

The anisotropic ground is intended to apply locally around a receiving antenna, which is excited by distant vertically or horizontally polarized sources of the earth-to-ionosphere waveguide. The conversion effects between waveguide modes for isotropic and anisotropic ground are neglected in this analysis. This neglect implies an extension of the region of ground anisotropy over distances that are sufficient for suppressing the isotropic waveguide modes. However, the final results of the calculations are nearly independent of the wave-propagation parameters of the airspace; and it is of little consequence as to what modes have been used for the exciting field. The anisotropic ground must be extended only over distances that are representative of the return current flow of a buried horizontal wire antenna. For isotropic ground, this distance range is of the order of a few skin depths $\delta = \sqrt{2/(\omega\mu_0\sigma_g)}$.

The fields induced in horizontal electric dipoles (short horizontal wires) will be proportional to the electric field components of the incident fields in the direction of the dipole axis. The horizontal electric fields are examined for various directions β and incidence angles ψ. For T.M. modes, the anisotropy of the ground is shown to modify the electric fields and to shift their null positions; the horizontal magetic fields are not affected by the anisotropy of the ground.

6.7.1 *Fields in the Anisotropic Ground*

Assuming a suppressed $\exp(-i\omega t)$ harmonic time dependence of the fields, the electric and magnetic field vectors satisfy the Maxwell's equations

$$\nabla\times\mathbf{E} = i\omega\mu_0\mathbf{H}, \tag{137}$$

$$\nabla\times\mathbf{H} = -i\omega\varepsilon_0\boldsymbol{\epsilon}\cdot\mathbf{E}, \tag{138}$$

where μ_0 and ε_0 are the permeability and permittivity of free space. The wave propagation below the ground surface is considered in rectangular coordinates which are lined up with the axes of the anisotropy. The z-axis is considered to be in the upward vertical direction. The dyadic permittivity $\boldsymbol{\epsilon}$ contains only the diagonal elements and is of the form

$$\boldsymbol{\epsilon} = \begin{bmatrix} \varepsilon_1 & 0 & 0 \\ 0 & \varepsilon_2 & 0 \\ 0 & 0 & \varepsilon_3 \end{bmatrix} \tag{139}$$

where

$$\varepsilon_j = \varepsilon_r + i\sigma_j/(\omega\varepsilon_0) \tag{140}$$

and where ε_r is the relative dielectric constant of the earth and σ_j is the conductivity component of the appropriate direction. The ground surface is excited by a wave of complex wave number k_0S propagating in the space between the earth and the ionosphere at an angle ψ with respect

to the x-axis; the fields below the ground surface are assumed to be of the form

$$F_j = F_j^0 \exp[-i\omega t + ik_0S(x\cos\psi + y\sin\psi) + ikz], \tag{141}$$

where $F = E$ or H, $j = x, y$, or z, $k_0 = \omega\sqrt{\mu_0\varepsilon_0}$ is the wave number of free space, and k is a yet undetermined wave number for vertical propagation in the ground. The propagation parameter S characterizes the waves above the ground surface, and $\mathrm{Re}(S) = c/v_{ph}$, where c is the free-space velocity of electromagnetic waves and v_{ph} is the phase velocity, $\mathrm{Im}(S)$ is proportional to the attenuation rate α. The fields above the ground surface will exhibit the same x and y variations, but the z-dependence follows from the mode theory for the spherical earth-to-ionosphere waveguide. Equation (141) applies to distances from the source where a single mode characterizes the excitation. In the vicinity of the source, a large number of modes of the type (141) are required. For isotropic ground, such a mode sum has been shown in Chapter 4 to give near fields that are comparable to those of a dipole above a finitely conducting ground plane [Wait, 1961; Baños, 1966]. Introducing the notation

$$u = k_0S\cos\psi, \quad v = k_0S\sin\psi, \tag{142}$$

the components of (137) can be combined with the z component of (138) to give

$$E_x^0 = -\frac{u(\varepsilon_3 - S^2)}{kS^2}E_z^0 - \frac{\omega\mu_0 v}{k_0^2S^2}H_z^0, \tag{143}$$

$$E_y^0 = -\frac{v(\varepsilon_3 - S^2)}{kS^2}E_z^0 + \frac{\omega\mu_0 u}{k_0^2S^2}H_z^0, \tag{144}$$

$$H_x^0 = \frac{1}{(k_0S)^2}(\omega\varepsilon_0\varepsilon_3 vE_z^0 - ukH_z^0), \tag{145}$$

$$H_y^0 = \frac{1}{(k_0S)^2}(-\omega\varepsilon_0\varepsilon_3 uE_z^0 - vkH_z^0). \tag{146}$$

Substituting (144) and (145) in the y component of (137) gives

$$Y_1 = \frac{H_z^0}{E_z^0} = \frac{1}{\eta k_r}\frac{\varepsilon_3(k_r^2 - \varepsilon_2) + \varepsilon_2S^2}{k_r^2 - \varepsilon_2 + S^2}\frac{v}{u}, \tag{147}$$

where $k_r = k/k_0$, and $\eta = \sqrt{\mu_0/\varepsilon_0} = 120\pi$. Substituting (143) and (146) in the x component of (137) gives

$$Y_2 = \frac{H_z^0}{E_z^0} = -\frac{1}{\eta k_r}\frac{\varepsilon_3(k_r^2 - \varepsilon_1) + \varepsilon_1S^2}{k_r^2 - \varepsilon_1 + S^2}\frac{u}{v}. \tag{148}$$

The H_z^0/E_z^0 ratio should be the same in (147) and (148). Equations (147) and (148) can be combined to give the following biquadratic equation

$$k_r^4 + k_r^2[-\varepsilon_1 - \varepsilon_2 + S^2 + (\varepsilon_1u^2 + \varepsilon_2v^2)/(\varepsilon_3k_0^2)] + (1 - S^2/\varepsilon_3\cdot[\varepsilon_1\varepsilon_2 - (\varepsilon_1u^2 + \varepsilon_2v^2)/k_0^2] = 0 \tag{149}$$

in the unknown k_r^2. Noting that $|\varepsilon_j| \gg |S^2|$, (149) simplifies to

$$k_r^4 - k_r^2(\varepsilon_1 + \varepsilon_2) + \varepsilon_1\varepsilon_2 \approx 0, \tag{150}$$

the solutions of which become $k_r^2 \approx \varepsilon_1$ or ε_2. Substitution of $k_r = \sqrt{\varepsilon_1}$ in (147) shows that $H_z^0 = 0$ for $v = 0$ (the wave is T.M. for propagation along the x-axis) and that $E_z^0 = 0$ for $u = 0$ (the wave is T.E. for propagation along the y-axis). Similarly, a substitution of $k_r = \sqrt{\varepsilon_2}$ in (148) shows that a T.M. wave may propagate along the y-axis and a T.E. wave along the x-axis. The horizontal E-field component of the above waves lies in the direction of ε_j, which results in $k_r = \sqrt{\varepsilon_j}$.

A numerical solution of (149) will not be sufficiently accurate to obtain identical values of Y_1 and Y_2 in the limits of u or $v \to 0$. Alternatively, one may define

$$Y = \frac{H_z^0}{E_z^0} = \sqrt{Y_1 Y_2}. \tag{151}$$

After substituting (147) and (148) and multiplying out the product, (149) is applied to simplify the numerator and denominator. This gives

$$Y = \pm \frac{i\varepsilon_3}{\eta k_r} \sqrt{\frac{N}{D}}, \tag{152}$$

where

$$N = k_r^2\left[-1+\frac{\varepsilon_1 v^2+\varepsilon_2 u^2}{\varepsilon_3 k_0^2 S^2}\right]+\left[1-\frac{S^2}{\varepsilon_3}\right]\cdot\left[-\frac{\varepsilon_1\varepsilon_2}{\varepsilon_3}+\frac{\varepsilon_1 u^2+\varepsilon_2 v^2}{k_0^2 S^2}\right], \tag{153}$$

$$D = k_r^2-\left[\frac{\varepsilon_1 u^2+\varepsilon_2 v^2}{\varepsilon_3 k_0^2 S^2}\right](k_r^2+S^2)+S^2+\frac{\varepsilon_1\varepsilon_2}{\varepsilon_3}-\frac{\varepsilon_1 v^2+\varepsilon_2 u^2}{k_0^2 S^2}. \tag{154}$$

The + and − signs of (152) apply to $k_r^2 \approx \varepsilon_2$ and ε_1 respectively. After substituting the approximation of k_r, Y of (152) is seen to exhibit the limiting values that were discussed following (150).

After computing k_r from a solution of (149) and $Y = H_z^0/E_z^0$ from (152), the field components E_x^0, E_y^0, H_x^0, and H_y^0 are obtained from (143) to (146). Equation (149) has two solutions with Im $k_r < 0$ that correspond to downgoing waves with two distinct wave numbers $k = k_0 k_r$ in (141) or with different amplitudes E_{zj}^0 in (143) to (146). The field components (143) to (146) can be expressed more compactly as

$$E_x^0 = p_{11}A_1+p_{12}A_2, \tag{155}$$

$$H_y^0 = p_{21}A_1+p_{22}A_2, \tag{156}$$

$$H_x^0 = p_{31}A_1+p_{32}A_2, \tag{157}$$

$$E_y^0 = p_{41}A_1+p_{42}A_2. \tag{158}$$

The relative amplitudes $A_1 = E_{z1}^0/\cos\psi$ and $A_2 = E_{z2}^0/\sin\psi$ of the two waves are determined from boundary conditions above the earth's surface.

The fields of the space between the earth and the ionosphere are described in geocentric spherical coordinates (r, θ, φ), where the θ direction corresponds to the ψ direction of the rectangular (x, y, z) coordinates that were used to characterize the fields below the ground surface. The x and y field components are related to the θ and φ field components of the

spherical coordinates by the transformation

$$F_\theta = F_x\cos\psi+F_y\sin\psi, \tag{159}$$

$$F_\varphi = -F_x\sin\psi+F_y\cos\psi, \tag{160}$$

where $F_i = E_i$ or H_i. Substitution of (155) to (158) in (159) and (160) shows that at the surface of the earth ($r = a$), the fields may be computed as

$$E_\theta(a) = q_{11}A_1+q_{12}A_2, \tag{161}$$

$$H_\varphi(a) = q_{21}A_1+q_{22}A_2, \tag{162}$$

$$H_\theta(a) = q_{31}A_1+q_{32}A_2, \tag{163}$$

$$E_\varphi(a) = q_{41}A_1+q_{42}A_2, \tag{164}$$

where

$$q_{1j} = p_{1j}\cos\psi+p_{4j}\sin\psi,$$

$$q_{2j} = p_{2j}\cos\psi-p_{3j}\sin\psi,$$

$$q_{3j} = p_{3j}\cos\psi+p_{2j}\sin\psi,$$

$$q_{4j} = p_{4j}\cos\psi-p_{1j}\sin\psi.$$

The downward-looking impedances that are seen by the T.M. and T.E. field components at the ground level $r = a$ may be computed from (161) to (164) as

$$Z_{ge} = -\frac{E_\theta(a)}{H_\varphi(a)} = -\frac{q_{11}+q_{12}(A_2/A_1)}{q_{21}+q_{22}(A_2/A_1)}, \tag{165}$$

$$Z_{gh} = \frac{E_\varphi(a)}{H_\theta(a)} = \frac{q_{41}+q_{42}(A_2/A_1)}{q_{31}+q_{32}(A_2/A_1)}. \tag{166}$$

Equations (165) and (166) may be solved for the amplitude ratio A_2/A_1, which gives

$$\frac{A_2}{A_1} = -\frac{q_{11}+q_{21}Z_{ge}}{q_{12}+q_{22}Z_{ge}} = -\frac{q_{41}-q_{31}Z_{gh}}{q_{42}-q_{32}Z_{gh}}. \tag{167}$$

The ground impedances of T.M. and T.E. field components Z_{ge} and Z_{gh} are related from (167) as

$$Z_{ge} = -\frac{a_{11}-a_{12}Z_{gh}}{a_{21}-a_{22}Z_{gh}} \quad \text{or} \quad Z_{gh} = \frac{a_{11}+a_{21}Z_{ge}}{a_{12}+a_{22}Z_{ge}}, \tag{168}$$

where

$$a_{11} = q_{11}q_{42}-q_{12}q_{41},$$

$$a_{12} = q_{11}q_{32}-q_{12}q_{31},$$

$$a_{21} = q_{21}q_{42}-q_{22}q_{41},$$

$$a_{22} = q_{21}q_{32}-q_{22}q_{31}.$$

The impedance Z_{ge} is related to the impedance Z_{gh}, which generally implies a coupling between T.E. $(E_r, E_\theta, H_\varphi)$ and T.M. $(E_\varphi, H_r, H_\theta)$ field components by the anisotropy of the

ground. However, there will be no coupling in the special cases of propagation along the axes of the anisotropy ($\psi = 0$ and $\pi/2$). This can be shown analytically using the solutions k_r of the simplified biquadratic equation (150).

For $k_r^2 \approx \varepsilon_1$ and ε_2, (147) and (148) simplify to

$$Y_1 \approx \frac{\varepsilon_3}{\eta\sqrt{\varepsilon_1}} \tan\psi; \qquad Y_2 \approx -\frac{\varepsilon_3}{\eta\sqrt{\varepsilon_2}} \cot\psi, \tag{169}$$

where it is assumed that $|\varepsilon_j| \gg |S^2|$. The parameters p_{ij} of (155) to (158) are computed as

$$[p_{ij}] \approx \begin{bmatrix} -\varepsilon_3/(\sqrt{\varepsilon_1}S) & 0 \\ -\varepsilon_3/(\eta S) & 0 \\ 0 & \varepsilon_3/(\eta S) \\ 0 & -\varepsilon_3/(\sqrt{\varepsilon_2}S) \end{bmatrix} \tag{170}$$

The simplified expressions for k_r and Y_j in (150) and (169) have been derived by assuming $|\varepsilon_j| \gg |S^2|$ in (147) to (149). This inequality is the basis of the so-called Leontovich boundary conditions which can be derived from (143) to (146)

$$Z_1 = \frac{E_x^0}{H_y^0} = \frac{\eta}{k_r}, \qquad Z_2 = \frac{E_y^0}{H_x^0} = -\frac{\eta}{k_r}. \tag{171}$$

A comparison with (170) shows that $k_r = k/k_0$ should be replaced by $\sqrt{\varepsilon_j}$ in the definition of Z_j. Also, the subsequent equations (180) to (184), which are based on (170), are consistent with the boundary conditions (171).

6.7.2 *Fields of the Airspace and the Modal Equation*

A homogeneous isotropic ionosphere is assumed as the upper boundary of the airspace at a height h above the ground surface. Following equations (97) and (101) of Chapter 4, the ionospheric boundary will present to T.M. and T.E. waves of the airspace the impedances

$$Z_e(h) = \frac{E_\theta(a+h)}{H_\varphi(a+h)} = \frac{\eta}{n_i}\sqrt{1-\left(\frac{aS}{r_m n_i}\right)^2},$$
$$Z_h(h) = -\frac{E_\varphi(a+h)}{H_\theta(a+h)} = \frac{\eta}{n_i}\Big/\sqrt{1-\left(\frac{aS}{r_m n_i}\right)^2}, \tag{172}$$

where the refractive index of the ionosphere is given by

$$n_i = \sqrt{1+i\sigma_i/(\omega\varepsilon_0)} \tag{173}$$

and where σ_i is the ionospheric conductivity and $r_m = a+0.5h$. For large values of the refractive index n_i, the impedances $Z_e(h) \approx Z_h(h)$; and the impedances are nearly independent of the propagation parameter S of the waves in the airspace. The impedances $Z_e(h)$ and $Z_h(h)$ of (36) can be transformed to the ground surface using wave representations of the airspace developed in Chapter 4. The transformed impedances are denoted as $Z_e(0)$ and $Z_h(0)$.

Continuity of the tangential field components at the ground surface $r = a$ requires that the downward-looking impedances Z_{ge} and Z_{gh} of (165), (166), or (168) should be the negative of the upward-looking impedances $Z_e(0)$ or $Z_h(0)$. Substituting $Z_e(0) = -Z_{ge}$ and $Z_h(0) = -Z_{gh}$ in (168), gives a single transcendental equation for determining the permissible propagation parameter S. After determining the propagation parameter S, $Z_{ge} = -Z_e(0)$ or $Z_{gh} = -Z_h(0)$ are uniquely determined; and it is possible to compute the amplitude ratio A_2/A_1 from (167). Subsequently, the field component ratios $E_\varphi(a)/E_\theta(a)$ or $H_\theta(a)/H_\varphi(a)$ may be calculated from (161) to (164).

The electric field induced in a horizontal wire located at the ground surface at an angle β with respect to the x (or ε_1) axis will be

$$E_\beta = E_\theta \cos(\beta-\psi) + E_\varphi \sin(\beta-\psi). \tag{174}$$

For T.M. waves

$$\frac{E_\beta}{E_r} = \frac{E_\theta}{E_r}(\psi)\left[\cos(\beta-\psi) + \frac{E_\varphi}{E_\theta}(\psi)\sin(\beta-\psi)\right]. \tag{175}$$

The wave tilt E_θ/E_r is determined from (161) and (165) as

$$\frac{E_\theta(a)}{E_r(a^+)} = \frac{E_\theta(a)}{\varepsilon_3 E_r(a^-)} = \frac{q_{11}+q_{12}(A_2/A_1)}{\varepsilon_3(\cos\psi+\sin\psi A_2/A_1)} = \frac{-Z_{ge}[q_{21}+q_{22}(A_2/A_1)]}{\varepsilon_3(\cos\psi+\sin\psi A_2/A_1)}, \tag{176}$$

where a^+ and a^- refer to fields above and below the surface of the earth. Expressing q_{ij} in terms of p_{ij} and applying (170), it is seen that

$$\frac{E_\theta(a)}{E_r(a^+)} = \frac{Z_{ge}}{\eta S}, \tag{177}$$

which is consistent with (108) of Chapter 4. For T.E. waves

$$\frac{E_\beta}{H_r} = \frac{E_\varphi}{H_r}(\psi)\left[\sin(\beta-\psi) + \frac{E_\theta}{E_\varphi}(\psi)\cos(\beta-\psi)\right]. \tag{178}$$

The ratio E_φ/H_r is computed from (164), (169), and (170) as

$$\frac{E_\varphi(a)}{H_r(a)} = \frac{q_{41}+q_{42}(A_2/A_1)}{\cos\psi Y_1 + Y_2\sin\psi(A_2/A_1)} = \frac{\eta}{S}, \tag{179}$$

which can be also obtained from (117) of Chapter 4. For a horizontal wire lying on the surface of a homogeneous and isotropic ground, $E_\varphi = 0$ for T.M. waves, $E_\theta = 0$ for T.E. waves, and E_θ/E_r or E_φ/H_r are independent of ψ. In this case, the induced fields E_β/E_r and E_β/H_r will be proportional to $\cos(\beta-\psi)$ and $\sin(\beta-\psi)$ respectively.

The factor E_φ/E_θ of the field expressions (175) and (178) can be also expressed using the approximation (170) in (161) and (164). This gives

$$\frac{E_\varphi}{E_\theta} \approx \frac{-\sqrt{\varepsilon_2}\tan\psi + \sqrt{\varepsilon_1}(A_2/A_1)}{\sqrt{\varepsilon_2} + \sqrt{\varepsilon_1}(A_2/A_1)\tan\psi}. \tag{180}$$

For T.M. modes, the amplitude A_2/A_1 is computed from the second half of (167) as

$$\frac{A_2}{A_1} \approx \sqrt{\frac{\varepsilon_2}{\varepsilon_1}}\,\frac{1-\sqrt{\varepsilon_1}\,\Delta_h(0)}{1-\sqrt{\varepsilon_2}\,\Delta_h(0)}\tan\psi, \tag{181}$$

where $\Delta_h(0) = Z_h(0)/\eta = -Z_{gh}/\eta$. Numerical calculations show that for wave numbers corresponding to T.M. modes, $\left|\sqrt{\varepsilon_j}\,\Delta_h(0)\right| \gg 1$ and A_2/A_1 simplifies to

$$\frac{A_2}{A_1} \approx \tan\psi. \tag{182}$$

E_φ/E_θ is computed substituting (182) in (180). This gives

$$\frac{E_\varphi}{E_\theta} \approx \frac{1-\sqrt{\varepsilon_2/\varepsilon_1}}{\tan^2\psi+\sqrt{\varepsilon_2/\varepsilon_1}}\tan\psi. \tag{183}$$

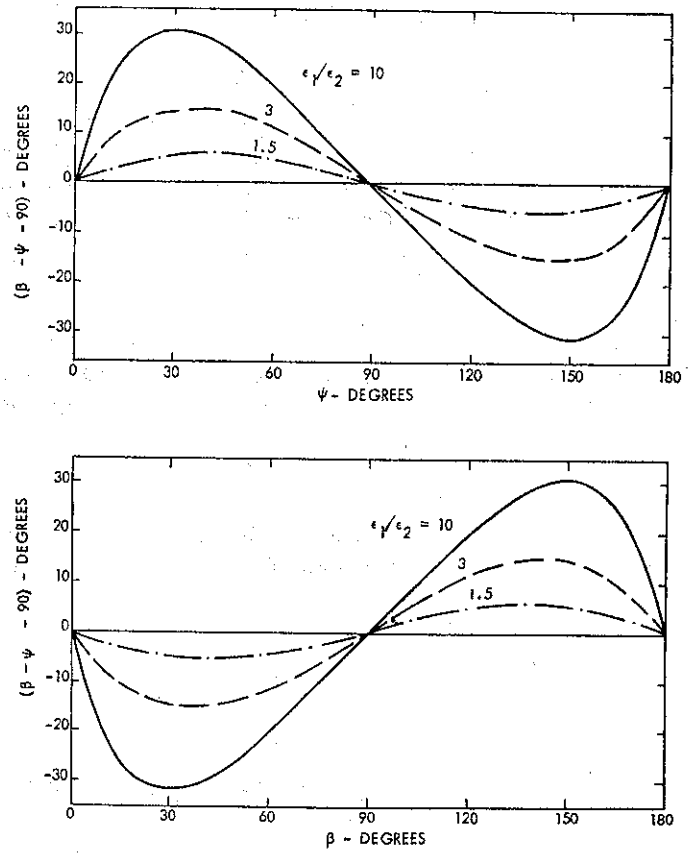

FIG. 6.4 Shift in the Null of the Horizontal Fields E_β for T.M. Modes and Various Angles ψ and β

Substitution of (183) in (175) shows that $E_\beta/E_r = 0$ for angles β and ψ satisfying the equation

$$\cot(\beta-\psi) = -\frac{1-\sqrt{\varepsilon_2/\varepsilon_1}}{\tan^2\psi+\sqrt{\varepsilon_2/\varepsilon_1}}\tan\psi. \tag{184}$$

It is shown in Appendix 6.8.4 that (184) can be also derived using simple, heuristic arguments. In the limit of decreasing anisotropy, $\varepsilon_2 \to \varepsilon_1$ and the nulls of E_β/E_r correspond to zeros of $\cot(\beta-\psi)$, one of which is given by $\beta-\psi = 90°$. After computing β and ψ from (184) from $\varepsilon_1 \neq \varepsilon_2$, a plot of $(\beta-\psi-90°)$ versus ψ or β will indicate the shift in the null of E_β/E_r relative to isotropic conditions when the null is given by $\beta-\psi-90° = 0$. Figure 6.4 indicates that the maximum shift in the pattern nulls of 31° for $\varepsilon_1/\varepsilon_2 = 10$ is decreased to 6° for $\varepsilon_1/\varepsilon_2 = 1.5$. For antennas oriented along the axes of anisotropy ($\beta = 0$, 90°, or 180°), there is no null shift; but for two mutually perpendicular antennas of other orientations, the shifts are of opposite signs: the nulls are shifted *towards* the axis of the largest ε_j value ($\beta = 0$ or 180°).

The horizontal magnetic field components and the pattern distortions of a horizontal magnetic dipole (small vertical loop) can be also determined. Also the complete field pattern of horizontal antennas have been determined [Galejs, 1969c]. It is shown in Appendix 6.8.4 that pattern distortions of a horizontal wire antenna are related to the horizontal current flow along the ground surface which may differ from the direction of the impressed electric field.

6.8 Appendix

6.8.1 *Reflection Coefficients*

The field components tangential to the ionospheric boundary have been expressed in (109) to (112) in terms of wave amplitudes in the ionosphere A_{iu} and matrix elements q_{ij}. The same field components can be also related to the fields incident from below the ionospheric boundary. It follows from chapter 8 of Budden [1961a] that

$$\left.\begin{aligned} C^{-1}E_\varphi &= (1-{}_\parallel R_\parallel)E_{\parallel i} - {}_\perp R_\parallel E_{zi},\\ \eta H_x &= (1+{}_\parallel R_\parallel)E_{\parallel i} + {}_\perp R_\parallel E_{zi},\\ C^{-1}\eta H_\varphi &= {}_\parallel R_\perp E_{\parallel i} + (-1+{}_\perp R_\perp)E_{zi},\\ E_x &= {}_\parallel R_\perp E_{\parallel i} + (1+{}_\perp R_\perp)E_{zi}. \end{aligned}\right\} \tag{185}$$

where $C = \sqrt{1-S^2}$. Equations (185) can be rearranged into

$$\left.\begin{aligned} {}_\parallel R_\parallel &= \left.\frac{C\eta H_x - E_\varphi}{C\eta H_x + E_\varphi}\right|_{E_{zi}=0}, \qquad {}_\parallel R_\perp = \left.\frac{CE_x+\eta H_\varphi}{E_\varphi+C\eta H_x}\right|_{E_{zi}=0},\\ {}_\perp R_\parallel &= \left.\frac{\eta H_x - E_\varphi}{E_x - \eta H_\varphi}\right|_{E_{\parallel i}=0}, \qquad {}_\perp R_\perp = \left.\frac{CE_x+\eta H_\varphi}{CE_x-\eta H_\varphi}\right|_{E_{\parallel i}=0}. \end{aligned}\right\} \tag{186}$$

Applying the condition $E_x - C^{-1}\eta H_\varphi = 2E_{zi}$, it follows from (111) and (112) that $E_{zi} = 0$ corresponds to

$$\frac{A_{3u}}{A_{1u}} = -\frac{q_{41}-\eta q_{31}/C}{q_{43}-\eta q_{33}/C}. \tag{187}$$

Applying the condition $C^{-1}E_\varphi+\eta H_z = 2E_{\parallel i}$, it follows from (109) and (110) that $E_{\parallel i} = 0$ corresponds to

$$\frac{A_{3u}}{A_{1u}} = -\frac{q_{11}+\eta q_{21}C}{q_{13}+\eta q_{23}C}. \tag{188}$$

The reflection coefficients (186) can be computed substituting (109) to (112) and by applying (187) or (188) for the amplitude ratios A_{3u}/A_{1u}.

Under isotropic conditions $E_\varphi/H_z = Z_e$ and $E_z/H_\varphi = -Z_h$ as in (97) and (101) of Chapter 4, respectively. Noting that $k_j/k_0 = n_j$ and letting $r_m = a$, the reflection coefficients ${}_\parallel R_\parallel$ and ${}_\perp R_\perp$ of (186) may be reduced to the forms (29) and (30) of Chapter 1.

6.8.2 *Solution of the Quartic Equation*

The quartic equation (116) will be solved following the method described by Zaguskin [1961] for equations with real coefficients, but this development applies also to equations with complex coefficients.

After dividing (116) with a_4, the quartic equation is expressed as

$$x^4+c_3x^3+c_2x^2+c_1x+c_0 = 0, \tag{189}$$

where $c_j = a_j/a_4$. Equation (141) can be formally factored into

$$(x^2+p_1x+q_1)(x^2+p_2x+q_2) = 0. \tag{190}$$

After multiplying out the two factors of (190) and equating coefficients of equal powers of x, it follows that

$$c_3 = p_1+p_2, \tag{191}$$

$$c_2 = p_1p_2+q_1+q_2, \tag{192}$$

$$c_1 = p_1q_2+p_2q_1, \tag{193}$$

$$c_0 = q_1q_2. \tag{194}$$

Letting

$$m = q_1+q_2 \tag{195}$$

and eliminating p_1 and p_2 from (191) to (193), the resulting equation can be rearranged using (194) into

$$m^3+b_2m^2+b_1m+b_0 = 0, \tag{196}$$

where

$$b_2 = -c_2, \quad b_1 = (c_3c_1-4c_0), \quad \text{and} \quad b_0 = (4c_2c_0-c_1^2-c_3^2c_0).$$

One root of the cubic equation (196) is computed as

$$m = u-\frac{p}{3u}-\frac{b_2}{3} \tag{197}$$

with

$$p = (3b_1-b_2^2)/3, \quad q = (2b_2^3-9b_2b_1+27b_0)/27, \quad \text{and} \quad u^3 = -(q/2)+[q/2)^2+(p/3)^3]^{0.5}.$$

With m given by (197), (194), and (195) are solved for q_j as

$$q_{1,2} = (m/2)\pm[(m/2)^2-c_0]^{0.5} \tag{198}$$

and p_j is computed from (191) and (193) as

$$p_1 = (c_3q_1-c_1)/(q_1-q_2), \tag{199}$$

$$p_2 = c_2-p_1. \tag{200}$$

Alternatively, (191) and (192) are solved for p_j as

$$p_{1,2} = (c_3/2)\pm[(c_3/2)^2-c_2+m]^{0.5}, \tag{201}$$

and the corresponding values of q_j are computed from (193) and (195) as

$$q_1 = (c_1-p_1m)/(p_2-p_1), \tag{202}$$

$$q_2 = m-q_1. \tag{203}$$

This completes the specification of the factors in (190). The two quadratic equations of (190) give four values of x that are roots of the original quartic (189).

The solution of the quartic equation (189) requires finding one root (197) of an auxiliary cubic equation (196); then the coefficients q_j and p_j of the quadratic factors of (190) are computed from (198) to (200) or from (201) to (203). The two quadratic factors are solved for the four roots of the quartic equation (189).

An alternative method, based on the work of Burnside and Panton [1904], has been recently described by Sheddy [1968]. This method requires the evaluation of a cube root and of several square-root expressions, and it appears to be comparable in complexity to the procedure described in this section. Considerably more involved numerical methods have been used by Johler and Walters [1960] for solving this same problem.

6.8.3 *Solutions for the Lower Ionosphere*

The limit of $|\nu-i\omega| \gg \omega_c$ (or $\varepsilon_3 = \varepsilon_1$ with $\varepsilon_2 \to 0$) will be examined for $\varphi = 0$, but with arbitrary values θ for the orientation of the static magnetic field. For $\varphi = 0$, the quartic (116) is reduced to a biquadratic equation; and it has roots of the form

$$k_r^2 = k^2/k_0^2 = \varepsilon_1-S'^2\pm i\varepsilon_2 \sin\theta\sqrt{1-S'^2/\varepsilon_1}. \tag{204}$$

The field components E_x^0 and E_y^0 are computed from (117) and (118) as

$$E_x^0 \approx -\frac{\sqrt{\varepsilon_1-S'^2}}{S'}E_z^0, \tag{205}$$

$$E_y^0 \approx \pm\frac{\sqrt{\varepsilon_1}}{S'}E_z^0. \tag{206}$$

The ratio E_x^0/E_y^0 is computed as

$$E_x^0/E_y^0 = \pm i\sqrt{1-S'^2/\varepsilon_1}. \tag{207}$$

The ratio is independent of ε_2 and remains finite for both values of k_r^2 given by (204). The T.M. field component E_x^0 is coupled with the T.E. field component E_y^0 for any of the wave numbers k_r that correspond to a solution of the quartic (204).

However, the complete field expression in a layer of finite thickness consists of four terms of arbitrary amplitudes A_j that correspond to the amplitudes E_z^0 for the various roots of the quartic (116). For $\varphi = 0$, E_z is of the form

$$\left.\begin{aligned} E_z &= A_1 \exp(ik_+z) + A_2 \exp(-ik_+z) + A_3 \exp(ik_-z) + A_4 \exp(-ik_-z) \\ &= A_1 \exp[i(k_s+k_d)z] + A_2 \exp[-i(k_s+k_d)z] \\ &\quad + A_3 \exp[i(k_s-k_d)z] + A_4 \exp[-i(k_s-k_d)z], \end{aligned}\right\} \tag{208}$$

where k_+ and k_- refer to the two roots $k = k_0 k_r$ of the biquadratic equation in (204) with $\operatorname{Im} k > 0$. The wave numbers k_s and k_d are defined as

$$k_s = 0.5(k_+ + k_-) = k_0 \sqrt{\varepsilon_1 - S'^2}, \tag{209}$$

$$k_d = 0.5(k_+ - k_-) = \frac{ik_0\varepsilon_2}{2\sqrt{\varepsilon_1}} \sin\theta. \tag{210}$$

For $k_d \to 0$, (208) can be rearranged into

$$E_z = (B_1 + B_3 ik_d z)\exp(ik_s z) + (B_2 - B_4 ik_d z)\exp(-ik_s z), \tag{211}$$

where the amplitudes B_j are related to A_j by

$$\begin{aligned} B_1 &= A_1 + A_3, \quad B_2 = A_2 + A_4, \\ B_3 &= A_1 - A_3, \quad B_4 = A_2 - A_4. \end{aligned} \tag{212}$$

The field components E_x and E_y are expressed similarly as

$$\left.\begin{aligned} E_x &= -\frac{\sqrt{\varepsilon_1 - S'^2}}{S'}[A_1 \exp(ik_+z) - A_2 \exp(-ik_+z) + A_3 \exp(ik_-z) - A_4 \exp(-ik_-z)] \\ &= -\frac{\sqrt{\varepsilon_1 - S'^2}}{S'}[(B_1 + B_3 ik_d z)\exp(ik_s z) - (B_2 - B_4 ik_d z)\exp(-ik_s z)], \end{aligned}\right\} \tag{213}$$

$$\left.\begin{aligned} E_y &= \frac{i\sqrt{\varepsilon_1}}{S'}[A_1 \exp(ik_+z) - A_2 \exp(ik_+z) - A_3 \exp(ik_-z) + A_4 \exp(-ik_-z)] \\ &= \frac{i\sqrt{\varepsilon_1}}{S'}[(B_3 + B_1 ik_d z)\exp(ik_s z) - (B_4 - B_2 ik_d z)\exp(-ik_s z)]. \end{aligned}\right\} \tag{214}$$

In the limit of $\varepsilon_2 \to 0$, $k_d \to 0$, and $E_x \sim B_1, B_2$ while $E_y \sim B_3, B_4$. E_x and E_y are proportional to different amplitudes B_j and are therefore uncoupled as $\varepsilon_2 \to 0$.

The field components H_x and H_y are computed by approximating the factors k_r of (120) and (121) by $k_s k_0$. It follows that

$$\left.\begin{aligned} H_x &= -\frac{i\sqrt{\varepsilon_1}\sqrt{\varepsilon_1 - S'^2}}{\eta S'}[A_1 \exp(ik_+z) + A_2 \exp(-ik_+z) - A_3 \exp(ik_-z) - A_4 \exp(ik_-z)] \\ &= -\frac{i\sqrt{\varepsilon_1}\sqrt{\varepsilon_1 - S'^2}}{\eta S'}[(B_3 + B_1 ik_d z)\exp(ik_s z) + (B_4 - B_2 ik_d z)\exp(-ik_s z)], \end{aligned}\right\} \tag{215}$$

$$\left.\begin{aligned} H_y &= -\frac{\varepsilon_1}{\eta S'}[A_1 \exp(ik_+z) + A_2 \exp(-ik_+z) + A_3 \exp(ik_-z) + A_4(-ik_-z)] \\ &= -\frac{\varepsilon_1}{\eta S'}[(B_1 + B_3 ik_d z)\exp(ik_s z) + (B_2 - B_4 ik_d z)\exp(-ik_s z)]. \end{aligned}\right\} \tag{216}$$

In the limit of $\varepsilon_2 \to 0$, $k_+, k_- \to k_s$. The impedances E_x/H_y and $-E_x/H_y$ are computed from (165) to (168) using the expressions involving A_j and B_j. It is seen that

$$\frac{E_x}{H_y} = \frac{\eta\sqrt{\varepsilon_1 - S'^2}}{\varepsilon_1} \frac{(A_1 + A_3)\exp(ik_s z) - (A_2 + A_4)\exp(-ik_s z)}{(A_1 + A_3)\exp(ik_s z) + (A_2 + A_4)\exp(-ik_s z)} \tag{217}$$

or

$$\frac{E_x}{H_y} = \frac{\eta\sqrt{\varepsilon_1 - S'^2}}{\varepsilon_1} \frac{B_1 \exp(ik_s z) - B_2 \exp(-ik_s z)}{B_1 \exp(ik_s z) + B_2 \exp(-ik_s z)} \tag{218}$$

$$-\frac{E_y}{H_x} = \frac{\eta}{\sqrt{\varepsilon_1 - S'^2}} \frac{(A_1 - A_3)\exp(ik_s z) - (A_2 - A_4)\exp(-ik_s z)}{(A_1 - A_3)\exp(ik_s z) + (A_2 - A_4)\exp(-ik_s z)} \tag{219}$$

or

$$-\frac{E_y}{H_x} = \frac{\eta}{\sqrt{\varepsilon_1 - S'^2}} \frac{B_3 \exp(ik_s z) - B_4 \exp(-ik_s z)}{B_3 \exp(ik_s z) + B_4 \exp(-ik_s z)}. \tag{220}$$

Noting the definitions of B_j in (212), the impedance expressions (218) and (220) based on decoupled amplitudes B_j are seen to be identical to the impedances (217) and (219) using amplitudes A_j of the original formulation.

6.8.4 *Shift of the Antenna Pattern*

Some results of Section 6.7 can be also derived using a more heuristic reasoning. A horizontal wire transmitting antenna located below the surface of the anisotropic ground of Fig. 6.3 is assumed to excite an average return current $\mathbf{I} = i_x I_x + i_y I_y$ at an angle α with respect to the x-axis. The current components I_x and I_y are causing potential differences V_x and V_y on the surface of the earth which are assumed to be proportional to the characteristic impedance of the ground in the x and y directions or to be inversely proportional to $\sqrt{\varepsilon_1}$ and $\sqrt{\varepsilon_2}$ respectively. The electric field or the voltage $\mathbf{V} = i_x V_x + i_y V_y$ will be at an angle γ with respect to the x-axis; this angle is given by

$$\tan\gamma = \frac{V_y}{V_x} = \sqrt{\frac{\varepsilon_1}{\varepsilon_1}}\frac{I_y}{I_x} = \sqrt{\frac{\varepsilon_1}{\varepsilon_2}}\tan\alpha. \tag{221}$$

The maximum fields will be radiated in the direction γ of the voltage gradient and not in the direction α of the current flow. However, α and γ coincide for isotropic ground ($\varepsilon_1 = \varepsilon_2$). The antenna pattern is shifted by an angle $(\gamma - \alpha)$ relative to isotropic conditions. This angle is computed as

$$\tan(\gamma - \alpha) = \frac{\tan\gamma - \tan\alpha}{1 + \tan\alpha\tan\gamma} = \frac{1 - \sqrt{\varepsilon_2/\varepsilon_1}}{\tan^2\alpha + \sqrt{\varepsilon_2/\varepsilon_1}}\tan\alpha. \tag{222}$$

For a given direction α of the current flow, γ denotes the direction of maximum fields; the null of the antenna pattern will be at an angle $\beta = \gamma - 90°$. Noting that

$$\tan(\gamma - \alpha) = -\cot(\beta - \alpha), \tag{223}$$

(222) is seen to be consistent with (184) if the direction of wave incidence ψ for the receiving antenna corresponds to the direction α of the current flow in a transmitting antenna.

6.9 References

AKSENOV, V. I., and I. V. LISHIN (1967) The ionosphere transmission factor for electromagnetic waves of low and ultra-low frequency, *Radio Eng. Electron. Phys.* **12**, 1690–1693.

ALTMAN, C., and H. CORY (1969) The generalized thin-film optical method in electromagnetic wave propagation, *Radio Sci.* **4** (5), 459–470.

BAÑOS, A. (1966) *Dipole Radiation in the Presence of a Conducting Half-Space*, Pergamon Press, Oxford.

BARBER, N. F., and D. D. CROMBIE (1959) V.L.F. reflections from the ionosphere in the presence of a transverse magnetic field, *J. Atmos. Terr. Phys.* **16**, 37–45.

BOSTICK, F. X., and H. W. SMITH (1962) Investigation of large-scale inhomogeneities in the earth by the magneto-telluric method, *Proc. IRE* **50** (11), 2339–2346.

BUDDEN, K. G. (1955) The numerical solution of differential equations governing the reflexion of long radio waves from the ionosphere, *Proc. Roy. Soc. London* A, **227** (1171), 516–537.

BUDDEN, K. G. (1961a) *Radio Waves in the Ionosphere*, Cambridge University Press, Cambridge.

BUDDEN, K. G. (1961b) *The Wave Guide Mode Theory of Wave Propagation*, Logos Press, London.

BUDDEN, K. G. (1962) The influence of the earth's magnetic field on radio propagation by wave-guide modes, *Proc. Roy. Soc. London* A, **265**, 538–553.

BUDDEN, K. G. (1969) Full wave solutions for radio waves in a stratified magnetoionic medium, *Alta Frequenza* **38**, num. spec., 167–179.

BURNSIDE, W. S., and A. W. PANTON (1904), *The Theory of Equations*, Dublin University Press, Dublin.

CAGNIARD, L. (1953) Basic theory of the magneto-telluric method of geophysical prospecting, *Geophysics* **18** (3), 605–635.

CANTWELL, T. (1960) Detection and analysis of low frequency magneto-telluric signals, Thesis, MIT, Cambridge, Massachusetts.

CLARK, S. P., JR. (ed.) (1966) *Handbook of Physical Constants*, revised edition, Geological Soc. Am. Memoir 97.

CROMBIE, D. D. (1961) Reflection from a sharply bounded ionosphere for V.L.F. propagation perpendicular to the magnetic meridian, *J. Res. Nat. Bur. Stand.* **65D** (5) (Radio Prop.), 455–464.

DOWLING, F. L. (1968) A magnetotelluric investigation of the crust and upper mantle across the Wisconsin arch, Ph.D. thesis, Department of Geophysics, University of Wisconsin, Madison, Wisconsin.

D'ERCEVILLE, I., and G. KUNETZ (1962) The effect of a fault on the earth's natural electromagnetic field, *Geophysics* **27** (5), 651–665.

GALEJS, J. (1961) E.L.F. waves in presence of exponential ionospheric conductivity profiles, *IRE Trans. on Antennas and Propagation* **AP-9** (6), 554–562.

GALEJS, J. (1964a) Terrestrial extremely-low-frequency propagation, *Proc. NATO Advanced Study Institute on Natural Electromagnetic Phenomena Below 30 kc/s*, Bad Homburg, W. Germany, July–August 1963, Plenum Press, New York, NY, pp. 205–258.

GALEJS, J. (1964b) E.L.F. and V.L.F. waves below an inhomogeneous anisotropic ionosphere, *Radio Sci. J. Res. NBS* **68D** (6), 693–707.

GALEJS, J. (1964c) Propagation of V.L.F. waves below a curved and stratified anisotropic ionosphere, *J. Geophys. Res.* **69** (17), 3639–3650.

GALEJS, J. (1965) On the terrestrial propagation of E.L.F. and V.L.F. waves in the presence of a radial magnetic field, *Radio Sci. J. Res. NBS/USNC-USSI* **69D** (5), 705–720.

GALEJS, J. (1967a) Propagation of V.L.F. waves below an anisotropic stratified ionosphere with a transverse static magnetic field, *Radio Sci.* **2** (6), 557–574.

GALEJS, J. (1967b) Propagation of V.L.F. waves below anisotropic ionosphere models with a dipping static magnetic field, *Radio Sci.* **2** (12), 1497–1512.

GALEJS, J. (1968a) Propagation of E.L.F. and V.L.F. waves below an anisotropic ionosphere with a dipping static magnetic field, *J. Geophys. Res.* **73** (1), 339–352.

GALEJS, J. (1968b) Propagation of E.L.F. and V.L.F. waves below a generally anisotropic ionosphere, *Radio Sci.* **3** (8), 781–786.

GALEJS, J. (1968c) E.L.F. and V.L.F. fields of a horizontal electric dipole, *IEEE Trans. Antenna Propagation* **AP-16** (6), 689–700.

GALEJS, J. (1969a) V.L.F. modes below an idealized anisotropic ionosphere, *Radio Sci.* **4** (6), 491–516.

GALEJS, J. (1969b) Near fields and antipodal fields in the terrestrial earth-to-ionosphere wave guide, *Proc. IEE* **116** (7), 1150–1158.

GALEJS, J. (1969c) Horizontally oriented antennas in the presence of an anisotropic ground, *Radio Sci.* **3** (11), 1047–1059.

GALEJS, J., and R. V. ROW (1964) Propagation of E.L.F. waves below an inhomogeneous anisotropic ionosphere, *IEEE Trans. Antenna Propagation* **AP-12** (1), 74–83; also *Radio Sci. J. Res. NBS* **68D** (1), 103–104.

GINZBURG, V. L. (1964) *The Propagation of Electromagnetic Waves in Plasmas*, Pergamon Press, Oxford, pp. 340–342.

HELLIWELL, R. A. (1965) *Whistlers and Related Ionospheric Phenomena*, Stanford University Press, Stanford, California.

INOUE, Y., and S. HOROWITZ (1966) Numerical solutions of full wave equation with mode coupling, *Radio Sci.* **1** (8), 957–970.

JOHLER, J. R. (1961) Magneto-ionic propagation in low- and very-low-radio-frequency waves reflected by the ionosphere, *J. Res. NBS Radio Propagation* **65D** (1), 53–66.

JOHLER, J. R., and J. D. HARPER (1962) Reflection and transmission of radio waves at a continuously stratified plasma with arbitrary magnetic induction, *J. Res. NBS Radio Propagation* **66D** (1), 81–99.

JOHLER, J. R., and L. C. WALTERS (1960) On the theory of reflection of L.F. and V.L.F. radio waves from the ionosphere, *J. Res. NBS Radio Propagation* **64D** (3), 269–285.

KAMKE, E. (1948) *Differential Gleichungen*, Chelsea Publishing Co., New York, NY.

KRASNUSHKIN, P. E. (1962) On the propagation of long and very long radio waves around the earth, *Nuovo Cimento*, Supp. **24**, 50–112.

LARGE, D. B., and J. R. WAIT (1968) Theory of electromagnetic coupling phenomena in the earth-ionosphere cavity, *J. Geophys. Res.* **73** (13), 4335–4362.

MADDEN, T. R., and W. THOMPSON (1965) Low-frequency electromagnetic oscillations of the earth-ionosphere cavity, *Rev. Geophys.* **3** (2), 211–254.

MARTIN, H. G. (1965) The polarization of low frequency radio waves in the terrestrial wave guide, *J. Atmos. Terr. Phys.* **27** (9), 995–1007.

PAPPERT, R. A. (1968) A numerical study of V.L.F. mode structure and polarization below an anisotropic ionosphere, *Radio Sci.* **3** (3), 219–233.

PAPPERT, R. A., E. E. GOSSARD, and I. J. ROTHMULLER (1967) A numerical investigation of classical approximations used in V.L.F. propagation, *Radio Sci.* **2** (4), 387–400.

PITTEWAY, M. L. V. (1965) The numerical calculations of wave fields, reflection coefficients, and polarizations for long radio waves in the lower ionosphere, Part I, *Philos. Tran. Roy. Soc. (London)*, A, **257** (1079), 219–241.

SHEDDY, C. H. (1968) A general analytical solution for reflection from a sharply bounded anisotropic ionosphere, *Radio Sci.* **3** (8), 792–795.

SWIFT, C. M. (1967) A magnetotelluric investigation of an electrical conductivity anomaly in the Southwestern United States, Ph.D. thesis, Department of Geology and Geophysics, MIT, Cambridge, Massachusetts.

THOMPSON, W. B. (1963) A layered model approach to the earth-ionosphere cavity resonance problem, Ph.D. thesis, Department of Geology and Geophysics, MIT, Cambridge, Massachusetts.

VOLLAND, H. (1962) The propagation of plane electromagnetic waves in a horizontally stratified ionosphere, *J. Atmos. Terr. Phys.* **24**, 853–857.

VOLLAND, H. (1964) On the theory of propagation of long electromagnetic waves: Part II, Curved anisotropic wave guide (in German), *Archiv Elektrischen Uebertragung* **18** (3), 181–188.

WAIT, J. R. (1961) The electromagnetic fields of a horizontal dipole in the presence of a conducting half-space, *Canadian J. Phys.* **39**, 1017–1028.

WAIT, J. R. (1962) *Electromagnetic Waves in Stratified Media*, Macmillan, New York, NY.

WAIT, J. R. (1963) Concerning solutions of the V.L.F. mode problem for an anisotropic curved ionosphere, *J. Res. NBS Radio Propagation* **67D** (3), 297–302.

WAIT, J. R. (1966) Electromagnetic fields of a dipole over an anisotropic half-space, *Canadian J. Phys.* **44**, 2387–2401.

WAIT, J. R., and K. P. SPIES (1965) Influence of finite ground conductivity on the propagation of V.L.F. radio waves, *Radio Sci.* **69D** (10), 1359–1373.

WAIT, J. R., and L. C. WALTERS (1964) Reflection of electromagnetic waves from a lossy magneto plasma, *Radio Sci.* **68D** (1), 95–101.
WALSH, E. J. (1967) Full wave solutions in terms of coupled vacuum modes, *Radio Sci.* **2** (8), 913–925.
WEAVER, J. T. (1963) The electromagnetic field within a discontinuous conductor with reference to geomagnetic micropulsations near a coastline, *Canadian J. Phys.* **41**, 484–495.
ZAGUSKIN, V. L. (1961) *Handbook of Numerical Methods for Solution of Equations*, Pergamon Press, Oxford.

CHAPTER 7

E.L.F. PROPAGATION AND SCHUMANN RESONANCES

Abstract. Propagation characteristics are calculated for a number of stratified and anisotropic model ionospheres. Tapered models of the lower ionosphere should include also ions at altitudes below the *D*-layer. During nighttime waves penetrate above the *D*-layer, and propagation parameters of the earth-to-ionosphere waveguide are dependent on the detailed ionospheric structure below the *F*-layer. The individual models advanced for the ionosphere are not representative of long-distance or global wave propagation; but the average of the propagation parameters derived for a number of propagation geometries is comparable to the parameters deduced from an isotropic nighttime ionosphere model.

The resonances of the earth to ionosphere can be analyzed in a symmetrical geometry, which is adequate for explaining observed resonance frequencies, *Q*-factors, power spectra, diurnal variations of power, and changes of resonance frequencies. The split modes that result from differences between normal day and night hemispheres are of negligible amplitudes.

7.1 Introduction and Summary

E.L.F. and V.L.F. fields in a spherical shell have been discussed in Chapter 4, where wave representations in the shell and propagation parameters are derived by idealizing the ground surface and also the ionospheric boundary of the waveguide as homogeneous isotropic conductors. In a more realistic representation, the surface properties will vary along the direction of wave propagation and the guide boundaries will be stratified and anisotropic. The ground surface exhibits a generally higher conductivity than the ionospheric boundary; and for purposes of calculating wave-propagation parameters, it may be approximated as a perfect conductor. (This idealization cannot be used for estimating the fields in the ground surface or the wave tilt above the ground.) For fields in the E.L.F. range, only T.M. $n = 0$ (or T.E.M.) waveguide mode will propagate; and the simple field expressions derived for homogeneous boundaries may be used provided that the surface impedance of the ionospheric boundary accounts for the stratification and the possible existence of T.E. field components, which arise in the guide from ionospheric anisotropy. However, the gradual variations of boundary characteristics are ignored in this approach.

Several of the basic field representations derived in Chapter 4 are summarized in Section 7.2. In the representation of zonal harmonics, the azimuthal or θ variations of the fields are denoted by Legendre polynomials $P_n(\cos\theta)$ and derivatives; in the residue series representation by Legendre functions $P_\nu(-\cos\theta)$, where ν is a complex parameter; but the latter function can be expressed also as a series of functions $P_n(\cos\theta)$. The final field representations based on zonal

harmonics and residue series both involve Legendre functions $P_n(\cos\theta)$, but these field representations differ for the vertical electric field component E_r of a vertical electric dipole source. The zonal harmonic series is slowly convergent, but the residue representation (which reproduces only the $n = 0$ waveguide mode) is converging rapidly. However, there are no differences between the two corresponding expressions for the horizontal magnetic field components H_φ. Other fields components, wave tilt, and other excitations are discussed in less detail.

The wave propagation in the spherical shell is characterized by the phase velocity v_{ph} and the attenuation rate α. The propagation parameters are illustrated for a number of ionosphere models.

The calculations for a sharply bounded homogeneous and isotropic ionosphere model do not account properly for phase-velocity and attenuation-rate variations over the E.L.F. range. The stratifications of the lower ionosphere may be represented most simply by an exponentially varying conductivity. This idealization approximates the observed daytime characteristics. The nighttime attenuation rate is lower, and it appears as too low for frequencies in the Schumann resonance range.

The observed differences between the general east–west (E.W.) and west–east (W.E.) directions of propagation can be modeled most simply with a purely horizontal static magnetic field [Galejs, 1964], but these directional effects can be accounted more accurately by allowing for the finite dip angle of the geomagnetic field. Significant differences between E.W. and W.E. directions of propagation are noted when the geomagnetic field is within 30° from the horizontal direction, but these differences are not necessarily the largest for a purely horizontal magnetic field in Section 7.3.3. The radial geomagnetic field component facilitates wave penetration in the nighttime ionosphere; and the nighttime attenuation rates are higher for frequencies in the Schumann resonance range, even when ignoring the presence of ions below the *D*-region.

The inclusion of lower altitude ions increases the attenuation rates for isotropic and anisotropic ionosphere models, but the presence of the radial geomagnetic field component increases also the difference between calculations and nighttime measurements reported in Section 7.3.4. In this work the ionosphere has been assumed to be homogeneous in the vertical (or radial) direction above 100 km, and the increased electron density of the *F*-layer has been ignored.

When considering the reflections from a nighttime *F*-layer in Section 7.3.5, it has not been possible to advance a single ionospheric model which produces gradually varying propagation parameters comparable to the ones obtainable from models of the lower ionosphere. The presence of the *F*-layer introduces standing waves above the *D*-region, the characteristics of which are determined by the propagating magneto-ionic mode. There appear absorption peaks and phase-velocity changes, the occurrence of which depends on electron density, boundary height of the *F*-layer, and the radial component of the static magnetic field. In long-distance or global propagation, the conditions for absorption peaks may be satisfied only locally. More refined models include ions above 100 km, a gradual electron density buildup at the bottom side of the *F*-layer, and a residual nighttime *E*-layer; these factors tend to decrease but do not eliminate the standing-wave effects in a given ionosphere model [Galejs, 1970a].

The average of the calculated propagation parameters tends to approximate the propagation parameters of the isotropic nighttime ionosphere model, and *not* the parameters of the lower ionosphere model with a radial static magnetic field. This may explain in part the success of past calculations based on isotropic ionosphere models in the E.L.F. range [Galejs, 1962; Cole, 1965; Jones, 1967]. However, nighttime models of an anisotropic lower ionosphere may give excessive attenuation rates; and such simplified ionosphere models should be carefully justified by comparisons with available experimental data.

Propagation under perturbed conditions is discussed in Section 7.3.6. The work of Crain and Booker [1964], Cole and Pierce [1965], Johler and Berry [1966], or Field [1969] show that the conductivity of the lower ionosphere is determined principally by ions and that ions will affect the characteristics of radio-wave propagation under perturbed conditions and/or for the lower frequencies, but there are uncertainties in parameters that characterize the ion contributions to the total conductivity. Ion collision frequencies ν_{in} which exceed the neutral particle collision frequency ν_{nn} and molecular weights M.W. that exceed M.W. = 29 of the typical lower atmosphere ions produce an agreement between calculated conductivity of the unperturbed daytime profile and available measurements. For unperturbed and slightly perturbed ionosphere profiles, the phase velocity is practically unaffected by the presence of ions; but there is some increase in the attenuation rate α. The propagation parameters are shown to depend on the choice of M.W. and ν_{in} figures.

The electromagnetic oscillations in the spherical shell between the earth and ionosphere that are due to azimuthal waves are frequently described as Schumann [1952a, b] resonances. These oscillations are excited by naturally occurring lightning discharges and are manifested by increased spectral field amplitudes near 8, 14, 20 c/s, and higher frequencies. At these frequencies the wavelengths are large, and the resonances are affected by ionospheric parameters averaged over comparable distances. The essential characteristics of the resonances can be explained even by assuming a perfect symmetry of the cavity, and the elementary field representations of Section 7.2 are used to calculate resonance frequencies and cavity quality (Q) factors in Section 7.4.2 and noise spectra in Section 7.4.3.

There is a close agreement between measured and calculated resonance frequencies, but certain ambiguities are associated with an interpretation of Q-factors. The half-power width of resonance curves is affected by the presence of adjacent resonances and of near-field noise, which may lead to low experimental Q estimates. It is shown that a close agreement with measured power spectra may be obtained with Q figures which are higher than the usually accepted experimental values. When used in conjunction with estimated source distributions, similar theoretical models are also useful for explaining diurnal changes of power levels and differences of noise levels observed at various locations on the globe.

The nonsymmetrical structure of the earth-to-ionosphere cavity has been analyzed numerically with a network analog of the varying surface impedances [Madden and Thompson, 1965], by perturbation techniques [Nelson, 1967; Bliokh *et al.*, 1968] or by a direct summation of the series of zonal harmonics, which allows for θ but no φ variations of the fields [Large and Wait, 1968]. In a uniform or φ-symmetrical cavity, the fields are expressed using Legendre polynomials $P_n(\cos\theta)$ while nonsymmetrical cavities can support additionally the so-called split modes characterized by Legendre functions $P_n^m(\cos\theta)$ with $|m| \ll n$. The various mode amplitudes of such a field representation are determined in Section 7.4.4, from a solution of linear equations the number of which increases quadratically with the number of modes $N \gg n$. The solution of the large number of linear equations is avoided by restricting N to two. In a geometry which distinguishes only between day and night hemispheres, the amplitudes of these additional split modes appear to be negligible under normal daytime and nighttime conditions [Galejs, 1970b].

The diurnal frequency variations described in Section 7.4.5 differ when observing vertical electric or horizontal magnetic field components. The fundamental resonance frequency of the magnetic field is smoothly varying. The frequency variations of the electric field appear discontinuous near the null of the fields when the equatorial point source is separated from the observation point by 90° in longitude, but the magnitude of these frequency changes is decreased for sources spread out in the azimuthal direction. The complete observed diurnal frequency variations can be explained by noting that the peak activity of local thunderstorms, which occurs in late afternoon over land, is shifted to nighttime for sources over the Pacific. High-altitude nuclear explosions and also natural ionospheric perturbations are shown to affect the earth-to-ionosphere cavity resonances by lowering resonance frequencies.

In agreement with Madden and Thompson [1965] or Nelson [1967], the frequency shifts of resonance frequencies are explained by the interaction of adjacent resonance modes. Bliokh *et al.* [1968] proposed a mechanism where the difference in the response of daytime and nighttime hemispheres to an eccentric geomagnetic field caused frequency changes for a single mode. For such frequency changes it is necessary that the nighttime phase velocity is decreased with an increased radial component of the geomagnetic field; but in multi-layer ionosphere models, which consider F-layer reflections, there can be also an increase of phase velocity.

7.2 Field Representations for a Uniform Cavity

Several of the basic field representations that have been derived for a uniform spherical cavity in Section 4.9 will be summarized in this section. In the E.L.F. range, T.E. modes do not propagate and the propagating T.M. $n = 0$ (or T.E.M.) mode contains only E_r, E_θ, and H_φ field components for azimuthally symmetric (vertical electric dipole) excitation in an isotropic environment.

The E.L.F. fields can be represented by a series of zonal harmonics. After expressing the radial functions in a Taylor series and neglecting the height variations of the fields, the radial electric fields E_r excited by a vertical electric dipole of moment $I\,ds$ are expressed following (268) of Chapter 4 as

$$E_r \approx \frac{iI\,ds}{4\pi\omega\varepsilon_0 h a^2} \sum_n \frac{n(n+1)(2n+1)}{n(n+1)-\nu(\nu+1)} P_n(\cos\theta), \tag{1}$$

where

$$\nu(\nu+1) = (k_0 aS)^2 = (k_0 a)^2 \left[1 + \frac{i\Delta_e}{k_0 h}\right] \tag{2}$$

and $\Delta_e = Z_e/\eta$ is the normalized surface impedance of the ionosphere for T.M. field components and h is the height of the ionospheric boundary. The impedance of the ground surface Δ_g is much smaller than Δ_e, and the ground can be approximated by a perfect conductor for purposes of calculating the propagation parameter ν. The approximation (1) is valid only for $nh < a$, and it will become inaccurate for large values of n. The exponential approximation of the radial functions (Section 4.9.1.2) shows that the terms of the sum should become proportional to $n^2 P_n(\cos\theta)$ for $n > k_0 a$, and further manipulations of the summation are necessary to increase its rate of convergence.

More convenient for numerical work is the residue series representation of the fields which contains only one propagating term for frequencies in the E.L.F. range. Equation (291) of Chapter 4 is rewritten as

$$E_r = -\frac{iI\,ds}{4\omega\varepsilon_0 h a^2} \frac{\nu(\nu+1)}{\sin \nu\pi} P_\nu(-\cos\theta), \tag{3}$$

where ν is obtained from (2) as

$$\nu = -0.5 + \sqrt{0.25 + (k_0 aS)^2} \approx k_0 aS - 0.5. \tag{4}$$

The latter approximation introduces an approximately 10 percent error in ν for frequencies near the fundamental Schumann resonance; however, the error becomes small at higher frequencies. The Legendre function of (3) can be also expressed as a summation of Legendre polynomials, which gives following (293) of Chapter 4

$$E_r = \frac{iI\,ds\nu(\nu+1)}{4\pi\omega\varepsilon_0 h a^2} \sum_{n=0}^{\infty} P_n(\cos\theta) \frac{2n+1}{n(n+1)-\nu(\nu+1)}. \tag{5}$$

For frequencies where Re ν approaches an integer value n, the resonant terms of equation (5) are approximately the same as in (1). However, the total field that is represented by (1) will generally differ from (5), where all the terms of the summation represent only one propagating waveguide mode.

In the representation of zonal harmonics (238), (257), (260), and (261) of Chapter 4 show that

$$\left.\frac{\eta H_\varphi}{E_r}\right|_n = \frac{ik_0 a}{n(n+1)P_n(\cos\theta)} \frac{d}{d\theta} P_n(\cos\theta). \tag{6}$$

Equations (16) and (17) of Chapter 4 imply that

$$\eta H_\varphi = \frac{ik_0 a}{\nu(\nu+1)} \frac{\partial}{\partial\theta} E_r. \tag{7}$$

Substituting either (6) in (1) or (7) in (5) one obtains

$$H_\varphi = -\frac{I\,ds}{4\pi a h} \sum_n \frac{2n+1}{n(n+1)-\nu(\nu+1)} \frac{d}{d\theta} P_n(\cos\theta). \tag{8}$$

There is only one rapidly convergent H_φ representation (8) which corresponds to two different E_r expressions (1) and (5). In (8) the derivatives of Legendre polynomials can be expressed in terms of the associated Legendre functions of order 1 by

$$P_n^1(\cos\theta) = \frac{d}{d\theta} P_n(\cos\theta) \tag{9}$$

following Erdélyi [1953] or Abramowitz and Stegun [1964] although in the notation of Stratton [1941] or Morse and Feshbach [1953], the right-hand side of (9) is multiplied with (-1).

More complete field expressions contain also the height-gain functions [(205) to (207) of

Chapter 4], which are near unity for the propagating waveguide mode in the E.L.F. range. In this approximation (1) to (8) apply at any height in the earth-to-ionosphere waveguide ($0 \ll z \ll h$). A comparison of (206) and (207) of Chapter 4 shows that the E_θ field component is related to the H_φ field component by a height-dependent impedance as

$$\frac{E_\theta(z)}{H_\varphi(z)} = \Delta_0(z)\eta = Z_e(z). \tag{10}$$

At the ground surface $z = 0$, $\Delta_0(0) = -\Delta_g$; at the ionospheric boundary $z = h$, $\Delta_0(h) = \Delta_e$; the height variations of $\Delta_0(z)$ illustrated in Fig. 4.5 (p. 95) show that $\Delta_0(z) \sim z$ near the ionospheric boundary.

The θ-dependence of the individual resonance modes of (1) and (5) or (8) are characterized by the functions $P_n(\cos\theta)$ or $P_n^1(\cos\theta)$. The lower order functions are $P_0 = 1$, $P_1 = \cos\theta$, $P_2 = (3\cos 2\theta + 1)/4$, $P_3 = (5\cos 3\theta + 3\cos\theta)/8$; $P_1^1 = -\sin\theta$, $P_2^1 = -1.5\sin 2\theta$, $P_3^1 = -\left(\frac{3}{8}\right)(\sin\theta + 5\sin 3\theta)$. The amplitude distributions of the first two resonance modes are illustrated in Fig. 7.1 following Polk [1968]. E_r of (1) and (5) is equal to 0 with $n = 1$ for the

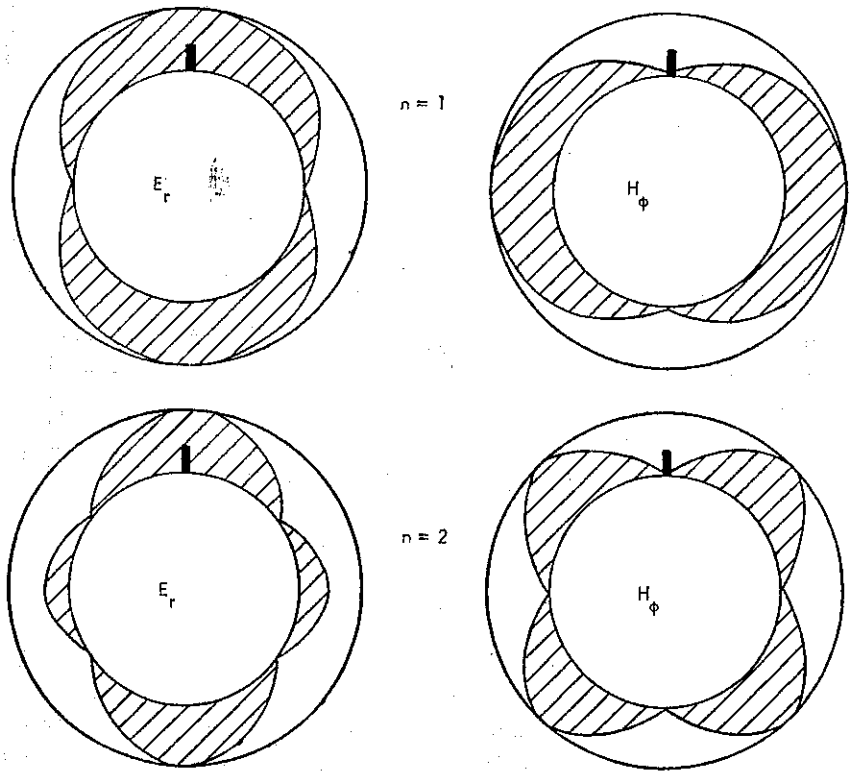

FIG. 7.1 Amplitude Distributions for First and Second Modes Excited by a Vertical Electric Dipole

polar angle $\theta = 90°$ and with $n = 2$ for $\theta = 55°$. H_φ of (8) vanishes with $n = 1$ for the angles $\theta = 0$, 180° and with $n = 2$ for $\theta = 0$, 90, and 180°. E_r and H_φ field components exhibit different θ variations; the relative amplitudes of E_r and H_φ are principally dependent on the polar angle θ between the source and the receiver, and they are less sensitive to the propagation parameters ν or S. Measurements of E_r and H_φ carried out at a number of frequencies may provide an indication of the distance from active thunderstorm regions [Polk, 1968; Jones and Kemp, 1969].

The field components E_φ and H_θ are significant for horizontal dipole sources when at frequencies near the fundamental Schumann resonances they are comparable in magnitude to E_θ and H_φ field components following (125) of Chapter 4. Nonpropagating T.E. modes are also significant in the near-field range of horizontal dipole sources following Section 4.6.2. The T.E. field components are also considered in the treatment of anisotropic waveguide boundaries.

7.3 Propagation Parameters

The propagation parameter S is determined from the solution of (2) for ionospheric models denoted by a surface impedance Δ_e. The phase velocity v_{ph} is characterized by $\mathrm{Re}\,(S) = c/v_{ph}$, and the attenuation rate α by $\mathrm{Im}\,(S) = \alpha/0.028933\omega$, where c is the freespace velocity of electromagnetic waves and α is the attenuation rate in decibels per 1000 km. Such calculations will be reported for several classes of ionospheric models.

7.3.1 *Models of One and Two Isotropic Layers*

Phase velocities and attenuation rates of E.L.F. waves have been illustrated in Section 4.3.1 for the rather simple sharply bounded homogeneous and isotropic ionosphere model. It was pointed out that a particular ionospheric model which may account for the attenuation rates at frequencies less than 300 c/s does not provide the correct attenuation rate at higher frequencies nor the proper phase velocity at any frequency. It has been possible to construct empirical two-layer isotropic ionosphere models that are more satisfactory for explaining measurement data [Jean *et al.*, 1961; Chapman and Jones, 1964a, b]. However, the parameters of such ionosphere models cannot be deduced from physical properties of the ionosphere; and these models will not be discussed in more detail.

7.3.2 *Exponential Isotropic Ionosphere*

The electron density N_e can be approximated by an exponential function through much of the lower ionosphere, and also the collision frequencies ν exhibit an exponential height variation. This leads to an exponential height variation of the conductivity

$$\sigma_e = \frac{\varepsilon_0\omega_{pe}^2}{\nu} = 0.0283\,\frac{N_e}{\nu}, \tag{11}$$

where ω_{pe} is the plasma frequency of the electrons, N_e is defined per cm^3, and where it is assumed that $\nu \gg \omega$. This conductivity is represented as

$$\sigma_e = \sigma(z_0) \exp [\beta(z - z_0)]. \tag{12}$$

Letting $z_0 = 60$ km, daytime conditions may be represented with $\sigma(z_0) = 4.63 \times 10^{-8}$ and $\beta = 0.308$ and nighttime with $\sigma(z_0) = 6.5 \times 10^{-10}$ and $\beta = 0.44$ [Galejs 1962, 1964]. The daytime and nighttime conductivity profiles have been extended downward to altitudes of

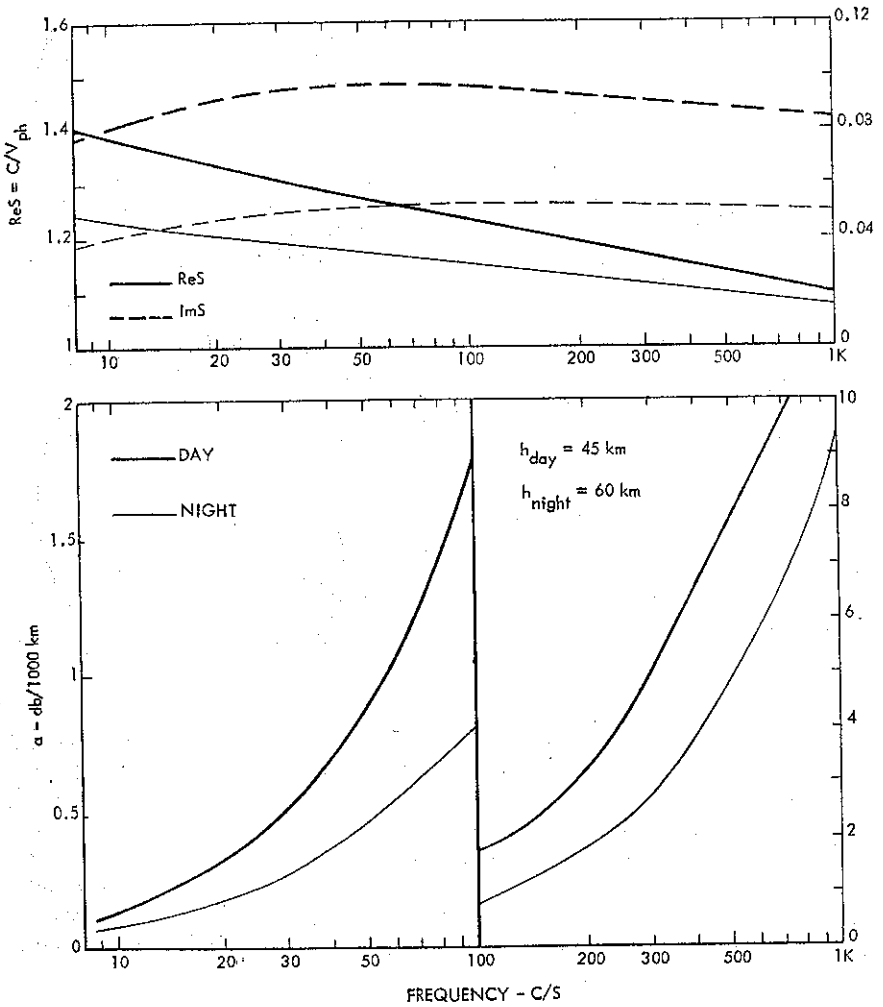

FIG. 7.2 Phase Velocity and Attenuation Rates of E.L.F. Waves for an Exponential Isotropic Ionosphere Model

$z = 45$ and 60 km, where the refractive index $n = [1 + i\sigma/(\omega\varepsilon_0)]^{0.5}$ is near 1 in magnitude. However, there is no evidence of ionospheric reaction rates which could support such conductivity figures near these lower boundaries. After computing the ionospheric surface impedance following Galejs [1961b], the propagation parameter S is determined from (2). The top part of Fig. 7.2 shows the real and imaginary parts of S which can be interpreted as the complex sine of the wave incidence angle at the ionospheric boundary. The corresponding attenuation rates α are shown in the lower part of Fig. 7.2. In distinction from Fig. 4.3 (p. 91), which depicts the propagation parameters for the homogeneous sharply bounded ionosphere model, α is below 0.5 in the frequency range of Schumann resonances; and it exceeds 10 db per 1000 km for frequencies near 1 kc/s. Re S is near 1.3 for Schumann resonances and is near 1.1 for $f = 1$ kc/s. Similar figures of the propagation parameters can be also seen from the experimental data summarized in Fig. 7.12 (p. 260). The exponential isotropic ionosphere model exhibits a nighttime attenuation rate that is lower than the daytime figure for all frequencies, and the nighttime attenuation rate is too low in the frequency range of Schumann resonances. The attenuation rates are increased by atmospheric losses that are due to ionic conductivity [Galejs, 1961b]. Also the more elaborate ionosphere models of Figs. 7.6 and 7.7 (pp. 252 and 253) give nighttime attenuation rates that exceed the daytime figures in the lower part of the E.L.F. range.

7.3.3 *Composite Electron Density Profiles*

The phase velocities and attenuation rates have been also calculated using the electron-density profiles of Deeks [1966] and the collision-frequency profile of Piggott and Thrane [1966] that are shown in Figs. 2.2 and 2.6 (pp. 22 and 26). The ionosphere model is anisotropic, and the geomagnetic field is at an angle θ relative to the horizontal plane ($\theta = \pi/2, 0, -\pi/2$ at the south pole, magnetic equator, and the north pole respectively; the dip angle $I = -\theta$) with $B_0 = 0.5$ gauss. The lower boundary of the ionospheric model is assumed at an altitude h_b. The procedure of these calculations is summarized in Section 6.5.

Calculated daytime phase-velocity and attenuation data are shown in Figs. 7.3A and 7.4A. For $\theta = 45°$ the attenuation rate differs between east–west (E.W.) and west–east (W.E.) directions by approximately 0.5 db per 1000 km at 100 c/s, and by 1.5 to 2 db at 300 c/s. The data of polar propagation ($\theta = 90°$) are nearly the same as the data for W.E. propagation at $\theta = 45°$. The maximum differences between E.W. and W.E. attenuation rates occur for $\theta \approx = 15°$ at 100 c/s. In the modified profiles, the electron-density data have been extended to lower altitudes following the dashed curve in Fig. 2.2. The modification increases Re (S) and also the attenuation rate α and decreases the difference between E.W. and W.E. propagation characteristics.

The nighttime data of Figs. 7.3B and 7.4B show attenuation rates that differ by less than 0.3 db per 1000 km for E.W. and W.E. directions of propagation at $f = 100$ c/s and $\theta = 45°$, and the same difference is less than 1.5 db per 1000 km at $f = 300$ c/s. The maximum difference between E.W. and W.E. attenuation rates occurs near $\theta = 15°$ for $f = 100$ c/s. Figure 7.4B shows distinct differences between the propagation data for the electron density profiles of Deeks and the smoothed nighttime profile, which is obtained by replacing the curved Deeks profile of

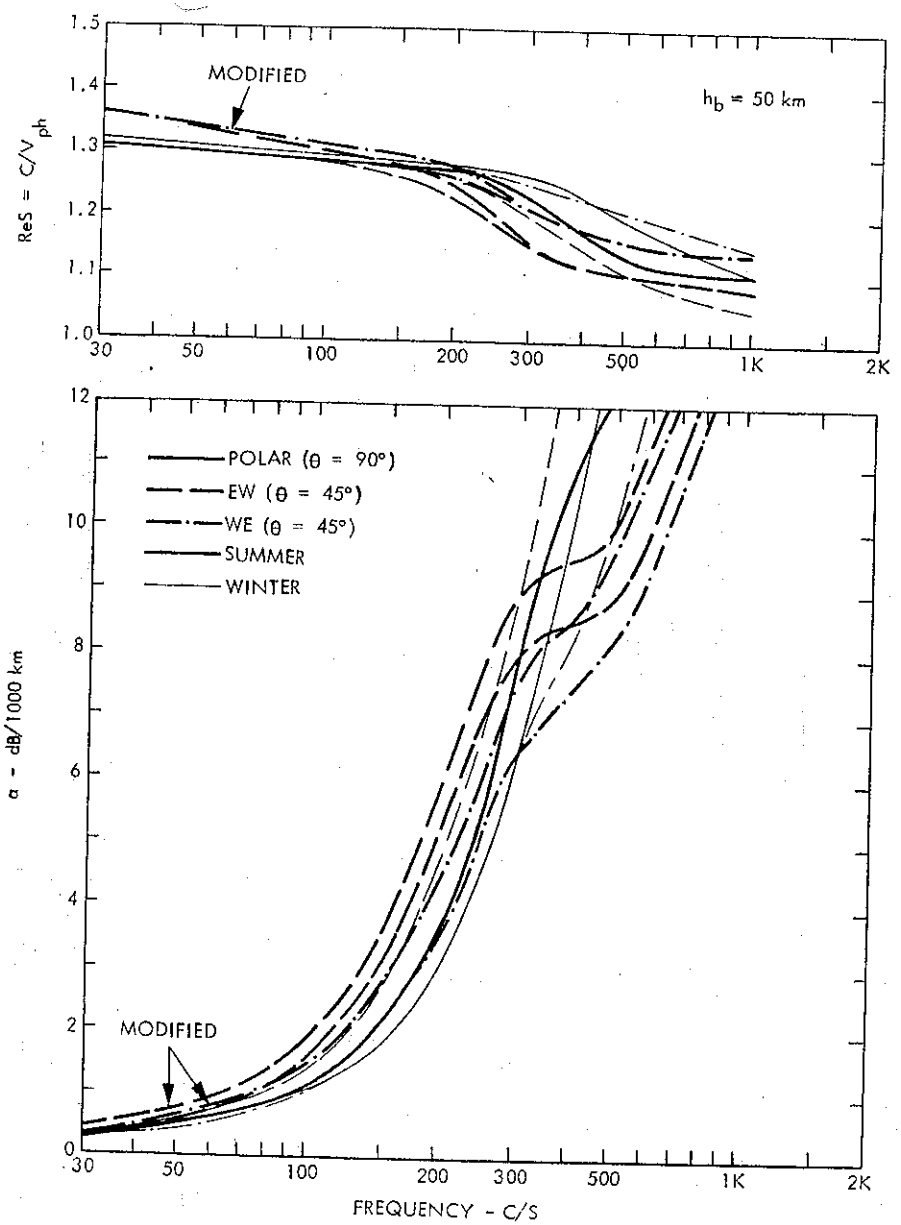

FIG. 7.3A Daytime Phase Velocity and Attenuation Rates of E.L.F. Waves. θ = Const.

Fig. 2.2, by a straight line in the altitude range between 70 and 95 km. The propagation data of the smoothed profiles exhibit larger nonreciprocity (or directional effects) near $\theta = 0°$ and also larger differences between the E.W. and W.E. attenuation at other values of θ.

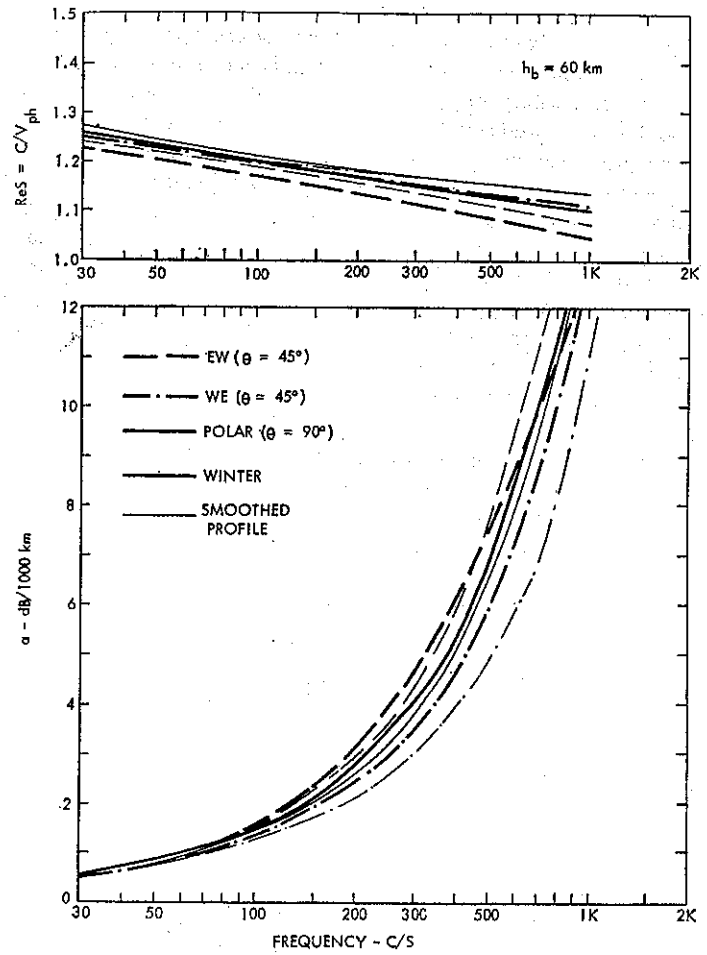

FIG. 7.3B Nighttime Phase Velocity and Attenuation Rates of E.L.F. Waves. θ = Const.

The penetration of E.L.F. waves in the ionosphere is investigated by computing the ratio $H_z(h)/H_z(h_b)$ for various heights h. The computed field strength ratio, shown in Fig. 7.5, is approximately 0.6 for $h > 110$ km and for the angle $\theta > 15°$. For a given penetration depth, the field strength is higher for E.W. direction of propagation, which exhibits also a higher attenuation rate than the W.E. direction of propagation.

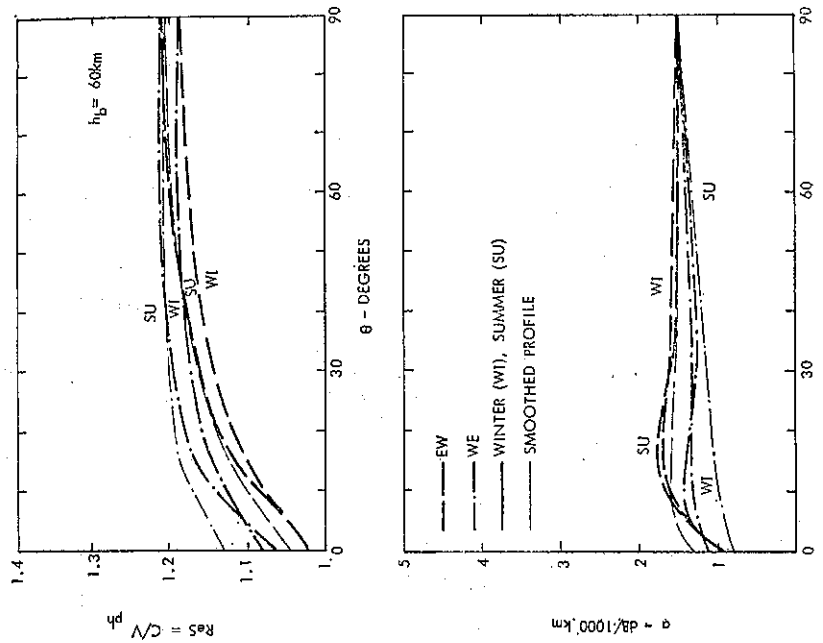

FIG. 7.4B Nighttime Phase Velocity and Attenuation Rates of E.L.F. Waves. $f = 100$ c/s

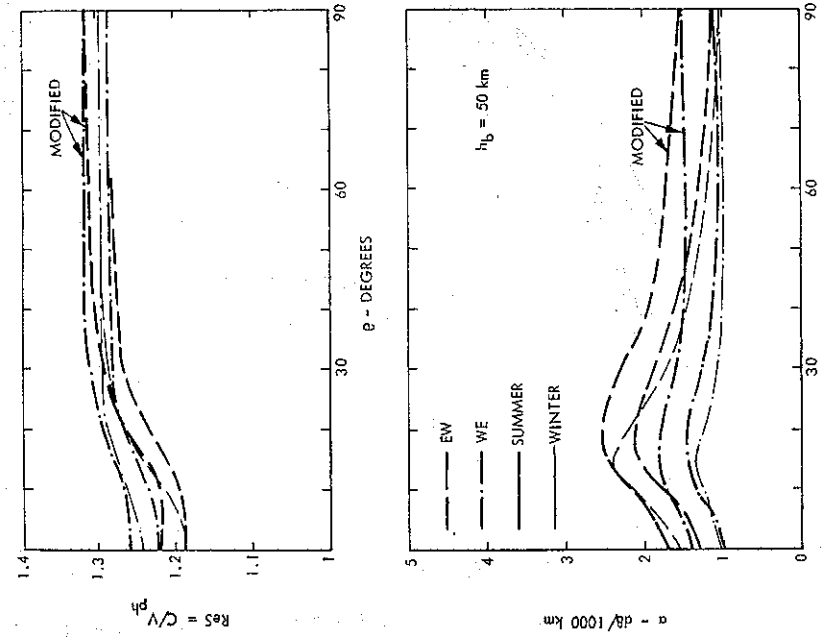

FIG. 7.4A Daytime Phase Velocity and Attenuation Rates of E.L.F. Waves. $f = 100$ c/s

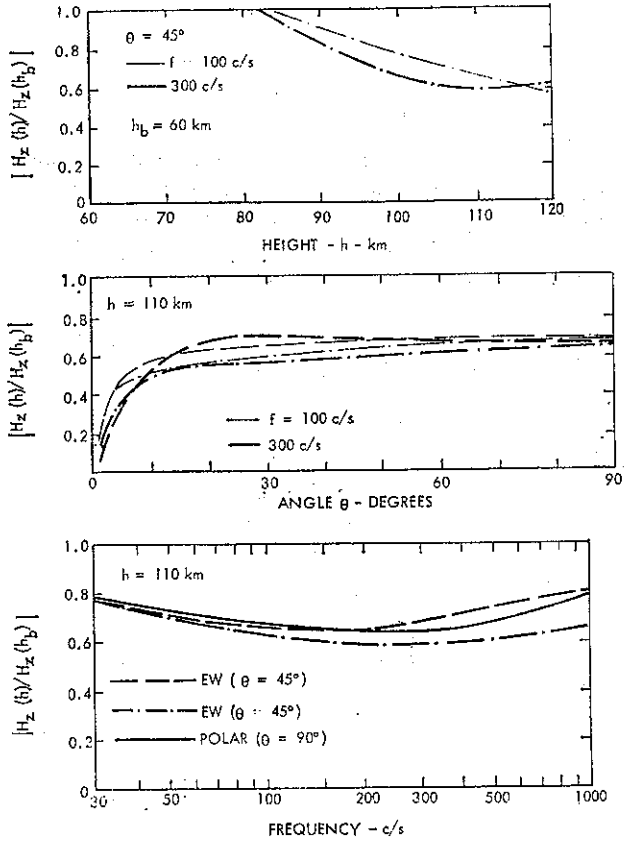

FIG. 7.5 Penetration of E.L.F. Waves in the Nighttime Ionosphere

The numerical calculations will also compare the propagation data of the ionospheric profiles of Deeks [1966] with those of simpler exponential approximations. The exponential profiles, shown in Fig. 2.2 are of the form $N_e = 350 \exp[\alpha(z - z_0)]$, where for daytime $\alpha = 0.138$ and $z_0 = 72.5$ km, and for nighttime $\alpha = 0.35$ and $z_0 = 85$ km. The collision-frequency profile of Piggott and Thrane [1966] is approximated as $\nu = 0.725 \times 10^6 \exp[0.164(85 - y)]$. Applying (11), the conductivity component σ_0 assumes the form of equation (12), with $\beta = 0.302$ in daytime and $\beta = 0.514$ in the nighttime model. The ionosphere is assumed to be homogeneous of constant electron density N_e and collision frequencies ν above the altitude h_u, and the lower boundary of the ionosphere is assumed at h. The static magnetic field $B_0 = 0.36$ gauss is assumed to be purely radial. The modified summer daytime profile, which produced the dotted conductivity curve in Fig. 2.10 (p. 33) gives in Fig. 7.6 for frequencies less than 100 c/s lower attenuation figures than the exponential profile; but the winter nighttime profile of Deeks [1966] results in slightly higher attenuation rates than the nighttime exponential model.

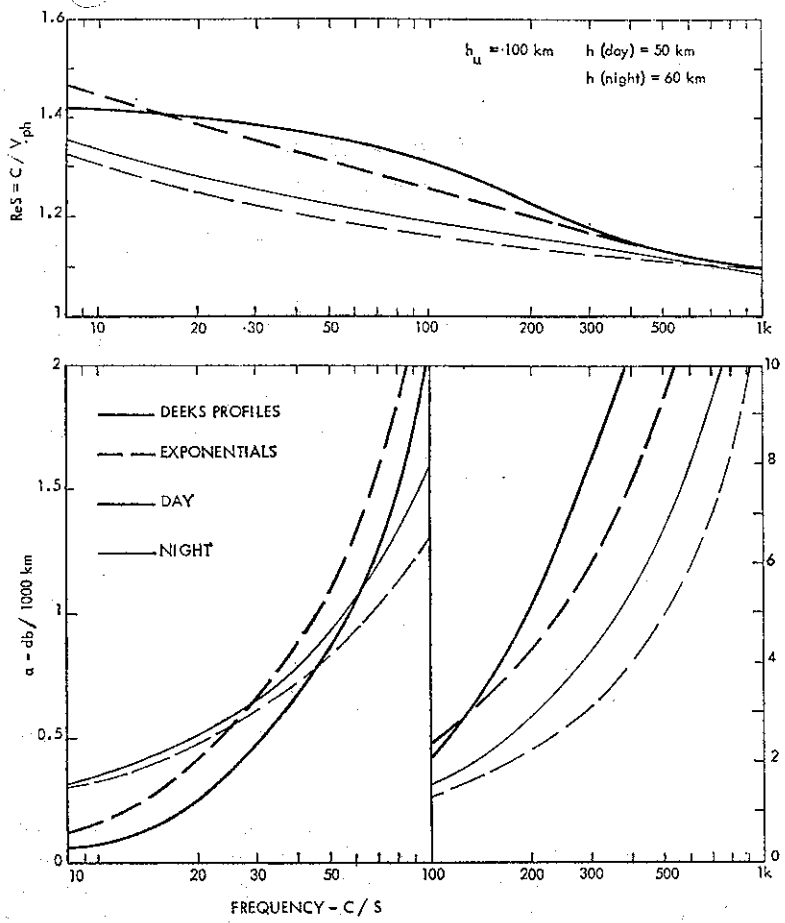

FIG. 7.6 Phase Velocity and Attenuation Rates of E.L.F. Waves. Electron Profiles with Radial Static Magnetic Field of 0.36 Gauss

7.3.4 *Ions of the Lower Ionosphere*

Ion effects will be studied in conjunction with the electron-density profiles of Deeks [1966] by assuming an ion density of $N_i = 2000\ \text{cm}^{-3}$ in the altitude range from 65 to 40 km (Fig. 2.4, p. 24), ion neutral-collision frequency $\nu_{in} = \nu_{nn}$ and the molecular weight M.W. = 29 although larger values of ν_{in} and M.W. may be justified following the arguments outlined in Section 7.3.6. The resulting conductivity σ_0 exhibits the altitude variation shown in Fig. 2.10.

Inclusion of ions increases the attenuation rates for the lower frequencies in Fig. 7.7 relative to the data shown in Fig. 7.6. The static magnetic field affects the daytime data to a lesser degree than the nighttime data when the attenuation rates of the isotropic model ($B_0 = 0$) are

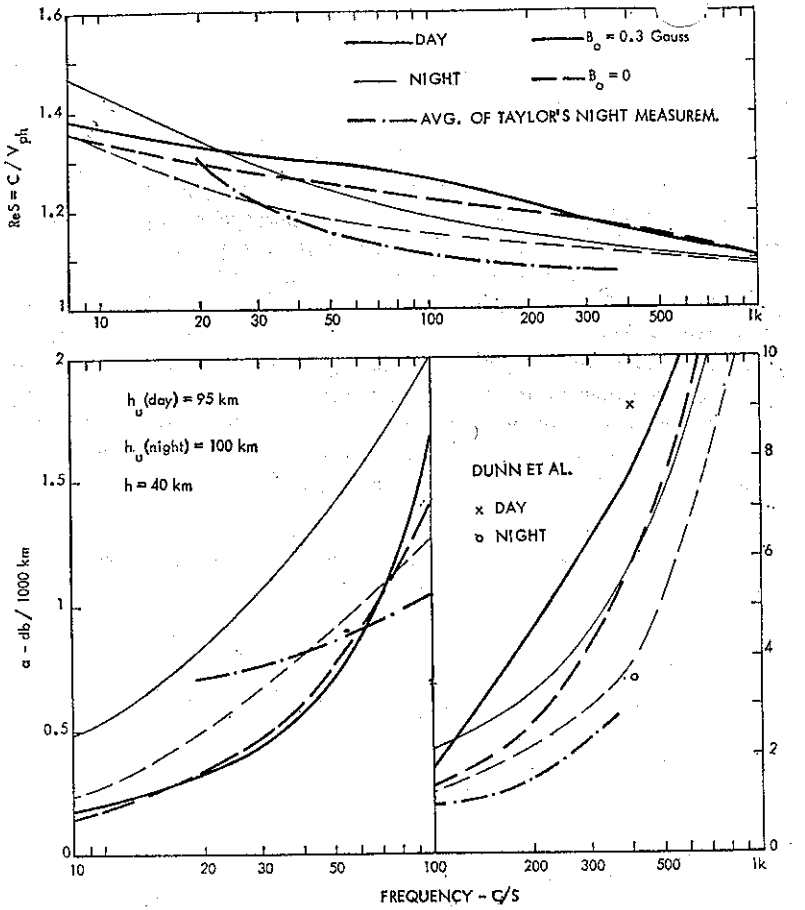

FIG. 7.7 Phase Velocity and Attenuation Rates of E.L.F. Waves. Electron Profiles of Deeks with Added Ions

significantly lower. The isotropic nighttime ionosphere model yields propagation parameters in Fig. 7.7 that are comparable to the average of Taylor's [1969] measurement data that were obtained by observing atmospheric waveforms in a transpacific geometry. The experimental Re S and α figures are lower than in calculations, except for frequencies less than 40 c/s, where Taylor expects his data to become less accurate. The attenuation rates of 400 c/s measurements made by Dunn *et al.* [1964] over a 3000 km propagation path between California and New York are also indicated in Fig. 7.7. The daytime attenuation rate is approximated by the calculations for the anisotropic model, but the nighttime attenuation rate is represented more closely by the isotropic model. The inclusion of a static magnetic field should provide more realistic propagation parameters, but it increases the difference between calculations and

nighttime measurements. The magnetic field increases the attenuation rate, which may signify wave penetration above the upper boundary of the present nighttime model, where the ionosphere has been assumed to be homogeneous in the vertical (or radial) direction and where the presence of an increase of electron density near the F-layer has been ignored.

7.3.5 *F-Layer Reflections*

The effects of the F-layer will be investigated using several idealized electron-density profiles. It is frequently assumed that the electron density which is of the order of 10^3 cm^{-3} at an altitude near 100 km is gradually increased in the height range between 100 and 200 km; a more rapid increase is observed near the bottom side of the F-layer, where N_e exceeds 10^4 cm^{-3} [Hanson, 1961; Maeda and Matsumoto, 1962; Prince and Bostick, 1964]. Such electron-density data are further idealized by the profile A of Fig. 7.8, where the electron density used for the lower nighttime ionosphere [Deeks, 1966] is extended upward to a height h_F where it is changed to $N_e = 10^5$ of the F-layer. For altitudes between 100 and 200 km, the electron density varies from experiment to experiment; and it is in the range from 300 to 5000 cm^{-3} [Wakai, 1967; Maeda, 1969]. In the model B of Fig. 7.8, the electron density is assumed to have a constant value $N_e = N_t$ in the height range between 105 and $(h_F - \Delta h)$ km; N_e is increased to 2×10^4 cm^{-3} $\Delta h = 40$ km below the F-region, where at h_F N_e is changed to the value 2×10^5 cm^{-3}. An E-layer peak that is reported near 100 km with densities of 3000 to 10^4 cm^{-3} in the review of Maeda [1969] is approximated by the profile C of Fig. 7.8, which follows profile B at altitudes above

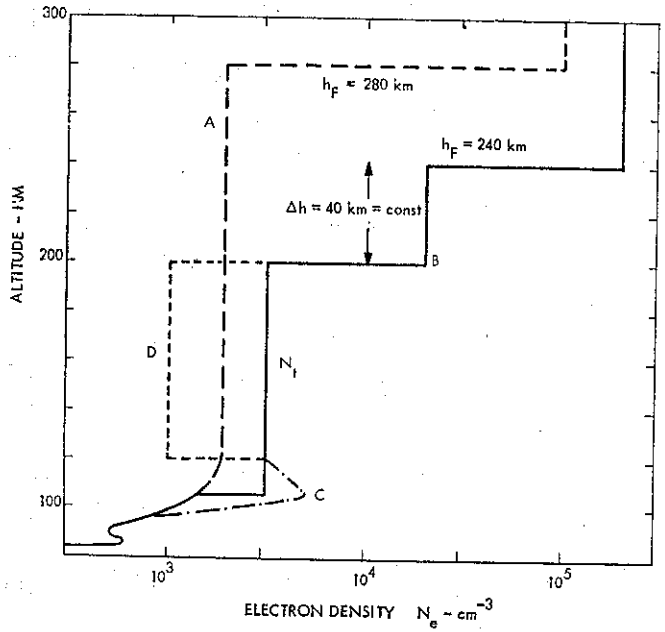

FIG. 7.8 Models of Nighttime Electron Density

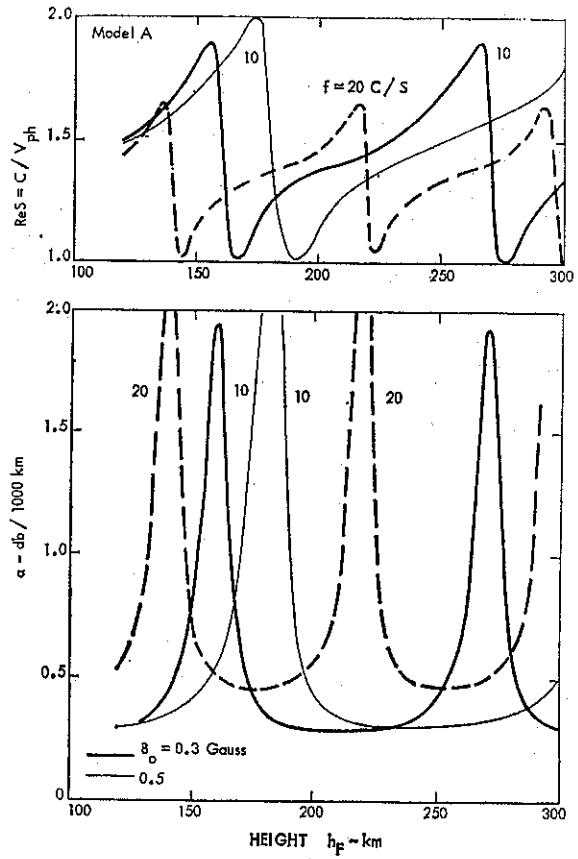

FIG. 7.9 Phase Velocity and Attenuation Rates for Ionosphere Model A with no Ions above 100 km. Effects of F-Layer Height

120 km. The profile D considered in conjunction with the electron density curve C represents lower densities than the profile B in the altitude range from 120 to $(h_F - \Delta h)$ km.

The F-layer may be considered simplest by introducing at the height h_F a semi-infinite layer of higher electron density $N_e = 10^5$ cm^{-3}, as indicated in the model A of Fig. 7.8. The effects of various boundary heights h_F are illustrated in Fig. 7.9, where larger heights approximate the conditions near local midnight and smaller values of h_F are representative of evening or early morning hours. The attenuation rates are decreased on average relative to the 0.55 and 0.85 db per 1000 km values shown in Fig. 7.7 for $B_0 = 0.3$ gauss and $f = 10$ and 20 c/s respectively. There are heights h_F of high absorption, where Re (S) is rapidly changing. In an electron plasma with a radial static magnetic field, the radial wave number k of the propagating magnetoionic mode can be computed from the approximation [Galejs, 1965a]

$$(k/k_0)^2 \approx \varepsilon_1 - i\varepsilon_2 \approx \omega_{pe}^2/(\omega\omega_{ce}), \tag{13}$$

where ω_{pe} and ω_{ce} are the plasma and cyclotron frequencies of electrons and k_0 is the wave number of free space. This wave number is in the first approximation independent of collision frequencies, and the radial wavelengths $\lambda_r = 2\pi/k$ can be calculated as 222, 157, and 286 km for the curves of $f = 10$ and 20 c/s with $B_0 = 0.3$ and $f = 10$ c/s with $B_0 = 0.5$ gauss respectively. It is apparent that the distance between the absorption peaks is approximately equal to $\lambda_r/2$ and that the lower peak is $\lambda_r/4$ above the altitude of 100 to 110 km. The absorption peaks are therefore associated with standing waves in the radial direction between D- and F-layers of the model ionosphere.

These standing waves cause an almost periodic variation in the effective surface impedance that is used in the calculation of the guided wave parameters. The normalized surface impedance Δ_e of the T.M. $n = 0$ mode exhibits $|\text{Im}\,\Delta_e| > \text{Re}\,\Delta_e$ for h_F below the resonance height. At the resonance height $|\text{Im}\,\Delta_e| \ll \text{Re}\,\Delta_e$; above the resonance height $\text{Re}\,\Delta_e$ is decreased in magnitude and $|\text{Im}\,\Delta_e|$ is increased. In the example of $f = 10$ c/s and $B_0 = 0.3$ gauss of Fig. 7.9, $\Delta_e = 0.011 - i0.018$, $0.026 - i0.0002$, $0.006 - i0.0005$, $0.0038 - i0.004$, and $0.027 - i0.003$ at $h_F = 150$, 160, 170, 180, and 260 km respectively. The propagation parameters can be computed from the formula

$$S = \sqrt{1 + \frac{i\Delta_e}{k_0 h}} \approx \sqrt{1 + i120\,\Delta_e} \quad \text{for} \quad f = 10 \text{ c/s} \quad \text{and} \quad h = 40 \text{ km}.$$

This equation gives $S = 1.88 + i0.38$, $1.46 + i1.07$, $1.03 + i0.35$, $1.23 + i0.187$, and $1.58 + i1.06$ for the h_F values of the earlier example. The S changes of Fig. 7.9 are therefore correlated with changes of the effective surface impedance.

The reflection coefficients ${}_{\parallel}R_{\parallel} \approx {}_{\perp}R_{\perp}$, which exceed 0.99 in magnitude for most of the h_F values shown in Fig. 7.9, are decreased to 0.96–0.97 near the absorption peaks. The reflection coefficients ${}_{\parallel}R_{\perp} = {}_{\perp}R_{\parallel}$ are correspondingly increased from 0.01 to approximately 0.05. Their changes appear to be less drastic than the corresponding changes of propagation parameters.

Calculations have been also made for a dipping geomagnetic field. The numerical results are nearly identical to those for a radial geomagnetic field provided that the radial magnetic field components are the same in both cases. This is not surprising because the direction dependence of propagation parameters nearly disappears for $f < 50$ c/s in Fig. 7.3.

The effects of frequency variations have been investigated for several fixed values of h_F. The minima of the various α curves are closely approximated by the attenuation rate of the nighttime isotropic ionosphere model of Fig. 7.7, but the Re (S) curves are discontinuous near the absorption peaks that occur under the same conditions as in Fig. 7.9. An introduction of ions for altitudes above 100 km decreases the range of Re (S) variations, shifts the absorption peaks, and raises the minima of the attenuation rate.

The ionospheric model A shows the standing-wave effects caused by F-layer reflections, but the geometry is too idealized to yield propagation data comparable to measurements. In the ionospheric model B of Fig. 7.8, the electron density assumes the value $N_e = N_t$ at an altitude of 105 km; and an intermediate electron density of $N_e = 2\times10^4$ precedes by $\Delta h = 40$ km the F-layer with $N_e = 2\times10^5$ at the altitude h_F. Electron densities $N_t = 2000$ to 6000 give roughly comparable propagation parameters in the left-hand side of Fig. 7.10, but $N_t = 1000$ cm^{-3} (and lower values) cause high absorption and also Re (S) changes that are radically different from those observed with the higher values of N_t. The effects of several h_F and B_0 values are

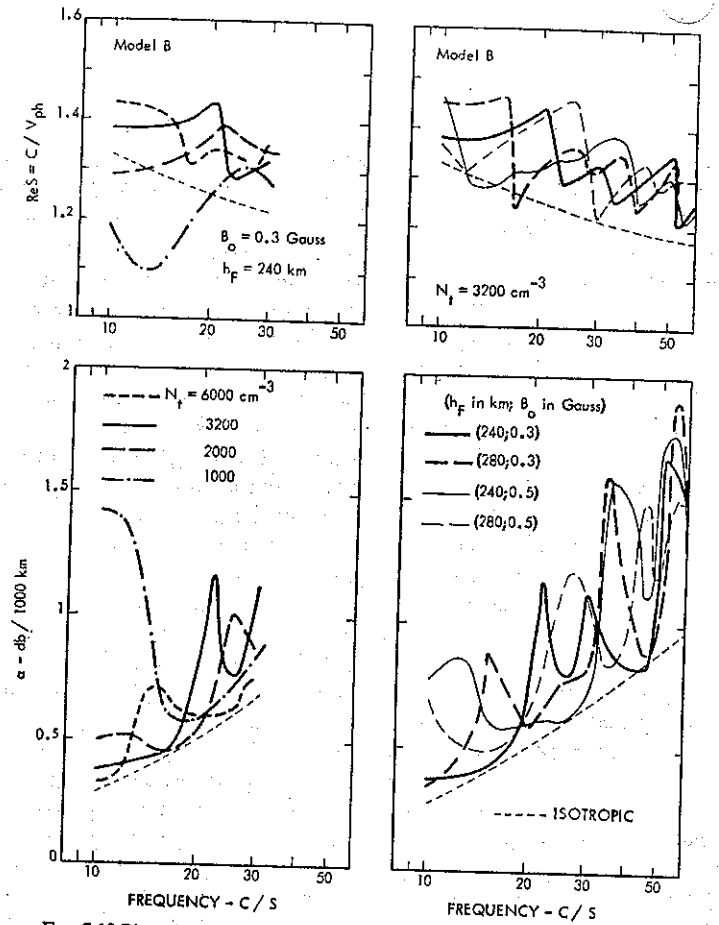

FIG. 7.10 Phase Velocity and Attenuation Rates for Ionosphere Model B

further illustrated in the right-hand side of Fig. 7.10. When increasing the frequency, Re (S) is decreased and Im (S) is increased on average. Most of the absorption peaks do not overlap, but the average of the α curves is larger than under isotropic conditions for frequencies exceeding 30 c/s.

The surface impedance changes will be illustrated for the 22 c/s absorption peak in the right-hand side of Fig. 7.10 for $h_F = 240$ km and $B_0 = 0.3$ gauss. The normalized surface impedance $\Delta_e = 0.0081 - i0.016$, $0.014 - i0.013$, and $0.0094 - i0.013$ for $f = 19$, 22, and 25 c/s respectively. The corresponding propagation parameters $S = 1.43 + i0.18$, $1.34 + i0.295$, and $1.29 + i0.174$. The reflection coefficients ${}_{\parallel}R_{\parallel}$ or ${}_{\perp}R_{\perp}$ are 0.977 at the absorption peak and are increased to 0.99 in magnitude at the other frequencies. The corresponding values of ${}_{\perp}R_{\parallel}$ or ${}_{\parallel}R_{\perp}$ are 0.025 and 0.01 respectively. These changes of Δ_e, S, or of the reflection coefficients

are less than for the ionosphere model A, where the standing-wave effects are more pronounced.

In the lower ionosphere, ions of greater mass can be produced by clustering and aerosols or attachment to dust and nuclei [Cole and Pierce, 1965]. An increase of the molecular weight from 29 to 60 for the ions of the lower ionosphere can be shown to modify the Re (S) and α curves only slightly. The Re (S) curve for the ionospheric model B remains between 1.4 and 1.2 for frequencies between 10 and 60 c/s, but the minima of the α curves are decreased from approximately 0.85 to 0.65 db per 1000 km for frequencies near 40 c/s.

The models C and CD of Fig. 7.8 include a residual E-layer of peak electron density 5000 cm^{-3} as an idealization of the electron-density profiles shown in the review of Maeda [1969] and the work of Wakai [1967]. Above the E-layer peak, the higher electron densities of model C approximate late evening or early morning hours. The lower electron density of model CD

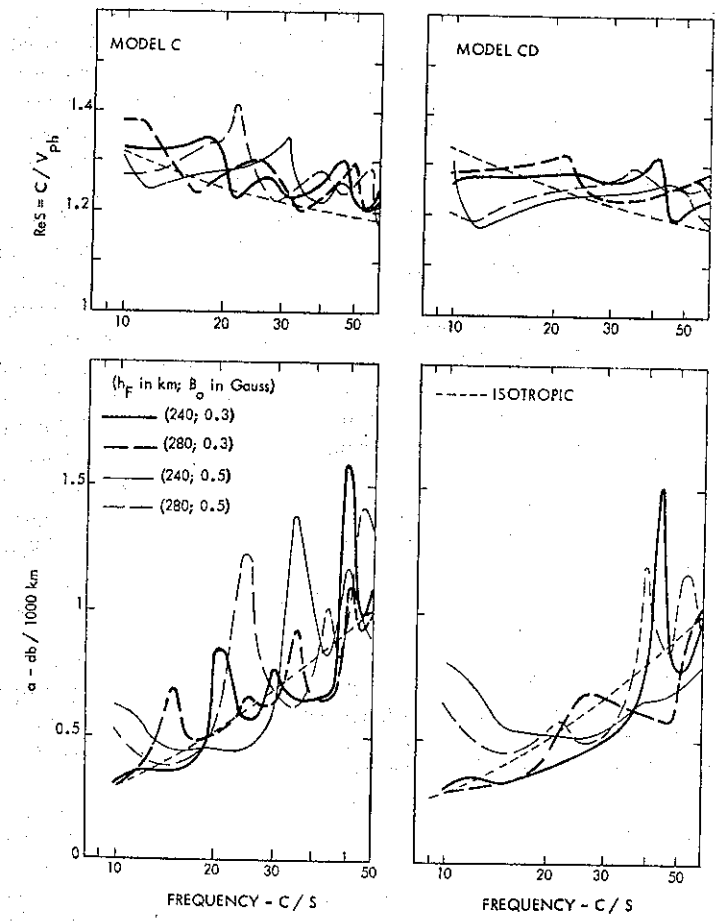

FIG. 7.11 Phase Velocity and Attenuation Rates for Ionosphere Models C and CD

is more representative of conditions near midnight. The calculated propagation parameters of Fig. 7.11 illustrate the effects of varying h_F and B_0. The average of the calculated curves tends to approximate the propagation parameters of the isotropic ionosphere model more closely than the calculations shown in the earlier figures.

It can be shown that the propagation parameters S computed as the average of the four curves for the model CD near $f = 10$ c/s is the same as the propagation parameter S computed for an average of the four corresponding surface impedances Δ_e. The surface impedances Δ_e may change drastically along a propagation path of changing ionosphere parameters. The formula of S calculations is based on a uniform wave guide, and v_{ph} and α cannot be expected to undergo sudden changes with changing boundary properties. Although the averaging of surface impedances Δ_e may seem to be more appropriate, either an average value of S or an average of Δ_e with a corresponding single S value can be used for computing long-distance propagation parameters.

The above calculations illustrate only a few of the many possible ionospheric models. Other results, not shown in the figures, indicate that ionospheric models similar to B of Fig. 7.8, but with increased values of Δh are more representative of magnetically perturbed conditions and show average α values that are of the order of 0.8 db per 1000 km for frequencies between 10 and 30 c/s. A gradual increase of N_e from 1000 at $h = 100$ to approximately 6000 cm^{-3} at $h = 200$ km can be viewed as a modification of the profile B, but the resulting Re (S) curves exhibit larger variations of Re (S) and even higher absorption for frequencies above 30 c/s than indicated in Fig. 7.10. Resonance peaks are also found in ionosphere models which are similar to B of Fig. 7.8, but exhibit a smooth transition from N_t to N_e of the F-layer. The finite thickness of the F-layer has been investigated by assuming a constant electron density for a few hundred km above h_F, with N_e reverting to a lower value at larger altitudes. This introduces a fine structure in the resonance curves near frequencies where the layer thickness becomes an integer multiple of $\lambda_r/2$ (λ_r is the radial wave number of the propagating mode in the F-layer); but this does not alter the basic frequency dependence of the Re (S) curves.

The propagation parameters of the daytime model of the lower ionosphere with a radial geomagnetic field and of the isotropic nighttime ionosphere of Fig. 7.7 are indicated by the dashed lines in Fig. 7.12. The isotropic nighttime model was shown in Fig. 7.11 to approximate an average of propagation parameters derived for more elaborate models which consider ionospheric anisotropy and reflections from the F-layer. In the frequency range of Schumann resonances, the average of propagation parameters of the theoretical curves approximates the data of Chapman *et al.* [1966]; Taylor [1969] does not consider his transpacific measurements accurate for frequencies less than 40 c/s, and for higher frequencies there is a reasonable agreement between the theoretical curves and the data of Taylor [1969], the 400 c/s California to New York measurements of Dunn *et al.* [1964], and the atmospherics measurements of Chapman *et al.* [1966]. The measurements of Jean *et al.* [1961] made on a mixed daytime and nighttime path are intermediate between the daytime and nighttime measurements shown in Fig. 7.12. The estimated propagation parameters of Jones [1967], who does not distinguish between daytime and nighttime conditions, are intermediate between those of the present anisotropic daytime and isotropic nighttime models shown in Fig. 7.12. The propagation parameters are affected by the selection of ion models of the lower ionosphere. An increase of ion density and/or a decrease of the ion-neutral collision frequency ν_{in} may lead to daytime and nighttime models

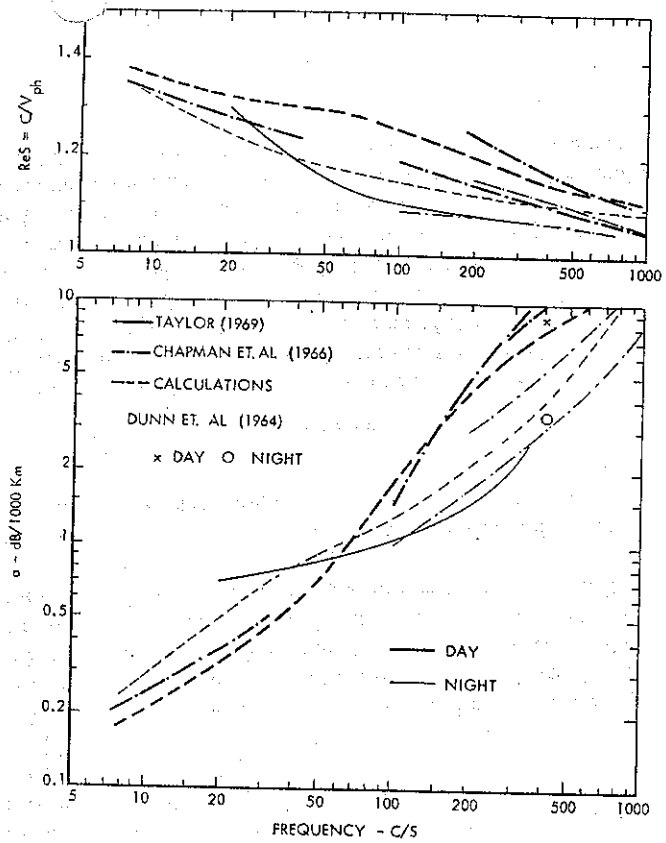

FIG. 7.12 Measured and Calculated E.L.F. Propagation Parameters

which exhibit $\alpha \approx 1$ db per 1000 km for $f = 30$ c/s [Field, 1969]. If adopted for the analysis of global propagation phenomena, such ionosphere models would produce a rather high damping of Schumann resonances.

7.3.6 *Models of a Perturbed Ionosphere*

A number of perturbed electron-density profiles have been shown in Fig. 2.3 (p. 23). Calculations [Galejs and Mentzoni, 1968] indicate higher attenuation rates for frequencies below 100 c/s for profiles which exhibit higher electron concentrations in the height range between 50 to 55 km; this emphasizes the sensitivity of E.L.F. propagation parameters to ionosphere characteristics at relatively low altitudes.

E.L.F. propagation parameters are also calculated for the idealized electron- and ion-density profiles of Fig. 2.5 (p. 25), where the profile 0 approximates the unperturbed daytime

conditions; profiles 1 and 2 could arise during polar cap absorption events while profile 3 is more representative of nuclear perturbations. The effects of various choices of ion collision frequencies ν_{in} and molecular weights are also illustrated. The relevant formulas for ν_{in} are summarized in Section 2.2.2. The measurement data shown in figs. 8.18 and 8.20 of Valley [1965] show that for moderate northern latitudes and for the altitude range of 20–28 km, the small ion concentration is near 2500 cm^{-3} and the atmospheric conductivity σ is 2 to 5×10^{-12} mho/m with variations up to ± 40 percent. Calculations for the unperturbed particle density (profile 0) based on M.W. = 29 and $\nu_{in} = \nu_{nn}$ show that $\sigma = 7$ to 20.5×10^{-12}; for M.W. = 60 and $\nu_{in} = 2\nu_{nn}$, $\sigma = 1.75$ to 5.1×10^{-12} mho/m. This comparison tends to justify the use of larger molecular weights M.W. and of collision frequencies ν_{in}, which are larger than ν_{nn}.

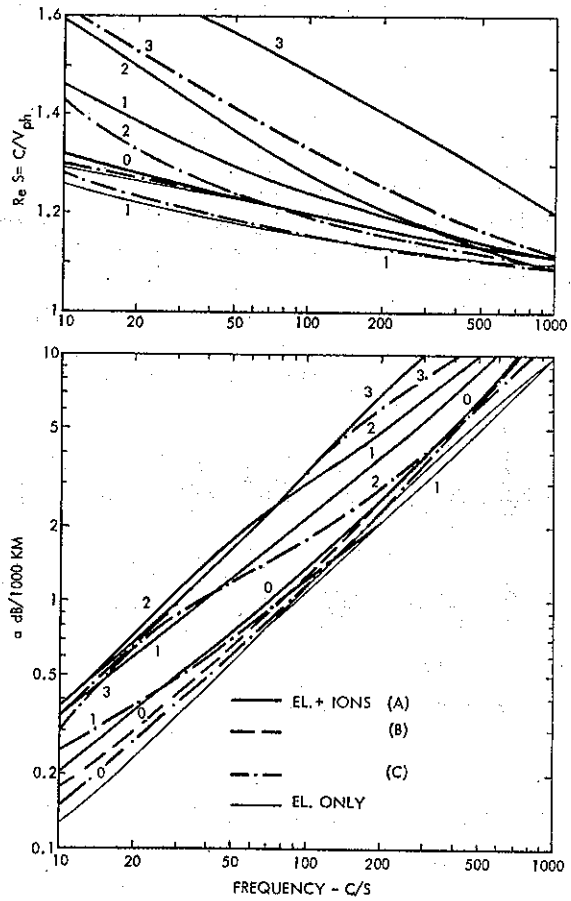

FIG. 7.13 Phase Velocity and Attenuation Rates of E.L.F. Waves
(A) M.W. = 29, $\nu_{in} = \nu_{nn}$; (B) M.W. = 60, $\nu_{in} = \nu_{nn}$;
(C) M.W. = 60, $\nu_{in} = 2\nu_{nn}$

Ions of larger molecular weights have been also established by mass spectrometric measurements [Narcisi and Bailey, 1965].

The calculated propagation parameters are shown in Fig. 7.13. For profiles 0 and 1 the phase velocity is practically unaffected by the presence of ions; but there is some increase in the attenuation rate α. For profiles 2 and 3, the presence of ions increases Re (S) (or decreases v_{ph}) and α; in the absence of ions (not shown in Fig. 7.13), profiles 2 and 3 give Re (S) and α figures comparable to those of the electron profiles 1 and 2. For a frequency $f = 100$ c/s and the ion profile 2, a decrease of the molecular weight and the collision frequency from M.W. = 60 and $\nu_{in}/\nu_{nn} = 2$ to M.W. = 29 and $\nu_{in}/\nu_{nn} = 1$ increases Re (S) by 8 percent and increases the attenuation rate by 66 percent. The choice of M.W. and ν_{in} figures is critical in the E.L.F. range.

7.4 Schumann Resonances

Based on theoretical considerations, Schumann [1952a, b, 1957] postulated resonances of the earth-to-ionosphere cavity. Koenig [1958, 1959, 1961] obtained the first experimental indication of Schumann resonances by observing noise waveforms in the output of a narrow band amplifier. Detailed frequency spectra of this noise were first obtained by Balser and Wagner [1960]. Other measurements have been reported by Fournier [1960], Benoit and Houri [1961, 1962], Lokken *et al.* [1961, 1962], Polk and Fitchen [1962], Balser and Wagner [1962a, b, 1963], Rycroft [1963], Gendrin and Stefant [1964], Chapman and Jones [1964], Hughes [1964], Ogawa *et al.* [1966a], Nelson [1967], and Larsen and Egeland [1968]. Some of this work has been reviewed by Gendrin [1967a].

The fundamental theory of Schumann resonances [Schumann, 1952a, b, 1957] is discussed in a book by Wait [1962]. Summaries of other theoretical work which account for observed characteristics like the resonance frequency, Q-factors, and shape of the noise spectra and diurnal variations of the received power, have been presented by Galejs [1965b]. Madden and Thompson [1965] and also Nelson [1967] show that the interference of adjacent resonance modes gives rise to diurnal changes of the dominant frequency. Bliokh *et al.* [1968] have indicated that the eccentricity of the geomagnetic dipole field may also contribute to frequency changes.

After reviewing some of the experimental data, the largest part of this section will be devoted to the theory explaining such observations.

7.4.1 *Observed Waveforms and Frequency Estimates*

In wide-band recordings of atmospheric signals, an E.L.F. component or slow tail follows the initial V.L.F. component of the transient [Hepburn and Pierce, 1953; Liebermann, 1956a, b; Tepley, 1959; Pierce, 1960]. An oscillatory structure of the signal becomes noticeable by passing it through a band-pass filter. An example of a noise recording in the output of a 2–30 c/s band-pass filter [Lokken, 1964] is shown in Fig. 7.14. The two horizontal magnetic field components have been observed simultaneously in Canada and in Antarctica. There is a correlation between the high-intensity E.L.F. noise bursts observed at the various sites. A Sonagraph recording of one of the waveforms is shown in Fig. 7.15. The darkened areas indicate resonance frequencies around 8, 14, and 20 c/s. Noise waveforms in the 5–20 c/s band have been reported

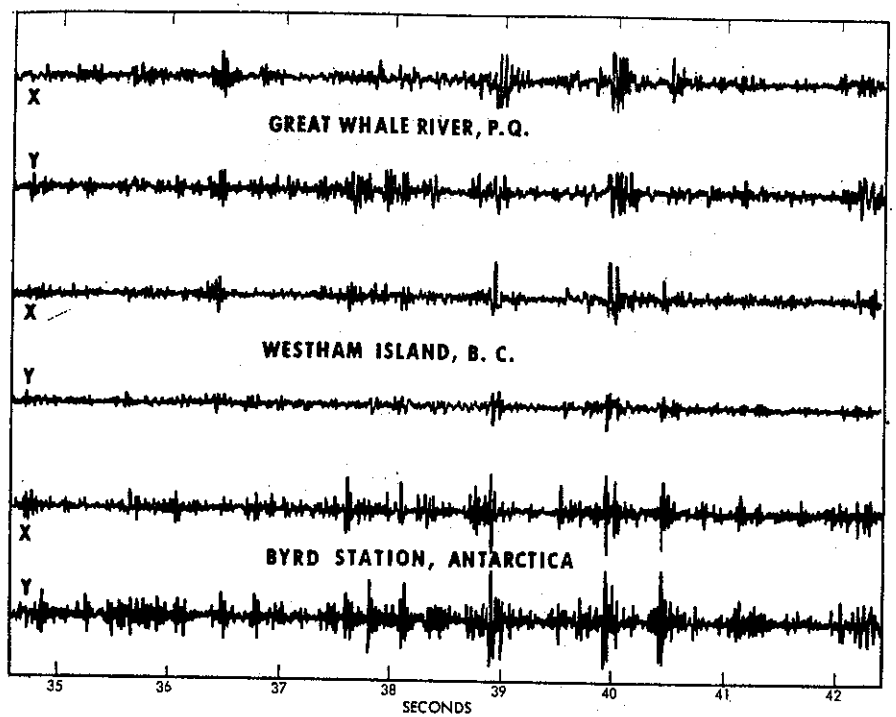

FIG. 7.14 Noise Recording in the 2 to 30 c/s Band

by Polk and Fitchen [1962] and Polk [1964]. Figure 7.16 shows sample recordings of the outputs of two coils the axes of which are oriented in the north–south (N.S.) and east–west (E.W.) directions. Frequency of these waveforms has been estimated by counting the cycles between the second markers shown on the records. The average frequency computed in this procedure should be higher than the resonance frequencies of a spectral analysis.

This can be established by computing the average frequency of a noise waveform based on the mean time interval between the crossings of its zero axis. This average frequency is given by Rice [1944, 1945] as

$$\bar{f} = \left[\frac{\int_0^\infty g(f) f^2 \, df}{\int_0^\infty g(f) \, df} \right]^{1/2} \tag{14}$$

where $g(f)$ is the power spectrum of the noise waveform. Noise of spectrum similar to that recorded by Balser and Wagner [1960, 1962a] is assumed to be passed through idealized filters with bandwidths of 5–12 and 5–20 c/s. For these two bandwidths, the average frequency is calculated from (14) as $\bar{f} = 8.7$ and 12.9 respectively. This average frequency $\bar{f}$ depends on the

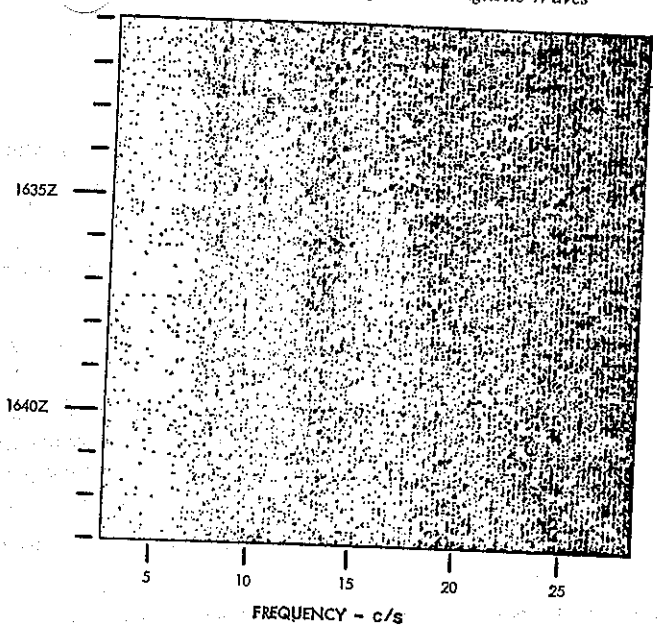

FIG. 7.15 Sonagraph Recording of the Noise Waveform X of Westham Island, B.C.

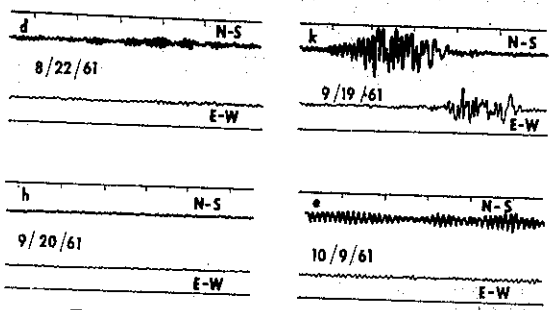

FIG. 7.16 Noise Recording in the 5 to 20 c/s Band

bandwidth of the waveform and is generally higher than the frequency of the first two spectral peaks.

The power spectra of the received signal are obtained after a frequency analysis of wide-band waveforms that are similar to the ones shown in Figs. 7.14 or 7.16. The power spectrum computations by Larsen and Egeland [1968] from 30 sec of data show clearly the various resonance frequencies in Fig. 7.17a. Further recordings of the fundamental resonance computed from 2 min of data are shown in Fig. 17b and c. The spectra are frequently skew about the center frequency and undergo variations of up to 1 c/s in peak frequency in periods of the order of a minute. A split of the peak frequency into three distinct separate peaks is observed very

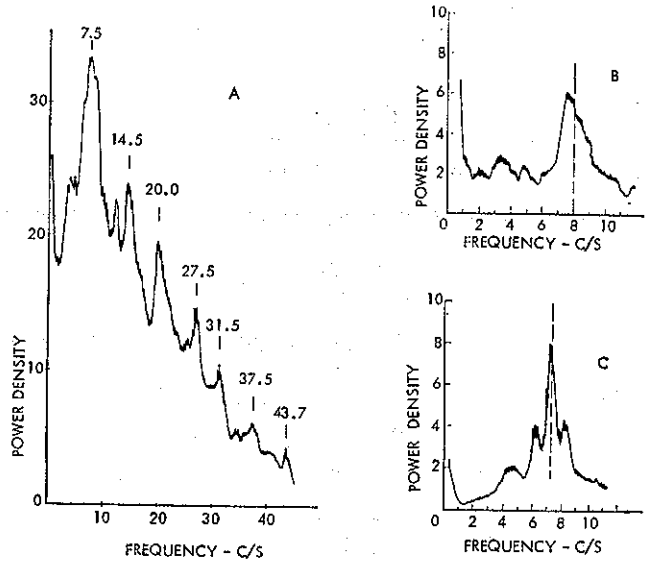

FIG. 7.17 Short-period Spectrum Measurements

seldom. The fine structure of resonance curves has been observed also by Hughes [1964] and Rycroft [1965]. Short time-frequency spectra are extremely jagged, but there is no regular splitting of the mode n into $m = 2n+1$ sublevels. Rycroft [1965] concludes that the fine structure is spurious and is brought about by statistical fluctuations due to the finite length of the sample.

Most of the E.L.F. energy is of terrestrial origin and is caused by thunderstorm activity although there are some high latitude events of an apparent extraterrestrial origin. Such emissions of approximately 650 c/s have been detected near Kiruna, Sweden, by Egeland [1964]. Similar observations have been made by Béghin [1967] in Iceland using rocket-borne and ground-based receivers. These signals of the auroral chorus propagate quasi-longitudinally through the ionosphere with a minimum attenuation near 700 c/s. Gendrin and Stephant [1964, private communication] have recorded emissions in the 14–17 c/s frequency band on Kerguelen Island in the southern part of the Indian Ocean. The Spectran recording of the signals received at Kerguelen is shown in Fig. 7.18. The upper trace shows a normal signal with resonances near 8, 14, 20, and 25 c/s. There is an additional signal of 14–17 c/s on the two lower traces. Similar E.L.F. noise bursts of 14–18 c/s have been observed by Ogawa *et al.* [1966b] during solar flares at midlatitudes. Morozumi [1965] and Gendrin [1967b] show a simultaneity of increased riometer absorption, noise near 1 kc/s, E.L.F. signals in the 2–30 c/s band, and of micro-pulsations between 0.001 and 5.0 c/s during auroral zone geophysical disturbances.

Further measurement data appear in Figs. 7.19–7.22, 7.24, 7.30, and 7.31; and they will be discussed in conjunction with the appropriate theoretical models.

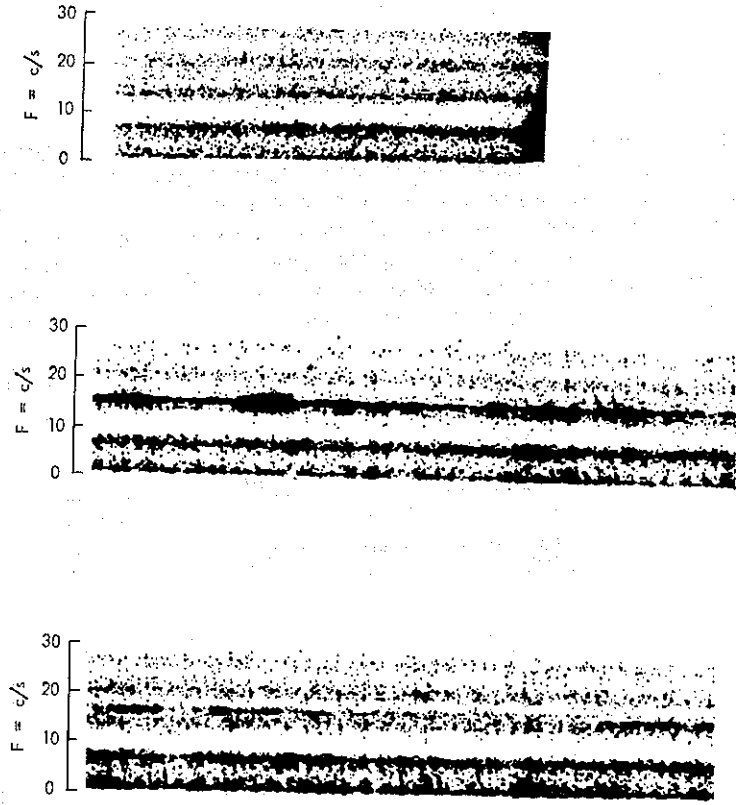

FIG. 7.18 Spectran Recordings of Noise Waveforms at Kerguelen Island

7.4.2 *Resonance Frequencies and Quality Factors*

Resonance frequencies and Q-factors of the earth-to-ionosphere cavity may be calculated from the field representations summarized in Section 7.2.

The fields will exhibit their maximum values at the resonance frequencies of the individual modes; E_r of (1) or H_φ of (8) will exhibit maxima near

$$|n(n+1)-\nu(\nu+1)| = \min. \tag{15}$$

Applying (2), this implies

$$n(n+1) \approx (k_0 a S)^2, \tag{16}$$

and the resonance frequency f_n is computed as

$$f_n \approx \frac{7.5\sqrt{n(n+1)}}{\operatorname{Re} S}. \tag{17}$$

Typical values of Re S are 1.4–1.2 for frequencies in the resonance region. The same maxima

occur near $|\sin \nu\pi| = \min$ in (3). Applying (4), this condition is equivalent to

$$n = \operatorname{Re} \nu \approx -0.5+[0.25+(k_0 a \operatorname{Re} S)^2]^{0.5}, \tag{18}$$

where n is an integer. Equation (18) can be readily rearranged into the form (17). The resonance conditions (15) to (18) are only approximate ones. In the representation (1), (5), or (8), there will be slight shifts of maxima due to the finite slopes of the adjacent $(n+1)$ and $(n-1)$ modes. In the representation (3), other terms of the equation are also frequency dependent.

The cavity Q may be determined as a ratio between the stored energy and energy loss per cycle or simply by the width of the resonance curves. The basic definition of the Q-factor of a cavity with lossy walls is

$$\frac{1}{Q} = \frac{\iint \mathbf{E}\times\mathbf{H}^*\cdot ds}{\frac{\omega\varepsilon_0}{2}\iiint \mathbf{E}\cdot\mathbf{E}^*\, dv+\frac{\omega\mu_0}{2}\iiint \mathbf{H}\cdot\mathbf{H}^*\, dv}, \tag{19}$$

where the surface integral is extended over the cavity walls and the volume integral covers the inside of the cavity. The ground surface is assumed to be a perfect conductor, and E_θ is related to H_φ at the ionospheric boundary by the surface impedance Z_e as $E_\theta = Z_e H_\varphi$. However, E_θ is assumed to be small relative to E_r for vertically polarized waves. Equation (19) is rewritten as

$$\frac{1}{Q} = \frac{2\iiint \operatorname{Re} Z_e\,|H_\varphi|^2 (a+h)^2 \sin\theta\, d\theta\, d\varphi}{\omega\iiint [\varepsilon_0|E_r|^2+\mu_0|H_\varphi|^2] r^2\, dr \sin\theta\, d\theta\, d\varphi}, \tag{20}$$

$$\approx \frac{2\operatorname{Re} Z_e}{\omega h}\,\frac{\int |H_\varphi|^2 \sin\theta\, d\theta}{\int [\varepsilon_0|E_r|^2+\mu_0|H_\varphi|^2]\sin\theta\, d\theta}. \tag{21}$$

Substituting the leading terms of (1) and (8) and evaluating the integrals gives

$$\frac{1}{Q} = \frac{2\operatorname{Re}\Delta_e}{k_0 h\left[\frac{n(n+1)}{(k_0 a)^2}+1\right]}, \tag{22}$$

where $k_0 = \omega\sqrt{\mu_0\varepsilon_0}$. From (2) it can be seen that

$$2\operatorname{Re} S \operatorname{Im} S = \frac{\operatorname{Re}\Delta_e}{k_0 h}. \tag{23}$$

Applying (23) and the resonance condition (16), (22) simplifies to

$$\frac{1}{Q} = \frac{4\operatorname{Re} S \operatorname{Im} S}{(\operatorname{Re} S)^2+1}. \tag{24}$$

For different characteristics of the day and night hemispheres, it can be shown that

$$\frac{1}{Q} \approx \frac{2\left[\operatorname{Re} S \operatorname{Im} S\big|_{\text{day}}+\operatorname{Re} S \operatorname{Im} S\big|_{\text{night}}\right]}{\left(\operatorname{Re} S\big|_{\text{avg}}\right)^2+1}. \tag{25}$$

When considering only the magnetically stored energy, the E integral at (21) is neglected and the value of the H integral is doubled. The resulting quality factor is given by

$$Q_h = \frac{1}{2 \operatorname{Re} S \operatorname{Im} S}. \tag{26}$$

For a given set of propagation parameters, this will give a lower Q figure than (24). Considering only the electrically stored energy, the H integral of (21) is neglected and the value of the E integral is doubled. This gives

$$Q_e = \frac{\operatorname{Re} S}{2 \operatorname{Im} S}. \tag{27}$$

The last expression can also be derived from the concept of complex resonance frequencies [Wait, 1964; Madden and Thompson, 1965] or by considering the half-power bandwidth of the resonance curve. All three Q definitions yield the same results as Re S approaches unity, but they will differ near the lower resonance frequency of the earth ionosphere cavity.

TABLE 7.1. RESONANCE FREQUENCIES OF THE SPHERICAL SHELL BETWEEN THE EARTH AND IONOSPHERE

	n	1	2	3	4
Resonance frequency f_n in c/s	Lossless cavity	10.6	18.3	25.9	33.5
	Exponential isotropic daytime model of Fig. 7.2	7.6	13.5	19.4	25.4
	Day and nighttime models of Fig. 7.12	7.8	14.0	20.2	26.4
	Measurements	8.0	14.1	20.3	26.4

TABLE 7.2. Q-FACTORS OF EARTH-IONOSPHERE CAVITY RESONANCES

	f in c/s	10	30	100
$Q(Q_e)$ factors	Exponential isotropic daytime model of Fig. 7.2	6.5(8.5)	5.4(6.8)	5.2(6.4)
	Daytime and nighttime model of Fig. 7.12	3.8(4.9)	5.1(6.3)	6.1(7.3)
	Measurements	4.0	6.0	

The resonance frequencies (17) and Q-factors of (25) and (27) are listed in Tables 7.1 and 7.2 for the isotropic exponential daytime ionosphere model of Fig. 7.2 and for the daytime and nighttime models of Fig. 7.12, where the average of day and nighttime parameters are used in (17) and (27). It is also permissible to average the $(1/Q_e)$ figures computed under daytime and nighttime conditions, but *not* the respective Q_e values. Also indicated are resonance frequencies of a lossless cavity (Re $S = 1$) and the measurement averages of Balser and Wagner [1960],

which do not reflect diurnal variations. Comparable resonance frequencies (with deviations up to 0.2 c/s) have been observed by many other authors, and Larsén and Egeland [1968] have obtained $Q = 4.1 \pm 0.2$ for the $n = 1$ mode based on a study of over a hundred different spectra. The calculations made for the combined daytime and nighttime models are particularly close to the measured values.

Experimentally determined Q values that are estimated from the half-power bandwidths of the resonance curves neglect the effects of adjacent resonances and of near-field noise that will tend to add to the background level. Hence, the half-power level is estimated too low, the apparent half-power bandwidth is larger, and the estimated Q factor may be too low. This observation is also borne out in the subsequent Figs. 7.19 and 7.20, where a reasonable agreement with experimental spectra is obtained using theoretical models with Q figures that are higher than the usually accepted experimental values indicated in Table 7.2.

7.4.3 *Noise Spectra*

The power spectrum received by a vertical stub antenna that is due to a distribution of vertical electric dipoles is computed starting with (3). It follows [Galejs, 1961a] that

$$G(i\omega) = \int_0^{2\pi} \int_0^{\pi} g(i\omega, \theta, \varphi)\, a^2 \sin\theta \cdot \left| \frac{\nu(\nu+1)}{4k_0 h a^2} \frac{P_\nu(-\cos\theta)}{\sin \nu\pi} \right|^2 d\theta\, d\varphi, \tag{28}$$

where $g(i\omega, \theta, \varphi)$ is proportional to the squared dipole moment of the sources per unit area. Assuming that

$$g(i\omega, \theta, \varphi) = g(i\omega) \sim \exp(-0.0091\omega) \tag{29}$$

for $\theta_1 < \theta < \theta_2$ and is equal to zero elsewhere, equation (28) may be evaluated with the aid of 3.12.3 of Erdélyi [1953]. The integral of (28) may also be evaluated after replacing the Legendre functions by their asymptotic expansions. Applying (44) of Chapter 4 gives

$$\left.\begin{aligned} G(i\omega) = {} & \frac{g(i\omega)\,|\nu(\nu+1)|^2}{8(ak_0h)^2\,|\nu+\frac{1}{2}|\,[\cosh(2\pi \operatorname{Im}\nu) - \cos(2\pi \operatorname{Re}\nu)]} \\ & \left\{ \frac{\sinh[2 \operatorname{Im}\nu(\pi-\theta)]}{\operatorname{Im}\nu} + \frac{\sin[(2 \operatorname{Re}\nu+1)(\pi-\theta) - (\pi/2)]}{\operatorname{Re}\nu+\frac{1}{2}} \right\}_{\theta_2}^{\theta_1}, \end{aligned}\right\} \tag{30}$$

where the parameter ν is defined by (4).

Power spectra have been calculated from (30) by assuming that Re (S) represents the average of daytime and nighttime parameters of Fig. 7.2, but Im (S) is changing from 0.095 to 0.066 and Q_e is changing from 6.8 to 9.4 in the frequency range between 10 and 30 c/s. The calculations made for two intervals of the angle θ in Figs. 7.19 and 7.20 compare with several measurements.

Spectra can be also obtained for highly localized sources, like unusually large atmospherics. For signals originating from a distance $D = 10000$ km ($\theta = 90°$), equations (5) and (8) show that $E_r = 0$ for odd values of n and $H_\varphi = 0$ for even values, which can be seen from Fig. 7.1 for the two lowest modes. This is borne out in the measurements and calculations of Jones and

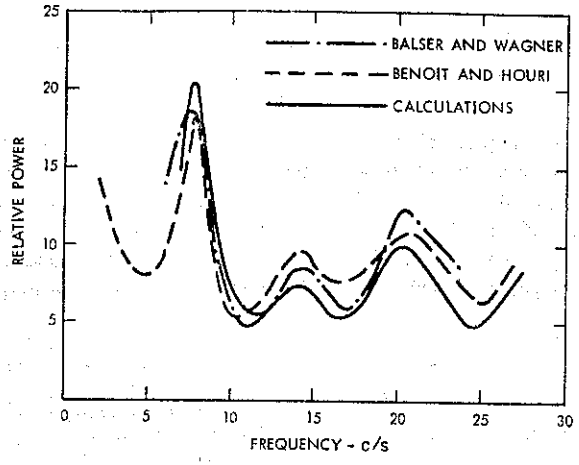

FIG. 7.19 Noise Spectrum for $38° \leqslant \theta \leqslant 72°$

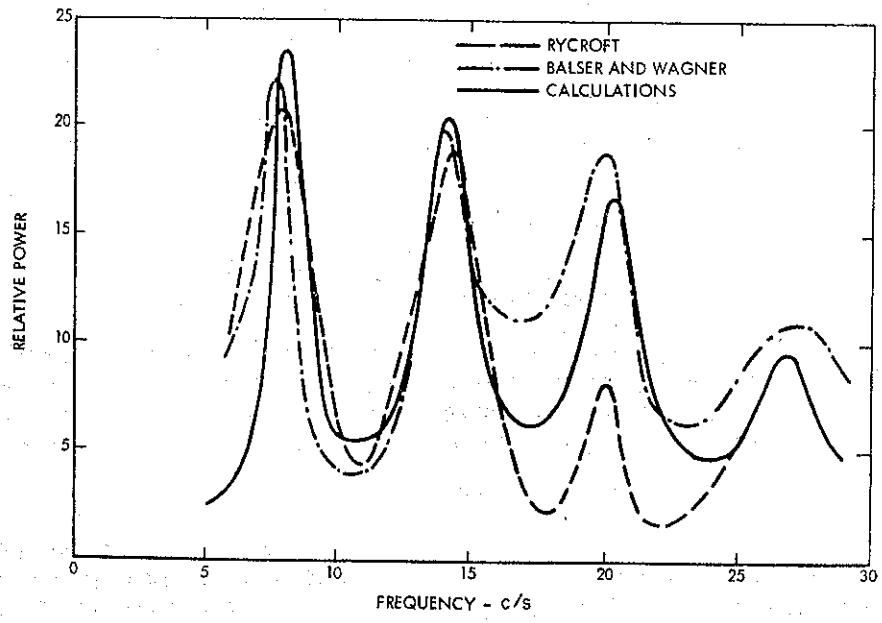

FIG. 7.20 Noise Spectrum for $47° \leqslant \theta \leqslant 128°$

Kemp [1969] that are based on estimated values of ν for $D = 10500$ km and on source dipole moments Ids that decrease by a factor of 3 in magnitude as frequency is increased from 0 to 50 c/s. The data shown in Fig. 7.21 indicate a close agreement between measurements and calculations, the absence of odd resonances for E_r at $f \approx 8, 20, 32$ c/s and the absence of even resonances for H_φ at $f \approx 14, 26, 38$ c/s.

The above spectra show a gradual decrease with frequency, which can be attributed to the form of $g(i\omega)$ in (29) used for Figs. 7.19 and 7.20 or to the decrease of the dipole moment assumed in the calculations of Fig. 7.21. The frequency spectra computed by Large and Wait

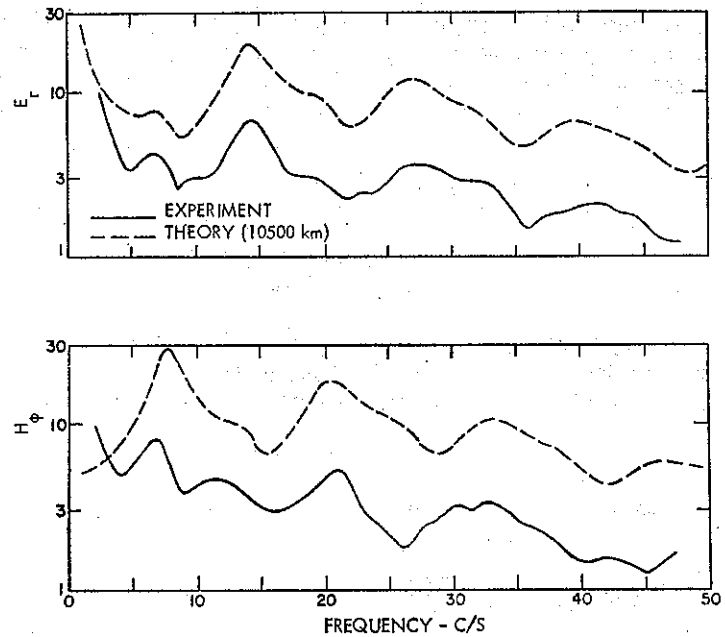

FIG. 7.21 Spectra of Large E.L.F. Atmospherics

[1968] increase linearly with frequency in a geometry which is excited by a small magnetic ring current. A magnetic current K flowing around an area da produces the same fields as an electric dipole of moment $Ids = \pm i\omega\varepsilon_0 Kda$, which increases linearly with frequency ω and accounts for the increase in spectral amplitudes. Their nighttime and composite spectra are excessively damped; the high nighttime attenuation rates are manifested in the nighttime quality factors $Q = 1.2$ to 1.4 of the fundamental resonance that are much lower than in the present calculations.

Balser and Wagner [1962a] have recorded diurnal variations of measured noise spectra. Their measurements of the diurnal variations of the power level at the first three resonance frequencies are shown in Fig. 7.22 together with similar measurements by Gendrin and Stefant [1964]. Diurnal variations of the fields near the two lower resonance frequencies have been

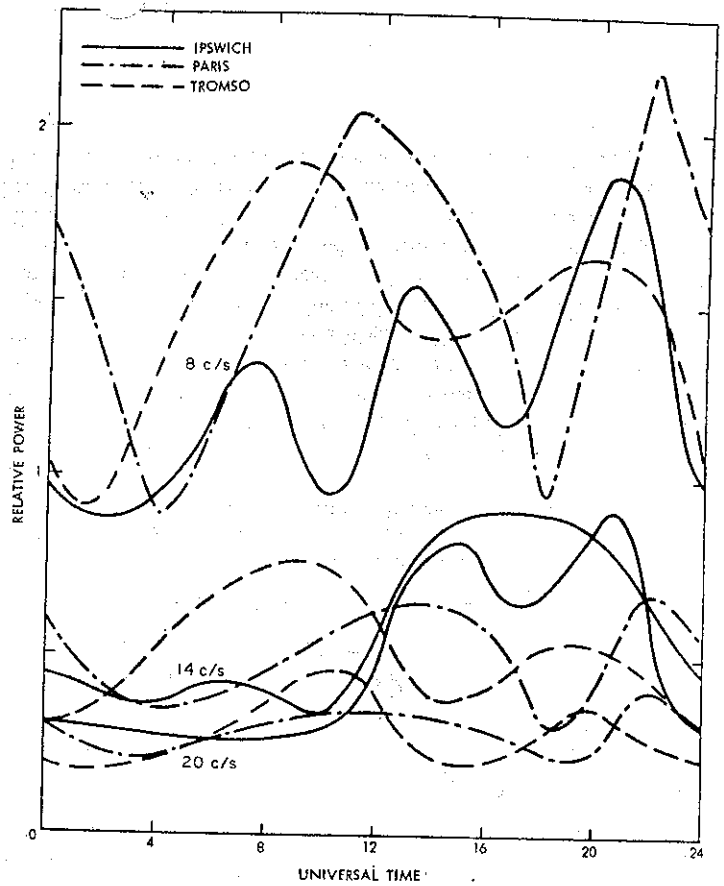

FIG. 7.22 Diurnal Variation of the Resonance Modes at Ipswich, Massachusetts, February 1961 (Vertical Electric Field), Chambon-la-Forêt (Near Paris), July 1962, and at Tromso (Norway), April 1962 (Horizontal Magnetic Field)

measured at Kingston, Rhode Island, by Polk *et al.* [1963]. The maximum signal intensity occurs between 1500 and 1800 U.T. In an amplitude versus time plot, the signal peak is broader during summer than winter. Seasonal and diurnal variations of the noise power in the E.L.F. frequency band below 35 c/s have been described by Wright [1964] without singling out the individual resonance modes. The measurements are made at Byrd Station, Antarctica (80° S, 120° W), and show peak intensities near 1000 U.T. during spring and summer and near 2300 U.T. during most of the year.

The gross features of the spectrum, such as the number of peaks and their approximate time of occurrence, may be explained qualitatively by noting areas of globe with particularly high

thunderstorm activity and by measuring the polar angle θ from these source regions to the observation point. The vertical electric field E_r and the horizontal magnetic field H_φ of the mode n exhibit the θ dependence of

$$E_r \sim P_n(\cos\theta) \tag{31}$$

$$H_\varphi \sim \frac{d}{d\theta} P_n(\cos\theta), \tag{32}$$

where $P_n(\cos\theta)$ is a Legendre polynomial of the order n. A particular geographical region will contribute to the measured values of E_r or H_φ in the mode n if the right-hand sides of (31) or (32) are sizable for those values of θ. Such considerations have been reported by Balser and Wagner [1962a] and Gendrin and Stefant [1964].

More detailed calculations have been carried out by Abraham [1965] and Galejs [1964], who used available estimates of geographical distributions of the noise sources and who calculated the day and night propagation effects after expressing the fields as a sum of recirculating azimuthal waves.

In the expression for the electric field component E_r of (3), the Legendre function is replaced by the leading term of its asymptotic expansion. The function $\sin \nu\pi$ is expanded into

$$(\sin \nu\pi)^{-1} = -2i \sum_{n=0}^{\infty} \exp\left[i(2n+1)\nu\pi\right] \tag{33}$$

which is valid for $\operatorname{Im} \nu > o$. This results in

$$\left.\begin{aligned} E_r = \frac{I\,ds}{2\omega\varepsilon h a^2} \frac{\nu(\nu+1)}{\sqrt{2\pi\left(\nu+\frac{1}{2}\right)\sin\theta}} \exp\left[i\left(\frac{3\pi}{4}\right)\right] \sum_{n=0}^{\infty} \exp\left[i\left(\nu+\frac{1}{2}\right)(\theta+2n\pi) - i2n\frac{\pi}{2}\right] \\ + \exp\left\{i\left(\nu+\frac{1}{2}\right)[2\pi(n+1)-\theta] - i(2n+1)\frac{\pi}{2}\right\}. \end{aligned}\right\} \tag{34}$$

The first term of the summation represents a wave which has traveled the direct distance from the source to the observation point (θ) plus n full circles around the sphere ($2n\pi$), while experiencing a phase shift of $(-\pi/2)$ radians at each traversal of the source point or its antipode. The other term of the summation represents a wave which has traveled toward the observation point across the antipode of the source ($2\pi - \theta$) and has made furthermore n circles around the sphere ($2n\pi$) and has also experienced a phase shift of $(-\pi/2)$ radians at each traversal of the source point or its antipode. This physical interpretation of (34), which is equivalent to (3) for $\nu = \text{const}$, permits a heuristic consideration of the ν differences between the day and night hemispheres. The multiplicative ν factors in front of the n summation are assumed to be constant and equal to $\bar{\nu}$, which is intermediate between the day and night ν values. The θ factors of the exponentials are replaced by integrals in order to account for the ν variation seen by the circular wave front as it propagates in the θ direction with respect to the source. The amplitude changes at the day and night boundary can be also considered for each traveling wave by assuming that the energy of the wave remains constant after passing the day and night boundary. This results in decreased amplitudes for the larger ionospheric height of the night hemisphere. In the numerical work the surface of the earth was subdivided into 10° cells. Each cell had a constant surface density of noise sources, but a variation was allowed from cell to cell. The plots

of thunderstorm days T_m over the world were used to set relative values of lightning activity for each of the cells by assuming that the thunderstorm day plots were directly proportional to the distribution of squared dipole moment per unit area according to the *Handbook of Geophysics* [1960]. The diurnal variations were accounted for by a multiplicative factor in terms of local time at the source [Williams, 1959]. The final equation used in the spectrum calculations is similar to (30) although it is algebraically more involved.

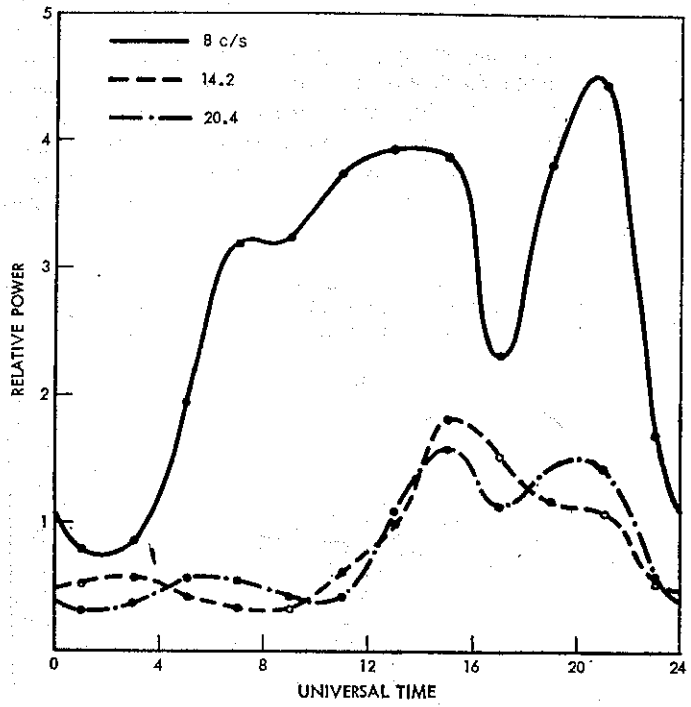

FIG. 7.23 Calculated Diurnal Variation of Noise Power at the Peak of the Resonance Modes – Wintertime – Boston, Massachusetts

The diurnal variations of the noise power at the first three Schumann resonances have been computed using the exponential ionosphere model of Fig. 7.2 and are shown in Fig. 7.23. The calculations have disregarded the noise sources near the antipode, where the usual asymptotic approximation of the Legendre functions is inaccurate. Figure 7.23 shows a qualitative agreement with the measurements of Balser and Wagner [1962a] that were shown in Fig. 7.22.

Based on measurements at one location of the earth, it is also possible to estimate the noise levels at other locations using this procedure of noise spectrum calculations. The noise that is due to a worldwide distribution of thunderstorms depends on the frequency variation and also on the absolute value of the power spectrum of the mean dipole moment of source $g(i\omega, \theta, \varphi)$. The θ and φ dependence may be estimated from the thunderstorm frequency maps as was indicated before, which leaves the absolute value and the frequency dependence of $g(i\omega)$

as an unknown. Assuming that $g(i\omega)$ is the same for all noise sources, it may be determined by making the calculations to agree with measurements at one particular location. This gives a uniquely determined noise distribution over the surface of the earth, and the accuracy of this model can be checked by comparing the calculations with measurements at other locations. In an example, measurements by D.E.C.O. at Boulder, Colorado [Maxwell, 1967], and by R.C.A. at Long Island, New York [Powers, 1964, private communication], were used to determine $g(i\omega)$. The calculations by Abraham [1965] have been based on these values of $g(i\omega)$ and are compared with simultaneous measurements made in Malta and Alaska [Maxwell, 1967]. As seen from Fig. 7.24, the analytic curves agree in shape with the measurements. The noise level at Alaska is lower for higher frequencies because of increased distance from the sources and higher net attenuation. The normalization with respect to Boulder gives somewhat higher predictions of the noise level. This may possibly be caused by summertime thunderstorm activity in the mountains near Boulder, Colorado, that would give significant near fields and a high estimate for the function $g(i\omega)$. The calculations are extended above the region of the earth-ionosphere cavity resonances to show that more significant noise level changes occur at higher frequencies.

In the calculations leading to Figs. 7.23 and 7.24, the day and night effects are considered most accurately if the day and night boundary is located symmetrically with respect to source (i.e. source at local noon or midnight). For nonsymmetrical day and night boundaries, it is

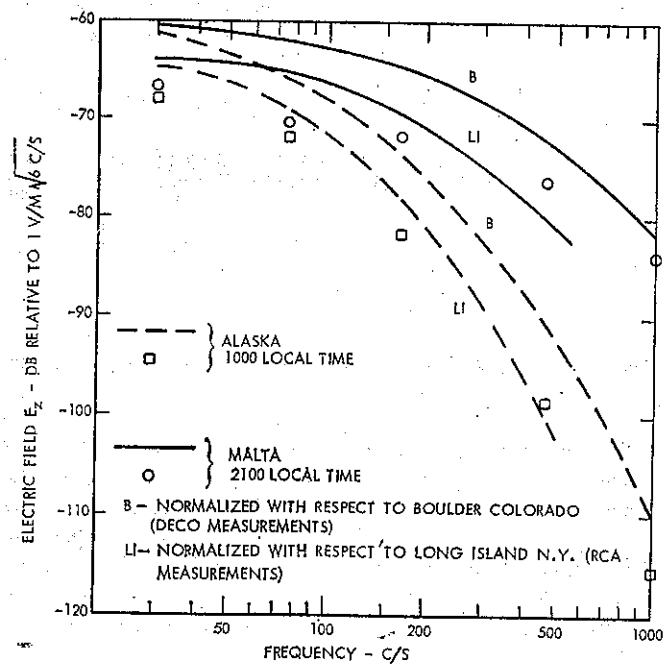

FIG. 7.24 Comparison of Calculated Field Strengths Data with July 1963 Measurements by DECO and RCA

difficult to estimate the effects of wave-front distortion. When neglecting such distortions (or assuming propagation strictly in the θ-direction), this method can account for $\nu(\theta)$ variations, which may be caused by ionosphere parameter changes or by changes of the static magnetic field along the surface of the earth. Also, the assumption of a proportionality between source power density and thunderstorm days T_m may be inaccurate in analysis. Pierce [1968] has shown that the monthly density of lightning flashes σ_m (per km^2) is related to T_m as $\sigma_m^2 = aT_m + a^2T_m^4$ with $a = 0.03$, and an assumed linearity leads to low values of σ_m in tropical areas where $T_m \approx 20$.

7.4.4 *Fields in a Nonuniform Cavity*

The previous analysis is strictly valid only in a uniform spherical shell where the ionosphere is characterized by a constant boundary height and constant surface impedance at any point along the globe. This is an obvious idealization, and more accurate theoretical models should account for the nonuniformities of the actual geometry. In the work of Madden and Thompson [1965], the lower ionospheric boundary is represented by a surface impedance that accounts for differences between daytime and nighttime conditions and for the magnetic field effects at various latitudes. They present a numerical solution for a network analog of this nonuniform spherical transmission line, and Nelson [1967] considers a perturbation solution of the same problem. The resonance frequency changes of the nonuniform cavity are essentially the same as in a uniform cavity and depend primarily on the interaction between adjacent resonance modes. Bliokh *et al.* [1968] have analyzed the fundamental $n = 1$ Schumann resonance in the presence of an eccentric geomagnetic field and obtained frequency changes that are comparable to those obtained in the presence of higher order modes ($n > 1$) in a uniform cavity. Large and Wait [1968] provide a general formulation of the problem, and investigate numerically coupling in a cavity where the surface properties vary with the polar angle θ but remain independent of the azimuth φ.

In a uniform or φ-symmetrical cavity, the fields can be expressed using Legendre polynomials $P_n(\cos\theta)$ while nonsymmetrical cavities can support additional so-called split modes characterized by Legendre functions $P_n^m(\cos\theta)$ with $m \neq 0$. Any deviation from a spherical geometry will introduce the split modes and these include such possibilities as ionospheric depressions in the polar regions, variations in ionospheric structure with solar zenith angle, anisotropy of the ionosphere due to the geomagnetic field, or variable ground conductivity. Ionospheric depressions associated with polar cap absorption (P.C.A.) events involve a small area of the earth's surface and have a smaller effect on Schumann resonances than some sudden ionospheric disturbances (S.I.D.) [Madden and Thompson, 1965]. With the possible exception of the low conductivity ice cap of Greenland or Antarctica, other ground surfaces appear as near-perfect conductors in the lower E.L.F. range and could not cause effective unsymmetries. Variations of ionospheric structure with solar zenith angle should be less significant than differences between grossly averaged day and night hemispheres. The discussion will be limited to unsymmetries caused by differences between daytime and nighttime conditions. There is no firm experimental evidence. A split of the peak frequency of the $n = 1$ mode into three distinct separate peaks is observed very seldom [Larsen and Egeland, 1968]. A fine structure of resonance curves has been observed also by Hughes [1964] and Rycroft [1965].

Short time-frequency spectra are extremely jagged, but there is no regular splitting of the mode n into $m = 2n+1$ sublevels. Rycroft [1965] concludes that the fine structure is spurious and is brought about by statistical fluctuations due to the finite length of the sample. Line splitting may contribute to the changes of resonance frequencies [Bliokh, 1968], but its significance has not been established in relation to the energy spillover from adjacent fundamental modes of $m = 0$.

For a nonsymmetrical cavity the number of mode amplitudes (and also the number of the corresponding linear equations) increases quadratically with the number of modes n: there will be $n(n+2)$ equations for T.M. modes and an equal number for T.E. modes, which are coupled by nonuniformities of the cavity and by ionospheric anisotropy to T.M. modes. In the formulation of waveguide modes θ variations of fields are described by Legendre functions $P_\nu(-\cos\theta)$ of complex order ν and only the zero order T.M. mode propagates for frequencies in the E.L.F. range. The highly attenuated T.E. modes are present near nonuniformities of the cavity, but T.E. field components will also accompany the propagating T.M. mode in the presence of ionospheric anisotropy. In a uniform cavity these T.E. field components must be considered in the process of determining the ionospheric surface impedance of the T.M. mode, but the latter T.E. field components do not contribute directly to the observed vertical electric field. (Such considerations are not valid in the V.L.F. range, where both T.E. and T.M. modes are significant.) The subsequent development considers only hemispherical differences between daytime and nighttime conditions. The T.E. modes are neglected near the day to night transition and the presence of T.E. fields caused by ionospheric anisotropy is implicit in the calculation of the T.M. surface impedance [Galejs, 1968a]. This assumption reduces the number of simultaneous equations of the $P_n^m(\cos\theta)$ formulation by one-half. The problem of inverting large matrices is further avoided by restricting the numerical solution to modes $n = 1, 2$ and $m = 0, \pm 1$. Such a truncation of a doubly infinite system of equations implies a restriction of the θ variations of the fields to cosine and sine functions of arguments θ and 2θ; the φ variations are restricted to $\sin\varphi$ and $\cos\varphi$. More rapid θ or φ variations can be expected near localized perturbations of the spherical boundaries, and the accuracy of a truncated solution has not been investigated. Calculations indicate that the frequency variations of the fundamental Schumann resonance can be approximated using the two lower fundamental modes ($n = 1, 2$ with $m = 0$). The addition of $m = -1$ split modes alters the fields only to a negligible degree for ionospheric models that provide empirical propagation parameters.

The calculations will distinguish only between daytime and nighttime hemispheres; the model of the daytime ionosphere considers a radial geomagnetic field component, but the nighttime ionosphere is assumed to be isotropic. One usually expects stronger magnetic field effects at night than in day. However, the usual nighttime profiles of the *D*-region may yield very high attenuation rates when including a radial geomagnetic field component. More complete profile models must be used at night, and an *F*-layer has been considered in Section 7.3.5 to obtain more realistic propagation parameters from anisotropic nighttime profiles. The propagation data of the latter models are closely approximated by an isotropic ionosphere.

7.4.4.1 Formal Solution

The spherical earth of radius a is surrounded by a shell of free space of thickness $h = c - a$, and ionosphere occupies the space of $r > c$. This geometry is described in the spherical coordinates of Fig. 7.25. The source is at the point Q in the φ or $\varphi' = 0$ plane at $r = b \gg a$ and at an angle ψ from the north pole. The fields are observed at the point P. The (r, θ, φ) coordinates

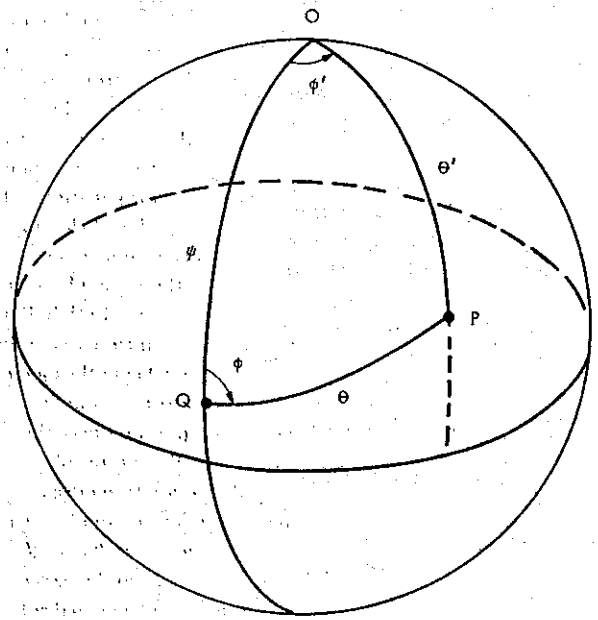

FIG. 7.25 The Spherical Geometry

will be used for calculating the fields, but the boundaries of the shell will be described in the (r, θ', φ') coordinates. Examination of the spherical triangle OPQ shows that

$$\begin{aligned} \cos\theta &= \cos\theta' \cos\psi + \sin\theta' \sin\psi \cos\varphi', \\ \cot\varphi &= -\cot\varphi' \cos\psi + (\sin\psi \cot\theta')/\sin\varphi'. \end{aligned} \tag{35}$$

For an equatorial source, $\psi = 90°$ and (1) simplifies to

$$\cos\theta = \sin\theta' \cos\varphi', \quad \tan\varphi = \tan\theta' \sin\varphi'. \tag{36}$$

It follows from sections 7.1 and 7.11 of Stratton [1941] that T.M. field components of the space between the earth and the ionosphere that are characterized by $H_r = 0$ can be derived from a scalar function U_j as

$$E_r = \left(k_0^2 + \frac{\partial^2}{\partial r^2}\right)(rU_j), \tag{37}$$

$$E_\theta = \frac{1}{r}\frac{\partial^2}{\partial r\,\partial\theta}(rU_j), \tag{38}$$

$$E_\varphi = \frac{1}{r\sin\theta}\frac{\partial^2}{\partial r\,\partial\varphi}(rU_j), \tag{39}$$

$$H_\theta = -\frac{i\omega\varepsilon_0}{r\sin\theta}\frac{\partial}{\partial\varphi}(rU_j), \tag{40}$$

$$H_\varphi = \frac{i\omega\varepsilon_0}{r}\frac{\partial}{\partial\theta}(rU_j), \tag{41}$$

where

$$rU_j(r, \theta, \varphi) = \frac{1}{k_0}\sum_{n=0}^{\infty}\sum_{m=-n}^{n}[A_{nm}^j U_n(u) + B_{nm}^j V_n(u)]\,P_n^m(\cos\theta)\exp(im\varphi), \tag{42}$$

$$U_n(u) = uh_n^{(1)}(u); \qquad V_n(u) = uh_n^{(2)}(u), \tag{43}$$

$$h_n^{(m)}(u) = \sqrt{\frac{\pi}{2u}}\,H_{n+0.5}^{(m)}(u). \tag{44}$$

$H_q^{(m)}(u)$ is the Hankel function of kind m, $u = k_0 r$, and $P_n^m(\cos\theta)$ is the associated Legendre function of degree n and order m. The subscript $j = 1$ refers to the region $a \leqslant r \leqslant b$ and $j = 2$ to $b \leqslant r \leqslant c$. Denoting the derivative with respect to the argument by a prime, the Wronskian of the radial functions (43) is computed as

$$U_n'(u)\,V_n(u) - U_n(u)\,V_n'(u) = 2i. \tag{45}$$

A radial electric dipole will be characterized by discontinuous θ components of the electric fields at $r = b$. It follows from (143) to (145) of Galejs [1964] that

$$\lim_{\Delta\to 0}[E_\theta(b+\Delta) - E_\theta(b-\Delta)] = -\frac{iI\,ds}{4\pi\omega\varepsilon_0 b^3}\sum_{n=0}^{\infty}(2n+1)\frac{\partial}{\partial\theta}P_n(\cos\theta). \tag{46}$$

The other tangential field components E_φ, H_φ, and H_θ will be continuous at $r = b$. In the E.L.F. range, the ground surface can be approximated by a perfect conductor as long as the ground conductivity σ_g is much larger than the effective ionospheric conductivity σ_i. In this approximation E_θ and $E_\varphi = 0$ for $r = a$. At the ionospheric boundary $r = c = a + h$, the tangential field components will satisfy impedance-type boundary conditions

$$\begin{aligned} Z_e(h) &= \frac{E_\theta(a+h)}{H_\varphi(a+h)} = \eta\,\Delta(\theta', \varphi'), \\ Z_h(h) &= -\frac{E_\varphi(a+h)}{H_\theta(a+h)} = \eta\,\Delta(\theta', \varphi'), \end{aligned} \tag{47}$$

where $\eta = \sqrt{\mu_0/\varepsilon_0} = 120\pi$. The θ' and φ' variations of the impedances arise from variations in the effective propagation parameters along the surface of the earth that depend on latitude or longitude variations of the ionosphere, diurnal and seasonal changes, and variations of

the geomagnetic field. The boundary conditions (47) are strictly valid under isotropic conditions, which is pointed out also by Large and Wait [1968]. For an anisotropic ionosphere Δ will also depend on the direction of propagation, but the direction dependence of the propagation parameters (and hence of surface impedance) is small for frequencies near the Schumann resonances following Figs. 7.3A, B. For a given ionosphere model the propagation parameter S (or the phase velocity v_{ph} and the attenuation rate α) of the propagating zero order waveguide mode is related in a *uniform* geometry to the normalized surface impedance of T.M. waves Δ by

$$\Delta = ik_0h\left[1-\left(\frac{aS}{a+0.5h}\right)^2\right] \tag{48}$$

for any degree of ionospheric anisotropy, and the parameters Δ and S can be used interchangeably for characterizing a particular model. An ionosphere varying along θ' or φ' may be characterized by $\Delta(\theta', \varphi')$, but the effective value of S will not necessarily follow from (48). The coupling between the T.E. and T.M. fields that arises by ionospheric anisotropy [Galejs, 1968a] is considered in the computation of Δ, but possible changes of the coupling by θ' and φ' variation of the geometry are not accounted for.

Using the boundary conditions at $r = a$ and b and letting $b \to a$, it can be shown that

$$B_{nm}V_n'(u_g) = -A_{nm}U_n'(u_g) - \frac{(2n+1)iI\,ds}{4\pi\omega\varepsilon a^2}\delta_{m0}, \tag{49}$$

where $u_g = k_0a$, the superscripts $j = 2$ of the amplitude coefficients have been omitted, and where the Kronecker delta $\delta_{mq} = 1$ for $m = q$ and $\delta_{mq} = 0$ for $m \neq q$. Applying (49), the impedance boundary conditions (47) and (48) can be expressed as

$$\begin{aligned}&\mathbf{i}_\theta \sum_{n=1}^{\infty}\sum_{m=-n}^{n}(A_{nm}R_n'+S_{nm}')\frac{\partial}{\partial\theta}P_n^m(\cos\theta)\exp(im\varphi)\\ &\quad = \mathbf{i}_\theta i\,\Delta(\theta',\varphi')\sum_{n=1}^{\infty}\sum_{m=-n}^{n}(A_{nm}R_n+S_{nm})\frac{\partial}{\partial\theta}P_n^m(\cos\theta)\exp(im\varphi)\end{aligned} \tag{50}$$

$$\begin{aligned}&\mathbf{i}_\varphi \sum_{n=1}^{\infty}\sum_{m=-n}^{n}A_{nm}R_n'\frac{m}{\sin\theta}P_n^m(\cos\theta)\exp(im\varphi)\\ &\quad = \mathbf{i}_\varphi i\,\Delta(\theta',\varphi')\sum_{n=1}^{\infty}\sum_{m=-n}^{n}A_{nm}R_n\frac{m}{\sin\theta}P_n^m(\cos\theta)\exp(im\varphi)\end{aligned} \tag{51}$$

with

$$R_n = R_n(u_i) = U_n(u_i) - \frac{U_n'(u_g)}{V_n'(u_g)}V_n(u_i), \tag{52}$$

$$S_{nm} = S_{nm}(u_i) = -\frac{(2n+1)iI\,ds}{4\pi\omega\varepsilon_0a^2}\frac{V_n(u_i)}{V_n'(u_g)}\delta_{m0}, \tag{53}$$

where $u_i = k_0(a+h)$ and $\mathbf{i}_\theta$ and $\mathbf{i}_\varphi$ are unit vectors in θ and φ directions. R_n' and S_{nm}' are computed by differentiating the functions of arguments u_i in the expressions of R_n and S_{nm}. Equations (50) and (51) are added, multiplied with $\exp(-il\varphi)$ and integrated from 0 to 2π.

This results in

$$\left.\begin{aligned}&2\pi\sum_n\left\{A_{nl}R_n'\left[\mathbf{i}_\theta\frac{\partial}{\partial\theta}P_n^l+\mathbf{i}_\varphi\frac{l}{\sin\theta}P_n^l\right]+S_{nl}'\mathbf{i}_\theta\frac{\partial}{\partial\theta}P_n\right\}\\ &\quad = i\sum_n(A_{n0}R_n+S_{n0})\mathbf{i}_\theta\frac{\partial}{\partial\theta}P_n\int_0^{2\pi}\Delta e^{-il\varphi}\,d\varphi\\ &\quad\quad + i\sum_{n,m}A_{nm}R_n\left[\mathbf{i}_\theta\frac{\partial}{\partial\theta}P_n^m+\mathbf{i}_\varphi\frac{m}{\sin\theta}P_n^m\right]\int_0^{2\pi}\Delta e^{i(m-l)\varphi}\,d\varphi,\end{aligned}\right\} \tag{54}$$

where arguments of the normalized impedance Δ and of the Legendre functions P_n^m have been omitted. The double summation

$$\sum_{n,m} = \sum_{n=1}^{\infty}\left(\sum_{m=-n}^{-1}+\sum_{m=1}^{n}\right)$$

excludes the $m = 0$ term. The orthogonality of Legendre functions implies that

$$\int_0^{\pi}\left[\frac{\partial}{\partial\theta}P_n^m\frac{\partial}{\partial\theta}P_p^m+\frac{m^2}{\sin^2\theta}P_n^mP_p^m\right]\sin\theta\,d\theta = \begin{cases}0 & \text{for } n\neq p,\\ f_n^m = \dfrac{2n(n+1)}{2n+1}\dfrac{(n+m)!}{(n-m)!} & \text{for } n=p,\end{cases} \tag{55}$$

which is valid also for $m = 0$. Integrating the scalar product of (54) and $\{\mathbf{i}_\theta\,\partial P_p^l/\partial\theta+\mathbf{i}_\varphi lP_p^l/\sin\theta]\sin\theta$ from $\theta = 0$ to π results in

$$2\pi(A_{pl}R_p'+S_{pl}')f_p^l = i\sum_n(A_{n0}R_n+S_{n0})I_{np}^{0l}+i\sum_{n,m}A_{nm}R_nI_{np}^{ml}, \tag{56}$$

where $S_{pl}' = 0$ for $l = 0$ from the definition in (53) and where

$$I_{np}^{ml} = \int_0^{\pi}d\theta\sin\theta\left[\frac{\partial}{\partial\theta}P_n^m\frac{\partial}{\partial\theta}P_p^l+\frac{ml}{\sin^2\theta}P_n^mP_p^l\right]\int_0^{2\pi}d\varphi\,\Delta\exp[i(m-l)\varphi]. \tag{57}$$

Introducing the notation

$$C_n^m = A_{nm}R_n \tag{58}$$

for the coefficients and

$$Q_p^l = -\sum_n S_{n0}I_{np}^{0l} - i2\pi S_{pl}'f_p^0 \tag{59}$$

for the source terms, equation (56) is rewritten as

$$Q_p^l = 2\pi iC_p^l\frac{R_p'}{R_p}f_p^l+\sum_n C_n^0I_{np}^{0l}+\sum_{n,m}C_n^mI_{np}^{ml}. \tag{60}$$

After restricting n and p to values less than a maximum value N, (60) is seen to represent a set of $N(N+2)$ linear equations that can be solved for the unknown coefficients C_n^m. The subsequent numerical calculations will emphasize the fundamental Schumann resonance of

$n=1$. For a perfectly symmetrical cavity, all the $m \neq 0$ terms vanish; and the resonance of $n=1$ will be also affected by fields of the adjacent $n=2$ resonance mode. For some unsymmetries also, the $m=1$ and -1 terms will contribute to the $n=1$ resonance. This reduces the number of equations (60) to six ($n=1$ and 2 with $m=-1$, 0, and $+1$); and some calculations will also be made by further neglecting the $n=2$, $m=\pm 1$ terms.

7.4.4.2 *Equatorial Excitation of Day–Night Hemispheres*

Equation (60) contains integrals I_{np}^{ml} that must be evaluated numerically for a general θ' and φ' dependence of Δ. In the subsequent calculations, Δ will distinguish only differences between day and night hemispheres. It is further assumed that the vertical electric dipole source is located on the equator at the day–night boundary, which is observed at 6 p.m. local time. Such an assumption is not inconsistent with past work, where equatorial thunderstorms of 4 p.m. local time have been considered to be the principal sources of cavity excitation [Madden and Thompson, 1965]. Following (36), the day–night boundary of $\varphi'=0$ or π corresponds to $\varphi=0$ or π; the night conditions prevail for $0 \ll \varphi \ll \pi$, and day conditions for $\pi \ll \varphi \ll 2\pi$, with no θ variations of Δ. The integral of (57) is rewritten as

$$I_{np}^{ml} = I_\varphi(m,l) \int_0^\pi d\theta \sin\theta \left[\frac{\partial}{\partial\theta} P_n^m \frac{\partial}{\partial\theta} P_p^l + \frac{ml}{\sin^2\theta} P_n^m P_p^l \right], \tag{61}$$

where

$$I_\varphi(m,l) = \Delta_n \int_0^\pi e^{i(m-l)\varphi}\, d\varphi + \Delta_d \int_\pi^{2\pi} e^{i(m-l)\varphi}\, d\varphi. \tag{62}$$

Evaluation of (62) shows that

$$I_\varphi(m,l) = \begin{cases} \pi(\Delta_n+\Delta_d) & \text{for } m=l, \\ 0 & \text{for } (m-l)=\text{even}, \\ 2i(\Delta_n-\Delta_d)/(m-l) & \text{for } (m-l)=\text{odd}. \end{cases} \tag{63}$$

The θ integrals of (61) become zero if $(n+m+p+l)$ is equal to an odd integer. I_{np}^{ml} will be zero if either the θ or φ integrals are equal to zero. After inserting the appropriate zero terms in (60), the six equations can be separated into two sets of three equations each. This results in

$$\begin{bmatrix} Q_n^0 \\ Q_p^{-1} \\ Q_p^1 \end{bmatrix} = \begin{bmatrix} D_n^0 & I_{np}^{0,-1} & I_{np}^{01} \\ I_{pn}^{-10} & D_p^{-1} & 0 \\ I_{pn}^{10} & 0 & D_p^1 \end{bmatrix} \cdot \begin{bmatrix} C_n^0 \\ C_p^{-1} \\ C_p^1 \end{bmatrix} \tag{64}$$

where ($n=1$ and $p=2$) or ($n=2$ and $p=1$). Noting that $I_{np}^{0l} = -I_{pn}^{l0}$, the solutions of (64) are readily computed as

$$C_n^0 = \frac{Q_n^0 - \sum_l I_{np}^{0l} Q_p^l / D_p^l}{D_n^0 + \sum_l (I_{np}^{0l})^2 / D_p^l}, \tag{65}$$

$$C_p^l = (Q_p^l + I_{np}^{0l} C_n^0)/D_p^l, \tag{66}$$

where $l=1$ and -1. The diagonal coefficients are defined by

$$D_n^m = 2\pi i \frac{R_n'}{R_n} f_n^u + I_{nn}^{mm} = \pi f_n^m \left[2i \frac{R_n'}{R_n} + \Delta_n + \Delta_d \right] \tag{67}$$

and the remaining coefficients are evaluated as

$$I_{12}^{01} = -2I_{21}^{01} = -4I_{21}^{0,-1} = 6I_{12}^{0,-1} = 3\pi i(\Delta_d - \Delta_n)/2. \tag{68}$$

With the six amplitude coefficients C_n^m determined from (65) and (66), the fields can be determined from (37) to (42) in conjunction with (49) and (59). Using (37) and (42), the radial electric field E_r is expressed as

$$E_r(u) = \frac{1}{kr^2} \sum_{n=1}^{2} \sum_{m=-1}^{1} n(n+1) \left[C_n^m \frac{R_n(u)}{R_n(u_l)} + S_{nm}(u) \right] P_n^m(\cos\theta) \exp(im\varphi) \tag{69}$$

The horizontal magnetic field is obtained from (40), (41), and (42) as

$$H_t(u) = \frac{i}{r\eta} \sum_{n=1}^{2} \sum_{m=-1}^{1} \left[C_n^m \frac{R_n(u)}{R_n(u_l)} + S_{nm}(u) \right] \times \left[-\mathbf{i}_\theta \frac{im}{\sin\theta} P_n^m(\cos\theta) + \mathbf{i}_\varphi \frac{\partial}{\partial\theta} P_n^m(\cos\theta) \right] \exp(im\varphi). \tag{70}$$

Following (6) of Galejs [1968b] or (269) of Chapter 4, the radial functions (43) are proportional to $\exp(\pm iK_n r)$, where

$$K_n^2 = k_0^2 - n(n+1)/(a+0.5h)^2. \tag{71}$$

It follows that

$$\frac{R_n(u)}{R_n(u_l)} = \frac{\cos K_n(r-a)}{\cos K_n h}; \qquad \frac{R_n'(u_l)}{R_n(u_l)} = -\frac{K_n}{k_0} \tan K_n h, \tag{72}$$

$$S_{nm}(u) = \frac{(2n+1)I\, ds}{4\pi\omega\varepsilon_0 b^2} \frac{\exp[-iK_n(r-a)]}{(K_n/k_0)} \delta_{m0}. \tag{73}$$

$$S_{nm}'(u_l) = (-iK_n/k_0)\, S_{nm}(u_l). \tag{74}$$

For a uniform cavity $\Delta_n = \Delta_d = \Delta$, I_{np}^{0l} of (61) and (63), Q_p^l of (59), S_{pl} of (53), and C_p^l of (66) are all equal to zero for $l \neq 0$. Equations (65), (59), and (67) show that

$$C_n^0 = \frac{Q_n^0}{D_n^0} = -\frac{\Delta S_{n0}(u_l) + iS_{n0}'(u_l)}{\Delta + iR_n'(u_l)/R_n(u_l)}. \tag{75}$$

Substitution of (72) to (75) shows that (69) and (70) simplify for $r=a$ and $nh \ll a$ to the elementary forms (1) and (8). The convergence rate of the E_r expression becomes particularly slow for large values of n, where the approximations leading to (1) are no longer valid; special techniques must be used to assure numerical accuracy [Galejs, 1969b; Johler and Lewis, 1969]. However, the H_φ representation is rapidly convergent, which can be also seen from the zonal harmonics analysis of Large and Wait [1968].

It was pointed out following (48) that in the present computations, coupling between T.E. and T.M. field components by ionospheric anisotropy is considered as in a uniform geometry.

It is shown in the Appendix that T.E. modes arise also by the discontinuity of surface impedance between day and night hemispheres; additional terms of (38) to (41) are required to account for such modes, and the number of simultaneous equations [corresponding to (60)] is doubled for a given value of N. In the representation of residues or waveguide modes, the T.E. waves are highly attenuated and may be present only in the direct vicinity of the day-to-night boundary. Their presence is neglected in this analysis.

The analytical method of Large and Wait [1968] tends to lump the mode coupling caused by the presence of an anisotropic ionosphere together with mode coupling caused by a discontinuity between day and night hemispheres; a comparison of their figs. 10 and 17 suggests that the former coupling is the dominant one. The present formulation neglects the T.E. and T.M. mode coupling due to the daytime and nighttime discontinuity; but the coupling caused by ionospheric anisotropy is implicit in the calculation of Re S and α, as is pointed out in the discussion following equation (47). The propagation parameters can be also computed by assuming a magnetic conductor at the lower ionospheric boundary [equation (23) of Galejs, 1967] in the computation of ionospheric T.E. fields, which implies that the presence of T.E. fields below the ionosphere is neglected. For the anisotropic daytime ionosphere model of Fig. 7.12, this causes an approximate 2 percent decrease of the attenuation rate α and increase of Re S by 0.5 percent. For the corresponding nighttime ionosphere model of Fig. 7.7, $Q_e = 2.2$ following (27); and the neglect of T.E. fields decreases α by approximately 13 percent and Re S by less than 1 percent. These latter changes are qualitatively similar as in fig. 10 of Large and Wait [1968], where Q is changed from 1.2 to 1.4. For the isotropic nighttime ionosphere model of Fig. 7.12, there is no coupling between T.E. and T.M. fields. The propagation parameters of this isotropic nighttime ionosphere tend to approximate the average parameters for a number of anisotropic nighttime ionosphere models in Fig. 7.11, which include also the effects of F-layer reflections; in the individual anisotropic nighttime ionosphere models, α is decreased but Re (S) may be increased or decreased by the neglected presence of T.E. fields.

The coupling between T.M. and T.E. modes that tends to decrease the resonance frequencies and Q-factors in the work of Large and Wait [1968] appears to be caused principally by ionospheric anisotropy; these effects are less significant for the higher Q ionosphere models of the present study.

7.4.4.3 *Amplitude Variations of Field Components and Mode Splitting*

The amplitude variations of the electric and magnetic fields of (69) and (70) or (1) and (8) are investigated for a hypothetical ionosphere model with Re $S = c/v_{ph} = 1.36$ and with various amounts of losses. For losses characterized by Im $S = 0.087$ and 0.261, the corresponding attenuation rates $\alpha = 0.126$ and 0.378 db/1000 km for $f = 8$ c/s. The thin-line curves of Fig. 7.26 consider only the $n = 1$ term and exhibit $Q_e = 2.6$, the half-power width of the H-field gives $Q = 2.7$, but the halfpower bandwidth remains undetermined for the E-field curves in Fig. 7.26 because of an amplitude increase at lower frequencies. In the presence of a second-order mode ($n = 2$), there may be similar ambiguities in the definition of Q from the width of the E curves for $\theta = 45°$ and from the H curves for $\theta = 135°$ when the resonance curves do not reach the half-power points for $Q < 3$.

The change of the angle θ from 45 to 135° tends to increase the resonance frequencies of E

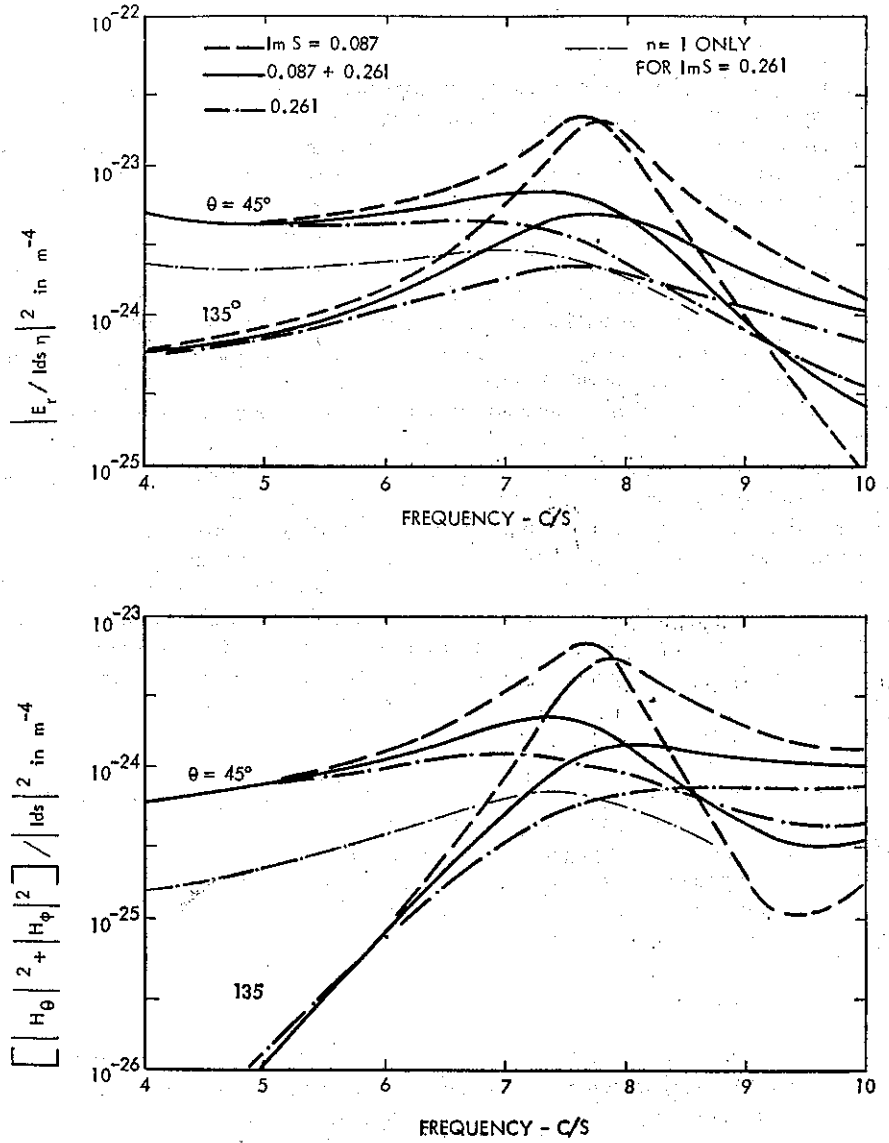

FIG. 7.26 Frequency Variation of the Electric and Magnetic Field Components Re S = 1.36 = Const.

and H fields. The largest change $\Delta f = 1.6$ c/s, shown in Fig. 7.26, occurs for the H-field with Im $S = 0.261$ or $Q = 2$; for E-field the corresponding change $\Delta f = 0.9$ c/s. The frequency changes are decreased with increasing Q, which has also been observed by Madden and Thompson [1965].

For a spherically homogeneous ionosphere model of identical day and night hemispheres ($\Delta_n = \Delta_d$), the summations (69) and (70) contain only the $m = 0$ terms. For a combined day and night ionosphere model, the resulting nonuniformity in the φ' direction gives rise to split modes or $m \neq 0$ terms in the summation, the relative amplitudes of which are shown in Table 7.3. For $Q = 2$, the $m = -1$ term is approximately 10 percent of the $m = 0$ term for $n = 1$;

TABLE 7.3 RELATIVE MODE AMPLITUDES

Day	Re (S)	1.36	1.36	1.38
	α	0.126	0.126	0.18
Night	Re (S)	1.36	1.36	1.34
	α	0.63	0.378	0.24
$Q(Q_s)$		2(2.6)	3(3.9)	3.6(4.7)
C_1^{-1}/C_1^0		0.1	0.05	0.015
C_2^{-1}/C_2^0		0.22	0.06	0.05
C_2^0/C_1^0		0.3	0.2	0.2

but the relative amplitudes of the $m = -1$ terms are decreased with increasing Q. For the ionosphere model of Fig. 7.12, $Q = 3.6$ and $C_1^{-1}/C_1^0 = 0.015$. The relative contributions of the $m \neq 0$ terms appear negligible, and their presence cannot be expected to affect the resonance frequencies of the cavity.

The $m \neq 0$ terms arise only from differences between day and night hemispheres, and their relative amplitudes are small if the propagation parameters of the two hemispheres differ only by the amounts indicated in Fig. 7.12; the propagation parameters of Fig. 7.12 will be adopted for the subsequent numerical examples.

7.4.5 *Variations of Resonance Frequencies*

Diurnal frequency variations of the earth-ionosphere cavity modes have been reported by Balser and Wagner [1962b], Stefant [1963], Rycroft [1963], Chapman and Jones [1964b], and Nelson [1967]. The resonance frequencies vary by about ± 0.2 to 0.3 c/s, but the changes are not simultaneous for the different modes; a low resonance frequency of one mode occurs simultaneously with a high frequency of a different mode. Madden and Thompson [1965] or Nelson [1967] explain the frequency shifts of resonance frequencies by the interaction of adjacent resonance modes. Bliokh *et al.* [1968] proposed a mechanism where the difference in the response of daytime and nighttime hemispheres to an eccentric geomagnetic field caused frequency changes for a single mode.

A high-altitude nuclear explosion has been shown to affect the earth-to-ionosphere cavity resonances by simultaneously lowering all the resonance frequencies [Gendrin and Stefant, 1962; Balser and Wagner, 1963], which suggests the lowering of the effective ionospheric boundary. More exact treatments of such ionosphere perturbations are possible with the analytical techniques of Madden and Thompson [1965] and Nelson [1967].

Frequency variations of the resonances will be investigated in this section using the representations (69) and (70) that apply to the fields of a single vertical electric dipole. Resonance frequencies will be also calculated for the power spectrum $G(i\omega)$ of (30) that is based on vertical electric dipoles uniformly distributed in the θ interval from θ_1 to θ_2. In subsequent calculations, $\theta_{1,2} = \theta \mp \Delta\theta/2$; θ_1 and θ_2 will be also computed from (36) for equatorial sources distributed over the φ'-interval from $(\varphi' - \Delta\varphi_1)$ to $(\varphi' + \Delta\varphi_2)$. Differences between day and night hemispheres are accounted for by averaging the respective Re S and α figures when computing ν of (30).

7.4.5.1 *Equatorial Thunderstorms at Sunset*

The resonance frequencies calculated for a uniform daytime ionosphere are shown in Fig. 7.27 when the representations (69) and (70) contain only $m = 0$ terms and are reduced to (1) and (8). The source is assumed to move along the equator, and it is located at the longitude of the observation point ($\varphi' = 0$) at 18 hours local time. Midlatitude ($\theta' = 45°$) and equatorial ($\theta' = 90°$) locations of the observation points are indicated by solid and dashed lines respectively. The vertical electric fields are computed from the waveguide mode representation (30) and using the zonal harmonics (1). The resonance frequencies exhibit a minimum for sources at the longitude of the observation point ($\varphi' = 0$) and are increased with an increased distance; for a source located at the opposite side of the globe ($\varphi' = 180°$), resonance frequencies exhibit a local maximum. Rapid frequency changes are observed near $\varphi' = 90$ and 270°. After relating φ' to θ by (36), $P_1(\cos\theta)$ and also E_r of (1) for a symmetrical $n = 1$ mode are seen to go through a zero for these values of φ'. The net frequency variation is larger for observation points near the equator. Similar frequency variations are also noted for a uniform ionosphere model in fig. 10 of Madden and Thompson [1965]. The resonance frequency variation of the horizontal H-field of (8) is gradual and does not exhibit the rapid changes near local noon and midnight observed for the vertical electric field. The frequency has its lowest value at the longitude of the source ($\varphi' = 0°$), and it reaches its maximum value for a source at the opposite side of the globe ($\varphi' = 180°$). Such a resonance frequency variation has been also noted by Large and Wait [1968]. The functional difference between the resonance frequency variations of vertical electric and horizontal magnetic fields arises from differences in the modal field patterns that are proportional to $P_n(\cos\theta)$ and its θ derivative in (1) and (8); rapid frequency changes are observed near the pattern nulls when the residual field amplitudes are caused by adjacent resonance modes. Such frequency changes are illustrated in Fig. 7.27 for the vertical electric field in the $n = 1$ mode and can be seen from table 8 of Large and Wait [1968] for the horizontal magnetic fields in higher modes ($n = 2$ and 3). It may not be appropriate to interpret measurements made for vertical electric fields [Balser and Wagner, 1962b] using theoretical calculations based on horizontal magnetic fields.

Subsequent calculations are made for ionosphere models which distinguish between the different properties of day and night hemispheres. The resonance frequency variations of Fig. 7.28 computed from (69), (70), and (30) remain similar to the frequency variations of the

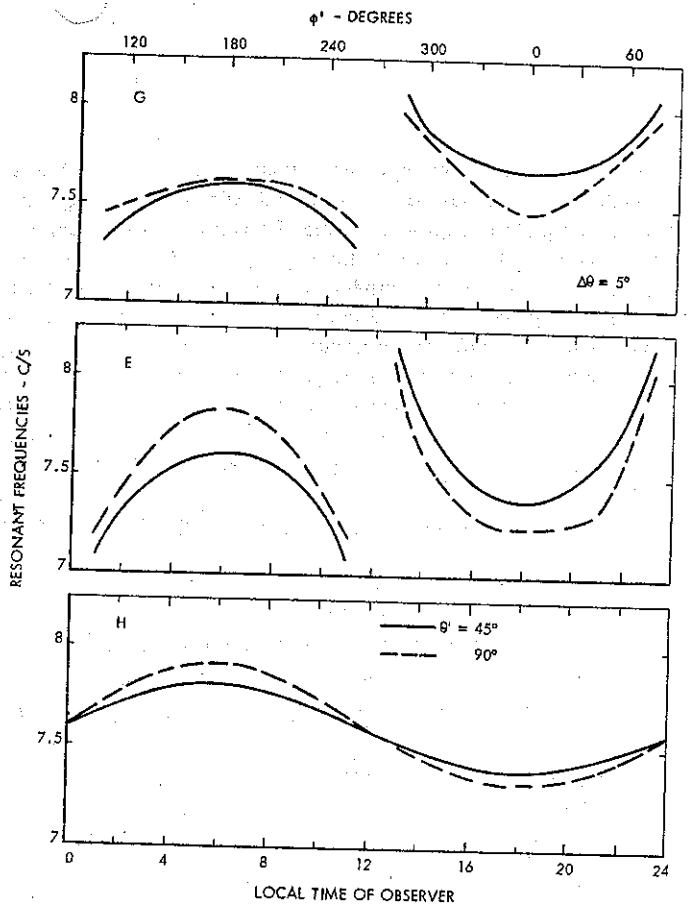

FIG. 7.27 Diurnal Variations of Resonant Frequencies for the Daytime Ionosphere Model. Equatorial Sources at Sunset Time (18 hrs or $\varphi' = 0$); Observer at Polar Angle θ'. $G-E_r$ of a Source Distributed Over $\Delta\theta$; E, $H-E_r$ and H_φ of Localized Sources

uniform ionosphere model in Fig. 7.27, except for some increases in the resonance frequency. In the propagation model of Fig. 7.12, Re (S) of the nighttime ionosphere is lower than at daytime, the effective Re (S) is decreased, and one may anticipate some increases in the resonance frequencies following (17).

The calculations for E_r or H_φ are based on a single dipole source located on the equator, but the power spectrum calculations are for sources extending over a θ interval $\theta \pm \Delta\theta/2$ around the equator. $\Delta\theta = 5°$ is indicated by solid curves, but the dashed curves of Fig. 7.28 show the effects of increasing the source region to $\Delta\theta = 20$, 40, and 60°. An increase of $\Delta\theta$ decreases the frequency variations observed near $\varphi' = 90$ and 270°. For $\Delta\theta = 40°$, there is an approximate 0.5 c/s frequency change in a 2-hour interval around noontime, which has been

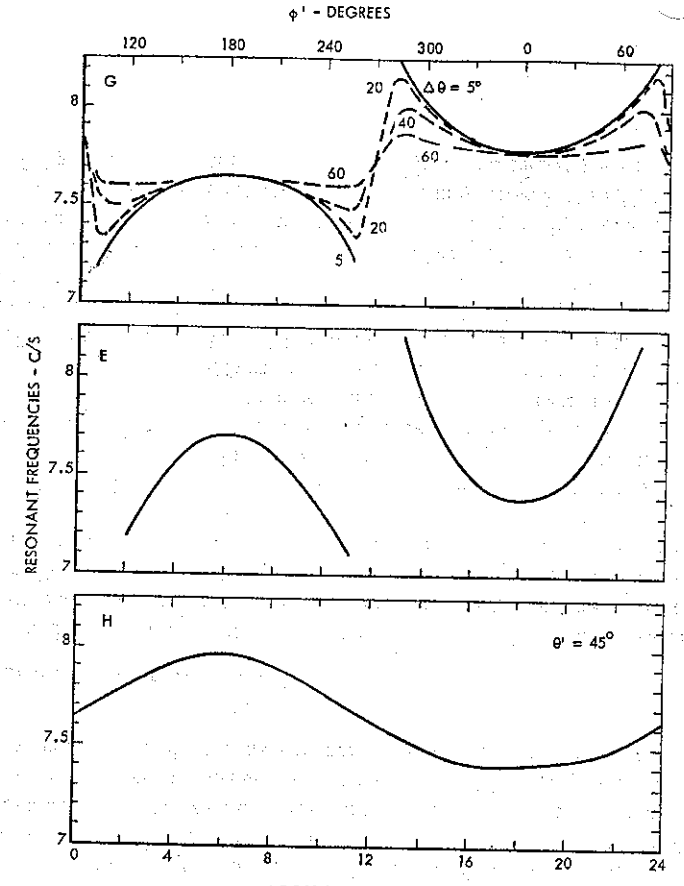

FIG. 7.28 Diurnal Variations of Resonant Frequencies; Equatorial Sources at Sunset Time (18 hrs or $\varphi' = 0$); Observer at Polar Angle θ'. $G-E_r$ of a Source Distributed Over $\Delta\theta$; E, $H-E_r$ and H_φ of Localized Sources

observed in several measurements [Balser and Wagner, 1962b; Nelson, 1967]; but there is also a comparable frequency change around midnight which is contrary to observations. These calculations are based on the assumption that the sources are symmetrical with respect to the day and night boundary at sunset.

7.4.5.2 *Effects of Different Diurnal Thunderstorm Activities*

Some of the data available on diurnal variations of local thunderstorm activities will be reviewed in order to establish limits on the θ interval (30). The data of Maxwell and Stone [1966] that are representative of Egypt, Europe, India, and New Zealand indicate in Fig. 7.29a

that local thunderstorm activity peaks around 18 hours and that the activity is near peak between 15 and 20 hours. Data of Solovyev [1969] for the Central Asia gives peak activity between 14 and 18 hours. The measurements reported by Whipple [1929] for the Indian Ocean peak near midnight, and the data of Solovyev [1969] for North Atlantic exhibit a peak in the early morning hours in Fig. 7.29b. There is a definite shift between times of peak activity for thunderstorms on landmasses and on oceans although a constant diurnal activity is frequently assumed for oceans [Pierce, 1969].

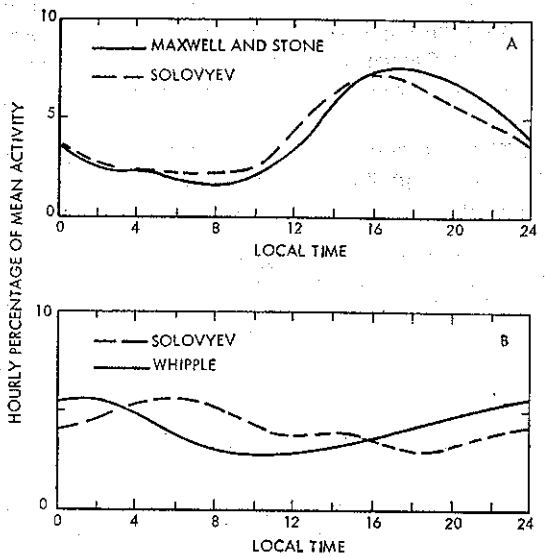

FIG. 7.29 Diurnal Variations of Local Thunderstorm Activity

A over land
B on oceans

Subsequent calculations will be made for land thunderstorms occurring in afternoon and early evening between 15 and 19 hours ($\Delta\varphi_1 = 45°$, $\Delta\varphi_2 = 15°$) and also for ocean thunderstorms that occur in late evening or night between 18 and 24 hours ($\Delta\varphi_1 = 0$, $\Delta\varphi_2 = 90°$) and 20 to 02 hours ($\Delta\varphi_1 = -30°$, $\Delta\varphi_2 = 120°$). The resulting frequency variations are compared in Fig. 7.30 with measurements of Balser and Wagner as reported by Nelson [1967]. Because of the wide azimuthal spread $\Delta\varphi_j$ of the thunderstorm areas, the overland figures will be applied from Southeast Asia to South America, the oversea figures will be applied to the Pacific. However, the selection of the transition points between the two curves may require further clarification. For an observer at a longitude of 70° W, 20 hours of observer time correspond to a sunset line at 100° W. The afternoon activity from 85° W to 145° W over the Pacific is switched to the late evening activity from 100° to 10° W, which includes also the South America. The afternoon activity over the Pacific appears to be equivalent to the reduced nighttime activity over South America. At 04 hours of the observer time, the day–night

boundary is at 130° E. The late evening activity over the Pacific from 140° E to 130° W is switched in the computational model to the afternoon activity over Southeast Asia extending from 95° E to 155° E without changes of the resonance frequency.

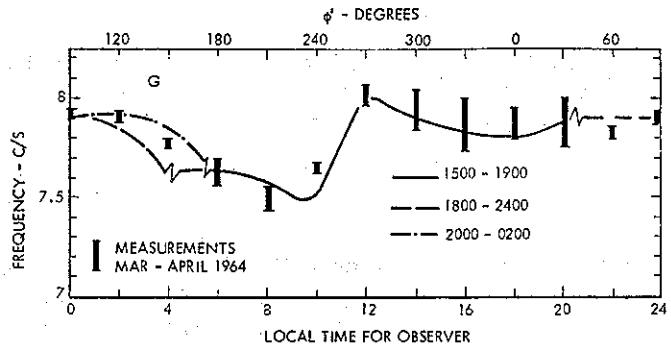

FIG. 7.30 Measured and Calculated Variations of Resonant Frequencies; Observer at 45° N, 70° W; Equatorial Sources Active During the Indicated Interval of Local Time

The above computational model is obviously idealized, but it is able to account for the complete diurnal frequency variations of North American measurements made during a season when local thunderstorm activity is low. In these calculations, it is essential to have an azimuthal extension of the equatorial sources; also, the afternoon or evening times of peak activity over landmasses are changed to a late evening peak activity over the Pacific Ocean, which is not inconsistent with the diurnal changes of thunderstorm activity shown in Fig. 7.29.

7.4.5.3 *Comparisons with Other Work*

Madden and Thompson [1965] and also Nelson [1967] explain diurnal variations of resonance frequencies by mode mixing without requiring any particular systematic variations of the ionosphere. Parts of diurnal frequency variations of the fundamental Schumann resonance have been correlated with peak activity for sources in Southeast Asia, Africa, and South America.

Bliokh *et al.* [1968] have calculated diurnal variations of the resonance frequencies in a model which distinguishes between differences of day and night hemispheres and allows for the eccentricity of the geomagnetic field. These frequency variations appear to be caused principally by differences in the response of daytime and nighttime hemispheres to changes in the radial magnetic field components, which can be also demonstrated in a simpler computational model.

The collision frequencies ν (3 and 0.17×10^7) and the plasma frequencies ω_p (5.5 and 1.3×10^6) quoted by Bliokh *et al.* [1968] (their electron density should be increased by a factor of 10) are used to calculate the propagation parameter S in the presence of a radial geomagnetic field, and the resonance frequencies of a uniform cavity are subsequently determined from (17). Under daytime conditions, the resonance frequency is 8.7 c/s; and it is not affected by the radial magnetic field. The nighttime resonance frequencies change from 8.9 to 7.5 c/s as B_r is increased from 0 to 0.5 gauss. The average of day and nighttime Re S figures gives a change of the fre-

quency from 8.45 to 8.05 c/s as B_r is changed from 0.3 to 0.5 gauss. It is seen from fig. 11.8 of Valley [1965] that the radial geomagnetic field component averaged over all latitudes is near 0.3 gauss for a longitude of 45° W and near 0.5 gauss at 120° E. After extending these magnetic field figures over the whole nighttime hemisphere, one would obtain a change of resonance frequency from 8.45 c/s for 03 hours U.T. to 8.05 c/s for 16 hours U.T. Except for a constant 0.2 c/s shift, these frequencies correspond to the peaks of the diurnal frequency variations depicted in fig. 2 of Bliokh *et al.* [1968]. These frequency changes are contingent on the proportionality between Re S and the radial component of the geomagnetic field, which changes in the nighttime ionosphere model of Bliokh *et al.* [1968] from 1.32 to 1.4 as B_r is increased from 0.3 to 0.5 gauss for $f = 8$ c/s. However, such changes of Re S are not observed in more complex ionosphere models, where an increase of B_r may cause an increase as well as a decrease of Re S in Figs. 7.10 and 7.11 and where propagation in the presence of radial geomagnetic field is approximated by the isotropic conditions on average.

7.4.5.4 *Ionosphere Perturbations*

A high-altitude nuclear explosion affects the earth-to-ionosphere cavity resonances by simultaneously lowering all the resonance frequencies. Tepley *et al.* [1963] noted also an increase of signal strength for observations near the conjugate point of the explosion. The

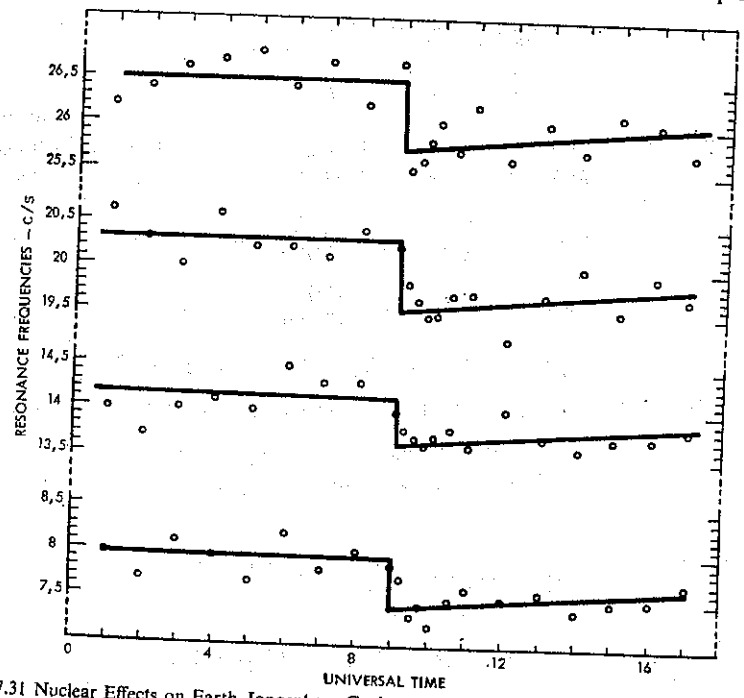

FIG. 7.31 Nuclear Effects on Earth–Ionosphere Cavity Resonances. Measurements by Gendrin and Stefant

lowering of resonance frequency, shown in Fig. 7.31, has been attributed to worldwide lowering of the effective ionosphere in a model of a single layer isotropic ionosphere [Gendrin and Stefant, 1962]. The depression of the resonance frequency can be also explained by assuming an exponential daytime ionosphere to be effective around the globe. As an illustration, the daytime resonance frequencies of Table 7.1 compare with the measured resonance frequencies of Fig. 7.31. There are V.L.F. observations [Zmuda *et al.*, 1963] that can be explained by a lowering (or increasing electron density) of the D-region boundary. Brady *et al.* [1964] interpreted V.L.F. diurnal phase shifts to show that some enhanced D-region ionization persists for several days following the event.

Although the effective ionosphere boundary is lowered over wide areas of the earth's surface, the frequency depressions of resonances are not universal [Madden and Thompson, 1965]. There are wide zones where only small changes of resonance frequencies are observed following a nuclear explosion. Also sudden ionospheric disturbances (S.I.D.) cause a lowering of resonance frequencies; polar cap absorption (P.C.A.) events that are confined to auroral zones involve a small area of the earth's surface and have a lesser effect on Schumann resonances.

7.5 Appendix. Combined T.M. and T.E. Fields

The solutions of Section 7.4.4 have been derived by neglecting the T.E. field components that are associated with a nonzero H_r field in a φ-dependent geometry. The inclusion of T.E. fields doubles the number of equations that are to be solved for amplitudes of the various spherical harmonics, which will be illustrated in the subsequent development.

The complete set of T.M. and T.E. fields can be expressed as

$$E_r = \left(k_0^2 + \frac{\partial^2}{\partial r^2}\right)(rU_j), \tag{76}$$

$$E_\theta = \frac{1}{r}\frac{\partial^2}{\partial r\,\partial\theta}(rU_j) + \frac{i\omega\mu_0}{r\sin\theta}\frac{\partial}{\partial\varphi}(rV_j), \tag{77}$$

$$E_\varphi = \frac{1}{r\sin\theta}\frac{\partial^2}{\partial r\,\partial\varphi}(rU_j) - \frac{i\omega\mu_0}{r}\frac{\partial}{\partial\theta}(rV_j), \tag{78}$$

$$H_r = \left(k_0^2 + \frac{\partial^2}{\partial r^2}\right)(rV_j), \tag{79}$$

$$H_\theta = -\frac{i\omega\varepsilon_0}{r\sin\theta}\frac{\partial}{\partial\varphi}(rU_j) + \frac{1}{r}\frac{\partial^2}{\partial r\,\partial\theta}(rV_j), \tag{80}$$

$$H_\varphi = \frac{i\omega\varepsilon_0}{r}\frac{\partial}{\partial\theta}(rU_j) + \frac{1}{r\sin\theta}\frac{\partial^2}{\partial r\,\partial\varphi}(rV_j), \tag{81}$$

where

$$rV_j(r,\theta,\varphi) = \frac{1}{k_0}\sum_{n=0}^{\infty}\sum_{m=-n}^{n}\left[C_{nm}^j U_n(u) + D_{nm}^j V_n(u)\right]P_n^m(\cos\theta)\exp(im\varphi). \tag{82}$$

U_j, $U_n(u)$, $V_n(u)$ are defined by (42) and (43). The primary E_θ field components (46) excited by a vertical electric dipole are independent of φ. As a consequence, the discontinuity of E_θ at the source will be reflected only in U_j of (42); the functions V_j of (82) will be valid for any value of

r in the range of $a \ll r \ll c$. The boundary conditions $E_\theta(a) = E_\varphi(a) = 0$ and the condition (47) for $r = c = a+h$ lead to the inclusion of terms proportional to C_{nm} in (50) and (51). The resulting equations are multiplied with $\exp(-il\varphi)$ and integrated from 0 to 2π. This gives

$$\left.\begin{aligned} 2\pi \sum_n \left\{ a'_{nl}\left[\mathbf{i}_\theta \frac{\partial}{\partial\theta} P_n^l + \mathbf{i}_\varphi \frac{l}{\sin\theta} P_n^l\right] - c_{nl}\left[\mathbf{i}_\theta \frac{l}{\sin\theta} P_n^l + \mathbf{i}_\varphi \frac{\partial}{\partial\theta} P_n^l\right]\right\} \\ = i \sum_{n,m} \left\{ a_{nm}\left[\mathbf{i}_\theta \frac{\partial}{\partial\theta} P_n^m + \mathbf{i}_\varphi \frac{m}{\sin\theta} P_n^m\right] \right. \\ \left. + c'_{nm}\left[\mathbf{i}_\theta \frac{m}{\sin\theta} P_n^m + \mathbf{i}_\varphi \frac{\partial}{\partial\theta} P_n^m\right]\right\} \int_0^{2\pi} \Delta \exp\left[i(m-l)\varphi\right] d\varphi, \end{aligned}\right\} \tag{83}$$

where

$$\begin{aligned} a_{nm} &= A_{nm}R_n + S_{nm}, \qquad a'_{nm} = A_{nm}R'_n + S'_{nm}, \\ c_{nm} &= \eta C_{nm} T_n, \qquad c'_{nm} = \eta C_{nm} T'_{nm}, \end{aligned} \tag{84}$$

and where the double summation $\sum_{n,m}$ does not exclude the $m = 0$ term. R_n and S_{nm} are defined as in (52), (53), or (72) to (74). The functions T_n and T'_n are computed from

$$T_n = T_n(u_i) = U_n(u_i) - \frac{U_n(u_g)}{V_n(u_g)} V_n(u_i) = 2i \sin K_n h \exp(iK_n a), \tag{85}$$

$$T'_n = T'_n(u_i) = U'_n(u_i) - \frac{U_n(u_g)}{V_n(u_g)} V'_n(u_i) = \frac{2iK_n}{k_0} \cos K_n h \exp(iK_n a), \tag{86}$$

where K_n is defined by (71). Integrating the scalar product of (83) and $[\mathbf{i}_\theta\, \partial P_p^l/\partial\theta + \mathbf{i}_\varphi l P_p^l/\sin\theta] \sin\theta$ or $[\mathbf{i}_\theta (l/\sin\theta) P_p^l + \mathbf{i}_\varphi\, P_p^l/\partial\theta] \sin\theta$ from $\theta = 0$ to π and applying (55) results in

$$2\pi a'_{pl} f_p^l = i \sum_{n,m} (a_{nm} I_{np}^{ml} + c'_{nm} J_{np}^{ml}), \tag{87}$$

$$-2\pi c_{pl} f_p^l = i \sum_{n,m} (a_{nm} J_{np}^{ml} + c'_{nm} I_{np}^{ml}), \tag{88}$$

where f_p^l is defined in (55), I_{np}^{ml} is given by (57) and

$$J_{np}^{ml} = \int_0^\pi d\theta \left[l P_p^l \frac{\partial}{\partial\theta} P_n^m + m P_n^m \frac{\partial}{\partial\theta} P_p^l\right] \int_0^{2\pi} d\varphi\, \Delta \exp\left[i(m-l)\varphi\right]. \tag{89}$$

After restricting n and p to values less than a maximum value N, (87) and (88) are seen to represent a set of $2N(N+2)$ linear equations that can be solved for the unknown coefficients a_{nm} and c_{nm}, which are related to A_{nm} and C_{nm} as indicated in (84). The calculations are simplified if it is assumed that Δ distinguishes only between day and night hemispheres and that the equatorial source is located at the day–night boundary. This makes Δ to (89) independent of θ and $J_{np}^{ml} = 0$ if $(n+m)$ and $(p+l)$ are both even or both odd or if $m = l$.

In the absence of source terms ($S_{nm} = S'_{nm} = 0$) the vector equation (83) corresponds to the two scalar equations (58) and (59) of Large and Wait [1968]; however, the subsequent θ integrations are different in these two formulations.

7.6 References

Abraham, L. G. (1965) Prediction of the E.L.F. background noise spectrum, paper presented at the URSI Fall Meeting, Hanover, New Hampshire.

Abramowitz, M., and I. A. Stegun (ed.) (1964) *Handbook of Mathematical Functions*, National Bureau of Standards, AMS 55.

Balser, M., and C. A. Wagner (1960) Observations of earth–ionosphere cavity resonances, *Nature* **188**, 638–641.

Balser, M., and C. A. Wagner (1962a) Diurnal power variations of the earth–ionosphere cavity modes and their relationship to worldwide thunderstorm activity, *J. Geophys. Res.* **67** (2), 619–625.

Balser, M., and C. A. Wagner (1962b) On frequency variations of the earth–ionosphere cavity modes, *J. Geophys. Res.* **67** (10), 4081–4083.

Balser, M., and C. A. Wagner (1963) Effect of a high-altitude nuclear detonation on the earth–ionosphere cavity, *J. Geophys. Res.* **68** (13), 4115–4118.

Béghin, C. (1967) Rocketborne observations of E.L.F. natural noise during an aurora (in French), *Ann. Géophys.* **23** (2), 275–284.

Benoit, R., and A. Houri (1961) Propagation of very-low-frequencies in the earth–ionosphere system (in French), *Ann. Géophys.* **17** (4), 370–373.

Benoit, R., and A. Houri (1962) Power spectrum measurements of geophysical noise: Application to earth-to-ionosphere cavity (in French), *CR Acad Sci.* **255**, 2496–2498.

Bliokh, P. V., A. P. Nikolayenko, and Yu. F. Filippov (1968) Diurnal variations of the natural frequencies of the earth-ionosphere resonator in relation to the eccentricity of the geomagnetic field, *J. Geomagnet. Aeron.* **8** (2), 198–206.

Brady, A. H., D. D. Crombie, A. G. Jean, A. C. Murphy, and F. K. Stede (1964) Long-lived effects in the *D*-region after the high altitude nuclear explosion of 9 July 1962, *J. Geophys. Res.* **69**, 1921.

Chapman, F. W., and D. L. Jones (1964a) Earth–ionosphere cavity resonances and the propagation of extremely low frequency radio waves, *Nature* **202**, 654–657.

Chapman, F. W., and D. L. Jones (1964b) Observations of earth–ionosphere cavity resonances and their interpretation in terms of a two-layer ionosphere model, *Radio Sci. J. Res. NBS* **68D** (11), 1177–1185.

Chapman, F. W., D. L. Jones, J. D. W. Todd, and R. A. Challinor (1966) Observations on the propagation constant of the earth–ionosphere waveguide in the frequency band 8 c/s to 16 kc/s, *Radio Sci.* **1** (11), 1273–1282.

Cole, R. K. (1965) The Schumann resonances, *Radio Sci.* **69D** (10), 1345–1349.

Cole, R. K., and E. T. Pierce (1965) Electrification in the earth's atmosphere for altitudes between 0 and 100 kilometers, *J. Geophys. Res.* **70** (12), 2735–2749.

Crain, C. M., and H. G. Booker (1964) The effects of ions on low frequency and very low frequency propagation in an abnormally ionized atmosphere, *J. Geophys. Res.* **69** (21), 4713–4716.

Deeks, D. G. (1966) *D*-region electron distributions in middle latitudes deduced from the reflection of long radio waves, *Proc. Roy. Soc.* **291** (1426), 413–427.

Dunn, G. R., P. F. Kuhnle, and R. D. Smith (1964) Experimental research investigation of extremely low frequency propagation, final report, Space General Corp., El Monte, California, Contract AF19 628 1603, AD-437 777 Div. 8.

Egeland, A. (1964) E.L.F. (500–1000 cps) emissions at high latitude, in *Natural Electromagnetic Phenomena Below 30 kc/s* (ed. D. F. Bleil), pp. 157–166.

Erdélyi, A. (ed.) (1953) *Higher Transcendental Functions*, **1**, McGraw-Hill, New York, NY.

Field, E. C. (1969) The propagation of E.L.F. waves under normally and naturally disturbed conditions, *J. Geophys. Res.* **74** (14), 3639–3650.

Fournier, H. (1960) Some aspects of the first high-frequency geomagnetic recordings obtained at Garchy (in French), *CR Acad. Sci.* **251** (7), 962–964.

Galejs, J. (1961a) Terrestrial extremely-low-frequency noise spectrum in the presence of exponential ionospheric conductivity profiles, *J. Geophys. Res.* **66** (9), 2787–2792.

Galejs, J. (1961b) E.L.F. waves in presence of exponential ionospheric conductivity profiles, *IRE Trans. Antenna Propagation* **AP-9** (6), 554–562.

Galejs, J. (1962) A further note on terrestrial extremely-low frequency propagation in the presence of an ionosphere with an exponential conductivity-height profile, *J. Geophys. Res.* **67** (7), 2715–2728.

Galejs, J. (1964) Terrestrial extremely-low-frequency propagation, *Natural Electromagnetic Phenomena Below 30 kc/s* (ed. D. F. Bleil), Proc. NATO Advanced Study Institute, Bad Homburg, Germany, 1963, Plenum Press, New York, NY, pp. 205–258.

GALEJS, J. (1965a) On terrestrial propagation of E.L.F. and V.L.F. waves in the presence of radial magnetic field, *Radio Sci.* **69D** (5), 705–720.
GALEJS, J. (1965b) Schumann resonances, *Radio Sci.* **69D** (8), 1043–1055.
GALEJS, J. (1967) Propagation of V.L.F. waves below anisotropic ionosphere models with a dipping static magnetic field, *Radio Sci.* **2** (12), 1497–1512.
GALEJS, J. (1968a) Propagation of E.L.F. and V.L.F. waves below an anisotropic ionosphere with a dipping static magnetic field, *J. Geophys. Res.* **73** (1), 339–352.
GALEJS, J. (1968b) E.L.F. and V.L.F. fields of a horizontal electric dipole, *IEEE Trans. Antenna Propagation* **AP-16** (6), 689–700.
GALEJS, J. (1969a) V.L.F. modes below an idealized anisotropic ionosphere, *Radio Sci.* **4** (6), 491–516.
GALEJS, J. (1969b) Near fields and antipodal fields in the terrestrial earth-to-ionosphere wave guide, *Proc. IEE* **116** (7), 1150–1158.
GALEJS, J. (1970a) *F*-layer Reflections and Ion Effects in the Propagation of Terrestrial E.L.F. Waves, *J. Geophys. Res.* **75** (13), 2529–2539.
GALEJS, J. (1970b) Frequency variations of Schumann resonances, *J. Geophys. Res.* **75** (16), 3237–3251.
GALEJS, J., and M. MENTZONI (1968) Propagation of E.L.F. and V.L.F. waves below models of naturally perturbed ionospheres, *J. Geophys. Res.* **73** (13), 4439–4443.
GENDRIN, R. (1967a) E.L.F. and micropulsations, Part I (in French), *Ann. Géophys.* **23** (1), 145–152.
GENDRIN, R. (1967b) E.L.F. and micropulsations: Part III (in French), *Ann Géophys.* **23** (2), 299–311.
GENDRIN, R., and R. STEFANT (1962) Effects of the very high altitude nuclear explosion of the July 9, 1962, on the earth to ionosphere cavity resonances. experimental results and interpretation (in French), *CR. Acad. Sci.* **255**, 2273–2275 and 2493–2495.
GENDRIN, R., and R. STEFANT (1964) Magnetic records between 0.2–30 c/s, in *Propagation of Radio Waves at Frequencies Below 300 kc/s* (ed. W. T. Blackband), Pergamon Press, Oxford, pp. 371–400.
Handbook of Geophysics (1960), USAF Air Research and Development Command, Air Force Cambridge Research Center, Macmillan Co., New York, NY.
HANSON, W. B. (1961) Structure of the ionosphere, in *Satellite Environment Handbook* (ed. F. S. Johnson) Stanford University Press, Stanford, California, pp. 27–46.
HEPBURN, F., and E. T. PIERCE (1953) Atmospherics with very-low-frequency components, *Nature (London)* **171**, 837–838.
HUGHES, H. G. (1964) Power spectral analyses of modulated earth–ionosphere cavity resonances, *J. Geophys. Res.* **69**, 4709–4712.
JEAN, A. G., JR., A. C. MURPHY, J. R. WAIT, and D. F. WASMUNDT (1961) Propagation attenuation rates at E.L.F., *J. Res. NBS Radio Propagation* **65D** (5), 475–479.
JOHLER, J. R., and L. A. BERRY (1966) On the effect of heavy ions on L.F. propagation, with special reference to the nuclear environment, *Radio Sci.* **1** (3), 303–307.
JOHLER, J. R., and R. L. LEWIS (1969) Extra low-frequency radio-wave field calculations with the zonal harmonic series, *J. Geophys. Res.* **74** (10), 2459–2470.
JONES, D. L. (1967) Schumann resonances and E.L.F. propagation for inhomogeneous, isotropic ionosphere profiles, *J. Atmos. Terr. Physics* **29**, 1037–1044.
JONES, D. L., and D. T. KEMP (1969) Experimental and theoretical observations on the impulse excitation of Schumann resonances, King's College, University of London.
KOENIG, H. (1958) Atmospherics of lowest frequencies (in German), dissertation at the Technical University of Munich.
KOENIG, H. (1959) Atmospherics of lowest frequencies (in German), *Z. Angew. Phys.* **11** (7), 264–274.
KOENIG, H., E. HAINE, and C. H. ANTONIADIS (1961) Measurement of atmospherics of lowest frequencies in Bonn, *Z. Angew. Phys.* **13** (8), 364–367.
LARGE, D. B., and J. R. WAIT (1968) Theory of electromagnetic coupling phenomena in the earth–ionosphere cavity, *J. Geophys. Res.* **73** (13), 4335–4362.
LARSEN, T. R., and A. EGELAND (1968) Fine structure of the earth–ionosphere cavity resonances, *J. Geophys. Res.* **73** (15), 4986–4989.
LIEBERMANN, L. (1956a) Extremely-low-frequency electromagnetic waves: I, Reception from lightning, *J. Appl. Phys.* **27** (12), 1473–1476.
LIEBERMANN, L. (1956b) Extremely-low-frequency electromagnetic waves: II, Propagation properties, *J. Appl. Phys.* **27** (12), 1477–1483.
LOKKEN, J. E., (1964) Pacific Naval Laboratory BC, private communication.
LOKKEN, J. E. J. A. SHAND, C. S. WRIGHT, L. H. MARTIN, N. M. BRICE, and R. A. HELLIWELL (1961) Stanford Pacific Naval Laboratory Conjugate Point Experiment, *Nature* **192**, 319.

LOKKEN, J. E., J. A. SHAND, and C. S. WRIGHT (1962) A note on the classification of geomagnetic signals below 30 c/s, *Canadian J. Phys.* **40**, 1000–1009.
MADDEN, T. R., and W. THOMPSON (1965) Low-frequency electromagnetic oscillations of the earth–ionosphere cavity, *Rev. Geophys.* **3**, 211–254.
MAEDA, K. (1969) Mid-latitude electron density profile as revealed by rocket experiments, *J. Geomagnet. Geoelectr.* **21** (2), 557–567.
MAEDA, K., and H. MATSUMOTO (1962) Conductivity of the ionosphere and current system, *Rep. Ionosphere Space Res. Japan* **16** (1), 1–26.
MAXWELL, E. L. (1967) Atmospheric noise from 20 Hz to 30 kHz, *Radio Sci.* **2** (6), 637–644.
MAXWELL, E. L., and D. L. STONE (1966) *V.L.F. Atmospheric Noise Predictions*, Report 92-F-1 on Contract Nobsr 93159, DECO Electronics, Inc., Boulder, Colorado.
MOROZUMI, H. M. (1965) Diurnal variation of aurora zone geophysical disturbances, *Rep. Ionosphere Space Res. Japan* **19**, (3), 286–298.
MORSE, P. M., and H. FESHBACH (1953) *Methods of Theoretical Physics*, McGraw-Hill, New York, NY.
NARCISI, R. S., and A. D. BAILEY (1965) Mass spectrometric measurements of positive ions at altitudes from 64 to 112 kilometers, *J. Geophys. Res.* **70** (15), 3687–3700.
NELSON, P. H. (1967) Ionospheric perturbations and Schumann resonance data, Ph.D. dissertation (geophysics), Massachusetts Institute of Technology, Cambridge, Massachusetts.
OGAWA, T., Y. TANAKA, T. MIURA, and M. OWAKI (1966) E.L.F. noise-bursts and enhanced oscillations. associated with the solar-flare of July 7, 1966, *Rep. Ionosphere Space Res. Japan* **20** (4), 528–536.
OGAWA, T., Y. TANAKA, T. MIURA, and M. YASUHARA (1966) Observations of natural E.L.F. electromagnetic noises by using the ball antennas, *J. Geomagnet. Geoelectr.* **18** (4), 443–454.
PIERCE, E. T. (1960) Some E.L.F. phenomena, *J. Res. NBS Radio Propagation* **64D** (4), 383–386.
PIERCE, E. T. (1968) A relationship between thunderstorm days and lightning flash density, *Trans. Am. Geophys. Un.* **49**, 686.
PIERCE, E. T. (1969) *The Thunderstorm as a Source of Atmospheric Noise at Frequencies Between 1 and 100 kHz*, Report DASA 2299, Stanford Research Institute, Menlo Park, California.
PIGGOTT, W. R., and E. V. THRANE (1966) The electron densities in the *E* and *D* regions above Kjeller, *J. Atmos. Terr. Physics* **28**, 467–479.
POLK, C. (1964) Some recent magnetic field measurements in the earth–ionosphere resonance region, in *Propagation of Radio Waves at Frequencies Below 300 kc/s* (ed. W. T. Blackband), Pergamon Press, Oxford, pp. 435–456.
POLK, C. (1968) Relation of E.L.F. noise and Schumann resonances to thunderstorm activity, paper presented at the 4th International Conference on the Univ. Aspects of Atmospheric Electricity, May 12–18, Tokyo, Japan.
POLK, C., and F. FITCHEN (1962) Schumann resonances of the earth-ionosphere cavity-extremely low frequency reception at Kingston, RI, *J. Res. NBS Radio Propagation* **66D** (3), 313–318.
POLK, C., F. HUCK, and I. P. YU (1963) University of Rhode Island, private communication.
PRINCE, C. E., and F. X. BOSTICK (1964) Ionospheric transmission of transversely propagated plane waves at micropulsation frequencies and theoretical power spectrums, *J. Geophys. Res.* **69** (15), 3213–3234.
RICE, S. O. (1944, 1945) Mathematical analysis of random noise, *Bell System Tech. J.* **23**, 282–332; **24**, 46–156, eqn. 3.3–11.
RYCROFT, M. J. (1963) Low frequency disturbances of natural origin of the electric and magnetic fields of the earth, Ph.D. thesis, University of Cambridge.
RYCROFT, M. J. (1965) Resonances of the earth–ionosphere cavity observed at Cambridge, England, *Radio Sci.* **69D** (8), 1071–1081.
SCHUMANN, W. O. (1952a) On the radiation free selfoscillations of a conducting sphere, which is surrounded by an air layer and an ionospheric shell (in German), *Z. Naturforsch.* **7a**, 149–154.
SCHUMANN, W. O. (1952b) On the damping of electromagnetic selfoscillations of the system earth–air–ionosphere (in German), *Z. Naturforsch.* **7a**, 250–252.
SCHUMANN, W. O. (1957) Electrical selfoscillations of the cavity earth-air-ionosphere (in German), *Z. Angew. Phys.* **9**, 373–378.
SOLOVYEV, V. A. (1969) Time and space characteristics of thunderstorm activity, *Planetary Electrodynamics* (ed. S. C. Coroniti and J. Hughes), Gordon & Breach, New York, NY.
STEFANT, R. (1963) Application of an induction magnetometer to the study of Schumann resonances (in French), *Ann. Géophys.* **19** (3), 250–283.
STRATTON, J. A. (1941) *Electromagnetic Theory*, McGraw-Hill, New York, NY.
TAYLOR, W. L. (1969) Observed directional effects in E.L.F., attenuation rates and phase velocities from slow tail components of atmospherics, paper presented at the URSI Spring Meeting, Washington, DC.

TEPLEY, L. R. (1959) A comparison of sferics as observed in the very-low-frequency and extremely-low-frequency bands, *J. Geophys. Res.* **64** (12), 2315–2329.

TEPLEY, L., R. C. WENTWORTH, K. G. LAMBERT, H. V. PRENTISS, K. D. AMUNDSEN, and D. R. HILLENDAHL (1963) Sub E.L.F. geomagnetic fluctuations; III, Final Report Contract A.F. 19(628)-462, Lockheed Missile and Space Co., Palo Alto, California.

VALLEY, S. L. (ed.) (1965) *Handbook of Geophysics and Space Environments*, Air Force Cambridge Research Laboratories, McGraw-Hill, New York, NY.

WAIT, J. R. (1962) *Electromagnetic Waves in Stratified Media*, Macmillan, New York, NY.

WAIT, J. R. (1964) On the theory of Schumann resonances in the earth–ionosphere cavity, *Canadian J. Phys.* **42**, 575–582.

WAKAI, N. (1967) Quiet and disturbed structure and variations of the night-time E region, *J. Geophys. Res.* **72** (17), 4507–4517.

WHIPPLE, F. J. W. (1929) On the association of the diurnal variation of electric potential gradient in fine weather with the distribution of thunderstorms over the globe, *Quart. J. Roy. Met. Soc.* **55**, 1–17.

WILLIAMS, J. C. (1959) Thunderstorms and V.L.F. radio noise, Ph.D. thesis, Harvard University, Division of Engineering and Applied Physics.

WRIGHT, C. S. (1964) Micropulsations at near conjugate stations in the auroral zones and their association with other ionospheric phenomena, in *Natural Electromagnetic Phenomena Below 30 kc/s* (ed. D. F. Bleil), Proc. NATO Advanced Study Institute, Bad Homburg, Germany, 1963, Plenum Press, New York, NY, pp. 287–318.

ZMUDA, A. J., B. W. SHAW, and C. R. HAAVE (1963) V.L.F. disturbances and the high-altitude nuclear explosion of July 9, 1962, *J. Geophys. Res.* **68** (3), 745–758.

CHAPTER 8

V.L.F. PROPAGATION

Abstract. The T.M. and T.E. modes excited by horizontally and vertically polarized line sources are investigated for homogeneous, exponentially varying and composite daytime and nighttime ionosphere models. Ion effects are investigated for several models of a perturbed ionosphere. Because of ionospheric anisotropy, the vertically polarized source excites also T.M. field components with wave numbers corresponding to T.E. modes; and a horizontally polarized source excites T.E. fields corresponding to T.M. modes, particularly for the higher frequencies at nighttime and for propagation towards west. Among the field components tangential to the ground surface, T.M. fields tend to dominate with the exception of T.E. modes at daytime and for lower frequencies also at night. T.M. modes dominate in the nighttime mode sum (or interference pattern) for propagation towards east, but the two lower T.E. modes contribute significantly if propagation is towards west. For higher frequencies at nighttime, the ratio of T.E. to T.M. field components may change for various directions of propagation in such a way that a quasi-T.E. (or T.M.) mode appears to change into a quasi-T.M. (or T.E.) mode.

Simplified computational models which neglect the radial component of the earth's static magnetic field are justified under daytime conditions. At nighttime such calculations provide extreme changes in the attenuation rates and phase-velocity variations, which are opposite to the ones observed with a dipping static magnetic field. The direction dependence of the phase velocity is eliminated by decreasing the strength of the static magnetic field. The present calculations are compared with attenuation rate, mode interference, and phase delay fluctuation measurements. In nighttime propagation towards west at frequencies near 20 kc/s, the T.M. field components of the $T.E._1$ mode are excited more effectively and attenuated less than the field components of the $T.M._1$ mode.

8.1 Introduction and Summary

V.L.F. signals exhibit low attenuation, and this frequency band is widely used in low data rate communication systems. The phase of such transmissions is highly stable and it undergoes nearly reproducible diurnal variations [Pierce, 1955; Crombie, 1964; Westfall, 1967]. This phase stability leads to applications in navigational systems [Pierce, 1965], frequency comparisons [Blair *et al.*, 1967] and clock synchronization [Reder *et al.*, 1961] or timing systems [Fey and Looney, 1966]. Such applications will not be discussed here, but the developments will concentrate on propagational aspects: wave parameters like phase velocities, attenuation rates, and excitation factors will be derived under what are believed to be realistic conditions.

The basic field representations and also propagation characteristics have been discussed in Chapter 4 in conjunction with a uniform spherical shell bounded by a homogeneous ground surface and an isotropic sharply bounded ionosphere. Such an ionosphere model is obviously oversimplified, and a better accuracy may be expected from more refined models which consider the stratifications and/or anisotropy caused by the geomagnetic field. The T.E. and T.M. field components are uncoupled in an isotropic ionosphere and also in an ionosphere where the direction of wave propagation is perpendicularly to a horizontal geomagnetic field, as for

propagation alo[illegible]e magnetic equator. Under such conditions the wave propagation is relatively simple to analyze [Galejs, 1964a, b, 1967a]; assuming a constant value of the magnetic field B_0 it can be shown that the phase-velocity variations observed for different directions of nighttime propagation are opposite to the ones of experimental data. In other work [Wait and Spies, 1965; Watt, 1967] the strength of the magnetic field is not given explicitly, and the numerical results reflect varying amounts of anisotropy. For low reflection or reference heights B_0 is too high, and for larger reflection heights B_0 is extremely small, which results in nearly isotropic propagation conditions. However, such simplified ionosphere models may have certain merits under daytime conditions [Galejs, 1969b].

Ionosphere models with a purely horizontal magnetic field are restrictive, and most of the calculations will be reported for a dipping magnetic field. Such an anisotropic ionosphere will cause coupling between the T.E. and T.M. field components, and waves corresponding to T.E. modes may have significant T.M. components and vice versa. Baybulatov and Krasnushkin [1967] indicate that T.M.$_1$, T.E.$_1$, and T.M.$_2$ modes must be taken into account for nighttime propagation. Pappert [1968] and Snyder and Pappert [1969] discuss also higher order modes.

Terrestrial V.L.F. propagation should be considered in a curved geometry, but the differential equations of the fields in the ionosphere are separable for arbitrary directions of the static magnetic field only for cylindrical stratifications. Although it is possible to assume a cylindrical ionosphere on the top of a spherical air shell and a spherical earth [Madden and Thompson, 1965], the mathematical formalism appears to be more consistent by assuming a cylindrical geometry of Fig. 8.1 for the ionosphere, the airspace, and also for the ground surface. This geometry can be readily treated for excitation by vertically and horizontally polarized line sources located at $r_s = a+y_s$ and $\varphi = 0$. However, in this approach it will be necessary to relate the line source excited fields in a cylindrical shell to the more realistic dipole excited fields of a spherical shell. It is also possible to treat a spherical shell with anisotropic boundaries [Wait, 1963], but it will not be possible to determine the required ionospheric parameters in a corresponding spherical geometry.

The ionospheric fields for $r > r_i$ have been discussed in detail in Chapter 6, and the results are applicable to the derivation of field expressions in the space between the earth and the ionosphere. The line source excited fields can be expressed in a harmonic series, which is transformed in a residue series in Chapter 5. The final expressions of these residue series (or mode summations) involve height-gain functions and normalized impedances that are identical to those computed under isotropic conditions in Chapter 4. However, the excitation factors, can be reduced to, but cannot be deduced from, the excitation factors of the isotropic shell. There appear no simple methods for deducing the amplitudes of T.M. field components excited by vertically polarized sources with wave numbers corresponding to T.E. modes (or T.E. field components excited by horizontally polarized sources with wave numbers corresponding to T.M. modes). The T.E. field components excited by a vertically polarized source and the T.M. field components excited by a horizontally polarized source will also depend on a coupling impedance Z_{eh} that is defined as the ratio between the transverse horizontal electric and magnetic fields at the ground surface.

Idealized sharply bounded homogeneous or exponentially varying anisotropic ionospheric models are discussed in Sections 8.2 and 8.3. Vertically polarized sources excite T.M. field components with wave numbers corresponding to T.E. modes that may dominate over the

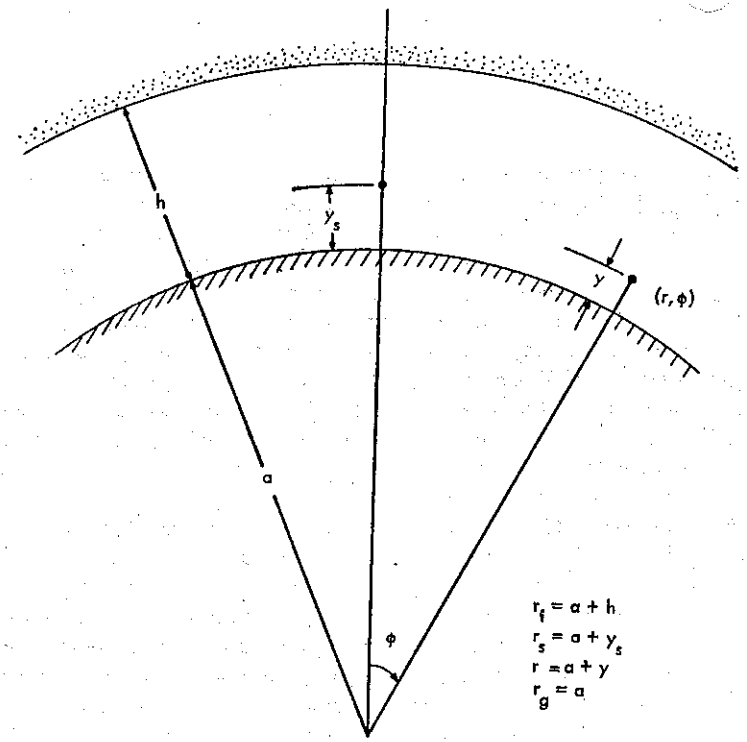

FIG. 8.1 Geometry of the Cylindrical Shell

corresponding components of T.M. modes, particularly at higher frequencies for the E.W. direction of nighttime propagation. Under similar conditions, horizontally polarized sources excite also significant T.E. field components with wave numbers corresponding to T.M. modes. For E.W. direction of propagation, the T.M.$_1$ mode becomes weakly excited for higher frequencies and for small dip angles of the static magnetic field. The characteristics of higher order T.M. modes depend also on the dip angle for east–west direction of propagation: modes, which for radial static magnetic field can be designated as modes n, exhibit the character of modes $(n-1)$ for a nearly horizontal static magnetic field.

Exponential ionosphere models of Section 8.3 have been considered in the presence of a purely horizontal static magnetic field. Under daytime conditions, it is permissible to neglect the radial component of the static magnetic field in the computations of mode characteristics. However, at nighttime this leads to excessive attenuation rates for the E.W. direction of propagation; the resulting phase velocities exhibit variations that are opposite to the variations observed for the various directions of propagation in the presence of a dipping static magnetic field. With a decreasing strength of the static magnetic field, the nighttime phase velocities become nearly independent of the directions of propagation; and also the variations of the attenuation rates are decreased.

The daytime ionosphere models of Deeks [1966] and of Bain and May [1967] of Section 8.4 exhibit propagation characteristics comparable to those of a simpler exponential ionosphere model. The exponential and sharply bounded nighttime ionosphere models exhibit lower attenuation rates for the quasi-T.E. $m = 2$ mode for the E.W. direction of propagation than the Deeks' wintertime model; for the former nighttime ionosphere models, the $m = 2$ mode perturbs significantly the nighttime mode summation for frequencies near 20 kc/s. A decreasing ground conductivity decreases phase velocities and increases attenuation rates; however, the daytime attenuation rates of the m modes are not affected by σ_g. For vertically polarized sources, a decreasing ground conductivity increases the excitation factors of the n modes; but it does not change the excitation factors of the m modes. For horizontally polarized sources, the excitation factors are inversely proportional to the ground conductivity.

Wave polarization is discussed in Section 8.5. In the fields tangential to the ground surface, the T.M. field components tend to dominate, with the exception of the T.E. modes at daytime and for lower frequencies also at night. The quasi-T.E. modes exhibit larger ratios of the T.E. to T.M. components than the quasi-T.M. modes; under nighttime conditions at higher frequencies, this ratio may change with a changing direction of propagation in such a way that an m type of mode appears to change into an n mode although both modes remain essentially T.M. in character.

Nighttime V.L.F. mode interference patterns of Section 8.6 indicate that T.M.$_1$ and T.M.$_2$ modes characterize the propagation in the W.E. direction; for E.W. propagation the T.E.$_1$ mode may dominate over the T.M.$_1$ mode and the interference patterns are further perturbed by the presence of T.E.$_2$ modes. Attenuation rates of the dominant waveguide mode cannot be readily deduced from the decay rate of an interference pattern.

The calculated attenuation rates compare with the attenuation rate measurements of Bickel [1967] for the frequency of 19.8 kc/s. The calculated propagation parameters are consistent with mode interference distance measurements of Crombie [1966] for the frequency range of 18–24 kc/s and with phase delay measurements of Burgess [1967] for frequencies near 10 kc/s, which cannot be explained using simpler exponential near isotropic ionosphere models [Wait and Spies, 1965]. The E.W. measurements of Bickel [1967] and Crombie [1966] are explained using T.M. field components of the quasi-T.E.$_1$ mode instead of the usually assumed components of the quasi-T.M.$_1$ mode.

A perturbed ionosphere is illustrated in Section 8.7 with electron-density profiles that are representative of solar flare induced sudden ionospheric disturbances (S.I.D.), auroral absorption and polar cap absorption (P.C.A.) events [Galejs and Mentzoni; 1968]. P.C.A. events (which give the most dramatic effects) cause a lowering of the effective ionosphere; the resulting propagation is nearly isotropic and the phase velocities are increased. The attenuation rates are increased also in the lower part of the V.L.F. band. The propagation parameters are affected to a lesser degree by the other events, which are not uniquely distinguishable from propagation characteristics obtainable under quiet daytime conditions.

Ion effects are considered for several models of a perturbed ionosphere and with various choices of ion collision frequencies and molecular weights. Comparisons with atmospheric conductivity measurements tend to justify the use of ion collision frequencies which exceed the collision frequency between neutral particles and of molecular weights that are larger than the molecular weights for the usually assumed atmospheric constituents. With the exception of extreme perturbations where particle densities exceed 10^0 cm^{-3}, the ion contributions appear to be marginal in the V.L.F. range.

Under isotropic conditions the fields excited by a vertical electric dipole are purely T.M. in character; the fields of a horizontal electric dipole are T.M. in the axial and T.E. in the broadside directions. For elevated horizontal electric dipoles the T.E. field components may become comparable to T.M. field components following Chapter 4, but the vertical electric field E_r^{he} still vanishes in the broadside direction. An anisotropic ionosphere causes coupling between T.E. and T.M. modes and for any given mode the field components of a horizontal electric dipole remain finite for both the axial and endfire directions, which may be seen from Section 8.8.

During daytime the ionospheric anisotropy is relatively weak and the vertical electric fields E_r^{he} of a horizontal electric dipole exhibit a minimum near the broadside direction for W.E. and at short distances also for E.W. propagation; during nighttime the fields exhibit maximum values near the broadside direction. For elevated sources and observation points, the field components E_r^{he} of a horizontal electric dipole become comparable to E_r^{ve} of a vertical electric dipole. Inclined electric dipoles exhibit amplitude variations of the vertical electric fields E_r with changes of the direction relative to the dipole axis. The amplitude variations are particularly pronounced for E.W. direction of nighttime propagation.

8.2 Propagation Parameters for a Sharply Bounded Homogeneous Ionosphere Model

The propagation parameters are investigated first for a homogeneous ionosphere of electron density $N_e = 350$ cm^{-3} and collision frequency $\nu = 10^6$ sec^{-1}, which is sharply bounded at a height $h = 85$ km. For this ionosphere model, the conductivity component σ_0 is computed following Chapter 2 as $\sigma_0 = 2.83\times10^{-2}\times N_e/\nu = 10^{-5}$, which is the same as the conductivity σ of one of the isotropic ionosphere models studied in Chapter 4. The parameters Re $S = c/v_{ph}$ and attenuation rate α are computed from (191) or from an iterative solution of (192) and (193) of Chapter 5. The static magnetic field of $B_0 = 0.5\times10^{-4}$ M.K.S. or 0.5 gauss (the gyro frequency $|\omega_c| = 8.8\times10^6$ sec^{-1}) has a dip angle $I = -\Theta$. The propagation is assumed to be either in the E.W. or in the W.E. directions along a constant magnetic latitude. In the curves plotted in Fig. 8.2, the quasi-T.M. modes are designated by numbers n and the quasi-T.E. modes by numbers m. There appear no ambiguities in mode numbering for W.E. direction of propagation. However, for propagation in E.W. direction, the phase velocity or Re S vary significantly with changes in the angle Θ. The solutions corresponding to the $n = 1$ mode become weakly excited with a decreasing angle Θ ($|A^e_{n=1}|$ changes from 0.17 to 0.03 as Θ is varied from 90 to 20°), and this solution could not be found for a horizontal static magnetic field ($\Theta = 0$). The lowest observed mode for E.W. propagation and $\Theta = 0$ is designated as $n = 2$ (1), which implies that the $n = 2$ mode of $\Theta = 90°$ assumes the character of the $n = 1$ mode for $\Theta = 0°$. This mode corresponds to the $n = 1$ mode for $\omega_c/\nu \approx 10$ in fig. 2 of Galejs [1967a] for a horizontal magnetic field; the $n = 2$ (1) mode corresponds to the $n = 1$ mode for $\Theta = 90° - \beta \neq 0$ and to the $n = 2$ mode for $\Theta = 90°$ in fig. 3 of Galejs [1967b]. Using the same convention, the mode $n = 3$ (2) assumes the character of mode 3 and 2 for Θ large and small, respectively.

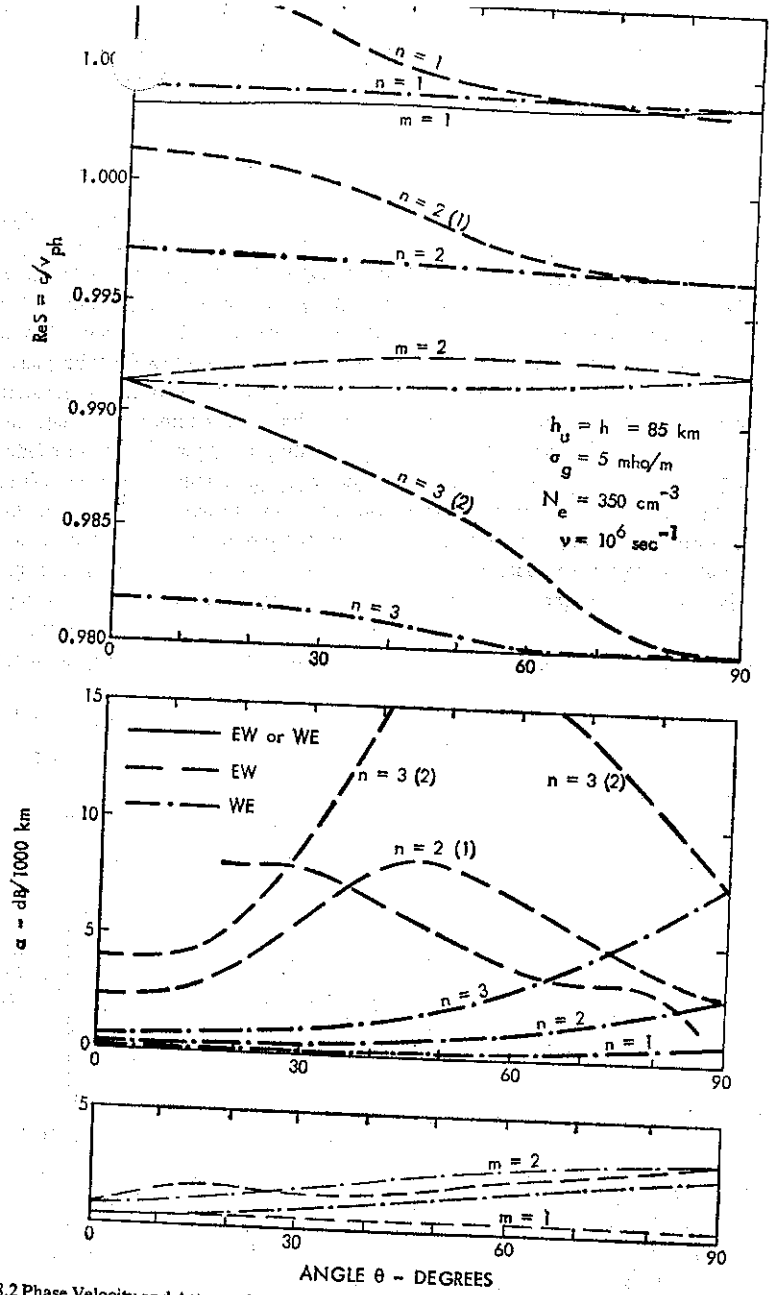

FIG. 8.2 Phase Velocity and Attenuation Rates for a Sharply Bounded Homogeneous Ionosphere Model. $f = 20$ kc/s

The characteristics of the various modes can be illustrated further by computing the height-gain functions from (272) and (275) of Chapter 5. All the functions $G_1^J(y)$ of Fig. 8.3A exhibit a single dip near the ionospheric boundary. $|G_1^e(y)| > 1$ for all values y in the $n = 1$ mode for E.W. direction of propagation and $\Theta = 45°$, which indicates from (282) of Chapter 5 that this mode becomes weakly excited with the decreasing angle Θ. For $\Theta = 0$, the $n = 2$ (1) mode exhibits also a single dip although at the somewhat lower altitude y than the other $n = 1$ or $m = 1$ modes. The function $G_q^J(y)$ of the n or $m = 2$ mode exhibits two dips over the y range shown in Fig. 8.3B. The function $G_q^e(y)$ of mode $n = 2$ (1) exhibits two shallow minima while the function $G_q^h(y)$ of the same mode exhibits only one minimum. The mode $n = 2$ (1) appears to exhibit a character that is intermediate between the n or $m = 1$ and 2 modes, respectively.

The height-gain functions $G_q^J(y)$ are quite similar for modes $n = 1$ and $m = 1$ or for modes $n = 2$ and $m = 2$. Consequently, the field components of T.E. and T.M. modes cannot be considered to be orthogonal in the presence of an anisotropic ionosphere.

The normalized impedance $|\Delta_1^J(y)|$ of Fig. 8.4 has been computed from (273) and (276) of Chapter 5. It is seen that the $n = 1$ mode for $\Theta = 45°$ and E.W. directional propagation and the $n = 2$ (1) mode of $\Theta = 0°$ approximate the characteristics of the other n or $m = 1$

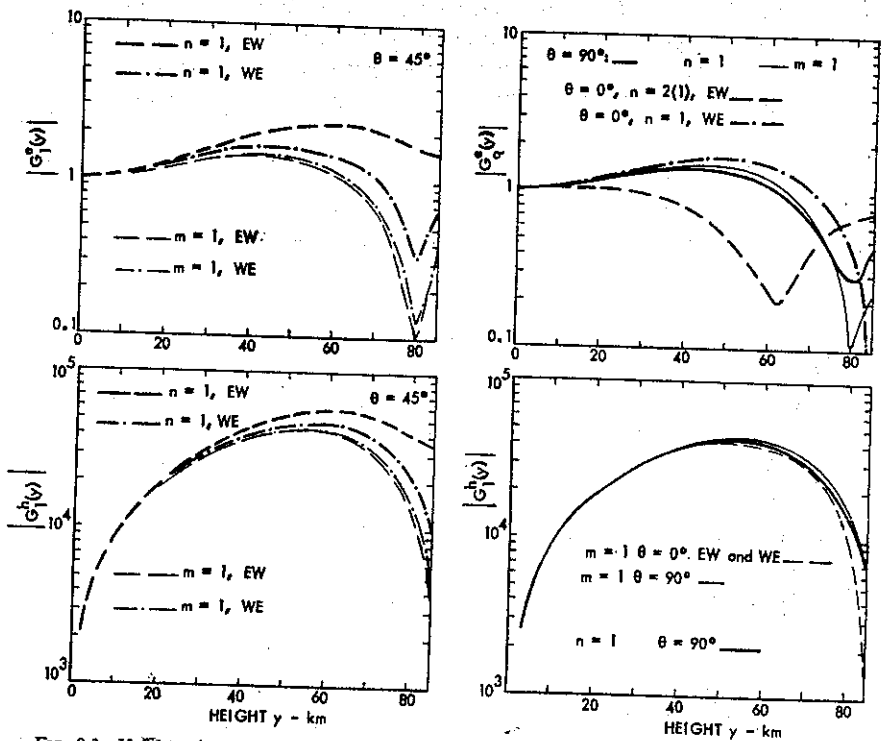

FIG. 8.3A Height-gain Functions $G_q^J(y)$ for a Sharply Bounded Homogeneous Ionosphere Model. $n = 1$ or 2(1); $m = 1$.

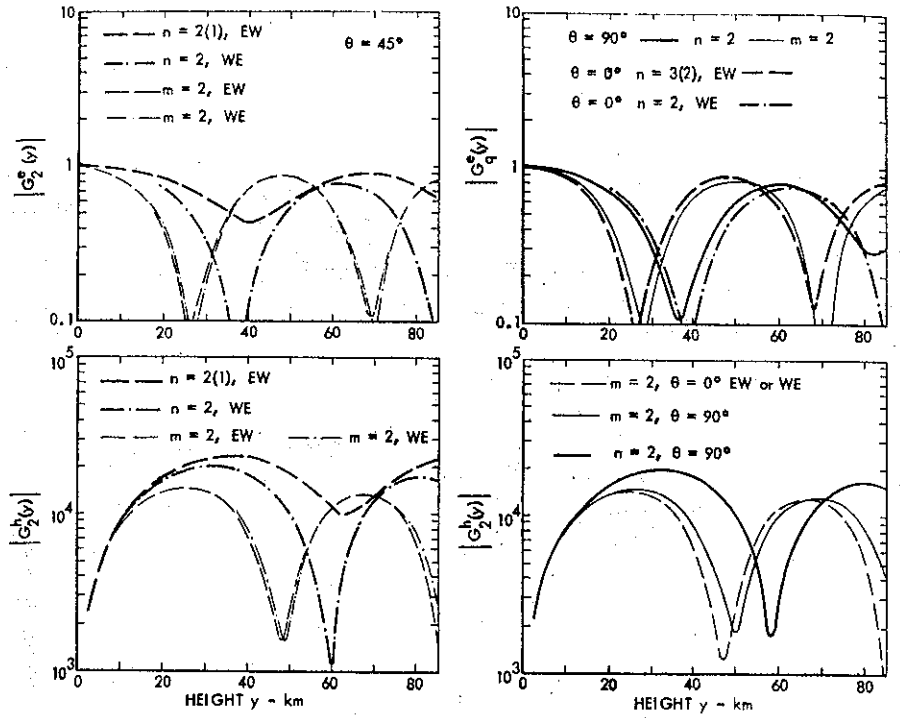

FIG 8.3B Height-gain Functions $G_q^l(y)$ for a Sharply Bounded Homogeneous Ionosphere Model. $n = 2, 2(1)$ or $3(2)$; $m = 2$.

modes, which are essentially the same as the n or $m = 1$ modes under isotropic conditions in Figs. 4.11A and B and 4.14A and B (pp. 117 and 120).

The propagation parameters S in the earlier work of Galejs [1967b, 1968] have been with a discontinuity at angles Θ, where the $n = 1$ mode becomes weakly excited. The method of finding the roots of the modal equation is more refined in the present study, and it is shown that the propagation parameters are continuous. However, the character of a given mode may change for various angles Θ. The changing character of the modes for E.W. direction of propagation is denoted by a double number $n = i(j)$, where the number i denotes the mode character for a radial static magnetic field and j denoted the mode character for a nearly horizontal static magnetic field.

The frequency variations of phase velocity and of attenuation rates are illustrated in Fig. 8.5 for the same sharply bounded homogeneous ionosphere model with $\Theta = 45° = \text{constant}$. For the quasi-T.M. modes (n), Re $S = c/v_{ph}$ and α are larger for propagation in the E.W. direction; for quasi-T.E. (m) modes, Re S is larger for E.W. direction but α is larger for the W.E. direction of propagation, which can be also seen from Fig. 8.2 for $f = 20$ kc/s and various angles Θ.

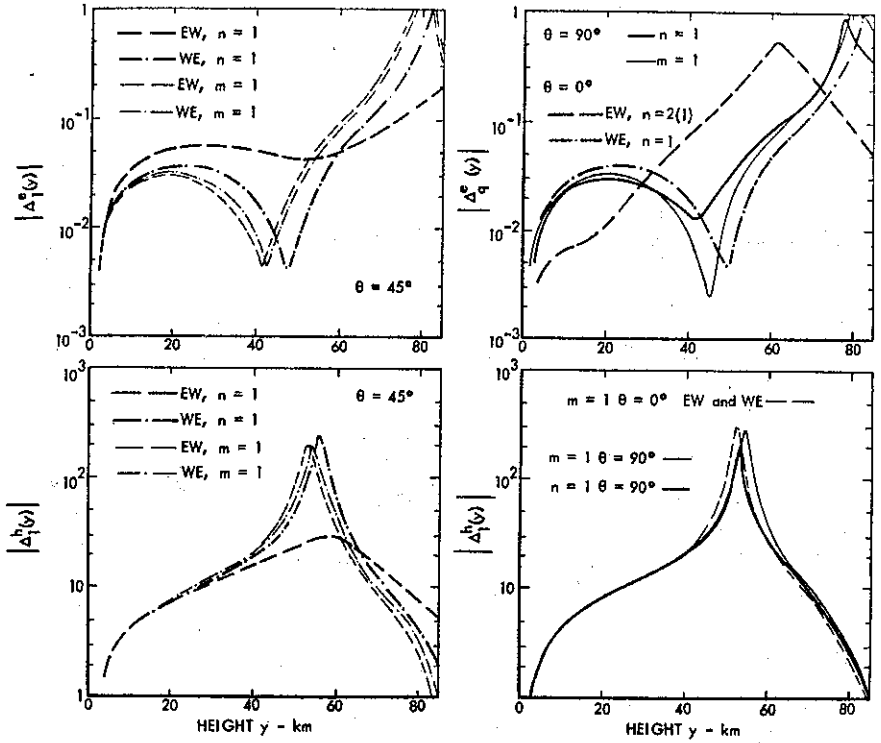

FIG. 8.4 Normalized Impedance $\Delta_q^l(y)$ for a Sharply Bounded Homogeneous Ionosphere Model. $n = 1$ or 2 (1); $m = 1$

The corresponding excitation factors are computed from (274) and (277) of Chapter 5 and are plotted in Fig. 8.6. For a vertically polarized source, the excitation factor of T.M. components, A_n^e, decays with increasing frequency in the $n = 1$ mode and remains of the order of unity in the $n = 2$ mode, similarly as for an isotropic ionosphere in Fig. 4.9 (p. 115). The excitation factors of T.M. components with wave numbers m corresponding to quasi-T.E. modes, A_m^e, are highest for E.W. direction of propagation when, following Fig. 8.14 (p. 320) the fields penetrate more deeply in the ionosphere. The excitation factor A_m^e may assume nonzero values only because of ionospheric coupling between the T.E. and T.M. field components; it can be expected to exhibit its largest values for propagation conditions favoring field penetration in the ionosphere. For $f \approx 10$ kc/s, $|A_m^e| < |A_n^e|$, but the excitation factors A_q^e become comparable in magnitude for the $n = 1$ and $m = 1$ modes in the high frequency end of the V.L.F. range. For propagation in the E.W. direction, $\alpha_{m=1} < \alpha_{n=1}$; and the T.M. field components of the quasi-T.E. $m = 1$ mode may dominate over the fields of the quasi-T.M. mode $n = 1$. Also, the excitation factor of the $m = 2$ mode A_m^e becomes comparable to $A_{n=2}^e$ for E.W. direction and the higher frequencies, and the corresponding attenuation rates $\alpha_{m=2} < < \alpha_{n=2}$ in Fig. 8.5.

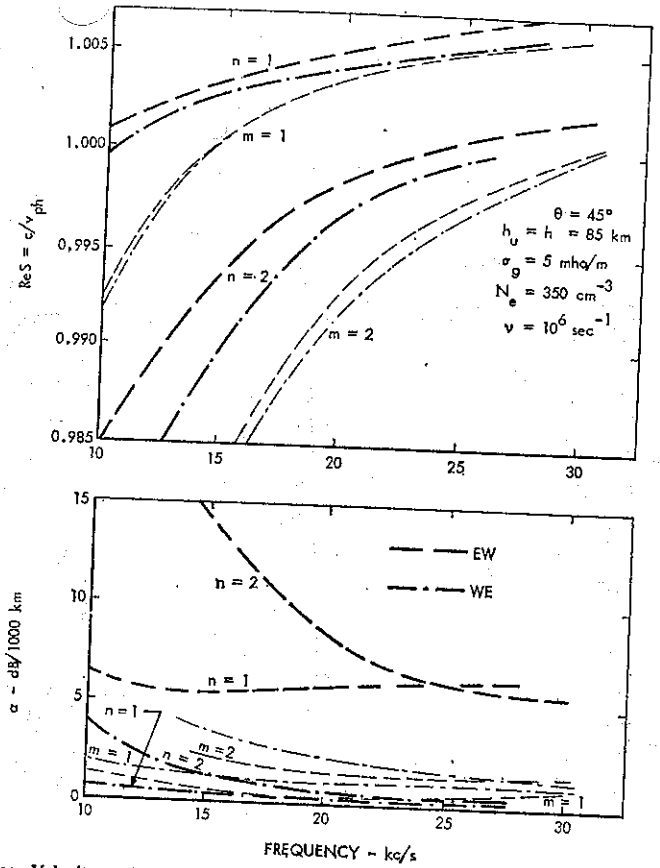

FIG. 8.5 Phase Velocity and Attenuation Rates for a Sharply Bounded Homogeneous Ionosphere Model. $\theta = 45°$

For a horizontally polarized source and wave numbers m corresponding to quasi-T.E modes, the excitation factors of the T.E. components A_m^h are comparable to the excitation factors of T.E. modes for an isotropic ionosphere in Fig. 4.12 (p. 118). The T.E. field components with wave numbers corresponding to quasi-T.M. modes (n) are excited more efficiently for propagation in the E.W. direction when the field penetration in the ionosphere is higher. For higher frequencies, $|A_{m=1}^h| \approx |A_{n=1}^h|$, similarly as for the excitation factors A_q^e.

8.3 Propagation Parameters for Exponential Ionosphere Models

A sharply bounded homogeneous ionosphere model is a rather gross idealization of the gradually varying lower ionosphere edge. This gradual taper may be approximated by an exponential height variation of collision frequencies and electron densities which provides

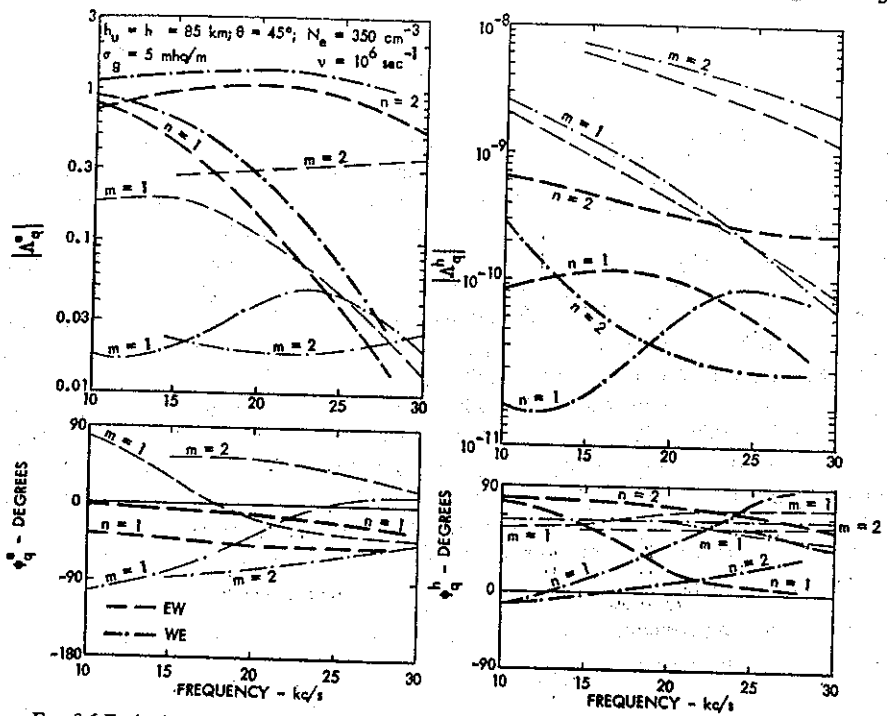

FIG. 8.6 Excitation Factors $A_q^i = |A_q^i| \exp(i\varphi_q^i)$ for a Sharply Bounded Homogeneous Ionosphere Model. $\theta = 45°$

an exponential change of the effective ionospheric conductivity in the form

$$\sigma = \sigma(y_0) \exp[\beta(y - y_0)], \tag{1}$$

where β is near 0.3 in daytime and in the range of 0.44–0.5 at night [Galejs 1961, 1962]. Similar ionosphere models have been used in conjunction with the purely horizontal static magnetic field by Galejs [1964a, b], Wait and Spies [1965], and Pappert *et al.* [1967]. In the present study, the homogeneous ionosphere model of $N_e = 350\,\text{cm}^{-3}$, sharply bounded at $y = 85$ km, is changed into $N_e = 350 \exp[0.35(y-85)]$ as an approximation of nighttime conditions. The daytime electron density is approximated by $N_e = 350 \exp[0.138(y-72.5)]$. The collision frequency profile of Pigott and Thrane [1966] is approximated as $\nu = 0.725 \times 10^6 \exp[0.164(85-y)]$. Noting that $\sigma \sim N_e/\nu$, the conductivity assumes the form (1) with $\beta = 0.302$ in daytime and $\beta = 0.514$ in the nighttime model.

The propagation parameters of the nighttime ionosphere model are shown in Figs. 8.7A, B, and 8.8. For the static magnetic field at an angle $\Theta = 45°$, Re S shown in Fig. 8.7A is larger than under isotropic conditions ($\omega_c = 0$). The parameter Re S is larger and the phase velocity is smaller for propagation in the E.W. direction. The attenuation rates of the isotropic model are comparable to the highest attenuation rates observed under anisotropic conditions,

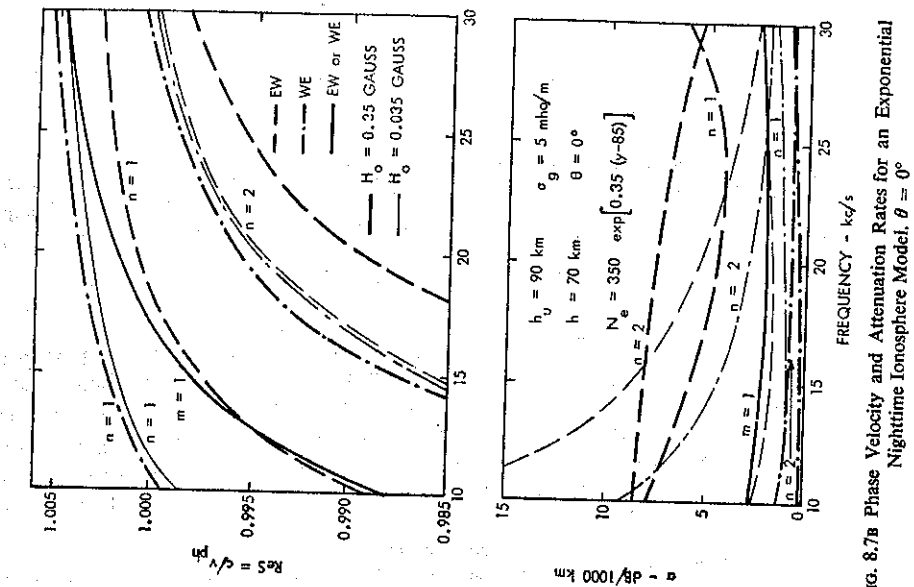

FIG. 8.7B Phase Velocity and Attenuation Rates for an Exponential Nighttime Ionosphere Model. $\theta = 0°$

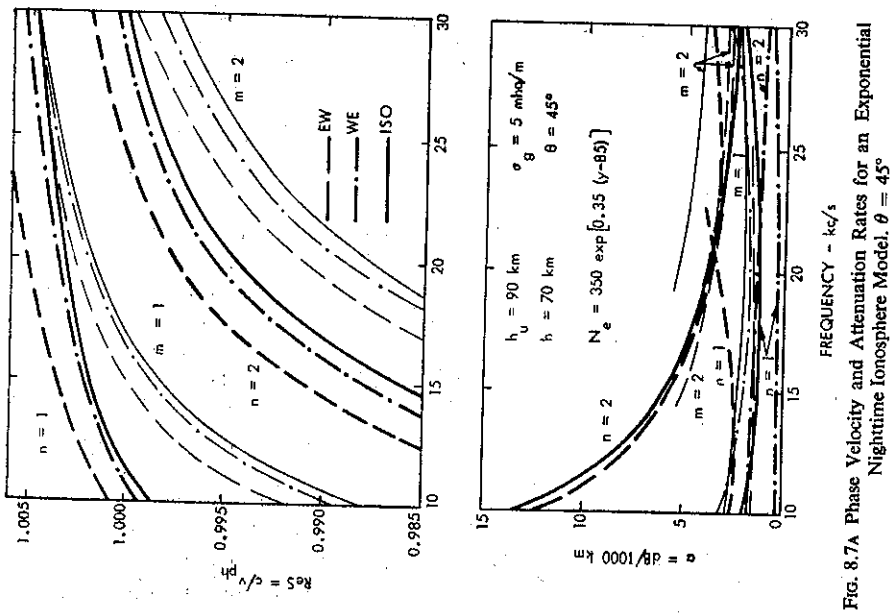

FIG. 8.7A Phase Velocity and Attenuation Rates for an Exponential Nighttime Ionosphere Model. $\theta = 45°$

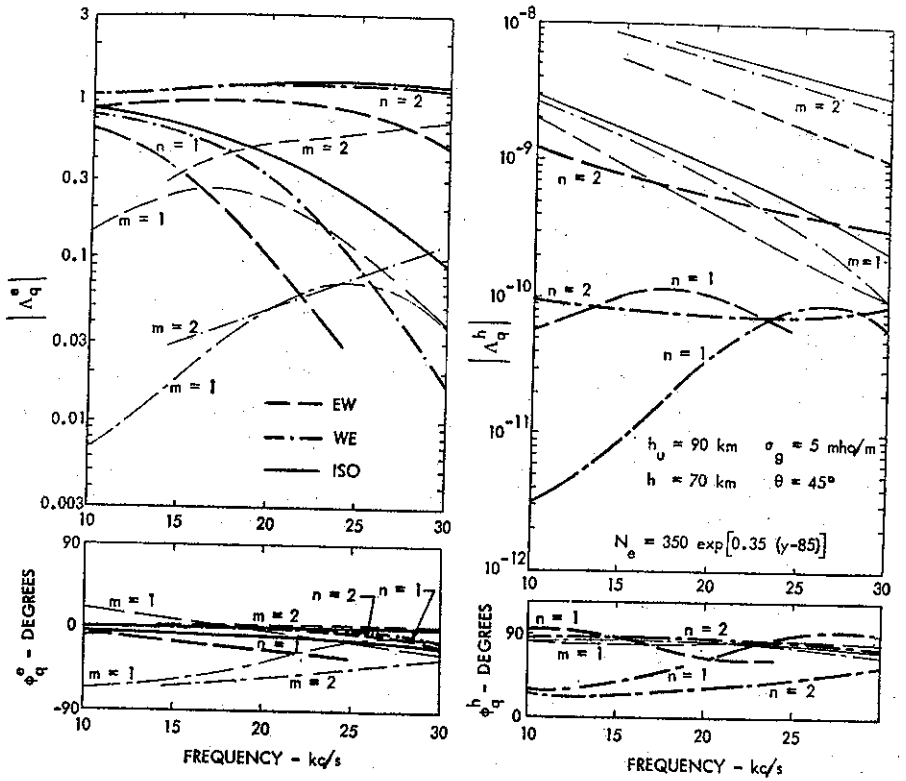

FIG. 8.8 Excitation Factors $A_q^j = |A_q^j| \exp(i\phi_q^j)$ for an Exponential Nighttime Ionosphere Model. $\theta = 45°$

except that in the $n = 1$ mode the isotropic attenuation rate is intermediate between the attenuation rates observed for different directions of propagation in the presence of a dipping static magnetic field. The corresponding excitation factors are shown in Fig. 8.8. The excitation factors are similar to the ones shown in Fig. 8.6 for the sharply bounded ionosphere model, except that $|A_{m=1}^e| > |A_{n=1}^e|$ at the higher frequencies where $|A_{m=1}^e|$ approaches $|A_{n=1}|$ of the isotropic model. Also, $|A_2^e| > |A_1^e|$ at the higher frequencies for either the n or m modes.

The excitation factors A_m^e (or A_n^h) which denote the excitation of T.M. (or T.E.) field components with wave numbers corresponding to T.E. (or T.M.) mode are significantly larger for E.W. direction of propagation when field penetration in the ionosphere is greater. A calculation following Section 6.8.1 shows that $_{\perp}R_{\parallel} \approx {}_{\perp}R_{\parallel}$ for propagation along a constant magnetic latitude, which can be seen also from figs. 4 and 5 of Johler [1961]. These reflection coefficients are approximately equal to 0.25 for E.W. direction and 0.1 for W.E. direction of propagation. The higher values of A_m^e and A_n^h occur for E.W. direction of propagation, which exhibits also the larger values of the reflection coefficients.

The exponential ionosphere model of Pappert [1968] is obtained by shifting the exponential

nighttime ionosphere models of Figs. 8.7A, B and 8.8 upward by approximately 13 km. The higher electron density profile should exhibit a stronger coupling between T.E. and T.M. field components. The excitation factor $|A^e_{m=1}| \approx 0.035$ of Pappert [1968] for an approximate E.W. direction of propagation at $f = 10$ kc/s is intermediate between the W.E. figure of 0.007 and the E.W. figure of 0.14 of the present calculations.

The propagation parameters of Fig. 8.7B are computed first by neglecting the vertical static magnetic field component of Fig. 8.7A, which gives an effective horizontal static magnetic field of 0.35 gauss or a gyro frequency $|\omega_c| = 6.2\times10^6$ sec^{-1}. The computations indicated by heavy curves show that Re S exhibits a different direction dependence than in Fig. 8.7A; for a horizontal static magnetic field $\mathrm{Re}\,S_{WE} > \mathrm{Re}\,S_{EW}$. It should be remembered that the $n = 1$ mode of $\Theta = 45°$ is not excited for $\Theta = 0°$. The $n = 1$ and $n = 2$ curves of Fig. 8.7B may be relabeled as $n = 2$ (1) and 3 (2) modes for E.W. direction of propagation following the notation adopted in Fig. 8.2. The $n = 1$ and $n = 2$ modes of E.W. directions for $\Theta = 0°$ of Fig. 8.7B are therefore identified as branches of the $n = 2$ and 3 modes for $\Theta = 45°$. Also the attenuation rates of the $n=1$ and 2 modes of Fig. 8.7B for E.W. propagation are higher than for a dipping static magnetic field or for isotropic conditions in Fig. 8.7A. The isotropic conditions can be approached by decreasing the static magnetic field by a factor of 10; for the thin-line curves of Fig. 8.7B, the phase velocity is practically independent of the direction of propagation and $\alpha_{EW} - \alpha_{WE}\big|_{n=1} \approx$ ≈ 1 db per 1000 km. The nighttime ionosphere model with a purely horizontal static magnetic field that is comparable to the field observed at the ground surface provides high attenuation rates for propagation in the E.W. direction, and also the resulting phase velocities exhibit variations that are opposite to the phase velocity changes observed with a dipping static magnetic field between E.W. and W.E. direction of propagation. This may explain the lack of success using realistic nighttime ionosphere models in the presence of horizontal static magnetic field [Galejs, 1964a, b, 1967a]. However, Wait and Spies [1965] observed no changes in the phase velocity and small changes in the attenuation rates for various directions of propagation even for electron profile heights that are representative of nighttime conditions. The strengths of the static magnetic field are implicit in their parameter $\Omega = \omega_c/\nu$, which is set equal to 1 in the numerical calculations. Assuming the collision frequency profile of Piggott and Thrane [1966], a variation of the reference height between 90 to 60 km corresponds to electron gyro frequencies ω_c of 2.8×10^5 to 4×10^7 or to a static magnetic field in the range from 0.016 to 2.3 gauss. Large reference heights in the work of Wait and Spies [1965] are therefore associated with very weak static magnetic fields, and one can expect nearly isotropic propagation conditions following the thin-line curves of Fig. 8.7B. Also it should be noted that Wait and Spies [1965] have used the daytime gradient ($\beta = 0.3$) exclusively; they have not claimed their model to be truly representative of nighttime conditions.

The propagation parameters of the exponential daytime ionosphere model are summarized in Figs. 8.9 and 8.10. The Re S curves show that the phase velocity is approximately the same for E.W. and W.E. directions of propagation; in the $m = 1$ mode, there are practically no changes in the phase velocities for the two directions of propagation. In a given mode, the attenuation rate is higher for the E.W. direction of propagation; and it is also higher than in the nighttime ionosphere model in Fig. 8.7A. The excitation factors of T.M. (or T.E.) components with wave numbers corresponding to T.E. (or T.M.) modes A^e_m (or A^h_n) are smaller in

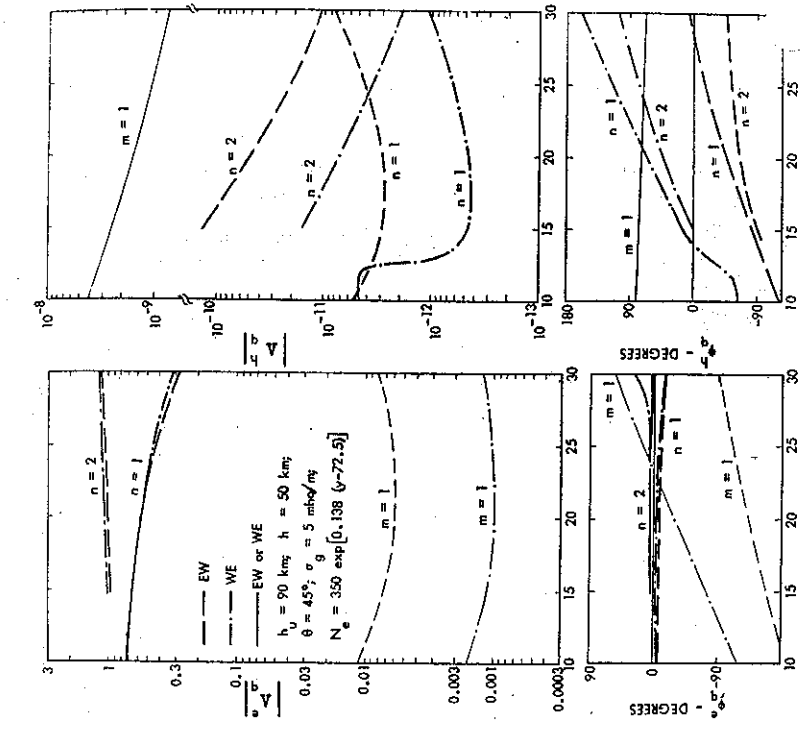

FIG. 8.10 Excitation Factors $A^e_n = |A^e_n| \exp(i\varphi^e_n)$ for an Exponential Daytime Ionosphere Model. $\theta = 45°$

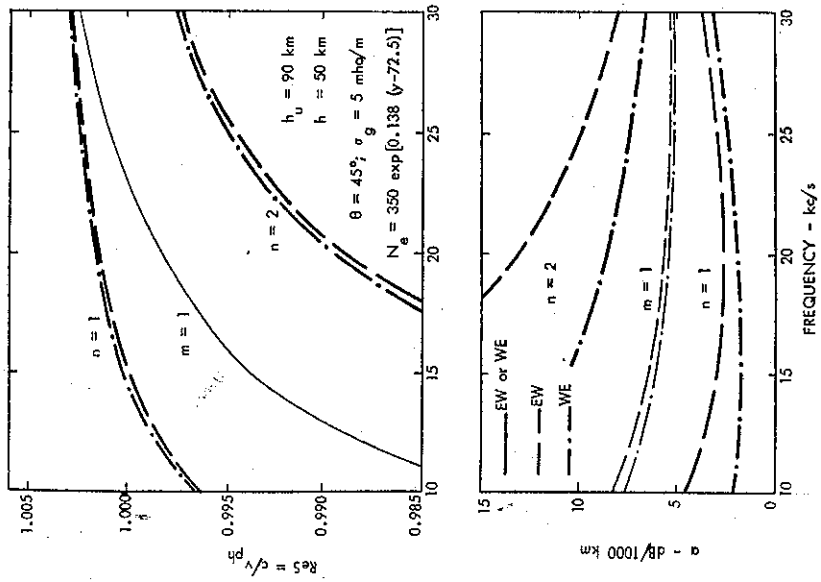

FIG. 8.9 Phase Velocity and Attenuation Rates for an Exponential Daytime Ionosphere Model. $\theta = 45°$

magnitude than for the nighttime ionosphere model in Fig. 8.8. The effective reflection level is lower at daytime, and also the reflection coefficients $_{\perp}R_{\parallel}$ and $_{\perp}R_{\parallel}$ are decreased in magnitude. For E.W. direction of propagation, the reflection coefficients are from 0.05 to 0.014 and for W.E. direction of propagation from 0.025 to 0.06 in the frequency range from 10 to 30 kc/s. The larger magnitude of the reflection coefficients for the E.W. direction of propagation corresponds to the larger values of A_m^e and A_n^h that are observed for this direction of propagation.

It is also possible to calculate the propagation parameters by neglecting the vertical component of the static magnetic field. The resulting Re S and α curves are numerically identical to those shown in Fig. 8.9 for a dipping static magnetic field, except that the attenuation rates in the $m = 1$ mode for a horizontal static magnetic field are the same for both directions of propagation and numerically equal to the attenuation rate for W.E. direction of propagation in Fig. 8.9. For ionospheric reflection heights corresponding to daytime conditions, it is therefore permissible to neglect the vertical component of the earth's magnetic field and to use the simpler computational model which considers only the static magnetic field component tangential to the earth's surface.

8.4 Propagation Parameters for Composite Ionosphere Models

The phase velocities and attenuation rates of the Deeks' [1966] summer daytime ionosphere model are shown in Fig. 8.11. For a given frequency, the phase velocity of the lowest order mode ($n = 1$) is practically independent of the angle Θ although the attenuation rate is somewhat higher for propagation in the E.W. direction ($\varphi = 180°$) than in the W.E. direction ($\varphi = 0°$) For the T.E. $m = 1$ mode, there are no differences within the accuracy of the graphical results between E.W. and W.E. directions of propagation. The largest difference between E.W. and W.E. directions of propagation occurs for the lowest frequencies ($f \approx 10$ kc/s). A decreasing ground conductivity (a change of σ_g from 5 to 0.001 mh/m) increases Re $S = c/v_{ph}$ and the attenuation rate α in the T.M. $n = 1$ and 2 modes but leaves the corresponding parameters of the T.E. $m = 1$ mode unaltered. The theoretical curves of Fig. 8.11 appear to be consistent with measurements by Bickel [1967], who reports $\alpha_{WE} = 2$ and $\alpha_{EW} = 2.7$ db per 1000 km for long distance measurements at $f = 19.8$ kc/s.

The ionospheric density model of Bain and May [1967] provides nearly the same attenuation rates as the ionosphere model of Deeks [1966], except that the attenuation rates of Bain and May are higher by about 1 to 2 db per 1000 km for frequencies near 30 kc/s. Also the excitation factors of the daytime ionosphere models of Deeks [1966] or Bain and May [1967] are similar to the corresponding parameters of an exponential daytime ionosphere model shown in Fig. 8.10. It is therefore permissible to replace these more elaborate ionosphere models by a simple exponential for purposes of calculating long-distance V.L.F. propagation parameters.

The phase velocity and attenuation data of the Deek's winter nighttime ionosphere model are shown in Figs. 8.12A and B. The curves of Fig. 12B indicate that Re $S = c/v_{ph}$ is larger for propagation towards west. The attenuation rates are higher for E.W. direction of propagation in the T.M. $n = 1$ and 2 modes but are lower for E.W. direction in the T.E. $m = 1$ and $m = 2$ modes for the higher ground conductivities ($\sigma_g = 5$ mho/m). A decreased ground conductivity increases the attenuation rates α_n and α_m of the n and m modes, which is contrary to

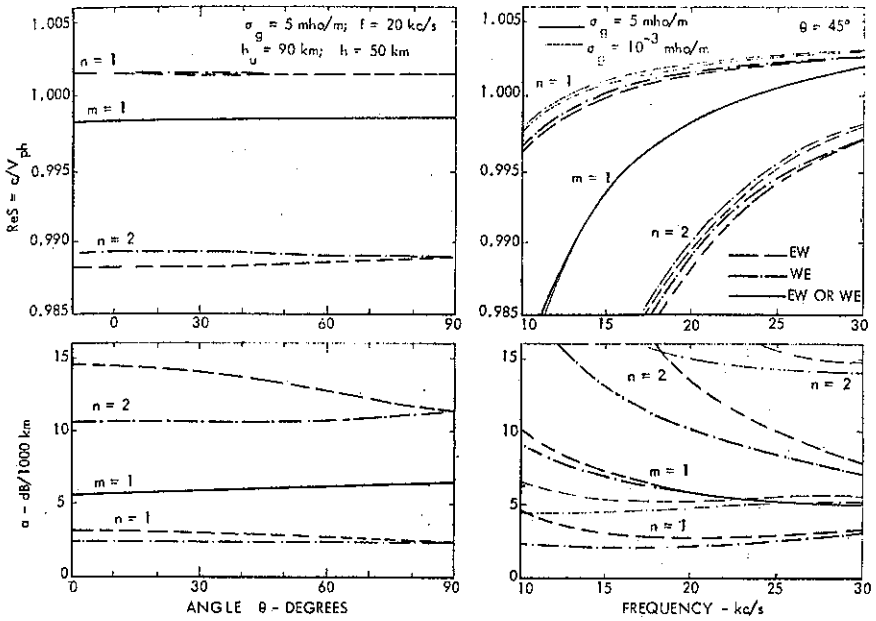

FIG. 8.11 Phase Velocity and Attenuation Rates for the Summer Daytime Ionosphere Model of Deeks

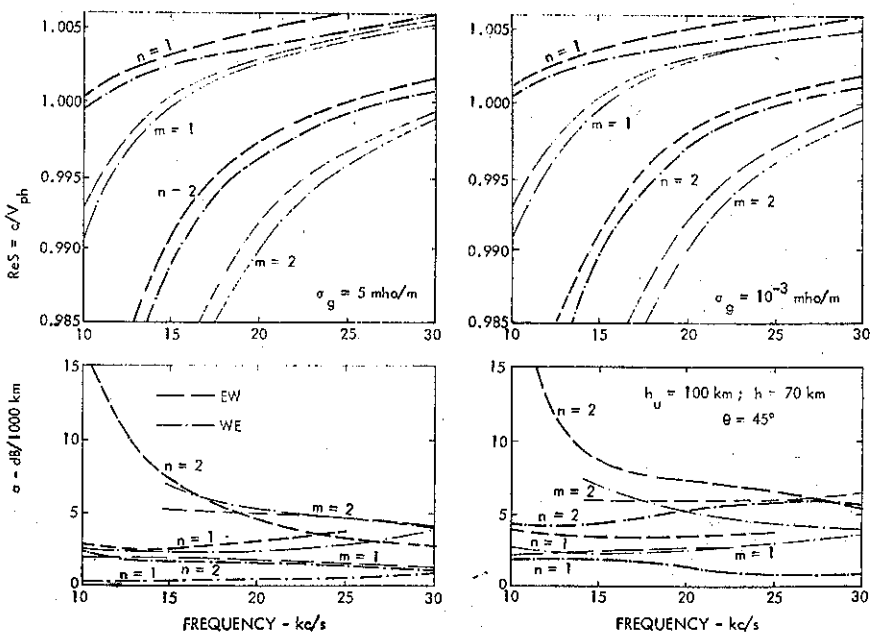

8.12A Phase Velocity and Attenuation Rates for the Winter Nighttime Ionosphere Model of Deeks

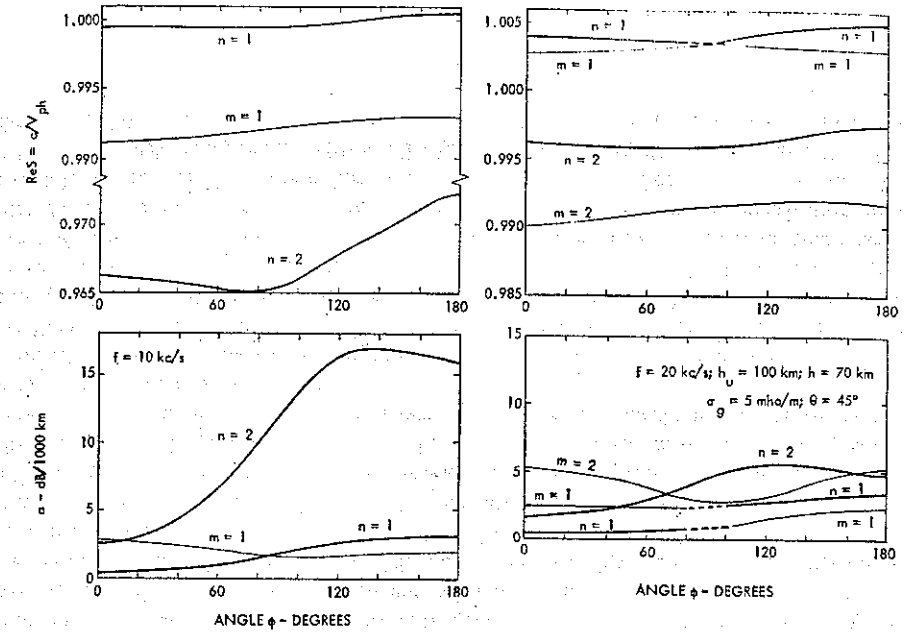

FIG. 8.12B Phase Velocity and Attenuation Rates for the Winter Nighttime Ionosphere Model of Deeks. Effects of a Varying Angle φ

daytime conditions when a decreasing σ_g leaves α_m unaltered. Under nighttime conditions, the m modes contain also significant amounts of T.M. field components (this can be seen from the data of Fig. 8.16 (p. 322); and the m modes should become more similar in their characteristics to n modes. For a decreasing ground conductivity and higher frequencies in the $m = 2$ modes, α_{EW} exceeds α_{WE}, which is similar to the behavior of the n modes.

Figures 8.12B shows the effect of varying the azimuthal angle φ. For $f = 10$ kc/s, the attenuation rates are smallest for W.E. direction of propagation ($\varphi = 0°$); but the attenuation rate is significantly increased with an increasing angle φ in the T.M. (n) modes. For this frequency, the excitation factors A_n^e are of comparable magnitudes in the $n = 1$ and 2 modes; and one may anticipate a significant interference between these modes for small values of φ. ($A_{m=1}^e$ is less than 0.01 in Fig. 8.6.A and the presence of T.E. modes may be neglected.) Such a mode interference is evident in the phase delay measurements discussed in Section 8.6. The attenuation rate of the $n = 2$ mode is increased to 6.5 db per 1000 km at $\varphi = 60°$ and the $n = 2$ mode will be attenuated much more rapidly than the $n = 1$ mode which exhibits $\alpha \approx 1$ db per 1000 km. The phase-velocity changes are almost linear with φ in the $n = 1$ and $m = 1$ modes, but Re S reaches a minimum and v_{ph} exhibits a maximum for $\varphi = 80°$ in the $n = 2$ mode.

For $f = 20$ kc/s, the various propagation parameters are changed more gradually with the angle φ. In the $n = 1$ and $m = 1$ modes, the phase velocities are comparable for $\varphi = 90°$;

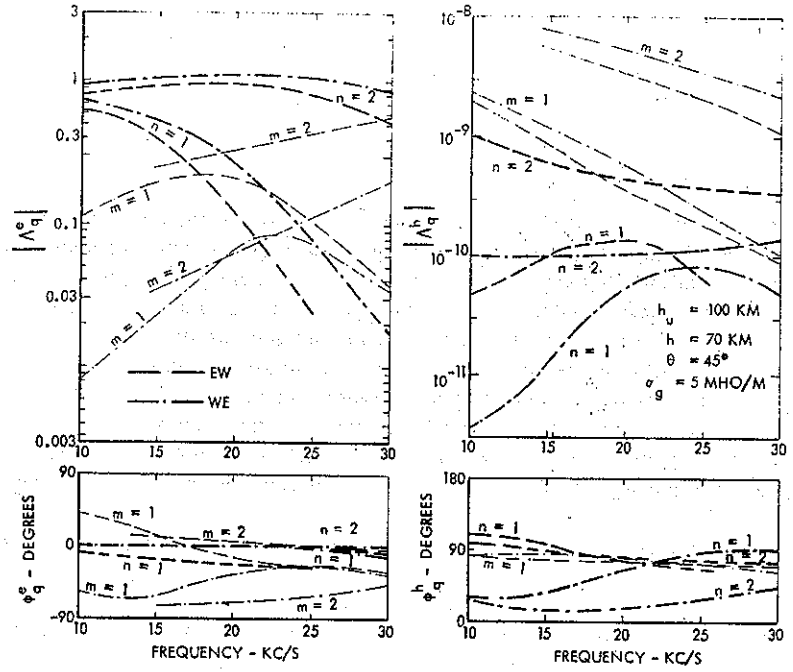

FIG. 8.13A Excitation Factors $A_q^j = |A_q^j| \exp(i\varphi_q^j)$ for Winter Nighttime Ionosphere Model of Deeks. $\sigma_g = 5$ mho/m

and the $n = 1$ and $m = 1$ curves of φ small appear to change over in the $m = 1$ and $n = 1$ curves for φ large. This is seen more clearly in the α curves of Fig. 8.12B, where attenuation rate of the $m = 1/n = 1$ curve remains near 2.5 while the $n = 1/m = 1$ curve exhibits α values in the range from 0.5 to 2.2 db per 1000 km.

The excitation factors for the nighttime ionosphere model are shown in Figs. 8.13A, B, and C. For a vertically polarized source, the excitation factor of the T.M. field components A_n^e decreases with frequency in the $n = 1$ mode because its fields become earth detached similarly as under isotropic conditions in Figs. 4.10A and B (p. 116); $A_{n=2}^e$ remains near unity over the whole frequency range. The excitation factor of T.M. components with wave numbers corresponding to m modes A_m^e increases with frequency for the lower frequencies, but $A_{m=1}^e$ decreases in magnitude at the higher frequencies. For propagation in the E.W. direction, $|A_{m=1}^e| > |A_{n=1}^e|$ for $f > 17.5$ kc/s; for W.E. direction of propagation, a similar inequality applies for frequencies larger than 25 kc/s. This indicates that T.M. field components with wave numbers corresponding to the $m = 1$ mode dominate over the T.M. field components with wave numbers corresponding to the $n = 1$ mode at the higher frequencies of the V.L.F. range, particularly for E.W. direction of propagation when $\alpha_{m=1} < \alpha_{n=1}$. For a horizontally polarized source, the excitation factor of T.E. field components with wave numbers corresponding to T.M. modes A_n^h are larger in magnitude for propagation towards west when the field pene-

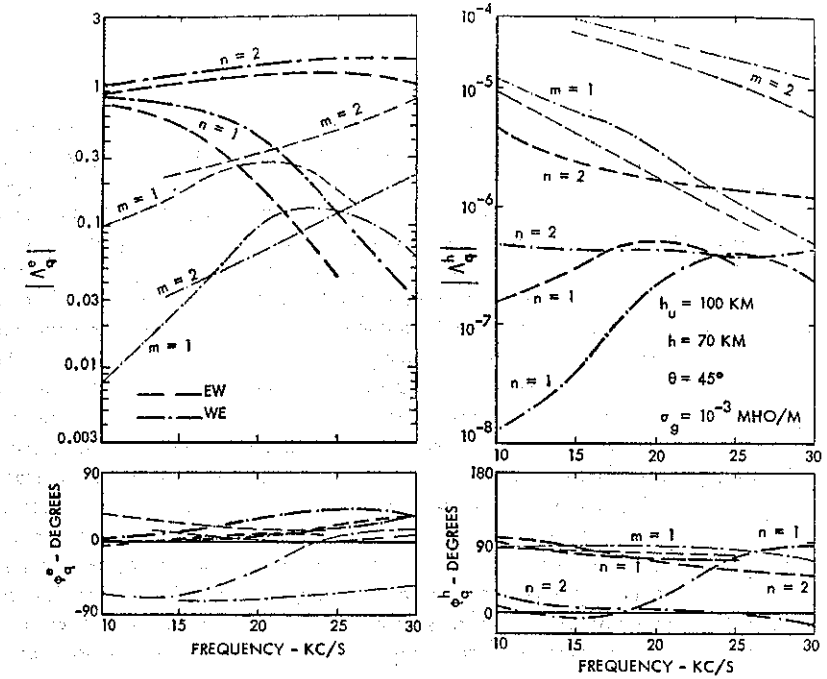

FIG. 8.13B Excitation Factors $A_q = |A_q^j| \exp(i\varphi_q)$ for Winter Nighttime Ionosphere Model of Deeks. $\sigma_g = 10^{-3}$ mho/m

tration in the ionosphere is higher. For lower frequencies, $|A_m^h| > |A_n^h|$; but for higher frequencies, the excitation of T.E. field components with wave numbers corresponding to n modes becomes comparable to the excitation of field components with wave numbers corresponding to m modes. For a decreasing ground conductivity, A_n^e is increased in Fig. 8.13B, but A_m^e remains nearly the same as in Fig. 8.13A. The excitation factors A_q^h are nearly proportional to σ_q^{-1} and are increased with a decreasing ground conductivity. Effects of various angles φ are shown in Figure 8.13C for $f = 20$ kc/s and $\Theta = 45°$. The $n = 1$ and $m = 1$ curves for φ small appear to continue as $m = 1$ and $n = 1$ curves for φ large, similarly as was shown for the parameters Re S and α in Fig. 8.12B.

Bickel [1967] reports measured nighttime attenuation rates of $\alpha_{WE} = 0.5$ and $\alpha_{EW} = 2$ db per 1000 km for a frequency $f = 19.8$ kc/s. These measurements correspond to $\alpha_{n=1}$ for $\varphi = 0$ and $\alpha_{m=1}$ for $\varphi = 180°$ in Figs. 8.12A and B. It was shown in Figs. 8.13A and C that the $m = 1$ mode is excited more efficiently than the $n = 1$ mode for $\varphi \approx 180°$; the T.M. field components of the $m = 1$ mode will dominate over the components of the $n = 1$ mode for frequencies near 20 kc/s. Although the mode $m = 1$ is labeled as a quasi-T.E. mode, its polarization does not differ appreciably from the polarization of the $n = 1$ mode. For $\varphi = 180°$, the ratio of T.E. to T.M. field components $R(0) = |H_\varphi(0)/H_z(0)| = |E_z(0)/E_\varphi(0)| = 0.075$ and 0.12 for the $n=1$ and $m=1$ modes respectively, in Fig. 8.16; in this example, the T.E. field components

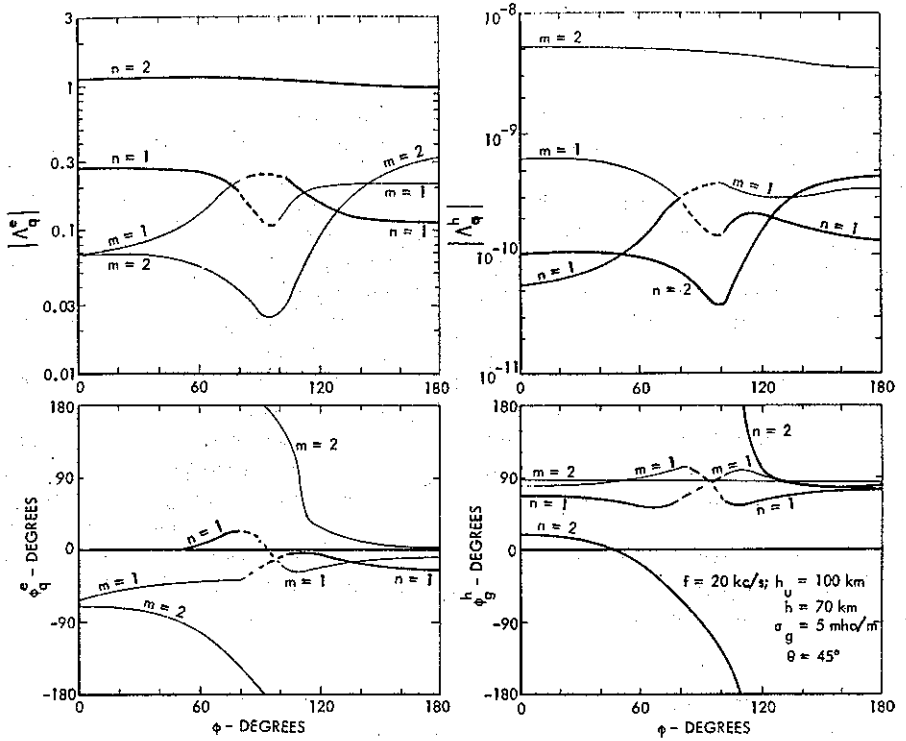

FIG. 8.13C Excitation Factors $A_q^j = |A_q^j| \exp(i\varphi_q^j)$ for Winter Nighttime Ionosphere Model of Deeks. $f = 20$ kc/s; $\theta = 45°$

are smaller in magnitude than the T.M. field components ($R < 1$) for both the m and n modes.

The field penetration in the ionosphere is illustrated in Fig. 8.14 for the winter nighttime model. The effective reflection height appears to be near the discontinuity of the electron density profile. The computations indicate a slight increase of the fields for $h > 100$ km, which is probably due to cumulative numerical errors. For $h = 110$ km the two up-going wave solutions of the quartic exhibit attenuation rates of 0.006 and 8 db/km and the field strengths should remain nearly constant for larger heights. However, there is a sharp increase of the computed field strength ratio at $h = 120$ km, and the computed propagation parameters become incorrect. For E.W. direction of propagation the fields in the ionosphere are larger in magnitude than for W.E. direction. E.W. direction of propagation exhibits also the higher attenuation rates α for the waves in the cylindrical shell between the earth and the ionosphere.

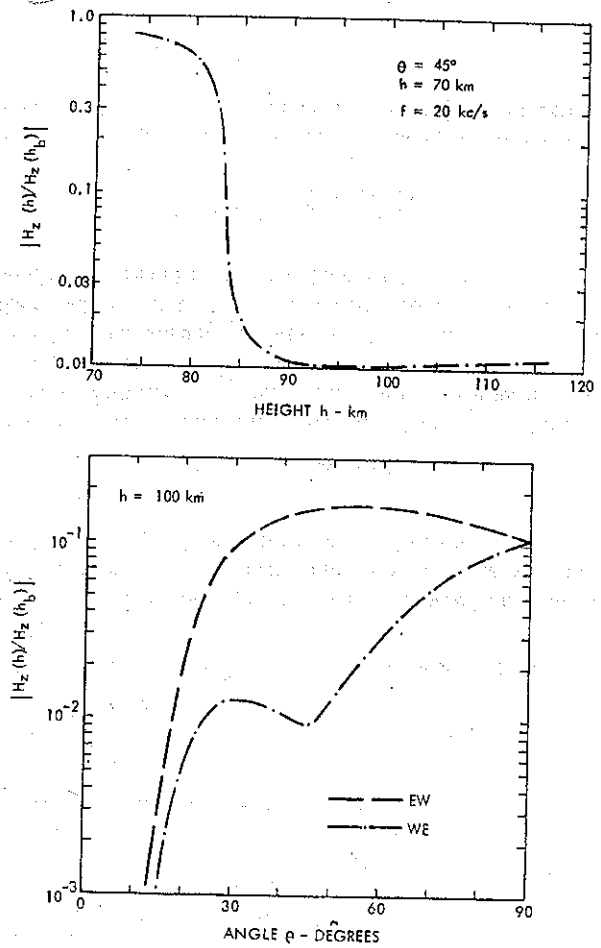

FIG. 8.14 Penetration of V.L.F. Waves in the Nighttime Ionosphere

8.5 Wave Polarization

The wave polarization is characterized by the ratios of T.E. to T.M. field components $R(y) = |H_\varphi(y)/H_z(y)| = |E_z(y)/E_\varphi(y)|$ or by the coupling impedance defined as $Z_{eh} = E_z(0)/H_z(0)$. Large ratios R or large values of the impedance Z_{eh} indicate predominantly T.E. field components, small ratios or impedances—predominantly T.M. field components.

Figure 8.15 shows that for the daytime ionosphere model of Deeks [1966], R exceeds unity in the $m = 1$ mode and R is larger for fields near the ionospheric boundary ($y = h$). In the $n = 1$ and 2 modes, R is of the order of 1% and $Z_{eh} \approx R/10$. Under nighttime conditions at

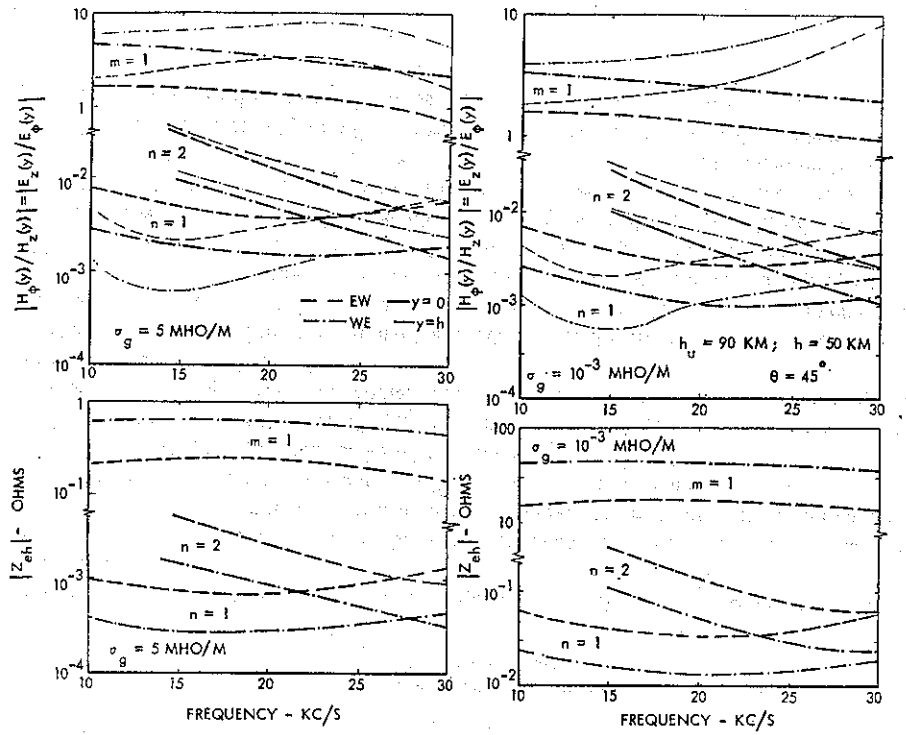

FIG. 8.15 Wave Polarization. Daytime Ionosphere Model of Deeks

the lower frequencies, the data of Fig. 8.16 indicate that $3 > R > 10^{-2}$; for the higher frequencies, $R \approx 0.1$. Also under nighttime conditions, $Z_{eh} \approx R/10$.

A decreasing ground conductivity does not affect the ratio R significantly except for an increase in $R(h)$ at the higher frequencies for some of the m modes. However, the coupling impedance Z_{eh} of the T.E. and T.M. field components is proportional to $\sigma_g^{-0.5}$, and it increases with a decreasing ground conductivity.

The quasi-T.E. or m modes exhibit larger T.E. field components than the quasi-T.M. or n modes. This can be seen from the wave polarization curves of Fig. 8.16, where the $m = 1$ mode exhibits the larger ratio R or the larger impedance Z_{eh} for both $\varphi = 0$ (W.E.) and $\varphi = 180°$ (E.W.). This justifies the labeling of the Re S, α, and Λ_q^j curves in Figs. 8.12B and C, where mode $n = 1$ (or $m = 1$) is shown to change into $m = 1$ (or $n = 1$) mode. Examination of the coupling impedance Z_{eh} for other angles of φ (not shown in Fig. 8.16) shows that for the propagation parameters of the $n = 1/m = 1$ curve, the fields exhibit the larger amounts of T.E. components for $80° < \varphi < 115°$ and for $\varphi > 150°$; however, Z_{eh} of both the $n = 1/m = 1$ and $m = 1/n = 1$ curves are nearly equal for φ in the range of $115° < \varphi < 150°$, and the mode labeling may be ambiguous in this latter range of φ.

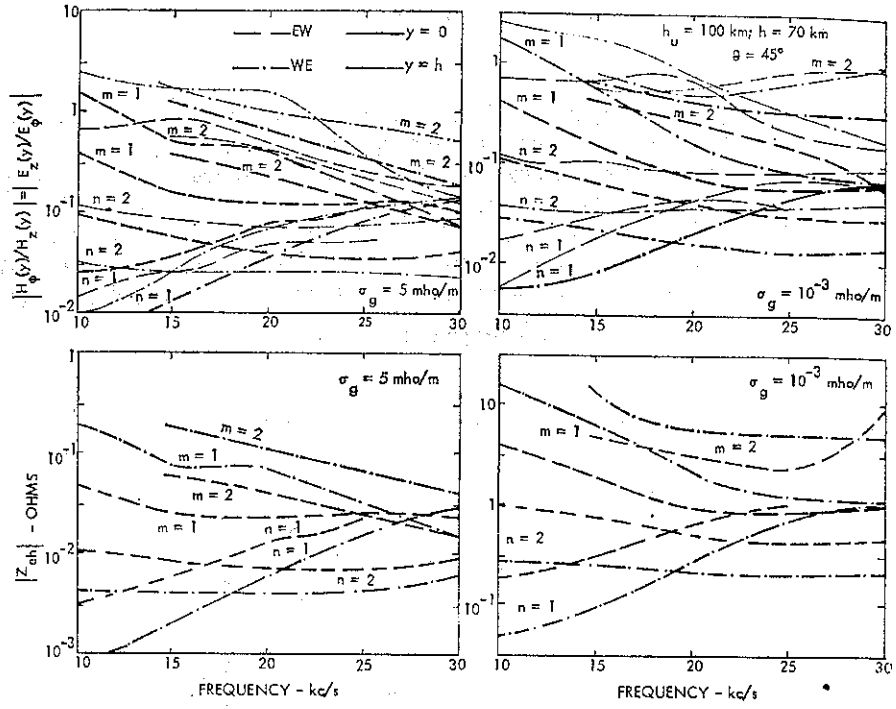

FIG. 8.16 Wave Polarization. Winter Nighttime Ionosphere Model of Deeks

The mode labeling in the various figures is therefore based on polarization of the field components; a change from an n mode to an m mode (or vice versa) with a change of the angle φ is correlated with the change of the relative wave polarization.

8.6 Mode Interference

In experimentally observed sunrise and sunset fading over long V.L.F. paths, the interference pattern changes with the movement of the sunrise or sunset line along the path. The distance between two successive minima of the interference pattern is approximately 1900 km for W.E. direction of propagation and 2800 km for E.W. propagation at moderate latitudes for frequencies in the range from 18 to 24 kc/s [Crombie, 1966]. The interference distance D_{ij} of two waveguide modes i and j can be computed from the formula

$$D_{ij} = \frac{\lambda_i \lambda_j}{\lambda_j - \lambda_i} = \frac{\lambda_0}{\mathrm{Re}\, S_i - \mathrm{Re}\, S_j}, \qquad (2)$$

where λ_i and λ_j are wavelengths of modes i and j, and λ_0 is a free-space wavelength. The excitation factor A_q^e of quasi-T.E. $m = 1$ mode is comparable to the excitation factor of the

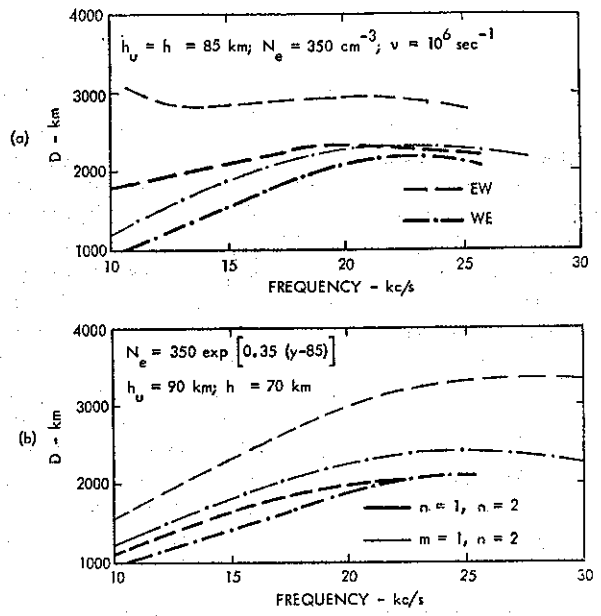

FIG. 8.17 Interference Distance D_{ij} Between the Modes n or $m = 1$ and $n = 2$. $\sigma_g = 5$ mho/m; $\theta = 45°$

a. Sharply Bounded Homogeneous Ionosphere
b. Exponential Nighttime Ionosphere

$n = 1$ mode, and it may be appropriate to examine the interference of modes n or $m = 1$ with the mode $n = 2$.

The calculations of Fig. 8.17 show that for W.E. propagation the interference of the $n = 1$ and $n = 2$ modes may explain the measurements. However, for E.W. direction of propagation, the interference of modes $n = 1$ and $n = 2$ gives only a marginal increase of D_{EW} relative to D_{WE}. The interference between modes $m = 1$ and $n = 2$, indicated by thin lines in Figs. 8.17A and B, provides a larger increase of D_{EW} that can also be shown to be less dependent on small changes of the ionospheric model. Similar data are obtained also from the ionospheric models of Deeks, not shown in Fig. 8.17.

The proper contributions of the individual modes can be illustrated more clearly by computing the mode sum (211) of Chapter 5. A four-term approximation of this sum involving the terms $n, m = 1$ and 2 is shown by heavy lines in Fig. 8.18. For W.E. direction of propagation, the distance between successive minima of the mode sum is approximately equal to 2000 km. For E.W. direction of propagation, the mode sum is highly oscillatory; and the presence of the $m = 2$ mode tends to mask the minima of the interference pattern between the modes $m = 1$ and $n = 2$. These minima are seen more clearly in the three-term mode summation ($n = 1, 2$; $m = 1$) that are indicated by thin lines in Fig. 8.18. The perturbations by the mode $m = 2$ are more pronounced for the exponential ionosphere model. A 5 km downward shift of the exponen-

tial nighttime electron density profile (not shown in Fig. 8.18) decreases the distance between the minima of the interference pattern to 2900 km for E.W. and to 1700 km for W.E. directions of propagation; an upward shift by 5 km increases this distance to 3400 km for E.W. and to

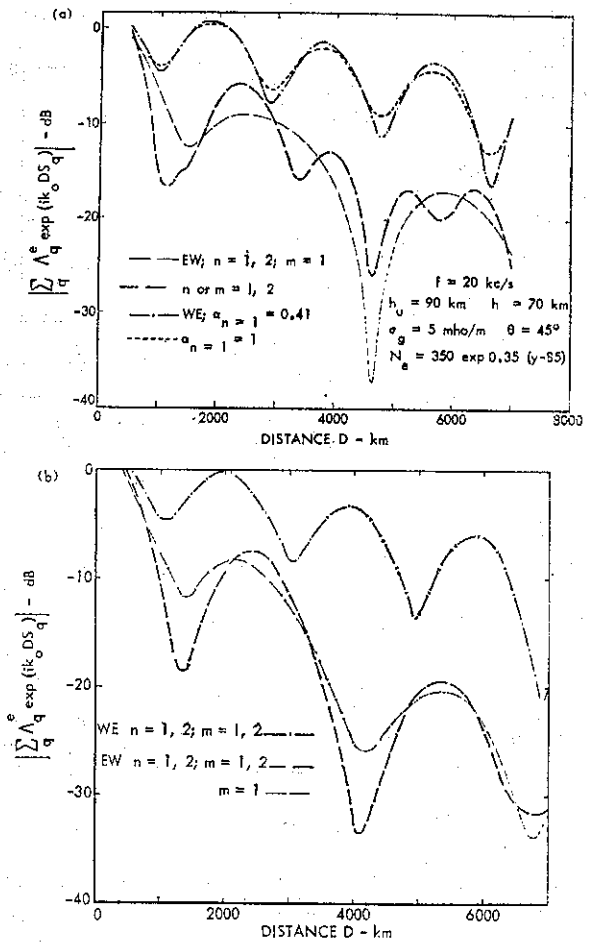

FIG. 8.18 Distance Variations of the Normalized Field-strength. (a) Exponential Nighttime Ionosphere Model. (b) Winter Nighttime Ionosphere Model of Deeks

2000 km for W.E. directions of propagation. The average slope of the interference pattern shown for the exponential nighttime ionosphere model in Fig. 18a gives an effective attenuation rate for W.E. direction of approximately 1.25 to 1.5 db per 1000 km and 2.5 db per 1000 km for E.W. direction of propagation, although the individual modes exhibit attenuation rates in the range of 0.3 to 4 db per 1000 km. The dotted curve of Fig. 8.18a is computed for W.E.

propagation using the same parameters as for the dotted-dashed curve, but by increasing the attenuation rate α of the $n = 1$ mode from 0.41 to 1 db per 1000 km. The increased attenuation rate of the $n = 1$ mode decreases the amplitude of the oscillations for the larger values of D, but it leaves the average slope of the interference pattern unchanged for the distances shown in Fig. 8.18a.

The field strength measurements available in experimental work represent interference patterns or mode summations. The average slope of an interference pattern can be readily determined, but it is not directly related to the attenuation rate of the lowest order mode. There may be ambiguities in determination of the various mode parameters. Figure 8.18a illustrates the minor changes of the mode interference pattern that may be associated with significant differences in mode parameters.

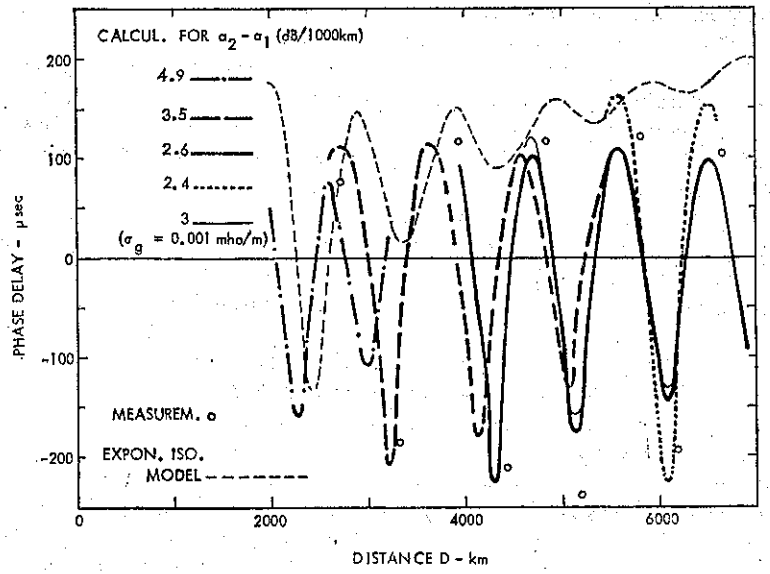

FIG. 8.19 Phase Delay Variability of 10462–10200 c/s Difference Frequency

Mode interference has been observed also in the V.L.F. navigational system Omega, which is based on relative phase measurements of transmissions in the frequency range from 10.2 to 13.6 kc/s. Recent nighttime measurements of Burgess [1967] made over the Trinidad/Bermuda/Azores/Farnborough (UK) flight path show phase delay variations of the 262 c/s difference frequency between the carriers of 10462 and 10200 c/s that are illustrated in Fig. 8.19. Ideally, the phase difference between the carriers A and B should increase linearly with the increasing distance D; but there will be further phase fluctuations because of the presence of higher order modes. In this frequency range, $A^e_{m=1} \approx 0.01$ for azimuthal angles φ in the range from 0° (W.E.) to 90° (S.N.); and the presence of the $m = 1$ mode can be ignored. The interference

between the modes $n = 1$ and 2 will cause a phase fluctuation

$$\Delta\varphi = \varphi_A - \varphi_B, \tag{3}$$

where

$$\varphi_J = \arg\left\{1 + \frac{A_{2J}^2}{A_{1J}^2} \exp\left[ik_0 D(S_{2J} - S_{1J})\right]\right\} \tag{4}$$

and $J = A$ or B. An isotropic exponential ionosphere model does not reproduce the negative excursions of the experimental points, but the theoretical model of an anisotropic ionosphere may reproduce the phase fluctuations if the attenuation rate $\alpha_2 - \alpha_1$ is decreased with an increasing distance D corresponding to a change of the direction of the effective azimuthal angle φ from the nearly N.S. direction ($\varphi = 60°$) to W.E. direction ($\varphi = 10°$).

The phase delay measurements of Burgess [1967] appear to be made in a propagation geometry where the effective attenuation rate is decreased with increasing distance from the source. Such variations of the attenuation rate can be considered using theoretical models of an anisotropic ionosphere with a dipping static magnetic field [Galejs, 1969a].

8.7 Perturbed Ionosphere

V.L.F. transmissions are highly stable and the phase of the carrier undergoes an approximately trapezoidal diurnal variation on a given transmission path. Examples of such phase variations [Reder and Westerlund, 1967] are indicated in Fig. 8.20a, where the standard

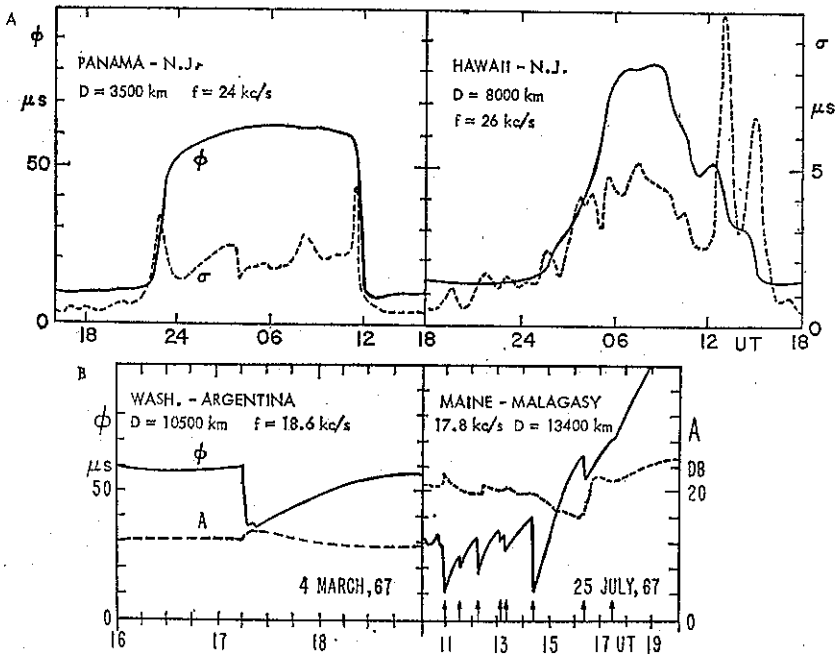

FIG. 8.20 Phase and Amplitude Patterns; A, Normal Diurnal Variation. B, S.I.D. effects

deviation σ of hourly phase values pertains to a 14 day average. The phase uncertainties are largest during periods of sunset or sunrise transitions and for some patterns also at night.

Sudden ionospheric disturbances (S.I.D.) caused by prominent solar flares are accompanied by a sudden enhancement of atmospherics (S.E.A.); spectral amplitudes are enhanced for frequencies above 15 kc/s and decreased below 12 kc/s. This change of signal amplitudes is associated with an increased electron density of the lower ionosphere and a lowering of its height; the cut-off frequency of the waveguide is higher; but above the cut-off, signal intensity is enhanced owing to better reflection conditions at the lower edge of the ionosphere [Obayashi, 1960]. Similar results are reported also by Pierce [1961]. These enhancement effects are not very pronounced in the frequency range of 16–18 kc/s investigated by Chilton *et al.* [1963], Crombie [1965], and Burgess and Jones [1967]. Phase anomalies associated with solar flares have been interpreted in the work of Chilton *et al.* [1963] by a change of reflection height in a sharply bounded homogeneous ionosphere model. Crombie [1965] shows that an increased gradient of an exponential ionosphere profile decreases attenuation rate and phase velocity. Burgess and Jones [1967] indicate that enhanced amplitudes and retarded phase during solar events can be explained by a lowering of the exponential ionosphere profile and by an increase of its gradient. Solar-flare effects have been interpreted over distances of about 1000 km using ray theory by Volland [1964]. Reder and Westerlund [1967] have recorded phase and amplitude variations shown in Fig. 8.20b. Coincident with a flare is the characteristic rapid phase advance (or decrease of φ) over a period of 1–30 minutes and a slower recovery over 0.5–2 hours. There are definite phase changes, but the changes of signal amplitudes are relatively small. Such phase and amplitude changes are readily detected if a given propagation path is continuously monitored. However, the corresponding changes of propagation parameters are minute. A 20 μsec phase change observed over a 10,000 km (or 33 msec) path is caused by a 0.6×10^{-3} change in phase velocity.

This is evidenced by propagation parameters calculated for S.I.D. profiles by Deeks [1966] and May [1966], solar-flare estimates of Jayaram and Chin [1967] and for the quiet-day data of Piggott and Thrane [1966] that have been shown in Fig. 2.3 (p. 23). The resulting phase velocities and attenuation rates lie within the shaded areas indicated in Fig. 8.21, and only the attenuation rate curves for the West to East direction of the $n = 2$ mode are shown individually. Also the quiet daytime summer profile of Deeks [1966] gives propagation parameters in Fig. 8.11, which would appear within the shaded areas of Fig. 8.21. These electron density profiles (D, M, P.T. in Fig. 2.3) exhibit approximately the same electron densities and the same average slopes in the height range between 60–90 km which includes the apparent reflection height of V.L.F. waves. Minor changes about this average slope are therefore of little significance in the calculation of propagation parameters for a nearly grazing incidence and for daytime or perturbed ionosphere conditions. However, when starting with a given ambient daytime profile and considering its modification by the X-ray flux of solar flares [Burgess and Jones, 1967; Field, 1969b], it is possible to show the small changes of attenuation rates noted in measurements [Obayashi, 1960; Pierce, 1961].

Egeland and Naustvik [1967] have correlated auroral absorption events with disturbances of V.L.F. propagation; a reduction of signal strength and of diurnal phase changes are noted particularly for frequencies below 12 kc/s. Aurora causes 5–10 μsec short-term phase fluctuations and also unstable signal amplitudes [Reder and Westerlund, 1967]. Phase velocities and

attenuation rates have been calculated for the ionosphere profile by Jespersen *et al.* [1966] for an auroral absorption event (*J* in Fig. 2.3) which exhibits higher electron concentrations for heights above 80 km. The computed phase velocities lie within the shaded areas of Fig. 8.21, but the attenuation rates of the $n = 1$ and 2 modes are by approximately 1 and 2 db per 1000 km higher than the upper boundaries of attenuation rates shown at a given frequency in Fig. 8.21.

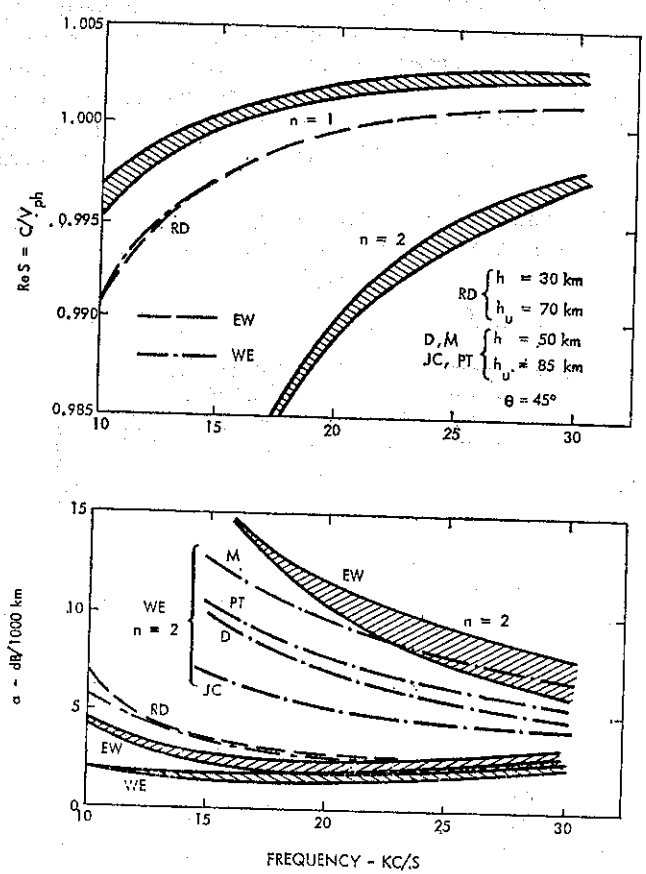

FIG. 8.21 Phase Velocity and Attenuation Rates of V.L.F. Waves. S.I.D. Data by Deeks (D) and May (M), Solar Flares by Jayaram and Chin (JC), Quiet Day by Piggot and Thrane (PT), P.C.A. Daytime Data by Reid (RD)

P.C.A. events cause more drastic changes of ionosphere parameters. During P.C.A. events V.L.F. reflection layers are depressed by about 25 km [Egeland and Naustvik, 1967], and a depression of the effective waveguide height by about 5 km is noted also by Bates [1962]. Bailey [1964] observes that during strong P.C.A. events diurnal variations of V.L.F. signals disappear and even sunrise and sunset effects are eliminated. Even relatively minor P.C.A.

events appear to depress the *D*-region for 4 to 5 days, which is evident from the V.L.F. phase measurement of Albee and Bates [1965]. Large decreases of signal strength are noted for paths crossing very low ground conductivity in Greenland and Antarctica [Westerlund *et al.*, 1969]. The recording of Fig. 8.22 exhibits amplitude changes of nearly 30 db following the onset of a P.C.A. event. However, the signal amplitudes are not necessarily decreased over paths on sea water.

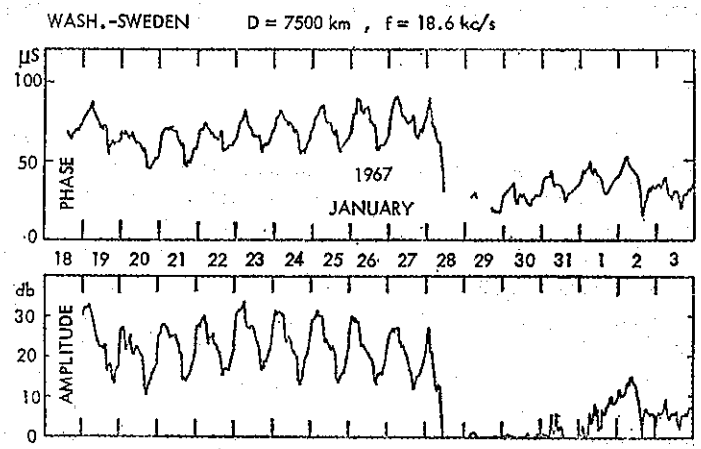

FIG. 8.22 Phase and Amplitude Recordings during a P.C.A. Event

The P.C.A. profiles of Reid [1966] show high electron concentrations at lower heights (*RD* and *RN* in Fig. 2.3). The phase velocity for the P.C.A. profile (*RD*) is significantly increased (Re $S = c/v_{ph}$ is decreased) relative to the other data shown in Fig. 8.21, particularly for the lower frequencies. The attenuation rates are higher near $f = 10$ kc/s, but they are approximately the same as for the E.W. direction of previous calculations at higher frequencies. There are practically no differences between E.W. and W.E. direction or propagation and the attenuation rates for daytime are approximately the same as at night. This is in agreement with the observations reported by Bailey [1964] who pointed out the disappearance of day to night or sunrise and sunset effects during P.C.A. events. Qualitatively similar propagation data can be also obtained from the simple sharply bounded homogeneous isotropic ionosphere model (figs, 3a and 4a, section 7.4, Wait, [1962]), when a lower effective ionosphere height causes increased phase velocities and attenuation rates at the lower frequencies, but a smaller change at the higher frequencies of the V.L.F. range.

The propagation parameters of Fig. 8.21 have been calculated without considering the effects of ions of the lower ionosphere. The work of Crain and Booker [1964], Cole and Pierce [1965], Johler and Berry [1966], or Field [1969a] show that the conductivity of the lower ionosphere is determined principally by ions and that ions will affect the characteristics of radio-wave propagation under perturbed conditions and/or for the lower frequencies. These ion effects will be illustrated using the simplified electron and ion density profiles shown in Fig. 2.5 (p. 25), where the profile 0 approximates the unperturbed daytime conditions; profiles 1 and

2 could arise during polar cap absorption evets while profile 3 is more representative of nuclear perturbations. It was shown in Chapter 2 that the collision frequencies between ions and neutral particles ν_{in} may be approximated by the collision frequency between neutral particles ν_{nn}, and that also higher and lower collision-frequency figures are in current use. The effective ion mass is also uncertain. A molecular weight of approximately 29 is frequently assumed for the average of NO^+, O_2^+, N_2^+, O_2^-, and O^- ions of the lower ionosphere. However, Cole and Pierce [1965] point out that ions of a greater mass can be produced by clustering and aerosols or attachment to dust and nuclei. Measurements of Narcisi and Bailey [1965] indicate that more than 50 percent of ions detected in the altitude range between 64 and 76 km have masses exceeding 45. In the measurement data shown in figs. 8.18 and 8.20 of Valley [1965] for moderate northern latitudes and for the altitude range of 20–28 km, the small ion concentration is near 2500 cm^{-3} and the atmospheric conductivity σ is 2 to 5×10^{-12} mho/m

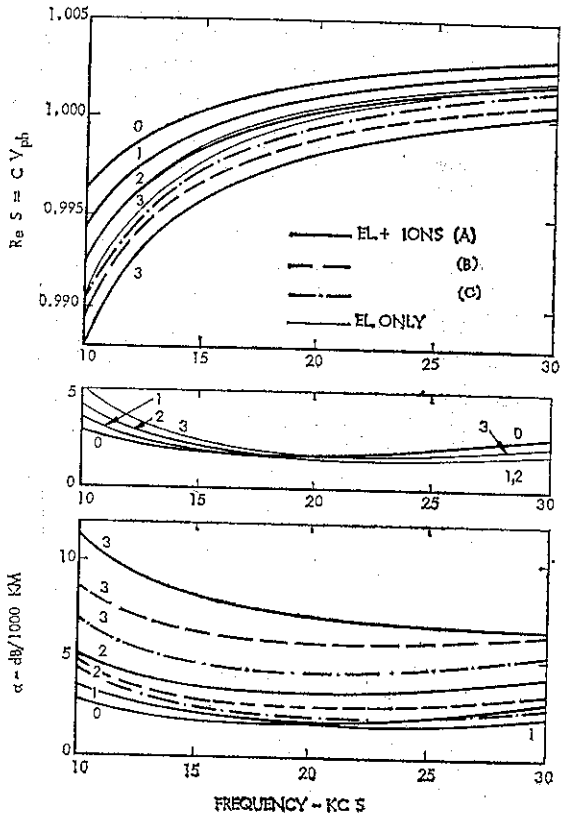

FIG. 8.23 Phase Velocity and Attenuation Rates of V.L.F. Waves
(A) MW = 29, $\nu_{in} = \nu_{nn}$; (B) MW = 60, $\nu_{in} = \nu_{nn}$; (C) MW = 60, $\nu_{in} = 2\nu_{nn}$

with variations up to ±40 percent. Calculations for the unperturbed particle density (profile 0) based on M.W. = 29 and $\nu_{in} = \nu_{nn}$ show that $\sigma = 7$ to 20.5×10^{-12}; for M.W. = 60 and $\nu_{in} = 2\nu_{nn}$, $\sigma = 1.75$ to 5.1×10^{-12} mho/m. This comparison tends to justify the use of larger molecular weights M.W. and of collision frequencies ν_{in}, which are larger than ν_{nn}.

The propagation parameters of V.L.F. waves of Fig. 8.23 are calculated using the ion collision frequencies $\nu_{in}/\nu_{nn} = 1$ and 2 and the molecular weights M.W. = 29 and 60, and ignoring the effects of the geomagnetic field. Ion effects are most pronounced for the lower M.W. and ν_{in} figures (solid curves); but even under these conditions, the phase velocity for the profiles 0, 1, and 2 remains the same as for the electron profiles only (thin lined curves). The attenuation rates of profiles 0 and 1 are not affected by ions; for profile 2, ions of larger molecular weight and higher collision frequencies (model *C*) produce nearly the same attenuation rate as the electron density profile with neglected ions. For profile 3, the ion effects are pronounced; and the neglect of ions will result in a slightly lower phase velocity and by about 2 db lower attenuation rate α. With the exception of extreme perturbations where particle densities exceed 10^6 cm^{-3}, the ion contributions appear to be marginal in the V.L.F. range. Ions would affect the propagation parameters more significantly if smaller values of ion collision frequencies and molecular weights could be justified in the conductivity calculations [Galejs, 1970].

8.8 Elevated Sources

Fields of vertical electric and horizontal dipoles have been examined in Sections 4.3.2.1 and 4.3.2.3 for isotropic waveguide boundaries. The vertical electric dipoles excite T.M. modes; the height-gain function of these modes are of the order of unity in Figs. 4.10A and B (p. 116), and no drastic field changes can be anticipated with a changing altitude of the source or observation point. The horizontal electric dipoles excite T.M. fields in the axial (or end fire) direction and T.E. fields in the broadside direction. For a ground based source the fields of the end fire direction dominate following (129) of Chapter 4. The height-gain functions of T.E. fields may exceed 10^4 in magnitude for elevated sources in Figs. 4.13A and B and the T.E. fields may become comparable to T.M. fields. An anisotropic ionosphere causes a further coupling between T.E. and T.M. modes, and the directional characteristics of the radiation from elevated horizontal dipole sources are not predictable from formulas for isotropic boundaries.

Effects of elevation and ground conductivity on horizontal dipole antennas have been studied by Pappert [1970] for anisotropic waveguide boundaries, and an inclined dipole antenna has been investigated by Kelly [1970] under isotropic conditions. Field expressions appropriate to anisotropic boundaries are listed in this section, and a comparison of elevated horizontal and vertical electric dipoles is also presented. Field variations of an inclined dipole antenna are discussed briefly.

8.8.1 Field Expressions

In a cylindrical shell a vertically polarized line source excites the field components listed in Section 5.6.2. For a vertical electric dipole in a spherical shell these field expressions are modified as shown in Section 5.6.3.1. For a height h of the spherical shell and the observer at a

distance $D = a\theta$ from the source it follows that

$$E_r^{ve} = -\frac{\eta I\, ds}{h\sqrt{a\lambda \sin\theta}} \sum_q S_q^{1.5} A_q^e G_q^e(z_s)\, G_q^e(z) \exp, \tag{5}$$

$$E_\theta^{ve} = \frac{\eta I\, ds}{h\sqrt{a\lambda \sin\theta}} \sum_q S_q^{0.5} A_q^e G_q^e(z)\, G_q^e(z_s)\, \Delta_q^e(z) \exp, \tag{6}$$

$$E_\varphi^{ve} = \frac{I\, ds}{h\sqrt{a\lambda \sin\theta}} \sum_q S_q^{0.5} A_q^e G_q^e(z_s)\, G_q^h(z)\, Z_{eh} \exp, \tag{7}$$

where

$$\exp \equiv \exp\,[ik_0 D S_q - i\pi/4] \tag{8}$$

and where the summation over q includes both the T.M.(n) and T.E.(m) modes. The excitation factors A_q^e of vertically polarized sources, the height-gain functions $G_q^e(z)$ and $G_q^h(z)$ of T.M. and T.E. field components and the normalized impedance $\Delta_q^e(z)$ in mode $q = n$ or m are given by (274), (272), (275), and (273) of Chapter 5. The coupling impedance $Z_{eh} = E_\varphi(0)/H_\varphi(0)$ denotes the ratio of horizontal field components perpendicular to direction of propagation at $z = 0$ following (284) of Chapter 5.

The field expressions of a horizontal electric dipole are derived from the fields of vertically and horizontally polarized line sources of Section 5.6.2 using the relations of Section 5.6.3.2. It follows that

$$E_r^{he} = -\frac{\eta I\, ds}{h\sqrt{a\lambda \sin\theta}} \sum_q \left[A_q^e G_q^e(z_s)\, \Delta_q^e(z_s) \cos\varphi + \eta \frac{A_q^h G_q^h(z_s)}{Z_{eh}} \sin\varphi \right] S_q^{0.5} G_q^e(z) \exp, \tag{9}$$

$$E_\theta^{he} = \frac{\eta I\, ds}{h\sqrt{a\lambda \sin\theta}} \sum_q \left[A_q^e G_q^e(z_s)\, \Delta_q^e(z_s) \cos\varphi + \eta \frac{A_q^h G_q^h(z_s)}{Z_{eh}} \sin\varphi \right] S_q^{-0.5} G_q^e(z)\, \Delta_q^e(z) \exp, \tag{10}$$

$$E_\varphi^{he} = \frac{I\, ds}{h\sqrt{a\lambda \sin\theta}} \sum_q \left[A_q^e G_q^e(z_s)\, \Delta_q^e(z_s)\, Z_{eh} \cos\varphi + \eta A_q^h G_q^h(z_s) \sin\varphi \right] S_q^{-0.5} G_q^h(z) \exp, \tag{11}$$

where the angle φ is measured from the dipole axis and where the symbols are defined as in (5) to (8). In addition, the excitation factor A_q^h of horizontally polarized sources is given by (277) of Chapter 5.

8.8.2 *Horizontal and Vertical Dipoles*

A comparison between elevated horizontal and vertical electric dipoles will be presented for the anisotropic exponential ionosphere models of Section 8.3. The static magnetic field is assumed at an angle $\theta = 45°$ with respect to the horizontal direction as is shown in Fig. 6.1 (p. 213). The propagation is in W.E. and E.W. directions along a constant magnetic latitude, $f = 20$ kc/s, and the ground surface exhibits a conductivity $\sigma_g = 5$ mho/m. The source is at an altitude $z_s = 10$ km and the observation point is on the ground surface $z = 0$.

Figure 8.24 shows the magnitude of E_r^{he}/E_r^{ve} computed from (9) and (5) for various distances D and angles φ. For W.E. direction of propagation and daytime conditions minimum fields are observed near the broadside direction ($\varphi = 90°$). For E.W. direction and D small, E_r^{he} is larger

for $\varphi = 0°$ than for $\varphi = 90°$, but a deep minimum is noted for $\varphi = 60°$. Only the mode of least attenuation contributes to the fields for D large, and E_r^{he} is approximately two times higher for $\varphi = 90°$ than for $\varphi = 0°$. Such a distance dependence of the daytime fields is noted also by Pappert [1970], who presents additional results for various source altitudes and ground conductivities. E_r^{he} of (9) is expressed as a sum of terms with $\sin\varphi$ and $\cos\varphi$ angular variations; depending on their relative phase and magnitude the two terms may essentially cancel at any angle φ and the minima of the curves do not necessarily occur for $\varphi = 0$ and 90°.

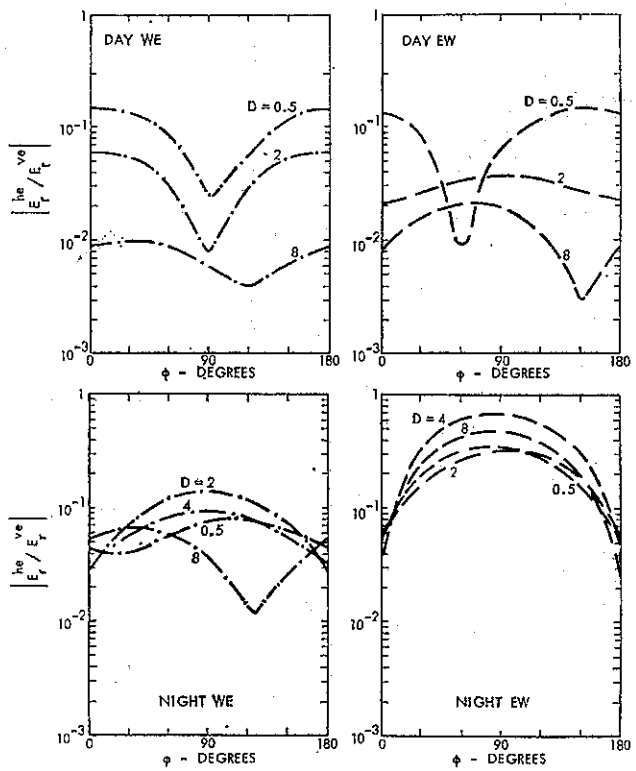

FIG. 8.24 Vertical Electric Fields of Elevated Horizontal and Vertical Dipoles. $z_s = 10$ km, $z = 0$, $f = 20$ kc/s, $\theta = 45°$, $\sigma_g = 5$ mho/m, D in mm

For nighttime W.E. propagation E_r^{he} exhibits the largest values near $\varphi = 90°$ for $D \leq 4000$ km, but the maximum shifts towards $\varphi = 0$ for larger values of D. For E.W. propagation the maximum values of E_r^{he} occur near $\varphi = 90°$; these maximum fields are only by a few decibels smaller than the fields E_r^{ve} of a vertical electric dipole. The sin φ terms of (9) are absent for isotropic ionosphere in (118) of Chapter 4; ionospheric coupling of T.E. and T.M. fields will cause the finite values of E_r^{he} for $\varphi = 90°$.

Figure 8.25 shows the magnitude of the horizontal fields E_θ^{he} and E_φ^{he} of horizontal electric dipoles in relation to the vertical field component E_r^{ve} of a vertical electric dipole. For an elevated source ($z_s = 10$ km) and a ground based observer ($z = 0$) the fields are maximum near $\varphi = 90°$, except for E_θ^{he} of daytime W.E. direction, when propagation is nearest to the isotropic conditions

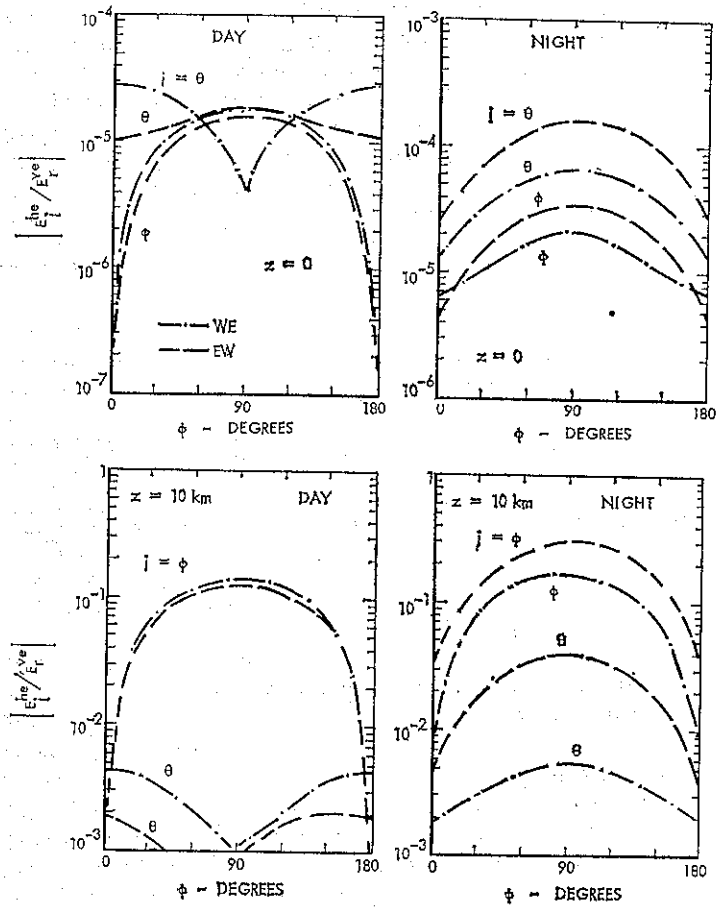

FIG. 8.25 Horizontal Electric Fields of Elevated Horizontal Electric Dipoles. $z_s = 10$ km, $f = 20$ kc/s, $D = 2000$ km, $\theta = 45°$, $\sigma_g = 5$ mho/m

discussed in Section 4.3.2.3. For an elevated source and observer ($z_s = z = 10$ km) E_φ^{he} of the broadside direction ($\varphi = 90°$) becomes comparable to E_φ^{ve}. The height-gain functions G_q^h in Figs. 8.3A and B (pp. 305 and 306) (or the functions $G_m(z)$ in Figs. 4.13A and B (p. 119)) are increasing with z or z_s in this range of altitudes and E_φ^{he} will be further increased for larger values of z and z_s.

8.8.3 The Inclined Dipole

An inclined antenna trailed behind an aircraft can be analyzed as a superposition of vertical electric and horizontal electric dipoles. Assuming that the antenna is at an angle γ relative to the vertical direction the effective dipole moment of the vertical and horizontal source component are $I\,ds\cos\gamma$ and $I\,ds\sin\gamma$ respectively. If $I\,ds$ designates the total dipole moment of the inclined antenna, the vertical electric field component E_r can be computed as

$$E_r = E_r^{ve}\cos\gamma + E_r^{he}\sin\gamma, \tag{12}$$

where E_r^{ve} and E_r^{he} are given by (5) and (8) respectively. E_r^{ve} is independent of the angle φ between the dipole axis and the direction of observation; E_r^{he} consists of terms proportional to $\cos\varphi$ and $\sin\varphi$ which exhibit the composite φ variations shown in Fig. 8.24. The magnitude and phase of (12) will exhibit a φ-dependence that is illustrated in the complex plane plots of Fig. 8.26 for daytime and nighttime conditions.

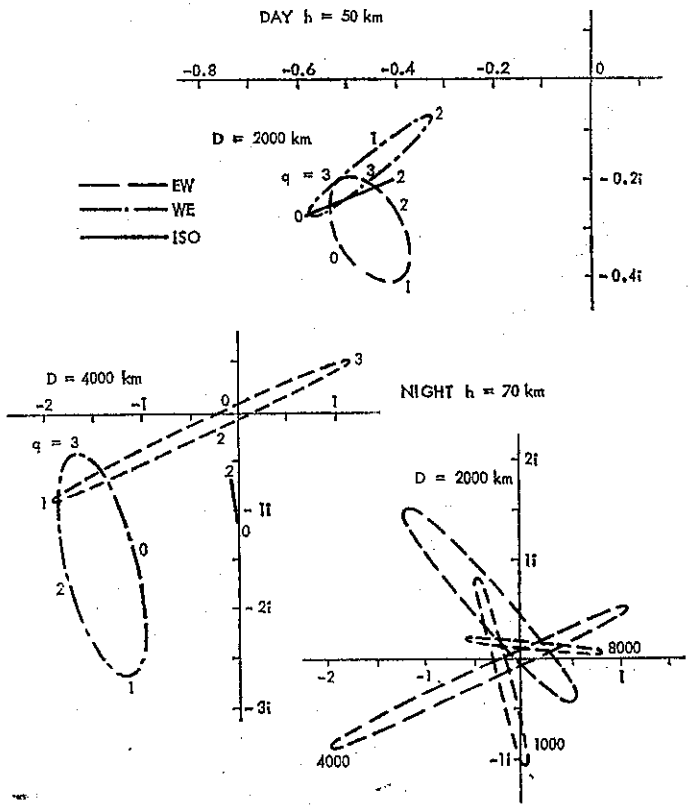

FIG. 8.26 Fields $E_r/(\eta\, I\,ds/hD)$ of an Elevated Inclined Dipole Antenna; $\gamma = 80°$, $\theta = 45°$, $\varphi = q(\pi/2)$; $z_s = 10$ km, $z = 0$; $E_r = E_r^{ve}\cos\gamma + E_r^{he}\sin\gamma$

For an isotropic ...ytime ionosphere E_r is largest in magnitude for $q = \varphi/(\pi/2) = 0$, smallest for $q = 2$ or $\varphi = \pi$, and a linear change is observed between these two extreme values. For anisotropic conditions (E.W. or W.E. propagation) E_r describes an ellipse in the complex plane, and the sense of rotation along the curve may be either clockwise or counterclockwise with increasing values of φ (or q). Under daytime conditions the ionosphere is only weakly anisotropic and the E_r variations observed under isotropic conditions may approximate the magnitude of variations for an anisotropic ionosphere.

During nighttime the isotropic ionosphere model is less satisfactory with its linear changes of E_r. For W.E. propagation there will be one minimum of E_r for a 2π change of φ, but for E.W. propagation there are two sharp minima corresponding to $\varphi = 0$ and π for $D = 4000$ km. The nighttime E.W. propagation is characterized by narrow ellipses as the locus of E_r for all the distances D investigated, and there appear to be 2 minima of E_r for every 2π change of φ.

A continuous variation of φ will be observed for transmitting antennas trailed behind a circling airplane [Kelly, 1970], and one may expect periodic changes of signal amplitude that are particularly pronounced for nighttime propagation in the general E.W. direction.

8.9 References

ALBEE, P. R., and H. F. BATES (1965) V.L.F. observations at College, Alaska, of various D-region disturbance phenomena, *Planet. Space Sci.* **13** (3), 175–206.

BAILEY, D. K. (1964) Polar cap absorption, *Planet. Space Sci.* **12** (5), 495–541.

BAIN, W. C., and B. R. MAY (1967) *D*-region electron density distributions from propagation data, *Proc. Inst. Elec. Engrs. (London)* **114** (11), 1593–1597.

BATES, H. F. (1962) V.L.F. effects from the November 10, 1961 P.C.A. event, *J. Geophys. Res.* **67** (7), 2745–2757.

BAYBULATOV, R. B., and P. E. KRASNUSHKIN (1967) Influence of the earth's magnetic field on the propagation of ultra long waves around the earth, *Doklady Akad. Nauk SSSR, Geofiz.* **174** (1), 84–87.

BICKEL, J. E. (1967) V.L.F. attenuation rates deduced from aircraft observations near the antipode of N.P.M., *Radio Sci.* **2** (6), 575–580.

BLAIR, B. E., E. L. CROW, and A. H. MORGAN (1967) Five years of V.L.F. world-wide comparison of atomic frequency standards, *Radio Sci.* **2** (6), 627–636.

BURGESS, B. (1967) Experimental observations on the phase variability of 200 Hz difference frequencies derived from V.L.F. transmissions obtained over large distances, *NATO/AGARD Symposium on Phase and Frequency Instability in Electromagnetic Wave Propagation, Ankara, Turkey, 9–11 October.*

BURGESS, B., and T. B. JONES (1967) Solar flare effects and V.L.F. radio wave observations of the lower ionosphere, *Radio Sci.* **2** (6), 619–626.

CHILTON, C. J., F. K. STEEL, and R. B. NORTON (1963) V.L.F. phase observations of solar flare ionization in the D-region of the ionosphere, *J. Geophys. Res.* **68** (19), 5421–5435.

COLE, R. K., and E. T. PIERCE (1965) Electrification in the earth's atmosphere for altitudes between 0 and 100 kilometers, *J. Geophys. Ces.* **70** (12), 2735–2749.

CRAIN, C. M., and H. G. BOOKER (1964) The effects of ions on low frequency and very low frequency propagation in an abnormally ionized atmosphere, *J. Geophys. Res.* **69** (21), 4713–4716.

CROMBIE, D. D. (1964) Periodic fading of V.L.F. signals received over long paths at sunrise and sunset, *Radio Sci. J. Res. NBS* **68D** (1), 27–34.

CROMBIE, D. D. (1965) On the use of V.L.F. measurements for obtaining information on the lower ionosphere (especially during solar flares), *Proc. IEEE* **53** (12), 2027–2034.

CROMBIE, D. D. (1966) Further observations of sunrise and sunset fading of V.L.F. signals, *Radio Sci.* **1** (1), 47–51.

DEEKS, D. G. (1966) *D*-region electron distribution in middle latitudes deduced from the reflexion of long radio waves, *Proc. Roy. Soc.* **291** (1426), 413–427.

EGELAND, A., and E. NAUSTVIK (1967) Influence of high latitude disturbances on V.L.F. propagation, *Radio Sci.* **2** (7), 659–667.

FEY, L., and C. LOONEY (1966) A dual-frequency V.L.F. timing system, *IEEE Trans. Instrumentation Measurement IM-15* (4), 190–195.

FIELD, E. C. (1969a) The propagation of E.L.F. waves under normally and naturally disturbed conditions, *J. Geophys. Res.* **74** (14), 3639–3650.

FIELD, E. C. (1969b) V.L.F. and E.L.F. propagation during sudden ionospheric disturbances, Memorandum RM-6124-PR, The Rand Corp., Santa Monica, Calif.

GALEJS, J. (1961) E.L.F. waves in the presence of exponential ionospheric conductivity profiles, *IRE Trans. Antennas Propagation* **AP-9** (6), 554–562.

GALEJS, J. (1962) A further note on terrestrial extremely low frequency propagaton in the presence of an isotropic ionosphere with an exponential conductivity height profile, *J. Geophys. Res.* **67** (2), 2715–2728.

GALEJS, J. (1964a) E.L.F. and V.L.F. waves below an inhomogeneous anisotropic ionosphere, *Radio Sci. J. Res. NBS* **68D** (6), 693–707.

GALEJS, J. (1964b) Propagation of V.L.F. waves below a curved and stratified anisotropic ionosphere, *J. Geophys. Res.* **69** (17), 3639–3650.

GALEJS, J. (1967a) Propagation of V.L.F. waves below an anisotropic stratified ionosphere with a transverse static magnetic field, *Radio Sci.* **2** (6), 557–574.

GALEJS, J. (1967b) Propagation of V.L.F. waves below anisotropic ionosphere models with a dipping static magnetic field, *Radio Sci.* **2** (12), 1497–1512.

GALEJS, J. (1968) Propagation of E.L.F. and V.L.F. waves below an anisotropic ionosphere with a dipping static magnetic field, *J. Geophys. Res.* **73** (1), 339–352.

GALEJS, J. (1969a) Phase variability of Omega navigational transmissions, *Electronics Letters* **5** (5), 106–107.

GALEJS, J. (1969b) V.L.F. modes below an idealized anisotropic ionosphere, *Radio Sci.* **4** (6), 491–516.

GALEJS, J. (1970) E.L.F. and V.L.F. propagation for models of a perturbed ionosphere, *Radio Sci.* **5**. (7), 1041–1044.

GALEJS, J., and M. MENTZONI (1968) Propagation of E.L.F. and V.L.F. waves below models of naturally perturbed ionospheres, *J. Geophys. Res.* **73** (13), 4439–4443.

JAYARAM, R., and G. Y. CHIN (1967) Analytical study of the D-region response to solar flares monitored by Ariel satellite (UK-1), *J. Geophys. Res.* **72** (7), 1889–1899.

JESPERSEN, M., A. HAUG, and B. LANDMARK (1966) Electron density and collision frequency observations in the arctic *D*-region, *Electron Density Profiles in Ionosphere and Exosphere* (edited by J. Frihagen), North-Holland, Amsterdam, p. 29.

JOHLER, J. R. (1961) Magneto-ionic propagation phenomena in low- and very-low-radiofrequency waves reflected by the ionosphere, *Radio Propagation* **65D** (1), 53–65.

JOHLER, J. R., and L. A. BERRY (1966) On the effect of heavy ions on L.F. propagation, with special reference to the nuclear environment, *Radio Sci.* **1** (3), 303–307.

KELLY, F. J. (1970) V.L.F. field strength variations from an orbiting inclined antenna, *Radio Sci.* **5** (5), 785–791.

MADDEN, T., and W. THOMPSON (1965) Low frequency electromagnetic oscillations of the earth-ionosphere cavity, *Rev. Geophys.* **3** (2), 211–254.

MAY, B. R. (1966) The behavior of the *D*-region at mid-latitudes during a sudden ionospheric disturbance, *J. Atmos. Terr. Phys.* **28**, 553–564.

NARCISI, R. S., and A. D. BAILEY (1965) Mass spectrometric measurements of positive ions at altitudes from 64 to 112 kilometers, *J. Geophys. Res.* **70** (15), 3687–3700.

OBAYASHI, T. (1960) Measured frequency spectra of V.L.F. atmospherics, *J. Res. NBS Radio Propagation* **64D** (2), 41–48.

PAPPERT, R. A. (1968) A numerical study of V.L.F. mode structure and polarization below an anisotropic ionosphere, *Radio Sci.* **3** (3), 219–233.

PAPPERT, R. A. (1970) The effects of elevation and ground conductivity on horizontal dipole excitation of the earth ionosphere wave guide, *Radio Sci.* **5** (3).

PAPPERT, R. A., E. E. GOSSARD, and I. J. ROTHMULLER (1967) A numerical investigation of classical approximations used in V.L.F. propagation, *Radio Sci.* **2** (4), 387–400.

PIGGOTT, W. R., and E. V. THRANE (1966) The electron densities in the *E* and *D* regions above Kjeller, *J. Atmos. Terr. Physics* **28**, 467–479.

REDER, F. H., G. WINKLER, and C. BICKART (1961) Results of a long-range clock synchronization experiment, *Proc. IRE* **49** (6), 1028–1032.

REDER, F. H., and S. WESTERLUND (1967) V.L.F. signal phase instabilities produced by propagation medium – experimental results, *Proceedings AGARD-EWP Symposium on Phase and Frequency Instability in Radio Wave Propagation, Ankara, Turkey, 9–12 October.*

REID, G. C. (1966) Physics of the *D*-region at high latitudes, *Electron Density Profiles in Ionosphere and Exosphere* (edited by J. Frihagen), North Holland, Amsterdam, p. 18.
SNYDER, F. P., and R. A. PAPPERT (1969) A parametric study of V.L.F. modes below anisotropic ionospheres, *Radio Sci.* **4** (3), 213–226.
VALLEY, S. L. (ed.) (1965) *Handbook of Geophysics and Space Environments*, Air Force Cambridge Research Laboratories, McGraw-Hill, New York, NY.
VOLLAND, H. (1964) On the solar flare effect of V.L.F. waves in the lower ionosphere, *J. Atmos. Terr. Phys.* **26**, 695–709.
WAIT, J. R. (1962) *Electromagnetic Waves in Stratified Media*, MacMillan, New York, NY.
WAIT, J. R. (1963) The mode theory of V.L.F. radio propagation for a spherical earth and a concentric anisotropic ionosphere, *Canadian J. Phys.* **41**, 299–315.
WAIT, J. R., and K. P. SPIES (1965) Influence of finite ground conductivity on the propagation of V.L.F. radio waves, *Radio Sci. J. Res. NBS* **69D** (10), 1359–1373.
WATT, A. D. (1967) *V.L.F. Radio Engineering*, Pergamon Press, Oxford.
WESTERLUND, S., F. H. REDER, and C. J. ÅBOM (1969) Effects of polar cap absorption events on V.L.F. transmissions, *Planet Space Sci.* **17** (7), 1329–1374.
WESTFALL, W. D. (1967) Diurnal changes of phase and group velocity of V.L.F. radio waves, *Radio Sci.* **2** (1), 119–125.

CHAPTER 9

L.F. PROPAGATION

Abstract. The propagation around a homogeneous spherical earth is examined using the residue (or mode) series representation. The phase velocity v_{ph} of the various modes is less than the free-space velocity of electromagnetic waves c, and the lower order modes of least attenuation dominate in the mode sum. The composite ground wave exhibits monotonic phase and amplitude changes with increasing distance.

In the presence of an isotropic ionosphere, the lower order modes of $v_{ph} < c$ are excited very weakly. The higher order modes of $v_{ph} > c$ are highly attenuated. Intermediate modes with $v_{ph} \approx c$ dominate in the mode sum, and the order of the dominant modes increases with increasing frequency. Several of the modes are of comparable amplitudes, and the phase and amplitude of the mode sum exhibits irregular distance variations.

9.1 Introduction

Several field representations can be used to characterize the terrestrial propagation of radio waves. The fields in a uniform spherical shell between earth and ionosphere can be expressed in a summation of spherical harmonics, which involves Legendre polynomials $P_n(\cos\theta)$ and spherical Bessel functions of integer order n. This series converges very slowly; and the number of terms required is of the order of 2–10 $k_0 a$, where $k_0 = 2\pi/\lambda$ and a is the radius of the earth. Although this series is directly applicable for frequencies in the E.L.F. or Schumann resonance range, the exceedingly slow convergence of this series may preclude its use for L.F. The Watson transformation changes the series of spherical harmonics into a residue or mode series, where fields are expressed using Legendre functions and spherical Bessel functions of complex order ν. Each term of the mode series can be identified as an azimuthal wave propagating in the θ direction with a distinct phase velocity and attenuation rate; for large distances from the source, the series is dominated by a few terms with a phase velocity approximately equal to the free-space velocity of the electromagnetic waves.

Basically different is the geometric-optical series. In this representation, the individual terms are identified as a ground wave that propagates along the surface of the earth and sky waves that reach receiver after a number of reflections from the ionosphere. This series provides results identical to those of the rigorous residue or mode series for distances up to 2000 km [Johler, 1964]. The individual terms of the geometric-optical series correspond to a sequence of waves that reach the receiver over different propagation paths. In a pulse transmission, the individual delays of the received pulses correspond to the path lengths of the ground wave and the various sky waves. However, in the residue series, a number of modes exhibit $v_{ph} > c$; and there is no 1 to 1 correspondence between the delay of the various pulses received in a pulse transmission and the phase velocities or the delay of the individual modes.

The more rigorous residue series representation will be used exclusively in this chapter. Such a mode series has been developed in Chapter 4 for propagation in the E.L.F. and V.L.F. ranges, but the ground-wave contributions have not been emphasized. The time delay between the arrivals of ground and sky waves does not exceed 1 cycle of the carrier frequencies for E.L.F. and V.L.F. ranges; because of the finite bandwidth of the transmissions, the higher amplitude sky waves will tend to corrupt the ground wave at larger distances from the source. However, for frequencies in the L.F. range, the period of the carrier frequency is decreased. The transmission bandwidth may be readily increased, and it will be possible to observe several cycles of the ground wave prior to the arrival of a sky wave for a pulse transmission. The ground-wave part of such a composite pulse is utilized in navigational transmissions (Loran C and D) which has stimulated some recent interest [Johler 1962, 1963] in this rather well-developed field. Although the ground wave is always followed by a sky wave, analytically it is possible to treat the ground-wave part separately by ignoring the presence of the ionosphere. Detailed references to the original work in this simplified geometry are available from a number of texts [Sommerfeld, 1949; Bremmer, 1949; Wait, 1962], and such references will not be given in this chapter.

For a spherical earth, the fields are expressed as a residue series that is usually developed after applying the Watson transformation to a series of spherical harmonics. However, the steady-state solutions of ground-wave propagation will be derived in Section 9.2 of this chapter by modifying the wave-guide mode theory developed in Chapter 4 by the absence of the ionosphere; the detailed characteristics of the individual ground-wave modes will be developed, and the composite ground wave will also be discussed.

The ground wave presents the initial part of a received signal pulse; and after the initial cycles, this low-amplitude ground wave will be swamped by the larger amplitude signal that arrives after reflections from the ionosphere. This can be seen from the transient response calculated for a residue series representation of the ground wave and the geometric-optical approximation of sky waves [Johler, 1963]. In this chapter, the total field will be expressed in a mode series; the characteristics of the individual waveguide modes and also of the mode sum will be examined in Section 9.3.

9.2 Ground Waves

The ground-wave part of the total fields that are observed on or near the surface of the earth can be determined in a geometry that neglects the presence of the ionosphere. The formal solution of this problem involves a summation of spherical harmonics, which are transformed in a more rapidly converging residue series using the Watson transformation [Sommerfeld, 1949; Bremmer, 1949]. The individual terms of this summation are characterized by distinct azimuthal wave numbers, and they can also be described as separate modes. A modal representation for the fields in the airspace between the earth and the ionosphere has been developed in Chapter 4, and this analysis can be readily modified for ground-wave computations.

A vertical electric dipole is assumed to be located at the height z_s above the surface of a spherical earth of radius $r = a$ on the $\theta = 0$ axis of a geocentric spherical coordinate system. The fields are observed at a distance $D = a\theta$ from the source at a height z above the surface of the earth. In the absence of the ionosphere, the fields will be evanescent in the radial direction; and the field representations (16) to (18) of Chapter 4 simplify for $B_e = 0$ to

$$E_r(r,\theta) = \sum_\nu C_\nu \frac{\eta\nu(\nu+1)}{iu} h_\nu^{(1)}(u) P_\nu(-\cos\theta), \tag{1}$$

$$E_\theta(r,\theta) = \sum_\nu C_\nu \frac{\eta}{iu} \frac{\partial}{\partial u}[uh_\nu^{(1)}(u)] \frac{\partial}{\partial\theta} P_\nu(-\cos\theta), \tag{2}$$

$$H_\varphi(r,\theta) = \sum_\nu C_\nu h_\nu^{(1)}(u) \frac{\partial}{\partial\theta} P_\nu(-\cos\theta), \tag{3}$$

where $P_\nu(-\cos\theta)$ is a Legendre function, $\eta = \sqrt{\mu_0/\varepsilon_0} = 120\pi$ ohms is the characteristic impedance of free space

$$h_\nu^{(m)}(u) = \left(\frac{\pi}{2u}\right)^{0.5} H_{\nu+0.5}^{(m)}(u). \tag{4}$$

$H_{\nu+0.5}^{(m)}(u)$ is the Hankel function of kind m and order $(\nu+0.5)$, $u = k_0 r$, $k_0 = 2\pi/\lambda$ is the wave number of free space, and ν designates the yet undetermined eigenvalues of the modes. The normalized surface impedance of the earth is computed as

$$\Delta_g = \frac{Z_g}{\eta} = \frac{-E_\theta(a)}{\eta H_\varphi(a)} = i \left.\frac{\frac{\partial}{\partial u}[uh_\nu^{(1)}(u)]}{uh_\nu^{(1)}(u)}\right|_{u=u_g=k_0 a}. \tag{5}$$

In the so-called third-order or Watson approximation, the spherical Bessel functions of large arguments and large complex order are replaced by Hankel functions of order $\left(\frac{1}{3}\right)$ or by Airy functions. It follows from Section 4.5 that

$$h_\nu^{(1)}(u) = -\frac{i}{\sqrt{2u}}\left(\frac{2}{k_0 a}\right)^{1/3} w_2(t), \tag{6}$$

where

$$-t = \left(\frac{\nu+0.5}{2}\right)^{2/3}\left[\left(\frac{u}{\nu+0.5}\right)^2 - 1\right] \approx \left(\frac{k_0 a}{2}\right)^{2/3}[1 - S^2 + 2(r-a)/a]. \tag{7}$$

The factor

$$\frac{\nu+0.5}{k_0 a} = \frac{\nu+0.5}{u} = S \tag{8}$$

can be interpreted as the ratio between the wave number along the surface of the earth k_g and the wave number of the free space k_0. The real part of S is inversely proportional to the phase velocity v_{ph}, and the imaginary part of S is proportional to the attenuation rate α of the waves in a particular mode. The Airy function $w_2(t)$ can be expressed alternately as

$$w_2(t) = \sqrt{\pi}[Bi(t) + iAi(t)], \tag{9}$$

where $Ai(t)$ and $Bi(t)$ are defined by Miller [1964] or Abramowitz and Stegun [1964]. Substituting (6) and noting that

$$\frac{\partial t}{\partial u} = -\frac{2^{1/3}u}{(\nu+0.5)^{4/3}} \approx -\left(\frac{2}{k_0 a}\right)^{1/3}, \tag{10}$$

(5) is rearranged into

$$w_2'(t_g) - q_g w_2(t_g) = 0, \tag{11}$$

where

$$q_g = i(k_0 a/2)^{1/3} \Delta_g. \tag{12}$$

The permissible eigenvalues t_g (ν or S) are determined from the solution of the transcendental equation (11).

The solutions of (11) can be determined more readily in the limits of low or high impedance ground surfaces ($|\Delta_g| = 0$ or ∞).

For a highly conducting ground, (11) simplifies to

$$w_2'(t_g) = \sqrt{\pi}[Bi'(t_g) + iAi'(t_g)] = 0. \tag{13}$$

Substituting

$$Bi(t) = \exp(i\pi/6)\, Ai[t \exp(2i\pi/3)] + \exp(-i\pi/6)\, Ai[t \exp(-2i\pi/3)], \tag{14}$$

dividing by $\exp(i\pi/6)$, applying the identity $t = -t\exp(\pm i\pi)$, and letting $z_i = t\exp(-i\pi/3)$, (13) is changed to

$$Ai'(-z_i) + \exp(-i\pi/3)\, Ai'[-z_i \exp(2i\pi/3)] + \exp(i\pi/3)\, Ai'[-z_i \exp(-2i\pi/3)] = 0. \tag{15}$$

Substitution of

$$Ai(t) = \exp(-i\pi/3)\, Ai[t \exp(2i\pi/3)] + \exp(i\pi/3)\, Ai[t \exp(-2i\pi/3)] \tag{16}$$

shows that

$$2Ai'(-z_i) = 0. \tag{17}$$

The zeros of $Ai'(t)$ are located on the negative real axis [Abramowitz and Stegun, 1964]. The parameter z of (17) is therefore real and positive. (The lowest values of the z_i sequence are 1.019, 3.248, 4.820, 6.163, 7.372....) The roots t_g of (13) become

$$t_g = z \exp(i\pi/3). \tag{18}$$

For a high impedance ground surface ($|\Delta_g| = \infty$), (11) is reduced to

$$w_2(t_g) = \sqrt{\pi}[Bi(t_g) + iAi(t_g)] = 0. \tag{19}$$

Substituting (14), dividing by $\exp(i\pi/6)$, letting $z_j = t\exp(-i\pi/3)$, and substituting (16), it can be shown that

$$2Ai(-z_j) = 0. \tag{20}$$

The zeros of $Ai(t)$ are located on the negative real axis; the parameter z_j of (20) is real and positive. (The lowest of the z_j sequence are 2.338, 4.088, 5.552, 6.787, and 7.944, which are all larger in magnitude than the corresponding values of z_i.) The roots t_g of (19) are also of the form (18).

For $|q_g| \to 0$ or ∞, (18) will represent also an approximate root t_0 of (11). Denoting the left-hand side of (11) as $f(t)$, a Taylor series expansion of the function $f(t)$ about its approx-

imate zero $f(t_n)$ gives a corrected t estimate for its zero as

$$t_{n+1} = t_n - \frac{f(t_n)}{df/dt\big|_{t=t_n}}. \tag{21}$$

Applying the differential equation

$$w''(t) - tw(t) = 0 \tag{22}$$

if follows that

$$t_{n+1} = t_n - \frac{w_2'(t_n) - q_g w_2(t_n)}{t_n w_2(t_n) - q_g w_2'(t_n)}. \tag{23}$$

For values of $q_g \neq 0$, (23) can be applied successively to a series of q values ($q = q_0, q_1, q_2, \ldots, q_m$) which cover the range from $q_1 \to 0$ (or ∞) to $q_m = q_g$. For calculations starting out with $q_0 = 0$, $w_2'(t_0) = 0$ following (13) and (23) simplifies to

$$t_1 = t_0 + \frac{q_1}{t_0}. \tag{24}$$

When starting with $q_0 = \infty$, $w_2(t_0) = 0$ following (19) and (23) becomes

$$t_1 = t_0 + \frac{1}{q_1}. \tag{25}$$

Noting that $t_0 = |t_0| \exp(i\pi/3)$ and $q_n = |q_n| \exp(i\pi/4)$, Re t is increased and Im t is decreased with increasing q in (24) and decreasing q in (25). This change of t corresponds to a decrease of phase velocity ($v_{ph} = c/\mathrm{Re}\, S$) and attenuation rate ($\alpha \sim \mathrm{Im}\, S$). Equations (24) and (25) represent the leading terms of a power series approximation to the zeros t_g of (11) [equations (III. 28) and (27) of Bremmer [1949], where in Bremmer's notation $t = 2^{1/3}\tau$, and $q = -1/(2^{1/3}\delta)$]. Both equations are of comparable accuracy if $|q^2/t| = 1$. The initial value $q_0 = 0$ can be used for $|t_0| > |q_g^2|$, and $q_0 = \infty$ for smaller values of $|t_0|$. The selection of the transition point between the two methods is not critical, and identical final values t_m may be obtained by either method in the vicinity of the transition point.

The mode amplitudes will be proportional to an excitation factor A_n. In the absence of an ionospheric boundary, (190) of Chapter 4 becomes

$$A_n = 0.5 k_0 h [h_\nu^{(1)}(u_g)]^2 \left\{ \lim_{\mu \to \nu} \frac{u^2}{2\mu + 1} \left[\frac{\partial}{\partial \mu} h_\mu^{(1)}(u) \frac{\partial}{\partial u} h_\nu^{(1)}(u) - h_\nu^{(1)}(u) \frac{\partial^2}{\partial \mu\, \partial u} h_\mu^{(1)}(u) \right]_{u=u_g} \right\}^{-1}, \tag{26}$$

where h denotes an arbitrary constant. Substituting (6), applying (22), and

$$\frac{\partial t}{\partial \nu} = \frac{1}{3}\left(\frac{2}{\nu + 0.5}\right)^{1/3} \left[2\left(\frac{u}{\nu + 0.5}\right)^2 + 1\right] \approx \left(\frac{2}{k_0 a}\right)^{1/3}, \tag{27}$$

$$\frac{\partial^2 t}{\partial \nu\, \partial u} = \frac{u}{3}\left(\frac{2}{\nu + 0.5}\right)^{7/3} \approx \frac{2}{3}\left(\frac{2}{k_0 a}\right)^{4/3}, \tag{28}$$

it is seen that

$$A_n = 0.5k_0h\left(\frac{2}{k_0a}\right)^{1/3}\left\{t_g - q_g^2 - \frac{2}{3}q_g\left(\frac{2}{k_0a}\right)^{2/3}\right\}^{-1}. \tag{29}$$

The term proportional to q_g will be small relative to q_g^2 at $f = 100$ kc/s; for $\sigma_g < 5$ mho/m, $\left|\left(\frac{2}{3}\right)(2/k_0a)^{2/3}/q_g\right| < 0.08$.

The fields of the vertical electric dipole are expressed as a mode sum in (104) of Chapter 4. This equation is rewritten as

$$E_r = \frac{i\eta I\,ds}{\sqrt{a\lambda}\sin\theta}\sum_n S_n^{1.5}(A_n/h)\,G_n(z)\,G_n(z_s)\exp\,(i\pi/4 + ik_0DS_n), \tag{30}$$

where z and z_s are the heights of the receiver and transmitter above the ground surface, $I\,ds$ is the dipole moment of the source, $\lambda = 2\pi/k_0$ is the free-space wavelength, and $D = a\theta$. The height-gain functions $G_n(z)$ are defined as

$$G_n(z) = \frac{h_\nu^{(1)}(u)}{h_\nu^{(1)}(u_g)} = \frac{w_2(t)}{w_2(t_g)}. \tag{31}$$

For ground-based transmitter and receiver, $(z_s = z = 0)$, $t = t_g$, and $G_n(z) = 1$. Applying (7) and (29) and assuming that $S_n \approx 1$ and $z = z_s = 0$, (30) is rearranged into

$$E_r = E_0\theta\sqrt{\frac{i\pi}{\sin\theta}}\left(\frac{k_0a}{2}\right)^{1/6}\sum_n \frac{\exp\,[it_n(k_0a/2)^{1/3}\theta]}{t_n - q_g^2}, \tag{32}$$

where

$$E_0 = \frac{i\eta I\,ds}{\lambda D}\exp\,(ik_0D) \tag{33}$$

represents the free-space fields of a dipole above a perfectly conducting flat ground plane. This equation agrees with (IV. 1) of Bremmer [1949] if it is noted that the R.M.S. value of a dipole moment $I\,ds = 5/k_0$ for 1000 W of radiated power. Equation (32) has been also listed by Spies and Wait [1966]. The individual terms of the mode series (30) are characterized by distinct values of the propagation parameter S_n, of the excitation factors A_n, and of height-gain functions $G_n(z)$. The number of terms required for an accurate field representation increases with a decreasing distance to the source. For small distances, it is advantageous to rearrange the field expressions in a way that yields the Sommerfeld–Norton ground wave as its leading term; higher order terms of this modified summation appear as correction terms accounting for the earth's curvature [Bremmer, 1949].

When the source and the observation point are on the ground surface, this ground wave representation follows from Sommerfeld [1949] or Norton [1937] as

$$E_r = E_0F(w), \tag{34}$$

where

$$F(w) = 1 + i\sqrt{\pi w}\exp\,(-w)\,\mathrm{erfc}\,(-i\sqrt{w}) = 1 - 2\sqrt{w}\exp\,(-w)\int_{i\infty}^{\sqrt{w}}\exp\,(u^2)\,du \tag{35}$$

and

$$w = \frac{\omega\varepsilon_0}{2\sigma_g}k_0D \tag{36}$$

is referred to as the Sommerfeld's numerical distance. Volland [1968] lists an approximation

$$F(w) \approx \frac{2 + 0.3w}{2 + w + 0.6w^2}\exp\left[i\pi\frac{(1.4 + w)w^{0.5}}{2.5 + w^{0.5} + w^{1.5}}\right] \tag{37}$$

that is convenient for numerical estimates under conditions where displacement currents of the ground are negligible.

The equation (30) or (32) is strictly valid for free space surroundings of the spherical finitely conducting earth. However, the lower atmosphere is inhomogeneous and the refractive index $n = \sqrt{\varepsilon_r}$ is known to increase nearly linearly with height. Under such conditions, it is shown by Bremmer [1949] or Wait [1962] that the radius of the earth a should be replaced by an effective radius a_e. It can be shown that

$$\frac{1}{a_e} = \frac{1}{a} + \left.\frac{d\varepsilon_r/dr}{2\varepsilon_r}\right|_{r=a}. \tag{38}$$

Formulas have been worked out that relate a_e to the gradients of temperature and water vapor pressure. The value of

$$K = \frac{a_e}{a} = \frac{4}{3} \tag{39}$$

is frequently adopted as representative of mean meteorologic conditions. For $K \neq 1$, a of the previous equations should be replaced by $a_e = Ka$ and θ by $\theta_e = D/a_e = D/(Ka)$.

The characteristics of several of the lower order ground-wave modes are illustrated in Fig. 9.1 for $f = 100$ kc/s and various ground conductivities σ_g; the attenuation rates α and the excitation factors A remain nearly constant for σ_g exceeding 0.01 mho/m, and the higher modes (n larger) are affected less than the lower order modes by a decreasing ground conductivity. For the higher modes, the phase velocity is low; and Re S is larger. It follows from (7) that also the parameter t is larger in magnitude, and it can be shown that $|t| \gg |q_g|$. It is seen from (24) that for these modes, the value of t (and hence S) does not differ significantly from the t_0 value computed for a perfectly conducting ground ($q_g = 0$). The excitation factor A_n is decreased with increasing values of n; for $\sigma_g = 0.001$ mho/m, the phase angle changes from $+32$ to $-52°$ as n is varied from 1 to 10. However, for $\sigma_g = 5$ mho/m, the phase angle remains near $-60°$ and does not change with n.

The height-gain functions of several modes are illustrated in Fig. 9.2. The height-gain functions are equal to unity at the ground surface. They decrease slightly in magnitude with increasing height for the lower ground conductivity, but increase at larger heights. At a height of 100 km, not shown in Fig. 9.2, $|G_1(z)| = 4.5$ to 16 and $|G_{10}(z)| > 10^{10}$ for the various ground conductivities. The height-gain function of (31) is proportional to the spherical function $h_\nu^{(1)}(u)$ or to Airy functions $w_2(t)$. The parameter t of (7) exhibits a positive real part for Re $S > 1$ at

the ground surface $r = a$, but Re t becomes increasingly negative for increasing heights $h = r - a$. Substituting the asymptotic form of Airy functions for arguments with large negative real parts [equation (167) of Chapter 4], it is seen that

$$h_\nu^{(1)}(u) = \left(\frac{2}{k_0 a}\right)^{1/3} \frac{\exp(-i\pi/4)}{\sqrt{2u}(-t)^{1/4}} \exp\left[i\frac{2}{3}(-t)^{3/2}\right], \tag{40}$$

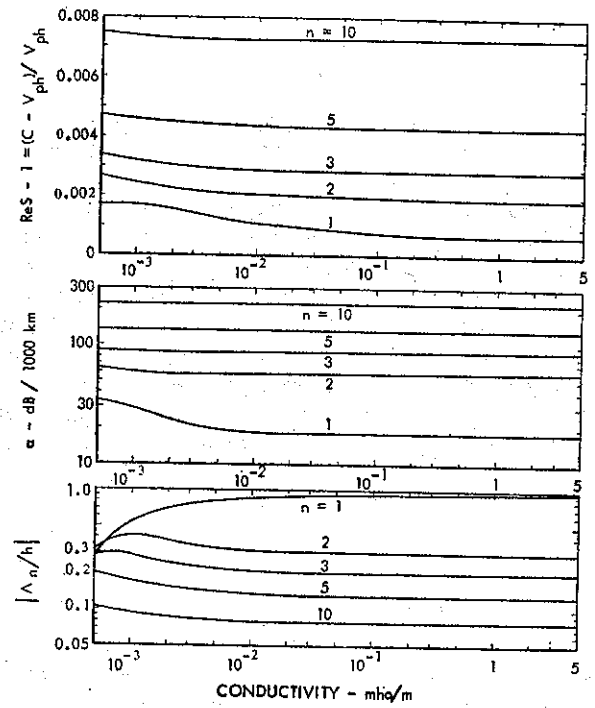

FIG. 9.1 Propagation Parameters of Ground-wave Modes for $f = 100$ kc/s; $K = \frac{4}{3}$

where $u = k_0 r = k_0(a+z)$ and $t = (k_0 a/2)^{2/3}(S^2 - 1 - 2z/a) = t_g - y$. For large heights where $|y| \gg |t_g|$, the r or h dependent factors of (40) are approximated applying (8) to give

$$|h_\nu^{(1)}(u)| \sim \frac{1}{(u^2 2z/a)^{0.25}} \exp\left[\text{Im}\,(\nu+0.5)\sqrt{2z/a}\right], \tag{41}$$

which indicates an exponential increase with increasing height z. For large heights where $|u-\nu| \gg u^{1/3}$, the second order or Debye approximation [equations (109) and (110) of Chapter 5] can be used in (4). For $\nu \ll u$, this results in

$$h_\nu^{(1)}(u) \approx \frac{1}{\sqrt{u}[u^2 - (\nu+0.5)^{0.25}} \exp\left[iu - i\pi(\nu+0.5)/2 - i\pi/4\right], \tag{42}$$

where $\nu = k_0 aS - 0.5 \approx k_0 a$. The exponential terms of (41) and (42) are of comparable magnitudes for $z \approx a$ (or $r \approx 2a$), where neither of the approximations are strictly valid. [This can be seen from the more complete expressions for $H_\nu^{(1)}(u)$ given in (159) and (160) of Chapter 4 or (109) and (110) of Chapter 5.] At larger distances from the sphere ($r \gg a$), the exponential term of (42) remains of constant magnitude; the individual modes are reduced to outgoing spherical waves with amplitudes proportional to $(1/r)$.

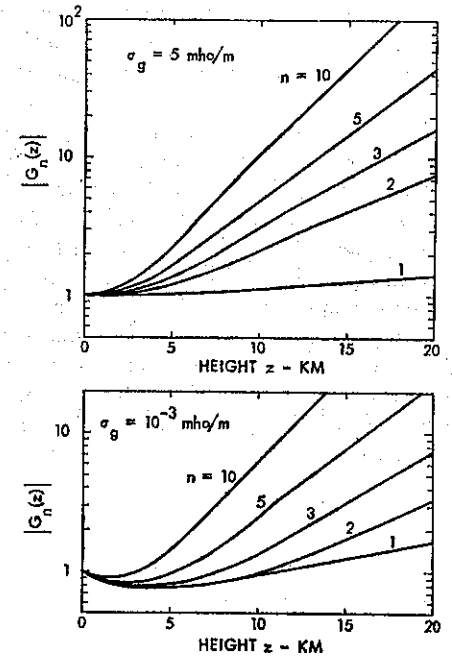

FIG. 9.2 Height-gain Functions of Ground-wave Modes for $f = 100$ kc/s; $K = \frac{4}{3}$

The distance variations of the ground-wave fields are illustrated in Fig. 9.3 by computing the mode summation (32). A decreased ground conductivity increases the attenuation rate and decreases the phase velocity. Consequently, the amplitude of the composite waveform is decreased; and its phase delay is increased with a decreasing ground conductivity. Changing the effective earth radius from $K = a_e/a = 1.33$ to 1 increases the effective curvature of the earth; this increases the attenuation rate and phase shift of the waveform. The fields have been also calculated for an observation height $h = 10$ km, when the height-gain functions of Fig. 9.2 exceed one in magnitude; the resulting ground-wave fields are slightly increased in magnitude, and there is an added approximately constant phase delay. For small distances D, the fields (32) can be approximated by the Sommerfeld ground wave (34), which is indicated by the dashed thin lines in Fig. 9.3.

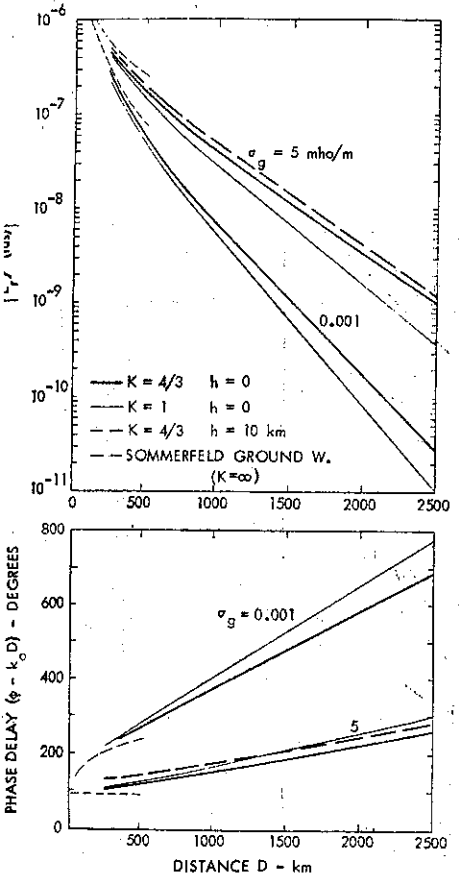

FIG. 9.3 Distance Variation of the Composite Ground-wave Fields; $f = 100$ kc/s

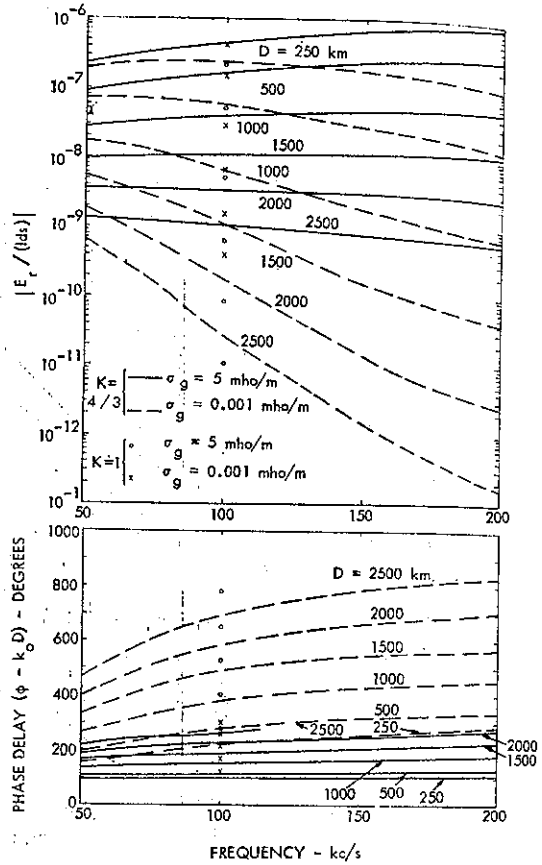

FIG. 9.4 Field Variations of the Composite Ground Wave

The distance and frequency variations of the ground-wave fields are further illustrated in Fig. 9.4. The attenuation and phase shift of the ground-wave fields are increased with increasing frequency and distance.

9.3 Waves in the Earth-to-ionosphere Waveguide

For frequencies in the L.F. range, the fields can be represented using a mode summation similar to the one developed for V.L.F. The radial (or vertical) electric field component of a vertical electric dipole is represented following (104) of Chapter 4 as

$$E_r^{ve}(r, \theta) = \frac{i\eta I\, ds}{\sqrt{D\lambda h}} \sqrt{\frac{D/a}{\sin (D/a)}} \sum_n S_n^{1.5} G_n(z)\, G_n(z_s) \Lambda_n \exp (i\pi/4 + ik_0 D S_n), \qquad (43)$$

where $D = a\theta$, $\lambda = (2\pi/k_0)$ is the free-space wavelength; and in the Airy function approximation of the radial functions, the excitation factor Λ_n and the height-gain functions $G_n(z)$ are given by (194) and (196). The subscript n designates modes with eigenvalues S_n determined from a solution of (178) or (83), where the above equations refer to Chapter 4. The real part of S is inversely proportional to the phase velocity v_{ph} of the waves, and the imaginary part of S is proportional to the attenuation rate α.

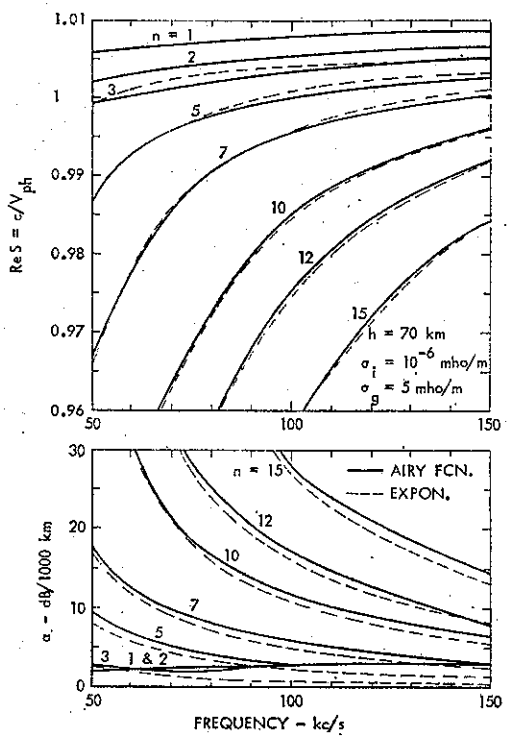

FIG. 9.5 Phase Velocity and Attenuation Rates of L.F. Waveguide Modes

The upper boundary of the terrestrial wave guide is assumed to be a homogeneous ionosphere of conductivity $\sigma_i = 10^{-6}$ mho/m at the height $h = 70$ km, and the lower boundary is a ground surface of conductivity $\sigma_g = 5$ mho/m. The calculated phase velocities and attenuation rates of the individual modes are shown in Fig. 9.5. At the lower frequencies Re $S < 1$, and the phase velocity of the individual modes exceeds the free space velocity c; Re S is increased, and v_{ph} is decreased with increasing frequency and $v_{ph} < c$ for the higher frequencies. The phase velocity v_{ph} and the attenuation rate α are increased with an increasing mode number n; but in distinction from Re S, the attenuation rate α is decreased with increasing frequency.

The exponential approximation of the radial functions, used in (83) of Chapter 4, gives nearly the same values of Re S and α as the more accurate Airy function approximation of (178) for

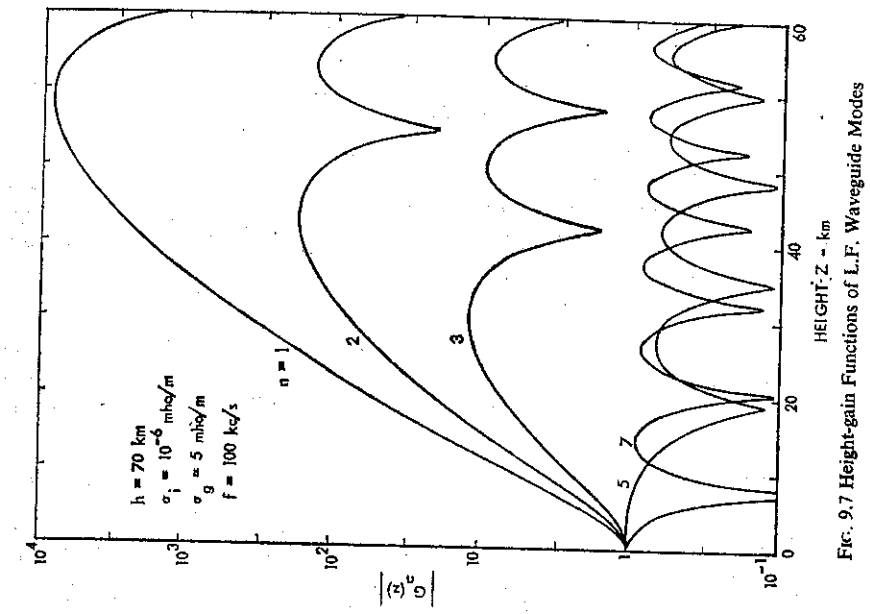

FIG. 9.7 Height-gain Functions of L.F. Waveguide Modes

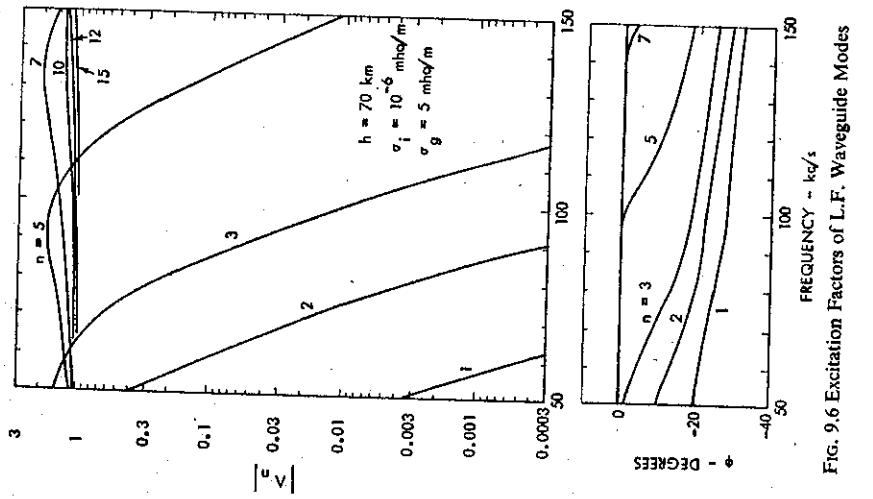

FIG. 9.6 Excitation Factors of L.F. Waveguide Modes

modes of Re $S < 1$. However, the height-gain functions $G_n(z)$ and excitation factors Λ_n become inaccurate in the exponential approximation; and they will be calculated using Airy functions in Figs. 9.6 and 9.7.

The excitation factors are illustrated in Fig. 9.6 for the same propagation geometry. The lower order modes are weakly excited by a ground-based source. The excitation factor of the higher modes initially increases with frequency, reaches the maximum value, and decreases rapidly with further increase of frequency. The phase angle of the excitation factor is near 0°, except that it may exhibit a phase angle of approximately $-30°$ in the frequency range where a particular mode becomes weakly excited.

The height-gain functions $G_n(z)$ are shown in Fig. 9.7 for $f = 100$ kc/s. $G_n(0) = 1$ by definition. For n small, $|G_n(z)| > 1$; and particularly large values of $|G_n(z)|$ are noted for the modes of smaller Λ_n values. For higher order modes, $|G_n(z)| < 1$; and the functions become increasingly oscillatory with increasing values of n. Λ_n and $G_n(z)$ are interrelated by (94) of Chapter 4, which is rewritten as

$$\Lambda_n = \frac{h}{2}\left\{\int_0^h [G_n(z)]^2\, dz\right\}^{-1}. \tag{44}$$

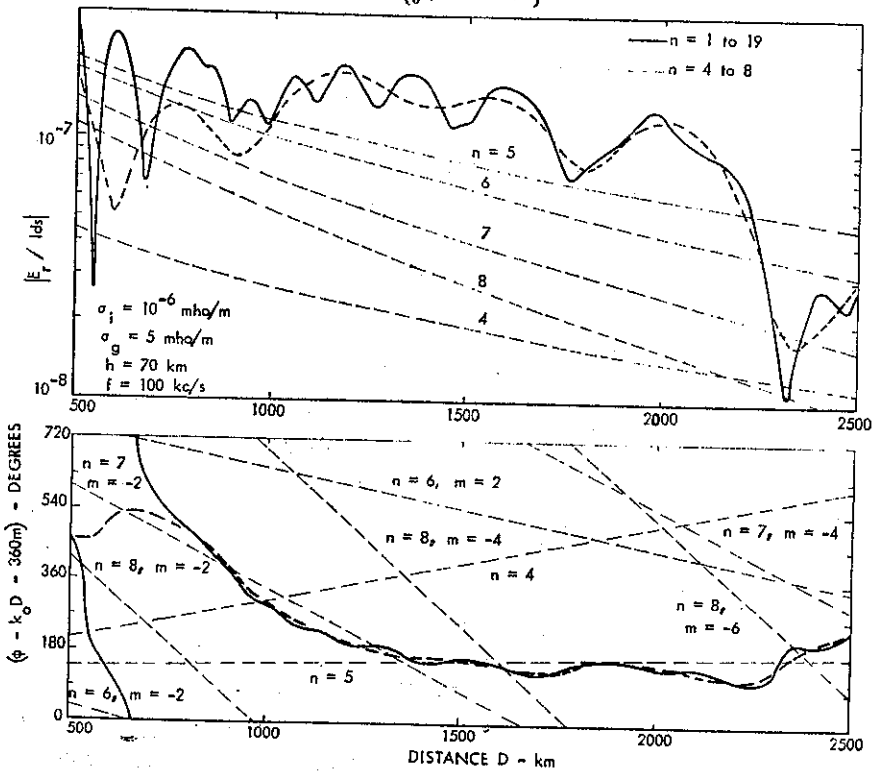

FIG. 9.8 Distance Variation of Waveguide Fields

It is apparent that A_n can be small in magnitude only if the average value of $G_n(z)$ is large compared to 1.

The distance variation of fields is illustrated in Fig. 9.8. The thin-line curves show the amplitude and phase variations of the individual modes $n = 4$ to 8, which are the five dominant modes for $D > 1500$ km; the mode $n = 5$ exhibits the largest amplitude over the indicated distance range. The phase of the individual modes when extrapolated to $D = 0$ gives 135° plus the phase of A_n. The phase is delayed (positive) for modes of $v_{ph} < c$, and advanced (negative) for modes of $v_{ph} > c$. The summation of these five modes results in the dashed amplitude and phase variations. The amplitude exhibits a number of interference minima and maxima, and rapid phase changes occur near the deepest minima. In the convention adopted in Fig. 9.8, the phase curve is shown to be similar to the phase of the dominant $n = 5$ mode for large distances. However, it is also possible to plot the cumulative phase by starting out with small angles at small distances. The solid curve of Fig. 9.8 is computed using the $n = 1$ to 19 terms in the summation; this curve exhibits a more detailed fine structure, and several of the interference minima are more pronounced.

The frequency variations of mode amplitudes are shown in Fig. 9.9 for a fixed distance of $D = 2000$ km. The lower order modes exhibit the largest amplitudes at lower frequencies, and the index n of the dominant mode is increased with an increasing frequency. There is a phase advance (φ negative) at lower frequencies which is changed to a phase delay (φ positive) at higher frequencies. A mode exhibits the largest relative amplitude for phase angles near 180° when $v_{ph} \approx c$.

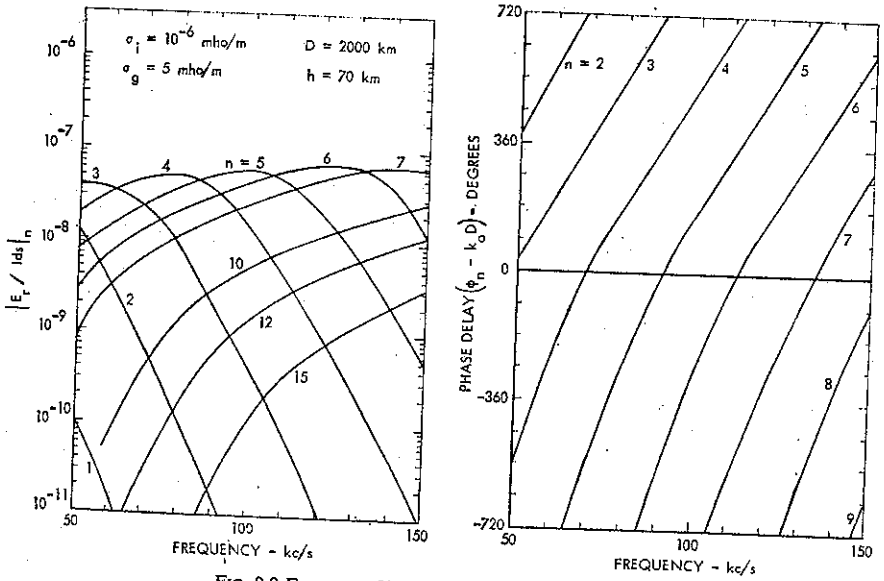

FIG. 9.9 Frequency Variation of Mode Amplitudes

9.4 References

ABRAMOWITZ, M., and I. A. STEGUN (1964) *Handbook of Mathematical Functions*, National Bureau of Standards, AMS 55.

BREMMER, H. (1949) *Terrestrial Radio Waves*, Elsevier, New York, NY.

JOHLER, J. R. (1962) Propagation of the low-frequency radio signal, *Proc. IRE* **50** (4), 404–427.

JOHLER, J. R. (1963) Radio pulse propagation by a reflection process in the lower ionosphere, *Radio Propagation* **67D** (5), 481–499.

JOHLER, J. R. (1964) Concerning limitations and further corrections to geometric-optical theory for L.F., V.L.F. propagation between the ionosphere and the ground, *Radio Sci.* **68D** (1), 67–78.

MILLER, J. C. P. (1946) *The Airy Integral*, British Association Mathematical Tables, Part-Volume B, University Press, Cambridge.

NORTON, K. A. (1937) The propagation of radio waves over the surface of the earth and in the upper atmosphere, Part II, *Proc. IRE* **25** (9), 1203–1236.

SOMMERFELD, A. (1949) *Partial Differential Equations in Physics*, Academic Press, New York, NY.

SPIES, K. P., and J. R. WAIT (1966) On the calculation of the ground wave attenuation factor at low frequencies, *IEEE Trans. Antennas Propagation*, **AP-14** (4), 515–517.

VOLLAND, H. (1968) *Propagation of Long Waves* (in German), F. Vieweg & Sohn, Braunschweig, Germany.

WAIT, J. R. (1962) *Electromagnetic Waves in Stratified Media*, Macmillan, New York, NY.

AUTHOR INDEX

SUBJECT INDEX